UNIVERSIDAD DE GRANADA
FACULTAD DE CIENCIAS

Departamento de Electrónica y Tecnología de Computadores

Tesis Doctoral

Compact Modeling of Memristors Based on Resistive Switching Devices

Programa de Doctorado en Tecnologías de la información y la Comunicación

Doctorando:
Gerardo Manuel
González Cordero

Directores:
Juan Bautista Roldán Aranda
Francisco Jiménez Molinos

Granada a 5 de diciembre 2019

A mis hijos Sofía, Gerardo y Ulises

A Ana

Agradecimientos

▪ Dr. Mario Lanza, Institute of Functional Nano & Soft Materials (FUNSOM), Collaborative Innovation Center of Suzhou Nano Science & Technology, Soochow University, China por las medidas del dispositvo Au/Ti/TiO$_2$/SiO$_X$/n^{++}Si utilizado en la sección 3.4.4.

▪ Profesor Aarik del Instituto de Física de la Universidad de Tartu en Estonia, por proporcionar las muestras del dispositivo Pt/TiO$_2$/Al$_2$O$_3$/TiO$_2$/Ru/Si.

Finalmente, quiero dedicar el trabajo que he realizado durante todos estos años a:

La memoria de mi padre Gerardo. Aunque nos dejaste muy pronto, siempre estás presente en nuestras vidas.

Mi madre Esther, por haberme dado la vida y ser un ejemplo de resistencia y lucha constante.

Mis hermanos Esther, Marcela y Javier, que me han ayudado tantas veces y con los que he compartido tantos buenos momentos.

Mis hijos Sofía, Gerardo y Ulises que cada día me sorprenden con sus logros y la ilusión que ponen en todas las cosas que hacen.

A mis suegros Julián y Ana por habernos ayudado en tantas ocasiones, por su disposición y su apoyo incondicional.

Y Especialmente a Ana, por apoyarme en cada proyecto que emprendo. Todo el camino recorrido no tendría sentido sin tí.

G. González Cordero
Granada, a 5 de diciembre de 2019

iv

Index

Chapter 1. Simulation and Modeling of Resistive Switching Devices, State of the Art 1

Chapter 2. Modeling of Conductive Bridge RRAMs..... 27

Chapter 3. Modeling of Valence Change Memories. Electrochemical Memories 57

Chapter 4. Quantum and Thermal Effects in Resistive Switching Memristor Models 99

Chapter 5. Random Telegraph Noise Modeling.......... 137

Chapter 6. Simulation Study of Circuits Based on Resistive Switching Memristors.................................... 197

Chapter 7. Conclusions... 235

Appendix A. Device Fabrication and Measurement Description 239

Appendix B. Additional Developments to the CB-RRAM Model.. 251

Appendix C. Additional Developments to the UGR-VCM Model.. 259

List of Figures

List of Tables

List of Abbreviations

Abbreviation	Description
1S1R	One Selector One Resistor
1T1R	One Transistor One Resistor
AC	Alternative Current
AFM	Atomic Force Microscopy
ALD	Atomic Layer Deposition
ANN	Artificial Neural Network
AVD	Atomic Vapor Deposition
BE	Bottom Electrode
BRS	Bipolar Resistive Switching
BEOL	Back-end-of-line
BL	Bit line
BRS	Bipolar Resistive Switching
C-CMS	Current-Controlled Memristive System
CCTLP	Color Code Time Lag Plot
CBM	Conductive Bridge Memories
CBRAM	Conductive Bridge RAM
CF	Conductive Filament
CMOS	Complementary metal–oxide–semiconductor
CNN	Convolutional Neural Network
CVD	Chemical Vapor Deposition
CZ	Czochralski
DC	Direct Current
DCS	Direct Current Sputtering
DFT	Density Functional Theory
DNN	Deep Neural Network
DRAM	Dynamic RAM
DT	Direct Tunneling
ECM	Electrochemical Metallization
EDA	Electronic Design Automation
EDX	Energy Dispersive X-ray
EMF	Electromotive Force
EMC	Electrochemical Metallization Cells
eNVM	Emerging Non-Volatile Memories
ETLP	Enhanced Time Lag Plot
FN	Fowler-Nordheim Tunneling
FEM	Finite Element Method
FF	Forming Free
FeRAM	Ferroelectric RAM
FR	Forming Required
FRH	Fixed Range Hopping
FOM	Figures of Merit
GT	Generalized Tunneling
GTA	Generalized Trap Assisted
GTT	Generalized Tunneling with temperature dependent
HC	Hopping Conduction
HDD	Hard Disk Drive
HRS	High Resistance State
IC	Integrated Circuit
IoC	Ionic Conduction
IoT	Internet of Things
IRS	Intermediate Resistance State
KMC	Kinetic Monte Carlo
LRS	Low Resistance State

Abbreviation	Description
MIM	Metal-Insulator-Metal
MIS	Metal-Insulator-Semiconductor
MOCVD	Metal-Organic Chemical Vapor Deposition
MOM	Metal–Oxide–Metal
MRAM	Magnetoresistance RAM
NVM	Non-Volatile Memories
OhC	Ohmic Conduction
OL	Oxide Layer
OxRAM	Oxide Random-Access Memory
PCM	Phase-Change Memory
PC-RAM	Phase-Change RAM
PLD	Pulsed Laser Deposition
PMC	Programmable Metallization Cell
PUF	Physical Unclonable Function
PVS	Pulsed Voltage Stresses
QPC	Quantum Point Contact
RAM	Random Access Memory
RAID	Redundant Array of Independent Disks
RFMS	Radio Frequency Magnetron Sputtering
RR	Resistance Ratio
RRAM	Resistive Random-Access Memory
RTN	Random Telegraph Noise
RTLP	Radio Time Lag Plot
RS	Resistive Switching
SCLC	Space Charge Limited Conduction
SE	Schottky Emission
SEP	Shklovskii-Efros percolation
SM	Simmons' Modified Schottky equation
SRAM	Static RAM
SSD	Solid-State Drive
SOM	Self-Organizing Maps
SPICE	Simulation Program with Integrated Circuits Emphasis
STT-RAM	Spin-Transfer Torque RAM
TAT	Trap-Assisted Tunneling
TCAD	Technology computer-aided design
TCM	Thermochemical Memories
TE	Top Electrode
TEM	Transmission electron microscope
TF	Thin Film
TLP	Time Lag Plot
TMO	Transition Metal Oxide
TRNG	True Random Number Generator
URS	Unipolar Resistive Switching
V-CMS	Voltage-Controlled Memristive System
VCM	Valence Change Memory
VMM	Vector-Matrix Multiplier
Vo	Oxygen Vacancies
VRH	Mott Variable Range Hopping
VRRAM	Vertical RRAM
WENO	Weighted Essentially Non Oscillatory
WL	Word Line
WTLP	Weighted Time Lag Plot

Contributions

1. Journal Papers

[1] **G. Gonzalez-Cordero**, J. B. Roldan, F. Jimenez-Molinos, J. Suñé, S. Long and M. Liu, "A new compact model for bipolar RRAMs based on truncated cone conductive filaments, a Verilog-A approach," *Semiconductor Science and Technology*, vol. 31, no. 11, pp. 1–13, 2016.
DOI: 10.1088/0268-1242/31/11/115013

Web of Science: Impact factor: 2.3, Q2   Scimago: SJR: 0.793, Q1

[2] **G. González-Cordero**, F. Jiménez-Molinos, J. B. Roldan, M. B. González and F. Campabadal "In-depth study of the physics behind resistive switching in TiN/Ti/HfO$_2$/W structures,". *Journal of Vacuum Science and Technology B*. **35**, 01A110 (2017). DOI: 10.1116/1.4973372

Web of Science: Impact factor: 1.31, Q3   Scimago: SJR: 0.467, Q2

[3] **G. González-Cordero**, M. B. González, H. García, F. Campabadal, S. Dueñas, H. Castán, F. Jiménez-Molinos and J. B. Roldán, "A physically based model for resistive memories including a detailed temperature and variability description", *Microelectronic Engineering*, Volume 178, 25 June 2017, Pages 26-29. DOI: 10.1016/j.mee.2017.04.019

Web of Science: Impact factor: 2.02, Q2   Scimago: SJR: 0.604, Q1

[4] J.B. Roldán, E. Miranda, **G. González-Cordero**, P. García- Fernández, R. Romero-Zaliz, P. González-Rodelas, A. M. Aguilera, M.B. González, F. Jiménez-Molinos. "Multivariate analysis and extraction of parameters in resistive RAMs using the Quantum Point Contact model" *Journal of Applied Physics*, 2018, 123, 014501. DOI: 10.1063/1.5006995

Web of Science: Impact factor: 2.17, Q2   Scimago: SJR: 0.739, Q2

[5] **Gerardo González-Cordero,** Mireia B. González, Francisco Jiménez-Molinos, Francesca Campabadal, and Juan Bautista Roldán. "New method to analyze random telegraph signals in resistive random access memories" *Journal of Vacuum Science and Technology B*. 37, 012203 (2019).
DOI: 10.1116/1.50593840

Web of Science: Impact factor: 1.31, Q3   Scimago: SJR: 0.467, Q2

[6] **G. González-Cordero**, M. Pedro, J. Martin-Martinez, M.B. González, F. Jiménez-Molinos, F. Campabadal, N. Nafría, J.B. Roldán. "Analysis of resistive switching processes in TiN/Ti/HfO$_2$/W devices to mimic electronic synapses in neuromorphic circuits" *Solid State Electronics*, Volume 157, July 2019, Pages 25-33. DOI: 10.1016/j.sse.2019.04.001

Web of Science: Impact factor: 1.666, Q3   Scimago: SJR: 0.492, Q2

[7] **G. González-Cordero**, M.B. González, F. Campabadal, F. Jiménez-Molinos, J.B. Roldán. "A new technique to analyze RTN signals in resistive memories" *Microelectronic Engineering*, Volume 215, 15 July 2019, 110994
DOI: 10.1016/j.mee.2019.110994

Web of Science: Impact factor: 2.02, Q2   Scimago: SJR: 0.604, Q1

[8] **G. Gonzalez-Cordero**, M.B. González, A. Morell, F. Jiménez-Molinos, F. Campabadal, J.B. Roldán, "Neural network based analysis of Random Telegraph Noise in Resistive Random Access Memories," *Semiconductor Science and Technology*, (Accepted for publication on December 4, 2019).

Web of Science: Impact factor: 2.654, Q2   Scimago: SJR: 0.74, Q1

2. *Proceedings of IEEE Xplore Digital Library*

[1] **G. González-Cordero**, F. Jiménez-Molinos, J. B. Roldan, M. B. González and F. Campabadal, "Transient SPICE simulation of Ni/HfO$_2$/Si-n+ resistive memories," in *XXXI edition of the Design of Circuits and Integrated Systems Conference (DCIS)*, 2016 in Granada, Spain.
DOI: 10.1109/DCIS.2016.7845384

Scimago Journal & Country Rank h-index:2

[2] **G. González-Cordero**, J. B. Roldan, and F. Jiménez-Molinos, "Simulation of RRAM memory circuits, a Verilog-A compact modeling approach," in *XXXI edition of the Design of Circuits and Integrated Systems Conference (DCIS)*, 2016 in Granada, Spain. DOI: 10.1109/DCIS.2016.7845386

Scimago Journal & Country Rank h-index:2

[3] **G. González-Cordero**, J. B. Roldán, F. Jiménez-Molinos, "SPICE simulation of RRAM circuits. A compact modeling perspective", in *11th edition of the Spanish Conference on Electron Devices (CDE)*, 2017 in Barcelona, Spain. DOI: 10.1109/CDE.2017.7905250

Google Scholar Metrics h5-index:6 h5-median:8

[4] **G. González-Cordero**, M. B. González, H. García, F. Jiménez-Molinos, F. Campabadal, S. Dueñas, H. Castán and J. B. Roldán, "A Physically Based Model to describe Resistive Switching in different RRAM technologies", in *11th edition of the Spanish Conference on Electron Devices (CDE)*, 2017 in Barcelona, Spain. DOI: 10.1109/CDE.2017.7905223

Google Scholar Metrics h5-index:6 h5-median:8

[5] F. Jiménez-Molinos, **G. González-Cordero**, P. Cartujo and J. B. Roldán, "SPICE modelling of thermal reset transitions for circuit simulation", *in 11th edition of the Spanish Conference on Electron Devices (CDE)*, 2017 in Barcelona, Spain. DOI: 10.1109/CDE.2017.7905227

Google Scholar Metrics h5-index:6 h5-median:8

3. International Conferences

[1] **G. González-Cordero**, J. B. Roldan and F. Jiménez-Molinos, "A model for circuit simulation of bipolar RRAMs based on conductive filaments with truncated cone shapes," en *Jornadas de Investigadores en Formación Fomentando la interdisciplinariedad (JIFFI)*, 2016 in Granada, Spain.

[2] **G. González-Cordero**, M. B. González, F. Jiménez-Molinos, F. Campabadal, and J. B. Roldan, "An in-depth study of the physics behind resistive switching in TiN/Ti/HfO$_2$/W structures," in *19th Workshop on Dielectrics in Microelectronics (Wodim)*, 2016 in Catania, Italy.

[3] **G. González-Cordero**, F. Jiménez-Molinos, M. A. Villena and J. B. Roldan, "SPICE simulation of thermal reset transitions in Ni/HfO$_2$/Si-n+ RRAMs including quantum effects," in *19th Workshop on Dielectrics in Microelectronics (Wodim)*, 2016 in Catania, Italy.

[4] **G. González-Cordero**, F. Jiménez-Molinos, J. B. Roldan, M. B. González and F. Campabadal, "Transient SPICE simulation of Ni/HfO$_2$/Si-n+ resistive memories," in *XXXI edition of the Design of Circuits and Integrated Systems Conference (DCIS)*, 2016 in Granada, Spain.

[5] **G. González-Cordero**, J. B. Roldan, and F. Jiménez-Molinos, "Simulation of RRAM memory circuits, a Verilog-A compact modeling approach," in *XXXI edition of the Design of Circuits and Integrated Systems Conference (DCIS)*, 2016 in Granada, Spain.

[6] **G. González-Cordero**, J. B. Roldán, F. Jiménez-Molinos, "SPICE simulation of RRAM circuits. A compact modeling perspective", in *11th edition of the Spanish Conference on Electron Devices (CDE)*, 2017 in Barcelona, Spain.

[7] **G. González-Cordero**, M. B. González, H. García, F. Jiménez-Molinos, F. Campabadal, S. Dueñas, H. Castán and J. B. Roldán, "A Physically Based Model to describe Resistive Switching in different RRAM technologies", in *11th edition of the Spanish Conference on Electron Devices (CDE)*, 2017 in Barcelona, Spain.

[8] F. Jiménez-Molinos, **G. González-Cordero**, P. Cartujo and J. B. Roldán, "SPICE modelling of thermal reset transitions for circuit simulation", *in 11th edition of the Spanish Conference on Electron Devices (CDE)*, 2017 in Barcelona, Spain.

[9] **G. González-Cordero**, M. B. González, H. García, F. Campabadal, S. Dueñas, H. Castán, F. Jiménez-Molinos and J. B. Roldán, "A physically based model for resistive memories including a detailed temperature and variability description" In *20th Conference on "Insulating Films on Semiconductors" (INFOS)*, 2017 in Potsdam, Germany.

[10] **G. González-Cordero**, J. B. Roldán, F. Jiménez-Molinos, "A time dependent thermal model for RRAM circuit simulation" In *20th Conference on "Insulating Films on Semiconductors (INFOS)*, 2017 in Potsdam, Germany.

[11] **G. González-Cordero**, J. Martín-Martínez, M.B. González, F. Jiménez-Molinos, F. Campabadal, N. Nafría, J.B. Roldán, "A new method to analyze Random Telegraph signals in the high-resistance state of Ni/HfO$_2$/Si-n+ RRAMs" In *20th Workshop on Dielectrics in Microelectronics (Wodim)*, 2018 in Berlin, Germany.

[12] **G. González-Cordero,** M.B. González, F. Campabadal, F. Jiménez-Molinos, J.B. Roldán, "A new technique to analyze RTN signals in resistive memories" In *21th Workshop on Dielectrics in Microelectronics (INFOS)*, 2019 in Cambridge University, Cambridge, UK.

4. Invited Talk

[1] Samuel Aldana, **G. González-Cordero,** F. Jiménez-Molinos, J.B. Roldán, "Simulation and physical compact modeling of resistive switching devices" In *7 th Workshop and MC Meeting on Memristors - Devices, Models, Circuits, Systems and Applications*, in Dubrovnik, Croatia, during march 12-13, 2018. Presented by: F. Jiménez-Molinos.

5. Other Publications

[1] **G. González-Cordero**, "Verilog A MEMRISTOR HP (Linear Ion Drift model)". figshare. DOI: 10.6084/m9.figshare.5579662.v5. Retrieved: 07:06, Nov 09, 2017 (GMT)

[2] **G. González-Cordero**, "RRAM Electrochemical Metallization Cells (EMC). Verilog A compact model". figshare. DOI: 10.6084/m9.figshare.5588593.v2 Retrieved: 21:51, Nov 09, 2017 (GMT)

[3] **G. González-Cordero**, "Spice Compact model for bipolar RRAMs based on truncated-cone conductive filaments". figshare. DOI: 10.6084/m9.figshare.5591062.v1 Retrieved: 15:33, Nov 10, 2017 (GMT)

[4] **G. González-Cordero**, "Video: Time evolution of TiN/Ti/HfO2/W RRAM with truncated-cone conductive filament. Cycle 402". Researchgate. Retrieved: Nov 19, 2016 DOI:10.13140/RG.2.2.10854.01601. url: https://youtu.be/WNJMabLf6lM

[5] **G. González-Cordero**, "Video: Time evolution of RRAM based on Truncated-cone shaped CFs. With four conductive filaments". Researchgate. Retrieved: Nov 19, 2017. DOI: 10.13140/RG.2.2.11692.87688. url: https://youtu.be/SOX6IiNNm2I

[6] **G. González-Cordero**, "Presentation: Simulation of RRAM memory circuits, a Verilog-A compact modeling approach". Researchgate. Retrieved: 07:06, Nov 09, 2017. DOI: 10.13140/RG.2.2.30940.80002. url: https://youtu.be/xlrZXIwwifc

[7] **G. González-Cordero**; Roldan, J.B.; Jiménez-Molinos, F.," A model for circuit simulation of bipolar RRAMs based on conductive filaments with truncated cone shapes." figshare. Retrieved: 18:15, Nov 12, 2017 (GMT). DOI: 10.6084/m9.figshare.5593516

[8] **G. González-Cordero**; Roldan, J.B.; Jiménez-Molinos, F. "A time dependent thermal model for RRAM circuit simulation". figshare. Retrieved: 18:18, Nov 12, 2017 (GMT). DOI: 10.6084/m9.figshare.5593513

[9] **G. González-Cordero**; Roldan, J.B.; Jiménez-Molinos, F. "SPICE simulation of RRAM circuits. A compact modeling perspective". figshare. Retrieved: 18:20, Nov 12, 2017 (GMT), DOI: 10.6084/m9.figshare.5593510

Abstract

In this doctoral thesis we have focused on the modeling of memristors implemented with different technologies. The models are used both for analog and digital applications. This doctoral thesis includes eight publications in scientific journals indexed in the Journal Citation Report of Science Citation Index, five Proceedings published in IEEE Xplore digital library and twelve contributions to International Conferences. The outline is the following:

Chapter 1 shows a review of the state of the art of memristors and in the simulation and modeling of these devices based on resistive switching mechanisms. First, we introduce the memristor elements in general for non-linear circuit modeling, next resistive switching devices are described in terms of the different technologies used. Several levels of simulation of memristors are discussed. Compact modeling is also addressed and the several possibilities available are discussed. The last section of this chapter is devoted to the actual context of the application of these devices.

Chapter 2 introduces the most representative models Conductive Bridge Resistive Memories (IM2NP-CBM and IM2NP-CBF). A new compact model (UGR-VCM) is presented. This latter model uses a conductive filament for charge conduction. In particular a filament with truncated-cone geometry is employed and a temperature description with two temperature values (top and bottom) is assumed. The model was checked with a $Ti/ZrO_2/Pt$ technology, these RRAMs were made at the Lab of Nanofabrication and Novel Device Integration, Institute of Microelectronics, Chinese Academy of Sciences. For testing their potential applications as memory devices, a simple 1T1R architecture is used for simulation purposes.

This chapter include the contribution ***Gonzalez-Cordero et al.*** [González-Cordero2016a], "A new compact model for bipolar RRAMs based on truncated cone conductive filaments, a Verilog-A approach," *Semiconductor Science and Technology*, vol. 31, no. 11, pp. 1–13, 2016. DOI: 10.1088/0268-1242/31/11/115013.

Chapter 3 deals with Valence Change Memories. We review the more important models of this kind of memories: the unidimensional compact model for VCM bipolar RRAM (SU-VCM) and the bidimensional compact model for VCM bipolar RRAM (PU-VCM). In this context, a new model for bipolar resistive RRAMs UGR-VCM is presented. It is based on redox and diffusion processes to describe in detail the physics behind the filamentary resistive switching (RS) mechanisms. The model includes truncated-cone shaped filaments which are known to be close to the real conductive filament geometry and a detailed thermal approach. The new model is tested with different technologies and the variability of cycle to cycle is included in the model.

This chapter includes the following contributions:

▪ ***González-Cordero et al.*** [González-Cordero2017a], "In-depth study of the physics behind resistive switching in $TiN/Ti/HfO_2/W$ structures", *Journal of Vacuum Science and Technology B*. **35**, 01A110 (2017). DOI: 10.1116/1.4973372.

▪ ***González-Cordero et al.*** [González-Cordero2017d], "A Physically Based Model to describe Resistive Switching in different RRAM technologies", in *11th edition of the Spanish Conference on Electron Devices (CDE)*, 2017 in Barcelona, Spain. DOI: 10.1109/CDE.2017.7905223.

▪ ***González-Cordero et al.*** [González-Cordero2017b], "A physically based model for resistive memories including a detailed temperature and variability description", *Microelectronic Engineering*, Volume 178, 25 June 2017, Pages 26-29. DOI: 10.1016/j.mee.2017.04.019.

Chapter 4 focuses on devices with unipolar switched resistance, this chapter present previous models (IM2NP-U and QPC) and two new models that stand upon the Quantum Point Contact (QPC) representation: UGR-QPC1 and UGR-QPC2 with different thermal description approximations (thermal resistance variable and thermal capacity variable respectively). A new technique of extraction of characteristics of the QPC model based on second derivative of current is presented and introduced.

This chapter includes the following contributions:

▪ ***Roldán et al.*** [Roldán2018] "Multivariate analysis and extraction of parameters in resistive RAMs using the Quantum Point Contact model" *Journal of Applied Physics*, 2018, 123, 014501. DOI: 10.1063/1.5006995.

▪ ***González-Cordero et al.*** [González-Cordero2016e], "A Physically Based Model to describe Resistive Switching in different RRAM technologies", in *11th edition of the Spanish Conference on Electron Devices (CDE)*, 2017 in Barcelona, Spain. DOI: 10.1109/CDE.2017.7905223.

▪ ***Jiménez-Molinos et al.*** [Jiménez-Molinos2017], "SPICE modelling of thermal reset transitions for circuit simulation", *in 11th edition of the Spanish Conference on Electron Devices (CDE)*, 2017 in Barcelona, Spain. DOI: 10.1109/CDE.2017.7905227.

Chapter 5 studies the Random Telegraph Noise signals in the memristors under study here. We review the graphical methods of representation of these signals and propose two new methodologies: the LWTLP and dLWTLP. They present high computational efficiency in comparison with the previous ones. The methods are used to represent long time sequences of RTN, and finally an application of LWTLP technique is presented were Neural Networks are employed. The analysis of RTN with LWTLP for classified RTN traces with the help of a structured and organized methodology based on neural networks is presented.

This chapter includes the following contributions:

▪ ***González-Cordero et al.*** [González-Cordero2019a]**,** "New method to analyze random telegraph signals in resistive random access memories" *Journal of Vacuum Science and Technology B*. 37, 012203 (2019). DOI: 10.1116/1.50593840.

▪ ***González-Cordero et al.*** [González-Cordero2019c], "A new technique to analyze RTN signals in resistive memories" *Microelectronic Engineering*, Volume 215, 15 July 2019, 110994 DOI: 10.1016/j.mee.2019.110994.

Chapter 6 describes simulations of resistive switching memristors with different models implemented in this doctoral thesis in different circuits, based on analog and digital applications. For example, 1T1R and 3x3 matrix of memory cells in digital applications and also an application for controlling the conductance of a device that can be used as electronic synapses in an analog applications, in particular neuromorphic circuits.

This chapter includes the following contributions:

▪ ***González-Cordero et al.*** [González-Cordero2016f], "Simulation of RRAM memory circuits, a Verilog-A compact modeling approach," Proceedings of IEEE of the *Design of Circuits and Integrated Systems Conference (DCIS)*, 2016 in Granada, Spain.
DOI: 10.1109/DCIS.2016.7845386.

▪ ***González-Cordero et al.*** [González-Cordero2017c], "SPICE simulation of RRAM circuits. A compact modeling perspective", in *11th edition of the Spanish Conference on Electron Devices (CDE)*, 2017 in Barcelona, Spain. DOI: 10.1109/CDE.2017.7905250.

▪ ***González-Cordero et al.*** [González-Cordero2019b], "A physical model to describe electronic synapses based on resistive switching devices" *Solid State Electronics*, Volume 157, July 2019, Pages 25-33. DOI: 10.1016/j.sse.2019.04.001.

Chapter 7 lists the main conclusions of this thesis.

Appendix A describes the fabrication processes and measurement set-ups for the different experimental devices used here.

Appendix B and *C* introduce additional development used to model CBRAM and VCM models respectively.

And finally, *Appendix D* presents different thermal approaches reported in the literature and some new ones used in this doctoral thesis.

Introduction

In the current electronic industry there is a growing demand for temporary (volatile) and permanent (non-volatile) data storage. In portable devices this demand is even higher and also requires low power consumption. This memory needs become evident in smartphones, laptops, internet of things (IoT) devices, 5G circuits, solid-state drives (SSD), cloud storage, data mining, artificial intelligence, among others applications [Gupta2019]. RRAMs are the main memory emerging technology since it is the more viable alternative due to its ease of integration into the current CMOS technology in the Back-End-Of-Line (BEOL), good scalability, data retention, endurance, speed and latency, low energy consumption and the possibility of 3D integration and multibit programming. RRAMs are part of a broad family known as memristors.

The dominant technology in the current solid state memory market is focused on static memories (SRAM), DRAM dynamic memories and Flash memories. The latter ones are non-volatile memories (Non-Volatile Memories, NVM), a memory that stores information when the power systems are turned off. In the context of NVM, different technological alternatives are being studied both at the academia and at the industry: RRAMs (Resistive Switching RAMs), PCM (Phase Change Memories) and STT-RAMs (Spin-Transfer Torque RAMs), which are being the subject of research in all large companies and research centres of the electronics sector actively [Xie2014]. The increase in R&D activities arises in a context where information storage is key in the electronic industry. The incessant increase in the amount of information circulating on the planet means that storage memory needs are more and more pressing and they are conditioned by electronic systems that reduce their execution time (at the level of nanoseconds), which have low consumption of energy and show retention times greater than ten years.

There are two main reasons to focus research efforts on non-volatile memories:

1.- They have a great potential for growth if their main facet (non-volatility) is accompanied by a high switching speed. They could gain part of the market space currently occupied by the SRAM or DRAM volatile memories in the midterm [Xie2014].

2. - This type of memories are the key components of devices that represent almost half of the memory market currently [Xie2014].

Non-volatile memories based on silicon technology, Flash memories, have been used in mobile phones, video games, scientific instrumentation, industrial robotics, etc. Despite this, the technological limit for these devices is close and this is a very important hurdle [Gupta2019, Xie2014, Waser2007, Waser2012]. RRAMs are well positioned candidates within emerging technologies in comparison to other alternatives such as magnetic memories MRAMs (Magnetic RAMs), STT-RAM memories or PCM memories [Lanza2019, Xie2014, Waser2007, Waser2012].

Resistive memories work making use of resistive switching (RS) phenomena, which were discovered in the early 60's. Many different materials show RS, i.e., switching with a hysteretic behavior. Although the activity in these devices was reduced by the competence of (DRAM, EEPROM), it was retaken in the nineties. A great rise of the number of publications happened after these new efforts. In IEDM (International Electron Devices Meeting), a world reference in the subject, many contributions have been received in the last few years. A huge number of research centres and company Labs are currently working on the subject. This is the reason why we present this doctoral thesis proposal.

If the non-volatile memories of the future are made with RRAMs, the current electronic technology landscape would change dramatically: new electronic applications would appear and even new computer architectures that could use the advantages of having large amounts of non-volatile memory, including to the extreme of replacing volatile memories in their usual functions. This technology is simple, it consists of structures of two terminals of nanometric size that offers very low

currents of programming and erase, high speed, high durability (endurance) and viability for the integration in CMOS technologies and the manufacture of structures stacked in 3D [Lanza2019, Munjal2019, Gupta2019, Carboni2019, Xie2014, Waser2007, Waser2012, Zahurak2014].

A RRAM memory is usually manufactured with a MIM (Metal-Insulator-Metal) structure although they have also been manufactured with MIS (Metal-Insulator-Semiconductor) structures. In RRAM structures, an insulating material is usually placed between the two electrodes; in general, this material is an oxide that the electrical conduction properties can be changed as a result of the transport of ions in its core. RS phenomena have been observed in many different materials [Lanza2019, Munjal2019, Gupta2019, Carboni2019, Waser2012]:

1.- Transition metal oxides (transition metal oxides, TMOs), for example: TiO_2, Cr_2O_3, FeO_x and NiO.

2.- TMO of the perovskite family that have paraelectric, ferroelectric, multiferroelectric and magnetic functionality, for example: $(Ba, Sr) TiO_3$, $Pb (Zr_xTi_{1-x}) O_3$, $BiFeO_3$ and $Pr_xCa_{1-x}MnO_3$.

3.- High bandwidth prohibited materials: Al_2O_3, HfO_2 and Gd_2O_3.

4.- Graphene oxides.

The good results obtained at the device level have also recently been verified at the circuit level, where an integrated RRAM memory circuit of 16 GBs has been manufactured successfully by the company Sony [Zahurak2014] or a 32Gbits memory using a 24nm CMOS process, based in a MeO_x RRAM device reported at [Liu2013] [Liu2014]. This fact makes it clear that the possibilities of these devices and the corresponding circuits are very promising. A recent press release from Sony announces that in 2020 it will begin marketing ReRAM drives of 128GB and 256GB more cheaper than NAND with PCIe support and transfer rates 25.6 GB/s read times, 9.6 GB/s write (128GB) and 51.2 GB/s read and 19.2 GB/s write (256GB). This issue converts ReRAM technology in a real candidate for future memory chips both for massive NVM solutions and for embedded storage class memory in processor and microcontroller integrated circuits [Sony2019].

The RRAMs memories belong to a larger group of electronic devices: memristors [Chua1971, Chua2011, Kozma2012]. The functioning and existence of these devices were predicted at the end of the 1960s. They have great potential for applications ranging from non-volatile memories to the manufacture of neuromorphic circuits (circuits that analogically reproduce biological systems, particularly neuronal circuits). There are currently many technologies that serve to manufacture memristors; among others, RRAMs manufacturing technology, although the other types of emerging NVM discussed above such as MRAMs, PCMs and STT-RAMs are also memristors [Kozma2012]. In the context of this work, henceforth we will use RRAMs and memristors as similar devices, although for memory applications the first option is preferred, the second one is more commonly employed for analog and neuromorphic circuit applications.

Objectives

The objectives that are proposed for this work are the following:

A.- Compact modeling of RRAMs for circuit simulation.

In this objective we pursue the development of compact circuital models and techniques for extracting parameters for these models. We have had plenty experimental data to carry out these studies. They provide mainly from the National Microelectronics Center of Barcelona where they manufacture and measure various types of devices, both for MIM and MIS structures.

This objective is subdivided into the following points:

   a) Compact modeling of RRAMs to obtain the corresponding analytical equations.

   b) Development of the numerical techniques needed for model parameter extraction.

   c) Design of optimization methods to improve the set of extracted parameters.

   d) Implementation of compact models in circuit simulators using the Verilog-A language.

   e) Simulation of cell circuits and arrays of memory cells based on RRAMs.

B.- Compact modeling and simulation of circuits with memristors

For this point we have followed the usual trend in the field of memristor compact modeling.

   a) Development of models using flux and charge instead of current and voltage. We used data from experimental RS devices, although we will incorporated data obtained with memristors of other technologies.

   b) Implementation in circuit simulators using Verilog-A.

   c) Simulation of different neuromorphic circuits to describe biological systems with the use of memristors, in particular circuits that replicate neuronal functioning.

Methodology

The methodology followed and the tasks carried out to achieve the objectives proposed in the previous point are described below.

A.- Compact modeling of RRAM for circuit simulation

Task 1.1.- Development of physical models oriented to obtain analytical equations. The equations that describe the oxidation-reduction chemical processes, the heat equation and the equations of the currents were solved. These equations, dependent on time, were simplified to obtain explicit models of reasonable algebraic complexity.

Task 1.2.- The second step was to extract parameters from the models developed by comparing experimental curves of RRAM devices.

Task 1.3.- Preparation of the equations for the different models and the files with the set of parameters necessary to characterize a certain technology, and they were implemented in Verilog-A code in the ADS simulator of the Keysight company.

Task 1.4.- Test of models in the simulator to reproduce the experimental data. Analysis of the effects of variability.

Task 1.5.- Simulation of circuits based on standard non-volatile memories.

B.- Compact modeling and simulation of circuits with Memristors

Task 2.1.- Development of memristor models adapted to the type of circuit applications to be simulated and studied. Use of different work spaces, such as flow-load.

Task 2.2.- Design of strategies for extracting parameters for previously developed models. Test of the models with data of experimental devices supplied by the CNM of Barcelona

Task 2.3.- Implementation of the models in Verilog-A in the ADS simulator of the Keysight company.

Task 2.4.- Simulation of different neuromorphic circuits.

Simulation and Modeling of Resistive Switching Devices, State of the Art

In this chapter, the memristor is introduced as a new passive fundamental circuit element and a mathematical description is presented [Chua1971]. The memristive system is shown as an extension of a memristor with n dimensional states and higher order memristors as a generalization with dependencies on m-even derivatives of the input signal [Chua2011]. The extension to non-linear circuit element is presented (with high order derivatives/integral dependences of currents and voltages) [Chua2012], and the modification of the memristive system general equation, a particular case, for nanobatteries is discussed.

Different memristors based on resistive switching operation (RRAMs are good examples as highlighted at the introduction) are specifically revised. The basic cell composition as a capacitor (such as metal-insulator-metal) is described. The main types of memristors are presented (electrochemical metallization memories, valence change memories and thermochemical memories), and the different operation modes as a function of the bias scheme are described (unipolar, bipolar, non-polar and threshold). The main figures of merit were described (off/on ratio, endurance, data retention, variability, scalability, speed and power consumption) to correctly evaluate RRAM technology.

With the focus on the simulation and modelling point of view, we describe the different simulation approaches presented in the literature (microscopic or atomistic description, macroscopic simulator such as Finite Element Method or kinetic Monte Carlo, and compact models as a support to design circuits based on memristors). A new compact model developed in this doctoral thesis for RRAMs is presented and some previous models are commented.

Finally, some applications of memristor in the digital and analogue realms are presented.

1.1. Memristors

Memristor is the contraction of the words memory and resistor. It is a new passive two terminal device introduced theoretically in 1971 by Leon Ong Chua (at University of California, Berkeley), in a general nonlinear circuit theory context [Chua1971]. The memristor completes the classical passive elements: resistor, capacitor and inductor, in terms of the relationships between the four basic electrical magnitudes, voltage, intensity, charge and flux (the two latter defined axiomatically by means of equations (1.2) and (1.3)) and represented graphically in **Figure 1.1**.
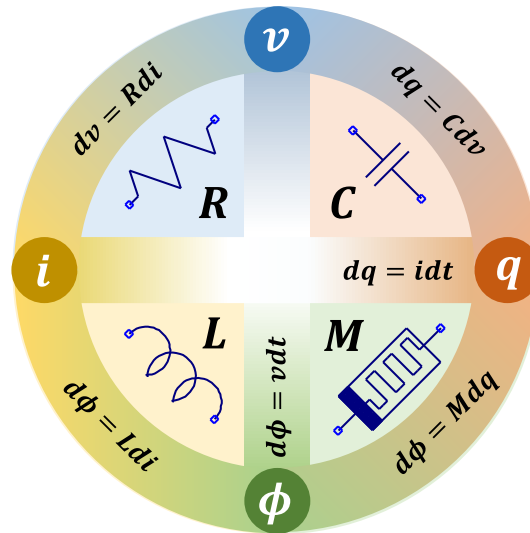
Figure 1.1 Four basic passive elements (*R*, *C*, *L* and *M*). Their symbols and mathematics relationships with the basic electrical magnitudes (v, i, q and ϕ) are also shown (v is the voltage, i is the current, q is the charge, ϕ is the flux), R is the electrical resistance (Georg Ohm, 1827), C is the capacitor (Ewald Georg von Kleist, 1745), L is the inductor (Michael Faraday, 1831) and M is the Memristor (Leon Ong Chua,1971) [Strukov2008].

The initial memristor concept was developed by Chua and it was implemented by an active circuit composed of operational amplifiers, transistors, diodes, resistors and capacitors (Figure 2 in [Chua1971]). The memristor presents a loop in current versus voltage plots. That is, for the same bias voltage is possible to obtain two different current values. The current at a time t depends on the previous device history. This property allows the memristor to be in different stable states for the same applied voltage and, therefore, it has the capability of working as a non-volatility memory (NVM) [Chua1971].

In 2008, a research team at Hewlett Packard Lab led by R. Stanley Williams [Strukov2008] fabricated the first memristor at the nanometre scale (**Figure 1.2 a**) based on a Pt/TiO$_2$/Pt stacks (**Figure 1.2 b**). Its operation was described by a current based on ionic transport dependent on the applied bias voltage. The voltage determines the width (w) of a doped region into de oxide layer (**Figure 1.2 c**). In order to model this behaviour, a circuit of two serial variable resistors (R_{on} and R_{off}) is used (**Figure 1.2 d**). The values of the two resistors depend on the length of the doped region, w. The evolution of the current versus a sinusoidal applied voltage is shown in **Figure 1.2 e**, while the ratio between the doped layer length and the oxide thickness (w/D) is shown in **Figure 1.2 f**. The $i - v$ plot is shown in **Figure 1.2 g**, where the hysteretical behaviour is observed. Note that the amplitude of the loop decreases as the frequency increases (in **Figure 1.2 g,** the loop turns into a straight line when the frequency is above $10\omega_0$) [Strukov2008].
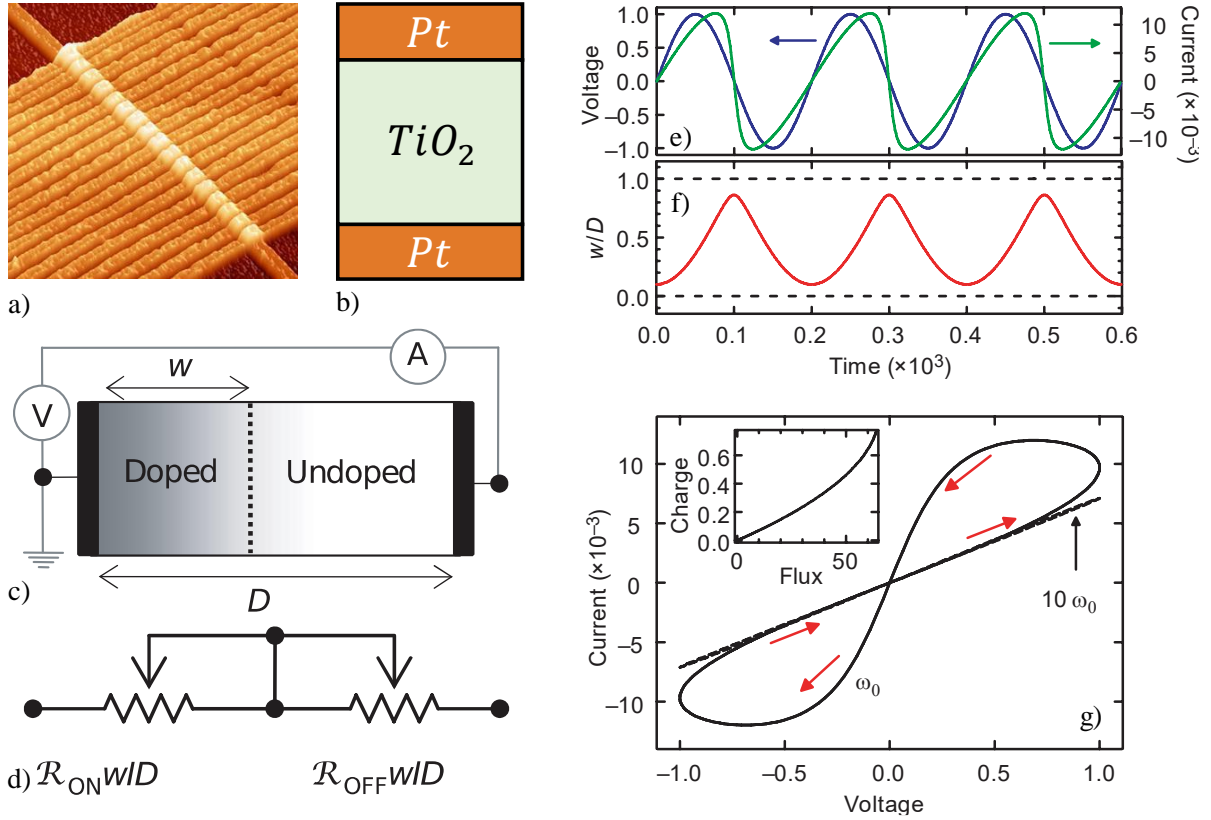
Figure 1.2 a) Atomic force microscope image of a memristor array (the wire width was 50nm). **b)** Sketch of the memristor stack structure, Pt/TiO$_2$/Pt. **c)** Representation of the measurement instrument connection (V: voltmeter and I: ammeter). The doped (w) and undoped (D-w) regions are drawn, where D is the thickness of the oxide layer. **d)** Equivalent serial variable resistors (R_{on} is the value of the resistance in the ON state, and R_{off} is the value of the resistance in the OFF state). **e)** Sinusoidal voltage applied to the device and current flowing through the device versus time. **f)** Plot of w/D versus time. **g)** Current versus voltage plot for two frequencies (inset: charge versus flux plot) [Strukov2008].

After the publication of the article presented by the research team of Williams [Strukov2008], a great interest has been triggered in the development of this type of devices, because of their great features for both digital and analog applications, as we will comment later.

1.1.1. Mathematical Description of Memristors

The memristor is a device defined by the relation between the flux ϕ and the charge q [Chua1971, Chua2011],

$$d\phi = M \cdot dq \tag{1.1}$$

where M is called the memristance and the flux $\phi(t)$ and charge $q(t)$ are defined axiomatically as functions of voltage $v(t)$ and current $i(t)$ by the following expressions [Chua1971 ,Chua2011]:

$$\phi(t) \triangleq \int_{-\infty}^{t} v(\tau)d\tau \tag{1.2}$$

$$q(t) \triangleq \int_{-\infty}^{t} i(\tau)d\tau \tag{1.3}$$

3

The memristor is defined as a passive element in which the flux ϕ is controlled by the charge q or vice versa, by constitutive relationships expressed as [Chua1971 ,Chua2011]

$$\phi = \hat{\phi}(q) \tag{1.4}$$

$$q = \hat{q}(\phi) \tag{1.5}$$

The constitutive function described in equation (1.4) and (1.5) may be continuous and piecewise-differentiable functions with bounded slopes [Chua2011].

If equation (1.4) is derived with respect to time, we obtain [Chua1971 ,Chua2011]:

$$v(t) = \frac{d\phi}{dt} = \frac{d\hat{\phi}(q)}{dt} = \frac{d\hat{\phi}(q)}{dq}\frac{dq}{dt} = M(q)i(t) \tag{1.6}$$

where $M(q)$ is the memristance (units in Ohms, Ω). Note that the memresistance value in time t_i depends on the previous current that flowed through the device from $-\infty$ to t_i.

In the same way, deriving equation (1.5) with respect to time, we obtain [Chua1971 ,Chua2011]:

$$i(t) = \frac{dq}{dt} = \frac{d\hat{q}(\phi)}{dt} = \frac{d\hat{q}(\phi)}{d\phi}\frac{d\phi}{dt} = M_G(\phi)v(t) \tag{1.7}$$

where $M_G(\phi)$ is defined as the memductance (units in Siemens, Ω^{-1}).

The electric power dissipated in a memristor, with menristance $M(q)$ or menductance $M_G(\phi)$, can be calculated as [Chua1971]

$$p(t) = i(t)v(t) = i^2(t)M(q) = v^2(t)M_G(\phi) \tag{1.8}$$

If $M(q) \geq 0$ (or $M_G(\phi) \geq 0$) then the power at each time satisfies that $p(t) \geq 0$ and, therefore, the memristor is a passive element [Chua1971].

An example of a voltage versus current plot is shown in **Figure 1.3**. A sinusoidal current with amplitude 1 A, with three different angular frequencies, is applied to a memristance M, with a constitutive flux-charge relationship defined by the inset equation in **Figure 1.3**. The characteristic pinched hysteresis loops can be observed.
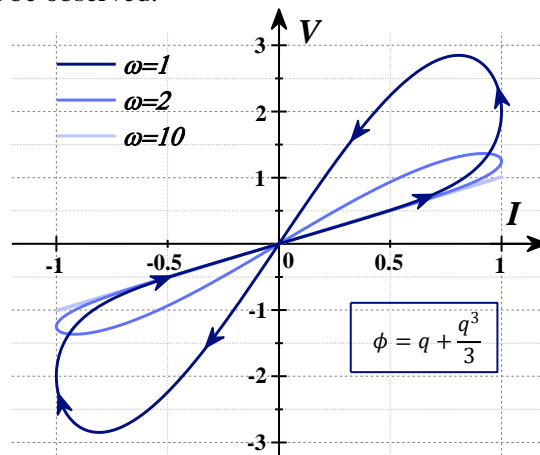
Figure 1.3 Voltage versus current ($v(t)$, $i(t)$) plotted for a sinusoidal current (amplitude equal to 1A) and three values of ω (1, 2 and 10). Inset equation: constitutive memristor relation $\hat{\phi}(q)$.

1.1.2. Memristive Systems

The memristive system is a generalization of a memristor that considers that the memristance (or memconductance) depends also on a n-dimensional state vector X and on the input signal, $u(t)$. It can be represented mathematically by the followings expressions [Chua1976]

$$y(t) = g_0(\text{X}, u)u(t) \tag{1.9}$$

$$\frac{d\text{X}}{dt} = f(\text{X}, u) \tag{1.10}$$

$$\text{X} = [x_1, x_2, \dots . x_n] \tag{1.11}$$

where $y(t)$ is the output signal, X is the n-dimensional state vector that contains the internal state-variables $x_1, x_2, \dots . x_n$, all independent on $u(t)$, and g_0 and f are two continuous functions.

According to the type of input/output signal (voltage or current) the memristive system is classified as shown in **Table 1.I**

Table 1.I Memristive system types in function of input control signal ($i(t)$ or $v(t)$)

Memristive System Types	$u(t)$	$y(t)$
Current-Controlled Memristive System (CCMS)	$i(t)$	$v(t)$
Voltage-Controlled Memristive System (VCMS)	$v(t)$	$i(t)$

Therefore, the memristors described in the previous section are an especial case of memristive systems, for which the state vectors are one-dimensional (X = q in CCMS or X = ϕ in VCMS).

1.1.3. High Order Memristive Systems

The high order memristive systems incorporate into the output signal, $y(t)$, the contribution of m-even derivatives of the input signal $u(t)$ weighted with m-state functions, g_1 to g_m:

$$y(t) = g_0(\text{X}, u)u(t) + g_1(\text{X}, u)\frac{d^2u}{dt^2} + g_2(\text{X}, u)\frac{d^4u}{dt^4} + \dots + g_m(\text{X}, u)\frac{d^{2m}u}{dt^{2m}} \tag{1.12}$$

where m is a positive integer, $y(t)$ is the output signal, $u(t)$ is the input signal, X is the n-dimensional vector that contains the internal state-variables $x_1, x_2, \dots . x_n$, and g_i are continuous functions. This new representation produces zero-crossing hysteresis curves too, as memristive systems, but it presents different frequency responses.

1.1.4. Extension of Circuits Elements (α,β)

For axiomatically defined circuit elements, let us introduce the equation $x^{(\gamma)}(t)$ defined as [Chua2012, Tetzlaff2013]

$$x^{(\gamma)}(t) \triangleq \begin{cases} \dfrac{d^\gamma x(t)}{dt^\gamma} & , \quad if \ \gamma = 1, 2, \dots, \infty \\ x(t) & , \quad if \ \gamma = 0 \\ \displaystyle\int_{-\infty}^{t} x(\tau)d\tau & , \quad if \ \gamma = -1 \\ \displaystyle\int_{-\infty}^{t}\int_{-\infty}^{\tau_{|\gamma|}} \dots \int_{-\infty}^{\tau_2} x(\tau_1)d\tau_1 d\tau_2 \cdots d\tau_{|\gamma|} & , \quad if \ \gamma = -2, \dots, -\infty \end{cases} \tag{1.13}$$

where γ is an integer number. If γ is and integer positive, the function $x^{(\gamma)}(t)$ is equal to γ-order time differential of $x(t)$, if γ is an integer negative, the function $x^{(\gamma)}(t)$ is equal to γ-order time integral of $x(t)$, and finally, if γ is equal to cero, the function $x^{(\gamma)}(t)$ is equal to $x(t)$.

Namely $v^{(\alpha)}(t)$ and $i^{(\beta)}(t)$ the high order differential/integral or linear voltages and current circuits relations, since the α, β are integers, is possible to define infinity of new circuits elements in function of the pair of values (α, β).

The basic element can be derived easily with this notation. The **Table 1.II** represent the constitutive equations in terms of voltages and current and the **Figure 1.4** shown the symbols used circuit representations.

Table 1.II Axiomatic definition of basic circuit elements as a function of the (α, β) values.

α	β	χ	$v^{(\alpha)}(t)$	$i^{(\beta)}(t)$	*Element Name*
0	0	0	$v(t)$	$i(t)$	Resistor
0	-1	1	$v(t)$	$\int_{-\infty}^{t} i(\tau)d\tau$	Capacitor
-1	0	1	$\int_{-\infty}^{t} v(\tau)d\tau$	$i(t)$	Inductor
-1	-1	2	$\int_{-\infty}^{t} v(\tau)d\tau$	$\int_{-\infty}^{t} i(\tau)d\tau$	Memristor
-1	-2	3	$\int_{-\infty}^{t} v(\tau)d\tau$	$\int_{-\infty}^{t}\int_{-\infty}^{\tau_2} i(\tau_1)d\tau_1\, d\tau_2$	Memcapacitor
-2	-1	3	$\int_{-\infty}^{t}\int_{-\infty}^{\tau_2} v(\tau_1)d\tau_1\, d\tau_2$	$\int_{-\infty}^{t} i(\tau)d\tau$	Meminductor

where the χ is a complexity metric of circuit elements defined as [Chua2012]

$$\chi \triangleq |\alpha| + |\beta| \tag{1.14}$$
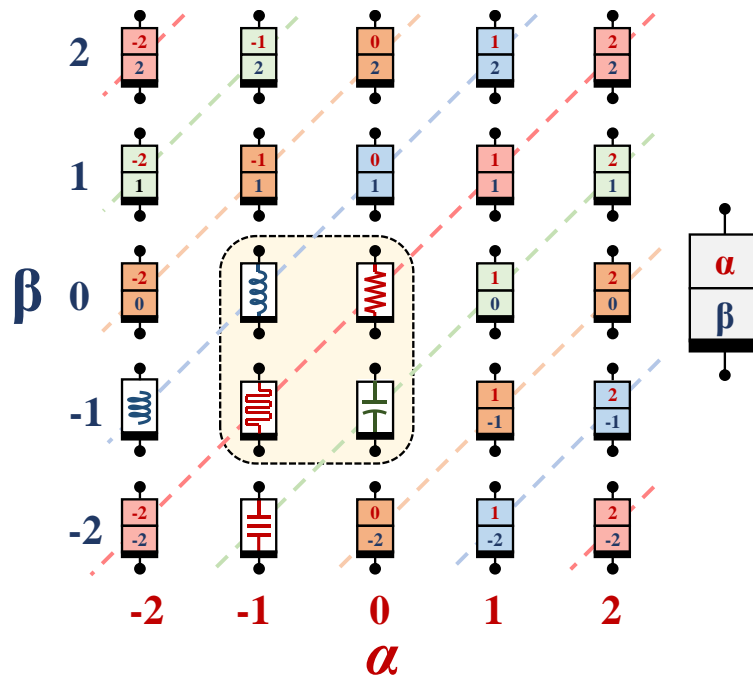
Figure 1.4 Periodic table of first 25 axiomatically defined circuits elements in function of (α, β). The columns are the integer values of α (|α|≤ 2) and the rows are the integer values of β (|β|≤ 2). The symbols of the four fundamental circuits element: Resistor (0,0), Capacitor (0,-1), Inductor (-1,0), Memristor (-1,-1). The symbol of Memcapacitor (-1,-2), and Meminductor (-2,-1) [Chua2012, Tetzlaff2013].

The general circuits elements with $|\alpha| + |\beta| > 2$ are active, this supposes the need of an external power supply and the use of active elements (like transistor or operational amplifiers) [Tetzlaff2013, Chua2012].

1.1.5. Memristor Model Extension for Nanobateries

The observed presence of voltage in the absence of current in some specific memristive devices that work as nanobatteries [Valov2013] forced to extend the memristor theory because the I-V curves do not cross the origin, which is against the basic principle of a memristor [Valov2013]. Three factors contribute to the formation of the electromotive force voltage V_{emf} in this type of devices: the Nernst potential V_N, the diffusion potential V_d and the Gibbs–Thomson potential V_{GT} [Valov2013]. The electromotive forces measured in different types of nanobatteries are shown in With the same description for the time evolution of the state variables (1.10) and for the state variables (1.11).

Table 1.III.

This potential produces nonzero-crossing pinched hysteresis in the I-V curve, since when the current is cero the voltage in the extremes of the device is equal to V_{emf}. In order to include an offset value a in the general memristor model, the expression (1.9) can be rewritten as,

$$y(t) = g_0(\mathrm{X}, u)(u(t) - a) \tag{1.15}$$

With the same description for the time evolution of the state variables (1.10) and for the state variables (1.11).

Table 1.III Electromotive force (emf) measured in different types of nanobattery cells. (Values extracted from [Valov2013]).

TE	Insulator	BE	Type	Vcell
Pt	Ta_2O_5	Ta	VCM	$50\mu V$
Pt	$SrTiO_3$	Ti	VCM	$1.3mV$
Pt	$SrTiO_3$ (as deposited)	Ti	VCM	$200mV$
Ag	AgI	Pt	ECM	$2.8mV$
Cu	WO_3	Pt	ECM	$36mV$
Ag	$GeSe_x$	Pt	ECM	$97mV$
Ag	GeS_x	Pt	ECM	$116mV$
Ag	SiO_2	Pt	ECM	$133mV$
Cu	SiO_2	Pt	ECM	$321mV$

1.2. Resistive Switching Devices. RRAM Technology

1.2.1. RRAM Structure

A wide and well known subset of memristors is based on resistive switching operation. These devices are called RRAMs (Resistive Random Access Memories). The basic RRAM cell consists of a capacitor with a Metal-Insulator-Metal (MIM) or Metal-Insulator-Semiconductor (MIS) structure. The insulator allows ion movement under proper temperature or/and electric field conditions [Waser2009]. Waser et al. [Waser2007] showed two basic configuration for arrays of RRAMs following a vertical stack arrangement or a lateral planar allocation (Figure 2 in [Waser2007]).

When a high number of RRAM cells are required, a cross-bar structure is adopted. The structure consists of a bottom wire (BE) and a perpendicular top wire (TE). Between them, the insulator layer (usually a transition metal oxide, TMO) is deposited [Lim2015]. A basic cross-bar structure with four cells is shown in **Figure 1.5**.
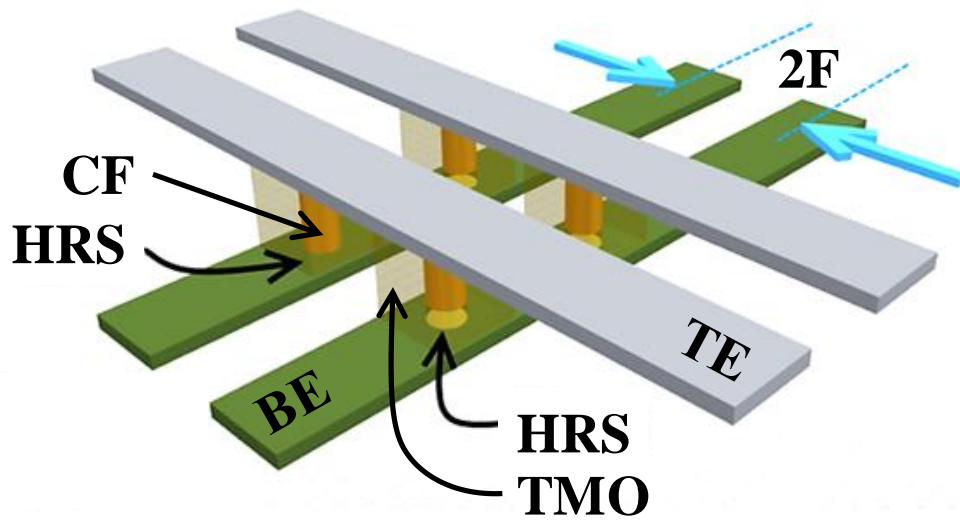
Figure 1.5 Sketch of a RRAM array following a crossbar architecture with a cell area of $4F^2$. Each device has a stack composed of TE/TMO/BE [Lim2015]. One of the devices has a formed conductive filament (CF) and, therefore, it is in a low resistance state (LRS) (it assumed filamentary conduction). The other three devices have disrupted CFs and, consequently, they are in a high resistance state (HRS).

For a great integration density is possible used the different metal layer in a 3D cross-point integration architecture (see **Figure 1.6** a), or in a vertical RRAM (VRRAM) integration architecture **Figure 1.6 b)** [Park2012b].
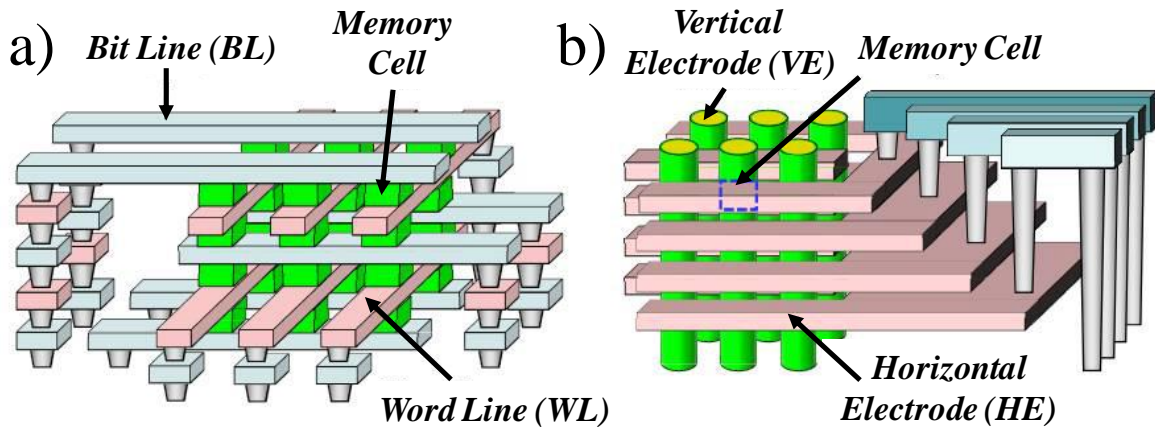
Figure 1.6 a) High density RRAM integration following a 3D cross-point configuration [Park2012b]. **b)** Vertical RRAM (VRRAM) integration architecture [Park2012b].

1.2.2. Resistive Switching Devices

Resistive switching devices can be used for non-volatile memory applications to store digital information. **Figure 1.7** shows a variety of physical phenomena that can be employed for resistive switching [Waser2009].
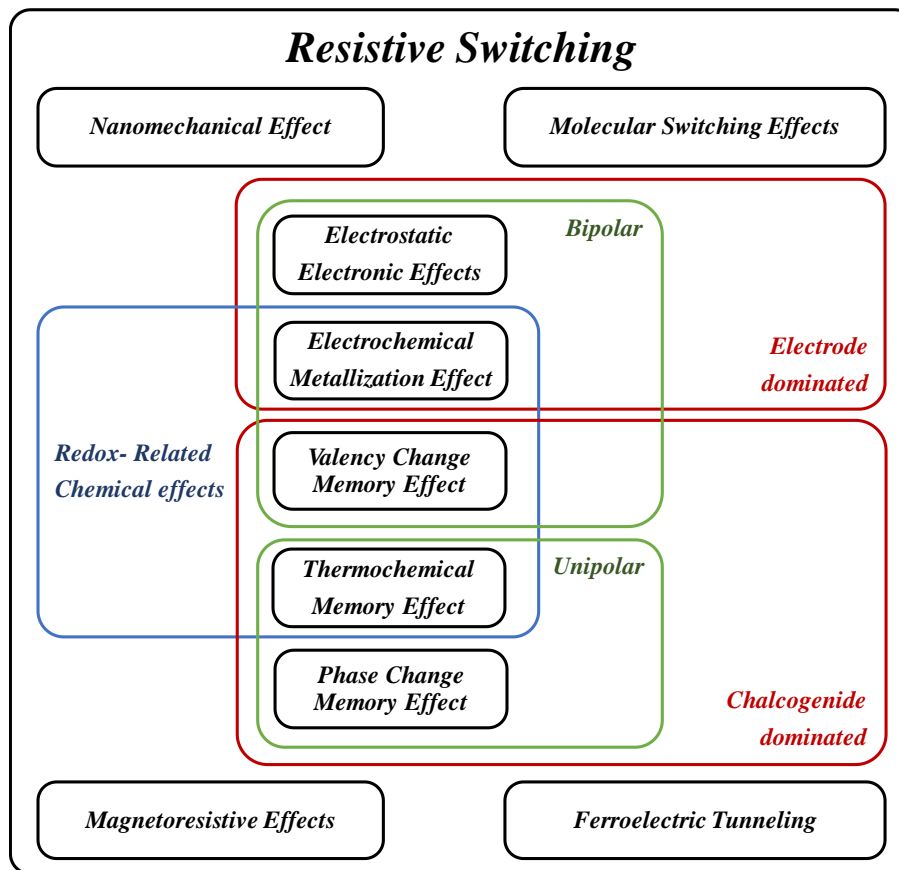
Figure 1.7 General classification of physical phenomena observed in resistive switching devices, in the context of non-volatile memories (NVMs) [Waser2009].

Among them, the most common RRAM devices are those characterized by redox-related chemical reactions and include the following physical phenomena (summarized in **Table 1.IV**).

Table 1.IV Description of the main characteristics of resistive switching mechanisms in RRAM [Li2015b].

Switching mechanism	ECM Electrochemical Metallization Memories	VCM Valence Change Memories	TCM Thermochemical Memories
Dominated charged species	Metal cations	O anions or oxygen vacancies Vo	
Type of CF	Metal	Vo-CF (bipolar)	Vo-CF (unipolar)
Dominant driving force	Electric field applied to the device		Thermal gradient
Top Electrode	An electrochemically active metal: Ag, Cu or Ni	A low function metal not easily reduced back after oxidation: Ti, Al or Nb	Inert electrodes: Pt, Pd, Ir, Ru, W or Au
RS layer materials	Ion-conducting solid electrolyte: Ag_2S, GeSe, Cu_2S Ag_2Se or Ag-Ge-Se Bynary or complex oxides: HfO_2, ZrO_2, SiO_2, WO_3, etc.	Transition metal oxides:TiO_2, HfO_2, ZrO_2, $SrTiO_3$, TaO_x, WO_3 Doped: SiO_2, amorphous: C	Transition metal oxides: HfO_2, NiO, CoO, CuO, Fe_2O_3
Bottom electrode	Inert electrodes: Pt, Pd, Ir, Ru, W or Au		
Dominant material	Electrode	Electrode and RS layer	RS layer

▪ *Electrochemical metallization (ECM) memories*: they are also called Programmable Metallization Cells (PMCs) or Conductive Bridge (CB) memories in the literature [Waser2009]. The ECM-RRAM cell stack is composed of a metallic or electrochemically active top electrode such as Ag, Cu or Ni, a solid electrolyte sandwiched in the middle, and an inert bottom electrode such as Pt, Pd, Ir,

Ru, W or Au. The set process is due to the formation of a CF from the top active electrode to the bottom inert electrode by the drift/diffusion of metallic ions, which form a conductive path between both electrodes. The reset process causes the CF rupture by oxidation [Gupta2019, Villena2017, Li2015b, Waser2009].

▪ *Valence-Change Memory (VCM)*: The VCM-RRAM cell stack is composed by a top metal electrode, not easily reducible after oxidation such as Ti, Al or Nb. A transition metal oxide is sandwiched between both electrodes (such as TiO_2, HfO_2, ZrO_2, $SrTiO_3$, TaO_x, WO_3, among others). Finally, the bottom electrode is an inert metal such as Pt, Pd, Ir, Ru, W or Au. The set process is activated when a positive voltage is applied (between the TE and the BE), the electric field produces pairs of oxygen ions (O^{2-}) and oxygen vacancies (V_0), the O^{2-} ions drift to the TE. The conductive filament is formed by the accumulation of oxygen vacancies that allows electrons to flow through. In the reset process a negative voltage is applied (between the TE and the BE), the O^{2-} ions migrate to the resistive switching layer to recombine with oxygen vacancies, V_0, causing the partial rupture of the CF. [Gupta2019, Villena2017, Li2015b, Waser2009].

▪ *Thermochemical Memory (TCM):* The TCM cell is formed by top and bottom inert electrodes (Pt, Pd, Ir, Ru, W or Au) and a transition metal oxide sandwiched between them, such as HfO_2, NiO, CoO, CuO, Fe_2O_3, among others. The set and reset processes are linked to a combination of the electric field and thermal effects, being the latter very important for these type of devices. In particular, for the reset process (also named fuse), the thermal diffusion (as a result of Joule heating) is key to explain the device behavior [Gupta2019, Villena2017, Li2015b, Waser2009].

In all the cases, if a conductive filament shorts both electrodes, it is said that the RRAM is in a Low Resistance State (LRS). On the other hand, if the filament is disrupted, the RRAM is in a High Resistance State (HRS).

1.2.3. Key Figures-of-Merit of RRAM Devices

In order to compare alternative RRAM technologies different Figures Of Merit (FOM) could be considered [Munjal2019, Gupta2019, Villena2017, Wong2012].

1.2.3.1. Off/On ratio

The on/off ratio is defined as the ratio between the current in the LRS and in the HRS measured at a given applied voltage. It is desirable to have the highest possible ratio, usually expressed as a power of 10. As an example, an on/off ratio of $3.2 \cdot 10^{10}$ is reported in a device with a Ge_xSe_y insulator [Kozicki2005, Kund2005].

1.2.3.2. Endurance

Endurance is defined as the number of Set/Reset cycles that one device can tolerate, maintaining the on/off ratio [Munjal2019, Gupta2019, Lanza2019, Villena2017, Wong2012]. The resistance on/off ratio is degraded with the cycle number. When the value is close to a certain value (given by the RRAM technology and operation) the device starts to fail. The endurance can be determined by performing different measurements, the most common are: I–V sweeps, Pulsed Voltage Stress (PVS), and current-blind PVS [Lanza2019].

1.2.3.3. Data Retention

Retention is defined as the time a certain conductance state (LRS or HRS) remains stable after a set/reset process [Munjal2019, Gupta2019, Villena2017, Wong2012]. The LRS retention is observed to be dependent on the compliance current employed in the set process and it decreases at high temperatures due to a greater probability of atomic rearrangements. The desired retention time for NVMs is of 10 years @85ºC [Lanza2019].

1.2.3.4. Variability

Variability is one of the key obstacles for a massive implementation of RRAM technologies. It can be observed for a single device, what is called cycle to cycle variability, or for different devices (device to device variability). The variability is mainly due to two causes: the technological processes in the manufacture and the intrinsic stochastic nature of RS phenomena [Lanza2019, Munjal2019, Gupta2019].

1.2.3.5. Scalability

The scalability determines the number of devices per unit area that each technology node can integrate in a circuit. Each technological node is characterized by the F number, expressed in nm. Each memory design requires a minimum size area (that depends on F) for implementing a unitary memory cell. The best scalability for emerging memory technologies corresponds to RRAMs (F lower than 5 nm can be reached and a minimum cell area equal to $4F^2$ is required), followed by PCRAMs (F = 45nm and minimum cell area of $4F^2$), FeRAMs (F=180nm and minimum cell area of $22F^2$) and, finally, MRAMs (F=130nm and minimum cell area of $45F^2$). These data have been extracted from Table 1 in [Munjal2019]. From the point of view of RRAM modeling, it is important to highlight that RS characteristics reported for larger devices cannot be always directly applied to smaller devices because the RS mechanism could be affected by the size of RRAMs [Lanza2019].

1.2.3.6. Speed

A key FOM in memory applications is the read/write time. This speed determines the throughput of a memory system. A classification of the different emerging memory devices according to their transfer rate (Table 1 in [Munjal2019]) put RRAMs in the first place, with a write/erase time lower than 1ns, followed by MRAMs (10ns), FeRAMs (65ns) and, finally, PCRAMs (100ns).

1.2.3.7. Power Consumption

Portable devices (such as smart phones, smart watches or laptops) demand a great amount of memory and a low energy consumption for a large time battery use. The RRAM power consumption depends on the device materials and the physics behind RS operation: filamentary conduction leads to a higher power consumption than distributed conduction [Lanza2019]. A comparison of emerging NVMs in terms of power consumption is presented in Carboni et al. It shows that FeRAMs and SST-MRAMs have a write energy ≈ 0.1pJ/bit, RRAMs between 0.1 to 1 pJ/bit and PCMs around 10pJ/bit (Table 1 in [Carboni2019]).

More information about the FOMs of these NVM technologies can be found in [Munjal2019, Carboni2019, Pan2014, Zangeneh2014, Wong2012].

1.2.4. RRAM Operation Modes

Based on the bias schemes for RS, RRAMs can be classified as bipolar, unipolar, non-polar and threshold RS [Gupta2019, Munjal2019, Lanza2019, Villena2017, Ielmini2016].

▪ *Bipolar*: under this operation regime, the set and reset processes occur with opposite bias polarity. **Figure 1.8 a)** shows a typical bipolar I-V curve with $V_{Set} > 0$, $V_{Reset} < 0$ [Yang2009c], while **Figure 1.8 b)** shows a bipolar behavior with $V_{Set} < 0$, $V_{Reset} > 0$ [Chen2011b, Lee2011b]. In terms of endurance, variability and power consumption bipolar RRAMs work better than unipolar devices [Gupta2019, Gao2018, Li2013].

▪ *Unipolar*: in this operation regime, set and reset processeses occur with the same polarity. Some devices have unipolar polarity with positive bias ($V_{Set} > 0$, $V_{Reset} > 0$), as shown in **Figure 1.8 c)**, and others require negative bias ($V_{Set} < 0$, $V_{Reset} < 0$). Unipolar devices in applications like crossbar with

selector diodes allow higher integration densities than bipolar devices and require a simpler control circuit [Gupta2019, Gao2018].

▪ ***Non-polar***: in this operation regime, the set and reset processes may occur with any polarity. Therefore, four cases are possible: $V_{Set} > 0$, $V_{Reset} < 0$ or $V_{Set} < 0$, $V_{Reset} > 0$ or $V_{Set} > 0$, $V_{Reset} > 0$ or $V_{Set} < 0$, $V_{Reset} < 0$. In other words, the non-polar devices have the ability to operate as unipolar or bipolar RRAMs. Examples of non-polar devices are described in references [Huang2012d, Guan2008].

▪ ***Threshold RS***: Threshold behavior is characterized by the fact that the set happens when a voltage ramp is applied. If the applied voltage is lowered again, the device returns to its HRS [Gupta2019, Lanza2019,Villena2017].
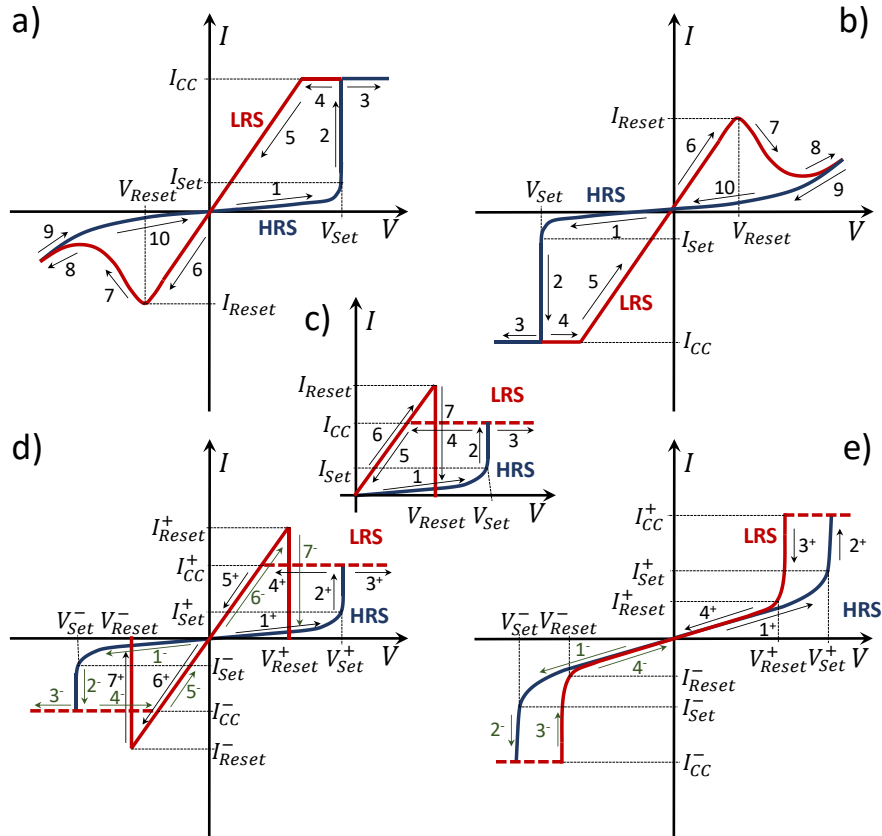
Figure 1.8 Types of RS according to I-V sweps. Bipolar behavior is characterized by having set and reset voltages with different polarity: **a)** bipolar I-V curve with $V_{Set} > 0$ and $V_{Reset} < 0$ **b)** bipolar I-V curve with $V_{Set} < 0$ and $V_{Reset} > 0$ **c)** Unipolar behavior is characterized by having set and reset voltages the same sign $V_{Set} > 0$ and $V_{Reset} > 0$ or $V_{Set} < 0$ and $V_{Reset} < 0$, **d)** In nonpolar RRAMs, set and reset voltages do not depend on the polarity of the applied voltage, **e)** Threshold behavior is characterized by the fact that the set happens when a voltage ramp is applied. If the applied voltage is lowered again, the device returns to its HRS. Adapted from References [Lanza2019, Villena2017, Ielmini2016, Gupta2019, Munjal2019] I_{CC} stands for the compliance current used in order to prevent permanent breakdown.

Other RRAM classification is based on the type of charge conduction that takes place: filamentary or distributed [Gupta2019]. Filamentary switching is characterized by the formation/destruction of one or more conductive filaments in the insulator, like small nanometric wires that short the top and bottom electrodes [Gupta2019, Lanza2019, Villena2017, Waser2007]. Distributed switching is a homogeneous phenomenon produced in the insulator volume [Ielmini2017]. In general, the filamentary switching consumes more power than the distributed switching [Lanza2019, Xiao2017].

Xiao et al. [Xiao2017] introduced a RRAM with simultaneous filamentary and distributed resistive switching in a bilayer TiO₂/SiOₓ insulating stack device used to improve the electrical characteristics.

1.2.5. Forming Process

Usually, RRAM devices require an initialization process for creating a region with a high concentration of defects in the insulator to ease and stabilize resistive switching. This process is called forming and it is like a soft dielectric breakdown [Ielmini2017].

The forming process need a much higher bias voltage (V_{form}) than a normal transition between RS states (set or reset processes). In some devices this voltage may be incompatible with CMOS technology operating conditions [Ielmini2017]. The electroforming process in RRAMs can be performed by pulsed or ramped voltages. In a ramped voltage scheme, the voltage is gradually increased till a limiting value. Furthermore, a compliance current is set to prevent the irreversible breakdown of the insulator. **Figure 1.9** shows I-V curves for different devices reported in the literature.
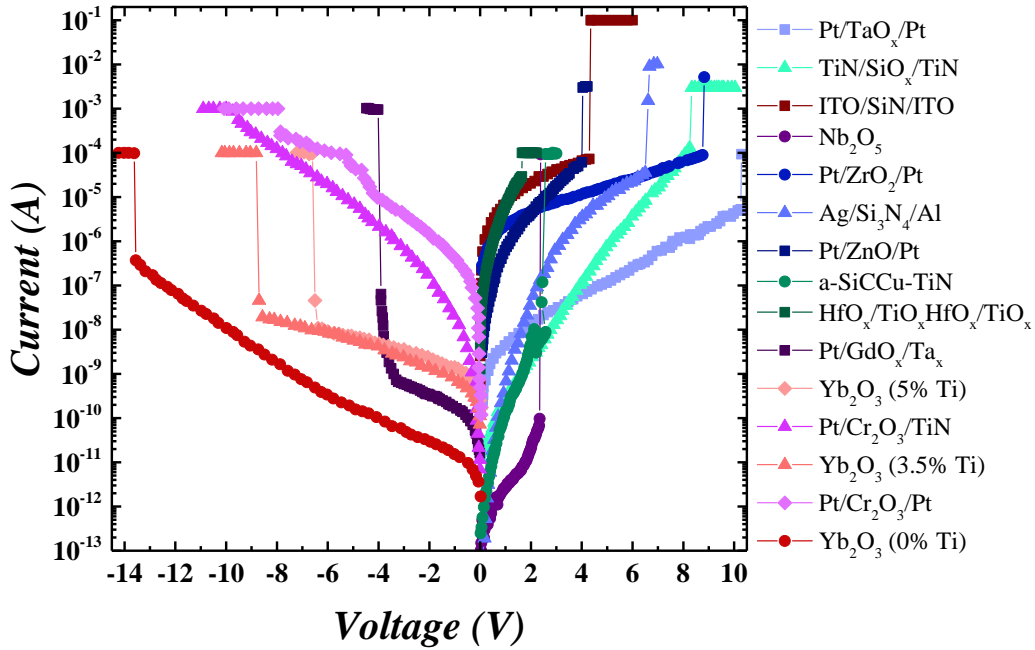
Figure 1.9 Electroforming processes by means of voltage sweeps of several RRAMs reported in the literature. The corresponding references and characteristics are shown in **Table 1.V**.

Table 1.V Summary of the electroforming characteristics in some devices. V_{FM} is the forming voltage, I_{FM} is the measured current at V_{FM} and I_{CC} is the compliance current used to prevent device damage.

Structure	Type	V_{FM}	I_{FM}	I_{CC}	Reference
Pt/TaO$_x$/Pt	unipolar	10.3	5.3μA	10μA	[Kurnia2013]
TiN/SiO$_x$/TiN	unipolar	8.25	130μA	3mA	[Montesi2016]
ITO/SiN/ITO	unipolar	4.3	73μA	100mA	[Kim2012b]
Nb$_2$O$_5$	unipolar	2.35	96.9pA	100μA	[Baek2013]
Pt/ZrO$_2$/Pt	bipolar	8.8	89.3μA	5mA	[Lin2007c]
Ag/Si$_3$N$_4$/Al	bipolar	6.5	35.8μA	10mA	[Kim2010f]
Pt/ZnO/Pt	bipolar	4	61.2μA	3mA	[Chiu2012]
a-SiCCu-TiN	bipolar	2.5	120nA	100μA	[Garcia-Redondo2016]
HfO$_x$/TiO$_x$/HfO$_x$/TiO$_x$/	bipolar	1.6	29.3μA	100μA	[Ma2016]
Pt/GdO$_x$/Tax	bipolar	-3.9	64nA	1mA	[Zhou2014]
Yb$_2$O$_3$(5% Ti)	bipolar	-6.4	10.9nA	100μA	[Mondal2012]
Pt/Cr$_2$O$_3$/Pt	bipolar	-7.8	0.3mA	1mA	[Chen2011b]
Yb$_2$O$_3$(3.5% Ti)	bipolar	-8.5	19.3nA	100μA	[Mondal2012]
Pt/Cr$_2$O$_3$/TiN	bipolar	-9.74	0.9mA	1mA	[Chen2011b]
Yb$_2$O$_3$(0% Ti)	bipolar	-13.5	370nA	100μA	[Mondal2012]

Grossi et al. [Grossi2016] used three different forming schemes based on pulsed operation to initialize a memory of 4 kbits implemented by RRAMs based on a TiN/Ti/HfO$_2$/Ti/TiN stack:

▪ *Single pulse (SP)*, a rectangular voltage pulse with limited amplitude and width is applied. Rise and fall times (t_{rise}, t_{fall}) are set in order to avoid overshoot currents.

▪ *Incremental Form (IF)*. A sequence of pulses with increasing amplitude is applied until a given voltage is reached.

▪ *Incremental Form and Verify (IFV)*. A sequence of pulses with increasing amplitude is applied. After each pulse, a reading pulse (with low amplitude) is applied. If the read current is higher than a given threshold, the forming process is supposed to be completed and the programming pulsed sequence is stopped.

According to the need of forming process, RRAMs can be classified as forming-free (FF) and forming-required (FR) cells [Kurnia2013]. Forming- free devices do not require extra processes in order to initialize the RS layer [Wang2010c, Li2010]. **Table 1.VI** shows the main characteristics of some free-forming RRAMs reported in the literature.

Table 1.VI Main characteristic of free-forming RRAM devices reported in the literature (adapted from [Wang2010c, Li2010]).

Reference	[Wang2010c]	[Guan2008]	[Sun2009b]	[Liu2009b]	[Li2010]
Device structure	Ti/Mo-embedded	Cu/Cu-doped	TiN/ZrO$_2$/Pt	Cu/Ti ZrO$_2$/Pt	Au/ZrO$_2$/Ag
Switching operation	BRS	NRS	BRS	BRS	BRS
R_{on}	90 to 300	~100	300 to 800	~500	100 to 1k
R_{off}	6k to 30k	~100M	4k to 80k	~5M	8M to 1G
V_{on}	0.6 to 1	2.1 to 3.6	0.7 to 1.1	0.6 to 2.1	0.2 to 0.8
V_{off}	1.2 to 1.5	0.8 to 1.5	0.5 to 0.8	0.5 to 1.1	0.2 to 1.1
Endurance	1000	-	600	250	500
t_{on}	10ns	50ns	1µs	50ns	50ns
t_{off}	10ns	100ns	1µs	100ns	50ns
retention	10^7	10^4	10^4	10^7	10^4

Other free-forming devices reported in the literature are in the references [Kurnia2013, Kim2013c, Bishop2012, Kurnia2011, Fang2011, Zhu2009].

1.2.6. Charge Transport

The charge transport in a metal-insulator metal (MIM) or metal- insulator-semiconductor (MIS) structure takes place via different physical mechanism depending of the electrical properties of electrodes and dielectric in a RRAM. The electron transport depends of many properties, for example: the energy barrier height, the presence of traps (levels, density and spacing between them), the charge carrier drift mobility, etc. [Chiu2014]. **Figure 1.10** shows the main charge transport mechanisms based in the band diagram of a MIM or MIS device with possible electron conduction paths. The Schottky emission occurs when the electrically activated electrons on the TE side are injected over the potential barrier (E_b) to the conduction band (E_c), crossing the TMO and reaching the BE (see **Figure 1.10 a)**). The Fowler–Nordheim tunneling occurs when the electrons tunnel from the TE into the conduction band (E_c) usually happens when a high electric field is applied to the device (see **Figure 1.10 b)**). Direct tunneling occurs when the electron cross the TMO (from TE to BE) directly; it usually happens when the TMO is thin enough (see figure **Figure 1.10 c)**). When enough traps are present in the TMO, they introduce additional energies levels (E_t) (for example by the presence of oxygen vacancies); it is possible electron transport by trap-assisted tunneling following the following steps: tunneling from TE to traps (**Figure 1.10 (d)**); Poole–Frenkel emission: an electron in a trap reaches the conduction band generally thermal active (**Figure 1.10 e)**); Fowler–Nordheim: an electron in a trap reach the conduction band by tunneling (**Figure 1.10 f)**); electron hopping or tunneling inter traps, by Mott hopping or

metallic conduction depending of electrons specific positions (specific or extended states respectively) see figure **Figure 1.10 g)**); and tunneling from traps to BE (**Figure 1.10 h)**)[Lim2015, Chiu2014, Wong2012, Yu2011b]. Is important to remark than charge transport mechanisms describe the current in the static states (HRL or LRS) but they not explain the dynamic of creation/destructions of CFs.
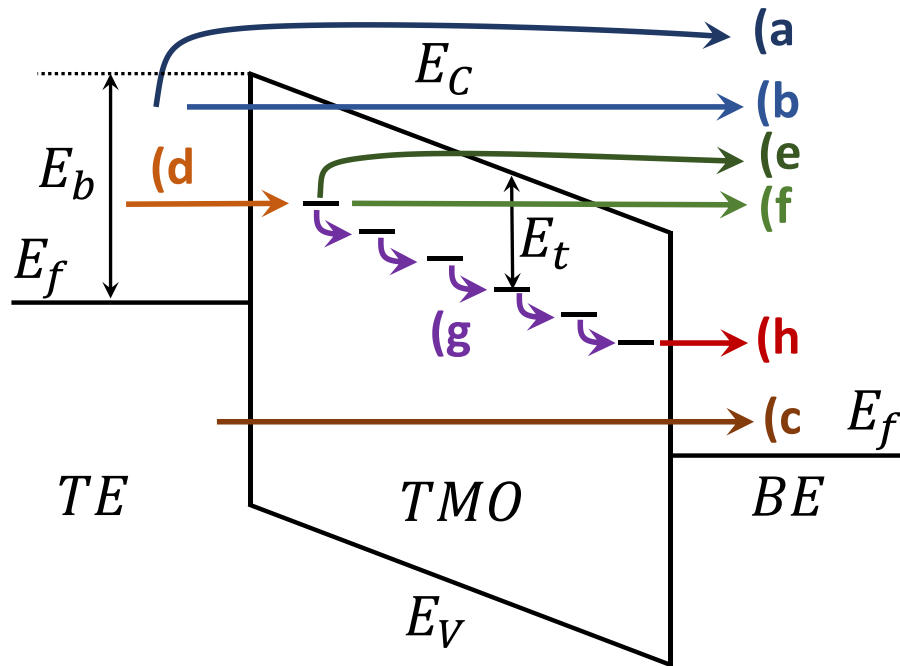
Figure 1.10 Band diagram in a MIM or MIS device with possible electron conduction paths [Lim2015, Chiu2014, Wong2012, Yu2011b]. **a)** Schottky emission **b)** Fowler–Nordheim tunneling **c)** Direct tunneling. **d)** tunneling from TE to traps; **e)** Poole–Frenkel emission **f)** Fowler–Nordheim **g)** inter traps electron hopping or tunneling and **h)** tunneling from traps to BE.

The equations of the main conduction mechanism in resistive switching memory are summarized in **Table 1.VII** and the symbols used are described in [Lim2015, Chui2014, Garcia-Redondo2016,Yen2019].

Table 1.VII. Current density expression of typical conduction mechanisms in dielectric films [Lim2015, Chui2014, Garcia-Redondo2016,Yen2019]

Conduction Mechanism	Expression	
Schottky Emission (SE)	$J_{SE} = \dfrac{4\pi q m^*(kT)^2}{h^3} \exp\left[\dfrac{-q\left(\Phi_B - \sqrt{qE/4\pi\epsilon}\right)}{k_b T}\right]$	(1.16)
Simmons' modified Schottky equation (SM)	$J_{SM} = \alpha_m T^{\frac{3}{2}} E \mu_B \left(\dfrac{m^*}{m_0}\right)^{3/2} \exp\left[\dfrac{-q\left(\Phi_B - \sqrt{qE/4\pi\epsilon}\right)}{k_b T}\right]$	(1.17)
Fowler-Nordheim Tunneling (FN)	$J_{FN} = \dfrac{q^2}{8\pi h \Phi_B} E^2 \exp\left(\dfrac{-8\pi\sqrt{2qm^*}}{3hE}\Phi_B^{3/2}\right)$	(1.18)
Direct Tunneling (DT)	$J_{DT} \approx \exp\left(-\dfrac{8\pi\sqrt{2q}}{3h}(m^*\Phi_B)^{1/2}\kappa t_{eq}\right)$	(1.19)
Poole-Frenkel Emission (PF)	$J_{PF} = q\mu N_C E \exp\left[\dfrac{-q\left(\Phi_T - \sqrt{qE/\pi\epsilon}\right)}{k_b T}\right]$	(1.20)
Space Charge Limited Conduction (SCLC)	$J_{SCLC} = \dfrac{9}{8}\epsilon\mu\theta\dfrac{V^2}{d^3}$	(1.21)
Hopping Conduction (HC)	$J_{Hop} = qanv \exp\left(\dfrac{qaE}{k_b T} - \dfrac{E_a}{k_b T}\right)$	(1.22)
Ionic Conduction (IoC)	$J_{Io} \propto vr\exp\left(-\dfrac{\Delta G^{\neq}}{k_b T}\right)\left\{\exp\left(\dfrac{\frac{1}{2}re}{k_b T}E\right) - \exp\left(-\dfrac{\frac{1}{2}re}{k_b T}E\right)\right\}$	(1.23)
Ohmic Conduction (OhC)	$J_{Oh} = \sigma E = q\mu N_C E\exp\left[-\dfrac{E_C - E_F}{k_b T}\right]$	(1.24)
Nearest Neighbor Hopping (NNH) or fixed range hopping (FRH)	$J_{NNH} = \sigma_0 \exp\left(-\dfrac{T_0}{T}\right)E$	(1.25)
Mott Variable Range Hopping (VRH)	$J_{VRH} = \sigma_0 \exp\left(-\dfrac{T_0}{T}\right)^{\frac{1}{4}}E$	(1.26)
Trap-Assisted Tunneling (TAT)	$J_{TAT} = A \exp\left(\dfrac{-8\pi\sqrt{2qm^*}}{3hE}\Phi_T^{3/2}\right)$	(1.27)
Generalized Trap Assisted (GTA)	$J_{GTA} \propto a_1\left(\dfrac{V}{d}\right)^{a_2}$	(1.28)
Generalized Tunneling (GT)	$J_{GT} = I_o \exp\left(-\dfrac{g}{g_0}\right)\sinh\left(\dfrac{V}{V_0}\right)$	(1.29)
Generalized Tunneling with temperature dependent (GTT)	$J_{GTT} = I_o \exp\left(-\dfrac{g}{g_0}\right)\sinh\left(\dfrac{V}{k_b T V_1}\right)$	(1.30)
Quantum Point Contact (QPC)	$I_{QPC} = \dfrac{2eN}{h}\left\{eV + \dfrac{1}{\alpha}ln\left[\dfrac{1 + \exp\{\alpha(\Phi - \beta eV)\}}{1 + \exp\{\alpha[\Phi + (1-\beta)eV]\}}\right]\right\}$	(1.31)
Shklovskii-Efros percolation (SEP)	$I_{SEP} = I_0 \exp\left(-\dfrac{W_e - \left(\frac{Ce}{d}Va_f V_0^{\gamma}\right)^{\frac{1}{1+\gamma}}}{k_b T}\right)$	(1.32)

1.3. Simulation and Modelling of Memristor and RRAM

The semiconductor industry is continuously introducing new electronic devices to improve circuit performance. In order to gain an in-depth knowledge of the device operation and provide circuit designers with suitable tools, the development of device models and simulation tools is a crucial issue [Panda2018]. General reviews of memristor simulation and modelling are presented in references [Lanza2019, Lekshmi2019, Panda2018, Ielmini2017, Villena2017].

RRAM simulation approaches can be classified according to the degree of accuracy in the description: atomistic or microscopic models (few nm^3), macroscopic solvers (about 100 nm^3 to 1000nm^3) and compact models (several µm^3) [Ielmini2017]. Macroscopic models include kinetic Monte Carlo (kMC) simulators and tools based on the Finite Element Method (FEM), although the former are sometimes classified as microscopic simulation tools [Lanza2019, Lekshmi2019, Panda2018, Ielmini2017, Villena2017].

Each simulation methodology provides different results:

- Atomistic tools can calculate the energy barriers of defects, band structures and other physical material properties.

- kMC models provide I-V characteristics taking into account the inherent stochastic behavior of the processes and provide a plethora of internal variables which are very useful to understand the physics behind resistive switching.

- FEM models can simulate I-V characteristic, variability and noise. The possibility of simulation several devices or even a region of a cross-bar structure is open in this case.

- Compact models calculate the current versus the applied voltage, generally by solving a simplified 1D differential equations. These models allow circuit simulation including several memristors in reasonable computation times.
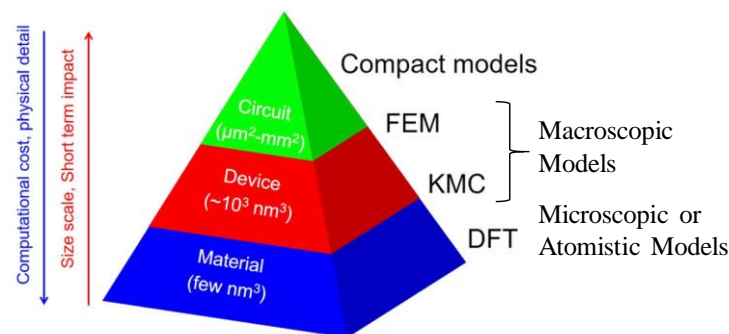
Figure 1.11 Comparison of different approaches for memristor modelling and simulation, as a function of the computation cost, physical detail, scale, and short term impact [Ielmini2017].

1.3.1. Microscopic or Atomistic Description

Microscopic or atomistic models use the density functional theory (DFT) for simulating devices at very low scale, in the range of few nm^3. The goal of this method is to understand the material structure, the ion/atom diffusion processes, the migration mechanisms, the impact of the oxide composition and the influence of defects, among other issues. The simulator calculates physical quantities, e.g., energy barriers for defect generation and migration, band structure, etc. [Ielmini2017]. An example of a simulation result of a Cu/a-SiO$_2$ device is shown in **Figure 1.12**.
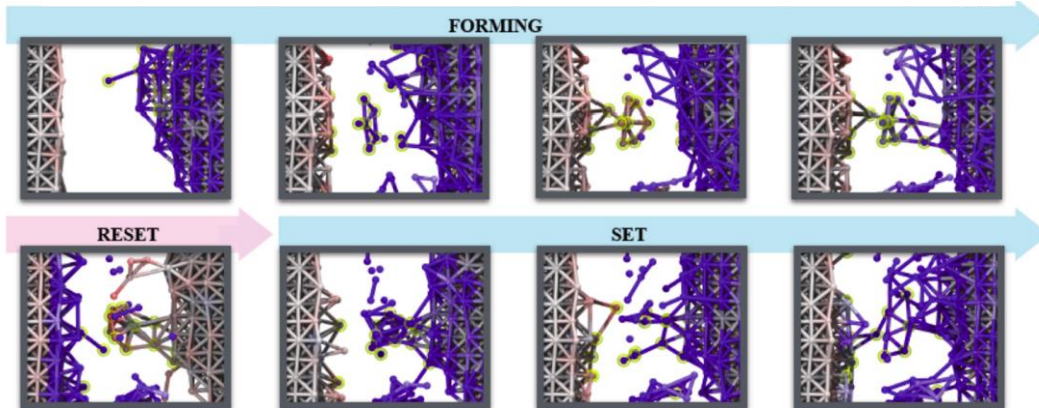
Figure 1.12 Example of a microscopic or atomistic model representation of a Cu/a-SiO$_2$ device with the description of forming, reset and set processes [Ielmini2017, Onofrio2015].

1.3.2. Macroscopic Simulator

Macroscopic simulators describe the RRAM in terms of differential equations that are solved by numeric methods such as Runge-Kutta. As said before, two different approaches can be distinguished: simulators based on the finite elements method (FEM) and kinetic Monte Carlo (kMC) algorithms.

1.3.2.1. Finite Element Method

In the finite element method technique, the device geometry is discretized in a 2D or 3D mesh, and transport, heat and Poisson equations are numerically solved with the corresponding boundary conditions [Ielmini2017, Lanza2019, Villena2017]. Furthermore, for RRAM simulation, ion migration and redox reactions have also to be considered because they determine the conductive filament evolution [Panda2018].

The device is biased with a voltage V_{RRAM}. Each grid point (x, y, z) is characterized by physical local properties, such as: potential φ, temperature T, thermal conductivity K_{th}, thermal lateral dissipation h and electric conductivity σ.

The ion-migration current density J_D, in general, is given by the combination of the drift current density, J_{Driff}, and the diffusion current density, J_{Diff}

$$J_D = J_{diff} + J_{drift} = -D\nabla n_D + \mu E n_D \tag{1.33}$$

where n_D is the ionized defect concentration, D is the ionic diffusion coefficient, E is the applied electric field, and μ is the ionic mobility. The ion diffusivity D is thermally activated following the Arrhenius law (1.34) [Nardi2012], while the ion mobility μ depends on the ionic diffusion coefficient D according to Einstein relation, equation (1.35) [Larentis2012].

$$D = D_0 e^{-\frac{E_A}{k_b T}} \tag{1.34}$$

$$\mu = \frac{qD}{k_b T} \tag{1.35}$$

where T is the temperature, D_0 is a pre-exponential factor, E_A is the energy barrier for hopping transport, k_b is the Boltzmann constant and q is the electron charge.

The electrical conductivity σ at each (x, y, z) point in the device depends on the local defect concentration n_D, which is usually dependent on the temperature according to the Arrhenius law [Larentis2012],

$$\sigma = \sigma_0 e^{-\frac{E_{AC}}{k_b T}} \qquad (1.36)$$

where σ_0 is a pre-exponential factor and E_{AC} is the activation energy for the electrical conduction.

The temperature at each (x, y, z) point in the device is described by the Fourier heat equation given by [Panda2018, Russo2009].

$$-\nabla \times (K_{th} \nabla T) = \rho J^2 \qquad (1.37)$$

Where K_{th} is the thermal conductivity, J is the current density and ρ is the electrical resistivity. If the CF is metallic-like for the charge conduction, the following thermal dependence is assumed [Russo2009]:

$$\rho_{CF}(T) = \rho_{CF0}[1 + \alpha(T - T_0)] \qquad (1.38)$$

where α is the temperature coefficient and ρ_{CF0} is the value of the resistivity at room temperature, T_0.

The evolution of ionized defects concentration, n_D, is determined by the continuity equation for the drift-diffusion [Larentis2012],

$$\frac{\partial n_D}{\partial t} = \nabla \times (D \nabla n_D - \mu E n_D) \qquad (1.39)$$
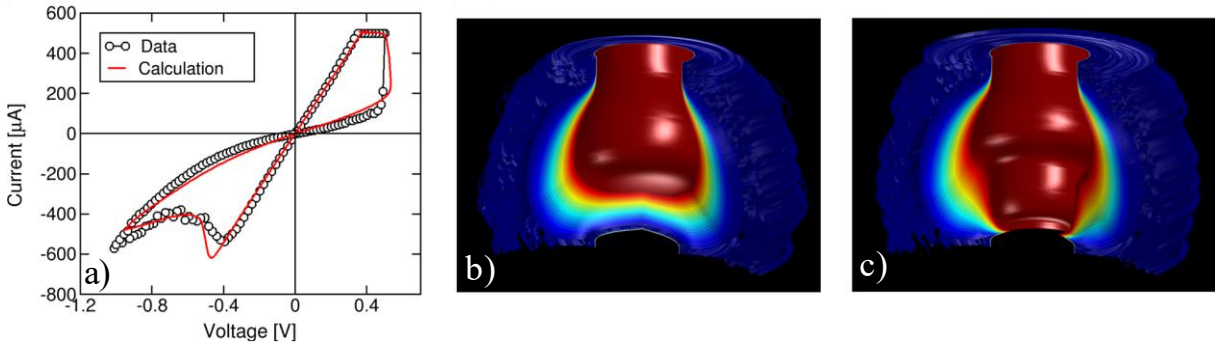
Figure 1.13 Example of FEM simulation of a TiN/HfOx/TiN bipolar RRAM device. **a)** Measured and simulated I-V curve; **b)** concentration of defects in the HLR; c) concentration of defects in the LRS [Ielmini2017, Larentis2012].

1.3.2.2. Kinetic Monte Carlo Simulators

Kinetic Monte Carlo (kMC) simulators take into account the number and position of defects, vacancies or ions and treat them individually following a Monte Carlo approach [Ielmini2017, Lanza2019]. The main difference with respect to FEM simulators is that kMC simulators can describe current fluctuations and the forming process, while FEM simulators describe an averaged behavior [Lanza2019].

For example, in kMC simulators of VCMs, the generation, migration and recombination of oxygen vacancies play a crucial rule in the device operation [Lanza2019]. The oxygen vacancy generation rate G is modelled by an exponential function of the temperature and electric field F given by [Ielmini2017]:

$$G(x,y,z) = \nu \, e^{-\frac{E_A(x,y,z)-bF(x,y,z)}{k_bT(x,y,z)}} \tag{1.40}$$

where ν is the particle vibration frequency, b is the bond polarization factor, k_b is the Boltzmann constant, and E_A is the defect formation effective energy at $F = 0$. The increase of oxygen vacancies results in an increase of trap assisted tunneling current.

Figure 1.14 shows an example of a kMC simulation employed to model a HfO$_x$ bipolar RRAM device following a 2D approach [Yu2011d, Ielmini2017].
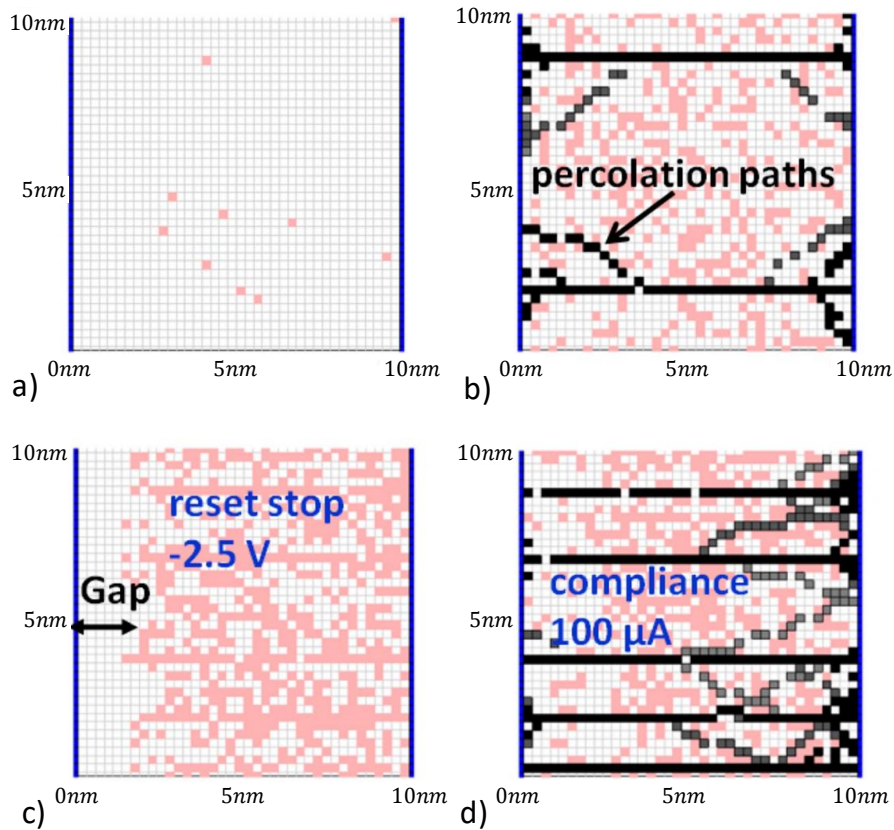
Figure 1.14 Example of kMC model simulation of a 10 nm HfO$_x$ bipolar RRAM device **a)** Initial pristine state **b)** percolation paths created after the forming process **c)** gap produced between the bottom electrode and the tip of conductive filament as a consequence as a consequence of a reset process, **d)** percolation paths created by a positive applied voltage with a compliance current of 100μA [Yu2011d, Ielmini2017].

1.3.3. Memristor Compact Modelling

Modeling of memristors is a key issue in circuit computer-aided design (TCAD). The previous models provide different degrees of accuracy and physical description at the simulation level. In general, a more detailed description implies more computational cost. In some applications, in which the number of devices to simulate is large (for example in a cross-bar architecture of a Kbit or Gbit memory), analytical simple models are required. These models must have very low computational cost and they should be able to work on standard electrical simulators. These models are named compact models if they provide a consistent simulation solution for circuit design [Ielmini2017, Lanza2019, Villena2017].

Compact models provide support to designer of circuits including RRAMs, with a reduced set of equations that describe the device switching characteristics: set/reset voltages and LRS and HRS resistances [Lanza2019, Ielmini2017].

Different review papers of published compact models can be found in references [Lanza2019, Lekshmi2019, Panda2018, Villena2017, Zha2017]. Most of these reviews propose a compact model classification based on two groups: empirical or phenomenological and physically based.

1.4. Applications and Circuits

A large amount of circuits and applications have been reported using memristors. Generally, in the context of analog applications, the term memristor is employed to name the device. However, in the field of digital applications, the term RRAM is widely used, taking into consideration that, as explained at the introduction, the RRAM are a particular case of memristors.

Mazumder et al. presented (Fig. 1 in [Mazumder2012]) a taxonomy of the memristor applications, a classification graph that divided the application of memristors in a primary level, formed by discrete elements and cross bar configurations. The second level of this classification includes analog and digital applications reported for the two previous groups (discrete or cross-bar), see **Figure 1.16** for an uptated taxonomy.

In the next sections, we are going to describe the most representative circuits grouped in digital or analog applications.

1.4.1. Digital Applications

The main use of memristors in digital applications is as non-volatile memories. Ielmini et al. [Ielmini2015] and Yu et al. [Yu2014] showed a pyramidal memory hierarchy with relative data about size, access cycles, speed and cost. On the other hand, **Figure 1.15** shows a memory hierarchy of typical von-Neumann computer system architectures [Wong2015]. This architecture may be inefficient when the memory is used intensely. In fact, access to memory is a bottleneck for computing system performance [Yu2014].

Chen [Chen2016] reported digital applications for implementing different levels of this hierarchy by emerging NVM technologies. For example, L2/L3 cache could be implemented by STTRAMs instead of SRAMs or DRAMs, and the external memory by RRAMs instead of Flash memories.
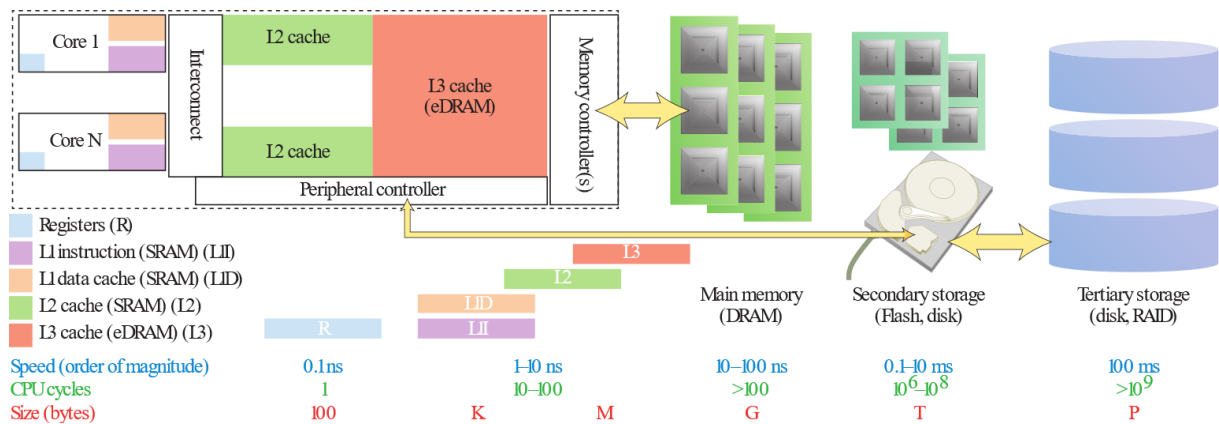
Figure 1.15 Memory hierarchy diagram of typical von-Neumann computer architectures. Data about speed, CPU cycles and size are provided [Wong2015].

In the NVM realm, various prototypes of RRAM memory chips have been fabricated and reported in the literature. Among them, the following can be highlighted:

- Fackenthal et al. [Fackenthal2014] and Zahurak et al. [Zahurak2014], reported a 16Gbits memory using a 27nm CMOS process and a Cu-based/oxide. They obtained a 1GB/s read throughput and a 200MB/s write speed.
- Ma et al. [Ma2015] reported a 16Mbits RRAM array based on a HfOx/CMO device with a 130nm CMOS process technology.
- Other memory circuits can be found in references [Symanczyk2007], [Sheu2009], [Chevallier2010], [Kawabata2010], [Yi2011], [Otsuka2011], [Sheu2011], [Kawahara2012], [Chang2012], [Lee2012], [Liu2013], [Liu2014] and [Pan2015].

Two reviews of RRAM memory prototypes can be found in:

- Table 1 in [Ielmini2016] shows a summary of RRAM prototypes from year 2010 to 2015.
- Figure 11 in [Chen2016] shows a graph with a summary of industry test chips for different emergent technologies (PCM, STTRAM and RRAM). They are compared in terms of capacity versus year (from 2003 to 2015) and considering the technological node used. The emerging memory with more capacity reported up to date is the 32Gbits SanDisk/Toshiba implemented in a 24nm node CMOS technology with RRAMs.

Furthermore, some examples of multi-levels memories have been also published in the context of RRAMs:

- Chen et al. [Chen2015] reported a simple one selector one resistor (1S1R) array structure with prevention of the sneak current path.
- Emara et al. [Emara2014] reported a one transistor two memristor differential memory cell that presents the capability of multilevel operation with 2 bits stored in each RRAM cell.
- Chien et al. [Chien2010] reported a four level (2bits) memory based on RTO WO_x unipolar RRAM devices.
- Ma et al. [Ma2016] reported a seven levels memory based on a $HfO_x/TiO_x/HfO_x/TiO_x$ multilayer RRAM. The levels are obtained by means of different pulse amplitudes with the same duration.

Apart from the use of memristors as memories, other digital applications are found in the literature, such as:

- Programmable logic circuits [Rose2012].
- Non-Volatile FPGAs [Gaillardon2012].
- Content addressable memories [Eshraghian2011].
- Logic gates:
  - Implication logic [Kim2011, Bickerstaff2010, Lehtonen2009].
  - Threshold logic [Rajendran2010].
  - Normally-off Logic Based on Resistive Switches [Balatti2015].
- Nonvolatile ternary content-addressable-memory (nvTCAM) 3T1R [Chang2017, Chang2015], 4T2R [Chang2016b] [Huang2014].
- RRAM-based 7T1R nvSRAM using HfO_x RRAM and a 90nm CMOS process [Lee2015b].

Finally, Wu et al. [Wu2019] reported a microcontroller made with a 130nm silicon CMOS process, with a RRAM instruction memory of 12Kbyte, a RRAM data memory of 4Kbyte and 8Kbyte of SRAM. The chip was designed for multibit operation and it was able to store five resistance levels in each cell. It was used for control, machine learning and cryptography applications.

1.4.2. Analog Applications.

Some review studies on analog applications and circuits with RRAMs can be found in the following papers:

- [Chen2016] presented and summarized emerging memories technologies (PCM, STTRAM, FeFET and RRAM), distinguishing two kinds of analog categories: neuromorphic applications and hardware security.
- Carboni et al. reviewed the current state of the art regarding hardware security [Carboni2019], and provided an overview of security applications: pseudo-true random number generator (PRNG) and true random number generator (TRNG) as hardware primitives for providing secret keys for physical unclonable functions (PUF); and neuromorphic and stochastic computing systems where memristors act as a source of entropy.

1.4.2.1. General Purposes Analog Memristor Circuits

Some analog applications have been reported in the literature:

- Chaotic circuits [Xiong2016, Zhao2016, Vaidyanathan2015, Lu2014, Chua2014, Sun2013b, Li2013b, Wen2013, Buscarino2012, Muthuswamy2010, Driscoll2011, Iu2011a, Wen2011, Bao2011, Lehtonen2010a, Muthuswamy2010b, Muthuswamy2009].
- Programmable resistors [Shin2009].
- Oscillator [Itoh2008].
- Analog filters [Ascoli2013, Wang2009, Corinto2012, Iu2011b, Driscoll2010].
- Programmable gain amplifiers [Sangho2011, Shin2011, Pershin2010b].
- RF switches [Gregory2015].
- Receivers for ultra-wide band wireless systems [Witrisal2009a, Witrisal2009b].
- Image encryption [Yang2015, Duan2013, Lin2010, Lin2009] and image processing [Shim2016, Secco2016].
- Nanofabricated wires for biosensing purposes [Carrara2012, Sacchetto2011].
- Programmable threshold comparators and Schmitt triggers [Pershin2010b].

1.4.2.2. Neuromorphic Circuits

Neuromorphic circuits emulate the behavior of biologic nervous systems. Specifically, memristor behavior is analogous to synaptic plasticity. Therefore, in the last years, a great amount of neuromorphic circuits based on memristors have been published. Among them, the following can be cited:

- Neuromorphic circuits: [Milo2019, Chang2016, Chang2013, Kosta2011, Yu2012, Yu2011, Shi2011, Pershin2010, Pershin2009].
- Artificial synapses: [Indiveri2013, Waser2007, Pershin2010, Ambrogio2016].
- Cellular nonlinear networks: [Lehtonen2010b].

1.4.2.3. In-Memory Processing Memristor Circuits

Other kind of analog circuits (named in-memory processing designs) are related to non-Von Neumann architectures. For example, the following applications can be cited:

- Song et al. [Song2018] used RRAMs to build blocks to perform matrix-vector multiplications in an accelerating graph processing (named GraphR).
- Kvatinsky et al. [Kvatinsky2014] described the IMPLY logic based on memristors and with this logic primitive, they implemented an 8 bits full adder.

- Bojnordi et al. [Bojnordi2017] used RRAMs in a Boltzmann machine, which is a parallel computational model capable of solving a broad class of combinatorial optimization problems and deep learning.
- Shafiee et al. [Shafiee2016] presented "ISAAC", an architecture that uses memristors in a crossbar array to store input weights of convolutional neural networks.
- Song et al. [Song2017] presented "PipeLayer", an architecture based on a RRAM array accelerator for deep learning.
- Qiao et al. [Qiao2018] presented "Atomlayer", an architecture based on a RRAM crossbar accelerator for deep neural networks (DNNs). The ReRAM crossbar is employed to perform vector-matrix multiplication in the analog domain.
- Pedró et al. [Pedro2019] proposed a Self-Organizing Neural Network based on a crossbar architecture of TiN/Ti-HfO$_2$-W devices under a fully unsupervised training.

1.4.2.4. Circuits for Cryptographic Purposes

True random number generators are an essential component of cryptographic hardware. They are used, for example, for generating keys in mobile phones or Internet of Things (IoT) devices [Huang2012], smart cards [Liu2016], radio frequency identification (RFID) applications [Balachandran2008] or in data encryption for secure communication systems [Huang2012, Yang2015].

The entropy source of random number generator could be based on thermal noise [Chen2015], phase jitter [Liu2016, Balachandran2008], trapping and detrapping processes in oxide defects [Brederlow2006, Fujita2004], and random telegraph noise (RTN) in resistive memories [Arumi2016, Wei2016].

To conclude this section, **Figure 1.16** shows a taxonomy of memristor applications in digital and analog contexts (updated from [Mazumder2012]).

Memristor Aplications

Crossbar
- **Analog**
  - Neuromorphic Networs
  - Field Programmable Array
- **Digital**
  - Content Addresable Memory — NVTCAM
  - Nonvolatile memory
    - Vertical stack
    - Horizontal stack
  - NVRAM
    - 1T1R
    - 1D1R
    - 1TNR — 1T4R, 1T8R
  - NVSRAM
    - 4T2R
    - 6T2R
    - 7T2R
    - 8T2R
  - Logic Circuits
    - 7T1R

Discrete
- **Analog**
  - Programmable resistor
  - Chaos circuits
  - Schmitt trigger
  - Variable gain amplifier
  - Difference comparator
  - Cellular Neural Networks
  - Oscilators
  - Analog filter
  - RF switches
  - Image
    - Processing
    - Encription
- **Digital**
  - Logic operations
  - Digital gates
  - Reconfigurable logic circuits
    - Implication logic
    - Theshold logic — AND, OR, NAND,XOR,XNOR
    - Rationed logic
    - Normally-off logic
      - single pulse
        - AND
        - implication
        - NOT
        - bit transfer
      - Multiple pulse
        - OR, XOR

Figure 1.16 Taxonomy of memristor applications (updated from reference [Mazumder2012]).

Modeling of Conductive Bridge RRAMs

2.1. Introduction

This chapter reviews the two main models of conductive bridge RRAMS previously described in the literature and presents a new model, named UGR-CB.

The IM2NP model assumes that the dynamic evolution of the conductive filament (CF) is based on redox chemical reactions in the surface between the insulator and the CF. The conductive filament is described as a resistor with cylindrical shape, heated by the current by Joule effect. In addition to the current through the CF, a trap assisted current component through the oxide layer is also assumed [Bocquet2013, Bocquet2014b].

The IM2NP-EF model is similar to IM2NP, but it includes an electroforming process described by an intermediate switching sub-oxide layer represented geometrically by a cylinder with an electrical conductivity greater than the electrical conductivity of the oxide in the pristine state [Bocquet2014].

The new model for bipolar RRAMs, UGR-CB, has been developed and implemented in Verilog-A code within ADS circuit simulator. The model is based on redox and diffusion processes and describes in detail the physics behind the filamentary resistive switching mechanisms in the CB-RRAMs under study. It assumes truncated-cone shaped filaments as a close but simple representation of the real conductive filament geometry. A detailed thermal approach has been developed: instead of an unique temperature for describing the thermal state of the filament, two temperatures have been considered to achieve a better thermal description of the conductive filament. One temperature is linked to the narrowest part of the CF, where the rupture process takes place. The other one describes the thermal state of the main part (the widest part) of the CF body [González-Cordero2016a].

Current measurements in DC and pulsed voltage regimes in Ti/ZrO$_2$/Pt RRAM devices have been used in order to tune and validate the model. The model results show a good agreement with experimental data. The flexibility of the model is illustrated by a simulation of a device with multiple conductive filaments. And finally, the potential application of the devices as memories is tested by means of the simulation of a 1T1R memory cell.

2.2. Compact Model of Bipolar CB-RRAM (IM2NP)

This compact model was proposed by Bocquet et al. [Bocquet2013, Bocquet2014b] and it uses a physically based macroscopic approach for redox memories, which covers Conductive Bridge RAM (CBRAM) and Oxide Resistive RAM (OxRAM) bipolar devices.

The CF is represented by a cylinder that connects the top electrode with the bottom electrode through the insulator (see **Figure 2.1**). Its radius, r_{CF}, is the internal variable that determines the CF state and it is changed according to the rates of the redox processes. The conduction in the CF is assumed to be ohmic. Therefore, electrical conductivities of the CF and the surrounding oxide are considered, σ_{CF} and σ_{Ox}, respectively.
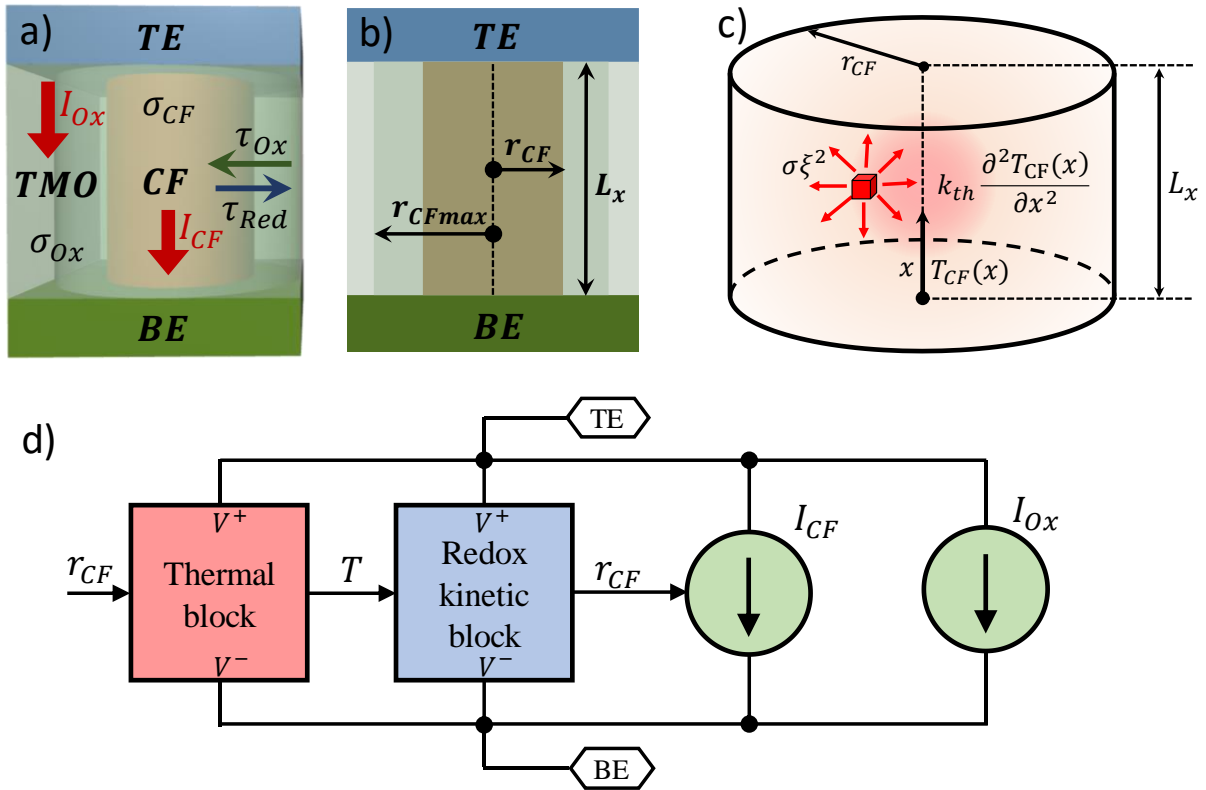
Figure 2.1 a) Three-dimensional view of the cylindrical structure of the CF assumed by the IM2NP model. The creation/destruction of the CF in the TMO depends on the kinetics of the redox processes. **b)** Geometrical parameters involved in the model. **c)** Thermal representation of the CF. **d)** Electrical sub-circuit used for implementing the IM2NP model.

Initially $r_{CF} \approx 0$ and the device is in the HRS. The conduction mechanism in the oxide is described by a generalized function for describing trap assisted tunnel current through the oxide, I_{Ox}, (equation (1.28)) in the IM2NP model [Bocquet2013]

$$I_{OX} = A_{HRS} \cdot S_{Cell} \cdot \left(\frac{V_{cell}}{L_x}\right)^{\alpha_{HRS}} \tag{2.1}$$

Where A_{HRS} and α_{HRS} are fitting parameters, S_{Cell} is the area of the device, V_{Cell} is the applied voltage between the top and the bottom electrode and L_x is the oxide thickness. This current component only depends on the applied voltage V_{cell} at simulation time. It is dominant in the HRS, but negligible in the LRS. In the circuital representation of the model (see **Figure 2.1 d**), it corresponds to the current source, I_{OX}.

An ohmic conduction mechanism is assumed in the LRS, with and equivalent resistance R_{eq} that takes into account the region formed by the CF (bounded by the radius r_{CF} and with an electrical conductivity σ_{CF}) and the surrounding oxide region (until the radius r_{CFmax}, with electrical conductivity σ_{Ox}). More details can be found in Appendix B.1. Therefore, the current in the device can be calculated as [Bocquet2013, Bocquet2014b]

$$I_{CF} = \frac{V_{cell}}{R_{eq}} = \frac{V_{cell}}{L_x}[r_{CF}^2 \cdot \pi \cdot (\sigma_{CF} - \sigma_{Ox}) + r_{CFmax}^2 \cdot \pi \cdot \sigma_{Ox}] \tag{2.2}$$

At simulation time, this current component depends on the applied voltage V_{cell} and the CF radius, r_{CF}. The other parameters are constant: geometrical parameters (L_x, r_{CFmax}) as well as electrical properties of the device materials (σ_{CF}, σ_{Ox}). In the sub-circuit representation (see **Figure 2.1 d)**, this current is calculated by the dependent current source I_{CF}.

The size of the CF (r_{CF}) depends on the electrochemical oxidation/reduction rates at the interface between the CF and the surrounding oxide. It is governed by the Butler-Volmer equation [Oldham2011, Bard2001, Allen2002]. The SET process begins when the CF is increased by a dominant electrochemical reduction rate, described by the next equation [Bocquet2013, Bocquet2014b]

$$\frac{1}{\tau_{Red}} = A_{RedOx} \cdot e^{-\frac{E_a - q \cdot \alpha_{Red} \cdot V_{cell}}{k_b T}} \tag{2.3}$$

On the other hand, the RESET process occurs when the CF is narrowed down by a dominant electrochemical oxidation rate described by the following equation [Bocquet2013, Bocquet2014b],

$$\frac{1}{\tau_{Ox}} = A_{RedOx} \cdot e^{-\frac{E_a + q \cdot \alpha_{Ox} \cdot V_{cell}}{k_b T}} \tag{2.4}$$

In these equations, τ_{Red} (τ_{Ox}) is the time constant for the electrochemical reduction (oxidation) rate, A_{RedOx} is the nominal redox rate, E_a is the activation energy, q is the electron charge, α_{Red} and α_{Ox} are the transfer coefficients (with values between 0 to 1), k_b is the Boltzmann constant, T is the device temperature and V_{cell} is the applied voltage. Note that electrochemical reduction/oxidation rates depend on the applied voltage (V_{cell}) and the local CF temperature (T). In this simple thermal model we assume that the device temperature is the same than the CF temperature. The sign of the applied voltage in expression (2.3) and (2.4) makes one of the processes dominate over the other one. See Appendix B.3. for more details.

The rate of the CF radius change is calculated by means of the next equation [Bocquet2013, Bocquet2014b]

$$\frac{dr_{CF}(t)}{dt} = \frac{r_{CFmax} - r_{CF}(t)}{\tau_{Red}} - \frac{r_{CF}(t)}{\tau_{Ox}} \tag{2.5}$$

In order to increase the simulator efficiency, a recursive equation in terms of r_{CF} is used (See Appendix B.5. for details)

$$r_{CF_{i+1}} = \left(r_{CF_i} - r_{CFmax} \cdot \frac{\tau_{eq}}{\tau_{Red}}\right)e^{-\Delta t/\tau_{eq}} + r_{CFmax} \cdot \frac{\tau_{eq}}{\tau_{Red}} \tag{2.6}$$

Where τ_{eq} is defined as,

$$\tau_{eq} = \frac{\tau_{Red} \cdot \tau_{Ox}}{\tau_{Red} + \tau_{Ox}} \qquad (2.7)$$

The redox kinetic block in the IM2NP model is implemented with the equations (2.3), (2.4), (2.6) and (2.7) (see **Figure 2.1 d).**

The temperature evolution inside the cylinder-shaped CF is calculated by solving the heat equation [Bocquet2013, Bocquet2014b]

$$\sigma_{eq} \cdot \xi^2 = -K_{th} \frac{\partial^2 T(x)}{\partial x^2} \qquad (2.8)$$

Where σ_{eq} is the equivalent electrical conductivity (see appendix B.1. for details), ξ is the electric field applied, $T(x)$ is the temperature across the x axis defined in the **Figure 2.1 c**), and K_{th} is the thermal conductivity. With boundary conditions $T(0) = T(L_x) = T_0$ is determined the location of x that corresponds to maximum temperature ($\text{T}(x) = T_{max}$ when $x = L_x/2$), and this is used to thermally characterize the device [Bocquet2013, Bocquet2014b] (see appendix D.3.).

$$T_{max} = T_0 + \frac{V_{cell}^2}{8 \cdot K_{th}} \cdot \sigma_{eq} \qquad (2.9)$$

$$\sigma_{eq} = (\sigma_{CF} - \sigma_{Ox}) \frac{r_{CF}^2}{r_{CFmax}^2} + \sigma_{Ox} \qquad (2.10)$$

Where T_0 is the room temperature. At simulation time, the temperature depends on the applied voltage (V_{cell}) and the CF radius (r_{CF}). The other parameters are constant: geometrical parameter, r_{CFmax}, electrical properties (σ_{CF}, σ_{Ox}) and thermal characteristics (K_{th}, T_0) of the device. The thermal block in the IM2NP is implemented by means of equations (2.9) and (2.10) (see **Figure 2.1 d**)

The IM2NP model is fully compatible with electrical simulators based on SPICE. **Figure 2.1d**) shows the model block diagram. Only two current sources are needed: I_{Ox} is an independent current source and I_{CF} is a current source that depends on the radius, r_{CF}, as explained above. The two subcircuits employed are: the thermal block that is electrically activated (V_{cell}) and depends on the CF radius (r_{CF}) and provides the CF temperature (T), and the redox kinetic block that is electricaly activated (V_{cell}) and depends on the CF temperature (T), and calculates the CF radius (r_{CF}) at every time.

Figure 2.2 shows the simulation results obtained by the IM2NP model implemented in SPICE when a ramped voltage is applied to the device. The initial state of the device is the HRS (the current is low and r_{CF} is close to 0.25nm). When the voltage is increased the set process begins, the temperature increases and the radius r_{CF} reaches the maximum value (4nm in this example), and the device state changes to LRS, while the current goes up. If the voltage polarity is reversed, the reset process is triggered and the CF radius decreases as well as the device current.
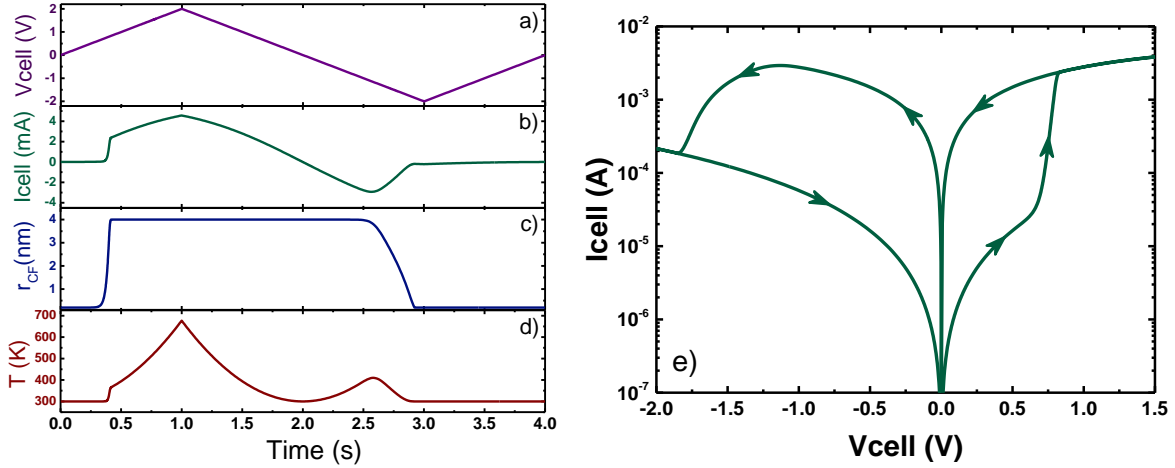
Figure 2.2 a) Triangular applied voltage. IM2NP model implemented in SPICE has been used in order to calculate: **b)** current versus time response, **c)** transient evolution of internal variable r_{CF}, **d)** evolution of CF temperature, T, and **e)** semi logarithmic I-V curve.

2.3. Compact Model of CBRAM with Electroforming Process (IM2NP-EF)

Bocquet et al. introduced the electroforming process in the model described previously [Bocquet2014]. The cell structure is shown in the **Figure 2.3 a)**. The IM2NP-EF model assumes a pristine oxide layer in an initial resistance state (IRS) with very low electric conductance. The electroforming process creates progressively a cylinder with radio r_{CFmax} between the TE and the BE, named switchable sub-oxide, with a conductivity σ_{Ox} that stimulates the creation/destruction of the CF. Finally, a second cylinder with radio r_{CF} (used as an internal variable) and electrical conductivity $\sigma_{CF} \gg \sigma_{Ox}$ emulates the region where RS takes place. **Figure 2.3 b**) shows the sub circuit diagram of the IM2NP-EF model with electroforming process.
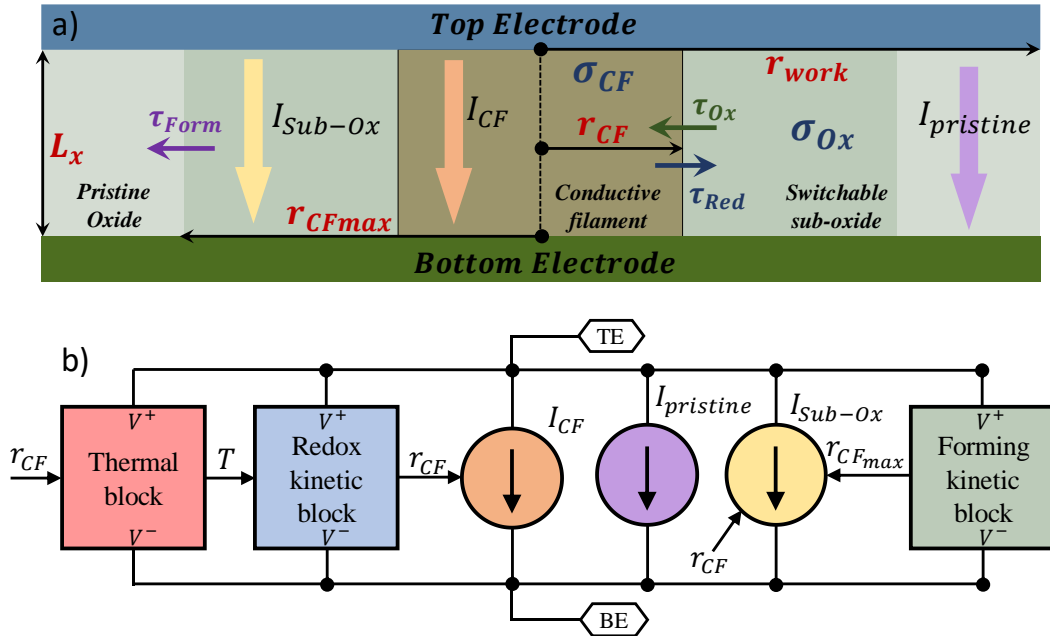
Figure 2.3 a) Cross section of a RRAM device, showing an sketch of the main components considered by the IM2NP-EF model: oxide region (pristine oxide, conductive filament and switchable sub-oxide), path currents ($I_{pristine}$, I_{Sub-ox} and I_{CF}), main geometric dimensions (r_{work}, r_{CFmax}, r_{CF} and L_x), electrical conductivities (σ_{CF} and σ_{Ox}) and the time constants of the electrochemical proccesses (τ_{Red}, τ_{Ox}, τ_{Form}) that determine the time evolution of the radii r_{CF} and r_{CFmax}. **b)** Sub-circuit diagram of the IM2NP-EF model with electroforming process.

In a fresh device the model assumes that the rate of change of r_{CFmax} is expressed as [Bocquet2014]

$$\frac{dr_{CF_{max}}}{dt} = \frac{r_{work} - r_{CF_{max}}}{\tau_{Form}} \qquad (2.11)$$

where r_{work} is the maximum radio admitted in the electroforming process and τ_{Form} is defined by the equation [Bocquet2014]

$$\tau_{Form} = \tau_{Form0} \cdot e^{\frac{E_{aForm} - q \cdot \alpha \cdot V_{cell}}{k_b T}} \qquad (2.12)$$

where τ_{Form} is the electroforming rate, E_{aForm} is the electroforming activation energy , τ_{Form0} is the pre exponential forming rate and α is the transfer coefficient (with values between 0 to 1).

Solving the differential equation (2.11) in a recursive way, the following equation in terms of $r_{CF_{max}}$ is obtained,

$$r_{CF_{max_{i+1}}} = \left(r_{CFmax_i} - r_{work}\right)e^{-\Delta t/\tau_{Form}} + r_{work} \qquad (2.13)$$

The current that flows into the switching sub-oxide layer is determined by the resistance of the hollow cylinder delimited by the radii r_{CFmax} and r_{CF} (see **Figure 2.3 a**) and whose height is given by the oxide thickness L_x. Taking into account the electrical conductivity σ_{Ox}, this current can be expressed as [Bocquet2014]

$$I_{Sub-Ox} = \xi \cdot \pi \cdot \sigma_{Ox} \cdot (r_{CFmax}^2 - r_{CF}^2) \qquad (2.14)$$

where ξ is the electric field applied between the top and bottom electrodes,

$$\xi = \frac{V_{cell}}{L_x} \qquad (2.15)$$

The current component through the CF is determined by a cylindrical resistance with radio r_{CF} and height L_x, and electrical conductivity σ_{CF} [Bocquet2014]:

$$I_{CF} = \xi \cdot \pi \cdot \sigma_{CF} r_{CF}^2 \qquad (2.16)$$

The pristine current component is assumed to be linked to tunnel conduction mechanisms and it is calculated by [Bocquet2014]:

$$I_{Pristine} = S_{Cell} \cdot A \cdot \xi^2 e^{-B/\xi} \qquad (2.17)$$

where S_{Cell} is the device area and A and B are defined as [Bocquet2014]:

$$A = \frac{m_e \cdot q^3}{8 \cdot \pi \cdot h \cdot m_e^{ox} \cdot \phi_b} \qquad (2.18)$$

and

$$B = \begin{cases} \frac{8\pi\sqrt{2m_e^{ox}}}{3hq}\left[\phi_b^{3/2} - (\phi_b - qL_x\xi)^{3/2}\right] & if \quad \phi_b \geq qL_x\xi \\ \frac{8\pi\sqrt{2m_e^{ox}}}{3 \cdot h \cdot q}\phi_b^{3/2} & if \quad \phi_b < qL_x\xi \end{cases} \qquad (2.19)$$

where m_e is the effective electron mass in the electrode, m_e^{ox} is the effective electron mass into the oxide layer, h is the Planck constant and ϕ_b is the metal-oxide barrier height.

The equivalent electrical conductivity is reformulated taking into account the new oxide regions, and it is expressed as [Bocquet2014] (See Appendix B.2. for details)

$$\sigma_{eq} = \sigma_{CF} \cdot \frac{r_{CF}^2}{r_{work}^2} + \sigma_{Ox} \cdot \frac{r_{CFmax}^2 - r_{CF}^2}{r_{work}^2} \qquad (2.20)$$

Table 2.I summarizes the equations of the IM2NP-EF compact model with electroforming process, implemented following the circuit diagram of **Figure 2.3**.

Table 2.I Summary of equations of the CB-RRAM compact model with electroforming process

Block	Equations	Comment
Redox kinetic block	(2.3),(2.4)	now $\alpha_{Red} = \alpha$ and $\alpha_{Ox} = 1 - \alpha$
Forming kinetic block	(2.12), (2.13)	
Thermal block	(2.9),(2.20)	new equivalent electrical conductivity
Depended source current I_{CF}	(2.16),(2.15)	
Depended source current I_{Sub-ox}	(2.14),(2.15)	
Source current $I_{pristine}$	(2.17),(2.15),(2.18),(2.19)	

2.4. New Bipolar CB-RRAM Compact Model (UGR-CB)

González-Cordero et al. presented a new compact model (UGR-CB) implemented in Verilog A code with ADS circuit simulator for Bipolar CB-RRAMs [González-Cordero2016a]. The main characteristics of this model are:

1. The CF evolution in our model is based on the description of redox chemical reactions by means of the Butler-Volmer equation [Allen2002, Oldham2011, Bard2001, Bocquet2013, Bocquet2014, Bocquet2014b] that modifies the geometrical shape of the CF behind the operation of the modeled RRAM.

2. The CF shape is based on a truncated-cone [Lee2015, Villena2014, Wu2013, Kwon2010] with two variable radii (top r_{CF_T} and bottom r_{CF_B}), which vary independently depending on the applied voltage and the thermal state of the filament.

3. The CF temperature in our model is computed analytically after solving the heat equation in an equivalent simplified structure, taking into account Joule heating and lateral heat dissipation (Villena2013). Our approach considers two relevant temperatures, T_{CF_T} and T_{CF_B}, in order to describe the thermal behavior of the filament. More details can be found in Appendix D.5.

4. Three current paths are considered by the model: two linear components (resistances R_{CF} and R_{OX}, which are calculated and described in detail in Appendix C.4.3. and C.4.4. respectively) and one nonlinear current contribution, I_{OX} [Bocquet2013] (equation (2.1)).

In order to validate the model, we used a fabricated device Ti/ZrO$_2$/Pt RRAM structure with 100x100µm^2 area (details about the devices and their fabrication and measurement processes can be found in section A.1. Ti/ZrO$_2$/Pt Device). Two different electrical characteristics were considered in order to fit the model:

1. Hundreds of DC electrical characteristics (I-V curves) measured with a semiconductor characterization system (Keithley 4200-SCS).

2. Pulsed operation measured with the help of an Agilent B1525A HV-SPGU pulse generator and a Tektronix DPO7140 digital oscilloscope for displaying and recording the pulsed response of the device under test.

Finally, once the model was properly calibrated, it was used for simulating a basic 1T1R memory cell [Sheridan2011] and a RRAM device with multiple CFs.

This section was published in González-Cordero et al. Semiconductor Science and Technology, the accepted preprint paper is presented below.

González-Cordero et al. Semiconductor Science and Technology (2016)

Quality metrics

Data base	Rating	Quartile
Web of Science	Impact factor: 2.3	Q2
Scimago	Scientific journal ranking: 0.793	Q1

Publication citations

Google Scholar	Web of Science
24	**19**

A new model for bipolar RRAMs based on truncated cone conductive filaments, a Verilog-A approach

Authors: [1]G. González-Cordero, [1]J.B. Roldan, [1]F. Jiménez-Molinos, [2]J. Suñé, [3]S. Long, [3]M.Liu

Address:

[1]Departamento de Electrónica y Tecnología de Computadores. Universidad de Granada. Facultad de Ciencias. Avd. Fuentenueva s/n, 18071 GRANADA, Spain. Email: jroldan@ugr.es
[2]Departament d'Enginyeria Electrònica, Universitat Autònoma de Barcelona, Bellaterra 08193, Spain
[3]Lab of Nanofabrication and Novel Device Integration, Institute of Microelectronics, Chinese Academy of Sciences, Beijing 100029, People's Republic of China

ABSTRACT

A new model for bipolar resistive random-access memories (RRAMs) is presented in this manuscript. Redox and diffusion processes are used to describe in detail the physics behind the filamentary resistive switching (RS) mechanisms of the RRAMs under study. The model includes truncated-cone shaped filaments which are known to be close to the real conductive filament geometry and a detailed thermal approach, where two temperatures are considered to describe the rupture process at the conductive filament narrowest part and also the main CF body electrical conductivity variations. Ti/ZrO$_2$/Pt RRAM devices have been fabricated and measured, the model allowed us to reproduce the experimental data for all the cases analyzed. Finally, the model has been implemented in Verilog-A code within the ADS circuit simulator, the response of a device to pulsed external voltages within a characterization circuit has been simulated obtaining good results when compared with experimental measurements.

I. INTRODUCTION

Resistive switching memories (RRAMs) are considered one of the most promising non-volatile memory emerging technologies [1-4], along with other technologies such as phase change memories (PCM) [5, 6] and Spin-transfer torque RAMs (STT-RAM) [7]. RRAMs show an operation based on Resistive Switching phenomena which were first characterized in the sixties [3]. Among other important features we can list the following: low program/erase currents, fast speed (switching times $\sim 1ns$), good endurance and retention, viability for 3D memory stacks, ease of integration in the back end of line of standard CMOS processes and multilevel cell storage capability [2, 3, 4, 8, 9]. Their potential to substitute the main non-volatile memory technology based on flash devices is great, and the previously mentioned encouraging characteristics have been obtained for a wide variety of RRAM technologies, combining different oxides and electrodes [3, 4]. In addition, the success obtained for single devices have also been proved in the arena of complete memory chips [10]. This latter fact shows the real potential of this technology for the coming years.

Different resistance states can be measured in RRAMs based on metal oxides. In general, these states are connected with filamentary conduction; i.e., linked to the formation and rupture of one or several conductive filaments (CFs) [3, 11-16]. A low resistance state (LRS) is achieved if a CF is formed, it can be switched to a high resistance state (HRS) by the partial dissolution of the CF (reset). The HRS can be turned back again to the LRS through a set process. A deep analysis of the switching mechanisms and the physics involved in different RRAMs structures can be found in [3, 4, 9].

As we have pointed out above, successful applications of RRAM devices in the integrated circuit terrain have already been reported [10]. In this respect, and in order to go on along this promising path, the scientific community has to provide the means to accurately include RRAMs in the circuit design with a high number of components. To do so, good circuital models are needed. Apart from a good description of the physics behind RS mechanisms, these models have to address the occurrence of fluctuations on the characteristics of the different resistive states that lead to device-to-device and cycle-to-cycle variability [3, 17-20]. The role of thermal effects in their operation needs also to be included [21, 22].

Several SPICE models for RRAM simulation have been reported so far, the following references can be counted among them [14, 15, 23-28]. Few of these models for RRAMs include explicitly the device temperature as a variable that changes at simulation time [14, 25, 27, 28]. In general, the real shape of the CFs in the RRAM models reported above is not considered because of the algebraic difficulties that poses the solution of the equations that connect the device electric and thermal behavior with the CF dynamics. In fact, only one of the latter references uses filaments including different branches [14]; nevertheless, neither set processes nor the CF dynamics were implemented in this latter model. In one of these models [27, 28] the CF temperature is calculated at simulation time; however, the shape of the CF is assumed to be cylindrical. Although this geometric approximation is reasonable from a modeling approach, recent experimental works have shown that real CFs can be better approximated if truncated cone shapes were considered [4, 12, 29, 30]. Moreover, since some of the mechanisms behind RS are linked to cation or anion migration [3], and also to oxygen vacancies migration [4], the CFs could grow either from one electrode (active electrode in some cases) to the other (counter electrode) or vice versa; if this is so, a truncated-cone shaped CF seems to be more appropriate than a regular cylindrical CF to approximate real CF shapes [3, 4].

In most CFs the rupture is produced in a narrow section because of the self-accelerated process [11, 22, 31] that takes place when the temperature rises at the CF narrowing. The temperature rise is due to the increase of Joule heating produced by the concentration of current lines at this point. Therefore, a reasonable approach from the physical viewpoint would need a description of the temperature all along the CF since the thermal behavior at each CF region is essential. Nevertheless, from a circuital model viewpoint these description would mean the point-to-point solution of the heat equation for each device and this time-consuming scheme has to be discarded if thousands of RRAMs are going to be simulated in a standard memory circuit. As pointed out before, some authors have used a single temperature value to represent the device thermal behavior. Taking into consideration the complexity of the thermal distribution in a RRAM close to the set/reset points [22, 12], a more detailed description would be desirable, but accounting for the trade-off of simplicity-accuracy that is always present in circuital modeling, for our model we propose the use of two different temperatures: the first one to approximate the main CF body that is not destroyed in a reset process (this value allows the calculation of the CF main body electrical conductivity variation with temperature), the other to describe the CF narrowing. In truncated-cone shaped CFs we could associate these two temperatures with the wide region of the truncated cone and the narrow one, as will be shown in the next section.

We have included the characteristics reported above in the model we present here. To do so, we extended a previous model [28] to incorporate truncated-cone shaped CFs (including different temperatures at each of the CF regions, calculated at simulation time), among other features. We have validated our model by comparing with experimental measurement [32]. The differences of this model with a simpler model based on cylindrical CFs will be also shown for comparison.

The paper is organized as follows: in section II we describe the experimental devices, in section III the model and physics behind it are explained, in section IV the main results are discussed and finally some conclusions are drawn in section V.

II. DEVICE FABRICATION AND MEASUREMENTS DESCRIPTION

The devices used in this manuscript correspond to Ti/ZrO$_2$/Pt RRAM structures with 100x100 µm^2 area. The bottom electrode (BE) was made of a Ti/Pt layer, later a 15-nm-thick ZrO$_2$ layer was grown by ion-beam sputtering and finally a 10/70-nm-thick Ti/Pt layer above the oxide was employed as the top electrode (TE). More details in connection with the sample fabrication are given in [32].

The DC electrical characteristics are shown in Figure 1. They were obtained making use of a Keithley4200-SCS semiconductor characterization system, the bias voltage was applied on the TE while the BE was grounded. Pulse operation was also analyzed [32] by using an Agilent B1525A HV-SPGU pulse generator and a Tektronix DPO7104 digital oscilloscope.
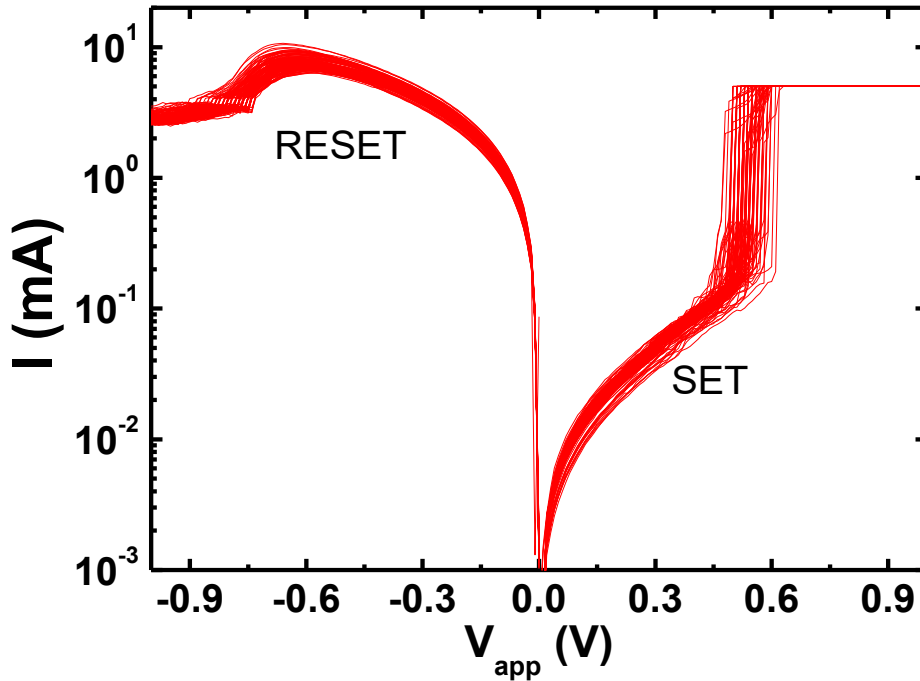
Figure 1. Experimental *I–V* curves of 128 continuous set/reset processes in a Ti/ZrO$_2$/Pt RRAM device.

III. MODEL DESCRIPTION

Our model is based on the description of redox chemical reactions by means of the Butler-Volmer equation [16, 33, 34]. Starting from this equation the CF evolution can be analyzed in a reasonable manner. As we pointed out in the previous section, the creation and destruction mechanisms that lead to RS switching [2, 3] are implemented to account for the evolution of the CFs. In our case, we take into consideration the CF dynamics at the regions close to the two interfaces between the CF and the electrodes.

The structure simulated is described in Figure 2. We assume a truncated-cone shaped CF in the device and, therefore, consider that the radius (r_{CF_T}) of the interface with the top electrode is always higher than the other radius, r_{CF_B} (corresponding to the interface between the filament and the bottom electrode). No particular assumptions are considered at the modeling level in relation to the orientation of the truncated cone; in this respect, it could be turned upside down to fit the particularities of other RRAMs if the model is used in another context. For the reset condition a null bottom radius is considered; in this respect, no variation of the vertical dimension of the CF is taken into consideration, i.e., no reduction of the truncated-cone height is assumed to leave a gap between the filament tip and the electrode. We have followed the results and numerical approaches of previous references [11, 12, 16, 14, 27, 28] to consider this simulation scheme.
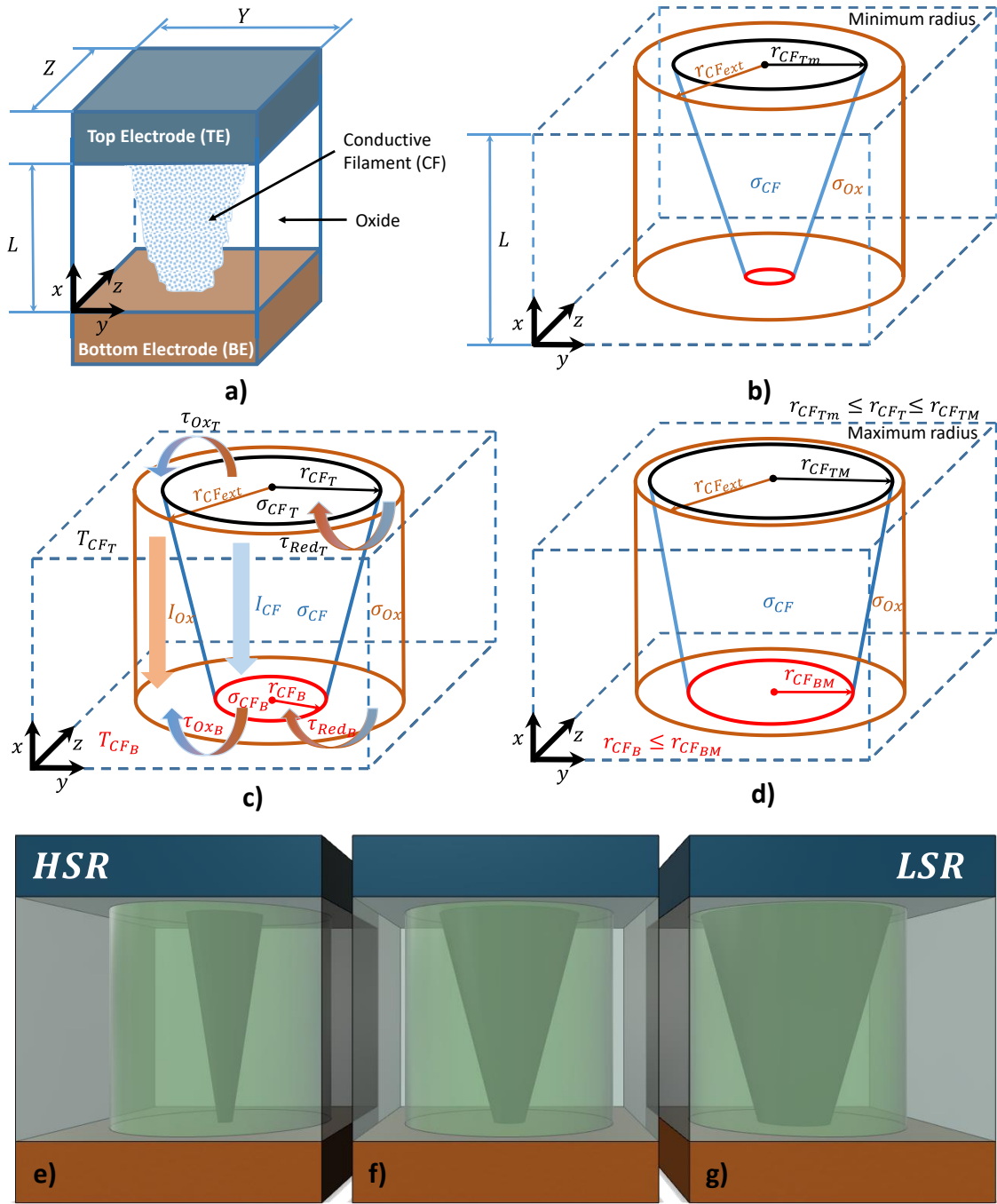
Figure 2. a) Schematic diagram of the modeled RRAM structure. The RRAM is formed by an oxide of thickness L sandwiched between a top electrode (TE) and a bottom electrode (BE). A truncated cone shaped CF can be created between the electrodes after a forming process. b) Scheme of the modeled structure. Different radii are used for the CF ends at the filament-electrode interfaces. An external cylinder in brown lines is considered to be the CF growth limit. c) Representation of the variables employed to solve the differential equations that control the CF creation and destruction processes. We highlight that the electric conductivity and the oxidation (τ_{Ox_B}, τ_{Ox_T}) and reduction (τ_{Red_B}, τ_{Red_T}) rates are different at each CF extreme because of the different temperatures used. d) CF with the maximum size assumed in the model after a set process. Three-dimensional representation of radii time evolution e) HRS f) intermediate state g) LRS

A forming process is assumed, although not included in the model that only accounts reset/set series. After this stage, a formed CF (Figure 2a and 2b) is obtained. We have considered the Butler-Volmer equation under the following assumptions [28]: 1) the electrodes potential with respect to the equilibrium potential is approximated to be equal to $-|Vapp|$ assuming isotropic redox reactions, where $Vapp$ is the voltage applied between the top and bottom electrodes; 2) the electron density available during set could not limit the reduction process and the parts of CF formed act as a virtual electrode [2].

III.A. ELECTROCHEMICAL REDOX REACTIONS

The set/reset operation of the device under study is based on a description of the redox reactions and diffusion processes that control the growth and rupture of the conductive filament that make the device switch between the LRS and the HRS. We have followed the procedure reported in [28] to adapt Butler-Volmer equation [33-35] to a device with a single CF. The electrochemical reduction rate $\tau_{Red_{(T,B)}}$ (the subindex T (B) corresponds to the top (bottom) electrode) can be obtained by means of Equation 1, and the oxidation rate $\tau_{Ox_{(T,B)}}$ is given in Equation 2. Both rates depend on the temperature; hence, as indicated in the previous section, we have to consider their values at both CF regions.

$$\frac{1}{\tau_{Red_{(T,B)}}} = A_{RedOx} \cdot e^{-\frac{E_a - q \cdot \alpha \cdot V_{(T,B)}}{k_b \cdot T_{CF_{(T,B)}}}} \tag{1}$$

$$\frac{1}{\tau_{Ox_{(T,B)}}} = A_{RedOx} \cdot e^{-\frac{E_a + q \cdot (1-\alpha) \cdot V_{(T,B)}}{k_b \cdot T_{CF_{(T,B)}}}} \tag{2}$$

Where k_b is the Boltzmann's constant, q is the charge of the electron. A_{RedOx} stands for the inverse of the nominal redox rate, E_a is the activation energy, α is the charge transfer coefficient (whose value lies between 0 and 1) and V_T, V_B are the voltages linked to the upper and bottom parts of the CF (see appendix C).

The increase/decrease velocity of the CF radius (at the top CF interface, Equation 3, and bottom CF interface, Equation 4) is given below [28].

$$\frac{dr_{CF_T}}{dt} = \frac{r_{CF_{TM}} - r_{CF_T}}{\tau_{Red_T}} - \frac{r_{CF_T}}{\tau_{Ox_T}} \tag{3}$$

$$\frac{dr_{CF_B}}{dt} = \frac{r_{CF_T} - r_{CF_B}}{\tau_{Red_B}} - \frac{r_{CF_B}}{\tau_{Ox_B}} \tag{4}$$

The following restrictions are imposed on the top and bottom CF radii ($r_{CF_{(T,B)}}$):

$$r_{CF_{Tm}} \leq r_{CF_T} \leq r_{CF_{TM}} \tag{5}$$

$$r_{CF_B} \leq r_{CF_{BM}} \tag{6}$$

where $r_{CF_{TM}}(r_{CF_{BM}})$ is the maximum top (bottom) radius that can be achieved and $r_{CF_{Tm}}$ stands for the minimum top radius (these three values will be fitted for each device cycle in our model). See that no restriction is imposed in Equation 6 for low radii; we assume that if r_{CF_B} is lower than the CF metallic atom radius the CF is considered to be broken. Equation 4 ensures that the CF geometry is a truncated cone with the top radius higher than the bottom one at all times. In this respect, this condition ensures that a maximum bottom radius higher than the minimum top radius could be chosen but the CF shape would be maintained.

Several authors proposed to include the role played by the local diffusion of metallic species [11, 16], previously proposed by other authors [22], in addition to the oxidation/reduction reaction in the description of the reset processes. Therefore, a term to account for this effect was included in their master equation (analytically close to our Equations 3 and 4). However, here, in order to maintain the symmetry

in Equations 3 and 4, we preferred to modify Equations 1 and 2 to include diffusion. We did so by assuming different activation energies for the reduction and oxidation rates ($E_{a_{Red}}$ for Equation 1 and $E_{a_{Ox}}$ for Equation 2). We performed this approximation taking into consideration that the metallic species diffusion velocity presents an expression quite close to Equation 2 [11, 16], so this diffusion effect was incorporated by merging the corresponding equations making use of a new (different to the value employed to account for the reduction process) activation energy for the oxidation process.

We employed the numerical scheme described in Ref. [28] for the solution of Equations 3 and 4. In our work we deal with two coupled differential equations for the calculation of the truncated cone radii.

III.B. TOTAL CURRENT IN THE RRAM

The total current flowing through the device has two components (see Figure 2c):

$$I = I_{CF} + I_{Ox}$$
(7)

a) *CF current* (I_{CF}): In this case, the CF resistance (R_{CF}) and the contribution of the oxide that surrounds the CF included in the cylinder of radius $r_{CF_{Ext}}$ (see Figure 1b) (R_{Ox}) are taken into account. The details of the calculation of R_{CF} and R_{Ox} are given in the Appendix.

This current component can be calculated as follows:

$$I_{CF} = \frac{V_{app}}{R_{CF}||R_{Ox}}$$
(8)

b) *Oxide current* (I_{Ox}): This component represents the current through the oxide accounting for the whole area of the device (save the cylinder of radius $r_{CF_{Ext}}$ where the CF is formed). We have used an expression based on a previous equation proposed in [27] that is given below:

$$I_{Ox} = \text{sign}(V_{app}) \, A_{HRS} \cdot S_{Cell} \cdot \left(\frac{|V_{app}|}{L}\right)^{\alpha_{HRS}}$$
(9)

Where S_{Cell} is the area of the RRAM device, and A_{HRS} and α_{HRS} are fitting constants.

III.C. TEMPERATURE EFFECTS

Temperature is a key factor in the reduction and oxidation rates [36], as can be seen in Equations 1 and 2. Therefore, an accurate description of the thermal features of the device under study is desirable. In this model, the CF geometry has axial symmetry along the axis perpendicular to the insulator-electrode interfaces; consequently, the heat equation can be simplified through a one-dimensional approach (see Figure 3).
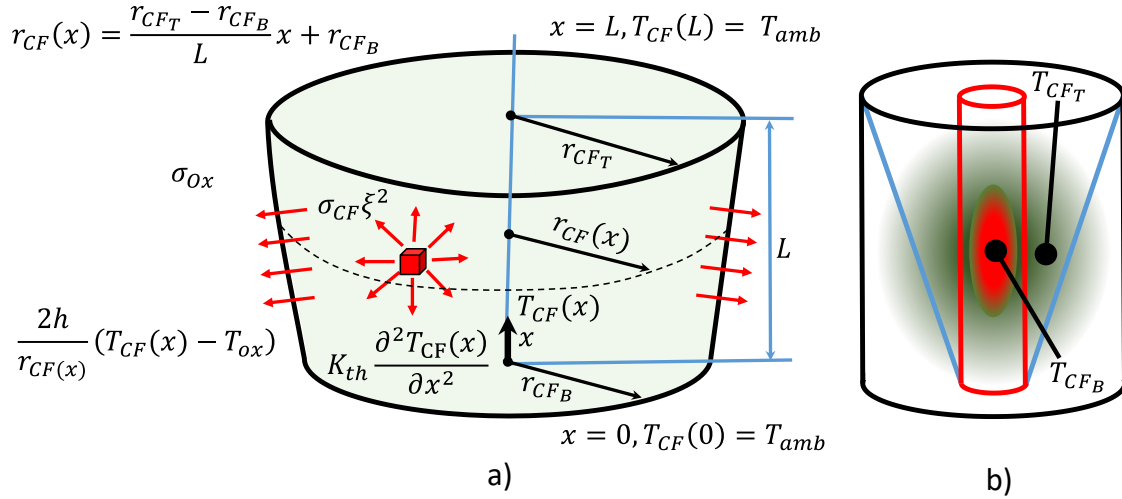
Figure 3. (a) Schematic representation of the CF used in our model. All the terms included in the heat equation are shown, in particular the terms that account for Joule heating and for the lateral heat dissipation. The temperature boundary conditions at the CF extremes are also included. (b) Schematic of the approach followed to obtain the two temperatures employed in the model.

$$\sigma_{CF} \cdot \xi(x)^2 - \frac{2h}{r_{CF}(x)}(T_{CF}(x) - T_{ox}) = -K_{th}\frac{\partial^2 T_{CF}(x)}{\partial x^2} \tag{10}$$

Where σ_{CF} is the CF electrical conductivity, $T_{CF}(x)$ the CF temperature, T_{amb} is the ambient temperature, K_{th} the CF thermal conductivity and $\xi(x)$ the electric field within the CF. This equation could be numerically solved for truncated-cone shapes [11] as explained in the introduction, but this procedure is not appropriate because of the need of simplicity for a circuit simulation model. Therefore, we use a different approach in order to get an analytical and simpler expression for the temperature.

In Ref. [28], a uniform radius is assumed (a cylindrical CF shape) without lateral dissipation of heat ($h = 0$). A unique temperature is calculated and it is supposed to be the same along the x-axis (see Figure 2). So, the cylinder (the CF) evolves thermally speaking as a whole. It is important to highlight that, since the electrodes are supposed to be at room temperature, the temperature value assumed for the CF was chosen at the CF center (the maximum value in the solution of the particularized version of the heat equation). This is a reasonable model; however, for the sake of a more detailed physical description, we have modified this approach to calculate two different temperature values: one connected with the hottest CF portion (where the reset process disrupt the CF) and the other to the main CF volume. In this way the truncated-cone shaped CF is better described since the two CF radii evolve independently with different oxidation/reduction rates. To get this modeling goal in a reasonably simple context, algebraically speaking, i.e. to obtain an analytical expression that can be easily implemented in a Verilog-A code, we have to perform a simplifying approximation. It is based on the consideration of uniform cylinders to represent the CF (see Figure 3b): one corresponding to the higher radius, r_{CF_T}, and the other with the lower one, r_{CF_B}. For each cylinder, the heat equation (expression 10) is solved making use of the boundary conditions sketched in Figure 2, in this manner an analytical expression can be achieved.

43

In our approximated approach we assume the electric field to be divided in two components associated with the top and bottom halves of the CF. In this respect the electric field can be calculated as $\xi_{(T,B)} = \frac{V_{(T,B)}}{L/2}$, where $V_{(T,B)}$ is obtained considering the voltage divider formed by the resistances associated with the top and bottom halves of the CF (see Appendix C). Then, the maximum temperature obtained for each cylinder is assumed to be the temperature at the main CF volume, T_{CF_T}, and at the narrowest part, T_{CF_B}:

$$
\begin{aligned}
T_{CF_{(T,B)}} = T_{amb} &+ \frac{\sigma_{CF_{(T,B)}} \cdot r_{CF_{(T,B)}} \xi_{(T,B)}^2}{2 \cdot h}\left(1 - cosh\left(\frac{\alpha_{(T,B)}L}{2}\right)\right) \\
&+ \frac{dT_{0_{(T,B)}}}{\alpha_{(T,B)}} sinh\left(\frac{\alpha_{(T,B)}L}{2}\right)
\end{aligned}
\tag{11}
$$

Parameters $\alpha_{(T,B)}$ and $dT_{0_{(T,B)}}$ are given in the equations below:

$$
\alpha_{(T,B)} = \sqrt{\frac{2h}{k_{th} \cdot r_{CF_{(T,B)}}}}
\tag{12}
$$

$$
dT_{0_{(T,B)}} = \frac{\sigma_{CF_{(T,B)}} \cdot r_{CF_{(T,B)}} \cdot \xi_{(T,B)}^2 tanh\left(\frac{\alpha_{(T,B)}L}{2}\right)}{\sqrt{2 \cdot K_{th} \cdot h \cdot r_{CF_{(T,B)}}}}
\tag{13}
$$

Equation 11 (also Equation 10) includes the CF conductance temperature dependence, assuming a metallic behavior [11, 13]:

$$
\sigma_{CF_{(T,B)}} = \frac{\sigma_{CF_0}}{1 + \alpha_T\left(T_{CF_{(T,B)}} - T_{amb}\right)}
\tag{14}
$$

where σ_{CF_0} stands for the CF conductivity at room temperature (T_{amb}) and α_T is the conductivity temperature coefficient.

These two temperature values are a simplifying approximation to the temperature distribution in a fine grid along the CF that would be obtained by solving the heat equation in a self-consistent procedure as reported in [37]; therefore, they have to be considered as such, taking into account the overall scheme of simplifications performed to develop the model.

III.D. MODEL COMPUTATIONAL IMPLEMENTATION

In the figure below it is shown the flowchart (Figure 4a) of the procedure employed to implement the model calculations. In addition, an equivalent circuit for the RRAM cell is given (Figure 4b) to better describe the different components included in the model. The capacitance of Figure 4b corresponds to a planar dielectric with constant thickness with two electrodes, the influence of a nanometric CF or CFs in a 100x100 μm² device is negligible.
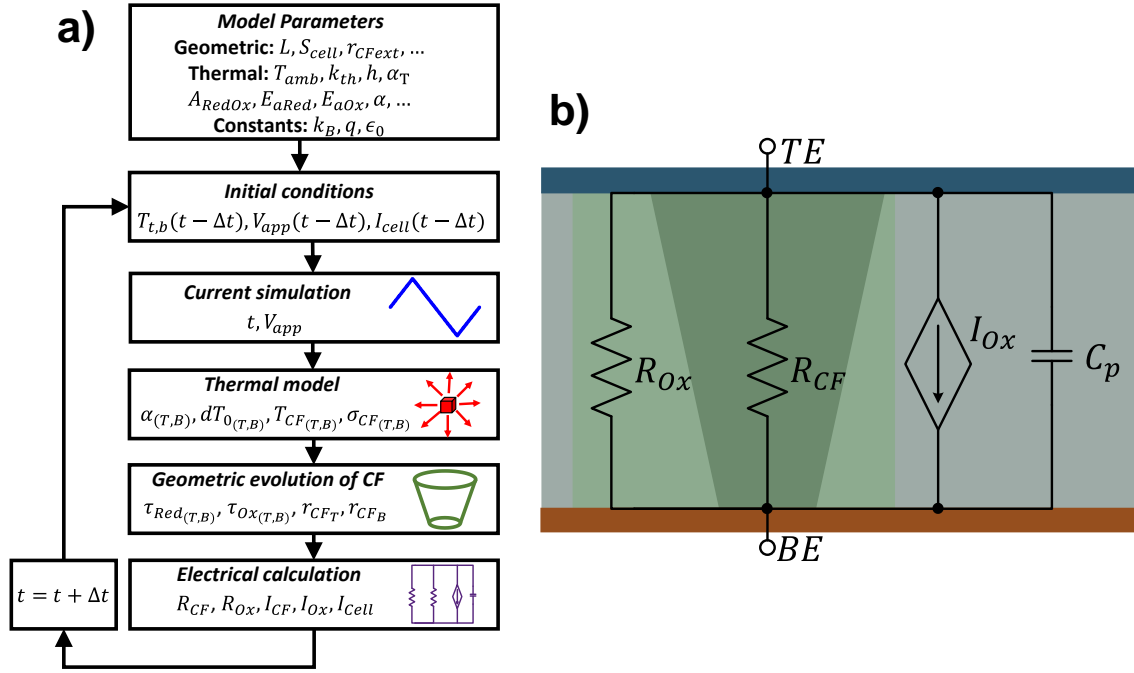
Figure 4. (a) Flowchart of the RRAM model, (b) equivalent circuit of the RRAM cell.

IV. RESULTS AND DISCUSSION

We have validated our model making use of more than a hundred I-V experimental curves (see Figure 1). The model allowed the fitting of the experimental data considered in a reasonable manner as can be seen in Figure 5. The physical constants used are given in Table I.
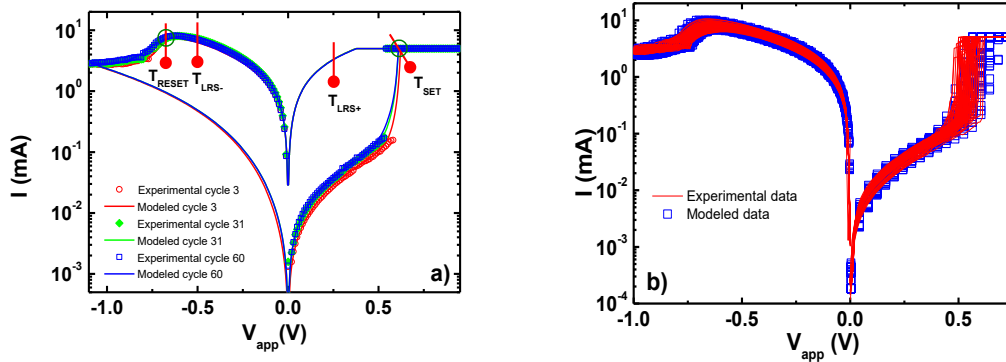
Figure 5. (a) RRAM current versus voltage for different cycles [32], the CF features employed to fit each curve were: $r_{CF_{TM}} = 45nm, r_{CF_{Tm}} = 15nm, r_{CF_{BM}} = 7nm$ for cycle 3, $r_{CF_{TM}} = 45nm, r_{CF_{Tm}} = 25nm, r_{CF_{BM}} = 7nm$ for cycle 31 and $r_{CF_{TM}} = 40nm, r_{CF_{Tm}} = 35nm, r_{CF_{BM}} = 7.8nm$ for cycle 60, (b) I-V curves for the devices under study along with different modeled data (the CFs dimensions considered to fit the whole set of curves have been generated randomly). Temperatures reached at the most representative points of the I-V curve, highlighted in (a) Cycle 3: $T_{SET_{(T,B)}} = [579,656]$, $T_{LRS+_{(T,B)}} = [349,368]$, $T_{LRS-_{(T,B)}} = [466,525]$, $T_{RESET_{(T,B)}} = [565,621]$, Cycle 31: $T_{SET_{(T,B)}} = [573,669]$, $T_{LRS+_{(T,B)}} = [349,368]$, $T_{LRS-_{(T,B)}} = [460,525]$, $T_{RESET_{(T,B)}} = [566,622]$, Cycle 60: $T_{SET_{(T,B)}} = [564,685]$, $T_{LRS+_{(T,B)}} = [347,367]$, $T_{LRS-_{(T,B)}} = [460,525]$, $T_{RESET_{(T,B)}} = [545,641]$.

We have considered the results highlighted in Ref. [29, 38] who reported the presence of metallic species in the CFs in addition to oxygen vacancies and other components. Because of this, electrical conductivity has been assumed to be a fitting parameter since the conductive nature of the CF (in the ohmic transport regime) is not well understood, and it is obviously affected by the final CF configuration [29]; in our case a value of $\sigma_0 = 2 \cdot 10^5 \ \Omega^{-1} \ m^{-1}$ was employed. The complex and stochastic processes behind the CF formation make its electrical and thermal characteristics different, in general, from the

ones corresponding to the 3D pure elements that can be found in the CFs; that is why we fit the main physical parameters of the equations describing the CF physics to reproduce the measurements instead of using the corresponding bulk values. See that in our case, the redox equations could account for different chemical processes taking place in the oxide, mostly at the CF tip.

In Figure 6 we plotted an experimental and several modeled curves. As can be seen in symbols, where no truncated-cone shaped CFs were employed (i.e. a previous model [28] based on cylindrical CFs was considered), the experimental data cannot be fitted accurately for any of the cylinder radii considered. This fact suggests the importance of the use of a correct CF shape.

The proposed model also allows the characterization of RRAMs with multiple conductive filaments. In Figure 6b, 6c and 6d it can represent I-V curves of devices including up to four filaments are shown. The filaments have truncated-cone shapes with different upper and lower radii. The effects of the inclusion of several filaments can be appreciated in the I-V curves; set processes with different activation steps and reset transitions with different slopes can be seen corresponding to the formation and disruption of the CFs included in the device.
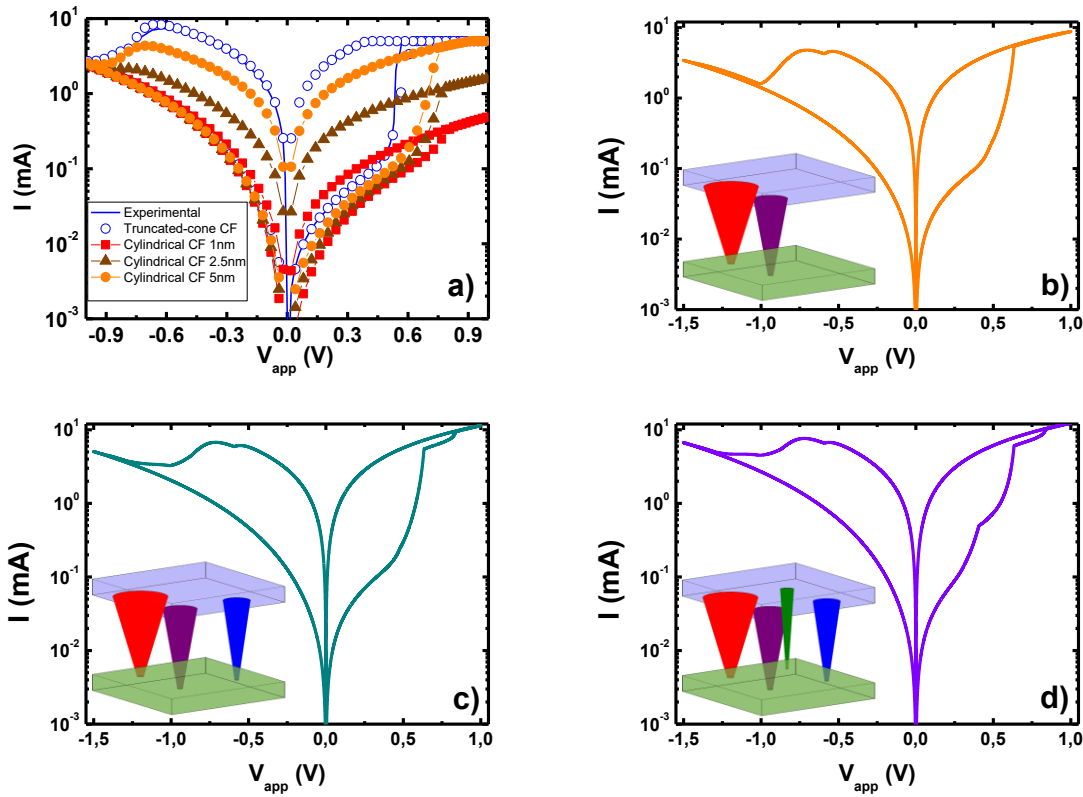
Figure 6. (a) I-V curves versus applied voltage, comparison of our model with the results of a previous model based on cylindrical CFs [28]. Blue hollow circles represent measured data for the Ti/ZrO$_2$/Pt cell. The modeled data considering truncated-cone shaped CFs are shown in solid blue lines. The other lines represent data modeled with cylindrical CFs (using only one temperature for the CF), the cylinder radii used were: $1 nm$ (red squares), $2.5 nm$ (brown triangles) and $5 nm$ (orange circles). The parameters employed in the simulations are given in Table I. (b) I-V curves for a device with two CFs (CF_1, CF_3), (c) three CFs (CF_1, CF_2, CF_3) and (d) four CF (CF_1, CF_2, CF_3, CF_4), where CF_1: $r_{CF_{TM}} = 40\ nm$, $r_{CF_{BM}} = 5\ nm$; CF_2: $r_{CF_{TM}} = 20\ nm$, $r_{CF_{BM}} = 3\ nm$; CF_3: $r_{CF_{TM}} = 25\ nm$, $r_{CF_{BM}} = 4\ nm$; CF_4: $r_{CF_{TM}} = 10\ nm$, $r_{CF_{BM}} = 2\ nm$. A 3D view of the devices modeled with the corresponding CFs are shown in the insets.

The model allows the extraction of interesting internal variables that cannot be easily measured; they might be of great help in the analysis of the device operation. In Figure 7 the applied voltage signal and corresponding current are plotted in different ways, see Figures 7a and 7b (the following geometrical features: $r_{CF_{TM}} = 45 nm, r_{CF_{Tm}} = 25 nm,\ r_{CF_{BM}} = 7 nm$ that corresponds to the experimental cycle 31, were considered). See that the input voltage can be positive and negative and the model works well in both cases, as it should be.
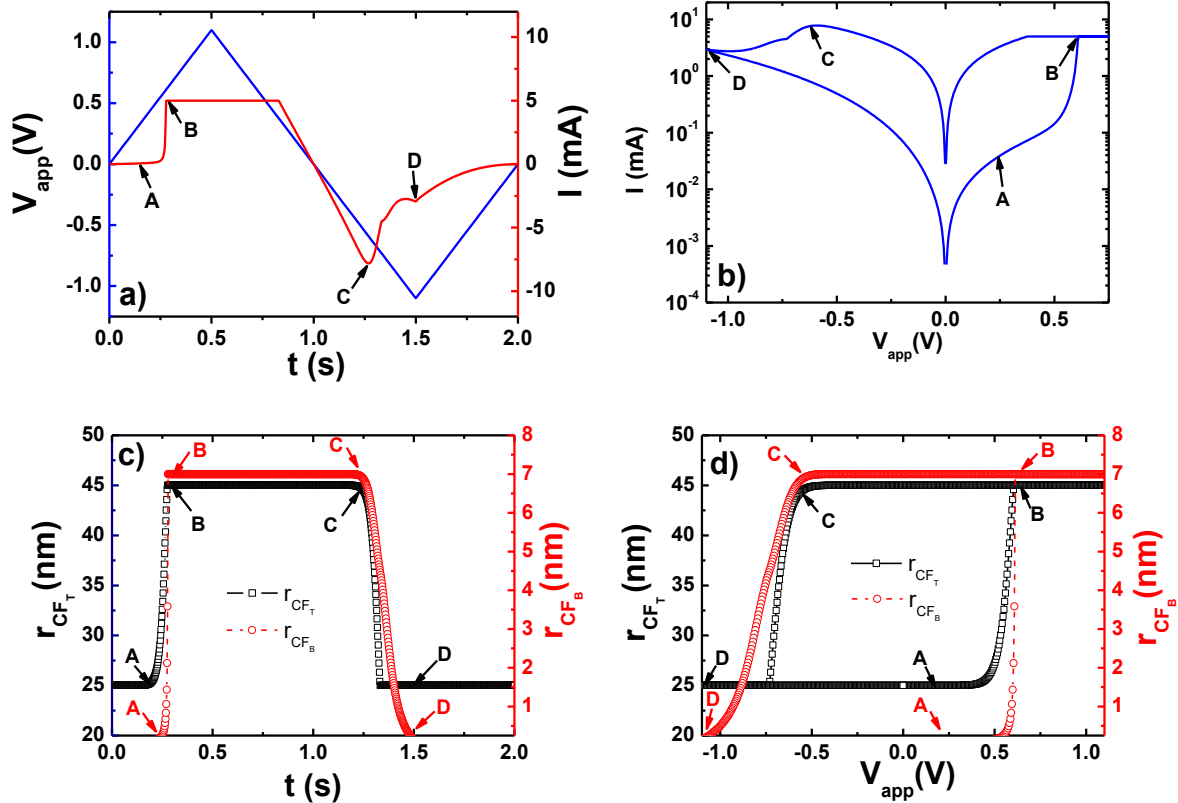
Figure 7. (a) Applied triangular voltage signal (blue) and corresponding device current (red) versus time, (b) RRAM current versus applied voltage, (c) top and bottom CF radii versus time for the devices under study, corresponding to Figures 7a, 7b and (d) top and bottom CF radii corresponding to Figure 7c versus applied voltage.

In the voltage range signaled between points B and C, the CF radii have the higher values allowed. This operation region is characterized by a full formed CF (the device is in the LRS) after a set process, see Figure 7c and 7d. The CF remains with the same geometry between points B and C, then the reset process starts to change the CF geometry for voltages lower than V_C (the voltage a point C in the previous figure). The top radius, r_{CF_T}, is the first to shrink due to diffusion of metallic species and oxidation processes for voltages lower than V_C, see that in Equations 3 and 4 the radius rate of change depends on the radius itself. In this particular case, there is a fast change from its maximum ($45 nm$) to its minimum value ($25 nm$). The CF resistance is therefore increased and the device current drops off. Between points C and D, the bottom radius shrinks till the CF is disrupted and the reset process concludes. A low current remains due to conduction in the oxide after the reset process. In our model both CF radii are strongly reduced in the reset process; however, it is the bottom radii the one that shrinks to a value where the CF is assumed to be disrupted. It is important to highlight that dissimilar shapes of the I-V curves are obtained for the reset and set processes because of the different activation energies employed and the different temperature evolution that takes place in each part of the curve.

We have made use of the model to reproduce the set of different experimental I-V curves shown in Figure 5b to plot Figure 8 where I_{reset} (I_{set}) versus V_{reset} (V_{set}) data are plotted for measured and modeled data. The fitting was achieved by changing the CF geometry, maintaining the physical constants given in Table I.
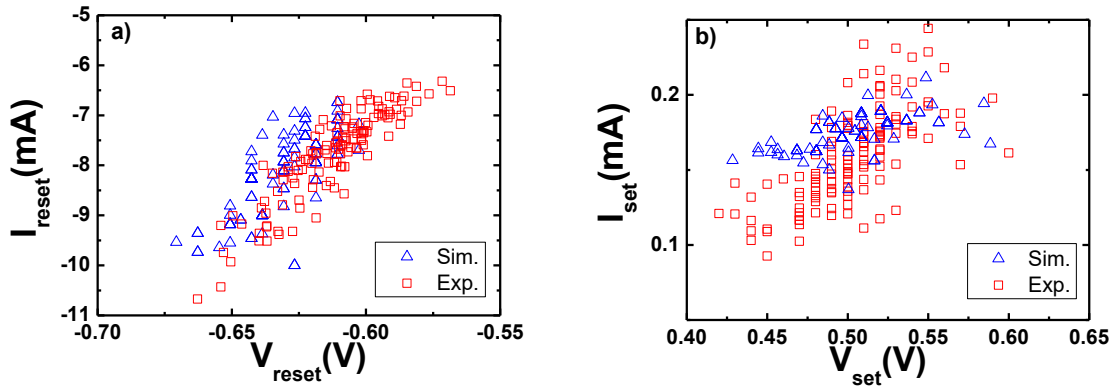
Figure 8. (a) I_{reset} versus V_{reset} calculated for experimental and simulated data. (b) I_{set} versus V_{set} calculated for experimental and simulated data.

See that although there are more experimental values in the plot, they are reproduced reasonably within the variability range that can be observed for the set and reset voltages. In this respect the model we are proposing shows its validity both in reproducing the most representative characteristics I-V curves and the V_{set} and V_{reset} values of the devices under study.

In addition to pure numerical calculations based on the solutions of the equations described in section III, we have implemented the model in Verilog-A in order to use it in a circuit simulation context within the ADS (an EDA tool by Keysight technologies). The model has been enhanced with a capacitance in parallel corresponding to the device structure with the geometrical features and the dielectric explained in section II. We have simulated a circuit introduced in [32], see the inset in Figure 9. The voltages at the RRAM electrodes (V_A and V_B) have been plotted in Figure 9, comparing experimental and modeled data.
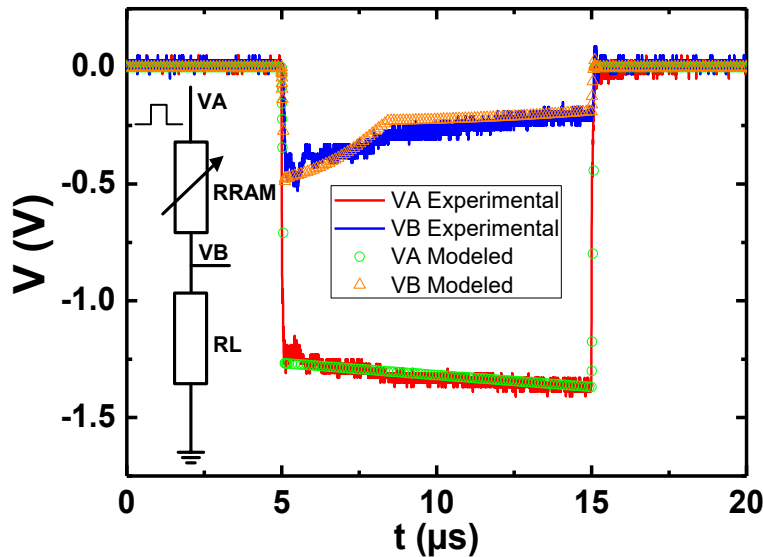
Figure 9. Experimental and modeled device current when operated under a pulsed applied voltage.

Voltage V_A represents the applied voltage pulse, the red solid line (green circles) shows the measured (experimental) voltage. Voltage V_B represents the signal in the load resistance. The time evolution of the device resistance is correctly modeled as shown in Figure 9. It can be observed that using an erase pulse of $1.25V$ in this circuit configuration, the devices require $3\mu s$ to switch from the LRS to HRS.

Table I. Technological parameters and fitting constants used in the model.

Parameters	*Ti/ZrO$_2$/Pt*	*Units*
L	15	nm
r_{CFext}	50	nm
$[\sigma_{CF0}, \sigma_{Ox}]$	$[2 \cdot 10^5, 1.65]$	$m^{-1}\Omega^{-1}$
α	0.5	
T_{amb}	300	K
α_T	1.1×10^{-3}	K
k_{th}	20	$\dfrac{W}{K \cdot m}$
h	10^{10}	$\dfrac{W}{K \cdot m^2}$
$[E_{a_{Red}}, E_{a_{Ox}}]$	$[0.62, 0.78]$	eV
A_{RedOx}	10^5	s^{-1}
A_{HRS}	10^{-13}	
α_{HRS}	2.23	
S_{Cell}	100×100	μm^2

V. CIRCUIT SIMULATION. SINGLE MEMORY CELL

Following the same simulation infrastructure reported before, the circuit sketched in Figure 10 a) has been analyzed.
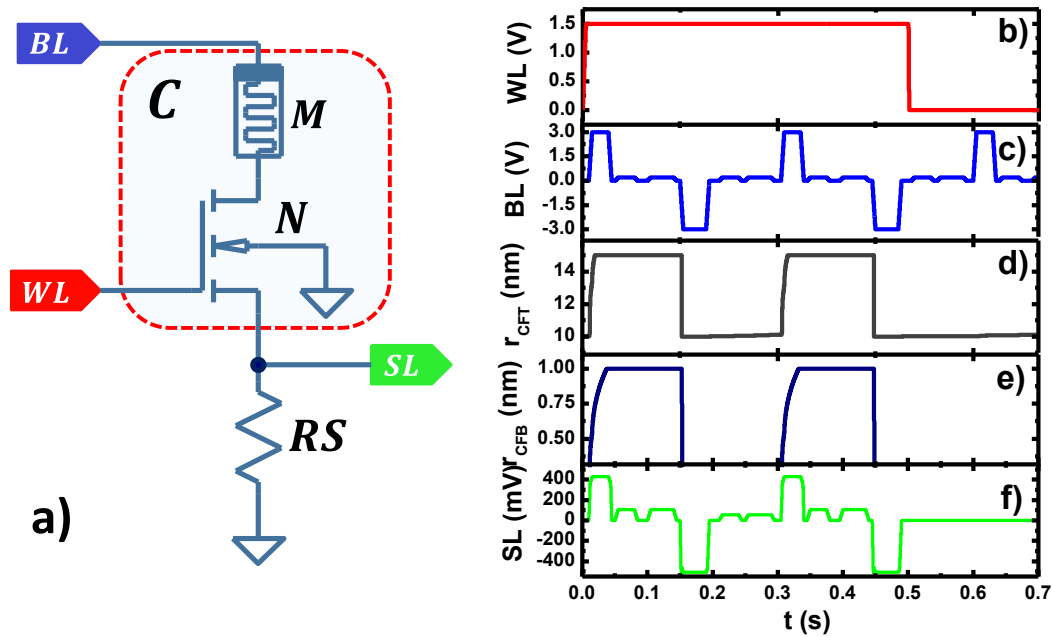
Figure 10. (a) Basic memory cell including a RRAM (M) based on the scheme proposed in Ref. [24]. This cell (C) could be part of a greater array. WL is the word line signal selector, BL is the bit line signal selector, and SL is the sensing line that connect to the sense amplifier. Voltage signals and RRAM parameters versus time. (b) Word line voltage at the gate of nMOS 130nm (PTM model used for the MOS transistor [39]) (c) Bit line voltage at the RRAM top electrode. (Two sequences are considered: Set-read-read-Reset-read-read), (d) RRAM CF top radius, (e) RRAM CF bottom radius, (f) Sense line voltage signal.

We have plotted in Figure 10 the input voltage signals and different RRAM model variables versus time. A 1.5 V signal for the Word Line (WL) is used. The operation voltage in the memory cell is introduced through the Bit Line (BL) (set or reset processes and resistance state reading operations are performed). The control signals have been chosen to show the operation of the circuit under study; in this respect, this facet could be further optimize. The cell selector element used was an nMOS transistor $W / L = 1$ with $L = 130nm$ described in Predictive Model Technology [39] using a BSIM model level 54.

The signals WL and BL are plotted in Fig. 10b and 10c. First, a voltage pulse to trigger a set process is introduced in the BL; after that, r_{CF_T} and r_{CF_B} reach its maximum value (the CF is fully formed) and the RRAM achieves its Low Resistance State (LRS). In case the other logic state is needed, then a negative voltage is introduced through BL. After this pulse, r_{CF_T} and r_{CF_B} reach its minimum values and the RRAM High Resistance State (HRS) is achieved. The maximum and minimum r_{CF_T} and r_{CF_B} values can be fitted to reproduce experimental results for a particular RRAM cycle. The cell can be read with a pulse $V_{Read} = 200\text{m}V$ in the BL with the same time features described above for Set/Reset voltages. The signal at the sense line is shown in green in the same figure.

V. CONCLUSIONS

A new model for bipolar RRAMs is presented. The model is based on the description of the redox and diffusion processes that modify the geometrical features of the conductive filaments that account for the RS mechanisms behind the operation of the modeled RRAMs. Truncated-cone shaped filaments and a detailed thermal description have been employed. As far as we know, it is the first time that two different temperature values are considered at simulation time in a circuital model to describe the CF main body region and the CF narrowing where the reset process takes place. The model has been compared to experimental data obtained from Ti/ZrO$_2$/Pt RRAM devices and the measurements were correctly reproduced in all the cases considered. Moreover, the model has been implemented in Verilog-A code within the ADS circuit simulator, the response of a device to pulsed external voltages has been simulated obtaining good results when compared with the experimental data.

VI. ACKNOWLEDGMENTS

APPENDIX

A. CONDUCTIVE FILAMENT RESISTANCE CALCULATION

The main geometrical features of a truncated cone shaped CF needed to calculate its ohmic resistance is given in Figure A1a.
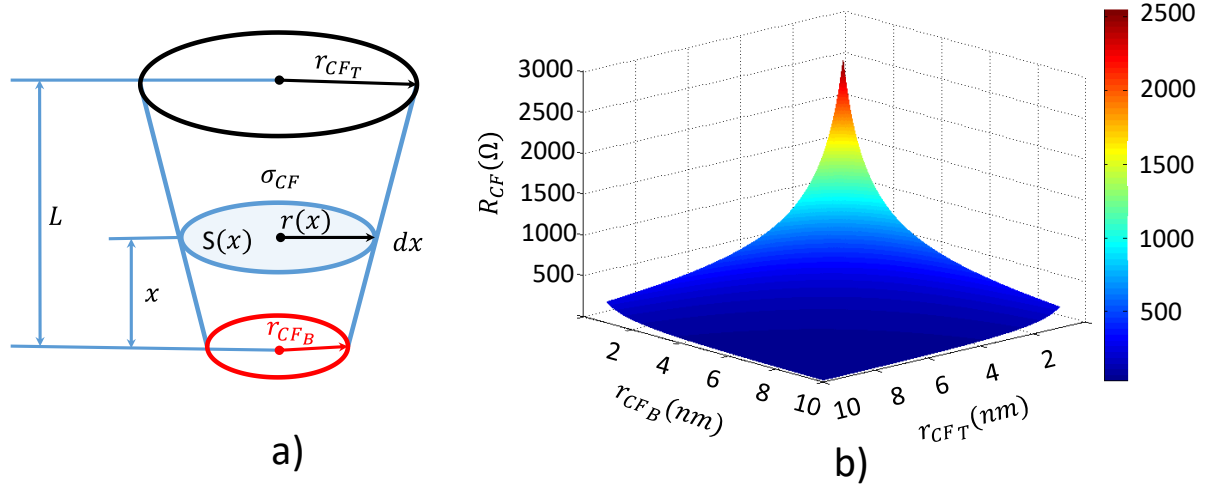
Figure A1. (a) Schematic diagram to compute the equivalent resistance of the truncated-cone shaped CF (R_{CF}) as a function of the top and bottom radii(r_{CF_T}, r_{CF_B}), the CF length (L) and the electrical conductivity (σ_{CF}). (b) 3D plot of the R_{CF} calculated for $\sigma_{CF} = 12.5 \; 10^5 m^{-1}\Omega^{-1}$ and $L = 10nm$.

The resistance of each infinitesimal section can be expressed as follows, assuming a homogeneous electrical conductivity:

$$dR_{CF} = \frac{dx}{\sigma_{CF} \cdot S(x)} \tag{A1}$$

Integrating the CF resistance from $x = 0$ to $x = L$ we obtain:

$$R_{CF} = \frac{L}{\pi \cdot \sigma_{CF} \cdot r_{CF_T} \cdot r_{CF_B}} \tag{A2}$$

B. EQUIVALENT RESISTANCE OF THE OXIDE SURROUNDING THE CF
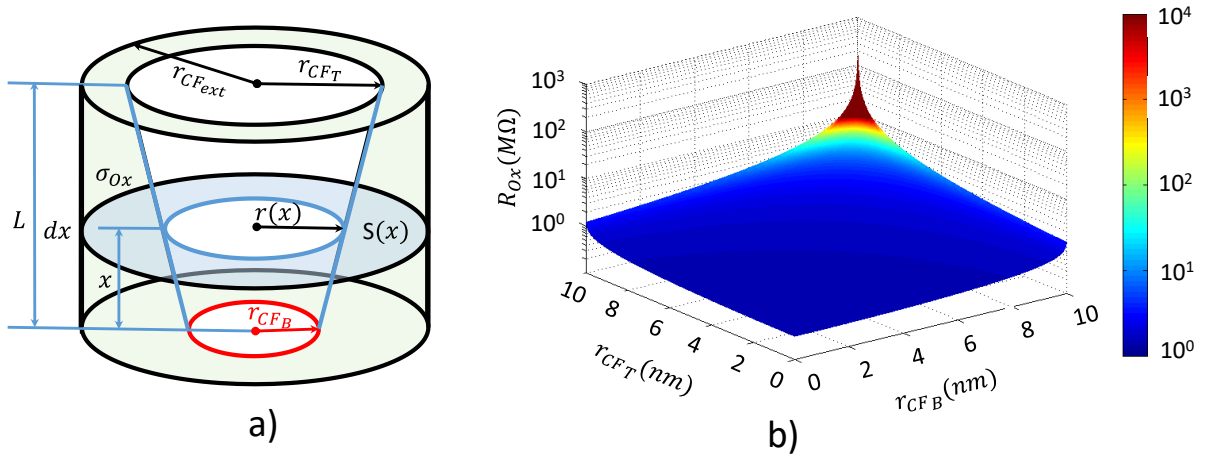
Figure B1. (a) Schematic diagram to compute the equivalent resistance of the oxide surrounding the truncated cone shaped CF (R_{ox}) as a function of the top and bottom CF radii (r_{CF_T}, r_{CF_B}), the CF length (L) and oxide electric conductivity (σ_{ox}). (b) 3D plot of the R_{ox} calculated for $\sigma_{OX} = 0.1 m^{-1}\Omega^{-1}$ and $L = 10nm$.

In this appendix section we perform the calculation of the resistance (R_{ox}) the oxide surrounding the CF as sketched in grey in Figure A2.a. Following the line described in the previous appendix section, the resistance of a slice of oxide of infinitesimal height can be calculated as follows:

$$dR_{ox} = \frac{dx}{\sigma_{CF} \cdot S(x)} \tag{B1}$$

Where $S(x)$ can be obtained from the following expression:

$$S(x) = \pi \cdot [A^2 - r(x)^2] \tag{B2}$$

Integrating Equation B1 from $x = 0$ to $x = L$, the following expression is obtained:

$$R_{Ox} = \begin{cases} \dfrac{L \cdot \beta}{2 \cdot \sigma_{ox} \cdot \pi \cdot r_{CFext} \cdot (r_{CF_B} - r_{CF_T})} & , r_{CF_T} \neq r_{CF_B} \\[4mm] \dfrac{L}{\sigma_{ox} \cdot \pi \cdot (r_{CFext}^2 - r_{CF_T}^2)} & , r_{CF_T} = r_{CF_B} \end{cases} \tag{B3}$$

$$\beta = ln\left[\frac{(r_{CFext} + r_{CF_B}) \cdot (r_{CFext} - r_{CF_T})}{(r_{CFext} + r_{CF_T}) \cdot (r_{CFext} - r_{CF_B})}\right] \tag{B4}$$

C. VOLTAGE DIVIDER FORMED BY THE TWO PARTS OF THE TRUNCATED-CONE SHAPED CF
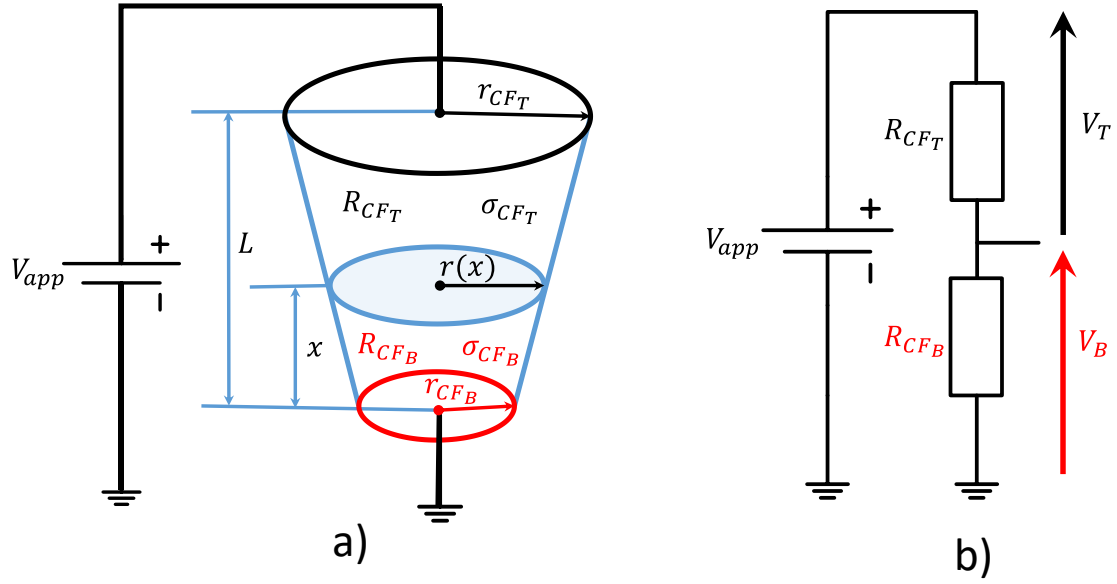
Figure C1. (a) Schematic diagram to compute the voltage divider formed by truncated-cone shaped top and bottom resistances (R_{CF_T}, R_{CF_B}) within the CF. These resistances can be calculated by considering the upper and bottom parts formed by dividing the CF by a plane placed at x, above the bottom CF interface. (b) Equivalent circuit.

The top and bottom resistances (R_{CF_T}, R_{CF_B}) can be calculated according with Appendix A as follows,

$$R_{CF_T} = \frac{L - x}{\pi \cdot \sigma_{CF_T} \cdot r_{CF_T} \cdot r(x)} \quad , R_{CF_B} = \frac{x}{\pi \cdot \sigma_{CF_B} \cdot r(x) \cdot r_{CF_B}} \tag{C1}$$

The top V_T and bottom V_B voltages are obtained using the following expressions,

$$V_T = \frac{R_{CF_T}}{R_{CF_T} + R_{CF_B}} V_{app} \, , V_B = \frac{R_{CF_B}}{R_{CF_T} + R_{CF_B}} V_{app} \tag{C2}$$

By developing the calculations they can be rewritten as follows,

$$V_T = \frac{D}{1 + D} V_{app} \, , V_B = \frac{1}{1 + D} V_{app} \tag{C3}$$

where D is shown in Equation C4.

$$D = \frac{L - x}{x} \cdot \frac{\sigma_{CF_B} \cdot r_{CF_B}}{\sigma_{CF_T} \cdot r_{CF_T}} \tag{C4}$$

REFERENCES

[1] R. Waser, M. Aono, "Nanoionics-based resistive switching memories," Nature Mater., vol. 6, no. 11, pp. 833–840, 2007. doi:10.1038/nmat2023

[2] R. Waser, R. Dittmann, G. Staikov, and K. Szot, "Redox-based resistive switching memories—Nanoionic mechanisms, prospects, and challenges," Adv. Mater., vol. 21, nos. 25–26, pp. 2632–2663, 2009. DOI: http://dx.doi.org/10.1166/jnn.2012.6652

[3] F. Pan, S. Gao, C. Chen, C. Song, F. Zeng, "Recent progress in resistive random access memories: materials, switching mechanisms and performance", Materials Science and Engineering, 83, pp. 1-59, 2014

[4] J.S. Lee, S. Lee., T.W. Noh "Resistive switching phenomena: A review of statistical physics approaches", Applied Physics Reviews, 2, 031303 ,2015.

[5] Young-Tae Kim, Young-Nam Hwang, Keun-Ho Lee, Se-Ho Lee, Chang-WookJeong, Su-JinAhn,Fai Yeung, Gwan-HyeobKoh, Heong-SikJeong, Won-Young Chung, Tai-Kyung Kim, Young-Kwan Park,Ki-Nam Kim and Jeong-Taek Kong, "Programming Characteristics of Phase Change Random Access Memory Using Phase Change Simulations", Japanese Journal of Applied Physics , vol. 44, no. No. 4B, pp. 2701-2705, 2005

[6] H.S. P. Wong, S. Raoux, S. Kim, J. Liang, J.P. Reifenberg, B. Rajendran, M. Asheghi, and K. E. Goodson, "Phase Change Memory", Proceedings of The IEEE - PIEEE, vol. 98, no. 12, pp. 2201-2227, 2010

[7] W. Zhao, S. Chaudhuri, C. Accoto, J.-O. Klein, D. Ravelosona, C. Chappert, P. Mazoyer, "High density spin-transfer torque (STT)-MRAM based on cross-point architecture", pp. 1-4,4th IEEE International Memory Workshop (IMW) 2012, doi: 10.1109/IMW.2012.6213618

[8] R. Waser (ed.), "Nanoelectronics and Information Technology", 3rd ed., Wiley-VCH, Berlin, 2012.

[9] Lanza, M., "A review on resistive switching in high-k dielectrics: A nanoscale point of view using conductive atomic force microscope". Materials, 7(3), 2155-2182, 2014.

[10] J. Zahurak, K. Miyata, M. Fischer, M. Balakrishnan, S. Chhajed, D. Wells, Li Hong, A. Torsi, J. Lim, M. Korber, K. Nakazawa, S. Mayuzumi, M. Honda, S. Sills, S. Yasuda, A. Calderoni, B. Cook, G. Damarla, H. Tran, Bei Wang, C. Cardon, K. Karda, J. Okuno, A. Johnson, T. Kunihiro, J. Sumino, M. Tsukamoto, K. Aratani, N. Ramaswamy, W. Otsuka,K. Prall. "Process integration of a 27nm, 16Gb Cu ReRAM," Electron Devices Meeting (IEDM), 2014 IEEE International, vol., no., pp.6.2.1,6.2.4, 15-17 Dec. 2014, doi: 10.1109/IEDM.2014.7046994

[11] Villena, M.A., Jiménez-Molinos, F., Roldán, J.B., Suñé, J., Long, S. Lian, X., Gámiz, F., And Liu,M., "An In-Depth Simulation Study Of Thermal Reset Transitions In Resistive Switching Memories", J. Appl. Phys., 2013, Vol. 114, Pp. 144505-144505-8.

[12] M.A. Villena, M.B. González, F. Jiménez-Molinos, F. Campabadal, J.B. Roldán, J. Suñé, E. Romera, E. Miranda, "Simulation of thermal reset transitions in RRAMs including quantum effects", J. Appl. Phys., vol. 115, p. 214504, 2014.

[13] U. Russo, D. Ielmini, C. Cagli, A. L. Lacaita, S. Spiga, C. Wiemer, M. Perego, and M. Fanciulli, in Proceedings of the IEEE International Electron Devices Meeting, IEDM 2007, 2007, pp. 775–778

[14] Jiménez-Molinos, F., Villena, M.A., Roldán, J.B., Roldán, A.M., "A Spice Compact Model For Unipolar Rram Reset Process Analysis", IEEE Trans. Elec. Dev., 2015, vol 62, n.3, Pp. 955-962.

[15] Peng Huang; Xiao Yan Liu; Bing Chen; Hai Tong Li; Yi Jiao Wang; Ye Xin Deng; Kang Liang Wei; Lang Zeng; Bin Gao; Gang Du; Xing Zhang; Jin Feng Kang, "A Physics-Based Compact Model of Metal-Oxide-Based RRAM DC and AC Operations," Electron Devices, IEEE Transactions on, vol.60, no.12, pp.4090,4097, Dec. 2013 doi: 10.1109/TED.2013.2287755

[16] M. Bocquet, D. Deleruyelle, C. Muller and J. M. Portal, "Self-consistent physical modeling of set/reset operations in unipolar resistive-switching memories". Appl. Phys. Letters, 98, 263507 2011.doi: http://dx.doi.org/10.1063/1.3605591

[17] J. Park, S. Jung, W. Lee, S. Kim, J. Shin, D. Lee, J. Woo, and H. Hwang, "Improved switching variability and stability by activating a single conductive filament", IEEE Elec. Dev. Lett., vol. 33, no. 5, pp. 646-648, 2012.

[18] S. Menzel, U. Böttger, and R. Waser, "Simulation of multilevel switching in electrochemical metallization memory cells", J. Appl. Phys. 111, 014501/1-5 (2012).

[19] M.B. Gonzalez, J.M. Rafí, O. Beldarrain, M. Zabala, and F. Campabadal "Analysis of the Switching Variability in Ni/HfO2-based RRAM Devices", IEEE Transactions on devices and material reliability, doi: 10.1109/TDMR.2014.2311231, 2014.

[20] R. Picos, J.B. Roldán, M.M. Al Chawa, P. García-Fernández, F. Jiménez-Molinos, E. García-Moreno, "Semiempirical Modeling of Reset Transitions in Unipolar Resistive-Switching based Memristors", Radioengineering Journal, vol 24, nº 2, pp. 420-424, 2015.

[21] M.A. Villena, M.B. González, J.B. Roldán, F. Campabadal, F. Jiménez-Molinos, F.M. Gómez-Campos, J. Suñé, "An in-depth study of thermal effects in reset transitions in HfO2 based RRAMs", Solid State Electronics, 2015, 111, pp. 47-51.

[22] U. Russo, C. Cagli y A.-L. Lacaita, "Self-accelerated thermal dissolution model for reset programming in unipolar resistive-switching memory (RRAM) devices". Transactions on Electronic Devices, Vol. 56, Nº 2, 193-200, Febrero 2009.

[23] Xudong Fang; Xuejun Yang; Junjie Wu; Xun Yi, "A Compact SPICE Model of Unipolar Memristive Devices," Nanotechnology, IEEE Transactions on, vol.12, no.5, pp.843-850, 2013 doi: 10.1109/TNANO.2013.2275178

[24] P. Sheridan, K.-H. Kim, S. Gaba, T. Chang, L. Chen and W. Lu, "Device and SPICE modeling of RRAM devices", Nanoscale, vol. 3, pp.3833-3840, 2011.

[25] X. Guan, S. Yu, and H-S. P Wong, "A SPICE Compact Model of Metal Oxide Resistive Switching Memory with Variations", IEEE Elec. Dev. Lett., vol. 33, pp. 1405-1407, 2012.

[26] A. Rák, G. Cserey, "Macromodeling of the memristor in Spice", IEEE Trans. On Computer-aided design of integrated circuits and systems, vol. 29, pp.632-636, 2010.

[27] M. Bocquet, D. Deleruyelle, H. Aziza, C. Muller, J.-M. Portal, "Compact modeling solutions for OxRAM memories", Faible Tension Faible Consommation (FTFC), 2013 IEEE, vol., no., pp.1, 4, 20-21, 2013 doi: 10.1109/FTFC.2013.6577779

[28] M. Bocquet, D. Deleruyelle, H. Aziza, C. Muller, J.-M. Portal, T. Cabout, E. Jalaguier, "Robust Compact Model for Bipolar Oxide-Based Resistive Switching Memories", Electron Devices, IEEE Transactions on, vol.61, no.3, pp. 674- 681, March 2014.doi: 10.1109/TED.2013.2296793

[29] X. Wu, D. Cha, M. Bosman, N. Raghavan, D.B. Migas, V. E. Borisenko, X. Zhang, K. Li and K. Pey, "Intrinsic nanofilamentation in resistive switching", J. Applied. Physics.113, 114503, 2013.

[30] D. H. Kwon, K. M. Kim, J. H. Jang, J. M. Jeon, M. H. Lee, G. H. Kim ... and C. S. Hwang, "Atomic structure of conducting nanofilaments in TiO2 resistive switching memory," Nature nanotechnology 5.2, 148-153, 2010.

[31] U. Russo, C. Cagli y A.-L. Lacaita, "Filament conduction and reset mechanism in NiO-based resistive-switching memory (RRAM) devices," Trans. Electron Devices 56(2), 186–192, 2009.

[32] Guoming Wang, Shibing Long, Zhaoan Yu, Meiyun Zhang, Tianchun Ye, Yang Li, Dinglin Xu, HangbingLv, Qi Liu, Ming Wang, Xiaoxin Xu, Hongtao Liu, Baohe Yang, Jordi Suñé, and Ming Liu, "Improving resistance uniformity and endurance of resistive switching memory by accurately controlling the stress time of pulse program operation", Appl. Phys. Letters, 106, 092103, 2015.

[33] K. B. Oldham, J. C. Myland A. M. Bond, "Electrochemical science and technology. Fundamentals and Applications", John Wiley & Sons, 2012

[34] A. J. Bard and L. R. Faulkner, "Electrochemical Methods: Fundamentals and Applications". New York, NY, USA: Wiley, 2001.

[35] Artjom V. Sokirko, Fritz H. Bark, Diffusion-migration transport in a system with butler-volmer kinetics, an exact solution, ElectrochimicaActa, Volume 40, Issue 12, September 1995, Pages 1983-1996, ISSN 0013-4686, http://dx.doi.org/10.1016/0013-4686(94)00359-9.

[36] B. Govoreanu, S. Clima, I. P. Radu, Y.-Y. Chen, D. J. Wouters, and M. Jurczak, "Complementary Role of Field and Temperature in Triggering ON/OFF Switching Mechanisms in Resistive RAM Cells," Electron Devices, IEEE Transactions on, vol.60, no.8, pp.2471,2478, Aug. 2013 doi: 10.1109/TED.2013.2266357

[37] M.A. Villena, F. Jiménez-Molinos, J.B. Roldán, J. Suñé, S. Long, E. Miranda and M. Liu, "A comprehensive analysis on progressive reset transitions in RRAMs", J. Phys. D: Appl. Phys. 47 205102, (2014).

[38] U. Celano, L. Goux, A. Belmonte, K. Opsomer, A. Franquet, A. Shulze, C Detavernier, O. Richard, H. Bender, M. Jurczak, W. Vandervorst, "Three-Dimensional Observation of the Conductive Filament in Nanoscaled Resistive Memory Devices", Nanoletters, 14, pp. 2401-2406, 2014

[39] Predictive Technology Model (PTM). Nanoscale Integration and Modeling (NIMO) Group at Arizona State University. Available: http://ptm.asu.edu/

Modeling of Valence Change Memories. Electrochemical Memories

3.1. Introduction

In this chapter we deal with the two most important Valence Change Memories (VCM) models described in the literature at the introductory level, and present the main features of a new model developed in our research group, UGR-VCM.

The unidimensional Compact Model for VCM (SU-VCM) [Guan2012, Guan2012b, Yu2012, Jiang2014, Jiang2016], developed initially by the group of Stanford University, describes RS mechanisms in terms of generation/recombination processes of oxygen vacancies in the oxide layer. The gap between the bottom electrode and the conductive filament tip acts as an internal state variable, the conduction mechanism is assumed to be a general tunneling current dependent on the gap and the applied voltage. The temperature dependence is modeled by means of a thermal resistance in most related papers, although more elaborated models are employed in some cases.

The bidimensional Compact Model for VCM (PU-VCM) is a natural evolution of the SU-VCM model development at Peking University [Huang2013, Li2014, Li2015]. This model introduces the CF radius as a second state variable. The current throughout the device has two components: a linear component dependent on the CF cylindrical geometry that it is assumed to have metallic-like conduction features and a non-linear current that depends on the gap and the applied voltage. The device temperature evolution is modeled by an effective thermal resistance.

The new UGR-VCM model, inspired in the previous models, improves the state-of-the-art on the compact modelling of these devices and adds an interesting set of novelties:

- A new differential equation that determines the filament volume is established to describe resistive switching operation.
- Truncated-cone shaped filaments are employed with metallic-like transport characteristics and the electrical conductivity associated is temperature dependent.
- The resistances connected with the metal electrodes are considered as well as the device capacitance.
- The temperature is obtained by solving the heat equation including the Joule heating effects in the CF and the lateral heat dissipation from the CF to the surrounding dielectric.
- The cycle-to-cycle variability is considered and included in the model equations.
- An additional current source is included to account for distributed and 3D conduction mechanisms in the dielectric.

The UGR-VCM model was tested with hundreds of experimental I-V RS cycles of different technologies based on the following stacks: $TiN/Ti/HfO_2/W$, $Pt/TiO_2/Al_2O_3/TiO_2/RuO_x/TiN$ and $Au/Ti/TiO_2/SiO_x/n^{++}Si$.

3.2. Unidimensional Compact Model for VCM Bipolar RRAMs (SU-VCM)

The unidimensional compact model of bipolar VCMs (SU-VCM) was develop initially at the Stanford University [Guan2012, Guan2012b]; nevertheless, more research groups made use of this original model to develop their own versions (see **Table 3.I** for details).

Table 3.I Institutions related to development the SU-VCM

Institution	Reference SU-VCM
Stanford University, USA	[Guan2012, Guan2012b, Yu2012, Jiang2014, Jiang2016]
South University of Science and Technology of china	[Yu2012]
Peking University, China	[Yu2012]
Institute of Microelectronics, A*STAR, Singapore	[Yu2012]
Arizona State University, USA	[Jiang2014, Chen2015, Jiang2016]
Oracle America, USA	[Jiang2014]
AIXTRON, USA	[Jiang2016]

The SU-VCM assumes RS operation to be described by generation/recombination of oxygen vacancies (V_o) and oxygen ions that allow the formation of a conductive filament that can short the electrodes. Due to the differences in the activation energies linked to the migration of oxygen vacancies and oxygen ions, the vacancies are supposed to be immobile while oxygen ions diffuse in the dielectric [Bersuker2011b]. **Figure 3.1** shows the band diagram for oxygen ion migration in the oxide layer and **Figure 3.2** shows how the SU-VCM model simplifies the CF structure in the dielectric layer.
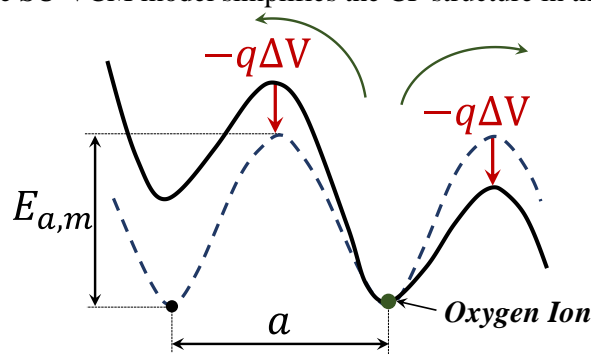
Figure 3.1 Band diagram for oxygen ion migration in the oxide layer. The blue dashed line represents the migration barrier without bias. The black curve accounts for the barrier when an external bias is applied. Adapted from [Guan2012b].
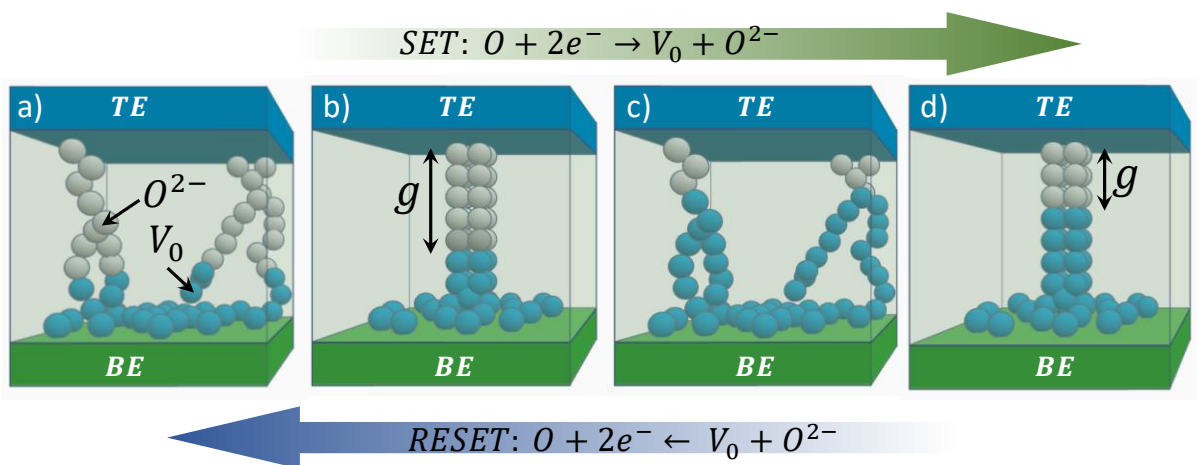
Figure 3.2 Sketch of CF configuration for the transition from HRS to LRS; **a)** filamentary configuration for the devices in HRS with a long gap distance, **b)** simplified configuration with a long gap, **c)** filamentary configuration when the gap is reduced, **d)** simplified stack structure assuming a short gap. (adapted from [Jiang2016, Jiang2014]).
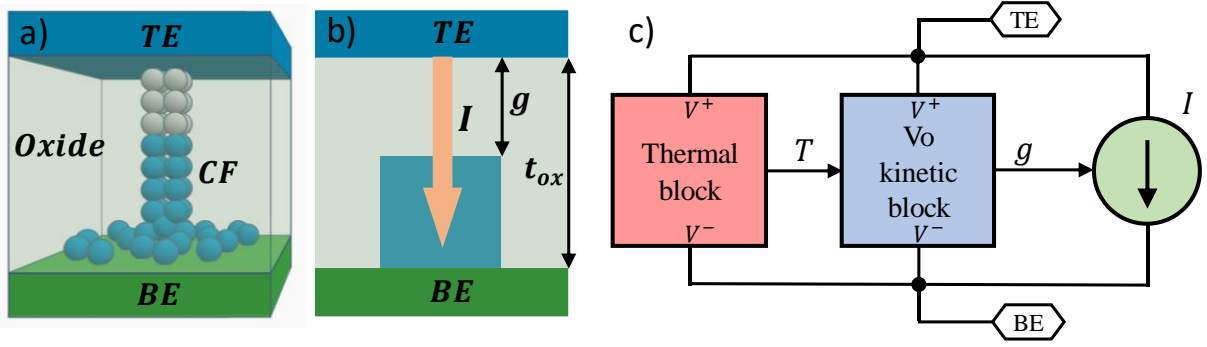
Figure 3.3 a) Three-dimensional view of the SU-VCM modelling structure with an indication of different device areas (TE, Oxide, CF and BE), **b)** geometrical parameters in the model. The gap (g) between the TE and the filament tip is one of the state variables, the other one is the temperature (T), **c)** sub-circuit for the model implementation.

The simplified structure of SU-VCM model is shown in **Figure 3.3 a)**, the gap (g) is the main internal state variable that controls RS operation. Derived from Arrhenius laws, accounting for the corresponding thermally activated RS physical mechanisms [Guan2012b], the gap variation (dg/dt) is calculated as follows [Guan2012, Guan2012b, Jiang2014, Yu2012],

$$\frac{dg}{dt} = v_0 \cdot e^{-\frac{E_{a,m}}{k_b T}} \cdot sinh\left(\frac{q \cdot \gamma \cdot a_0 \cdot V}{L \cdot k_b \cdot T}\right) \quad , \quad g \geq g_{min} \tag{3.1}$$

where v_0 is the velocity containing the attempt-to-escape frequency, E_a is the activation energy for vacancy generation that activates the set process, E_m is the migration barrier for oxygen migration that activates the reset process, k_b is the Boltzmann constant, q is the electron charge, a_0 is the atomic hopping distance, V is the applied voltage in the gap, L is the oxide layer thickness, g_{min} is the minimum gap distance, T is the device temperature and γ is the local enhancement factor that models the nonuniform potential distribution and the strong polarization in high-k dielectrics expressed as function of g, following refs. [Jiang2014, Yu2012],

$$\gamma = \gamma_0 - \beta \cdot g^3 \tag{3.2}$$

Where γ_0 and β are fitting parameters[1].

The kinetic block subcircuit shown in **Figure 3.3 c)** is implemented with equations (3.1) and (3.2). In this case all the parameters are constants except V, T and g.

The current in the dielectric layer is assumed to be linked to a tunneling mechanism (equation (1.29)), this means that there is no dominant conductive mechanism in the oxide layer and current components connected to trap-assisted tunneling, Poole–Frenkel tunneling, Fowler–Nordheim tunneling, or direct tunnelling could be feasible. The expression to account for a generalized tunneling current can be expressed as follows [Guan2012, Guan2012b Jiang2014, Yu2012, Chen2015, Jiang2016],

$$I = I_0 \cdot e^{-g/g_0} \cdot \sinh\left(V/V_0\right) \tag{3.3}$$

where I_0, g_0 and V_0 are fitting parameters. Equation (3.3) is implemented by the current source I in the subcircuit in **Figure 3.3 c)**. The oxygen ion dynamics is drastically affected by the local temperature [Guan2012b], thus affecting RS mechanisms such as generation/recombination of oxygen vacancies.

---

[1] In references [Guan2012, Guan2012b] show a linear dependence ($\gamma = \gamma_0 - c_0 \cdot g$), in reference [Jiang2016] a exponential relation ($\gamma = \gamma_0 - \beta \cdot g^\alpha$, where α is a fitting parameter) and in reference [Chen2015] a normalized exponential function ($\gamma = \gamma_0 - \beta \cdot (g/g_1)^3$, where g_1 is the inicial gap value)

Two thermal descriptions for the device operation are reported. In refs. [Guan2012b, Yu2012, Jiang2014, Jiang2016] the temperature is calculated making use of a simple effective thermal resistance (see appendix D.1.),

$$T = T_0 + V(t) \cdot I(t) \cdot R_{th} \tag{3.4}$$

where R_{th} is the effective thermal resistance of entire device, T_0 is the absolute room temperature and $V(t)I(t)$ describes the power dissipated by means of Joule heating. The temperature description including inertia can be implemented as follows [Guan2012, Chen2015] (see appendix D.2. for details),

$$\frac{dT}{dt} + \frac{T - T_0}{\tau_{th}} = \frac{|V(t) \cdot I(t)|}{C_{th}} \tag{3.5}$$

$$T(t + dt) = T(t) + dT \tag{3.6}$$

The high resistance state normally shows a prominent variability from cycle to cycle [Lee2010]. This is mainly due to 1) the stochasticity of ions related physical processes in the programming cycles and 2) the spatial variation of the gap size among multiple filaments. To model this issue, a transient noise signal is added to the average gap distance [Guan2012, Jiang2014, Yu2012, Jiang2016], which results in a random perturbation to the device resistance,

$$g|_{t+\Delta t} = \int \left(\frac{dg}{dt} + \delta_g(T) \cdot \chi(t) \right) dt \tag{3.7}$$

where $\chi(t)$ is a Gaussian noise sequence randomly generated with zero-mean and unitary root mean square generated at each simulation time step. Note that the gap without variability is obtained by integrating equation (3.1). To include variability, the gap is calculated by means of equation (3.6) and (3.7), considering that $\delta_g(T)$ is a sigmoid function dependent on the temperature that can be expressed as

$$\delta_g(T) = \frac{\delta_g^0}{1 + e^{\frac{T_{crit} - T}{T_{smth}}}} \tag{3.8}$$

where, δ_g^0 is a parameter to fit a set of RS cycles, T_{crit} is an activation temperature (for higher temperatures random fluctuations are activated) and T_{smth} is a fitting parameter that determines the gradual or abrupt transition for the activation of random fluctuations.

The complete set of parameter for the SU-VCM model is shown in **Table 3.II**.

The SU-VCB model is fully compatible with SPICE-like circuit simulators. **Figure 3.3 c)** shows the model block diagram. Only one current source is needed: (I) that depends on the applied voltage (V_{cell}) and the gap (g). The two subcircuits employed in this case are the following: a thermal block that is electrically activated (V_{cell}) and provides the device temperature (T), and the kinetic block that is electrically activated (V_{cell}) and depends on the device temperature (T), this latter block determines at each time step the gap (g).

Figure 3.4 shows the modeled results obtained by the SU-VCM model implemented in SPICE when a ramped voltage signal is employed. The initial state is assumed to be HRS (the current is low and the g value is close to 3nn). When the voltage increases the set process begins, the temperature rises and the gap g reaches the minimum value of 0.25nm (an oxygen vacancy approximated size), the device state changes to LRS, and the current increases. Then, the ramped voltage signal changes the polarity and a reset process begins. In this process the current drops off and the gap g increases.
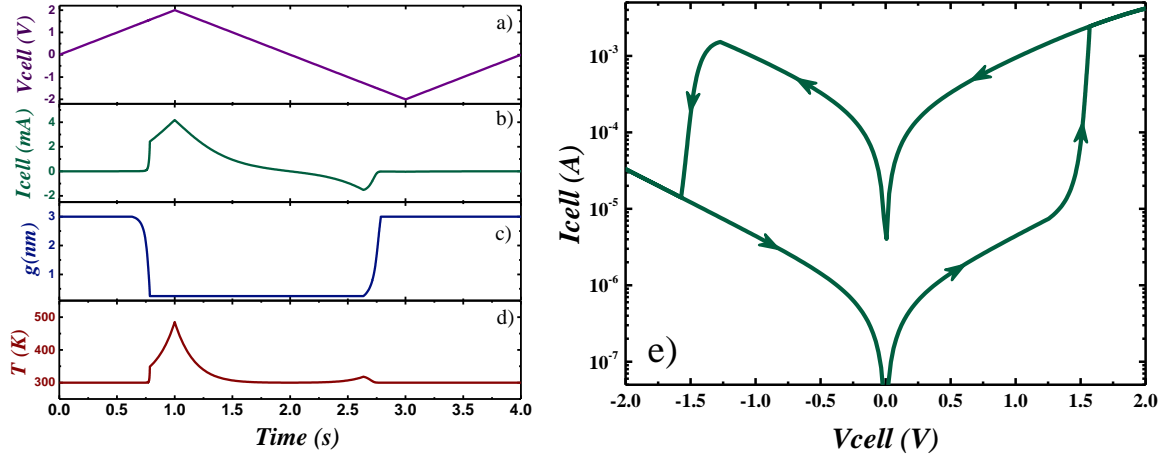
Figure 3.4 a) Ramped voltage applied to a RRAM. Temporal evolution of the main operational magnitudes: **b)** Current versus time response, **c)** gap time evolution, **d)** device temperature time evolution and **e)** corresponding I-V curve.

Table 3.II Summary of SU-VCM model parameters.

Symbol	Description	Unit
L	Oxide thickness	m
a_0	Atomic hopping distance	m
g_{min}	Minimum gap distance	m
g_{max}	Maximum gap distance	m
g_{ini}	Initial gap distance	m
E_a	Activation energy for vacancy generation	eV
E_m	Activation energy for oxygen ion migration	eV
v_0	Velocity containing the attempt-to-escape frequency	m/s
γ_0	Fitting parameter for field enhancement factor	
β	Fitting parameter for the field enhancement factor	
I_0	Fitting parameter for the tunneling current	A
g_0	Fitting parameter for the tunneling current	m
V_0	Fitting parameter for the tunneling current	V
T_0	Room absolute temperature	K
R_{th}	Effective thermal resistance	K/W
C_{th}	Effective thermal capacitance	
k	Boltzmann constant	J/K
q	Electron charge	C
V	Voltage applied to the RRAM	V
I	Current flowing through the RRAM	A
g	Gap distance from the CF tip to the TE	m
dg/dt	Gap velocity for filament growth/dissolution	m/s
γ	Local field enhancement factor	
T	Device temperature	K

Colour Code

Geometric properties   Thermal constants
Kinetic parameters   Physical constants
Hopping current parameter   Model Variables

3.3. Bidimensional Compact Model for VCM Bipolar RRAMs (PU-VCM)

The bidimensional compact model for bipolar RRAM PU-VCM was develop initially at the Peking University [Huang2013, Li2014, Li2015] based on the previous SU-VCM model [Guan2012, Guan2012b, Yu2012, Jiang2014, Chen2015, Jiang2016].

The model assumes an initial state in LRS, without gap (g), modelled by a cylindrical CF, whose resistance is R_{CF} with radius r_0 between the top and bottom electrodes. When the reset process is finished, the gap reaches the maximum allowed value[2], g_0; at this point, if a positive voltage is applied, the set process begins. It is mainly described by two geometric variables g and r. In the first step, the set process consists of a process where the cylindrical CF grows with a constant radius r, from the point of CF rupture to the TE, decreasing the gap. The second step of the set process begins when the gap reaches a minimum value ($g = 0$). This stage accounts for a CF expansion radially, i.e., the CF radius increases. [Huang2013, Li2014, Li2015]. This process is described in **Figure 3.5**.
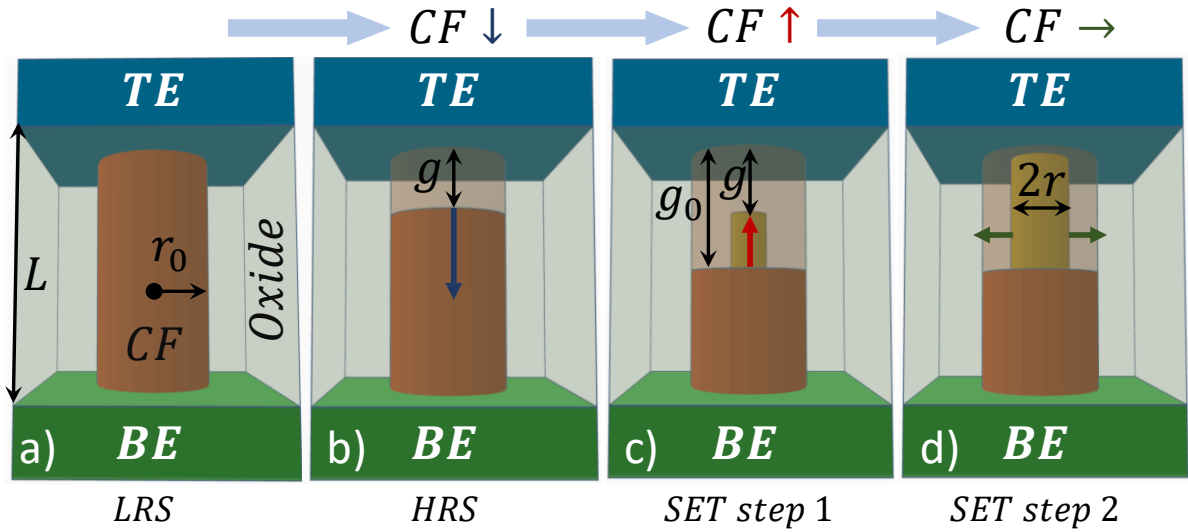
Figure 3.5 Diagram of SU-CVM model conductive filament evolution. **a)** Initial device state in LRS without gap (*g*) and modeled by a cylindrical CF that shorts the electrodes. The CF has an ohmic resistance R_{CF} with radius r_0. **b)** When the reset process is over the gap is non zero and it is limited by a value g_0. **c)** The first step in the set process consists of the growth of a cylindrical CF with radius *r*, from the point of rupture of the CF to the electrode. **d)** The second step on the set process begins when the gap is zero, then the CF expands radially increasing its radius. (Adapted from [Huang2013, Li2014, Li2015]).

The current in the CF has an ohmic nature, it is represented by I_{CF} that depends on the CF geometry (r, g) as given in equation (3.9) [Huang2013,Li2014, Li2015]. In addition, a tunneling current, also named hopping current, as described in the latter form by some authors due to important contribution of dielectric defects to the current, I_{hop} that depends on the CF geometry (r, g) too, and is given by equation (3.10) is employed [Huang2013, Li2014, Li2015].

$$I_{CF} = \frac{\pi r^2}{4} V_{CF} \cdot \rho(g_0 - g) \tag{3.9}$$

$$I_{hop} = I_0(\pi r^2/4)e^{-g/g_T} \cdot \sinh\left(\frac{V_{gap}}{V_T}\right) \tag{3.10}$$

where V_{CF} is the voltage that drops in the CF, V_{gap} is the voltage in the gap, ρ is the CF electrical resistivity, g_0 is the initial gap, I_0, g_T and V_T are fitting parameters of hopping current model.

---

[2] In the SU-VCM model g_0 is a fitting parameter for the tunneling current and g_{max} stands for the maximum gap. In the PU-VCM model g_0 denotes the maximum gap and g_T stands for the fitting parameter for the tunneling current.

In the set process, the CF evolves, this evolution is linked to the evolution of two geometric variables g and r described by equations (3.11) and (3.12) [Huang2013, Li2014, Li2015]

$$\frac{dg}{dt} = a_0 \cdot f \cdot e^{-\frac{E_a - \alpha_a \cdot Z \cdot q \cdot E}{k_b \cdot T}} \tag{3.11}$$

$$\frac{dr}{dt} = \left(\Delta r + \frac{\Delta r^2}{2r}\right) f \cdot e^{-\frac{E_a - \alpha_a \cdot Z \cdot q \cdot E}{k_b \cdot T}} \tag{3.12}$$

where a_0 is the atomic hopping distance, f is the vibration frequency of the vacancy oxygen atom, E_a is the activation energy for oxygen vacancies generation, Z is the charge number of oxygen ions, q is the unitary electron charge, α_a is an enhancement factor to lower E_a, E is the electric field across the gap, k_b is the Boltzmann constant, T is the temperature and Δr is the effective CF radial extension.

The reset process is modelled by accounting for the reduction of the gap distance g as a consequence of three possible mechanisms: electrode release of oxygen ions described by the equation (3.13), oxygen ion hopping in the oxide layer described by the equation (3.14) and recombination between oxygen vacancies and oxygen ions described by equation (3.15) [Huang2013, Li2014, Li2015]

$$\frac{dg}{dt} = a_0 \cdot f \cdot e^{-\frac{E_i - \gamma \cdot Z \cdot q \cdot V}{k_b \cdot T}} \tag{3.13}$$

$$\frac{dg}{dt} = a_0 \cdot f \cdot e^{-\frac{E_h}{k_b \cdot T}} sinh\left(\frac{\alpha_h \cdot Z \cdot q \cdot E}{k_b \cdot T}\right) \tag{3.14}$$

$$\frac{dg}{dt} = a_0 \cdot f \cdot e^{-\frac{\Delta E_r}{k_b \cdot T}} \tag{3.15}$$

where E_m, E_i and ΔE_r are the activation energy for oxygen ion migration, the energy barrier for the oxygen ion electrode release processes and relaxation recombination energy, respectively. The value of dg/dt is considered is given by the minimum value obtained of the three process mechanisms described above. In reference [Li2015] the equation (3.15) is supressed since it is considered that it is never dominant.

The ion dynamics is drastically affected by the local temperature [Guan2012b], thus affecting the generation/ recombination of V_o and oxygen ion pairs. In this model, the temperature is described making use of a simple effective thermal resistance [Huang2013, Li2014, Li2015] (see appendix D.1. for details)

$$T = T_0 + V(t) \cdot I(t) \cdot R_{th} \tag{3.16}$$

To model the cycle-to-cycle variation during set and reset processes, variations of g and r are introduced [Li2015].

$$g = \int \left[\frac{dg}{dt} + \delta g \cdot \chi(t)\right] dt \tag{3.17}$$

$$r = \int \left[\frac{dr}{dt} + \delta r \cdot \chi(t)\right] dt \tag{3.18}$$

Where $\chi(t)$ is a Gaussian noise sequence randomly generated with zero-mean and unitary root mean square, generated at each simulation time step, and δg and δr are sigmoid functions in line with equation (3.8) [Guan2012, Jiang2014, Yu2012, Jiang2016].

Additionally, a Monte-Carlo approach includes a random variable δ_{Ea} added to the activation energy E_a in equations (3.11) and (3.12) to model cycle-to-cycle variability (set). In the same way, for the reset process random variables δ_{Ei} and δ_{Eh} are added to the activation energies values E_i and E_h in equations (3.13) and (3.14) respectively [Li2015]. **Table 3.III** summarizes the parameters used in the bidimensional PU-VCM model.

$$g\ (set) = f(E_a + \delta_{E_a}) \tag{3.19}$$

$$g\ (reset) = f(E_i + \delta_{E_i}, E_h + \delta_{E_h}) \tag{3.20}$$

Table 3.III Summary of bidimensional PU-VCM model parameter

Symbol	Description	Unit
L	Oxide thickness	m
a_0	Atomic hopping distance	m
g_o	Initial gap distance	m
r_o	Initial radio of cylinder CF	m
E_a	Activation energy for vacancy generation	eV
E_m	Activation energy for vacancy migration	eV
E_i	Energy barrier between oxide and electrode	eV
ΔE_r	Relaxation recombination energy	eV
Δr	Effective CF radial extension	m
f	Vibration frequency of vacancy oxygen atom	Hz
γ_0	Fitting parameter for field enhancement factor	
β	Fitting parameter field enhancement factor	
α_a	Enhancement factor for lower E_a	m
α_m	Enhancement factor for lower E_m	m
ρ	Electrical resistivity of CF	$\Omega{\cdot}m$
I_0	Fitting parameter for hopping current	A
g_0	Fitting parameter for hopping current	m
V_0	Fitting parameter for hopping current	V
T_0	Room absolute temperature	K
R_{th}	Effective thermal resistance	K/W
k	Boltzmann constant	J/K
q	Elementary unit charge	C
V	Voltage applied to the RRAM	V
I	Current flowing through the RRAM	A
g	Gap distance from the CF tip to the TE	m
r	Radio of cylinder CF	m
dg/dt	Gap velocity for filament growth/dissolution	m/s
dr/dt	Radio velocity for filament growth/dissolution	m/s
T	Temperature	K

Colour Code

	Geometric properties		Thermal constants
	Kinetic parameters		Physical constants
	Electrical parameter		Model Variables

3.4. New Compact Model for Bipolar VCM (UGR-VCM)

3.4.1. Model Development

The UGR-VCM model has been developed for filamentary conduction in RRAMs based on Metal-Insulator-Metal (MIM) or Metal-Insulator-Semiconductor (MIS) structures and implemented in Verilog-A code for circuit simulation purposes. The model describes RRAM resistive switching processes by computing the formation and rupture of conductive filaments (CFs) formed by oxygen vacancies by means of a new differential equation in the dielectric that determines the filament volume. Truncated-cone shaped filaments were employed in the model developed with metallic-like transport characteristics. A hopping current in the gap (g) and in the lateral side of the truncated-cone shaped conductive filament are taken into account to describe the electron transport between the filament tip and the electrode. The hopping current is an essential component in the device in the high resistance state (HRS). The resistances of the electrodes, and of the dielectric between the CF tip and the electrode, are taken into consideration. The CF thermal description is included by solving the heat equation accounting for Joule heating and for lateral heat dissipation (see appendix D.6. for details). A table of the parameters used in the UGR-VCM model is shown in **Table 3.IV**.

The model has been employed to reproduce I-V curves of different RRAM technologies making use of the correct model parameters in each case:

- MIM devices: TiN/Ti/HfO$_2$/W and Pt/TiO$_2$/Al$_2$O$_3$/TiO$_2$/RuO$_x$/TiN (see appendix A.2. and A.3. for details).

- MIS device: Au/Ti/TiO$_2$/SiO$_X$/n^{++}Si (see appendix A.4. for details).

The model is suitable to be implemented in circuit simulators to analyze circuits based on RRAMs under different operation regimes. Variability can be included to account for the dispersion of experimental data due to the inherent stochasticity of RS operation.

Table 3.IV Summary of UGR-VCM model parameter.

Symbol	Description	Unit
L	Oxide thickness	nm
$[L_{CT}, L_{CB}]$	[Top, Bottom] electrode thickness	nm
$[g_{m,x}, r_{Tm,x}, r_{Bm,x}]$	Minimum, maximum [gap, top radio, bottom radio]	nm
L_{cell}	Side of the RRAM cell	μm
$[E_a, E_r]$	Average active energy of generation oxygen vacancies, Equivalent reset energy	eV
v_0	Volume velocity ($a_0^3 \cdot f$)	m^3/s
$[\alpha_a, \alpha_h]$	Enhancement factor of electric field for lowering of $[E_a, E_h]$	nm
γ	Enhancement factor of voltage during the O^{2-} release process	
$[T_0, T_C]$	[Initial room, Critical] temperature	K
k_{th}	Thermal conductivity	$WK^{-1}m^{-1}$
h	Heat transfer coefficient	$WK^{-1}m^{-2}$
α_T	Thermal conductivity coefficient	K^{-1}
$[\sigma_{Ox}, \sigma_{CF0}]$	[Oxide, C.F.] electrical conductivity	S/m
$[\sigma_{CB}, \sigma_{CT}]$	[Bottom, Top] electrode electrical conductivity	S/m
I_0	Density current fit coefficient	$A/\mu m^2$
g_0	Gap fit coefficient	nm
V_0	Voltage fit coefficient	V

Colour Code

	Geometric properties	Thermal constants
	Kinetic parameters	Electrical constants
	Hopping current parameter	Model Variables

The UGR-VCM model was selected in the review paper [Lekshmi2019] with other compact models previously reported in the literature. Analyzing the different materials and physical mechanisms adopted by each model, an error analysis was reported to determine the relative accuracy between the experimental and modeled data for each model. The results are listed in Table 3 [Lekshmi2019]. The UGR-VCM model is selected as the better model in terms of its minimum relative error (3%) reported.

Table 3.V Comparison of compact models. Error between the experimental and modeled data reported in the review study given in ref. [Lekshmi2019]

Device	Type	Error (%)	Reference
$TiN/TiO_x/HfO_x/Pt$	BRS	24	[Jiang2016]
$Pt/TaO_x/Ta$	BRS	23	[Siemon2014]
$Ag/ChG/Ni$	-	20	[Saremi2016]
$Pt/Ta_2O_5/TaO_x/Pt$	BRS	19	[Jagath2018]
$TiN/TiO_x/HfO_x/Pt$	BRS	12	[Jiang2016]
$Pd/Ta_2O_5/TaO_x/Pd$	BRS	9	[Kim2014b]
$TiN/HfO_2/TiN$	BRS	8	[Ambrogio2014]
$TiN/Ti/HfO_2/W$	BRS	3	[González-Cordero2017a]

A complete description of the UGR-VCM model is given in the Appendix C.

The UGR-VCM model was published in González-Cordero et al. Journal of Vacuum Science and Technology B (2017), the accepted preprint paper is presented below.

González-Cordero et al. Journal of Vacuum Science and Technology B (2017)

Quality metrics

Data base	Rating	Quartile
Web of Science	Impact factor: 1.31	Q3
Scimago	Scientific journal ranking: 0.467	Q2

Publication citations

Google Scholar	Web of Science
24	22

An in-depth study of the physics behind resistive switching in TiN/Ti/HfO₂/W structures

G. González-Cordero, F. Jiménez-Molinos, J.B. Roldán[a)]

Departamento de Electrónica y Tecnología de Computadores, Universidad de Granada (Spain)

M.B. González, F. Campabadal

Institut de Microelectrònica de Barcelona, IMB-CNM (CSIC), Campus UAB, 08193 Bellaterra, (Spain)

Electronic mail: jroldan@ugr.es

A physical simulation procedure was used to describe the processes behind the operation of devices based on TiN/Ti/HfO2/W structures. The equations describing the creation and destruction of conductive filaments formed by oxygen vacancies are solved in addition to the heat equation. The resistances connected with the metal electrodes also were considered. Resistive RAMs analyzed were fabricated and many of the characteristics of the experimental data were reproduced with accuracy. Truncated-cone shaped filaments were employed in the model developed with metallic-like transport characteristics. A hopping current also was taken into account to describe the electron transport between the filament tip and the electrode. Hopping current is an essential component in the device high resistance state.

INTRODUCTION

Many devices based on metal oxides are currently under study to analyze their capability as Resistive Random Access Memories (RRAMs) and analog memristors.[1, 2] The operating principle of the Resistive Switching (RS) mechanism is based on the ability of the devices to switch between two states with different electrical resistance: a Low Resistance State (LRS) and a High Resistance State (HRS). This RS process is linked to the creation and rupture of a conductive filament (CF) that connects the two device electrodes with a metallic-like path, when its fully formed.[2-5] The transition between states takes place due to Set (HRS to LRS) and Reset (LRS to HRS) processes. The potential for using RRAMs in industrial applications depends on a set of characteristics that make them a promising contender in the non-volatile memory landscape: low power consumption (low in program/erase currents), fast switching speed (~1ns), good endurance and retention, multilevel cell storage capability, viability for 3D memory stacks and ease of integration in the back end of line of standard CMOS processes.[2, 6-9] Fabrication, characterization and modeling activities for RRAMs have grown in the last few years, both in industry and academia. RRAM memory circuits that have been recently reported on include, 128Kb memory arrays,[10] 64Mb,[11] 4Mb memories with 2.3GB/s Read-Throughput and 216MB/s Program-Throughput,[12] and 8Mb,[13] 32Gb,[14] and 16Gb[15] memory circuits. However, some important issues have to be solved before these devices are used in massive industrial production. A key challenge is to create new and accurate compact models to translate the physics of RRAM operation to a set of analytical equations for the purposes of simulating resistive switching (RS) structures in circuits.

There are several important physical effects involved in the RS phenomena. These include thermal effects and quantum mechanical effects such as tunneling currents and redox reactions, which control the dynamics of CF creation and disruption. [2, 4, 8, 16, 17] In addition, parasitic effects such as series resistances, capacitors, etc., also must be considered to properly model RRAMs devices.[2, 4, 8, 16, 17] Models for circuit simulation have been published based on the formation and rupture of one or several CFs.[3-5, 8, 14, 17-26] However a detailed device thermal description, a correct CF geometrical implementation, and an accurate model for parasitic effects are needed to enhance these models.

In this paper and in the context of RRAM modeling, we present a physical model for bipolar RS devices where the electrode resistances and the CF temperature and geometry, among other features, are included in a comprehensive, analytical and compact numerical scheme. The simulation results using

the proposed model are compared to experimental data of TiN/Ti/HfO₂/W devices and the most representative modeling issues are discussed.

PHYSICAL MODEL

The analysis developed to describe the physics behind RS assumes filamentary RRAM operation, where CFs are formed by percolation paths made of oxygen vacancy clusters with metallic-like conduction features. These CFs are mainly formed in high temperature and high electric field dielectric regions.[21]
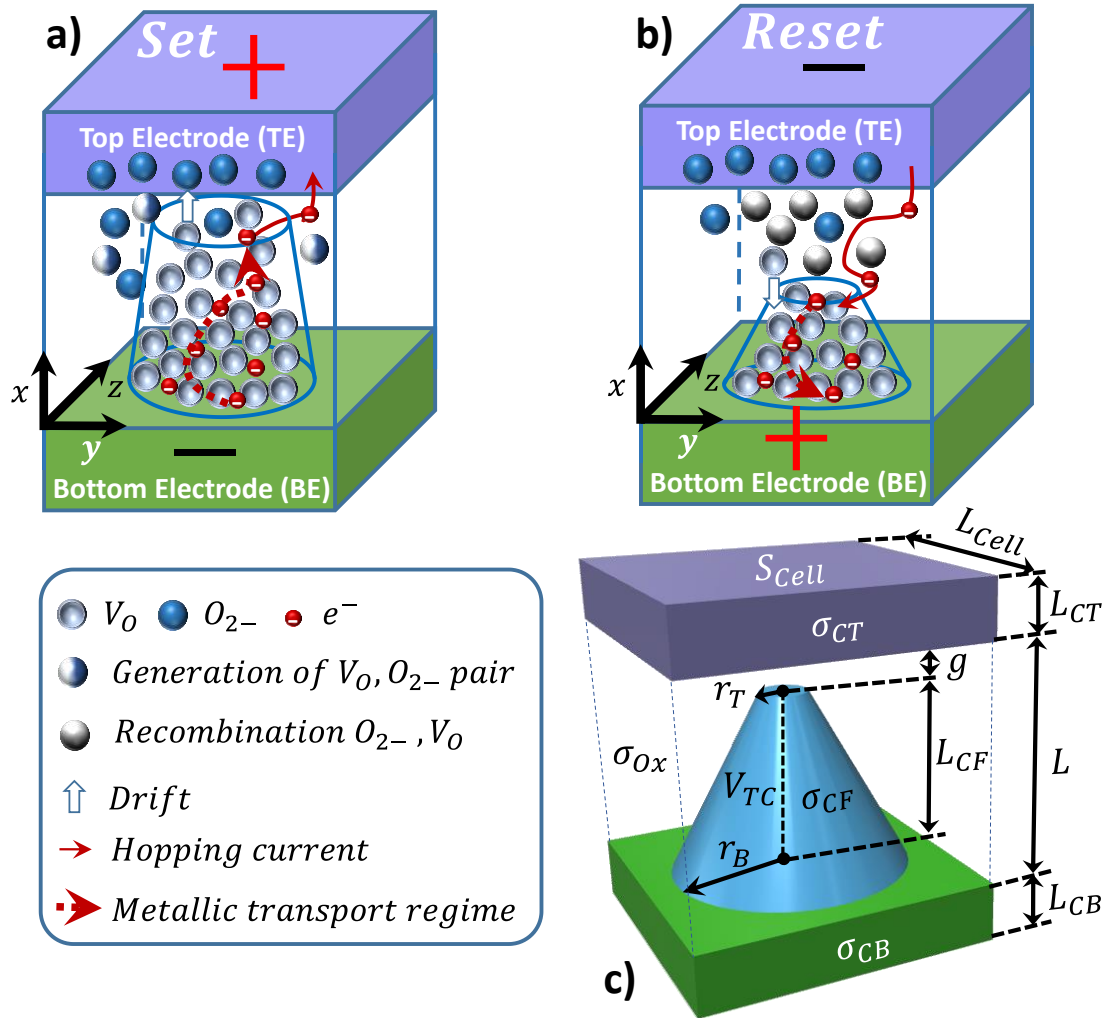
Fig. 1. (Color online) Diagram of the physical processes behind the RRAM RS mechanisms. (a) Set process, (b) Reset process, (c) RRAM scheme to represent the CF geometry and main modeling variables employed.

Truncated-cone shaped CFs were assumed for the description of RS operation in the devices, following previous experimental results (see Ref. 27). A diagram of the physical mechanisms behind the set/reset processes and the geometry of the CFs used in the device modeling are shown in Fig. 1. The distance between the CF tip and the electrode (g) modulates the hopping conduction[21] that was included in the study. The ohmic resistances of the electrodes (R_{CT}, R_{CB}) and of the CF (R_{CF}) were considered and the role of the dielectric surrounding the CF and the dielectric region filling the gap g also were included by means of two resistances (R_{ox}, R_g). Note that the CF geometry changes when g or the radii of the higher and lower truncated cone sides (r_B, r_T) are modified (see Fig. 1). Taking into account the CF shape, we have formulated its variation with time (t) as a function of its total volume. The variations for the set and reset processes, are expressed as equations 1 and 2, respectively:

$$\frac{dV_{TC}}{dt} = v_0 \exp\left(-\frac{E_a - \alpha_a Z e \xi}{k_b T}\right) \qquad (set) \qquad\qquad (1)$$

$$\frac{dV_{TC}}{dt} = -v_0 \exp\left(-\frac{E_r - \alpha_r(g) Z e \xi}{k_b T}\right) \qquad (reset) \qquad\qquad (2)$$

where V_{TC} is the CF volume; ξ is the electric field; T is the local temperature; k_b is the Boltzmann's constant; E_a is the average activation energy of oxygen vacancies; α_a is the enhancement factor of the electric field; v_0 stands for the product of the vibration frequency of the oxygen atom and the oxygen vacancy volume; $Z = 2$ is the charge number of oxygen ions; e is the unit charge; E_r is an average energy that accounts for the processes involved in the reset process[21] and $\alpha_r(g) = \gamma g + \alpha_h$, accounts for the electric field enhancement factor that lowers the hopping barrier (α_h) and for the external voltage enhancement factor (γ) during oxygen ion release. We would like to call the reader's attention to the fact that the electric field used in the previous equations was based on a 1D simplification of the real electric field distribution.

The CF volume depends on the bottom and top radii (r_B, r_T) and on the g parameter. Therefore, the volume can be modulated by varying the magnitudes of these three factors. Instead of focusing on the radii variation[17,24,28] and g variation,[21] we chose to merge all the dependencies and formulate the problem in terms of the CF volume to simplify calculations.

The heat equation also was solved to obtain the CF temperature.[17] This step helps provide information about the other magnitudes that control the CF geometry evolution.[28,29] Joule heating in the CF and lateral heat dissipation from the CF to the surrounding dielectric also are considered.[4, 5]

The volume of the CF is changed by considering variations of the g parameter between a maximum value (g_x) and a minimum value corresponding to the oxygen vacancy radius. Then, the variation of r_T is considered between a maximum value r_{Tx} and the oxygen vacancy radius. Setting this minimum value is coherent with the modeling approach followed here and avoids numerical instabilities. Finally, the variation of r_B is considered between a maximum value r_{Bx} and a minimum value r_{Bmin} which was chosen to be 25nm, a fitting parameter (the same value was used for all the curves considered) needed to reproduce the experimental data.

The hopping current can be calculated using Equation 3.[21]

$$I = I_0 \exp\left(-\frac{g}{g_0}\right) \sinh\left(\frac{V_g}{V_0}\right) \qquad\qquad (3)$$

where g_0 and V_0 are the characteristic length and voltage, respectively. We have taken into consideration both the contribution of the hopping currents from the top and lateral sides of the truncated-cone shaped CF. For the lateral sides, an average of the distance between the CF surface and the top electrode is calculated in order to compute the current.

DEVICE FABRICATION AND MEASUREMENT

The TiN/Ti/HfO₂/W devices were fabricated on (100) p-type CZ silicon wafers. After a standard wafer cleaning, a wet thermal oxidation process was performed at 1100 ℃, leading to a SiO_2 layer 200 nm in thickness. Then, a 200 nm W layer was deposited by magnetron sputtering and patterned by photolithography and a lift-off process. A 10 nm HfO_2 layer was deposited by atomic layer deposition (ALD) at 225 ℃ using TDMAH and H_2O as precursors, and N_2 as carrier and purge gas. The top electrode, consisting of a 200 nm TiN and a 10 nm Ti layer (as oxygen getter material), was deposited by magnetron sputtering and patterned by photolithography and lift-off. Finally, contact windows to the bottom electrode were opened by dry etching of the HfO_2 layer to allow electrical probing. The resulting device structures were square cells of 15 x 15µm². A schematic representation of the device cross-section is shown in Fig. 2(a).

The current-voltage (I-V) measurements were performed using a HP-4155B semiconductor parameter analyzer. The voltage was applied to the TiN/Ti top electrode, while the W bottom electrode was grounded. In order to evaluate the resistive switching (RS) properties and to automatically perform successive cycles, a software tool was been developed and implemented in Matlab to control the instrumentation via GPIB (General Purpose Instrumentation Bus). The measurement procedure consisted of the following steps: after a forming process with a current compliance of $100 \ \mu A$, several hundreds of RS cycles were measured in a double sweep mode, from 0 to 1 V for the set process and from 0 to -1.8 V for the reset process.

RESULTS AND DISCUSSION

In our numerical scheme, the equations to simulate the physical processes that lead to RS were put together and self-consistently solved. First, we fitted the parameters of equations (1), (2) and (3) accounting for the heat equation and using an experimental set of hundreds of RS cycles. As shown in Fig. 2(b), the experimental curves are well reproduced in both polarities. The modeled curves are shown in symbols.
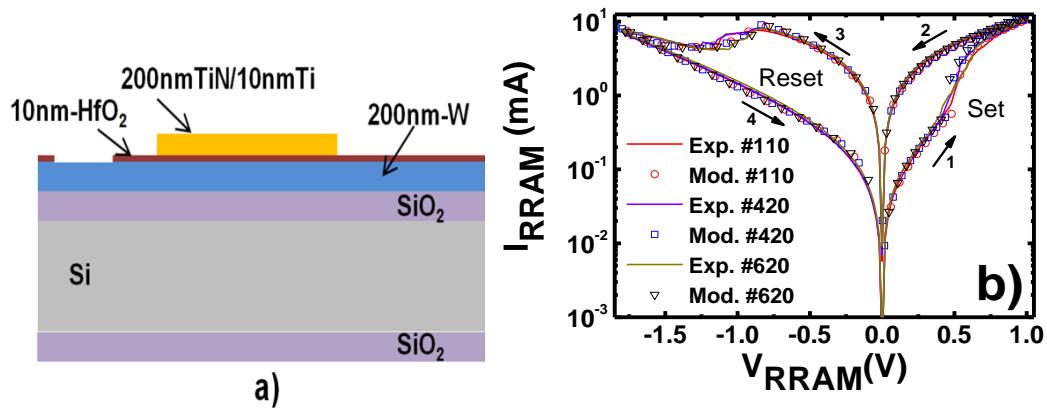
Fig. 2. (Color online) (a) Cross-section scheme of the devices under study. (b) Experimental and modeled current versus applied voltage for different cycles. The following CF geometrical parameters were employed in the modeling process: cycle 110, $r_{Bx} = 30nm$, $r_{Tx} = 3.9nm$ and $g_x = 3.3$nm; cycle 402, $r_{Bx} = 30 \ nm$, $r_{Tx} = 4nm$ and $g_x = 3.3$nm; and cycle 620, $r_{Bx} = 29nm$, $r_{Tx} = 4.5nm$ and $g_x = 2.8$nm.

We have considered several modeling situations in order to evaluate the accuracy of the model and the to include different features in the model (see Fig. 3). A curve with fixed temperature, T=300K, is included. As can be seen, no set or reset processes occur, as these processes are known to be activated by temperature.[1,4,5] A curve considering a cylindrical CF also is shown, though the experimental data fit poorly in this case. Finally, a curve with a much higher electrode series resistance is plotted. In this case the change with respect to the original curve (Fig. 2.b) is lower because the role of this resistance in comparison with the CF ohmic and tunneling components is less important; however, a non-negligible displacement can be seen for the higher current values.
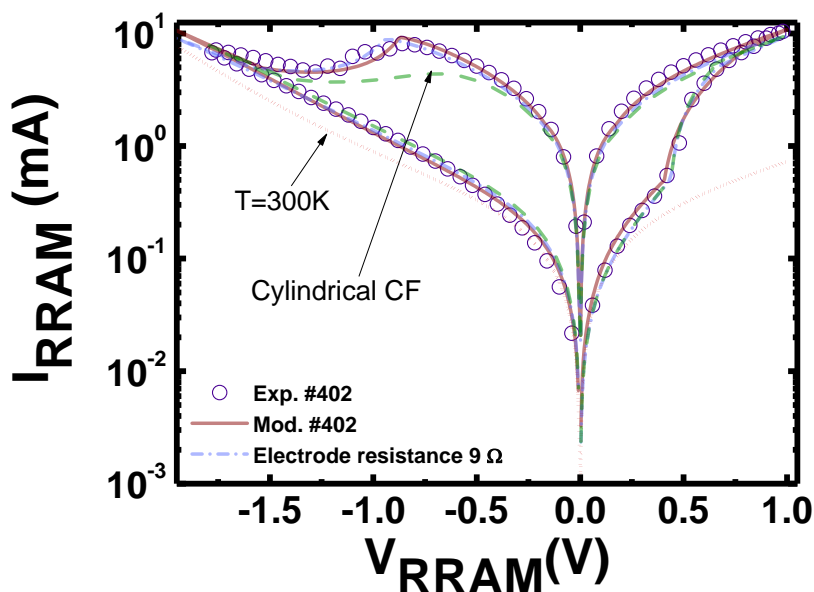
Fig. 3. (Color online) Experimental and modeled current versus applied voltage for the experimental 402 cycle with the following CF parameters: $r_{Bx} = 30\ nm$, $r_{Tx} = 4nm$ and $g_x = 3.3$nm. The dotted line represents a modeled curve with the temperature fixed at 300K, and it can be observed that no set or reset processes occur in this case. If a cylindrical CF is employed (dashed line) the fitting is not accurate. A higher electrode resistance is used in the curve shown in dashed-dotted line: a slight variation with the original curve can be seen, mostly at high currents.

After fitting the I-V curves, the variability during cycling of some of the most representative model parameters was explored. In particular, the statistical distribution of the main CF geometrical parameters was studied. It was observed that a Gaussian distribution of these parameters allowed the reproduction of a wide set of experimental cycles (728 curve, as shown in Fig. 4). Notice that the development of a physically based model allows the possibility of studying internal variables and their influence in RRAM filamentary operation, which can be of great use in understanding the device characteristics. Consequently, the inherent variability of RRAM devices can be analyzed to establish strategies for scaling in order to make this type of device feasible for industrial applications.
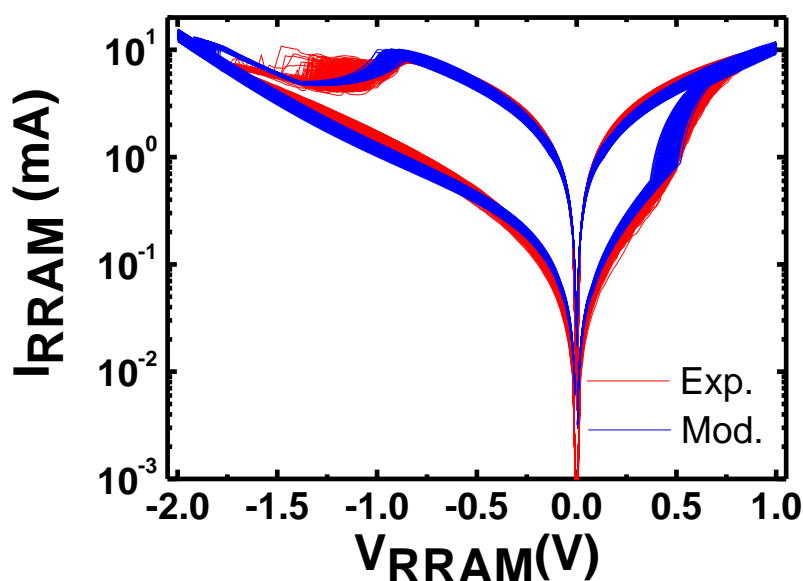
Fig. 4. (Color online) RRAM current versus applied voltage for a set of 728 experimental and modeled curves. A Gaussian distribution for the maxima of the main CF geometrical parameters (r_{Tx}, r_{Bx} and g_x) was used to generate the modeled curves.

See how the regions linked to the set and reset processes are reasonably well reproduced; however, as expected, the regions where more differences between the experimental and model data are these ones. This is due to the self-accelerated processes that lead to CF creation and disruption. They are characterized by a fast temperature rise as well as a rapid increase in the oxygen vacancy formation/recombination rates. The higher variability is consequently expected in these regions (Fig. 4), taking into consideration that a stochastic process is behind the oxygen vacancy generation and recombination events that contribute to the CF modification. It is worth highlighting that the gradual part of the reset curve is the most complicated region to model because here, a reduction in the CF radii and the increase of the CF-electrode gap take place. These parameters are linked but their variation is not completely simultaneous, that is why they contribute to the current reduction in different manners. Nevertheless, on average, the modeling of this region is quite accurate, as shown in Fig. 2(b).

Furthermore, the distributions of reset and set current voltage (I, V) pairs were modeled: In Fig. 5 the I_{reset} (I_{set}) versus V_{reset} (V_{set}) data are plotted for both measured and modeled results. The fitting was achieved by changing the CF geometry, while maintaining the physical constants given in Table I, as it was done in the previous figure. The simulated results agree well with experimental values obtained in real devices, providing a physical explanation of the key parameters that may induce cycle-to-cycle variability and reduce the device performance.
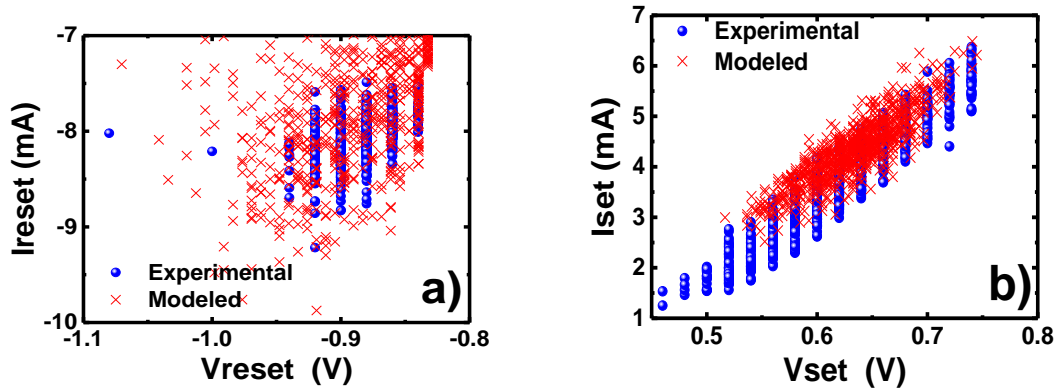
Fig. 5. (Color online) (a) I_{reset} versus V_{reset} calculated for experimental and modeled data. (b) I_{set} versus V_{set} calculated for experimental and modeled data.

Table I. Technological parameters and fitting constants used in the model.

Parameter	Value	Units
L	10	nm
$[L_{CT}, L_{CB}]$	$[210 , 200]$	nm
L_{cell}	15	μm
$[E_a, E_r]$	$[1.12, 1.35]$	eV
v_0	156.25	$\mu m^3/s$
γ	0.25	
k_{th}	5	$W/K \cdot m$
h	10^{10}	$W/K \cdot m^2$
α_T	$1.1 \cdot 10^{-3}$	K^{-1}
$[\sigma_{Ox}, \sigma_{CF0}]$	$[0.013, 5 \cdot 10^5]$	S/m
$[\sigma_{CB}, \sigma_{CT}]$	$[18 \cdot 10^6, 10^6]$	S/m
I_0	10	$A/\mu m^2$
g_0	1	nm
V_0	0.30	V

SUMMARY AND CONCLUSIONS

The operation of RRAMs built on the basis of the TiN/Ti/HfO$_2$/W stack has been analyzed by developing a numerical tool that describes the creation and destruction of conductive filaments formed by oxygen vacancies. The main equations involved in the physics of valence change memories are solved, and metallic-like and hopping transport mechanisms are considered in addition to the resistances corresponding to the metal electrodes. The RRAMs studied were fabricated and measured and their I-V curves were fitted with the modeled data. A set of hundreds of experimental cycles has been correctly described in terms of I-V curves as well as in the distributions of reset and set voltages and currents. Truncated-cone shaped filaments were assumed in the model with metallic-like transport characteristics. The equations controlling the CF dynamics were formulated using the filament volume for the first time, including the possibility of changing the cone radii and the gap between the filament tip and the electrodes.

ACKNOWLEDGMENTS

REFERENCES

[1]R. Waser and M. Aono, Nat. Mat. 6, 833 (2007).

[2]J. S. Lee, S. Lee and T. W. Noh, J. Appl. Phys. Rev. 2, 031303 (2015).

[3]M. Bocquet, D. Deleruyelle, C. Muller and J. M. Portal, J. Appl. Phys. Lett. 98, 263507 (2011).

[4]M. A. Villena, M. B. González, F. Jiménez-Molinos, F. Campabadal, J. B. Roldán, J. Suñé, E. Romera and E. Miranda J. Appl. Phys. 115, 214504 (2014).

[5]M. A. Villena, M.B. González, J. B. Roldán, F. Campabadal, F. Jiménez-Molinos, F. M. Gómez-Campos and J. Suñé, Solid State Electron 111, 47 (2015).

[6]R. Waser, R. Dittmann, G. Staikov and K. Szot, Adv Mater 21, 2632 (2009).

[7]R. Waser, Journal of Nanoscience and Nanotechnology 12, 7628 (2012).

[8]F. Pan, S. Gao, C. Chen, C. Song and F. Zeng, Mater. Sci. Eng. Reports 83, 1 (2014).

[9]M. Lanza, Materials 7, 2155 (2014).

[10]S. Kawabata, M. Nakura, S. Yamazaki, T. Shibuya, Y. Inoue, J. Onishi, Y. Tabuchi, Y. Tamai, Y. Yaoi, et al., presented at the 2010 IEEE International Memory Workshop, (2010).

[11]C. J. Chevallier, C. H. Siau, S. F. Lim, S. R. Namala, M. Matsuoka, B. L. Bateman, and D. Rinerson, presented at the 2010 IEEE International Solid-State Circuits Conference , (2010).

[12]W. Otsuka, K. Miyata, M. Kitagawa, K. Tsutsui, T. Tsushima, H. Yoshihara, T. Namise, Y. Terao, and K. Ogata, presented at the 2011 IEEE International Solid-State Circuits Conference,(2011).

[13]A. Kawahara, R. Azuma, Y. Ikeda, K. Kawai, Y. Katoh, Y. Hayakawa, K. Tsuji, S. Yoneda, A. Himeno, et al., IEEE J. Solid-State Circuits 48, 178 (2013).

[14]T.-y. Liu, T. H. Yan, R. Scheuerlein, Y. Chen, J. K. Lee, G. Balakrishnan, G. Yee, H. Zhang, A. Yap et al., IEEE J. Solid-State Circuits 49, 140 (2014).

[15]R. Fackenthal, M. Kitagawa, W. Otsuka, K. Prall, D. Mills, K. Tsutsui, J. Javanifard, K. Tedrow, T. Tsushima, et al., presented at the International Solid-State Circuits Conference Digest of Technical Papers, (2014).

[16]H.S. P. Wong, H.-Y. Lee, S. Yu, Y.-S. Chen, Y. Wu, P.-S. Chen, B. Lee, F. T. Chen and M.-J. Tsai Proceedings of the IEEE 100, 1951 (2012).

[17]M. A. Villena, F. Jiménez-Molinos, J. B. Roldán, J. Suñé, S. Long, X. Lian, F. Gámiz and M. Liu, J. Appl. Phys. 114, 144505 (2013).

[18]U. Russo, D. Ielmini,C. Cagli, A. L. Lacaita, S. Spiga, C. Wiemer, M. Perego and M. Fanciulli, presented at the 2007 IEEE International Electron Devices Meeting, (2007).

[19]P. Sheridan, K.H. Kim, S. Gaba, T. Chang, L. Chena and W. Lu, Nanoscale 3, 3833 (2011).

[20]X. Guan, S. Yu and H.-S. P. Wong, IEEE Electr. Device L. 33, 1405 (2012).

[21]P. Huang, X. Y. Liu, B. Chen, H. T. Li, Y. J. Wang, Y. X. Deng, K. L. Wei, L. Zeng, B. Gao, et al., IEEE T. Electron Dev. 60, 4090 (2013).

[22]M. Bocquet, D. Deleruyelle, H. Aziza, C. Muller and J. M. Portal, presented at the 2013 IEEE Faible Tension Faible Consommation, V,2,(2013).

[23] Stanford University Resistive-Switching Random Access Memory (RRAM) Verilog-A Model 1.0.0. https://nanohub.org/publications/19/1. Accessed: 2016-10-18

[24]M. Bocquet, , D. Deleruyelle, H. Aziza, C. Muller, J.-M. Portal, T. Cabout and E. Jalaguier, IEEE T. Electron Dev. 61, 674 (2014).

[25]F. Jimenez-Molinos, M. A. Villena, J. B. Roldan and A. M. Roldan, IEEE T. Electron Dev. 62, 955 (2015).

[26]R. Degraeve, A. Fantini, S. Clima, B. Govoreanu, L. Goux, Y.Y. Chen, D. J. Wouters, Ph. Roussel, G.S. Kar, et al., VLSI2012, T75 (2012)

[27]D. H. Kwon, K. M. Kim, J. H. Jang, J. M. Jeon, M. H. Lee, G. H. Kim, X.-S. Li, G.-S. Park, B. Lee, et al., Nature Nanotech 5, 148 (2010).

[28]G. Gonzalez-Cordero, J. B. Roldan, F. Jiménez-Molinos, J. Suñé, S. Long and M. Liu, Semicond. Sci. Technol., 31, 115013, (2016).

[29]S. Larentis, F. Nardi, S. Balatti, D. C. Gilmer, and D. Ielmini, IEEE T. Electron Dev. 59, 2468 (2012).

3.4.2. UGR-VCM Model Validation with other Technologies

To validate the UGR-Model it was tested with three different Metal-Insulator-Metal technologies: TiN/Ti/HfO$_2$/W with a 10 nm-thick dielectric, Pt/TiO$_2$/Al$_2$O$_3$/TiO$_2$/RuO$_x$/TiN with 28.4 nm oxide thickness (0.2nm of Al$_2$O$_3$) and finally, with the same structure reported previously with a 19.6 nm oxide thickness (0.4nm of Al$_2$O$_3$), see appendix A.2. and A.3. respectively for fabrication and measured set-up details.

Some key model parameters affect the device current. For instance: the dielectric layer thickness (D), lateral heat transfer coefficient (h) for dissipation between the CF and the surrounding dielectric, the average activation energy (E_r) accounting for the processes involved in the RESET process and activation energy for oxygen vacancy generation (E_a).

The model parameter fitting was carried out making use of several I-V curves of the experimental data set for each technology. After that, considering random distributions for the geometric model parameters (g, r_T, r_B), a set of simulated curves was obtained that fitted reasonably well the overall set curves of each experimental technology. Details of the model accuracy for some specific cycles for the three technologies are given. It is shown that the proposed model works well for different transition metal oxides and for a variety of dielectric thicknesses.

This section was published in González-Cordero et al. Proceedings of IEEE 11th Spanish Conference on Electron Devices (CDE 2017). IEEE Xplore digital library, the accepted preprint paper is presented below.

González-Cordero et al. Proceedings of IEEE 11th Spanish Conference on Electron Devices (CDE 2017). IEEE Xplore digital library

Quality metrics

Data base	Rating
Google Scholar Metrics	h5-index:6 h5-median:8

Publication citations

Google Scholar	Web of Science
1	**0**

2017 Spanish Conference on Electron Devices (CDE)

A Physically Based Model to describe Resistive Switching in different RRAM technologies

G. González-Cordero[1], M.B. González[2], H. García[3], F. Campabadal[2], S. Dueñas[3], H. Castán[3], F. Jiménez-Molinos[1], J.B. Roldán[1]

[1]Departamento de Electrónica y Tecnología de Computadores, Universidad de Granada (Spain), Email: jroldan@ugr.es
[2]Institut de Microelectrònica de Barcelona, IMB-CNM (CSIC), Campus UAB, 08193 Bellaterra, (Spain)
[3]Departamento de Electrónica, Universidad de Valladolid, Paseo de Belén 15, 47011 Valladolid, (Spain)

Abstract— **A model for filamentary conduction in RRAMs based on Metal-Insulator-Metal (MIM) structures has been developed. The model describes RRAM resistive switching processes by calculating the formation and rupture of conductive filaments (CFs) in the dielectric. The resistance of the electrodes, of the CF and the hopping current in the gap between the CF tip and the electrode, are taken into consideration. The thermal description of the CF is included by solving the heat equation. The model has been employed to reproduce I-V curves of different RRAM technologies making use of the correct model parameters in each case. Therefore, it is suitable to be implemented in circuit simulators to analyze circuits based on RRAMs under different operation regimes.**

Keywords—Compact model, device modeling, non-volatile memory, resistive RAM, Resistive swictching memory, RRAM .

I. INTRODUCTION

Resistive random-access memories (RRAMs) are built as stacks made of two electrodes, top and bottom, and a dielectric in between; for this technology, both MIM and MIS structures are employed. Several metal oxides have been used as dielectrics, among them: HfO_2, TiO_2, NiO, ZnO, Al_2O_3, SiO_2, ZrO_2 [1-5]. For RRAMs based on these dielectrics, resistive switching (RS) operation has been reported. RS shows up when a device switches between a high resistive state (HRS) to a low resistive state (LRS). This process is named SET and the inverse RESET. It should be noted that in devices with the same Transition Metal Oxide (TMO) as dielectric, the electrical behavior of the RRAMs can be different depending on the materials employed for fabricating the top electrode (TE) and bottom electrode (BE). For example, with a stack such us $Pt/HfO_2/Pt$ [3], the device could undergo both SET and RESET processes under the same voltage polarity (unipolar behavior); on the contrary, for a stack reported in Ref. [4], $Ti/HfO_2/TiO_x/Pt$, the devices show bipolar behavior, where the switching processes take place at different voltage polarities. The potential of RRAMs in the non-volatile memory realm is linked to features such as scaling simplicity, low program/erase currents, low switching voltages, fast switching speeds, excellent retention and endurance, capability of multi-bit storage, viability for 3D memory stacks and integration in the back-end-of-line (BEOL) of CMOS processes [1, 5-7]. The previously reported characteristics support RRAMs as viable candidates for the replacement of flash memory technology in future scaling nodes [5, 6].

To advance in RRAM development, and for the inclusion of these devices in future commercial ICs, good compact models are needed in circuit simulation tools. The link between process engineers and designers is made through compact models and reliable model parameters extraction algorithms which should be incorporated in future Electronic Design Automation (EDA) tools.

For these compact models to operate appropriately, the physics behind RS mechanisms has to be taken into account. Among the important physical effects to consider are thermal and quantum mechanical effects, parasitic effects, such as series resistances, redox reactions and other processes that affect the temporal evolution of the device conductance [1, 6-10]. In the last years, several compact models have been proposed by the scientific community [10-19] including different physical approaches to deal with the device temperature calculation. In few of these models the temperature is calculated at every simulation step; in addition, some of the models also consider the real shape and number of CFs, tunneling currents, etc. Parameter extraction has also been dealt with [11, 20-24]. In this work, we present a model for filamentary conduction in RRAMs accounting for the formation/disruption of CFs. The model has been validated with experimental data obtained from different technologies.

II. FABRICATED DEVICES

The devices based on the $TiN/Ti/HfO_2/W$ structure were fabricated on (100) p-type CZ silicon wafers. Wet thermal oxidation was performed at 1100 ºC, leading to a SiO_2 layer 200 nm thick. After that, a 200 nm W layer was deposited by magnetron sputtering. Then, a 10 nm HfO_2 layer was deposited by atomic layer deposition (ALD) at 225 ºC using TDMAH and H_2O as precursors, and N_2 as carrier and purge gas. A 200 nm TiN and a 10 nm Ti layer formed the top electrode, deposited by magnetron sputtering. The contact windows to the bottom electrode were opened by dry etching of the HfO_2 layer. The resulting device structures were square cells of 15 x 15μm². A schematic representation of the device cross-section is shown in Fig. 1(a).
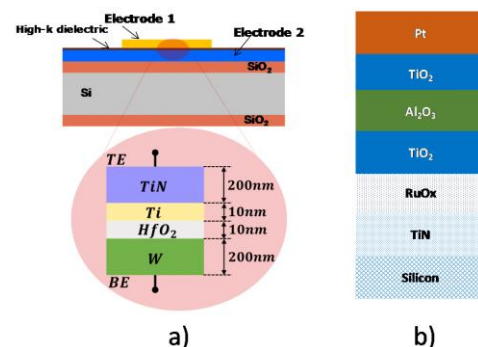
Figure 1: Cross-section sketch of the fabricated devices, a) $TiN/Ti/HfO_2/W$ structures fabricated at the Institute of Microelectronics of Barcelona, b) $Pt/TiO_2/Al_2O_3/TiO_2/RuO_x/TiN$ structures fabricated at the University of Tartu.

The devices made of $Pt/TiO_2/Al_2O_3/TiO_2/RuO_x/TiN$ stacks were deposited by ALD in a home-made flow-type reactor at substrate temperature of 350 °C. $TiCl_4$ was used as the Ti

precursor, TMA as Al precursor and H_2O as the oxygen source. $TiCl_4$ and TMA were kept at room temperature. The film thicknesses are given in Table 1. The ALD cycles used for TiO_2 deposition exposed the substrate to a $TiCl_4$ vapor for 2 s, a purge with pure nitrogen for 2 s, H_2O for 2 s, and a purge with pure nitrogen for 5 s. The ALD cycles used for deposition of Al_2O_3 contained exposure of the substrates to a TMA vapor for 3 s, a purge with pure nitrogen for 2 s, an exposure to H_2O for 2 s, and a purge with pure nitrogen for 5 s. A schematic representation of the device cross-section is shown in Fig. 1(b).

TABLE I.   DESCRIPTION OF THE EXPERIMENTAL DEVICES

Set	#1	#2	#3
Top electrode	Ti/TiN	Pt	
Bottom electrode	W	RuOₓ/TiN	
Dielectric TMO	HfO_2	TiO_2/Al_2O_3/TiO_2	
Dielectric thickness (nm)	10	28.2 TiO_2 0.2 Al_2O_3	19.2 TiO_2 0.4 Al_2O_3

III. MODEL DESCRIPTION

The geometrical features of the model are shown in Fig 2. It is based on the migration of oxygen ions and the formation/disruption of CFs made of oxygen vacancies. The master equations that control the CF geometry evolution and, therefore, the RRAM operation are given below:

$$\frac{dV_{TC}}{dt} = v_0 \exp\left(-\frac{E_a - \alpha_a Zq\xi}{k_b T}\right) \quad (set) \quad (1)$$

$$\frac{dV_{TC}}{dt} = -v_0 \exp\left(-\frac{E_r - \alpha_r(g)Zq\xi}{k_b T}\right) \quad (reset) \quad (2)$$

where V_{TC} stands for the CF volume, v_0 stands for the product of the oxygen atom vibration frequency and the oxygen vacancy volume and E_a is the average activation energy for the generation of oxygen vacancies.
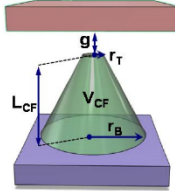
Figure 2: Three-dimensional geometrical representation of the modeled RRAMs.
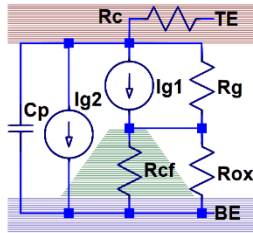
Figure 3: Equivalent circuit of the modeled RRAMs.

Other parameters in the above equations are the following: α_a is the enhancement factor of the electric field for the lowering of E_a, Z is the charge number of oxygen ions, q is the unit charge, ξ is the electric field, k_b is the Boltzmann's constant, T is the local temperature, E_r is an average energy that accounts for the processes involved in the RESET process and $\alpha_r(g)$ is a linear function of the dielectric gap between the CF tip and the

electrode (g) that takes into account the electric field enhancement factor that induces a lowering of the hopping barrier and the external voltage enhancement factor during oxygen ions release. The equivalent RRAM circuit is shown in the Fig. 3, where R_c stands for the ohmic resistances of the electrodes, R_{cf} for the resistance of the CF, I_{g1} and I_{g2} are hopping current components; finally, R_{ox}, R_g are the resistances of the dielectric surrounding the CF and the dielectric region filling the gap g, respectively [24].
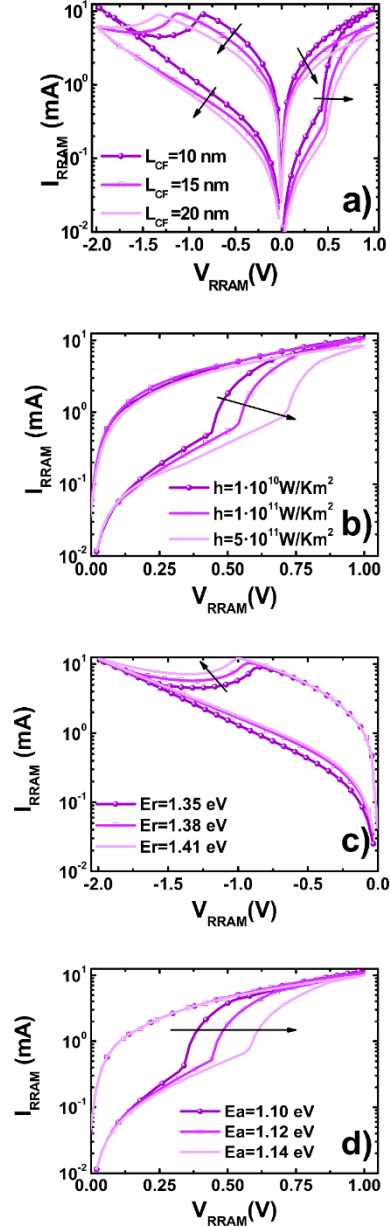
Figure 4: Modeled RRAM current versus applied voltage accounting for variations of different parameters used in the physical analysis: a) dielectric layer thickness, b) lateral heat transfer coefficient for dissipation between the CF and the surrounding dielectric, c) average activation energy accounting for the processes involved in the RESET process, d) activation energy for the generation of oxygen vacancies.

2017 Spanish Conference on Electron Devices (CDE)

IV. RESULTS AND DISCUSSION

The influence of some key model parameters on the device I-V characteristics has been studied in Fig. 4. Some changes in the parameters account for device-to-device variability while other features describe cycle-to-cycle variability. The proposed model was tested for different technologies (see Table I). Three types of RRAMs were employed: Set#1 TiN/Ti/HfO$_2$/W with a 10 nm-thick dielectric, Set#2 Pt/TiO$_2$/Al$_2$O$_3$/TiO$_2$/RuO$_x$/TiN with 28.4 nm oxide thickness (0.2nm of Al$_2$O$_3$) and Set#3 with the same structure than Set#2 but 19.6 nm oxide thickness (0.4 nm of Al$_2$O$_3$).

First, the model parameter fitting was carried out on the mean curve of the experimental data set for each technology. After that, considering random distributions for the geometric model parameters, a set of simulated curves was obtained that fitted well the experimental data (see Fig.5 Set#1 and Fig.6 Set#2 and Set#3). Some details of the model accuracy for some specific cycles of the three technologies are given in Fig.7 and Fig.8. It is shown that the proposed model reasonably fits the experimental data for different technologies and for a variety of dielectric thicknesses.
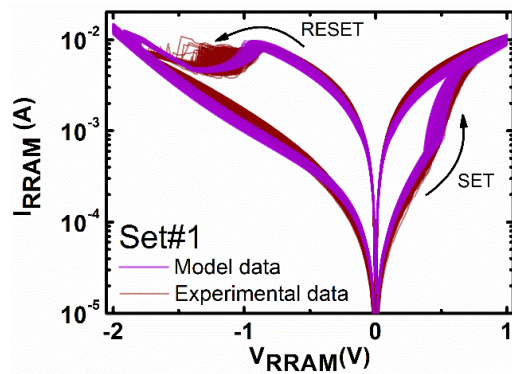
Figure 5: RRAM current versus applied voltage for Set#1 of 700 experimental RS cycles in TiN/Ti/HfO$_2$/W devices (fabricated at the IMB) and the corresponding modeled curves. For the modeled data a Gaussian distribution for the maxima of the main CF geometrical parameters (r_{Tx}, r_{Bx} and g_x) was used.
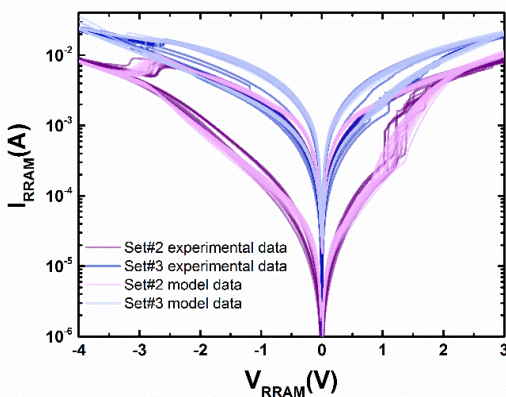
Figure 6: RRAM current versus applied voltage for Set#2 and Set#3 of experimental RS cycles in Pt/TiO$_2$/Al$_2$O$_3$/TiO$_2$/RuO$_x$/TiN devices and the corresponding modeled curves. For the modeled data a Gaussian distribution for the maxima of the main CF geometrical parameters (r_{Tx}, r_{Bx} and g_x) was used.
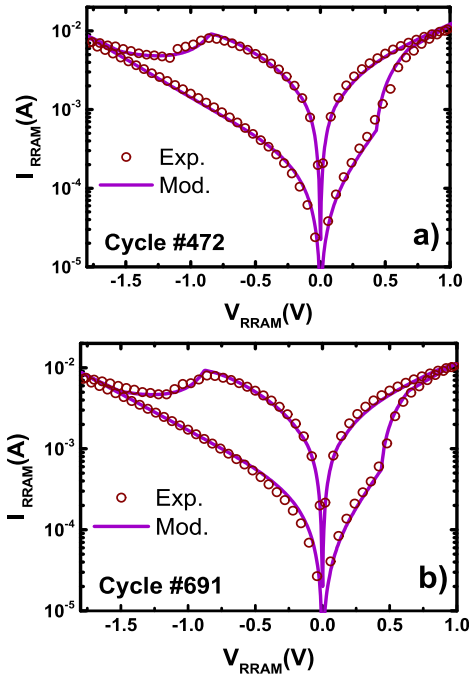
Figure 7: Current versus voltage for different cycles of samples Set#1 a) cycle #472 and b) cycle #691. The model reproduces accurately the experimental results.
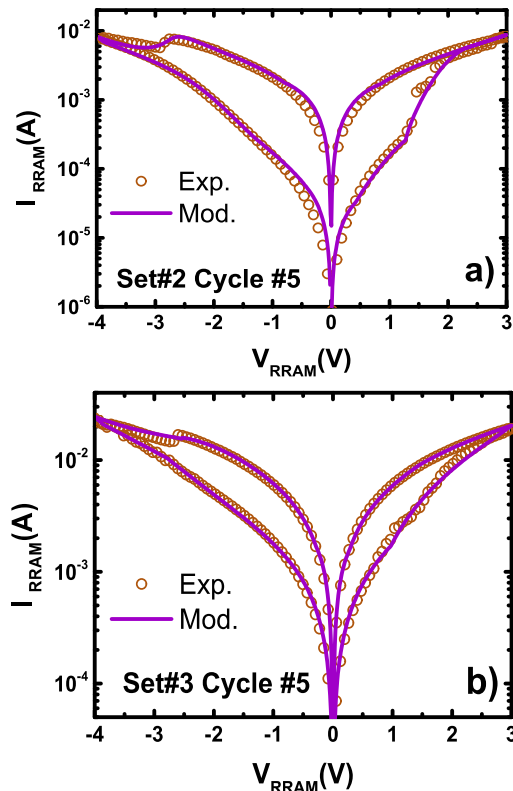
Figure 8: I-V curves corresponding to the cycles of samples a) Set#2 cycle #5 and b) Set#3 cycle #5. The experimental data are correctly fitted by the model.

V. Conclussions

A physically based model to describe resistive switching has been proposed. The model works well for several RRAM technologies that include different transition metal oxides (TMO), such as deposited HfO_2 and a three layer stack, $TiO_2/Al_2O_3/TiO_2$, with two combinations of layer thicknesses. The model is based on the migration of oxygen ions and the formation/disruption of CFs made of oxygen vacancies. The master equation proposed takes into account the variation of the volume of a conductive filament with a truncated-cone shape, a detailed thermal description, the influence of parasitic resistances of the dielectric surrounding the CF and the dielectric region filling the gap. The influence of some key model parameters on the device I-V characteristics has been also studied. The model reasonably fits experimental single I-V curves and several sets of RS cycles including SET and RESET transitions.

Acknowledgments

References

[1] F. Pan, S. Gao, C. Chen, C. Song, F. Zeng, "Recent progress in resistive random access memories: materials, switching mechanisms and performance", Materials Science and Engineering, vol. 83, pp. 1-59, 2014.

[2] J. Blasco, N. Ghenzi, J. Suñé, P. Levy, and E. Miranda, "Equivalent circuit modeling of the bistable conduction characteristics in electroformed thin dielectric films", Microelectron. Reliab., vol. 55, no. 1, pp. 1–14, 2015.

[3] Y.-M. Kim y J.-S. Lee, "Reproducible resistance switching characteristics of hafnium oxide-based nonvolatile memory devices", Journal of Applied Physics, vol. 104, no. 11, 2008.

[4] S. Lee, J. Woo, D. Lee, E. Cha y H. Hwang, "Internal resistor of multi-functional tunnel barrier for selectivity and switching uniformity in resistive random access memory", Nanoscale Research Letters, vol. 9, no. 1, pp. 1-7, 2014.

[5] R. Waser, R. Dittmann, G. Staikov, and K. Szot, "Redox-based resistive switching memories—Nanoionic mechanisms, prospects, and challenges", Advanced Materials, vol. 21, nos. 25–26, pp. 2632–2663, 2009.

[6] H. S. P. Wong, H. Y. Lee, S. Yu. Y.-S. Chen, Y. Wu, P.-S. Chen, B. Lee, F. T. Chen and M.J. Tsai, "Metal-Oxide RRAM", Proceedings of the IEEE, vol. 100, no. 6, pp. 1951-1970, June 2012.

[7] J.S. Lee, S. Lee., T.W. Noh, "Resistive switching phenomena: A review of statistical physics approaches", Applied Physics Reviews, vol. 2, p. 031303, 2015.

[8] M.A. Villena, F. Jiménez-Molinos, J.B. Roldán, J. Suñé, S. Long, X. Lian, F. Gámiz, and M. Liu, "An In-Depth Simulation Study Of Thermal Reset Transitions In Resistive Switching Memories", Journal of Applied Physics, vol. 114, pp. 144505-1–144505-8, 2013.

[9] M.A. Villena, M.B. González, F. Jiménez-Molinos, F. Campabadal, J.B. Roldán, J. Suñé, E. Romera, E. Miranda, "Simulation of thermal reset transitions in RRAMs including quantum effects", Journal of Applied Physics, vol. 115, pp. 214504-1–214504-6, 2014.

[10] Jiménez-Molinos, F., Villena, M.A., Roldán, J.B., Roldán, A.M., "A spice compact model for unipolar rram reset process analysis", IEEE Trans. Elec. Dev., vol 62, no. 3, pp. 955-962, 2015.

[11] X. Guan, S. Yu, and H.S.P. Wong, "A SPICE Compact Model of Metal Oxide Resistive Switching Memory with Variations", IEEE Elec. Dev. Lett., vol. 33, pp. 1405-1407, 2012.

[12] P. Y. Chen and S. Yu, "Compact Modeling of RRAM Devices and Its Applications in 1T1R and 1S1R Array Design," in IEEE Transactions on Electron Devices, vol. 62, no. 12, pp. 4022-4028, Dec. 2015.

[13] X. Fang, X. Yang, J. Wu, X. Yi, "A Compact SPICE Model of Unipolar Memristive Devices", IEEE Transactions on Nanotechnology, vol. 12, no. 5, pp. 843-850, 2013.

[14] R. Picos, J.B. Roldán et al., "Semiempirical Modeling of Reset Transitions in Unipolar Resistive-Switching based Memristors", Radioengineering Journal, vol 24, no. 2, pp. 420-424, 2015.

[15] S. Menzel, U. Böttger, R. Waser, "Simulation of multilevel switching in electrochemical metallization memory cells", J. Appl. Phys. vol. 111, pp. 014501-1–14501-5, 2012.

[16] M. Bocquet, D. Deleruyelle, C. Muller and J.-M. Portal, "Self-consistent physical modeling of set/reset operations in unipolar resistive-switching memories", Appl. Phys. Letters, vol. 98, pp. 263507-1–263507-3, 2011.

[17] G. Gonzalez-Cordero, J. B. Roldan, F. Jimenez-Molinos, J. Suñé, S. Long, and M. Liu, "A new compact model for bipolar RRAMs based on truncated cone conductive filaments, a Verilog-A approach", Semicond. Sci. Technol., vol. 31, no. 11, pp. 1–13, 2016.

[18] G. González-Cordero, J. B. Roldán, and F. Jiménez-Molinos, "Simulation of RRAM memory circuits, a Verilog-A compact modeling approach," in XXXI Edition of the Design of Circuits and Integrated Systems Conference, 2016.

[19] G. González-Cordero, F. Jiménez-Molinos, J. B. Roldán, M. B. González and F. Campabadal, "Transient SPICE simulation of Ni/HfO2/Si-n+ resistive memories", in XXXI edition of the Design of Circuits and Integrated Systems Conference, 2016.

[20] S. Long, L. Perniola, C. Cagli, J. Buckley, X. Lian, E. Miranda, F. Pan, M. Liu and J. Suñé. "Voltage and power-controlled regimes in the progressive unipolar RESET transition of HfO2-based RRAM", Scientific reports, vol. 3, pp. 2929-1–2929-8, 2013.

[21] S. Long, C. Cagli, D. Ielmini, M. Liu and J. Suñé, "Analysis and modeling of resistive switching statistics", Journal of Applied Physics, vol. 111, no. 7, pp. 074508-1–074508-19, 2012.

[22] M.A. Villena, J.B. Roldán, M.B. González, P. González-Rodelas, F. Jiménez-Molinos, F. Campabadal, D. Barrera, "A new parameter to characterize the charge transport regime in Ni/HfO2/Si-n+-based RRAMs", Solid State Electronics, vol. 118, pp. 56-60, 2016.

[23] P. Huang. et al., "A physics-based compat model of metal-oxide-based RRAM DC and AC operations", IEEE Trans. Elec. Dev., vol. 60, pp. 4090–4097, 2013.

[24] G. González-Cordero, F. Jiménez-Molinos, J. B. Roldán, M. B. González and F. Campabadal "In-depth study of the physics behind resistive switching in TiN/Ti/HfO2/W structures", J. Vac. Sci. Technol. B, vol 35, p. 01A110-1– 01A110-5, 2017.

3.4.3. UGR-VCM Model with Variability

The thermal characteristics of the UGR-VCM model are described in this section. They were obtained by simplifying the heat equation in one dimension, assuming the CF has metallic-like transport characteristics and taking into consideration the truncated-cone geometry. A compact analytical expression for the CF temperature was obtained (see details in appendix D.6.). This expression shows dependencies on the average electric field on the CF, the CF thermal conductivity and the heat transfer coefficient for the lateral heat dissipation from the CF to the surrounding dielectric.

To include the effects of cycle to cycle variability, the UGR-VCM model is modified introducing a random variation of CF volume linked to the self-accelerated process triggered by the temperature.

The modifications introduced into the UGR-VCM model are tested with three different devices:

1.- Pt/TiO$_2$(9.45nm)/Al$_2$O$_3$(0.5nm)/TiO$_2$(9.45nm)/RuOx/TiN (see details in appendix A.3.)

2.- Pt/TiO$_2$(14.1nm)/Al$_2$O$_3$(0.2nm)/TiO$_2$(14.1nm)/RuOx/TiN (see details in appendix A.3.)

3.- TiN/Ti/HfO$_2$ (10nm)/W (see details in appendix A.2.)

The model reproduced accurately specific cycles I-V of the three technologies. The cumulative probabilities of R_{on}, R_{off} and of V_{set}, V_{reset} are calculated, a good agreement between the experimental and simulated data is observed. The good fit obtained of a series of 729 experimental RS cycles of TiN/Ti/HfO$_2$ (10nm)/W devices is shown.

This section was published in González-Cordero et al. Microelectronic Engineering (2017), the accepted preprint paper is presented below.

González-Cordero et al. Microelectronic Engineering (2017)

Quality metrics

Data base	Rating	Quartile
Web of Science	Impact factor: 2.02	Q2
Scimago	Scientific journal ranking: 0.604	Q1

Publication citations

Google Scholar	Web of Science
4	3

A physically based model for resistive memories including a detailed temperature and variability description

G. González-Cordero[a], M.B. González[b], H. García[c], F. Campabadal[b],
S. Dueñas[c], H. Castán[c] , F. Jiménez-Molinos[a], J.B. Roldán [a,*]

aDepartamento de Electrónica y Tecnología de Computadores, Universidad de Granada, 18071 Granada, Spain
bInstitut de Microelectrònica de Barcelona, IMB-CNM (CSIC), Campus UAB, 08193 Bellaterra, (Spain)
cDepartamento de Electrónica, Universidad de Valladolid, Paseo de Belén 15, 47011 Valladolid, (Spain)

ABSTRACT

A new model to account for variability in resistive memories is presented. It is included in a previous general current model that considers the main physical mechanisms involved in the conductive filament formation and disruption processes that lead to different resistive states. The validity of the model has been proved for different technologies of metal-insulator-metal bipolar resistive memories. The model can be implemented in Verilog-A for circuit simulation purposes.

Keywords: Resistive RAM; ReRAM; physical model; stochastic variability

1. INTRODUCTION

Resistive Random Access Memories (RRAMs) are known to be one of the most promising alternatives to substitute flash technology in the non-volatile memory market [1, 2]. In addition to fabrication developments, simulation and compact modeling are essential facets to make a new technology pass into the maturity state. In this context, the variability of resistive switching (RS) based on the formation and disruption of Conductive Filaments (CF) in Metal-Insulator-Metal (MIM) structures has been modeled in this manuscript. The model works well for MIM structures fabricated with different technologies, once the corresponding model parameters are fitted. The resistance of the electrodes and that of the CFs in different stages of formation is considered, as well as the hopping current in the gap (g) between the CF tip and the electrode. The thermal description of the CF is included by solving the heat equation where Joule heating and lateral dissipation from the CF to the surrounding dielectric are taken into account [3-5]. Variability [6] has also been introduced by employing a sigmoid function that allows reproducing the stochastic nature of the device physics. The model is suitable for implementation in circuit simulators to analyze circuits based on RRAMs under different operation regimes.

---

2. FABRICATED DEVICES

Two types of MIM devices have been fabricated: $Pt/TiO_2/Al_2O_3/TiO_2/RuO_x/TiN$ and $TiN/Ti/HfO_2/W$.

The fabrication of RRAMs containing the $TiO_2/Al_2O_3/TiO_2$ stack was based on an ALD deposition performed in a flow-type reactor (substrate temperature of 350 °C). The Ti precursor was $TiCl_4$, the Al precursor was TMA and H_2O was used as oxygen source. $TiCl_4$ and TMA were kept at room temperature. In Fig. 1a and 1b the fabricated dielectric layer thicknesses and a schematic representation of the device cross-sections is shown.

The $TiN/Ti/HfO_2/W$ structures were fabricated on (100) p-type CZ silicon wafers. Wet thermal oxidation was performed at 1100 °C to create a 200 nm thick SiO_2 layer. A deposition of a W layer (200 nm) by magnetron sputtering followed. After this process, an ALD deposited 10 nm thick HfO_2 was formed at 225 °C using H_2O and TDMAH as precursors. The top electrode consisted of a 200 nm TiN and a 10 nm Ti layer. Dry etching of the HfO_2 layer was employed for the bottom electrode contact windows. The device area was a 15 x 15μm^2 square. A schematic of the device cross-section is shown in Fig. 1c.
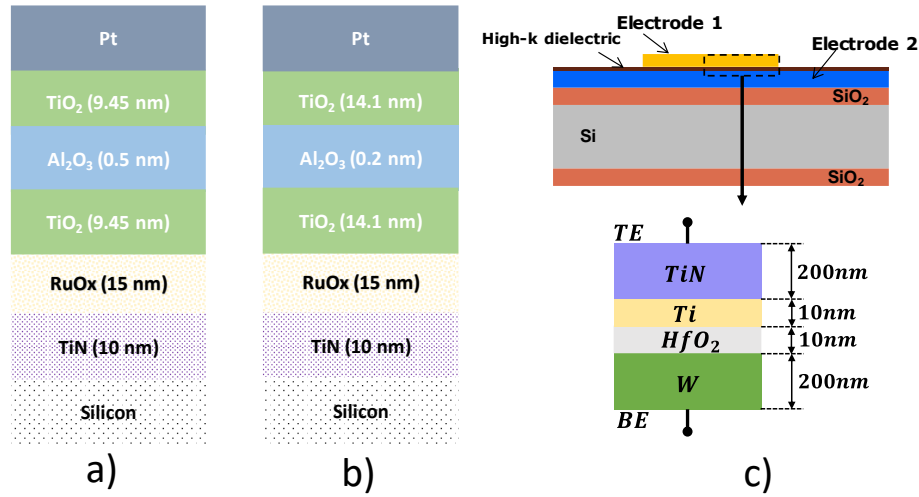
Fig 1. Cross-section sketch of the fabricated devices based on the following stacks: a) $Pt/TiO_2(9.45nm)/Al_2O_3(0.5nm)/TiO_2(9.45nm)/RuO_x/TiN$, b)$Pt/TiO_2(14.1nm)/Al_2O_3(0.2nm)/TiO_2(14.1nm)/RuO_x/TiN$ and c) $TiN/Ti/HfO_2 (10nm)/W$.

3. MODEL DESCRIPTION

The model is based on the geometric scheme shown in Fig 2a. The CF creation is linked to oxygen ion migration and the formation of percolation paths (the conductive filaments) made of oxygen vacancies [1-3, 5]. The CF time evolution is described by the following equations formulated in terms of the CF volume:

$$\frac{dV_{TC}}{dt} = v_0 \exp\left(-\frac{E_a - \alpha_a Zq\xi}{k_b T}\right) \quad (set) \tag{1}$$

$$\frac{dV_{TC}}{dt} = -v_0 \exp\left(-\frac{E_r - \alpha_r(g)Zq\xi}{k_b T}\right) \quad (reset) \tag{2}$$

V_{TC} stands for the CF volume, v_0 is obtained as the product of the oxygen vacancy volume and the oxygen atom vibration frequency [2], E_a is the oxygen vacancy activation energy, α_a is the electric field enhancement factor, Z is the oxygen ion charge number, q is the electron charge, ξ is the electric field, k_b

is the Boltzmann constant, T stands for the local temperature (obtained by solving the heat equation, see Fig. 3), E_r is an activation energy linked to the processes involved in the RESET process, and $\alpha_r(g)$ is a linear function of g that accounts for the electric field enhancement factor that induces a lowering of the hopping barrier and the external voltage enhancement factor during oxygen ions release [2].
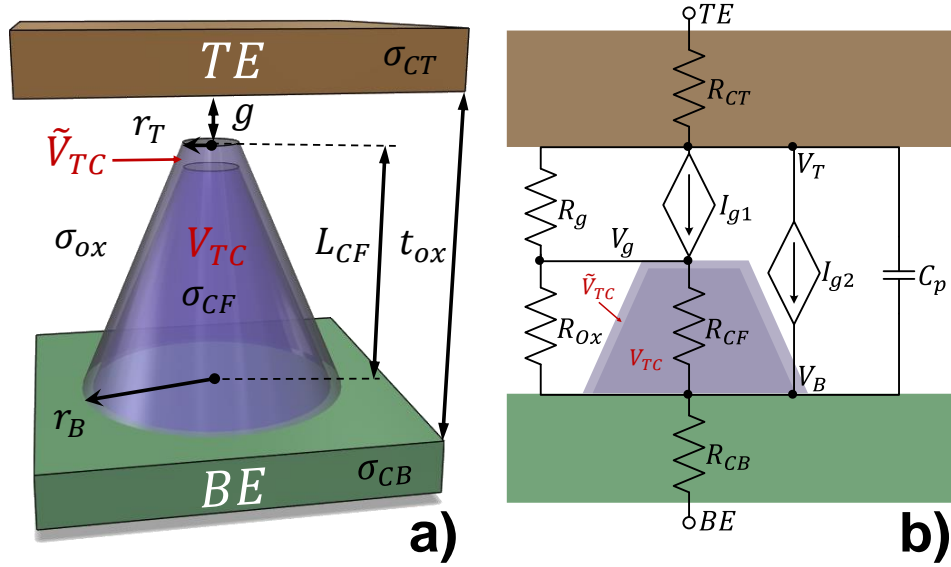
Fig.2. a) RRAM geometrical scheme, CF features and main model variables. The variability has been implemented as a random volume variation ($\tilde{V}_{TC}$), b) RRAM equivalent circuit including the different electrical components included in the model.
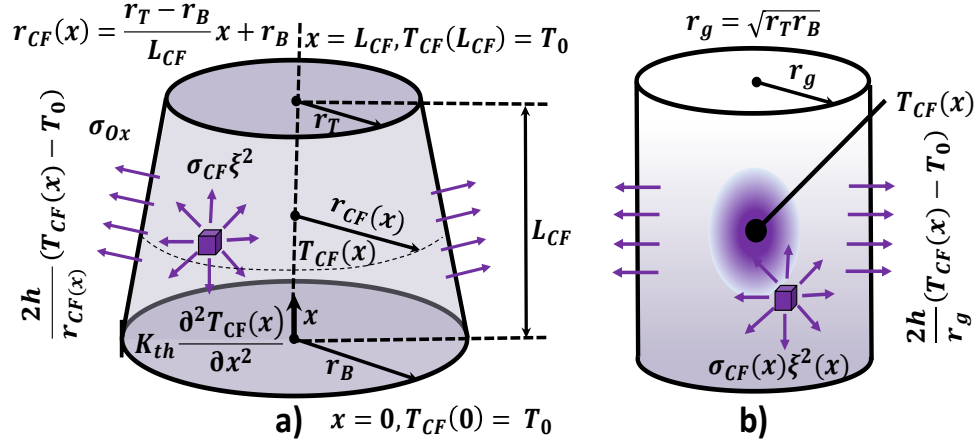
Fig.3. a) Energy dissipation terms included in the heat equation, and geometrical domain for the CF thermal description, b) equivalent cylindrical CF employed to simplify the heat equation solution and to obtain a compact analytical expression for the CF temperature.

The circuit that models the RRAM operation is sketched Fig. 2b. The scheme was used for the Verilog-A implementation of the model. The electrode ohmic resistances are R_{CT} and R_{CB}, the CF resistance is R_{CF}, the dielectric surrounding the CF resistance and the dielectric region filling the gap g associated resistance are R_{ox} and R_g, respectively. The no-linear current sources that account for the hopping current are modeled through I_{g1} and I_{g2}. The latter depends on the CF geometry and on the voltage applied to the gap g. A capacitance (C_p) is also included [7].

The thermal characteristics are obtained by solving the heat equation within the CF [3,4,7],

$$\sigma_{CF}\xi^2 = -k_{th}\frac{\partial^2 T(x)}{\partial x^2} + 2h\frac{T(x)-T_{ox}}{r_{CF}(x)} \tag{3}$$

σ_{CF} stands for the CF electric conductivity (we assume metallic-like temperature dependence [3, 7]), r_{CF} is the CF radius (variable because of a non cylindrical shape), ξ is the CF average electric field, k_{th} the CF thermal conductivity. The parameter h stands for heat transfer coefficient (accounts for the lateral heat dissipation from the CF to the dielectric). Eq. 3 cannot be solved analytically assuming a CF with variable r_{CF}. In order to obtain an approximated explicit solution we consider that a truncated-cone shaped CF with constant conductivity is equivalent (after an algebraic transform) to a cylindrical CF with r_g radius (r_T (r_B) stands for the top (bottom) CF radius) and a conductivity dependent on the spatial variable along the CF main axis (see Fig. 3). With this asumption the cylinder maximum temperature found is given in Eq. 4 and it is assumed as the CF temperature,

$$T = T_0 + \frac{\sigma_{CF} r_g r_B \xi^2}{r_T h}\left[\frac{1}{2} - \frac{e^{\frac{\alpha}{2}}}{e^{\alpha} + 1}\right] \tag{4}$$

where the α parameter is given below:

$$\alpha = L_{CF}\sqrt{\frac{2h}{k_{th}r_g}} \tag{5}$$

Finally, a random component $\tilde{V}_{TC}$ is included as a variation of the CF volume to account for the device variability. In this manner V_{TC} can be obtained as follows:

$$V_{TC}(t) = \int \frac{dV_{TC}}{dt}dt + \tilde{V}_{TC} \tag{6}$$

$$\tilde{V}_{TC} = V_{TCrnd}(\Delta t)F(T)rnd \tag{7}$$

where V_{TCrnd} is a random number whose Gaussian distribution presents a null mean value and a standard deviation σ_{VTC}, rnd is a flag parameter to introduce variability in the model and $F(T)$ is a sigmoid function that depends on the temperature, since the CF volume variation is connected with the kinetic energy of ions [6] (see Eq. 8):

$$F(T) = \frac{1}{2}\left[\tanh\left(\frac{T - T_c}{T_s}\right) + 1\right] \tag{8}$$

where T_C is a threshold temperature above which significant random variation of the gap size occurs, while T_S is a function smoothing parameter.

4. RESULTS AND DISCUSSION

The proposed model was tested for three different RRAM technologies (see Fig. 1). Batch#1 Pt/TiO$_2$/Al$_2$O$_3$/TiO$_2$/Ru/Si with 19.4nm oxide thickness (0.5nm of Al$_2$O$_3$), batch#2 with the same structure than batch #1 and 28.4nm oxide thickness (0.2nm of Al$_2$O$_3$) and batch #3 TiN/Ti/HfO$_2$/W with a dielectric 10nm thick (see Figures 4-5). The same physical constants were employed for all the I-V curves, the CF geometrical features were selected for each of the fitted curves in Figure 4.
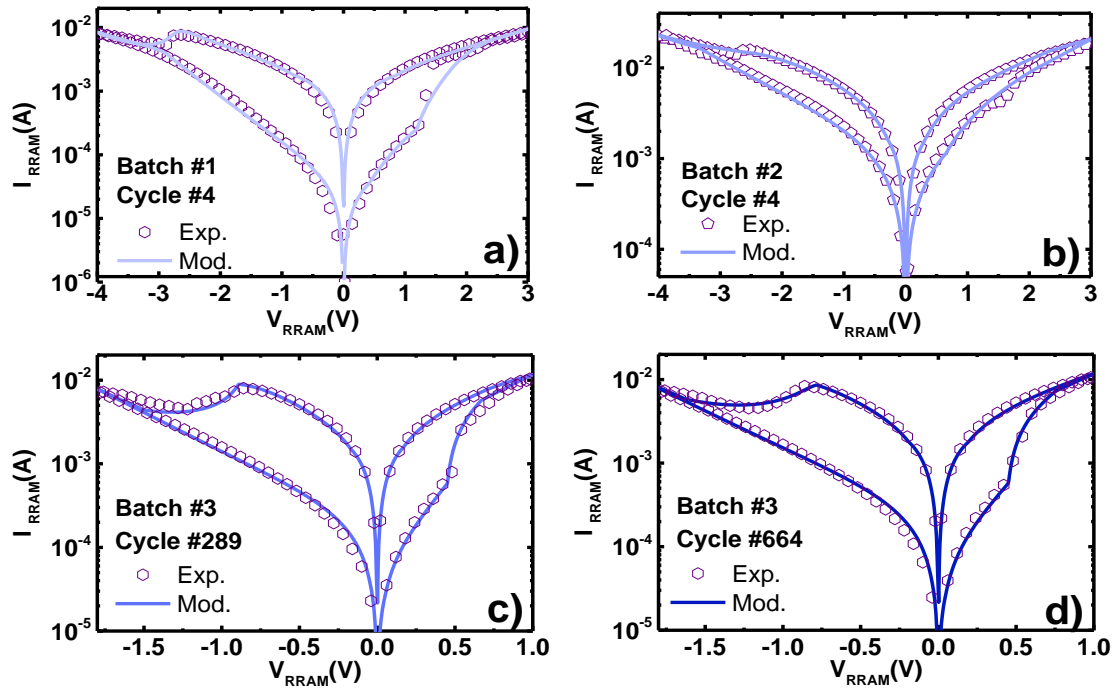
Fig.4. Current versus voltage for different RS cycles of the samples under study: a) batch#1 cycle #4 b) batch#2 cycle #4 c) batch#3 cycle #289 and d) batch#3 cycle #664. The model reproduces accurately the experimental results.

The variability is also correctly modeled as shown in Figures 5 and 6 by using Equation 6 and 7. A better fit than in previous approaches [3] was obtained (see Figure 6). The cumulative probabilities of R_{on}, R_{off} (Fig. 7 a) and of V_{set}, V_{reset} (Fig. 7 b) are also calculated, where a good agreement between the experimental and simulated data is observed.
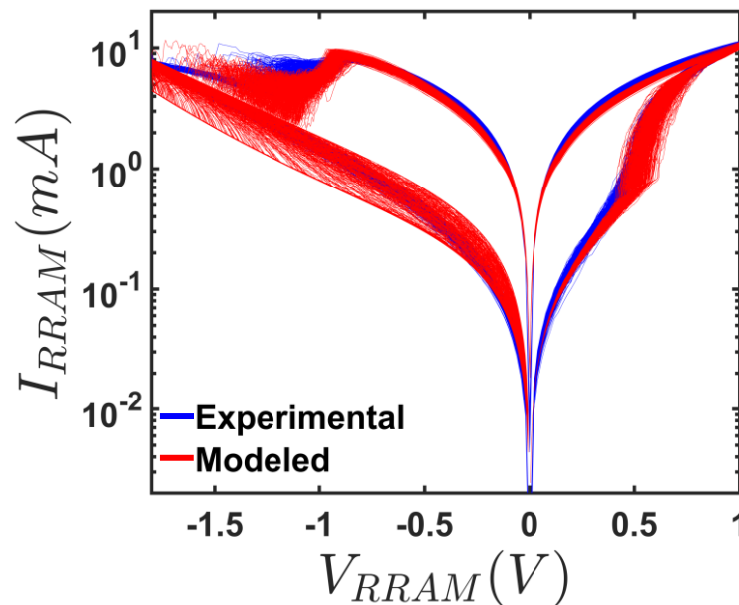
Fig.5. a) Batch #3: 729 experimental cycles and 400 modeled cycles.
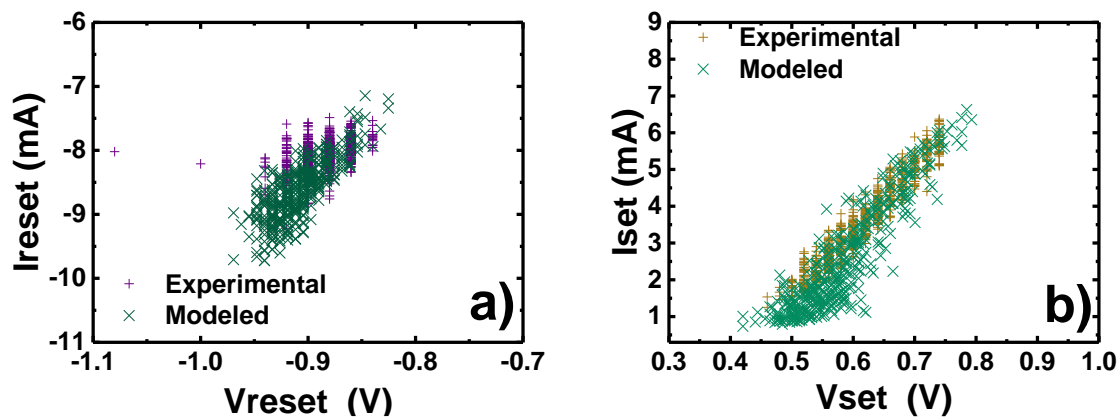
Fig.6. Batch #3 a)I_{reset} I_{reset} versus V_{reset} calculated for experimental and simulated data. b) I_{set} versus V_{set} calculated for experimental and simulated data.
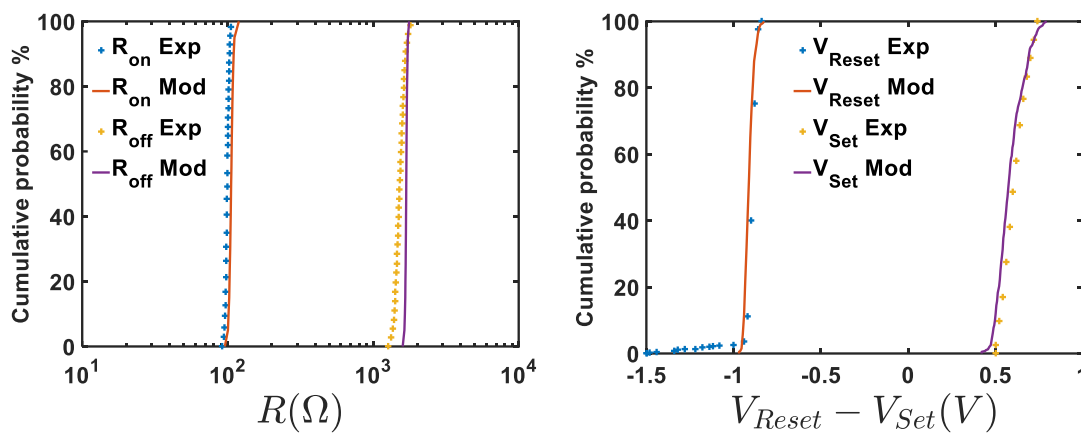
Fig.7. Cumulative probability comparative between experimental and modeled data for batch #3: a)I_{reset} R_{on} and R_{off} @V=0.1V b) V_{reset} and V_{set}.

The introduction of a threshold in a smooth sigmoid function makes sense since RS mechanisms, linked to cycle-to-cycle variability, are self-accelerated processes triggered by temperature. The good fit obtained in Figures 6 and 7 shows that the selected approach is appropriate.

5. CONCLUSIONS

A physically based model for bipolar MIM resistive memories is presented including a detailed temperature and variability description. The model was tested for three different RRAM technologies and a good agreement was obtained between the experimental and simulated data. The thermal features and the variability were modeled reasonably well in all the cases considered.

ACKNOWLEDGEMENTS

REFERENCES

[1] R. Waser, R. Dittmann, G. Staikov, and K. Szot, Adv. Mater., 21 (2009) 2632–2663.

[2] P. Huang et al., IEEE Transactions on Electron Devices, 60 (2013) 4090-4097.

[3] G. González-Cordero, F. Jiménez-Molinos, J. B. Roldan, M. B. González and F. Campabadal, J. Vac. Sci. Technol. B, 35 (2017) 01A110.

[4] M.A. Villena, M.B. González, J.B. Roldán, F. Campabadal, F. Jiménez-Molinos, F.M. Gómez-Campos, and J. Suñé, Solid State Electronics, 111 (2015) 47-51.

[5] G. González-Cordero, J. B. Roldán, and F. Jiménez-Molinos, in Conference on Design of Circuits and Integrated Systems (DCIS) (2016).

[6] X. Guan, S. Yu, and H.S.P Wong, IEEE Elec. Dev. Lett., 33 (2012) 1405-1407.

[7] G. González-Cordero, J. B. Roldán, F. Jiménez-Molinos, J. Suñé, S. Long and M. Liu, Semiconductor Science and Technology, 31 (2016) 115013.

3.4.4. UGR-VCM Model Improvement to Include Distributed Currents

To conclude with the validation of UGR-VCM model, a new device based on the Au/Ti/TiO$_2$/SiO$_x$/n^{++}Si stack was modelled (details of fabrication and measured set-up is presented in appendix A.4.). Previously, in references [González-Cordero2017b, González-Cordero2017d] included in the sections 3.4.2. and 3.4.3. the validation of UGR-VCM model with TiO$_2$/Al$_2$O$_3$/TiO$_2$ and TiN/Ti/HfO$_2$/W devices was presented.

Figure 3.6 shows the comparative of experimental data (red line) and the data obtained from the simulation of the UGR-VCM (blue line) of 100 cycles I-V. It can be seen that the current levels in the states of LRS and HRS are fitted with great precision.
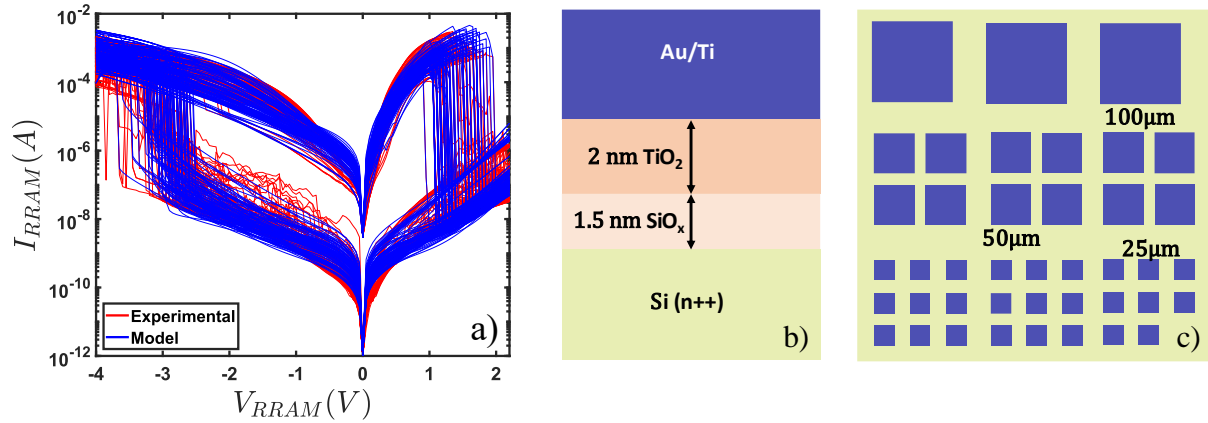
Figure 3.6 a) Current versus voltage for Au/Ti/TiO$_2$/SiO$_x$/n^{++}Si devices. RS cycles of experimental data (red line) and modeled data (blue line) are shown (100 cycles). **b)** Cross sectional sketch of Au/Ti/TiO$_2$/SiO$_x$/n^{++}Si stacks. **c)** sketch of the squared switching cells layout.

This new device works under filamentary and distributed switching mechanisms [Xiao2017]. For this new issue the UGR-VCM model is adapted by adding a semiempirical current source to account the distributed conduction at low voltages, as a generalized trap assisted current described in equation (1.28), controlled by the conductive filament volume (V_{TC}), see equation (3.21). The rest of the UGR-VCM model elements are the same as described in section 3.4.

$$I_k = \left(\frac{V_{TC} - V_{TCmin}}{V_{TCmax} - V_{TCmin}}\right) i_k V_{RRAM}^{a_k} \qquad for \qquad V_{RRAM} > 0 \tag{3.21}$$

where i_k and a_k are fitting parameters, V_{TC} is the filament volume and V_{TCmax} (V_{TCmin}) is the maximum (minimum) conductive filament volume. The maximum value of I_k is achieved when the CF is fully formed ($V_{TC} = V_{TCmax}$) and it has a minimum value is when $V_{RRAM} = 0$ or $V_{TC} = V_{TCmin}$.

Figure 3.7 a) shows the fit over the experimental data of cycle #6 with the inclusion of source current of I_k, and **Figure 3.7 b)** shows over the cycle #53 and how the inclusion or exclusion of the new current source I_k affects in the fitting process. A comparative of R_{on} and R_{off} measured and UGR-VCM modelled data for $V_{RRAM} = -1V$ versus cycle number is shown in **Figure 3.8 a)** and a comparative of V_{Reset} and V_{Set} versus cycle number for experimental and UGR-VCM modeled data is shown in the **Figure 3.8 b)**.
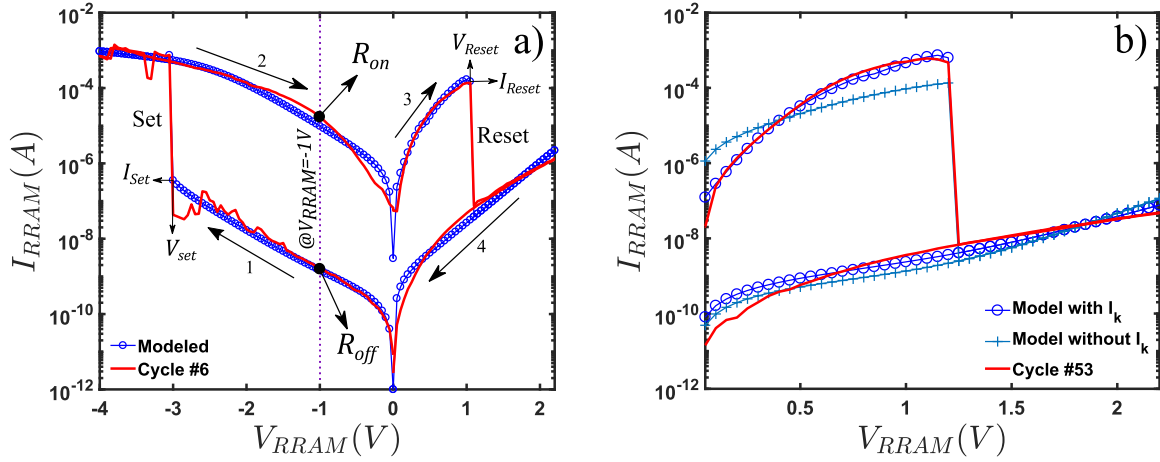
Figure 3.7 a) Current versus applied voltage of cycle #6 of RRAM Au/Ti/TiO₂/SiOₓ/n⁺⁺Si device, experimental data are shown in red lines and UGR-VCM modelled data in blue circles. The arrows marked 1 to 4 indicate the processes in a RS cycle and the reading voltage for R_{on} and R_{off} determination is shown; **b)** cycle #53, it is shown that the fitting process cannot be performed without the inclusion of I_k (Equation (3.21)).
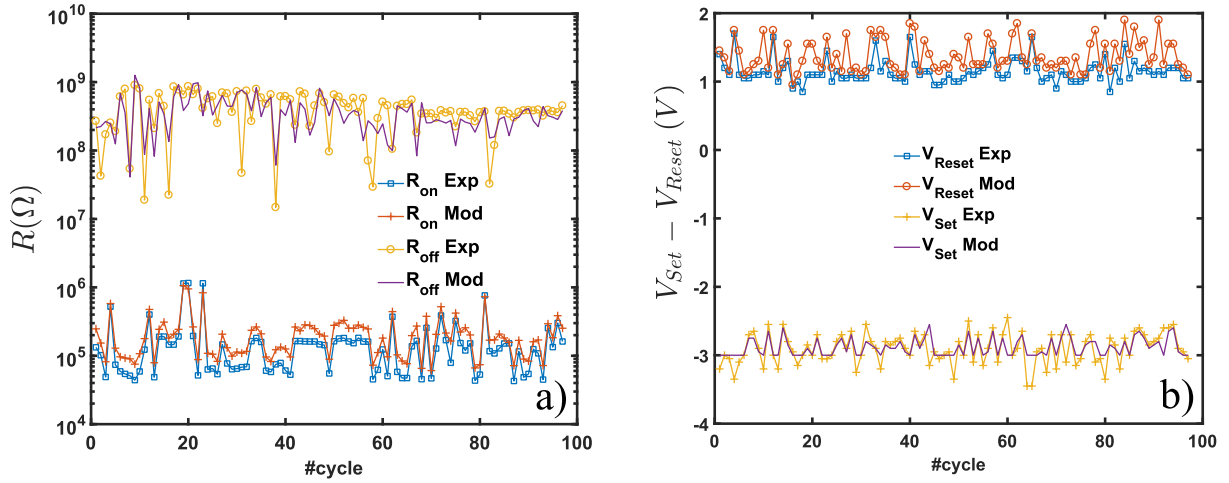
Figure 3.8 a) R_{on} and R_{off} calculated for V_{RRAM} = -1V versus cycle number for experimental and modeled data. **b)** V_{Reset} and V_{Set} versus cycle number for experimental and modeled data.

Finally **Table 3.VI** summarizes the technological parameters and fitting constants used in UGR-VCM model to fit experimental data based in the Au/Ti/TiO₂/SiOₓ/n⁺⁺Si device.

Table 3.VI UGR-VCM model parameters to fit Au/Ti/TiO2/SiOx/n++Si devices.

Parameter	Value	Units
L	3.5	nm
L_{cell}	100	μm
$[E_a, E_r]$	[0.95,1.2]	eV
v_0	125.17	$\mu m^3/s$
γ	0.3	
k_{th}	8.7	$W/K \cdot m$
h	$8.6 \cdot 10^9$	$W/K \cdot m^2$
α_T	$1.6 \cdot 10^{-3}$	K^{-1}
$[\sigma_{Ox}, \sigma_{CF0}]$	$[1.7 \cdot 10^{-10}, 8.9 \cdot 10^4]$	S/m
I_0	0.02	$A/\mu m^2$
g_0	0.4	nm
V_0	0.26	V

97

Quantum and Thermal Effects in Resistive Switching Memristor Models

4.1. Introduction

This chapter focuses on RRAM devices with unipolar operation. Some of the most representative compact models of these devices will be described; among them, the IM2NP-U and the quantum contact point model. In addition, a new technique for the extraction of the QPC model parameters is presented. This latter procedure is based on the calculation of the second derivative of the device current both for experimental and modeled data, the modeled data are obtained by means of an algebraic derivative of the QPC model equation. A comparison of modeled and experimental data for the current and the second derivative of the current allows the extraction of the QPC model parameters by means of a genetic algorithm. This methodology is based on the extraction of four important parameters (V_{Reset}, V_{Th_reset}, V_{2dmax1} and V_{2dmax2}) obtained by means of the first and second current derivatives with respect to the voltage. These parameters help to localize the operation regions where the QPC model is more important, i.e., the quantization due to the narrowing of the conductive filaments in RRAMs with filamentary conduction.

The thermal description of these devices is essential. In Appendix D. Thermal Description Used in the Devices Under Study, we have described different modeling approaches presented in the literature and some proposed in this doctoral thesis. In this Chapter, we present two contributions in this field:

The first one (UGR-QPC1), describes the conductive filament formed by two cylindrical sections of variable geometry (characterized by their radii). Under this premise a thermal model is proposed in which the equivalent thermal resistances depend on the two cylindrical sections. Secondly (UGR-QPC2) model employs the same hypotheses as the previous model; however, it includes a variable thermal capacity that allows a more precise characterization of the thermal response with respect to input voltage pulses.

4.2. Unipolar Compact Model IM2NP-U

Bocquet et al. proposed a physically based model for unipolar resistive switching devices for set/reset operation and checked it with a device based on the Pt/NiO/Pt stack [Bocquet2011]. The operation of the device is explained in terms of the formation and rupture of a conductive filament that shorts the top and bottom electrodes, both inert electrodes in this case. **Figure 4.1** shows a sketch of the CF formation and rupture that produces resistive switching operation in these devices.
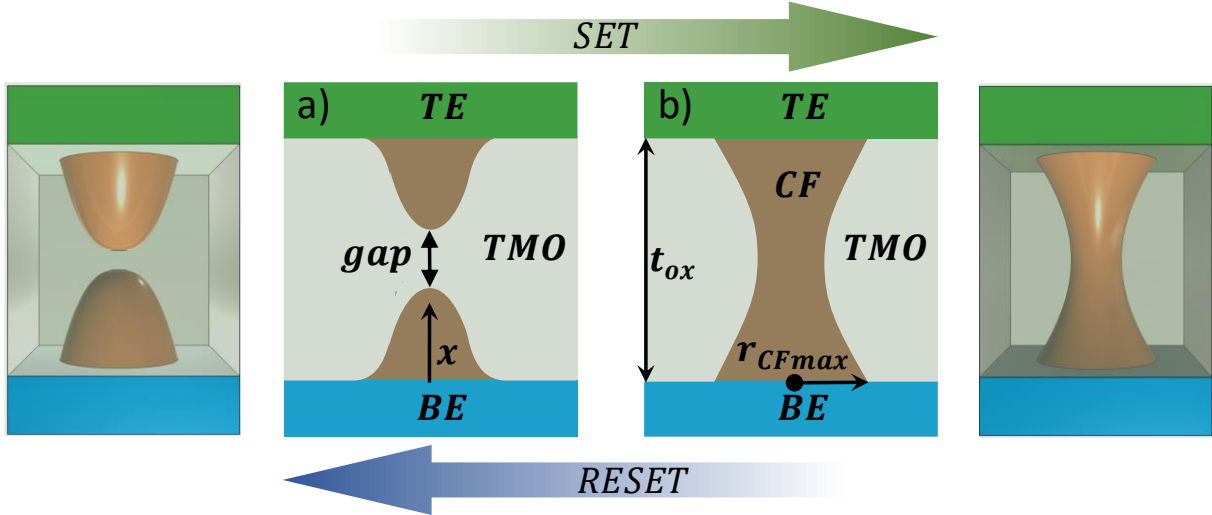
Figure 4.1 Sketch of conductive filament **a)** ruptured after a reset process, **b)** formed after a set process.

When the device is in the LRS, the CF is formed. It is assumed to be metallic-like with an electrical conductivity much higher than that of the device dielectric ($\sigma_{CF} \gg \sigma_{Ox}$). In contrast, when the device is in the HRS (the CF is broken), the resistance depends on the oxide gap that shows up between the two CF remnants left after the reset process [Bocquet2011].

The electric field can be calculated assuming the current conservation through the whole oxide layer [Bocquet2011]. Therefore, locally it can be obtained as follows,

$$\xi(x) = I_0 R(x) \tag{4.1}$$

where $R(x)$ is the resistance in each CF section, given as a function of x, in the vertical axis of the device [Bocquet2011, Bocquet2013] (more details are given in section B.1.)

$$R(x) = \frac{1}{r_{CF}^2(x)\pi(\sigma_{CF}(x) - \sigma_{Ox}) + r_{CFmax}^2 \pi \sigma_{Ox}} \tag{4.2}$$

where r_{CFmax} is the CF maximum radius. The CF conductivity, σ_{CF}, is of metallic nature. In this respect, its thermal dependence is assumed to be as follows [Russo2007],

$$\sigma_{CF}(x) = \frac{\sigma_{CF0}}{1 + \alpha_T(T_{CF}(x) - T_0)} \tag{4.3}$$

where σ_{CF0} is the CF conductivity at room temperature (T_0) and α_T is the linear temperature dependence coefficient. The ohmic current can be obtained making use of the previous equations by integration over the dielectric thickness,

$$I_0 = \frac{V_{cell}}{\int_0^{t_{Ox}} R(x)dx} \tag{4.4}$$

where V_{Cell} is the applied voltage between the top and bottom electrodes.

The evolution of the CF radius at each x section is governed by oxidation-reduction chemical reactions including also diffusion of the metallic species (this issue is described in detail in section B.4.). The device thermal evolution is obtained solving the heat equation using the CF thermal conductivity K_{th} and thermal constant to account for the lateral heat losses toward the dielectric, h [Bocquet2011] (see section D.4.)

$$\sigma_{CF}(x)\xi(x)^2 = -K_{th}\frac{\partial T_{CF}(x)}{\partial x^2} + h\frac{T_{CF}(x) - T_{Ox}}{r_{CF}} \tag{4.5}$$

where $\sigma_{CF}(x)$ is the CF electrical conductivity along x axis, $T_{CF}(x)$ the CF temperature along x axis, T_{Ox} the oxide temperature, r_{CF} the CF radius, and h the heat transfer coefficient between CF and surrounding oxide.

4.3. Quantum Point Contact Model

The quantum point contact model characterizes the electrical conduction in RRAMs where quantum effects are important being taken into consideration. The expression that describes these effects is obtained in a device with filamentary conduction in a dielectric film, the CF shorts the top and bottom electrode (see **Figure 4.2 a**). To obtain the current under a finite applied voltage under the zero-temperature limit, the equation below is employed [Datta1997],

$$I = \frac{2e}{h}N\int T(E)dE \tag{4.6}$$

where e is the electron charge, h is the Planck's constant, N is the number of active channels in the constriction (the conductive filament narrowing), $T(E)$ is the electron transmission probability and E is the electron energy. The Landauer approximation for quantum conductors in one dimension is assumed and this leads us to Landauer's integral. A transmission probability function $T(E)$ resembling an inverted parabolic function is used [Miranda2001,Miranda2010, Prócel2013]. The diagram of the energy band in the constriction that controls the current is shown in the **Figure 4.2 b**). Under this assumptions equation (4.6) can be expressed as follows,

$$I = \frac{2e}{h}N\int_{-(1-\beta)eV}^{\beta eV} \{1 + \exp[-\alpha(E - \Phi)]\}^{-1}\, dE \tag{4.7}$$

solving the integral, we obtain the general analytical equation for the current [Miranda2010, Prócel2013].

$$I = \frac{2eN}{h}\left\{eV + \frac{1}{\alpha}ln\left[\frac{1 + e^{[\alpha(\Phi-\beta eV)]}}{1 + e^{\{\alpha[\Phi+(1-\beta)eV]\}}}\right]\right\} \tag{4.8}$$

where e the charge of the electron, h the Planck's constant, V for the voltage drop between the two electrodes, β represents the fraction of voltage drop that falls at each end of the constriction, α is the parabolic factor assumed in the electron transmission probability function $T(E)$, Φ the height of the potential barrier with respect to the Fermi level (E_F),
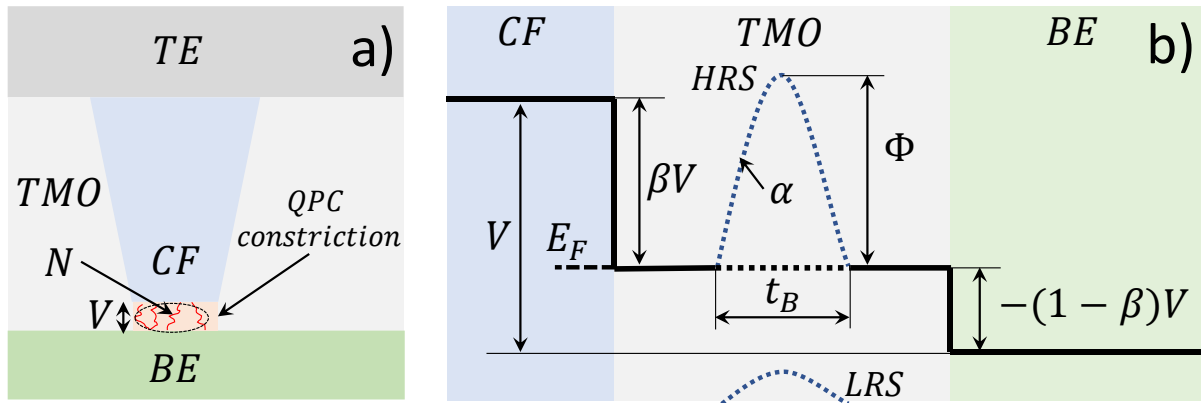
Figure 4.2 a) Scheme of the internal structure of the RRAM cell taking into account the quantum effects modeled the QPC currents. **b)** energy band diagram for the QPC current calculation, note that the potential is shown as a parabolic barrier.

The width of the potential barrier that has been used in the **Figure 4.2** b) is t_B, and is related to parameter α and the barrier height as follows [Miranda2001, Miranda2010],

$$\alpha = t_B \pi^2 h^{-1} \sqrt{\frac{2m^*}{\Phi}} \tag{4.9}$$

where m^* is the electron effective mass in the QPC constriction, a value of $m^* = 0.44m_0$ [Villena2014] (for HfO$_2$) could be employed where m_0 stands for the mass of the free electron. The QPC model has been used by several authors to model RRAMs in HRS state [Miranda2010, Lian2012, Prócel2013,], and for HRS and LRS too [Miranda2010, Lian2012, Prócel2013, Chen2013, Blasco2015, Jiménez-Molinos2017, González-Cordero2016e, Roldán2018]. The conductance quantization in RRAM devices (already measured, see **Figure 4.3**) is a clear proof that the QPC model is important in the modeling context of these devices.
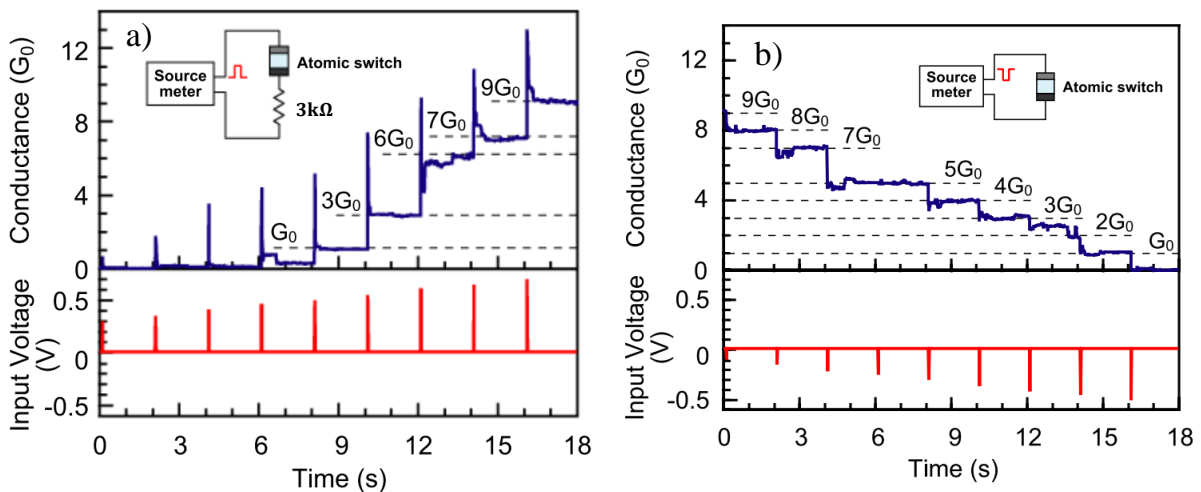
Figure 4.3 Conductance measurements in an Ag/Ta$_2$O$_5$/Pt devices. **a)** Quantized conductance in set process (by applying positive voltage pulses every 2s with a pulse width of 20ms). **b)** Decreasing quantized conductance in a reset process by using negative voltage pulses with a period of 2s and a pulse width of 20ms) [Tsuruoka2012].

Table 4.I Devices that exhibit conductance quantization effects reported in the literature (adapted from [Li2015b, Mehonic2013]). BRS stands for Bipolar Resistive Switching, URS for Unipolar Resistive Switching and V_o represents oxygen vacancies.

Device	Resistive switching mechanism	polarity	CF	Conductance level	observed	Reference
Ag₂S or Cu₂S (vacuum gap)	ECM	BRS	Ag	G_0	set	[Terabe2005]
Ag/AgI/Pt	ECM	BRS	Ag	G_0	set	[Tappertzhofen2012]
Ag/a-La1-xSrxMnO3/Pt	ECM	BRS	Ag	G_0	set	[Liu2013c]
Ag/ionic conductor-layer/W	ECM	BRS	Ag	G_0	set	[Geresdi2011]
Ag/GeS₂/W	ECM	BRS	Ag	G_0	set	[Jameson2012]
Ag/Ag₂S/Pt (STM tip)	ECM	BRS	Ag	G_0	reset	[Wagenaar2012]
Ag/SiO₂/Pt	ECM	BRS	Ag	$0.5G_0$	set	[Tappertzhofen2015]
Cr/p⁺-amorphous silicon/V	ECM	URS	Metal	$0.5G_0$	set	[Hajto1991]
Cu/HfOₓ/Pt	ECM	BRS	Cu	$0.5G_0$	set	[Lv2015]
Ag/Ta₂O₅/Pt	ECM	BRS	Ag	G_0	set/reset	[Tsuruoka2012]
Ag/P₃HT:PCBM/ITO	ECM	BRS	Ag	$G_0/0.5G_0$	set/reset	[Gao2013]
Nb/ZnOₓ/Pt	ECM	BRS	Nb or V_0	$G_0/0.5G_0$	set/reset	[Zhu2012]
Pt/HfO₂/Pt	VCM	URS	V_0	$0.5G_0$	reset	[Long2013b]
W/CeOₓ/SiO₂/NiSi₂	VCM	BRS	V_0	$0.5G_0$	reset	[Miranda2012]
ITO/ZnOₓ/ITO	VCM	URS	V_0	$0.5G_0$	set/reset	[Zhu2012]
Ti (Ta, W)/Ta₂O₅/Pt	VCM	BRS	V_0	G_0	set/reset	[Chen2013]
n-Si/SiOₓ/p-Si	VCM	U/BRS	V_0	$G_0/0.5G_0$	set	[Mehonic2013]
Ti/TiO₂/SrTiO₃/n-Si	VCM	BRS	V_0	G_0	set	[Hu2013]
Ti/HfO₂/TiN	VCM	BRS	V_0	G_0	reset	[Syu2013]
metal-a-Si:H-metal	-	-	-	G_0	set	[Hajto1996]
V/V₂O₅/V	-	-	-	$0.5G_0$	set	[Yun1993]

4.4. Parameter Extraction of QPC Model

Unipolar Ni/HfO₂/Si-based RRAMs were characterized using more than 2800 experimental I-V RS cycles (see Appendix A.5. for details of the fabrication process and measured set-up). For each I-V cycle (reset curve) four parameters are obtained: V_{Reset}, V_{Th_reset}, V₂dmax1 and V₂dmax2. The V_{Th_reset} corresponds with the voltage of the maximum value for the current first derivative with respect to voltage. V₂dmax1 and V₂dmax2 correspond with the voltages for the two maxima of the current second derivative with respect to the voltage. An initial study by multivariable analysis for the parameters V_{Reset}, V_{Th_reset}, V₂dmax1 and V₂dmax2 can help to understand the current components that contribute in the LRS. With the help of a genetic algorithm the 2800 I-V curves are fitted with the QPC current model and a set of (α, β, N and ϕ) parameters are obtained for each cycle. The flowchart of the overall process is shown in **Figure 4.4**.
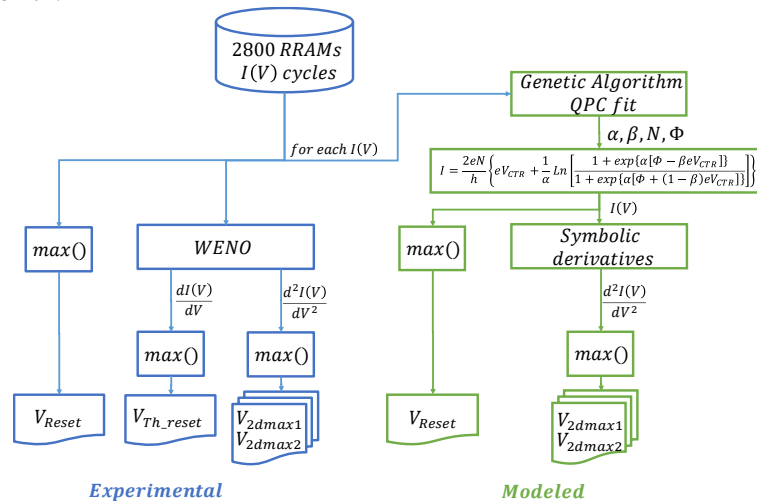
Figure 4.4 Flowchart of method for the Quantum Point Contact (QPC) current component is presented.

This section was published in Roldán et al. Journal of Applied Physics (2018), the accepted preprint paper is presented below.

103

Roldán et al. Journal of Applied Physics (2018)

Quality metrics

Data base	Rating	Quartile
Web of Science	Impact factor: 2.17	Q2
Scimago	Scientific journal ranking: 0.739	Q2

Publication citations

Google Scholar	Web of Science
4	3

Multivariate analysis and extraction of parameters in resistive RAMs using the Quantum Point Contact model

Authors: J.B. Roldán[1], E. Miranda[6], **G. González-Cordero**[1], P. García-Fernández[1], R. Romero-Zaliz[3], P. González-Rodelas[4], A. M. Aguilera[5], M.B. González[2], F. Jiménez-Molinos[1]

Address:

[1]Departamento de Electrónica y Tecnología de Computadores. Universidad de Granada. Facultad de Ciencias. Avd. Fuentenueva s/n, 18071 GRANADA, Spain. Email: jroldan@ugr.es

[2]Institut de Microelectrònica de Barcelona, IMB-CNM (CSIC), Campus UAB, 08193 Bellaterra, Spain

[3]Departamento de Ciencias de la Computación e Inteligencia Artificial. Universidad de Granada. Escuela Técnica Superior de Ingenierías Informática y de Telecomunicación, 18071 GRANADA, Spain

[4]Departamento de Matemática Aplicada. Universidad de Granada. ETSICCP (Edif. Politécnico). Avd. Fuentenueva s/n, 18071 GRANADA, Spain.

[5]Departamento de Estadística e Investigación Operativa and IEMath-GR. Universidad de Granada. Facultad de Ciencias. Avd. Fuentenueva s/n, 18071 GRANADA, Spain.

[6]Dept. Enginyeria Electrònica. Universitat Autònoma de Barcelona, Edifici Q. 08193 Bellaterra, Spain

Abstract:

A multivariate analysis of the parameters that characterize the reset process in RRAMs has been performed. The different correlations obtained can help to shed light on the current components that contribute in the Low Resistance State (LRS) of the technology considered. In addition, a screening method for the Quantum Point Contact (QPC) current component is presented. For this purpose the second derivative of the current has been obtained using a novel numerical method which allows determining the QPC model parameters. Once the procedure is completed, a whole RS series of thousands of curves is studied by means of a genetic algorithm. The extracted QPC parameter distributions are characterized in depth to get information about the filamentary pathways associated with LRS in the low voltage conduction regime.

Index Terms—Resistive switching memory, RRAM, Quantum Point Contact Model, Conductive filaments, Parameter extraction.

I. INTRODUCTION

Resistive Random Access Memory (RRAM) shows outstanding features to be considered a promising alternative technology for non-volatile memory applications [1]. Among the wide set of characteristics reported in the literature, the following can be accounted for: good scalability, low power, fast speed, the possibility of fabrication in the form of 3D memory stacks and compatibility with the BEOL of CMOS processes [1-14].

The viability of RRAMs has been proved at the device level and also in the integrated circuit arena as reported in Refs. [15-17]. The advantages of this technology with respect to Flash devices lie on remarkable improvements in the reading/writing speed, endurance, operation power, etc. Nevertheless, several hurdles have to be overcome to incorporate RRAMs into the industrialization lines, e.g.: the poor control of the switching uniformity and the lack of standardized compact models for circuit simulation. The stochastic nature of the switching features implies variations in the forming, set and reset voltages and in the resistance distributions [2, 11, 13, 18], both in the Low Resistance State (LRS) and in the High Resistance State (HRS). Great research efforts are needed to clarify the

mechanisms behind the physics of Resistive Switching (RS) and consequently behind the device variability. In terms of modelling for circuit simulation, there is also a long way to go: the introduction and acceptance by the scientific community of general compact models and clear parameter extraction algorithms, inclusion of these models into commercial circuit simulators, the consolidation of a publication corpus to offer alternatives to include the different physical effects that show up in RRAM operation for the technologies under study nowadays [2, 13, 14]. In this manuscript we deepen into the latest issue in line with previous papers in the literature [18-21].

In particular, a screening method for detecting if a current component, capable of being described by the QPC model [22, 23], is contributing to the current of a certain RRAM device is presented. Furthermore, once the QPC fingerprints have been detected, a method to extract the model parameters is proposed. To do so, we employed $Ni/HfO_2/Si$ devices. These RRAMs have been fabricated using the ALD technique [24] and were simulated and physically described in Ref. [25, 26]. The devices show a non-linear I-V relationship in LRS. The QPC model [22, 25, 27] was proposed in addition to an ohmic component to describe the charge transport in this operation regime. It was found that it worked well from the modelling viewpoint and helped to explain the device behaviour for different operations regimes [25, 27] and temperatures [26]. In RRAM devices showing non-linear I-V curves at low voltages in the LRS, different mechanisms can be thought to be responsible for this non-linearity; e. g., Schottky barriers, hopping conduction in an irregular contact between the filament tip and the electrode, presence of a nanometric constriction in the CF tip to be described by the QPC model, etc. The simultaneous contribution of several of these mechanisms is likely and consequently difficult to unveil under standard current measurements. That is why a numerical method to detect the presence of a current component (one linked to the QPC model in our case) is of utmost convenience.

Since the QPC model has been employed to describe the conduction both in the LRS and HRS [23], the proposed procedure might be used for both operation regimes; however, for the devices under study here we will only focus on the I-V curves in the LRS at low voltages. In the HRS, since there are no favoured conduction paths, different current mechanisms can take place depending on the dielectric nature, the electric field range and temperature [28, 29]. Taking into consideration all these issues, we find the application of our method extremely complicated. On the contrary, the LRS has been characterized in depth previously [25, 26] and a QPC component is recognizable; so, for the sake of simplicity, we will concentrate our analysis on this component here.

This new approach not only will allow the model parameters extraction but also will help us to deepen into the tunnelling barrier features behind the QPC current component. As it will be shown, we have obtained the QPC model parameters for all the curves in a long series of RS cycles by means of a genetic algorithm. The results will allow the analysis of device variability from a different perspective and the connection between important parameters such as the reset voltage, and others that can be extracted with this technique such as V_{Th_reset} introduced in Ref. [27]. For this purpose a multivariate statistical analysis has been considered.

The fabricated devices and measurement process are described in Section II, the numerical procedure in Section III and the main results and discussion in Section IV. Finally, the conclusions are given in Section V.

II. DEVICE DESCRIPTION AND MEASUREMENT

The devices measured were unipolar $Ni/HfO_2/Si$-based resistive RAMs. The RRAMs were fabricated on (100) n-type CZ silicon wafers with resistivity (0.007-0.013) Ω cm using a field-isolated process. Atomic layer deposition at 225ºC using tetrakis (Dimethylamido)-hafnium (TDMAH) and H_2O as precursors was employed to deposit 20nm-thick HfO_2 layers. The top Ni electrode with a 200nm thickness was deposited by magnetron sputtering [24]. A GPIB-controlled HP-4155B semiconductor parameter analyser was used to measure different long series of RS cycles under ramped voltage stress. The Si substrate was grounded and a negative voltage was applied to the Ni electrode.

III. NUMERICAL METHOD

The numerical procedure developed here is based on the calculation of the second derivative of the experimental I-V curves. In a previous work [27], we showed that a new parameter can be defined employing the first current derivative (see Fig. 1a). The current derivative shows a maximum and, the corresponding voltage was named threshold reset voltage V_{Th_reset}. It was found that this parameter is correlated with the reset voltage; as highlighted there, V_{Th_reset} can be used to estimate to some extent the reset voltage without the need of getting into the operation region where the self-accelerated processes that lead to the conductive filament rupture take place [27].
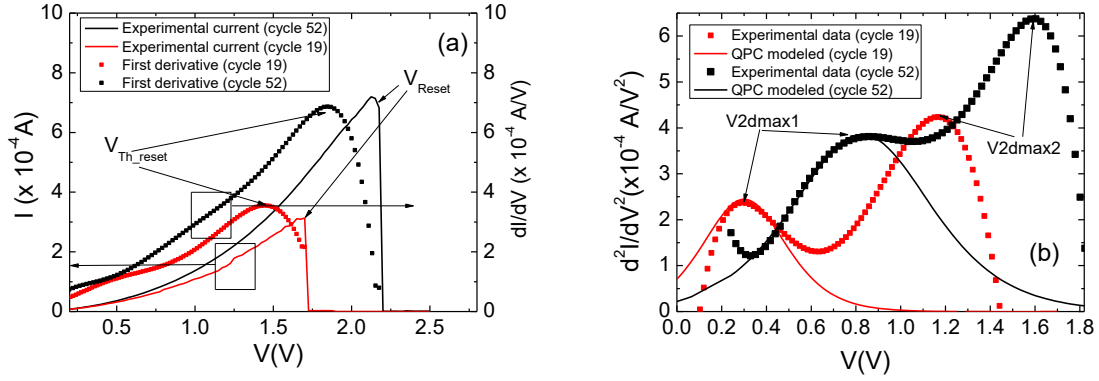
Figure 1: a) Experimental current versus applied voltage in the RRAMs under study and first derivative of the current versus voltage for two reset curves in a long series of RS. Second derivative of the experimental current versus voltage (symbols) for the two reset curves shown in a); the analytically calculated QPC modelled current second derivative (solid lines) is also shown. The parameters under analysis in this manuscript are shown for clarity: V_{Reset}, V_{Th_reset}, V2dmax1, V2dmax2.

We introduce now the analysis of the current second derivative (Fig. 1b). See that two maxima show up in this curve. The corresponding voltages were termed V2dmax1 and V2dmax2. After a massive calculation for a complete series of more than 2800 experimental RS cycles, it was found that 80% of the second derivative curves showed two maxima for the voltage range employed. The rest usually showed only one maximum and in a few cases three maxima were observed. As explained in Ref. [27], two conduction mechanisms in series (ohmic conduction and QPC based) are involved. Their different weights in each RS cycle, in addition to the stochastic mechanisms linked to the CF formation and rupture, can lead to the situations analysed here.

In Ref. [27] it was found that at low voltages the resistance component linked to the QPC model, i. e., to a quantum tunnelling conduction regime was the most important component. The current in the QPC model is given by Eq. 1 [22].

$$I = \frac{2eN}{h}\left\{eV_{CTR} + \frac{1}{\alpha}Ln\left[\frac{1 + exp\{\alpha[\Phi - \beta eV_{CTR}]\}}{1 + exp\{\alpha[\Phi + (1-\beta)eV_{CTR}]\}}\right]\right\} \qquad (1)$$

The Landauer's formalism for 1D quantum conductors and the zero-temperature limit were employed in the deduction of Eq. 1 [22, 30]. The following parameters are used in Eq. 1: Φ, the confinement potential barrier height measured with respect to the equilibrium Fermi level; α describes the curvature of the potential barrier in the longitudinal direction; V_{CTR} is the voltage which is assumed to drop at both ends of the CF constriction (a fraction of β and $(1-\beta)$ at each extreme [22]); e is the elementary electron charge and N is the number of active channels in the CF (assuming multi-filamentary contribution) [22, 30].

For the devices described in Section II, the ohmic conduction contribution at low voltages is negligible [25, 27]. Therefore, most of the external voltage drops at the ends of the CF constriction described by the QPC model so that $V_{RRAM} \approx V_{CTR}$. Hence, it is reasonable to expect that the device

current and its first and second derivatives can be described accurately by the QPC model in this operation regime. We have calculated the second derivative of two of the experimental reset curves in a long RS series, see the curves plotted in symbols in Fig. 1b. The numerical derivative was performed by means of a Weighted Essentially Non Oscillatory (W.E.N.O.) one-dimensional procedure [31, 32]. In this manner, we took advantage of the essentially non-oscillatory nature of the corresponding polynomial interpolation for the calculation. In this approach, a higher accuracy order can be obtained in smooth regions of the data with this procedure [31, 32]. The use of an advanced algorithm based on this technique greatly reduces the numerical oscillations and improves the results of the application of the usual finite differences techniques, especially when the presence of noise in the data cannot be disregarded (see for example [33]). In relation to this issue, an improvement in the noise treatment was included with respect to the algorithm employed in Ref. [27].

The corresponding analytical second derivative was calculated from Eq. 1. See that the QPC parameters can be tuned to reproduce the low voltage section of the experimental current second derivative around V2dmax1 as shown in Fig. 1b. The presence of the first maximum in the experimental current second derivative and the possibility to fit the curve with the QPC modelled current second derivative suggests that among different transport mechanisms, a QPC-based one is involved. The non-linear I-V relationship at low voltage also supports this assumption [25]. The shape of the current second derivative at low voltages, and most important, the value of V2dmax1 can be employed to obtain information related to the physical features of the transport through the CF constriction modeled by the QPC model. As shown in Fig. 2, were the role played by the different QPC model parameters can be seen in the analytically calculated current second derivative. The position of the curve maximum (V2dmax1) is linked to the parameters β and Φ. The steepness of the curve at the maximum sides is connected to the $\propto$ parameter.
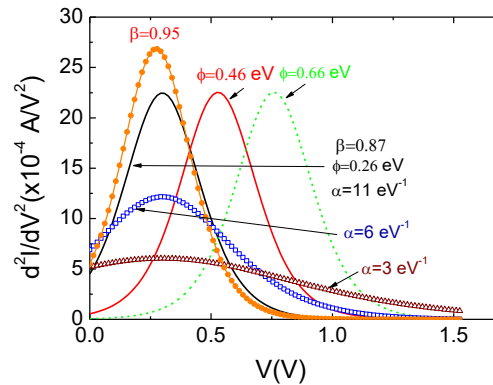
Figure 2: Second derivative of the QPC modeled current described in Eq. 1. The curve shapes for different model parameter values, in the voltage range where they are usually found [22], can be observed. The position of the curve maximum (V2dmax1) is linked to parameters β and Φ. The steepness of the curve at the maximum sides is connected to the $\propto$ parameter.

It is worth assessing now whether different conduction mechanisms in dielectrics are able or not to reproduce the experimental results. In particular, it is essential to analyse the voltage dependence of these mechanisms and their derivatives. To do so, we have focused the attention on the Poole-Frenkel (PF) and Fowler-Nordheim (FN) components in Fig. 3.

We employed a set cycle to obtain the best possible fit for both current components in order to determine their main parameters. Later on, the second derivative was calculated. The current second derivative of the FN presents tree terms, two of them negligible for the constants previously found, the third (the one with the higher value) shows a constant behavior for the voltage range plotted in Fig. 3, see the red curves. The ordeçr of magnitude of the current second derivative is much lower than those shown in previous figures and that in black line in Figure 3, since a set cycle has been employed for the fitting and the current magnitude is much lower than in the reset case.
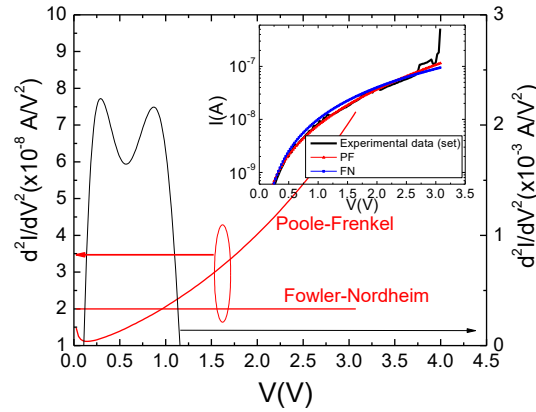
Figure 3: Second derivative of the current versus voltage for two different dielectric conduction mechanisms: Poole-Frenkel and Fowler-Nordheim (red lines). An experimental current curve corresponding to a set cycle has been employed as a reference to obtain the best fit for both current mechanisms, to determine the fitting constants, considering the electric field dependencies of the PF and FN current analytical expressions (see the inset). The experimental current second derivative for the reset curve corresponding to the set curve in the inset has also been plotted in black line for comparison.

Apart from PF and FN mechanisms, others could be considered, in particular Schottky emission. In that case, if the electron mean free path is lower than the Schottky barrier width, Simmons modified equation can be employed [29]. Under this assumption an expression analytically similar to the PF current is obtained, except for some differences in the constants. Therefore, a similar second derivative can be expected. In relation to the Space Charge Limited Conduction (SCLC), the ohmic region (low voltages) and the later region (at higher voltages) where Child's square law [29] can be applied will not produce a second derivative comparable to what we showed in Fig. 1b. For ionic conduction, nearest neighbor hopping as well as variable-range hopping no comparable second derivatives are expected since the current analytic dependence on the electric field is linear.

In the devices under study here, at low voltage, as commented below, the ohmic conduction contribution is negligible [25, 27]. This feature can be extended with respect to the considerations connected with the series resistance, although it has been proved that for other devices it could be of importance [23].

The origin of V2dmax2 could be linked to the overlapping of the conduction regimes described by the QPC and ohmic models. In addition, other conduction channels describable by the QPC model might be also important at higher voltages and could contribute to the existence of V2dmax2 in the experimental data.

IV. RESULTS AND DISCUSSION

A. Correlations

We have performed the first and second numerical derivatives for more than 2800 reset curves of a continuous RS series. The four parameters shown in Fig. 1 have been obtained and they were represented in Figs. 4 and 5.

A correlation between V_{Th_reset} and V_{Reset} was reported in [27], this correlation is not very clear in connection with V2dmax1, V2dmax2 and V_{Reset} as can be seen in Figure 5. To shed light on this issue, a multivariate analysis of correlation is needed and is presented below. In doing so, the correlation between V_{Th_reset} and V_{Reset} has been revisited within this statistical approach.
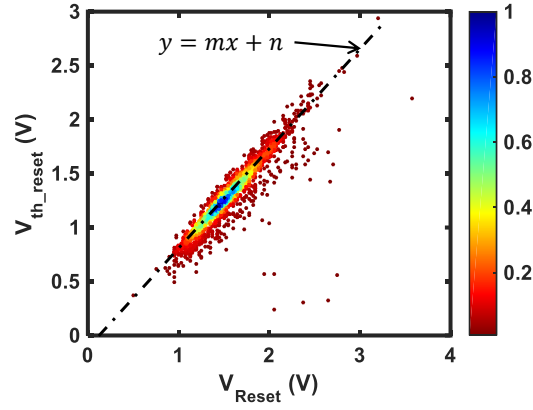
Figure 4: V_{Th_reset} versus V_{Reset} for the devices under study. Data relative to a normalized histogram are shown in a color map. The calculation of the numerical derivatives has been enhanced with respect to Ref. [27]. The dash-dot line shows a linear regression fit with the following parameters m=0.8475, n=-0.0357 V.
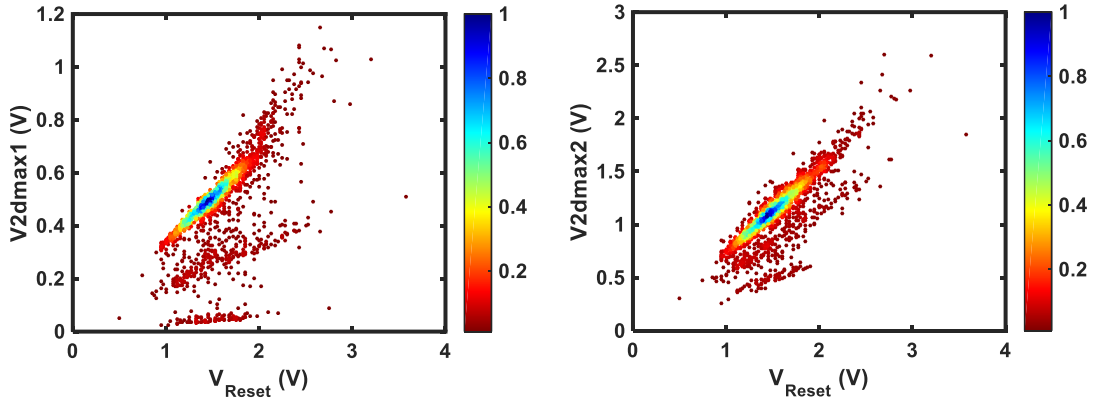
Figure 5: a) V2dmax1 versus V_{Reset} and b) V2dmax2 versus V_{Reset} for the devices under study. Data relative to a normalized histogram are shown in a color map.

It is well known that in the multivariate analysis of statistics [34] we must be aware of the dangers inherent to the interpretation of cross-correlations. In this respect, some of the variables (the parameters under study here) could be confounding variables that, in some sense, explain the relationship between reset voltage and each one of the others parameters (V_{Th_reset}, V2dmax1, V2dmax2). Taking this fact into consideration, computing and interpreting partial correlations for each pair of variables by controlling the others (statistically keeping them constant) is necessary. Summarizing the results obtained for the parameters for each cycle in the long RS series that we are considering, the partial correlations ordered by magnitude in the parameters under analysis are given in Table I.

Table I. Partial correlations between the different parameters considered in our analysis.

Parameter	Parameter	Correlation
V2dmax1	V2dmax2	0.826
V_{Reset}	V_{Th_reset}	0.655
V_{Reset}	V2dmax2	0.452
V_{Reset}	V2dmax1	-0.408
V_{Th_reset}	V2dmax2	0.206
V_{Th_reset}	V2dmax1	0.045

The only partial correlation that keeps the same value than the single correlation is the one between V2dmax1 and V2dmax2 parameters. The other correlations decrease and even change sign when calculating the partial correlations. Therefore, we can conclude that V2dmax1 and V2dmax2 are confounding variables that partly explain the correlation between other variables. V_{Reset} and V_{Th_reset} are also correlated (this was previously observed [27]). In addition, the correlations between V_{Reset} and the maxima of the current second derivative (V2dmax1, V2dmax2) are much smaller but statistically significant. Let us observe that the partial correlation between V_{Reset} and V2dmax1 is negative contrary to the associated single correlation that indicated positive correlation.

Assuming that V2dmax1 is linked to the current QPC modeled component, it is, however, not clear the connection of V2dmax2 with other current components, although we note that it is correlated with V2dmax1. Taking into account that this maximum shows up at higher voltages, a certain link to the ohmic current component is expected; that is why, these two variables, could explain partially the connection between V_{Reset} and V_{Th_reset}. In this manuscript we will focus on V2dmax1 and the information that can be extracted from the QPC model.

B. QPC model parameter extraction

See that in Figs. 1b and 2, apart from the fact that a QPC current component is detected, information related to the model parameters can be extracted. We have designed a fitting procedure where the Euclidean distance of the experimental and QPC current second derivative curves in the interval [V2dmax1-0.2V, V2dmax1+0.2V] (when it is possible) is minimized along with the Euclidean distance of the experimental and QPC currents in the interval [0, V2dmax1]. For the two cycles represented in Fig. 1, the fitting is shown in solid lines in Fig 1b.

The fitting process was reproduced for each curve in a complete RS series with more than 2800 cycles. The QPC model parameters were obtained or calculated accordingly to a Genetic Algorithm (GA) [35]. We employed a GA for this purpose because we are dealing with a non-polynomial optimization problem and because of the appropriateness of this approach for fitting constants searching problems like ours. In our particular case, the best possible fit is selected for obtaining the QPC model parameters for each reset cycle in complex spaces, achieving good results in a reasonable run time [36].

The GA was implemented using a real-valued encoding [35], that is, each chromosome was coded as an array of 4 floating point values, each one representing a QPC parameter. We chose a stochastic uniform selection operator, along with crossover and mutation operators using constraint dependence (that is, avoiding the creation of an invalid offstpring). The crossover operator specifies how the genetic algorithm combines two individuals, or parents, to form a crossover child for the next generation. The constraint dependent crossover operator creates children that are the weighted arithmetic mean of two parents. Mutation operators specify how the genetic algorithm makes small random changes in the individuals in the population to create mutation offsprings, generally adding or subtracting a small value. Mutation provides genetic diversity and enables the genetic algorithm to search a broader space. The constraint dependent mutation operator chooses a direction (this direction will correspond to an addition or substraction) and step length that satisfies bounds and linear constraints. The constraints are upper and lower values for each parameter (i.e., β between 0 and 1, ∝ between 0.1 eV^{-1} and 15 eV^{-1}, N between 1 and 100 and Φ between 0.25 eV and 3 eV). In (1), Φ can also be negative leading to nonlinear quantization. There is no limitation to the lower value of Φ; in this respect, if it is too negative (top of the barrier below the equilibrium Fermi level) it does not play any role. A population size of 500 chromosomes and 400 maximum generations were employed. The results are plotted in Figs. 6 and 7.
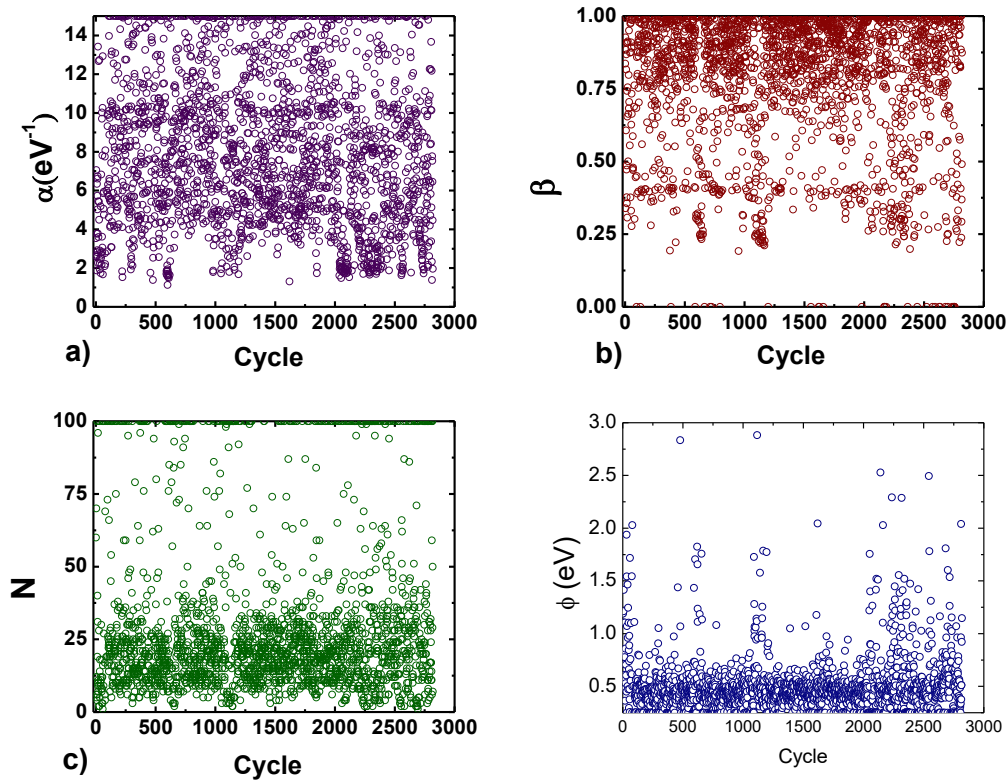
Figure 6: QPC model parameters versus cycle number for the devices under study. The calculation was performed by means of a genetic algorithm [35, 36].
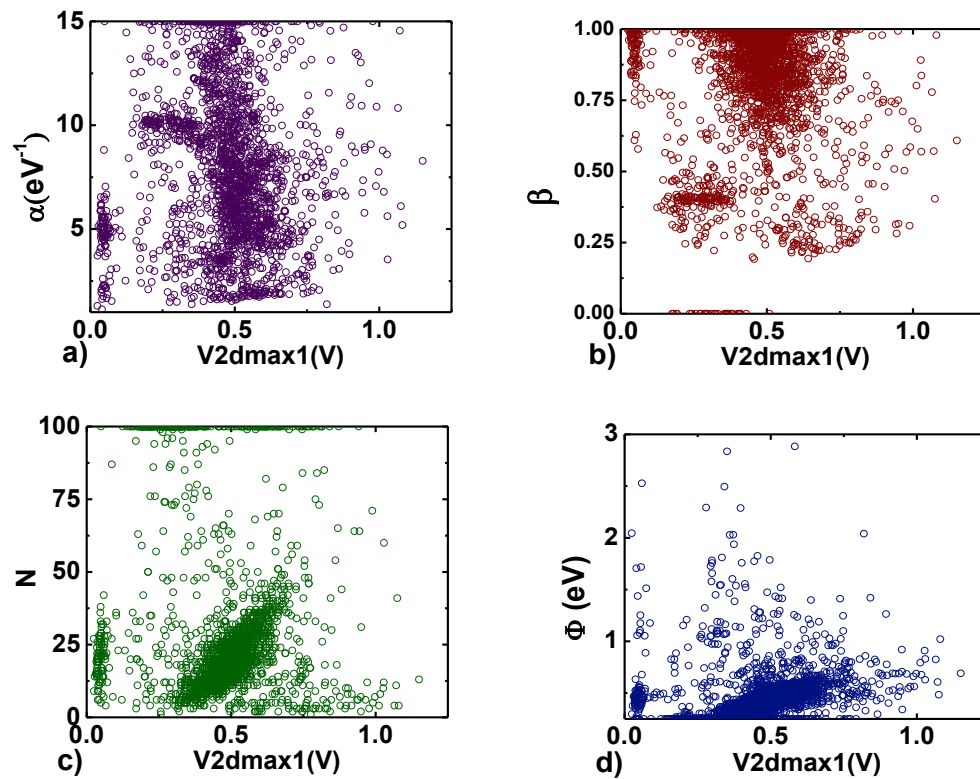
Figure 7: QPC model parameters versus V2dmax1 for the devices under study. The calculation has been performed by means of a genetic algorithm described above.

114

See that the N parameter (number of channels) is below 25 for most cycles, Here we assume that the channels are identical, this implies similar barrier height and shape, as well as the rest of features characterized by the QPC model parameters. In addition, the barrier height (measured from the Fermi level) is low, around 0.5 eV in most cycles. The parameters α and β are more spread out in a reasonable range of values [22].

If the parameters plotted in Fig. 6 are represented versus V2dmax1 (Fig. 7) we can analyze them from another perspective. A value of V2dmax1=0.5V is seen to be the most frequent and the corresponding parameters values concentrate in a narrow interval around; in particular, N=25 and Φ=0.5 eV, β=0.85 parameters are predominant values.

The barrier thickness along the CF constriction can be calculated as shown in Eq. 2 [22],

$$t_B = \frac{h\alpha}{2\pi^2}\sqrt{\frac{2\,\Phi}{m^*}}$$

(2)

where m* is the electron effective mass, and h is Planck's constant. For this particular calculation, we take an effective mass associated with HfO_2 with a value in between $0.11m_0$ [37] and $0.44m_0$ [38]. See Fig. 8b where t_B was plotted for the cycles considered here, the most frequent value is close to 1nm as can be seen.
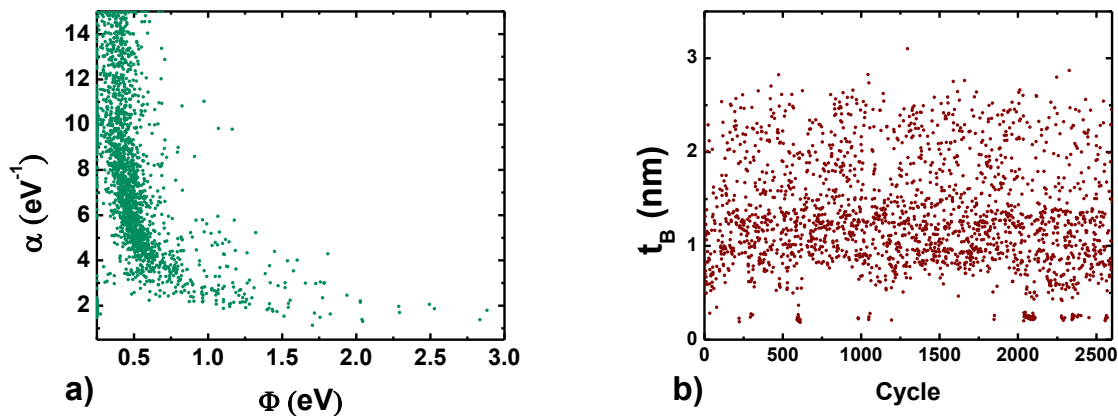
Figure 8: a) QPC model α parameter versus Φ parameter for the RS series considered. b) Barrier thickness (calculated by means of Eq. 2) versus cycle number. The QPC parameters have been obtained by means of a genetic algorithm applied to each curve in a whole RS series.

It is worth pointing out that assuming that the device CFs are formed by Ni atoms, for tB≈1nm there are several Ni atoms in the constriction linked to the potential barrier. There are, however, a few cases (see Fig. 8b) with tB≈0.25nm which could correspond to a single atom constriction.

V. CONCLUSIONS

A new screening method to detect the presence of a QPC modeled current mechanism has been developed. The new method is based on the calculation of the experimental current second derivative. The features of the second derivative allow the detection of the QPC model fingerprints, the model parameter extraction can be performed by minimizing the Euclidean distance between the current and the current second derivative in comparison to the analytical QPC model in the context of a genetic algorithm. The extracted parameter distributions have been analyzed to characterize the device LRS low voltage quantum transport regime. Finally, a multivariate statistical analysis of the correlations between the reset voltage and other reset curve characterization parameters has been performed.

VI. ACKNOWLEDGMENTS

REFERENCES

[1] P. Cappelletti, "Non volatile memory evolution and revolution", IEDM, p. 10.1.1-4, 2017.

[2] F. Pan, S. Gao, C. Chen, C. Song, F. Zeng, "Recent progress in resistive random access memories: materials, switching mechanisms and performance", Materials Science and Engineering, 83, pp. 1-59, 2014.

[3] D. Ielmini, R. Waser. "Resistive Switching: From Fundamentals of Nanoionic Redox Processes to Memristive Device Applications", Wiley-VCH, 2015.

[4] T. Hasegawa, K. Terabe, T. Tsuruoka, M. Aono. "Atomic Switch: Atom/Ion Movement Controlled Devices for Beyond Von-Neumann Computers", Advanced Materials, 24(2), pp. 252-267, 2012.

[5] T. Tsuruoka, K. Terabe, T. Hasegawa and M. Aono, "Forming and switching mechanisms of a cation-migration-based oxide resistive memory", Nanotechnology, *21*(42), pp. 425205, 2010.

[6] Y. C. Yang, F. Pan, Q. Liu, M. Liu, F. Zeng, "Fully room-temperature-fabricated nonvolatile resistive memory for ultrafast and high-density memory application", Nano letters, 9, pp. 1636-1643, 2009.

[7] Z. Wei, Y. Kanzawa, K. Arita, Y. Katoh, K. Kawai, S. Muraoka, S. Mitani, S. Fujii, K.Katayama, M. Iijima, T. Mikawa, T. Ninomiya, R. Miyanaga, Y. Kawashima, K. Tsuji, A. Himeno, T. Okada, R. Azuma, K. Shimakawa, H. Sugaya, T. Takagi, R. Yasuhara, K.Horiba, H. Kumigashira, M. Oshima, "Highly reliable TaOx ReRAM and direct evidence of redox reaction mechanism", IEEE International Electron Devices Meeting, pp. 1-4, 2008.

[8] S. Yu, X. Guan, H.S. Philip Wong, "On the switching parameter variation of metal oxide RRAM—Part II: Model corroboration and device design strategy", IEEE Transactions on Electron Devices, 59, pp. 1183-1188, 2012.

[9] W. Lu, D. S. Jeong , M. Kozicki , R. Waser, "Electrochemical metallization cells--blending nanoionics into nanoelectronics", MRS bulletin, 37, pp. 124, 2012.

[10] S. Gao, C. Song, C. Chen, F. Zeng, and F. Pan, "Formation process of conducting filament in planar organic resistive memory", Applied Physics Letters, 102(14), pp. 141606, 2013.

[11] R. Waser and M. Aono, "Nanoionics-based resistive switching 43

[12] M. Lanza, G. Bersuker, M. Porti, E. Miranda, M. Nafría, X. Aymerich, "Resistive switching in hafnium dioxide layers: Local phenomenon at grain boundaries", Applied Physics Letters, vol. 101, 193502, 2012.

[13] M. Lanza, "A Review on Resistive Switching in High-k Dielectrics: A Nanoscale point of View Using Conductive Atomic Force Microscope", Materials 7, pp. 2155-2182, 2014.

[14] R. Waser (ed.), "Nanoelectronics and Information Technology", 3rd ed., Wiley-VCH, Berlin, 2012.

[15] J. Zahurak, K. Miyata, M. Fischer, M. Balakrishnan, S. Chhajed,D. Wells, Li Hong, A. Torsi, J. Lim, M. Korber, K. Nakazawa, S. Mayuzumi, M. Honda, S. Sills,S. Yasuda, A. Calderoni, B. Cook, G. Damarla, H. Tran, Bei Wang, C. Cardon, K. Karda, J. Okuno, A. Johnson, T. Kunihiro, J. Sumino, M. Tsukamoto, K. Aratani, N. Ramaswamy, W. Otsuka,K. Prall. "Process integration of a 27nm, 16Gb Cu ReRAM", Electron Devices Meeting (IEDM), 2014 IEEE International, pp.6.2.1-6.2.4, 2014, doi: 10.1109/IEDM.2014.7046994

[16] T.Y. Liu, T. H. Yan, R. Scheuerlein, Y. Chen, J. K. Lee, G. Balakrishnan, G. Yee, H. Zhang, A. Yap et al., "A 130.7-mm^2 2-Layer 32-Gb ReRAM Memory Device in 24-nm Technology" IEEE J. Solid-State Circuits 49, pp. 140-153, 2014.

[17] A. Kawahara, R. Azuma, Y. Ikeda, K. Kawai, Y. Katoh, Y. Hayakawa, K. Tsuji, S. Yoneda, A. Himeno, et al., "An 8 Mb Multi-Layered Cross-Point ReRAM Macro With 443 MB/s Write Throughput", IEEE J. Solid-State Circuits 48, pp. 178-185, 2013.

[18] E. Miranda, and J. Suñé, "Modeling the conduction characteristics of broken down gate oxides in MOS structures", Microelectronics, *40,* pp. 1599-1603, 2000.

[19] C. Acha, "Graphical analysis of current-voltage characteristics in memristive interfaces", Journal of Applied Physics, vol. 121, p. 134502, 2017.

[20] F. Jiménez-Molinos, M.A. Villena, J.B. Roldán y A.M. Roldán, "A SPICE Compact Model for Unipolar RRAM Reset Process Analysis", IEEE Transactions on Electron Devices, 62, pp. 955-962, 2015.

[21] G. González-Cordero, J.B. Roldan, F. Jiménez-Molinos, J. Suñé, S. Long y M. Liu, "A new model for bipolar RRAMs based on truncated cone conductive filaments, a Verilog-A approach", Semiconductor Science and Technology, vol 31, p. 115013, 2016.

[22] E. Miranda, and J. Suñé, "Analytic modeling of leakage current through multiple breakdown paths in SiO_2 films", *Reliability Physics Symposium, 2001. Proceedings. 39th Annual. 2001 IEEE International,* pp. 367-379, 2001.

[23] E. Miranda, C. Walczyk, C. Wenger, T. Schroeder, "Model for the Resistive Switching Effect in HfO_2 MIM Structures Based on the Transmission Properties of Narrow Constrictions", IEEE Electron Device Letters, 31, pp. 609-611, 2010.

[24] M. B. González, J. M. Rafí, O. Beldarrain, M. Zabala, and F. Campabadal, "Analysis of the switching variability in Ni/HfO2-based RRAM devices," IEEE Trans. Device Mater. Reliab., vol. 14, no. 2, pp. 769–771, 2014.

[25] M.A. Villena, M.B. González, F. Jiménez-Molinos, F. Campabadal, J.B. Roldán, J. Suñé, E. Romera, E. Miranda, "Simulation of thermal reset transitions in RRAMs including quantum effects", Journal of Applied Physics, vol. 115, pp. 214504, 2014.

[26] M.A. Villena, M.B. González, J.B. Roldán, F. Campabadal, F. Jiménez-Molinos, F.M. Gómez-Campos y J. Suñé, "An in-depth study of thermal effects in reset transitions in HfO2 based RRAMs", Solid State Electronics, 111, pp. 47-51, 2015.

[27] M.A. Villena, J.B. Roldán, M.B. González, P. González-Rodelas, F. Jiménez-Molinos, F. Campabadal, D. Barrera, "A new parameter to characterize the charge transport regime in Ni/HfO_2/Si-n$^+$-based RRAMs", Solid State Electronics, vol. 118, pp. 56-60, 2016.

[28] Southwick R.G., Reed J., Buu C., Butler R., Bersuker G., Knowlton W.B.*,* "Limitations of Poole-Frenkel conduction in bilayer HfO2/SiO2 MOS devices", *IEEE Transactions on Device and materials reliability,* 10, pp. 201-207, 2010.

[29] E.W. Lim, R. Ismail, "Conduction mechanism of valence change resistive switching memory: a survey", Electronics, 4, pp. 586-613, 2015.

[30] L. M. Procel, L. Trojman, J. Moreno, F. Crupi, V. Maccaronio, R. Degraeve, L. Goux, and E. Simoen, "Experimental evidence of the quantum point contact theory in the conduction mechanism of bipolar HfO2-based resistive random access memories", Journal of Applied Physics, 114, 074509, (2013).

[31] G. Jiang and C. W. Shu, "Efficient implementation of weighted ENO schemes" Journal of Computational Physics, 126, pp. 202-228, 1996.

[32] X.D. Liu, S. Osher and T. Chan, "Weighted essentially non-oscillatory schemes", Journal of Computational Physics, 115, pp. 200-212, 1994.

[33] P. González, M.J. Ibáñez, A.M. Roldán y J.B. Roldán, "An in-depth study on WENO-based techniques to improve parameter extraction procedures in MOSFET transistors", Mathematics and Computers in Simulation, 118, pp. 248-257, 2015.

[34] D.C. Montgomery, E. A. Peck, G. G. Vining, "Introduction to linear regression analysis", Wiley, 2012.

[35] D. E. Goldberg, "Genetic Algorithms in Search, Optimization and Machine Learning", Addison-Wesley Longman Publishing Co., Inc. Boston, MA, USA, 1989.

[36] M. Kumar, M. Husian, N. Upreti and D. Gupta. "Genetic algorithm: review and application", International Journal of Information Technology and Knowledge Management, Vol. 2, pp. 451-454, 2010.

[37] S. Monaghan, P. Hurley, K. Cherkaoui, M. Negara, and A. Schenk, "Determination of electron effective mass and electron affinity in HfO2 using MOS and MOSFET structures," Solid State Electron., vol. 53, pp. 438–444, Apr. 2009.

[38] Y. Zheng, C. Troadec, A. Wee, L. Pey, S. O'Shea, and N. Chandrasekhar, "BEEM studies on metal high K-dielectric HfO2 interfaces", J. Phys.: Conf. Ser., vol. 61, pp. 1347–1351, 2007.

4.5. UGR-QPC1 model

This section introduces a new QPC SPICE model (UGR-QPC1). It is used for modeling conductive bridge memories (described in Chapter 2) with filamentary conduction through a constriction by the QPC model (described in section 4.3. Quantum Point Contact Model) and two cylindrical resistances with variable geometry (variable radius). The evolution of two radii is carried out at simulation time solving the differential equations of the chemical redox reactions (described in section 4.2. Unipolar Compact Model IM2NP-U).

A new thermal model is proposed using an equivalent electric circuit that includes longitudinal and transversal thermal resistances, both dependant on the radii of the two CF cylindrical sections (described in section II in Ref. [González-Cordero2016e]). The UGR-QPC1 model has been tested with I-V and I-t measured of Ni/HfO$_2$/Si-n+ devices (the fabrication and measurement set-up details are given in section A.5. Ni/HfO$_2$/Si-n^{++} Devices), a reasonable accurate fit was obtained.

This section was published in González-Cordero et al. Proceedings of IEEE. XXXI edition of the Design of Circuits and Integrated Systems Conference (DCIS 2016). IEEE Xplore digital library, the accepted preprint paper is presented below.

González-Cordero et al. Proceedings of IEEE. XXXI edition of the Design of Circuits and Integrated Systems Conference (DCIS 2016). IEEE Xplore digital library

G. González-Cordero, F. Jiménez-Molinos, J. B. Roldan, M. B. González and F. Campabadal, "Transient SPICE simulation of Ni/HfO$_2$/Si-n+ resistive memories," in *XXXI edition of the Design of Circuits and Integrated Systems Conference (DCIS)*, 2016 in Granada, Spain.
DOI: 10.1109/DCIS.2016.7845384

Quality metrics

Data base	Rating
Scimago Journal & Country Rank	h-index:2

Publication citations

Google Scholar	Web of Science
4	**0**

Transient SPICE simulation of Ni/HfO$_2$/Si-n$^+$ resistive memories

G. González, F. Jiménez-Molinos, J.B. Roldán

Depto. Electrónica y Tecnología de Computadores
Universidad de Granada.
Granada, Spain
jmolinos@ugr.es

M.B. González, F. Campabadal

Institut de Microelectrònica de Barcelona
IMB-CNM (CSIC)
Bellaterra, Spain

Abstract— A new SPICE model for the simulation of conductive bridge resistive memories has been developed. The model is based on filamentary transport and includes conduction through a constriction (by means of the quantum point contact model) and an accurate thermal description. It has been used for calculating thermally assisted reset transitions in Ni/HfO$_2$/Si-n$^+$ samples. Transient simulations have been carried out in order to obtain reset I-V and I-t curves, which are compared with experimental results showing a reasonably good fit. Finally, the role of the evolution at simulation time of the ohmic and thermal resistances is analyzed.

Keywords—Resistive Switching; RRAM; Conductive Filaments; Quantum Point Contact model (QPC); Circuital Model; Spice Simulation; Thermal Dissolution; Thermal Modeling.

I. INTRODUCTION

Resistive Random Access Memories (RRAMs) are one of the most preeminent emerging technologies in the non-volatile memory playground [1]. Although they will not replace 3D NAND flash memories in the short-medium term, they can fill the gap between DRAM and NAND performances [2]. RRAMs evolution in all their technological aspects (fabrication, characterization…) require a comprehensive understanding of their physical operation. In addition, RRAMs industrial implementation in fully functional memory circuits requires accurate SPICE models.

It is well known that in the modelling context, SPICE models can be found that are an evolution of previously developed physically based models. In this respect, the Institute of Microelectronics group (Peking University) has developed a SPICE model [3] to have an implementation of their physically based compact model for large scale array simulation [4]. In this case, switching is associated with the formation of a conductive filament (CF) made of oxygen vacancies clusters. The physical model deals with the generation and recombination of oxygen vacancies and the drift of the oxygen ions (O2-) to and from one of the electrodes in a bipolar operation scheme [4]. In this model, as in the well-known Stanford model [5], the gap parameter, g, the distance between the partially formed CF tip and the electrode, is the main parameter that controls the device resistive state. In these models, a simplified version of the heat equation is solved for

calculating the thermal evolution of the device (only one temperature value for each device state is considered).

In the same manner, we have developed a physically based differential simulator for unipolar RRAMs [6, 7] in which the evolution of conductive filaments (whose radii are not considered to be uniform, but dependent on the vertical coordinate) is calculated taking into account metallic species diffusion and redox reactions in the set/reset transitions. The temperature profile along the conductive filaments is calculated solving the heat equation for the structure. Finally, ohmic and quantum conduction through a constriction (by means of the Quantum Point Contact, QPC, model [7]) are also considered. Such a detailed physical description does not allow the fast RRAM simulation procedures needed in circuit analysis. Therefore, in order to make the simulation of circuits based on RRAMs easier and faster we have developed a SPICE model based on the simulation tool previously published [6]. This means that the physical principles and model parameters are the same, but the RRAM is treated with a discrete approach, using lumped circuital elements. A first version of this circuital model was introduced in [8]. The physics behind the device resistive switching processes and the numerical basis employed to articulate our present model are quite different from the previously reported models [4, 5], with some differences that are worth highlighting. First, the CFs in our simulator consist of several blocks that could form a tree branch structure including several subfilaments that allows a reliable reproduction of the RRAM operation [8], the previous models use a single changeable cylindrical CF [4, 5]. In addition, a more complete heat equation is employed in our case, incorporating the heat loss from the CF to the surrounding oxide; in particular, each block within the CF has a different temperature, therefore a more detailed thermal distribution can be considered in our case.

Besides the cited SPICE models [3, 5, 8], other models have also been reported so far [8-13]. Some of them develop the modeling equations assuming that RRAMs are a particular kind of memristors [14], defining a variable that determines the device state and whose temporal evolution is theoretically or empirically determined. Furthermore, some of them include the evolution of the device temperature at simulation time [3, 5, 8]. In the present work, we have improved our previous circuital
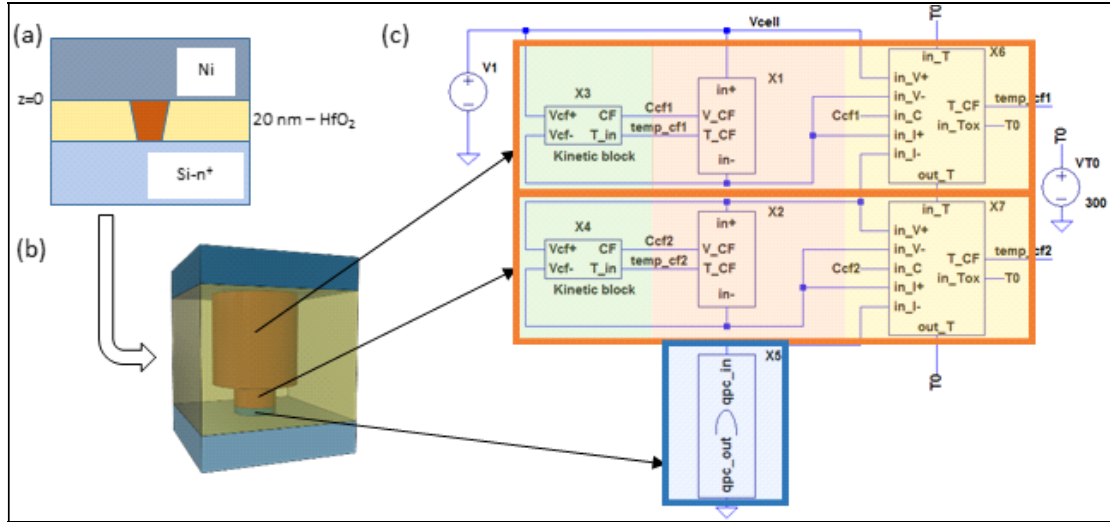
Fig. 1. (a) Cross section of the device structure. A truncated-cone shaped conductive filament (CF) is also shown. (b) For modeling purposes, the truncated-cone shaped filament is represented by two cylinders, with different radii and lengths. Furthermore, a tunnel barrier is also considered at the CF-Si interface. (c) LTspice schematic built in order to simulate the RRAM. Each portion of the CF (cylinder) is modeled with the subcircuits inside the brown rectangles. These include: thermal modeling (subcircuits X6, X7, orange colored), ohmic conduction through the filament (subcircuits X1 and X2, pink colored) and cylinder size and its temporal evolution (subcircuits X3, X4, green colored). Finally, the X5 subcircuit models the conduction through a constriction (making use of the QPC model [19]). As can be seen, all types of subcircuits which model each cylinder (thermal, conductive and kinetic subcircuits) are connected between them because they are interdependent.

model [8] that includes a detailed thermal description (different temperatures along the CF are considered) with the following new characteristics: (i) it allows the study of the transient evolution of CF radii and therefore, (ii) ohmic and thermal resistances can also change at simulation time; (iii) it includes quantum conduction in addition to ohmic transport (by using the QPC model).

II. MODEL DESCRIPTION

Figure 1 shows a schematic representation of the device and the model that describes it. The conductive filament is supposed to be formed by the serial connection of several cylinders, with different radii [8] (Fig. 1.b). With a reduced number of blocks (around 6-10), the modeling results are accurate enough when compared with those obtained by means of a numerical solver [8]. The thermal analysis of a reset process simulation allows distinguishing that only a small portion of the filament is deeply heated. This heated section of the filament is narrowed until the complete filament disruption takes place. According to previous results, the temperature of the CF main body is much lower throughout the reset process than in the narrowed portion, and, consequently, the CF shape remains almost unchanged [15, 16]. Therefore, we have chosen two cylinders for representing the CF. The big one (top cylinder, Fig. 1.b.) accounts for the CF main body, while the other one (bottom cylinder) models the hotter region where the breakdown is produced. In this manner, a balance between simplicity and accuracy is obtained while maintaining a reasonable physical description.

In this study, the simulations are performed using LTspice IV [17]. In order to model the device features, each cylinder is represented by a circuital block (shown inside the brown rectangles in Fig. 1.c). Each block is composed by three sections or subcircuits: an ohmic subcircuit (shown in pink in Fig. 1.c), a thermal subcircuit (orange) and a kinetic subcircuit (green). The last one stores the cylinder radius as a capacitor voltage. The capacitor charge is modified by current sources whose value depends on the diffusion and redox reaction rates [12, 18], which are temperature dependent. The ohmic subcircuit implements a voltage controlled resistor that reproduces the conduction through the CF. The actual value of the resistance depends on the cylinder radius and on its temperature and, therefore, evolves at simulation time. Finally, the thermal subcircuit leads to the calculation of the temperature using an equivalent electric circuit that includes longitudinal and transversal thermal resistances. These resistances also depend on the cylinder size and, therefore, are calculated at simulation time. This is an important novelty in this model. As can be seen, all the subcircuits are connected with each other (Fig. 1.c). Another important novelty in this new version of our SPICE model is that a new type of block (QPC subcircuit) has been introduced to account for the charge conduction through a constriction by means of the QPC model [7, 19] (see Fig.1.c).

III. VALIDATION OF THE MODEL AND RESULTS

The model has been previously validated [18] by means of a comparison with a numerical simulator that includes ohmic conduction, quantum conduction through a barrier (QPC

model), redox and diffusion reactions and the solution of the heat equation [6, 7]. As previously mentioned, this simulator uses the same physical principles and model parameters, but it solves the differential equations in a self-consistent scheme using a fine grid instead of following a lumped component scheme and circuital approximation, as in the present model. In this work, we extend the validation of the model by comparing with experimental data.

Ni/HfO$_2$/Si-n$^+$ RRAMs fabricated at IMB-CNM have been used [20]. These samples show a non-linear behaviour at low voltages that has been related to quantum conduction through a barrier [7, 21]. A negative voltage (-V_{app}) is applied to the top electrode while the bottom electrode is kept grounded. After a forming process, five successive reset-set cycles were performed with an approximated voltage ramp rate of 0.4 V/s. Figure 2 shows the I-V curves measured for the reset processes (dotted lines with symbols). Our new circuital model has been used in order to reproduce these curves (Fig. 2, solid lines). The model parameters are shown in Table I, while the cylinder

TABLE I. MAIN MODEL PARAMETERS

Acro-nym	Parameter[a]		
	Value	*Unit*	*Meaning*
σ_0	$3 \cdot 10^5$	$(\Omega m)^{-1}$	Ohmic conductance
α_T	$10 \cdot 10^{-3}$	K^{-1}	Temperature coefficient of resistivity
E_a	0.8	eV	Activation energy for diffusion
K_{diff}	$5 \cdot 10^{10}$	s^{-1}	Prefactor for diffusion velocity
N	35		Number of channels in QPC model
α_0	4.0	eV^{-1}	Related with barrier height and thickness [19]
ϕ_B	1.0	eV	Tunneling barrier height
β	0.9		Fraction of the voltage that drops at cathode side of the barrier
h	$4 \cdot 10^{10}$	$W/(K \cdot m^2)$	Heat transfer coefficient
κ_0	3	$W/(K \cdot m)$	Thermal conductivity

a. Background color indicates the corresponding model block in Fig. 1.c.

sizes are indicated in the figure caption. As can be seen, a good agreement has been reached. Different QPC parameters could have been used in each cycle since the resulting barrier after a set process could be different. However, in order to maintain the simplicity of the model, the same QPC parameters and cylinder lengths were used in all the simulations.

Fig. 2. Experimental (dotted lines with symbols) and simulated (solid lines) I-V curves obtained with an approximated voltage rate of 0.4V/s. Five set-reset cycles were carried out using the same sample (only the reset portion is shown). For the simulated curves, the initial values of the minimum radii are: 2.8nm (blue), 3.0nm (cyan), 3.4nm (green), 3.85nm (red) and 8.8nm (black). The initial maximum radius is 6.5nm for all the cases, except the black line (11.5nm). The other simulation parameters are the same for all the curves, and are indicated in Table I. The length of the biggest cylinder is 19nm, while the other is 1nm.

Fig. 3. Experimental (dotted line with symbols) and simulated (solid lines) current versus time curves obtained with an applied constant voltage of 1V. The sample is the same that has been previously subjected to five reset-set cycles (the reset I-V curves are shown in Fig. 2). The model parameters and cylinder sizes are the same than those used for the simulations in Fig. 2).

The model also allows transient simulations of RRAMs when a constant voltage is applied. Figure 3 shows the simulated current versus time obtained for V_{app} = 1V. The model parameters, including cylinder sizes, are the same than those given in Fig. 2. A comparison with the experimental current is also shown in Fig. 3. See that a perfect agreement has been achieved even taken into account that the filament configuration depends on the CF state after the last set process, and only a reasonable estimation of the transition time could be initially expected.

In most SPICE models the ohmic (R_{CF}) and thermal resistances (R_{TH}) are calculated before the simulation, taking into account the initial cylinder sizes [8]. In this work, we have improved our previous model and the ohmic and thermal resistances are calculated at simulation time, considering the actual filament size. Figure 4 shows the different results obtained using the full model and maintaining the thermal or the ohmic resistances at a fixed value (their initial value). At low voltages, a slight difference is observed because the filament evolves slowly (the temperature is not high enough and, therefore, the diffusion process and the corresponding filament destruction are hardly activated). However, close to the reset voltage, once the reset process is triggered through a self-accelerated process [22], the CF evolution is much faster and in these few tenths of a volt more differences can be found between the three models. Although the differences might be seen not very significant they depend on the model parameter choice. The accurate physical description is obtained when the full model is considered (that is, taking into consideration the influence of the actual cylinder sizes on the ohmic resistances values and, specially, the thermal resistances at simulation time).

If thermal resistances are not included another effect is observed (see inset of Fig. 4). Once the filament dissolution process has been triggered, the rupture is not completed because the self-accelerated process is not fully finished, in fact it is stopped. Then, a progressive reset [23] is obtained instead of the abrupt process observed with the full model. In order to illustrate this phenomenon, the temperature in the middle of the two cylinders that form the CF has been represented in Figure 5, as a function of the applied voltage (the inset shows the radii evolution). The dashed lines show the results obtained when the thermal resistances are fixed to their initial value. In this case, the temperature is maintained at a medium value instead of increasing almost in a divergent way as in the case when thermal resistances are not fixed (solid lines). In this latter case, the cylinder size reduction causes the increase of the thermal resistances and, therefore, a strong temperature increase (within a self-accelerated process). However, when the thermal resistances do not increase, the temperature is maintained at a lower value.

Figure 6 shows the thermal resistances versus the applied voltage for both cases (variable and fixed resistances). As can be seen, the values are similar and their only difference is significant near the reset voltage, when the temperature starts to increase, as explained above.

Finally, Fig. 7 shows the QPC and ohmic resistances. The QPC resistance is the resistance associated to the QPC barrier

(that is, the voltage drop between the QPC subcircuit pins divided by the CF current). The total ohmic resistance is also shown besides the partial resistance of each cylinder (top and bottom) which forms the CF. Two cases are shown: the full model and the case where the resistance dependence on the cylinder radius is deactivated (only the initial radius is considered for calculating the resistance). In this case, the resistance varies only because of its thermal dependence through the temperature coefficient of the resistivity (α_T). Again, the results are similar except for the region near the reset voltage, when the temperature of the bottom cylinder increases.

IV. CONCLUSIONS

A new SPICE model for the simulation of unipolar resistive switching memories has been introduced. The model includes an accurate thermal description and incorporates the quantum-point-contact model in order to account for the non-linear conductance observed at low voltages because of the quantum conduction through a channel constriction. The model has been validated by comparison with experimental data, both I-V and I-t curves. Another novelty of the model is the inclusion of the thermal and ohmic resistances dependence on the actual filament size. Therefore, their values can evolve at simulation time as the reset process advances. The role of this improvement has been analyzed.
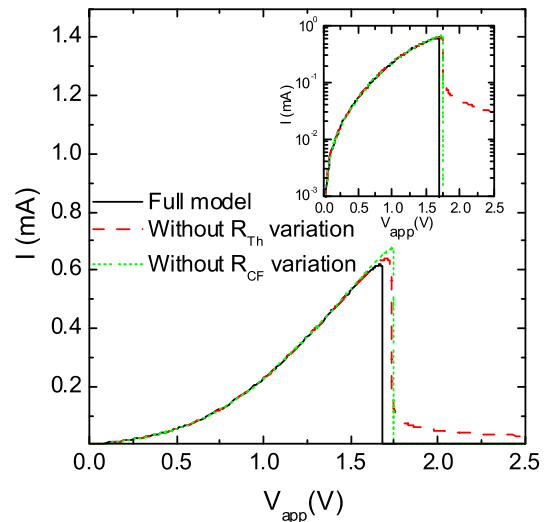
Fig. 4. Simulated I-V curves showing the effects when the dependence of the thermal and ohmic resistances on the cylinder radii is switched off. The solid black line has been calculated with the full model (including the variation of the resistances at simulation time), it is equal to the green curve (radius 3.4 nm) in Fig. 2. The dashed red line (dotted green line) shows the I-V curve when the thermal (ohmic) resistances are fixed at their initial values. Inset: the same graph with a vertical logarithmic scale.
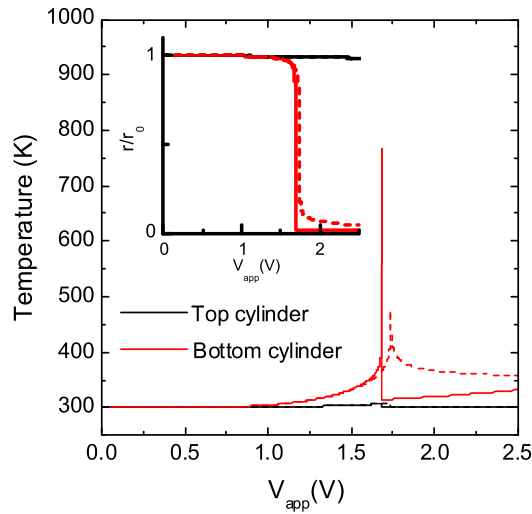
Fig. 5. Temperature at the center of the top (black) and bottom (red) cylinders. The inset shows the normalized radii evolution (r_0 is the initial radius for each cylinder). The results obtained with the full model are shown in solid lines, while dashed lines show the effects of fixing the thermal resistances to their initial values, that is, without including the cylinder size dependency.
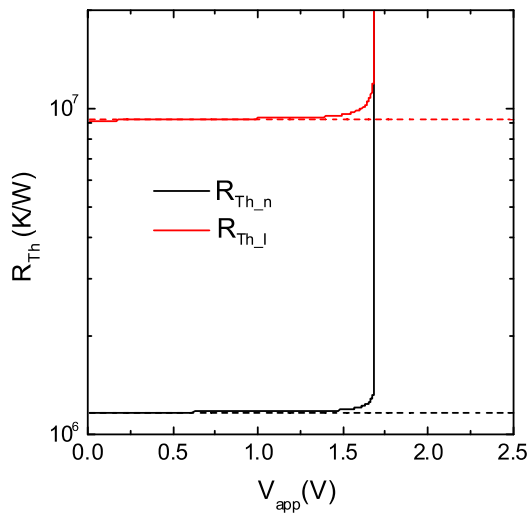
Fig. 6. Thermal resistances of the bottom cylinder versus applied voltage. The thermal resistance associated with the lateral heat leakage is shown in black lines, red lines correspond to the transversal heat conduction. Solid lines show the full model results while dashed lines show results for fixed thermal resistances (when the variation due to the radius evolution is not included).
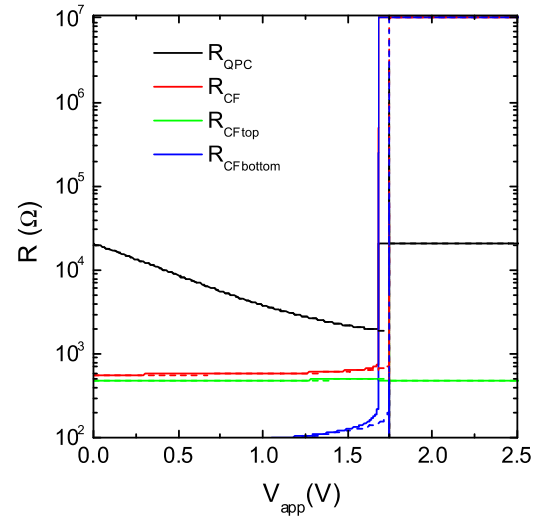
Fig. 7. Resistance versus applied voltage. The components are associated with the quantum barrier (R_{QPC}, black line) and ohmic transport: R_{CF} is the total ohmic resistance (red line), R_{CFtop} is the top cylinder resistance (green) and $R_{CFbottom}$ is the bottom cylinder resistance (blue). Solid lines show the results of the full model, while dashed lines show the case when the decrease of the radii is not taken into account for calculating the resistances (their variation is only due to the temperature coefficient).

REFERENCES

[1] F. Pan, S. Gao, C. Chen, C. Song, F. Zeng, "Recent progress in resistive random access memories: materials, switching mechanisms and performance", Materials Science and Engineering, 83, pp. 1-59, 2014.

[2] P. Cappelletti, "Non volatile memory evolution and revolution", in IEDM Proceedings, 2015.

[3] H. Li et al., "A spice model of resistive random access memory for large-scale memory array simulation", IEEE Electr. Dev. Lett., vol. 35, n. 2, 2014.

[4] P. Huang et al., "A physics-based compact model of metal-oxide-based rram dc and ac operations", IEEE Trans. Electr. Dev., vol. 60, no 12, 2013.

[5] *X. Guan, S. Yu, and H-S.P Wong, "A spice compact model of metal oxide resistive switching memory with variations", IEEE Elec. Dev. Lett., vol. 33, pp. 1405-1407, 2012.*

[6] M.A. Villena et al., "An in-depth simulation study of thermal reset transitions in resistive switching memories", J. Appl. Phys., vol. 114, p. 144505, 2013.

[7] M.A. Villena et al., "Simulation of thermal reset transitions in resistive switching memories including quantum effects",J. Appl. Phys., vol. 115, p. 214504, 2014.

[8]   F. Jiménez-Molinos, M.A. Villena, J.B. Roldán, A. Roldán, "A spice compact model for unipolar rram reset process analysis", IEEE Trans. on Elec. Dev, vol. 62, no. 3, pp. 955-962, 2015.

[9]   *A. Rák, G. Cserey, "Macromodeling of the memristor in Spice", IEEE Trans. On Computer-aided design of integrated circuits and systems, vol. 29, pp.632-636, 2010.*

[10] *S. Shin, K. Kin and S.-M. Kang, "Compact models for memristors based on charge-flux constitutive relationships", IEEE Trans. Comput.-Aided Design Integr. Circuits Syst., vol. 29, pp. 590-598, 2010.*

[11] *P. Sheridan, K.-H. Kim, S. Gaba, T. Chang, L. Chen and W. Lu, "Device and spice modeling of rram devices", Nanoscale, vol. 3, pp.3833-3840, 2011.*

[12] *X. Fang, X. Yang, J. Wu and X. Yi, "A compact spice model of unipolar memristive devices", IEEE Transactions on nanotechnology, vol. 12, pp 843-849, 2013.*

[13] *J.P. Strachan, A. C. Torrezan, F. Miao, M.D. Pickett, J.J. Yang, W. Yi, G. Medeiros-Ribeiro and R. S. Williams, "State dynamics and modeling of tantalum oxide memristors", IEEE Trans. Elec. Dev., vol. 60, pp. 2194-2202, 2013.*

[14] L. Chua, "Resistance switching memories are memristors", *Applied Physics*, vol. 102, pp. 765-783, 2011.

[15] M.A. Villena et al., "An in-depth study of thermal effects in reset transitions in HfO$_2$ based rrams", Solid-State Electronics, vol. 111, pp. 47-51, 2015.

[16] M.A. Villena, "Estudio, modelado y simulación de memorias rrams", Ph.D. Thesis, 2015.

[17] http://www.linear.com/designtools/software/#LTspice

[18] G. González, F. Jiménez-Molinos, M.A. Villena and J.B. Roldán, "Spice simulation of thermal reset transitions in Ni/HfO2/Si-n+ rrams including quantum effects", presented in Wodim 2016.

[19] E. Miranda, C. Walczyk, C. Wenger and T. Schroeder, "Model for the resistive switching effect in mim structures based on the transmission properties of narrow constrictions", Electron Device Letters, IEEE, vol. 31, no. 6, pp. 609–611, 2010.

[20] M.B. Gonzalez, J. M. Rafí, O. Beldarrain, M. Zabala and F. Campabadal, "Analysis of the switching variability in Ni/HfO$_2$-based rram devices", IEEE Trans. on dev. and mat.reliab., vol. 14, no. 2, 2014.

[21] M.A. Villena et al., "A new parameter to characterize the charge transport regime in Ni/HfO2/Si-n+-based rrams", Solid-State electr., vol. 118, pp. 56-60, 2016.

[22] U. Russo, D. Ielmini, C. Cagli and A.L. Lacaita, "Self-accelerated thermal dissolution model for reset programming in unipolar resistive switching memory (rram) devices", IEEE Trans. Electron Devices, vol. 56, nº2, pp. 193-200, 2009.

[23] M.A. Villena et al., "A comprehensive analysis on progressive reset transitions in rrams", J. Phys. D: Appl. Phys., vol. 47, p. 205102, 2014.

4.6. UGR-QPC2 model

This model is also employed for conductive bridge memories (described in Chapter 2). The charge conduction takes place through a filament with a constriction that can be described by the QPC model (described in section 4.3. Quantum Point Contact Model). The CF is represented by two cylinders with variable geometry (variable radii) with an associated resistance temperature dependent. In addition to CBRAM, these models can be employed also to devices with different RS operation such as VCMs. In the model under consideration, the evolution of the CF two radii is changed at simulation time by solving the differential equations of redox chemical reactions that account for the CF growth (described in section 4.2. Unipolar Compact Model IM2NP-U).

A new thermal model is proposed using an equivalent electric circuit that includes longitudinal and transversal thermal resistances and thermal capacitances. Both parameters depend on the radii of the two cylindrical sections (described in section II of [Jiménez-Molinos2017]). The UGR-QPC2 model has been tested in order to reproduce a transient current under a 3V pulse measured in Ni/HfO$_2$/Si-n+ devices. The model shows a reasonable fit.

This section was published in Jiménez-Molinos et al. Proceedings of IEEE. 11th Spanish Conference on Electron Devices (CDE 2017). IEEE Xplore digital library, the accepted preprint paper is presented below.

Jiménez-Molinos et al. Proceedings of IEEE. 11th Spanish Conference on Electron Devices (CDE 2017). IEEE Xplore digital library

Quality metrics

Data base	Rating
Google Scholar Metrics	h5-index:6 h5-median:8

Publication citations

Google Scholar	Web of Science
0	**0**

2017 Spanish Conference on Electron Devices (CDE)

SPICE modeling of RRAM thermal reset transitions for circuit simulation purposes

F. Jiménez-Molinos, G. González-Cordero, P. Cartujo-Cassinello, J.B. Roldán

Departamento de Electrónica y Tecnología de Computadores
Facultad de Ciencias. Universidad de Granada (Spain). Email: jmolinos@ugr.es

Abstract—A physically based SPICE compact model for unipolar resistive memories is presented. The model includes ohmic and quantum conduction accounting for filamentary resistive switching operation. In addition, a detailed description of thermal effects is incorporated. Different types of conductive filaments (CFs) can be taken into consideration; in particular, tree-branch shaped filaments. The implementation in a circuit simulation tool has been performed in a modular and comprehensive manner. The reset transient response under voltage pulse operation is simulated and analyzed in depth taking into account the evolution of electric and thermal internal variables. The thermal inertia in the RRAM response has been considered and characterized.

Keywords—*resistive switching; RRAMs; compact modeling; SPICE simulation, thermal capacitance.*

I. INTRODUCTION

Resistive random access memories (RRAMs) have become a serious contender in the non-volatile memory playground [1], [2]. In order to correctly design memory cells and complete ICs based on RRAMs in an industrial environment, circuital models are necessary. In this context we have developed a SPICE model for simulation of unipolar RRAMs. The physically based model introduced here accounts for: (i) temperature dependent ohmic conduction, (ii) quantum conduction through a constriction by means of the quantum-point-contact model (QPC) [3], [4] and (iii) an accurate thermal description that includes thermal resistances and capacitances that evolve at simulation time. To the best of our knowledge, the latter feature is a novelty in the RRAM circuit model playground. This model has been previously validated by comparison with a physically based differential simulator [5] and with experimental I-V and current versus time curves (the latter under Constant Voltage Stress CVS operation) [6], [7]. In this work we will focus on reset transitions operated under constant voltage, and on the corresponding thermal behavior.

II. SPICE MODEL DESCRIPTION

The model we proposed is based on the physics employed for the development of a previous RRAM simulator. That is, the model includes the same physical mechanisms and parameters than our former continuous differential solver [4], [8] (ohmic conduction through the CF with thermal dependency of the electric conductivity; quantum conduction through a constriction described by means of the QPC model; redox and diffusion process equations for controlling the CF

time evolution and a thermal equation solver to obtain a detailed temperature description). However, instead of using a continuous differential scheme, a lumped approach is followed here (for SPICE modeling and circuit simulation purposes). In this way, the CF is split off in several discrete regions which are supposed to be of cylindrical shape; each region is modeled by means of a SPICE subcircuit or block [6]. Consequently, the RRAM conductive filament (CF) consists of several of these blocks connected together.

Furthermore, a different kind of subcircuit (named QPC block) is added in this revised model version in order to include quantum conduction through a constriction in the CF or at the CF-electrode interface [3], [4].

The accuracy of the model is directly linked to the number of CF subcircuits employed to describe the conductive filaments; in this respect, the higher the number of subcircuits the closer the description to the physics implemented in the RRAM continuous macroscopic solver [4], [8]. Here we assume truncated-cone shaped CFs; thus, in order to look for a trade-off between simplicity and accuracy while maintaining a reasonable physical description, only two CF blocks are used to model the CFs. This approach is based on previous results obtained through physically based simulators [4], [9]. The simulations showed that the CF regions where the higher temperatures were achieved were narrow; indeed, the filament disruption that takes place in RESET processes is found in these high temperature narrow zones. This fact led us to propose a two block model for the CF: one to a represent the main body CF where the temperature does not change much and the other to account for the high temperature narrow zone where the rupture occurs.

A sketch of the proposed SPICE model is given in Fig. 1. As explained above and shown in Fig. 1.a the CF is implemented by two SPICE subcircuits, each one represents a cylinder with different radius. A subcircuit to account for quantum effects through the QPC model is also added. Each CF subcircuit is composed of other lower-level subcircuits following an hierarchical structure (see Fig. 1.b): (i) a kinetic block to calculate redox and metallic species diffusion rates and store the filament radii values; (ii) a block to implement an ohmic conductor with temperature dependent resistivity to calculate the device current and obtain Joule heating; and (iii) a thermal block to calculate the CF temperature considering Joule heating. The three referred blocks are interconnected because of their mutual dependence. Furthermore, the ohmic

and thermal components are linked to the corresponding subcircuits.
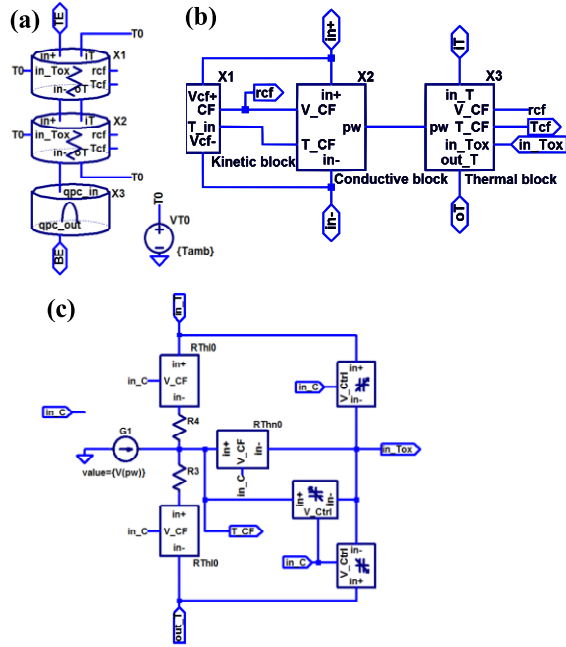
Fig. 1. Scheme of the SPICE model proposed which is based upon a subcircuit hierarchy including several levels. (a) The conductive filament is modeled by using three SPICE subcircuits: X1 and X2 account for the ohmic conduction in the two regions the CF is split off. X3 introduces the effect of a quantum constriction described by means of the QPC model. (b) Subcircuit to model each CF region. It includes: (i) a kinetic block to calculate redox and diffusion rates, and store filament radii values, (ii) a block to implement a temperature dependent resistance and to calculate Joule heating which is used as an input for (iii) the thermal block, where the CF temperature is obtained. (c) Subcircuit corresponding to the thermal block. Thermal capacitances and resistances (which depend on the filament radius) are considered.

Fig. 1.c shows the thermal block details which contains the main novelties of the present model with respect to previous versions [5]-[7]: the inclusion of thermal capacitances along with thermal resistances. Both of them are calculated considering the corresponding cylinder radii. They are also implemented as subcircuits because, as a novelty, the thermal capacitances change at simulation time as the CF size evolves. We call the readers' attention to the fact that thermal calculations are performed by means of an equivalent electric circuit, where temperature is treated as voltage and heat as current.

The model was previously validated [5] by comparing with our differential simulation tool [4], [8]. Furthermore, we succeeded to reproduce experimental data corresponding to devices based on the following stack, Ni/HfO$_2$/Si-n$^+$; the RRAMs were fabricated at the Institute of Microelectronics of

Barcelona (IMB-CSIC) [10]. These samples show a non-linear behaviour at low voltages in the low resistance state that has been related to quantum conduction through a barrier or constriction [4], [11]. Experimental data were accurately fitted in this operation regime with the QPC model both for I-V and I-t curves [7]. In both cases, the same model parameters were used, pointing out that a good description of the physics behind the device operation was fulfilled. More details on the RRAM structure and model parameters can be found in [7].

III. RESULTS AND DISCUSSION

Once the model was validated, it was used to simulate and analyze thermal reset transitions operated with pulses of different amplitudes. We have dealt with the same devices and model parameters previously reported (see [7]). Fig. 2 shows the current, temperature and radius of the narrower cylinder employed to model the CF during a transient corresponding to a RESET process, for different voltages. As can be seen, the lowest pulses are not enough to trigger a RESET event within the time scales employed here. However, the highest values made the device undergo a RESET process with very short transition times.
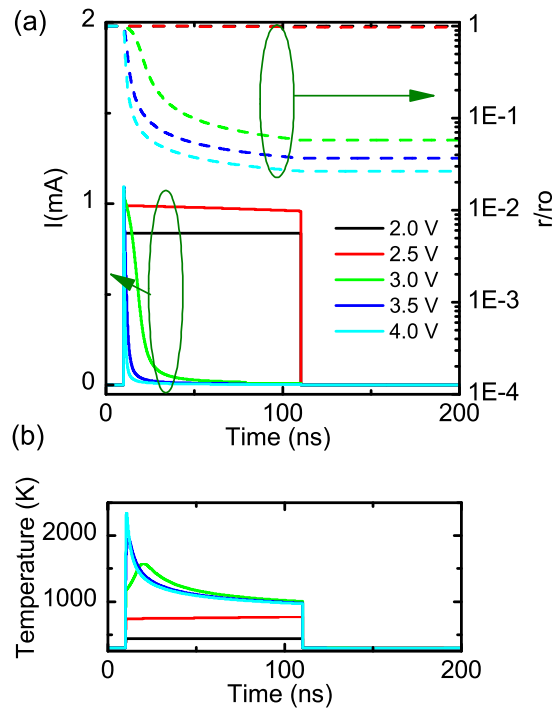
Fig. 2. Transient response of RRAMs operated with 100ns pulses, different amplitudes are employed. The device is assumed to be in the low resistance state. (a) Current and minimum radius (normalized with respect to its initial value), (b) temperature at the narrowest and hottest cylinder that is employed to model the conductive filament.

2017 Spanish Conference on Electron Devices (CDE)

A smooth transient can be observed for the 3V pulse. This is due to the fact that lower voltages slow down the CF dissolution process. As the CF shrinks within the disruption stage that takes place in the RESET process the temperature at the narrowest point goes up. For the simulations shown in Fig. 2 thermal capacitances were not considered in order to analyze their role separately.
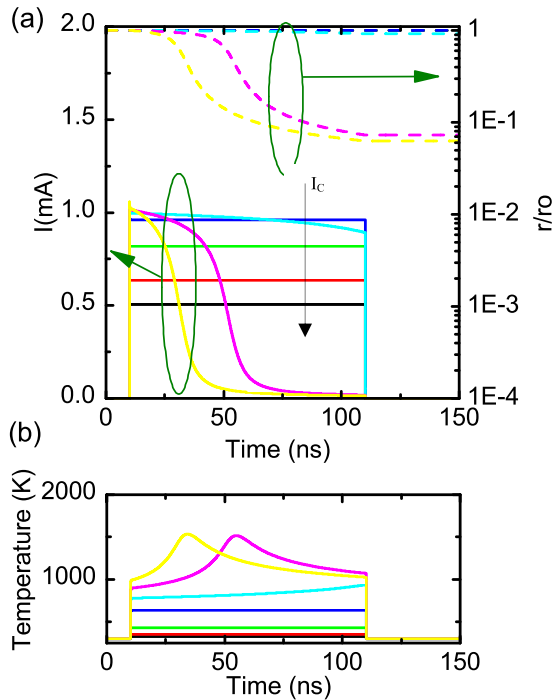
Fig. 3. RRAM transient response under decreasing compliance current, I_C (for a 3V voltage pulse). (a) Current and normalized minimum radius. (b) Temperature at the narrowest cylinder that is employed to model the conductive filament.

Fig. 3 shows the transient response under a 3V pulse when the current is limited with a MOS transistor in series. As expected, a limited current can totally avoid a successful RESET process, or at least slow it down.

The effect of the thermal capacitances is analyzed in Fig. 4. According to the used thermal model parameters and CF sizes the thermal capacitances can be estimated. Their value is around 10^{-3} fJ/K and agrees well with those reported in Ref. [12] which lead to time constants around 30 ps for switching transitions. None or little influence of thermal capacitances below 0.02fJ/K is observed (Fig. 4) at a time scale of nanoseconds. Other authors use higher thermal capacitances in their models [13], [14]. For example, for 0.2fJ/K and 2fJ/K, the

thermal capacitance role is more apparent, although not essential.

As a novelty, our model accounts for the thermal capacitance variation at simulation time. For comparison, Fig. 4 shows results obtained using fix capacitances (solid lines) and variable capacitances (dashed lines) whose values change as the filament size changes. In general, this latter effect is not relevant for the lower thermal capacitances (Fig. 4.b). As can be seen, during the reset process (in the high voltage part of the pulse) there is only a light influence of the thermal capacitance variation at simulation time on the current and temperature transient responses. On the contrary, when the CF has shrunk and the voltage pulse goes down again a difference can be found for the 2fJ/K case. This is because a complete reset process leads to a thermal capacitance reduction. A model without this effect could produce some differences in the simulation results (as it maintains the value of the formed CF thermal capacitance). This could be more apparent especially under pulsed operation with very short times between pulses [15].
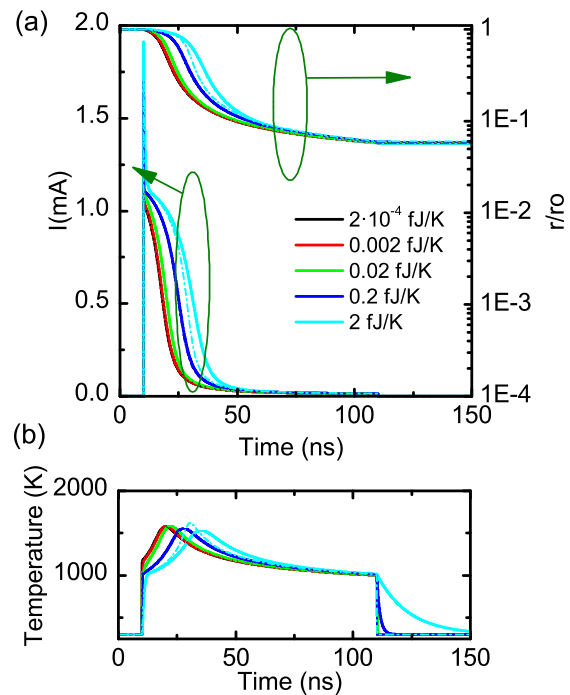
Fig. 4. Effects of the thermal capacitance on a RRAM transient response under the influence of a 3V pulse. Solid lines correspond to fixed thermal capacitance values and the dashed lines to the thermal capacitances that evolve at simulation time. (a) Current and normalized minimum radius. (b) Temperature of the narrowest cylinder that is employed to model the conductive filament.

2017 Spanish Conference on Electron Devices (CDE)

Finally, we want to call reader´s attention to the fact that even though the CF minimum size is reduced during the RESET process, the temperature remains high at the CF narrowest region with these voltage levels. Although the current is strongly reduced (around two orders of magnitude) it does not go to zero while the pulse is high (see Fig. 5, where the current curves in Fig. 4 are shown in logarithmic scale to show this effect).
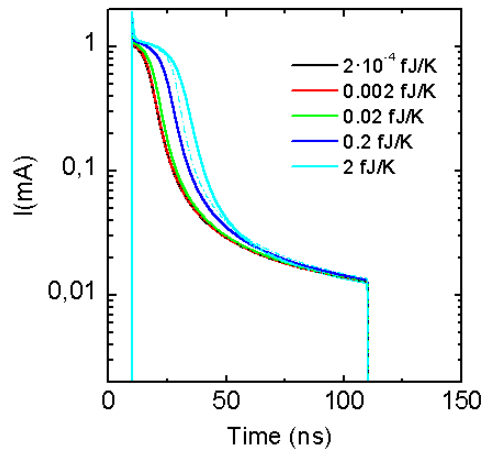
Fig. 5. Effect of the thermal capacitance on the RRAM transient current under a 3V pulse (a logarithmic scale has been used in order to show the lowest current values). Solid lines correspond to fixed thermal capacitance values and dashed lines to the thermal capacitances that evolve at simulation time.

IV. CONCLUSSIONS

We deal here with RESET process simulation of unipolar RRAMs by means of a new SPICE model. The physically based model includes quantum conduction through a constriction in addition to ohmic conduction through conductive filaments as well as a detailed thermal description. As a novelty, the thermal scheme incorporates thermal capacitances which evolve at simulation time. The model can be used for transient simulation of memory cells based on RRAMs under different voltage pulses. The influence of the thermal capacitance is investigated and the role of its transient variation is analyzed in depth.

REFERENCES

[1]   P. Cappelletti, "Non Volatile Memory Evolution and Revolution", in IEDM 2015 Proceedings. p. 10.1.1-4, 2015.

[2]   J. Zahurak et al, in IEDM 2014 Proceedings. p.6.2.1,6.2.4, 2014.

[3]   E. Miranda, C. Walczyk, C. Wenger and T. Schroeder, "Model for the resistive switching effect in mim structures based on the transmission properties of narrow constrictions", Electron Device Letters, IEEE, vol. 31, no. 6, pp. 609–611, 2010.

[4]   M.A. Villena et al., "Simulation of thermal reset transitions in resistive switching memories including quantum effects",J. Appl. Phys., vol. 115, p. 214504, 2014.

[5]   G. González, F. Jiménez-Molinos, M. A. Villena, J. B. Roldán, "SPICE simulation of thermal reset transitions in Ni/HfO2/Si-n+ RRAMs including quantum effects", Abstract Book of the 19th Workshop on Dielectrics in Microelectronics (Wodim), 2016.

[6]   F. Jiménez-Molinos, M. A. Villena, J. B. Roldán and A. M. Roldán, "A SPICE Compact Model for Unipolar RRAM Reset Process Analysis," in IEEE Trans. Electron Dev., vol. 62, no. 3, pp. 955-962, March 2015.

[7]   G. González, F. Jiménez-Molinos, J. B. González, M. B. González, F. Campabadal, "Transient SPICE simulation of Ni/HfO2/Si-n+ resistive memories", in the Proceedings of the XXXI Design of Circuits and Integrated Systems Conference (DCIS), 2016.

[8]   M.A. Villena et al., "An in-depth simulation study of thermal reset transitions in resistive switching memories", J. Appl. Phys., vol. 114, p. 144505, 2013.

[9]   U. Russo, D. Ielmini, C. Cagli and A. L. Lacaita, "Self-Accelerated Thermal Dissolution Model for Reset Programming in Unipolar Resistive-Switching Memory (RRAM) Devices," IEEE Trans. Electron Dev., vol. 56, no. 2, pp. 193-200, Feb. 2009.

[10] M.B. Gonzalez, J. M. Rafí, O. Beldarrain, M. Zabala and F. Campabadal, "Analysis of the switching variability in Ni/HfO2-based rram devices", IEEE Trans. on dev. and mat.reliab., vol. 14, no. 2, 2014.

[11] M.A. Villena et al., "A new parameter to characterize the charge transport regime in Ni/HfO2/Si-n+-based rrams", Solid-State electr., vol. 118, pp. 56-60, 2016.

[12] D. Ielmini, "Resistive switching memories based on metal oxides: mechanisms, reliability and scaling", Semic. Sci. Tech., vol. 31, p. 063002, 2016.

[13] *X. Guan, S. Yu, and H-S.P Wong, "A spice compact model of metal oxide resistive switching memory with variations", IEEE Elec. Dev. Lett., vol. 33, pp. 1405-1407, 2012.*

[14] P. Y. Chen and S. Yu, "Compact Modeling of RRAM Devices and Its Applications in 1T1R and 1S1R Array Design," IEEE Transactions on Electron Devices, vol. 62, no. 12, pp. 4022-4028, Dec. 2015.

[15] S. Kim, C. Du, P. Sheridan, W. Ma, S. Choi and W. D. Lu, "Experimental Demonstration of a Second-Order Memristor and Its Ability to Biorealistically Implement Synaptic Plasaticity",Nano Letters, vol. 15, pp. 2203-2211, 2015.

Random Telegraph Noise Modeling

5.1. Introduction

The read current of some memristors based on resistive switching devices presents Random Telegraph Noise (RTN) signals, particularly in the HRS. These fluctuations add serious difficulties for the device operation; i.e., they can reduce the noise margin in memory cells arrays [González-Cordero2016f, Publisi2013] or change the conductivity in devices employed to mimic electronic synapses in the context of neuromorphic circuits [González-Cordero2019c, Carboni2019]. These effects pose important hurdles to the use of these devices in highly-scaled integrated circuits, and represent a technological challenge. RTN fluctuations can also be beneficial as entropy sources of random number generators, in cryptography applications like secret key generation, stochastic neurons and stochastic spiking signals [Arumi2016, Wei2016, Puglisi2018, Carboni2019].

The particular operation of memristors, much different to what is seen in other electron devices such as MOSFETs, diodes, etc., make this issue more complicated from the mathematical viewpoint. Nevertheless, the accurate modeling these type of signals is essential for their use in digital and analog applications. RTN signals are linked to the emission and capture of electrons by traps or defects close to the conductive filament in devices with filamentary conduction. It is important to highlight, that RTN features depend on the number of active traps, on the interaction between these traps with time, on the occurrence of anomalous effects, and other related effects [Gonzalez2016, Puglisi2018, Puglisi2015, González-Cordero2019a].

This chapter begins with a review of the current methods of representation and analysis of RTN signals reported in the literature, which are the starting point for the subsequent synthesis in compact models. Two new analysis methodologies are reported: the Locally Weighted Time Lag Plot (LWTLP) as a fast method to generate a TLP with information of probability of occurrence, and the differential Locally Weighted Time Lag Plot (dLWTLP) that represents the derivative current in a TLP scheme that show new events (transitions between states and spikes) into the graph. Finally, we used the LWLTP to analyze a long time RTN trace with an artificial neural network (Self Organization Maps), that allow the classification of 1203 RTN traces intro six types of standard RTN classes.

5.2. Review of RTN Representation and analysis Methods

In the literature, we can find different methods to analyze and represent RTN signals [Nagumo2009, Martín-Martínez2014, Martín-Martínez2014b, Puglisi2013, Realov2013, Puglisi2015, Márquez2016, González-Cordero2019a, González-Cordero2019c]. In this section, we will describe them with the focus on their main characteristics, the recommended scopes of application, and their pros and cons.

5.2.1. Current versus Time Trace

Current versus time $(I - t)$ traces is the simplest way to represent RTN signals. It consists of a graph with N points (I_i, t_i) where N is the number of sampled data and i is an integer ($1 \leq i \leq N$). **Figure 5.1** shows a RTN trace #640 measured in a Ni/HfO$_2$/Si-n^{++} device in HRS (details about fabrication and measurement set-up can be found in section A.5. Ni/HfO$_2$/Si-n^{++} Devices). Two stable levels can be observed (labelled L_0 and L_1), with mean currents values $I_0 = 55nA$ and $I_1 = 72nA$; the current difference is named as Δ_I, the variability of the two stable levels, δ_0 and δ_1, and the emission (capture) time constants τ_e (τ_c) are marked too. This type of plot is useful when the RTN trace is short, but with long RTN traces, the information provided is less effective. It is important to highlight that with this representation method the information obtained (Δ_I, δ_0, δ_1, τ_e and τ_c) can be extracted in a visual or qualitative manner and it depends on the particularities of the signal. In this context other techniques are required.
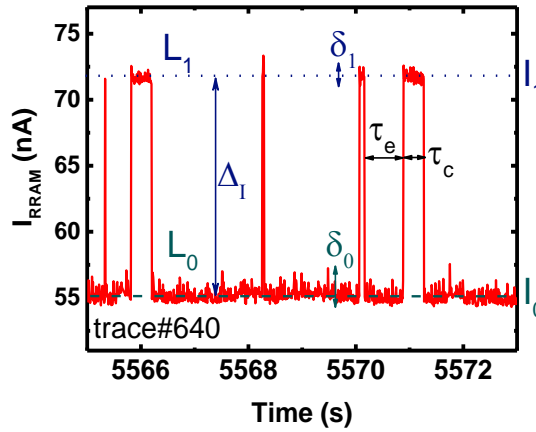
Figure 5.1 Current versus time of 1000 samples measured in Ni/HfO$_2$/Si-n^{++} device (trace #640).

5.2.2. Time Lag Plot

The Time Lag Plot (TLP) is a representation method in which the sampled current $i + 1$ is plotted versus the sample i. That is, it consists of a plot of $N - 1$ points (I_{i+1}, I_i) of RTN sampled data, where I_{i+1} is the current value at the time $i + 1$ and I_i is the current value at time i [Nagumo2009]. **Figure 5.2 a)** shows an $I - t$ trace, while **Figure 5.2 b)** is the corresponding TLP. In a TLP the stable levels of the RTN signal, marked as L_0 and L_1, appear as a cluster of points on the main diagonal (the line $I_{i+1} = I_i$). In the opposite diagonal, few points also appear. These points are linked to transitions between stable current levels. In **Figure 5.2**, these events are labelled as t_{0-1} (t_{1-0}) for transitions from I_0 to I_1 (I_1 to I_0). The variability of the current levels (δ_0, δ_1) can easily observed in the TLP. For example, it is clear that $\delta_0 > \delta_1$. The relative probability of each level is noticeable from the plot: the number of points in cluster L_1 is higher than in cluster L_0, but a numerical quantification is not obtained.
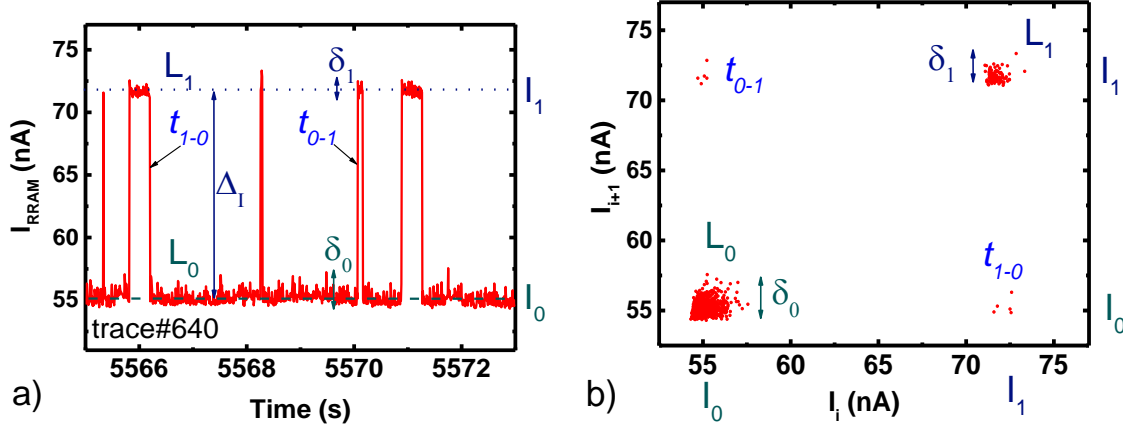
Figure 5.2 a) Current versus time of 1000 samples measured in Ni/HfO$_2$/Si-n^{++} device (trace #640), **b)** Time lag plot (TLP) of the same trace [Nagumo2009].

This type of plot is very useful for short RTN traces, but for long RTN traces, the information provided is less effective. For example, the proximity of stable levels, background noise and overlapping of points in the same region, make the interpretation and quantification of TLPs a very difficult task [Martín-Martínez2014, Martín-Martínez2014b, Puglisi2013, Márquez2016, González-Cordero2019a, González-Cordero2019c].

The approximated number of traps (N_T) presented in the RTN signal can be estimated by the expression [Nagumo2009, Realov2013]

$$N_T = \lceil \log_2(N_L) \rceil \tag{5.1}$$

where N_L is the number of local maxima presented in the main diagonal of TLP, and $\lceil \ \ \rceil$ is the ceiling function.

5.2.3. Color Code Time Lag Plot

The color code time lag plot (CCTLP) is a time lag plot that shows the occurrence probability of points (I_{i+1}, I_i) by means of a color spot (high probability: black, medium probability: yellow and low probability: red) [Puglisi2013]. **Figure 5.3** shows an example of this method.
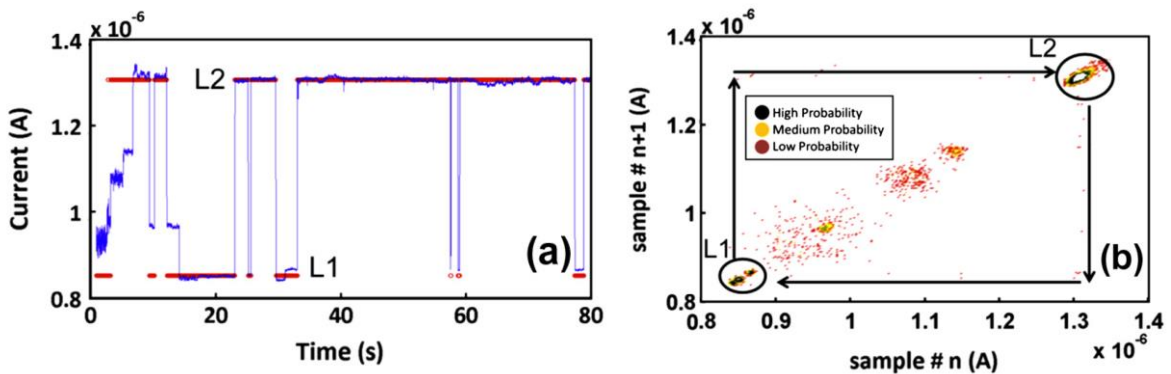
Figure 5.3 a) Current versus time with a two level RTN measured in TiN/HfO$_x$/TiN device **b)** Color code time lag plot (CCTLP) of the same trace [Puglisi2013].

This type of plot introduces in the TLP a visual representation of regions with different relative occurrence probabilities, but only with three non-zero possible values. As in the TLP, the number of local maxima in the main diagonal provides information about the number of current levels and indirectly on the number traps in the oxide layer influencing the RTN trace by equation (5.1).

5.2.4. Enhanced Time Lag Plot

The Enhacement Time Lag Plot (ETLP) is a two-dimensional histogram of I_i versus I_{i+1} obtained of the frequency analysis of each point of the TLP with a bin size equal to the less significative bit of current (I_{LSB}) of the analog to digital converter used in the data acquisition system [Realov2013]. **Figure 5.4** shows this technique applied for a RTN signal measured in a CMOS transistor of 45nm (TLP and ETLP representations are shown). The TLP shows a great quantity of dispersed points along the main diagonal. In this case, it is not possible to determine the current levels or the number of local maxima in order to obtain the number of traps. On the other hand, the ETLP shows in the main diagonal six regions with different probabilities, which allows us to conclude the presence of three traps influencing on the RTN trace.
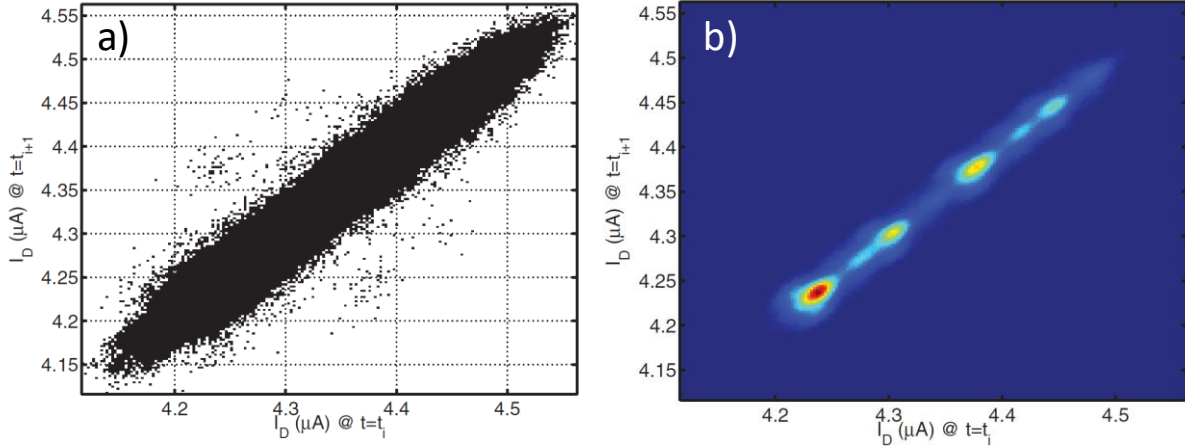
Figure 5.4 a) Time Lag Plot of a RTN trace measured in a 45nm CMOS transistor **b)** Enhanced Time Lag Plot of the same RTN data [Realov2013].

5.2.5. Radio Time Lag Plot

The Radio Time Lag Plot (RTLP) is a method to visualize the probability of a point (I_i, I_{i+1}) in the TLP, calculated as the number of counts in the neighborhood $\xi(i,j)$ delimited by an area region described by a circle of radius r [Márquez2016]. The RTLP method can be described by Equations (5.2) and (5.3).

$$RTLP\big(I(i), I(i+1)\big) = \sum_{j=1}^{N-1} \xi(i,j) \tag{5.2}$$

$$\xi(i,j) = \begin{cases} 1 & if \quad \sqrt{[I(j)-I(i)]^2 + [I(j+1)-I(i+1)]^2} \leq r \\ 0 & if \quad \sqrt{[I(j)-I(i)]^2 + [I(j+1)-I(i+1)]^2} > r \end{cases} \tag{5.3}$$

N is the number of sampled data of the RTN signal. The radius was assumed to be $10^{-6}\,\sigma$, where σ is the standard deviation of the current fluctuations in the RTN sequence [Márquez2016] (see **Figure 5.5 a)**. The plot shows the same points that the TLP (**Figure 5.5 b**) but a colour map is employed to represent the number of points in the defined neighborhood (a relative normalized probability is used). The most probable state is L_0 ($Pr(L_0) \approx 1$).The state L_1 (with a relative probability $Pr(L_1)$ close to 0.2) is shown in yellow. The main drawback of this method is related to the need of calculating the neighbourhood previously. Furthermore, for each point, the distance and counts added by the other neighbour points must be determined by an algorithm whose complexity depends on N^2.
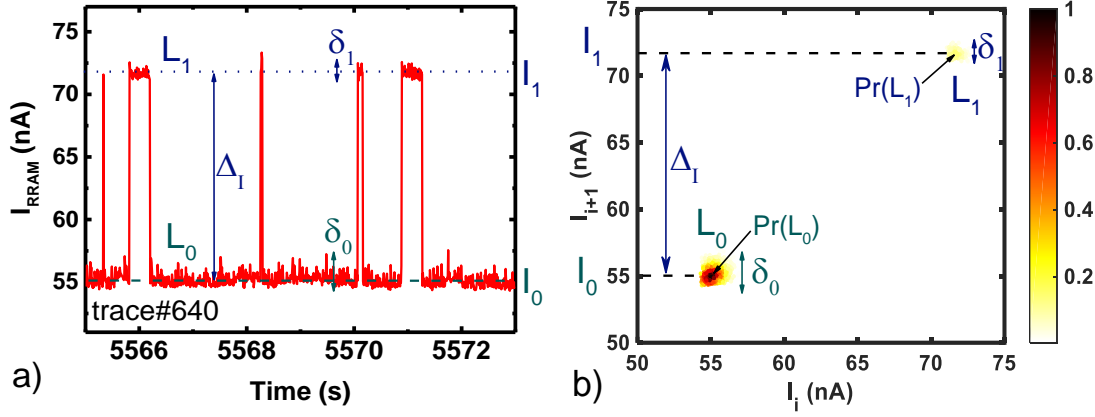
Figure 5.5 a) Current versus time plot of 1000 samples measured in a Ni/HfO$_2$/Si-n^{++} device (trace #640), **b)** Radius time lag plot (RTLP) of the same trace [Márquez2016].

5.2.6. Weighted Time Lag Plot

The Weighted Time Lag Plot (WTLP) provides information about the probability of occurrence in a given position of the TLP space considering the occurrences in the rest of positions of the graph by means of a bidimensional Gaussian distribution (BGD) [Martín-Martínez2014, Martín-Martínez2014b, Maestro2015]. It reduces the data space (I_{i+1}, I_i) of a trace to a $M \times M$ matrix ($M < N$); that is, for each position (x, y), the probability is calculated as a weighted sum of all the sampled data (I_{i+1}, I_i). The weights are given by the distance to each occurrence by the corresponding value of the BGD. The mathematical methodology can be described by Equation (5.4) [Martín-Martínez2014],

$$\psi(x, y) = \frac{k}{2\pi\alpha^2} \sum_{i=1}^{N-1} \exp\left(\frac{-[(I_i - x)^2 + (I_{i+1} - y)^2]}{2\alpha^2}\right) \tag{5.4}$$

The values of x and y depend on the range of values to be plotted and the numbers of points in the matrix accordingly to equation (5.5).

$$(x, y) = \left(\frac{\hat{x}}{M-1}(I_{max} - I_{min}) + I_{min}, \frac{\hat{y}}{M-1}(I_{max} - I_{min}) + I_{min}\right) \tag{5.5}$$

where $\hat{x}$ e $\hat{y}$ are the indices of the matrix of values to be displayed ($\hat{x} = 0,1, ... M - 1$ $\hat{y} = 0,1, ... M - 1$), and I_{max} e I_{min} are the maximum and minimum current values used in the plot. The current interval represented by each matrix cell depends on I_{max} e I_{min} and the numbers of points of the matrix M. **Figure 5.6** shows the WTLP of the trace #640 in logarithmic scale with a value of M=200. The state with the highest probability of occurrence can be easily visualized in the main diagonal making use of a color map. As can be seen, both methods (RTLP and WTLP) add information linked to the probability of occurrence in a third axis and, therefore, they solve problems related to hidden information in terms of current levels because of background noise or point overlapping found in the TLP. However, both techniques are computationally expensive.
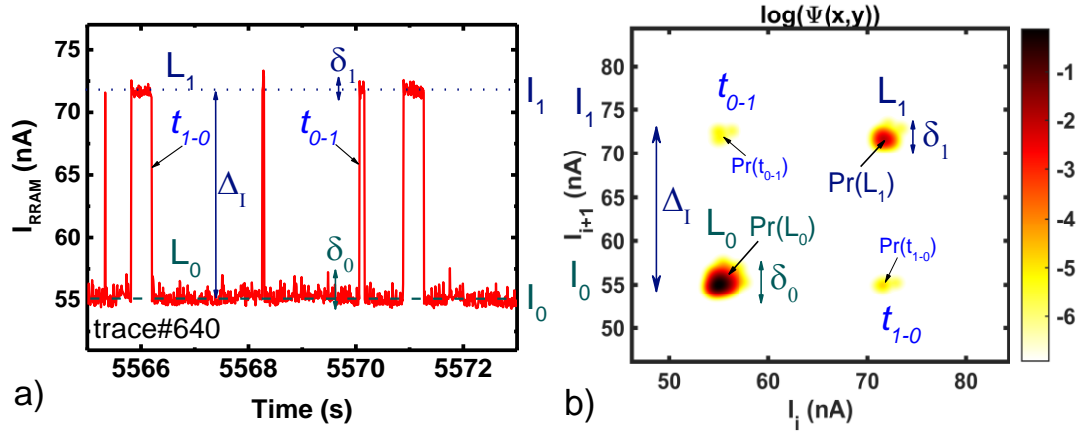
Figure 5.6 **a)** Current versus time plot of 1000 samples measured in a Ni/HfO₂/Si-n⁺⁺ device (trace #640). **b)** WTLP (M=200 points, α=0.1) of the same trace [Martín-Martínez2014].

5.2.7. The Locally Weighted Time Lag Plot

The Locally Weighted Time Lag Plot reduces the space (I_{i+1}, I_i) to $M \times M$ points (x, y) [González-Cordero2019a], for each of the $N - 1$ pairs of points (I_{i+1}, I_i) the method only uses the coordinates $(\hat{x}, \hat{y})$ that are determined by the following equation:

$$(\hat{x}, \hat{y}) = \left(int\left(M \frac{I_i - I_{min}}{I_{max} - I_{min}} \right), int\left(M \frac{I_{i+1} - I_{min}}{I_{max} - I_{min}} \right) \right) \quad (5.6)$$

Once the coordinates $(\hat{x}, \hat{y})$ are known, the matrix is updated, considering not only the corresponding cell but also the surrounding coordinates weighted by a function that depends on the distance. For the occurrence probability calculation, different submatrices were used (for example 3×3 or 5×5) [González-Cordero2019a]. A 5x5 matrix example is shown in **Figure 5.7**.

0.16	0.33	0.41	0.33	0.16	$\hat{y} + 2$
0.33	0.64	0.80	0.64	0.33	$\hat{y} + 1$
0.41	0.80	1	0.80	0.41	$\hat{y}$
0.33	0.64	0.80	0.64	0.33	$\hat{y} - 1$
0.16	0.33	0.41	0.33	0.16	$\hat{y} - 2$
$\hat{x} - 2$	$\hat{x} - 1$	$\hat{x}$	$\hat{x} + 1$	$\hat{x} + 2$	

Figure 5.7 Example 5x5 matrix used in the LWTLP method. The position in the matrix with same weights are presented with the same color. [González-Cordero2019a].

Figure 5.8 b) shows the LWTLP of trace #640 calculated for *M*=200 and a 5x5 sub-matrices. In this plot is easy to identify the regions in the main diagonal which represent the different current states. The main advantage of this method is its computational efficiency, approximately 750 times faster than WTLP or RTLP [González-Cordero2019a].
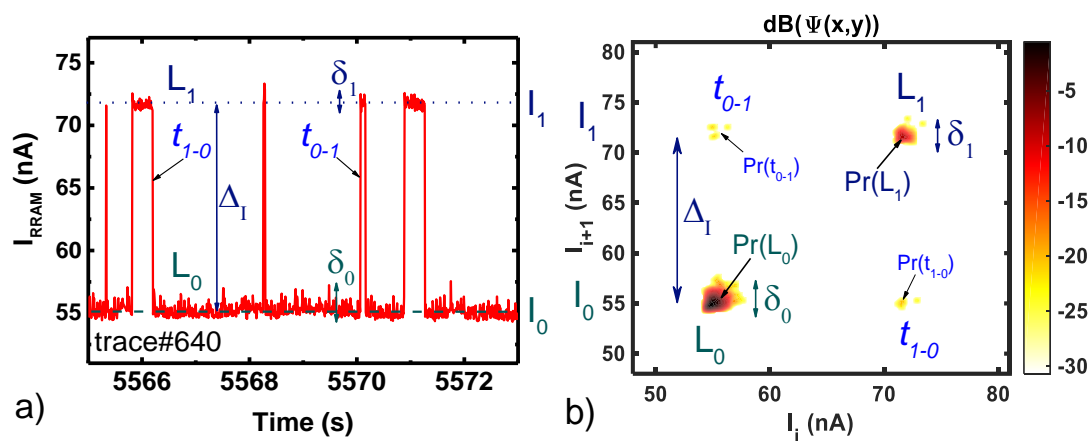
Figure 5.8 **a)** Current versus time plot of 1000 samples measured in a Ni/HfO$_2$/Si-n^{++} device (trace #640). **b)** LWTLP (*M*=200 points, M5x5, σ_f = 1.5) of the same trace [González-Cordero2019a].

This method was published in González-Cordero et al. Journal of Vacuum Science and Technology B (2019), the accepted preprint paper is presented below.

143

González-Cordero et al. Journal of Vacuum Science and Technology B (2019)

Quality metrics

Data base	Rating	Quartile
Web of Science	Impact factor: 1.31	Q3
Scimago	Scientific journal ranking: 0.467	Q2

Publication citations

Google Scholar	Web of Science
1	1

A new method to analyze Random Telegraph signals in resistive Random Access Memories

G. González-Cordero

Running Authors: G. González-Cordero et al.

Departamento de Electrónica y Tecnología de Computadores. Universidad de Granada. Facultad de Ciencias. Avd. Fuentenueva s/n, 18071 Granada, Spain.

M.B. González

Institut de Microelectrònica de Barcelona, IMB-CNM (CSIC), Campus UAB, 08193 Bellaterra, Spain

F. Jiménez-Molinos

Departamento de Electrónica y Tecnología de Computadores. Universidad de Granada. Facultad de Ciencias. Avd. Fuentenueva s/n, 18071 Granada, Spain.

F. Campabadal

Institut de Microelectrònica de Barcelona, IMB-CNM (CSIC), Campus UAB, 08193 Bellaterra, Spain

J.B. Roldán[a]

Departamento de Electrónica y Tecnología de Computadores. Universidad de Granada. Facultad de Ciencias. Avd. Fuentenueva s/n, 18071 Granada, Spain.

[a] Electronic mail: jroldan@ugr.es

A new technique to analyze Random Telegraph Noise (RTN) is proposed. It has been used for the analysis of current versus time measurements performed on Ni/HfO$_2$/Si-n+-based resistive random access memories (RRAMs). The method allows to study current-time traces with a massive number of data without losing the capability of dealing with background noise and discriminating the active defects responsible for current fluctuations. A comparison of this algorithm with previous ones is given in terms of computing time and RTN description accuracy. The computing efficiency and the validity of the model have been proved and, therefore, it is feasible to propose applications for real time analysis making use of this new algorithm.

I. INTRODUCTION

The next-generation of non-volatile memory technologies is getting wide attention among electronics manufacturers and the scientific community. The expected high-performance and cost-effective features of these emerging non-volatile memories will simplify memory hierarchy and incorporate non-volatility in logic circuits[1-7]. In addition, they will open paths for novel applications in neuromorphic computing and hardware security landscapes[3,8,9]. Among the technologies available for non-volatile memories, resistive random access memories (RRAMs) are promising devices due to their potential for scalability, low power operation, fast operation, high endurance, their CMOS compatibility and the possibility to be stacked in 3D architectures[1-5]. These features will be essential to introduce RRAMs in industrial production lines, which are focused by the growing prominence of mobile devices and the popularity of Internet-of-things (IoT).

A resistive memory consist of two electrodes made out of a metallic or highly doped semiconductor material that are separated by a dielectric material that can be fabricated by different types of oxides and even 2D materials. Research on these devices has been intensive in the last few years and dozens of devices have been analyzed where the materials employed for the electrodes and dielectric are different.

Although RRAM technology has been successfully employed at the integrated circuit level in a promising manner[10-12], some issues still exist that have to be urgently improved in order to introduce this technology in mass production channels. Variability and reliability have to be addressed. In addition, in order to assist design efforts in an industrial context, Electronic Design Automation (EDA) tools are needed. This implies the development of physical simulators[13-22], and reliable compact models for circuit design[3,23-29]. Recent reviews can be found in references[5,30].

Filamentary conduction is assumed to be the most common physical mechanism behind resistive switching (RS) in most of the RRAMs found in the literature. The formation and destruction of conductive filaments (CFs) inside the insulating layer permits the differentiation of two resistive states that allow the codification of the logic level for memory applications. Nevertheless, the presence of single or multiple traps inside or close to the conductive filaments can strongly influence the charge conduction giving rise to current fluctuations (named random telegraph noise, RTN) with relative larger amplitudes in the high-resistance state (HRS) than in the low-resistance state (LRS)[31,32]. In memory applications, these fluctuations can cause severe operation or read errors. On the other hand, this RTN fluctuations in resistive RAMs can be used as an entropy source of random number generators[33-35].

Different methods have been employed to characterize RTN[36-39]. In this context, an in-depth description of RTN signals is needed to unveil the contribution of defects responsible for the current fluctuations from the presence of background noise. Some of the previously proposed tecniques can deal with this task[37-39], but if long traces are under consideration these algorithms might be too expensive in terms of computing time because they need to sweep all the data in the current-time (*I-t*) trace several times.

In this contribution, we present a new method to analyze RTN signals, the Locally Weighted Time Lag Plot (LWTLP). This new method (see the details in section II) allows to reduce the computing time with respect to previous ones, being also an accurate technique that allows to perform a useful analysis as in the case of previous procedures[36-37]. The usefulness of the new method will be demonstrated for (*I–t*) traces with more than one million data points.

The paper is organized as follows. In Section II, a brief review of previous tecniques for analyzing RTN signals is presented and our new proposal, the LWTLP method, is detailed. In Sec. III, the fabricated devices and measurement set-up are described. In Sec. IV, we present the main results and the corresponding discussion. Finally, the conclusions are drawn in Sec. V

II. LOCALLY WEIGHTED TIME LAG PLOT TECHNIQUE

The Time Lag Plot (TLP) is a technique used to visualize RTN data[36]. Given a set of *N* data points of a current versus time trace, (I_i, t_i), with $i \in [1, N]$, the current value at a certain moment, I_{i+1}, is plotted versus the previous current, I_i. In this way, stable current values appear as clusters of points along the diagonal of the graph ($I_{i+1} = I_i$), while transitions between current levels show up outside this diagonal. The proximity of two stable levels and/or the background noise can produce the overlapping of point clusters, making the interpretation of the plot difficult[37-40]. Furthermore, the TLP does not provide a quantitative direct information about the number of points concentrated (or even overlapped) around a given plot region of the TLP space (for stable levels, this information would be related to the probability of measuring a particular current linked to these states). In order to overcome these drawbacks, alternative time lag plots have been proposed, among them, the Radius Time Lag Plot (RTLP)[39] and the Weighthed Time Lag Plot (WTLP)[37,38,41]. On the one hand, considering the RTLP method, the value associated to a given position (I_i, I_{i+1}) depends on the number of counts in the neighborhood (within a region described by a given radius). In that way, the zones with a higher concentration of points in the space are highlighted. On the other hand, the WTLP method calculates the occurrence probability in a given position of the space taking into consideration the occurrences in the rest of positions in the graph by means of the bidimensional Gaussian distribution (BGD)[37,38,41]. That is, for each position, the probability is calculated as a weighted sum of all the sampled data. The weights are given by the distance to each ocurrency and the corresponding value of the BGD. In that way, both methods (RTLP and WTLP) add information about the probability of occurrence in a third axis and, therefore, overcome the problem related to the hidden occurrence levels because of background noise. However, both techniques are computationally expensive. This is not the case for the technique we present here, the locally weighted time lag plot (LWTLP) method. In this new technique, the probability at a given position (I_i, I_{i+1}) is calculated also taking into account the distance to the counts in other positions (by means of a BGD), but only if those positions are close to the considered position (I_i, I_{i+1}). Hence, not all the plot domain is considered (as in the WTLP method), but only the neighborhood to each point of the space (as in the RTLP method). In that sense, the LWTLP technique holds the best features of both methods.

Given *N* data points, (I_i, t_i) (with $i \in [1, N]$), the LWTLP method reduces the data space (I_i, I_{i+1}) of a trace to a M×M matrix ($M < N$), as in the WTLP case[37-38]. Each pair of values (I_i, I_{i+1}) is linked to the corresponding matrix cell (indexed by the pair of variables $(\hat{x}, \hat{y})$). The number of events associated to this position are counted and also the neighbor sites of the matrix are updated with each event. These latter values are weighted by a function dependent on the distance to the point considered in each calculation. In our study, the neighbor regions considered for the calculation of the occurrence probability are described by 3×3 or 5×5 sub-matrices (a choice to be made at the beginning of the analysis). A more detailed algorithm description is given below.

The Locally Weighted Time Lag Plot method is based on the following procedure. First of all, the space (I_i, I_{i+1}) is reduced to $M \times M$ points (x, y), by means of equations (1) and (2):

$$x = \frac{\hat{x}}{M-1}(I_{max} - I_{min}) + I_{min} \tag{1}$$

$$y = \frac{\hat{y}}{M-1}(I_{max} - I_{min}) + I_{min} \tag{2}$$

where $\hat{x}$ e $\hat{y}$ are the indices of the matrix of values to be displayed ($\hat{x} = 0,1,...M-1$ $\hat{y} = 0,1,...M-1$) and I_{max} e I_{min} are the maximum and minimum current values used in the plot. The current interval that each matrix cell represents is determined by:

$$\Delta x = \Delta y = \frac{I_{max} - I_{min}}{M} \tag{3}$$

Once the matrix has been determined, for each of the $N - 1$ pairs of points (I_i, I_{i+1}) of the experimental current trace, their coordinates $\hat{x}, \hat{y}$ are calculated:

$$\hat{x} = int\left(\frac{I_i - I_{min}}{\Delta x}\right) \tag{4}$$

$$\hat{y} = int\left(\frac{I_{i+1} - I_{min}}{\Delta y}\right) \tag{5}$$

where $int(x)$ is the function that returns the integer closest to x. Once the coordinates $(\hat{x}, \hat{y})$ are known, the matrix is updated, considering not only the corresponding cell, but also the surrounding coordinates. For this latter action, two alternatives are offered (see Figure 1):

WL5TLP: the nearest cells (until a maximum change of the indices in 2 units from the central cell $\hat{x}, \hat{y}$) are taken into account (Figure 1b), which constitutes a 5×5 matrix centered on $(\hat{x}, \hat{y})$. The matrix values are updated with weights following a two-dimensional Gaussian distribution depending on the normalized distance between cells (see Figure 1b). That is:

$$WL_5TLP(\text{x}, \text{y}) = WL_5TLP(x, y) + d_k, \tag{6}$$

where the index k takes values from 0 to 5 (k=0 for the central cell $(\hat{x}, \hat{y})$ and k grows as shown in Figure 1b). The values of d_k are shown in Table I.

WL3TLP. It is a simplified version of the former case. Only the adjacent cells are considered, this option constitutes a 3×3 matrix centered on $(\hat{x}, \hat{y})$ (see Figure 1a). The weight values of the nine cells (d_0, d_1 and d_2) are shown in Table I.

Finally, once the calculations are performed, the matrix values are normalized.
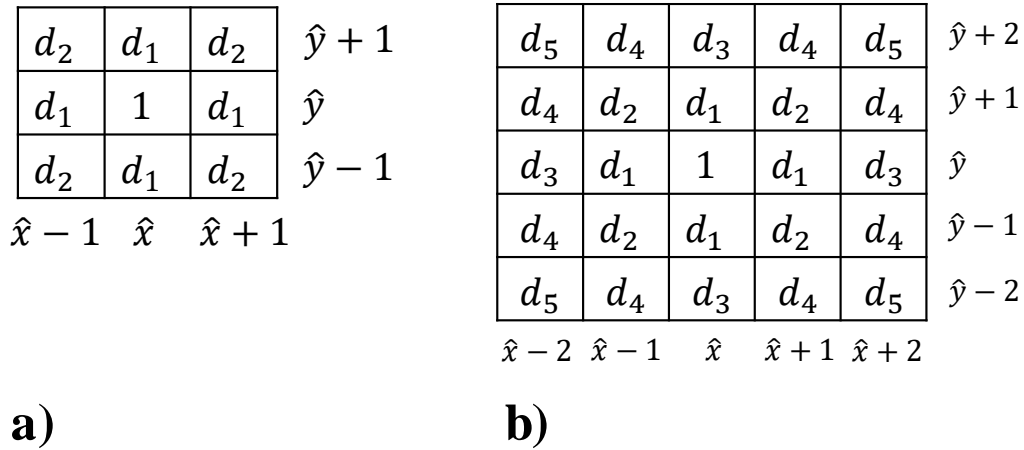
FIG. 1. Schema of the matrix cells updated for each event linked to the cell $(\hat{x}, \hat{y})$. Two cases have been considered: WL3TLP, only the adjacent cells are taken into account (a); WL5TLP, the 5x5 sub-matrix centered in $(\hat{x}, \hat{y})$ is calculated (b). The weight values (d_k, $k = 0..5$) are shown in Table I.

TABLE I. Weights used in the LWTLP technique (with $\sigma_f = 1.5$)

	d_0	d_1	d_2	d_3	d_4	d_5
$f(a) = e^{-\frac{a^2}{2\sigma_f^2}}$	$f(0)$	$f(1)$	$f(\sqrt{2})$	$f(2)$	$f(\sqrt{5})$	$f(2\sqrt{2})$
Value	1	0.8007	0.6412	0.4111	0.3292	0.1690

III. DEVICE FABRICATION AND MEASUREMENT

A. Device Description

Ni/HfO$_2$/Si devices were fabricated on (100) n-type CZ silicon wafers with resistivity (7-13) mΩ·cm following a field isolated process. The 20nm-thick HfO$_2$ layers were deposited by Atomic Layer Deposition at 498K using TDMAH and H$_2$O as precursors and N$_2$ as purge and carrier gas. The resulting structures are square cells of 5×5μm^2. A schematic cross-section of the final device is shown in the inset of Figure 2. More detailed information about the process flow can be found in References 42 and 43.

B. Characterization Setup

The current in both resistive states was recorded in the time domain using a HP-4155B semiconductor parameter analyzer. The voltage was applied to the top Ni electrode, while the Si substrate was grounded. Both the I-V curves for the forming process and RS cycles were measured making use of ramped voltage signals (some set and reset curves are shown in Figure 2). RTN data were measured in the high resistance state (HRS) of the devices employing different biases during observation periods of several seconds (thousands of data were obtained for each measurement series). The RTN signals were recorded by an automatic algorithm that considers the previous measured data making use of a smart procedure (a Matlab® software tool was employed to control the instrumentation). This algorithm could request to continue the RTN measurement or to measure a new voltage or switching cycle when the measured current values are not optimal for the detection of RTN traces. Figure 3 shows a long register of 1.2 million data points obtained at -0.5V for 6800 seconds and the detail of a time period of 100 seconds (where typical RTN signals can be recognized by current fluctuations between different levels).
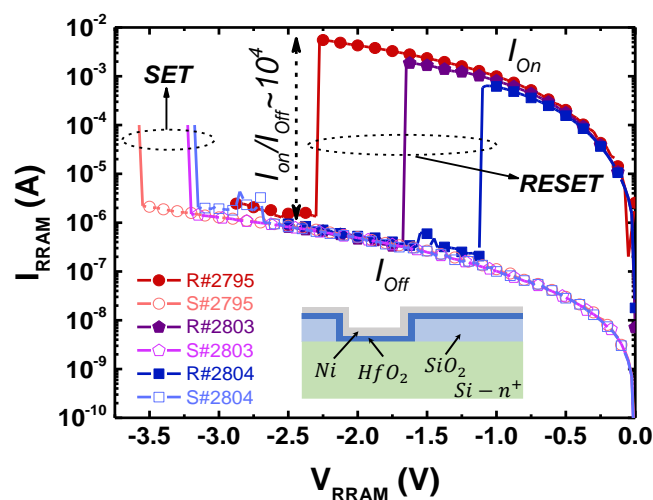
FIG. 2. (Color online) Current-voltage characteristics during typical set and reset cycles with a current compliance of 100μA. Inset: schematic cross-section of the device structure.
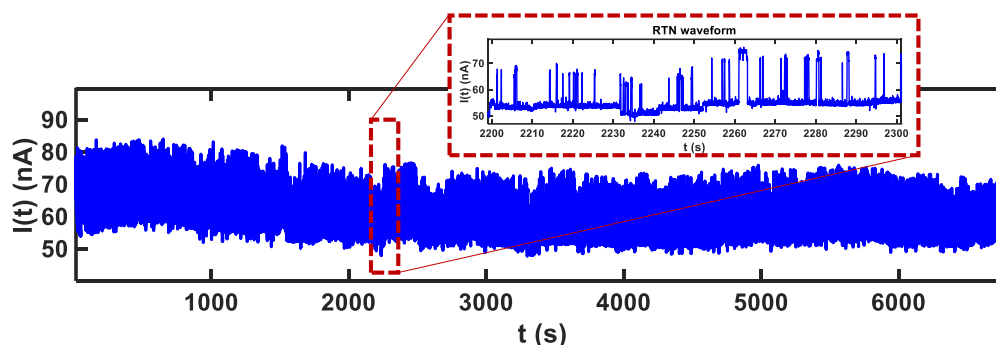
FIG. 3. (Color online) Current versus time plot measured at an applied voltage of - 0.5V for 6800 seconds (1.2 million of samples were recorded). A detail of a time period of 100 seconds is shown, where RTN signals are apparent.

IV. RESULTS AND DISCUSSION

As explained before, in order to characterize RTN signals, several techniques have been used, such as the Time Lag plot (TLP) and the Weighted Time Lag Plot (WTLP) methods[36-38,41].

The TLP representation method allows identifying the current levels present in a RTN signal when the number of data measured in the traces is low. As the amount of data rises, TLP shows a populated point cloud from which no clear information can be extracted. Furthermore, in the case of close current levels, clusters of points in the diagonal could overlap because of the background noise (see Figure 4a), leading to overlapping stretched clusters instead of rounded clusters[40]. To improve this technique, the RTLP and WTLP were proposed[37,39], adding information about the occurrence probability in a third axis (a Z axis), see Figure 4b and Figure 4c, as an example. Finally, in Figure 4d, the results of the proposed new LWTLP technique are shown for the same experimental samples.

Figures 4 and 5 show the time-lag plots of two RTN sequences of 2000 samples using the four methods analyzed in this study (the corresponding *I-t* traces can be seen in Reference 40, Table I, cell (6,1) and cell (5,1), respectively).
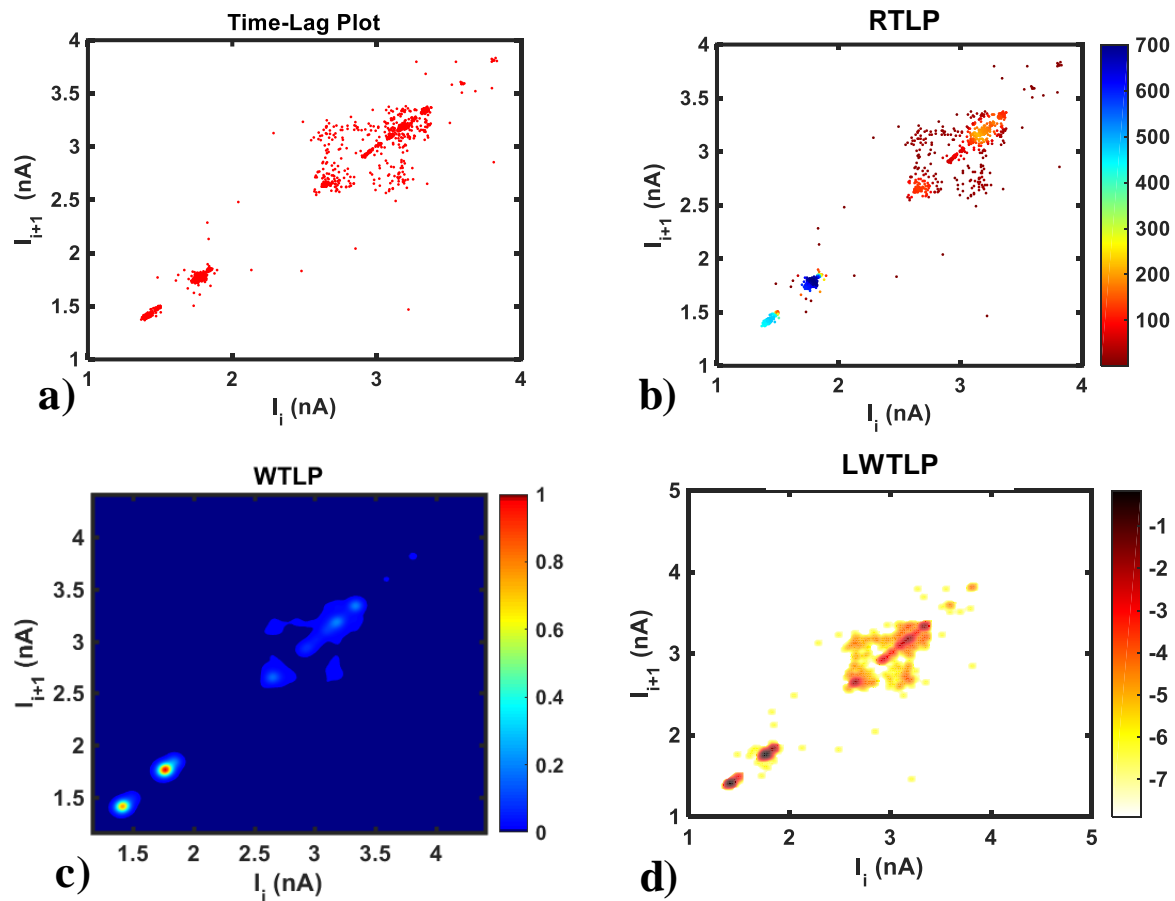
FIG. 4. (Color online) RTN plots for the RTN signals shown in Reference 40 (Table I, row 6). Trap density variations lead to irreversible changes in the current levels. The trace consists of 2000 data points measured at an applied voltage of - 0.28V on a RRAM in HRS. a) Time Lag Plot, b) RTLP, c) WTLP and d) LWTLP with a 5×5 matrix of neighbor points and M = 400.
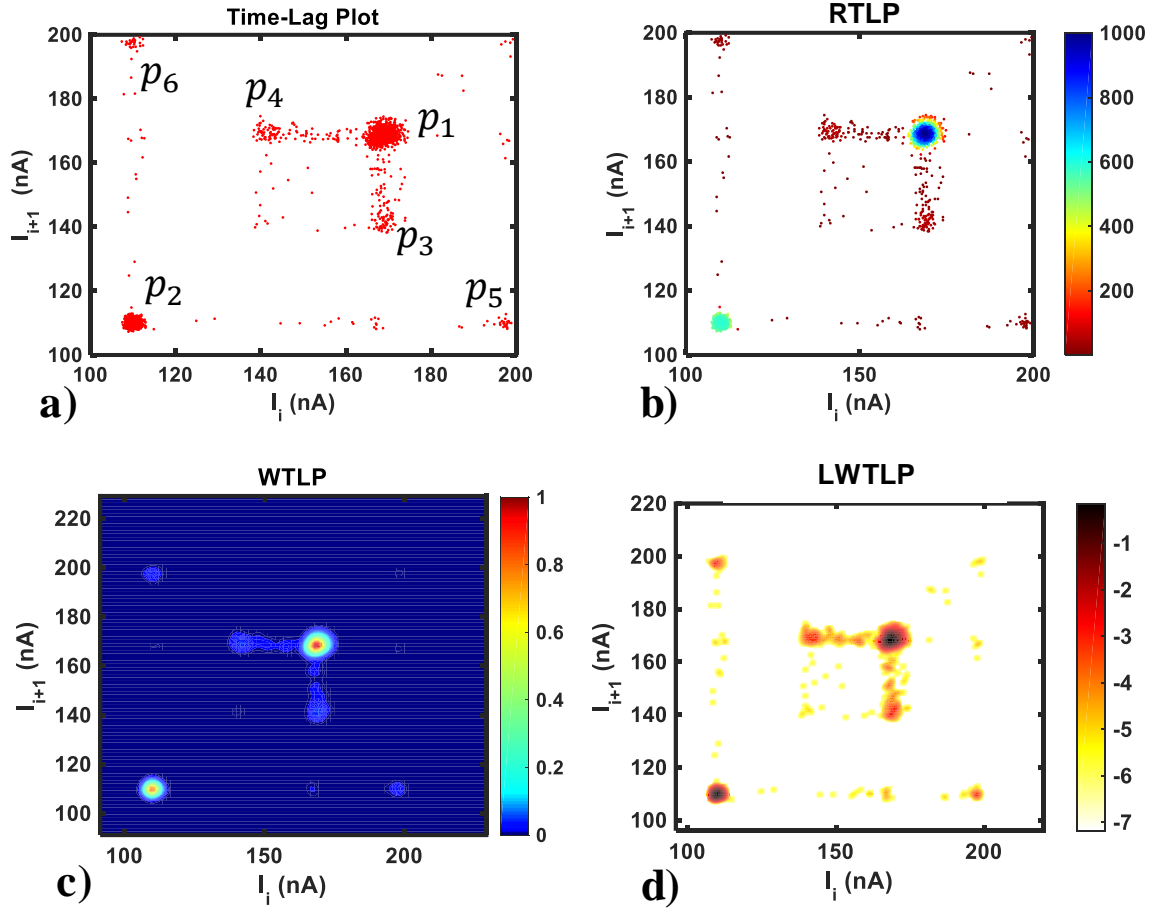
FIG. 5 (Color online) RTN plots for the case of activation and deactivation of two stable RTN signals. The corresponding *I-t* RTN signals and the physical interpretation are shown in Reference 40 (Table I, row 5). The trace consists of 2000 data points measured at an applied voltage of - 0.62V. a) Time Lag Plot, b) RTLP, c) WTLP and d) LWTLP with a 5×5 matrix of neighbor points and M = 400.

In order to shed light on the results plotted in Figure 5, and to evaluate the accuracy of the new methodology, we have compared the results of the RTLP, WTLP and LWTLP methods by extracting the coordinates of points p_1 to p_6 (see Figure 5a) in the TLP domain. They correspond to the location of the TLP cloud points where the higher occurrence probabilities are placed (Table II).

TABLE II. Evaluation of the regions of higher occurrence probability making use of the RTLP, WTLP and LWTLP (5x5 matrix) procedures (data corresponding to Figure 5 where the most populated regions in the TLP domain (p_1-p_6) are assumed as a reference).

		RTLP	WTLP	LWTLP
p_1	$I_i(nA)$	168.3±1.8	167.9±1.1	168.1±1.5
	$I_{i+1}(nA)$	168.2±1.8	167.9±1.1	168.1±1.5
p_2	$I_i(nA)$	109.7±1.9	109.7±0.6	109.9±0.85
	$I_{i+1}(nA)$	109.7±1.9	109.7±0.6	109.9±0.85
p_3	$I_i(nA)$	169.2±3.8	168.9±0.6	168.9±0.6
	$I_{i+1}(nA)$	140.9±1.2	140.3±0.6	140.3±0.6
p_4	$I_i(nA)$	140.9±1.2	140.3±0.6	140.3±0.6
	$I_{i+1}(nA)$	169.2±3.8	168.9±0.6	168.9±0.6
p_5	$I_i(nA)$	196.9±2.1	197.6±0.7	197.6±0.5
	$I_{i+1}(nA)$	110.5±2.3	109.7±0.6	109.7±0.5
p_6	$I_i(nA)$	110.5±2.3	109.7±0.6	109.7±0.5
	$I_{i+1}(nA)$	196.9±2.1	197.6±0.7	197.6±0.5

It can be seen (Table II) that the capacity to determine the regions where the higher occurrence probabilities are located for the LWTLP method is as good as in the other two methods. This new method

153

is especially useful when the number of samples is high. Figure 6 shows a trace of 1.2 million samples recorded at - 0.5V for 10500 seconds. The Locally Weighted Time Lag Plot (LWTLP) has employed 9.6 seconds (with M=400 and 5×5 matrix of neighbor points), while an equivalent representation of probability by means of the WTLP would require an estimated computation time of 11.5 hours.

a)

b)

c)
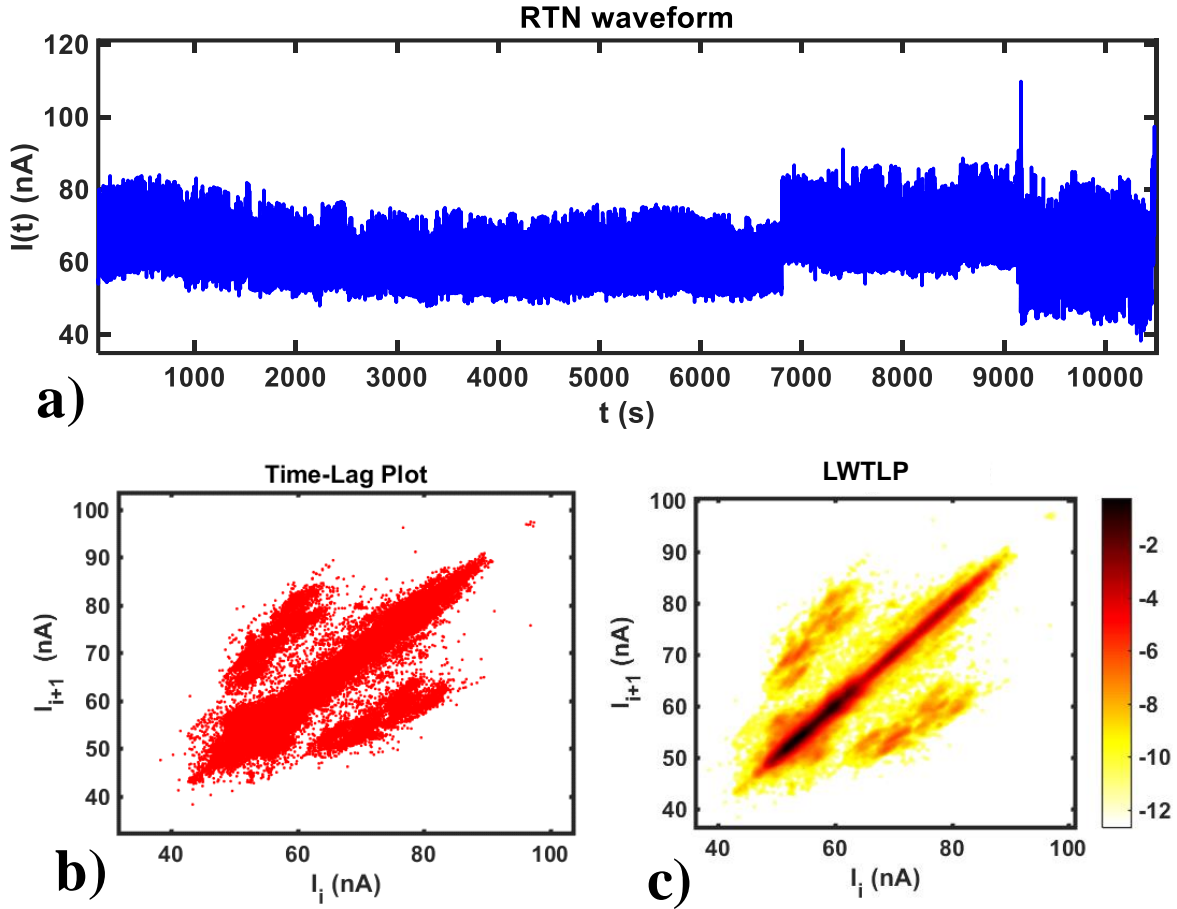
FIG. 6. (Color online) a) *I-t* trace of 1.2 million of samples measured at an applied voltage of - 0.5V for 10500 seconds. b) Corresponding Time Lag Plot of the RTN signal, c) Time Lag Plot obtained by means of the Locally Weighted method (LWTLP). A computation time of 9.6 seconds has been required for the whole data set (M=400 and 5×5 neighbor matrices have been employed). The WTLP method would require an estimated computation time of 11.5 hours for this long *I-t* trace.

For the sake of comparison, Table III shows the computation times to process these 2000-point signals. As commented above, although the four methods give information on the number of defects and the corresponding current levels, only the RTLP, WTLP and LWTLP represent the probability regions. Furthermore, the latter is much less computationally expensive than the others and, therefore, suitable for real time applications.

TABLE III. Computing time comparison for different RTN analysis methods for a (I-t) trace with 2000 samples. The calculations were performed in a PC with a processor Intel®Core™ I7 Q720 CPU@1.6Ghz. N is the number of samples in the trace, $n \times n$ is the matrix size used in the LWTLP method (where n<<M), and $M \times M$ is the matrix size of discrete (I_i, I_{i+1}) pairs. For the LWTLP we use N=2000, M =400 and n=5.

Method	Reduction of the space (I_i, I_{i+1}) to (x,y) (eqs. (1-2))	Order of complexity	Computation time	Probability	Fitting parameters
TLP	*No*	$N-1$	*0.31s*	*No*	*No*
WTLP	*Yes*	$(N-1) M^2$	*3.94s*	*Yes*	*Yes (α)*
RTLP	No	N^2	*3.68 s*	*Yes*	*Yes (r)*
LWTLP	*Yes*	$(N-1)n^2$	*5.23ms*	*Yes*	*No*

Different flavors of this method could be implemented if the 5×5 matrix is increased to 7×7 or 9×9 matrices, or reduced to 3x3 matrices, depending on the accurary required for a specific application. In these cases, there would be a trade-off between an agile computational implementation and the required accuracy in the occurrence probability description. In line with this consideration, and for the sake of clarity, we have compared the results obtained making use of 3x3 and 5x5 matrices (the I-t data related to Figures 4 and 5 are considered). The occurrence probabilities are described in a better manner in the 5x5 case at the cost of a slightly higher computation time, as it is shown in Figure 7.

Finally, it is worth pointing out that in relation to the weights employed in the LWTLP technique (given in Table I), we have tried different values of the σ_f parameter (Figure 8). We have found that for $\sigma_f=1.5$ a good trade-off is obtained for all the experimental data sets under study. In the LWTLP method we can change the σ_f parameter and matrix size, and these two options determine the LWTLP procedure accuracy. Nevertheless, we have shown that $\sigma_f=1.5$ works reasonably well in all cases and the option to refine accuracy could be just linked to the matrix dimension determination, although 3x3 and 5x5 matrices work well. In this respect, we determine a local weighting approach of the surrounding points in the TLP domain in the LWTLP; however, in the other plot methods, such as the WTLP, the standard deviation is used to perform the fitting parameter determination since the whole experimental data sequence is considered.
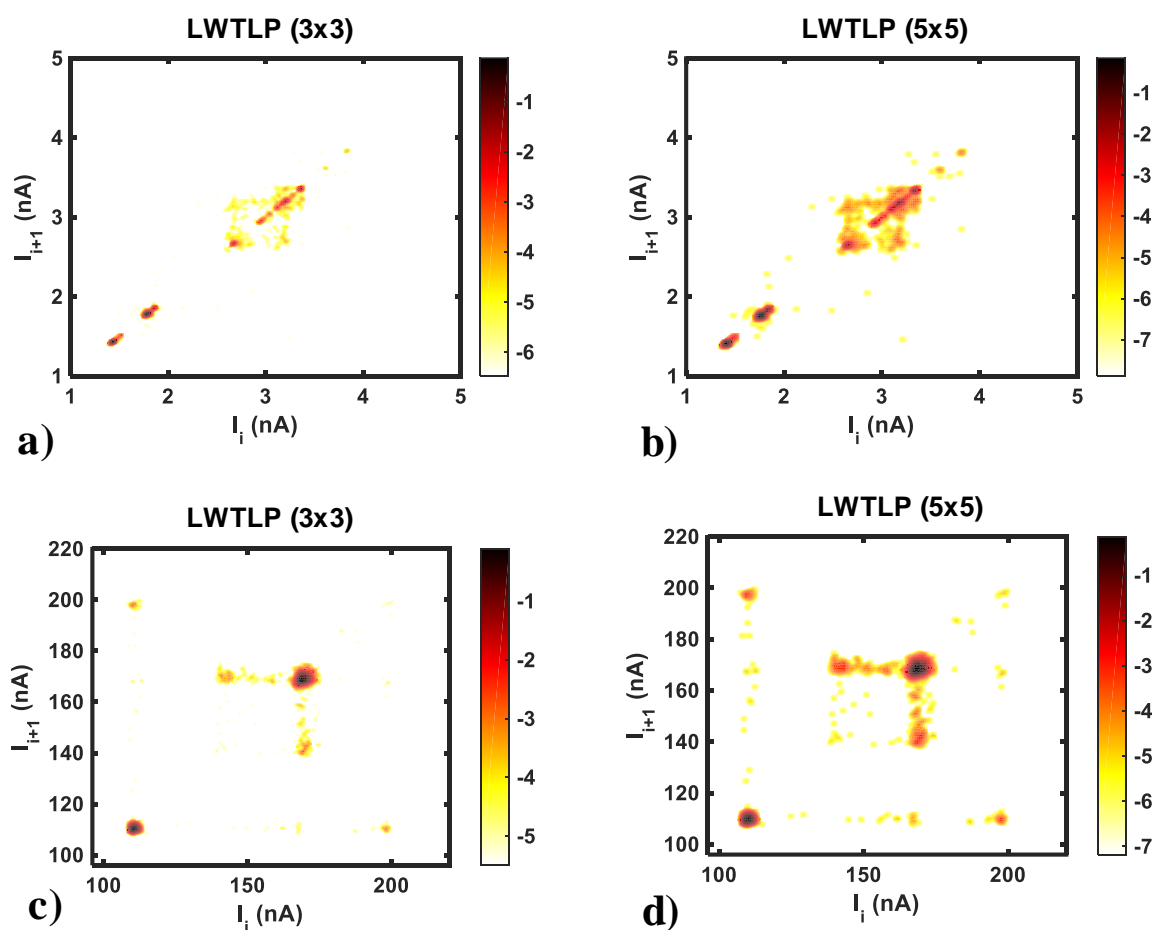
FIG. 7. (Color online) RTN plots for the RTN signals shown in Reference 40 (Table I, row 6). The trace consists of 2000 data points measured at an applied voltage of - 0.28V on a RRAM in HRS. a) LWTLP with a 3×3 matrix of neighbor points, M = 400 and computation time 4.9ms. b) LWTLP with a 5×5 matrix of neighbor points, M = 400 and computation time 5.23ms. RTN plots for the case of activation and deactivation of two stable RTN signals. The corresponding *I-t* RTN signals and the physical interpretation are shown in Reference 40 (Table I, row 5). The trace consists of 2000 data points measured at an applied voltage of - 0.62V. c) WTLP with a 3×3 matrix of neighbor points, M = 400 and computation time 4.9ms. d) WTLP with a 5×5 matrix of neighbor points, M = 400 and computation time 5.23ms.
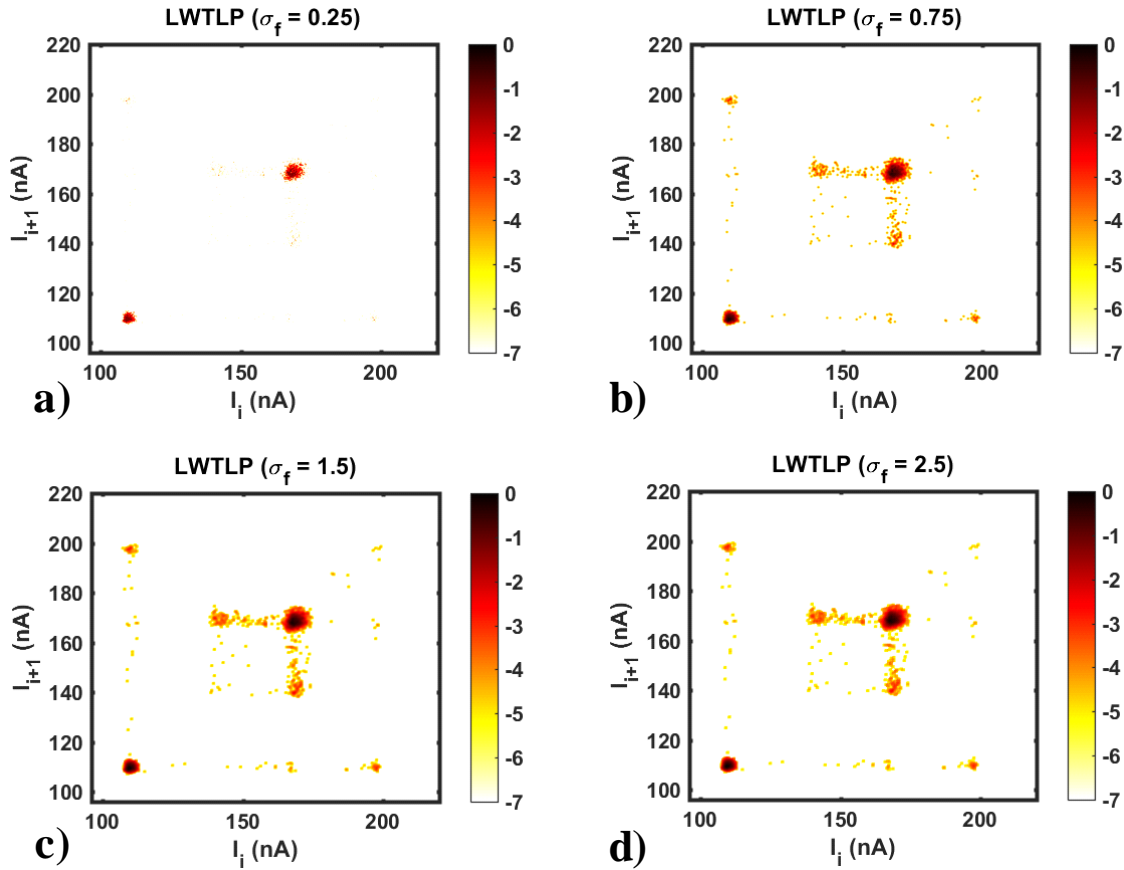
FIG. 8. (Color online) RTN plots for the case of activation and deactivation of two stable RTN signals for different σ_f values and 5x5 matrices (see Table I). a) $\sigma_f = 0.25$, the matrix central point is close to 1 and the others neighboring points are close to zero. The neighbor points scarcely contribute to the plot, b) $\sigma_f = 0.75$, the closest neighbor points slightly contribute, and the maximum occurrence probability regions are highlighted, c) $\sigma_f = 1.5$, a reasonable trade-off between the magnitude of the occurrence probability maxima and the contribution of non-null occurrence probability regions is achieved, d) $\sigma_f = 2.5$, the neighboring points contribute almost the same than the matrix central points.

V. CONCLUSIONS

A new technique to obtain time lag plots of Random Telegraph Noise (RTN) signals has been proposed and applied to *I*-t traces measured in Ni/HfO$_2$/Si-n+-based resistive RAMs (RRAMs). As other previously proposed methods (RTLP and WTLP), this new technique allows to calculate the probability associated to each position in the (I_i,I_{i+1}) plot, taking also in consideration the occurrences in the neighborhood. However, the computation time is much lower. In this way, the method allows the study of current-time traces with a massive number of data without losing the capability of dealing with background noise and discriminating the presence of active defects responsible for current fluctuations. A comparison of this algorithm with previous ones is given in terms of computing time and RTN description accuracy.

ACKNOWLEDGMENTS

REFERENCES

[1]F. Pan, S. Gao, C. Chen, C. Song and F. Zeng, Mat. Science and Eng. **83**, 1 (2014).

[2]M. Lanza, Mater. **7**, 2155 (2014).

[3]D. Ielmini, R. Waser, Resistive Switching: From Fundamentals of Nanoionic Redox Processes to Memristive Device Applications, (Wiley-VCH, 2015).

[4]M. Lanza, G. Bersuker, M. Porti, E. Miranda, M. Nafría and X. Aymerich, **Appl. Phy. Lett., 101**, 193502 (2012).

[5]M.A. Villena, J.B. Roldán, F. Jiménez-Molinos, E. Miranda, J. Suñé and M. Lanza, J. Comput. Electron., **16**, 1095 (2017).

[6]R. Waser (ed.), "Nanoelectronics and Information Technology", 3rd ed., Wiley-VCH, Berlin (2012).

[7]R. Waser and M. Aono, Nat. Mater., **6**, 833 (2007).

[8]S. Yu, Y. Wu, R. Jeyasingh, D. Kuzum, H.-S. Wong, IEEE Trans. Electron Devices, **58,** 2729 (2011).

[9]S. Yu (ed.), "Neuro-inspired computing using resistive synaptic devices", Springer (2017).

[10] J. Zahurak, K. Miyata, M. Fischer, M. Balakrishnan, S. Chhajed,D. Wells, Li Hong, A. Torsi, J. Lim, M. Korber, K. Nakazawa, S. Mayuzumi, M. Honda, S. Sills,S. Yasuda, A. Calderoni, B. Cook, G. Damarla, H. Tran, Bei Wang, C. Cardon, K. Karda, J. Okuno, A. Johnson, T. Kunihiro, J. Sumino, M. Tsukamoto, K. Aratani, N. Ramaswamy, W. Otsuka and K. Prall. IEEE International Electron Devices Meeting (IEDM), 6.2.1-6.2.4 (2014).

[11]T.Y. Liu et al, IEEE J. Solid-State Circuits 49, 140 (2014).

[12]A. Kawahara et al., IEEE J. Solid-State Circuits, **48**, 178 (2013).

[13]H.-S P. Wong, H.-Y. Lee, S. Yu, Y.-S. Chen, Y. Wu, P.-S. Chen, B. Lee, F. Chen, and M.-J. Tsai, Proceedings of IEEE, **100**, 951 (2012).

[14]S. Aldana, P. García-Fernández, A. Rodríguez-Fernández, R. Romero-Zaliz, M. B. González, F. Jiménez-Molinos, F. Campabadal, F. Gómez-Campos, J. B. Roldán, J. Phys. D, **50**, 335103 (2017).

[15]J. Guy, G. Molas, P. Blaise, M. Bernard, A. Roule, G. Le Carval, V. Delaye, A. Toffoli, G. Ghibaudo, F. Clermidy, B. De Salvo and L. Perniola, IEEE T. Electron Dev., **62**, 3482 (2015).

[16]A. Padovani, L. Larcher, O. Pirrotta, L. Vandelli and G. Bersuker, IEEE T. Electron. Dev., **62**, 1998 (2015).

[17]S. Aldana, J.B. Roldán, P. García-Fernández, J. Suñe, R. Romero-Zaliz, F. Jiménez-Molinos, S. Long, F. Gómez-Campos and M. Liu, J. Appl. Phys. **123**, 154501 (2018).

[18]M. Bocquet, D. Deleruyelle, C. Muller and J.M. Portal, Appl. Phy. Lett. **98**, 263507 (2011).

[19]S. Menzel, P. Kaupmann and R. Waser, Nanoscale, **7**, 12673 (2015).

[20]M.A. Villena, J.B. Roldán, M.B. González, P. González-Rodelas, F. Jiménez-Molinos, F. Campabadal and D. Barrera, Solid State Electron., **118**, 56 (2016).

[21]M.A. Villena, M.B. González, J.B. Roldán, F. Campabadal, F. Jiménez-Molinos, F.M. Gómez-Campos and J. Suñé, , Solid State Electron., **111**, 47 (2015).

[22]M.A. Villena, M.B. González, F. Jiménez-Molinos, F. Campabadal, J.B. Roldán, J. Suñé, E. Romera and E. Miranda, J. Appl. Phys., **115**, 214504 (2014).

[23]J.B. Roldán, E. Miranda, G. González-Cordero, P. García-Fernández, R. Romero-Zaliz, P. González-Rodelas, A. M. Aguilera, M.B. González and F. Jiménez-Molinos, J. Appl. Phys., **123**, 014501 (2018).

[24]Z. Jiang, S. Yu, Y. Wu, J. H. Engel, X. Guan, and H.-S. P. Wong, in International Conference on Simulation of Semiconductor Processes and Devices (SISPAD), 41 (2014).

[25]P. Huang, X. Y. Liu, B. Chen, H.T. Li, Y. J. Wang, Y.X. Deng, K.L. Wei, L. Zeng, B. Gao, G. Du, X. Zhang and J.F. Kang, IEEE T. Electron Dev., **60**, 4090 (2013).

[26]G. González-Cordero, F. Jiménez-Molinos, J.B. Roldan, M.B. González and F. Campabadal, J. Vac. Sci. Technol. B, **35**, 01A110 (2017).

[27]G. González-Cordero, J. B. Roldan and F. Jiménez-Molinos, in XXXI edition of the Design of Circuits and Integrated Systems Conference DCIS (2016) DOI: 10.1109/DCIS.2016.7845386

[28]X. Guan, Y. Shimeng and H-S. Philip Wong. IEEE Electr. Device L, **33**, 1405 (2012).

[29]M. Bocquet, D. Deleruyelle, H. Aziza, C. Muller, J. Portal, T. Cabout and E. Jalaguier, IEEE T. Electron Dev., **61**, 674 (2014).

[30]D. Panda, P.P Sahu and T.Y. Tseng, Nanoscale Res. Lett, **13**, 8 (2018).

[31]F. M. Puglisi, P. Pavan, A. Padovani, L. Larcher and G. Bersuker," Solid-State Electron., **84**, 160 (2013).

[32]Z. Chai, W. Zhang, P. Freitas, F. Hatem, J.F. Zhang, J. Marsland, B. Govoreanu, L. Goux, G.S. Kar, S. Hall, P. Chalker and J. Robertson, IEEE Electr. Device L., **39**, 955 (2018).

[33]D. Arumí, S. Manich, R. Rodríguez-Montañés and M. Pehl, 2016 Conference on Design of Circuits and Integrated Systems (DCIS), Granada, 2016, pp. 1-6. doi: 10.1109/DCIS.2016.7845382

[34]Z. Wei et al., in IEEE International Electron Devices Meeting (IEDM), San Francisco, 4.8.1-4.8.4 (2016). doi: 10.1109/IEDM.2016.7838349

[35]F.M. Puglisi, N. Zagni, L. Larcher and P. Pavan, IEEE T. Electron. Dev., **65**, 2964 (2018).

[36]T. Nagumo, K. Takeuchi, S. Yokogawa, K. Imai and Y. Hayashi, in IEEE International Electron Devices Meeting IEDM, 32.1.1 (2009).

[37]J. Martin-Martinez, J. Diaz, R. Rodriguez, M. Nafria and X. Aymerich, IEEE Electr. Device L., **35**, 479 (2014).

[38]J. Martin-Martinez, J. Diaz, R. Rodriguez, M. Nafria, X. Aymerich, E. Roca, F. V. Fernández and A. Rubio, in Proc. 5th Eur. Workshop CMOS Variability (VARI), 1 (2014).

[39]C. Márquez, N. Rodríguez, F. Gámiz, R. Ruiz, and A. Ohata, Solid State. Electron., **117**, 60 (2016).

[40]M. B. Gonzalez, J. Martin-Martinez, M. Maestro, M. C. Acero, M. Nafría and F. Campabadal, IEEE T. Electron Dev., **63**, 3116 (2016).

[41]M. Maestro, J. Martin-Martinez, J. Diaz, A. Crespo-Yepes, M.B. Gonzalez, R. Rodriguez, F. Campabadal, M. Nafria and X. Aymerich, Microelectron. Eng., **147**, 176 (2015).

[42]M. B. Gonzalez, J. M. Rafí, O. Beldarrain, M. Zabala and F. Campabadal, IEEE T. Dev. Mat. Reliab. **14**, 769 (2014).

[43]M.B. Gonzalez, J. Martin-Martinez, R. Rodriguez, M.C. Acero, M. Nafria, F. Campabadal and X. Aymerich, Microelectronic Eng., **147**, 59 (2015).

5.2.8. Differential Locally Weighted Time Lag Plot

The Differential Locally Weighted Time Lag Plot (DLWTLP) is a method that plots the current derivative with respect to time in the sample $i+1$ versus the current derivative with respect to time of sample i in a LWTLP. The current derivative is calculated numerically by the quotient of the current and time increments, as described in equation (5.7) This plot offers information about the temporal sequence of current values, such as the probability of occurrence of changes between current states (p_1, p_2, p_3 and p_4) and the presence of spikes (p_5), described in the **Table 5.I**. **Figure 5.9 b)** shows the DLWTLP of the trace #640, the occurrence of p_5 indicates the presence of spikes in the RTN signal. The marks p_1 and p_2 indicate the transition from state 0 to state 1, and the presence of marks p_3 and p_4 indicates the transition from state 1 to state 0.

$$\frac{dI_i}{dt} \approx \frac{I_{i+1} - I_i}{t_{i+1} - t_i} \quad , i = 1..\,\mathrm{N} - 1. \tag{5.7}$$
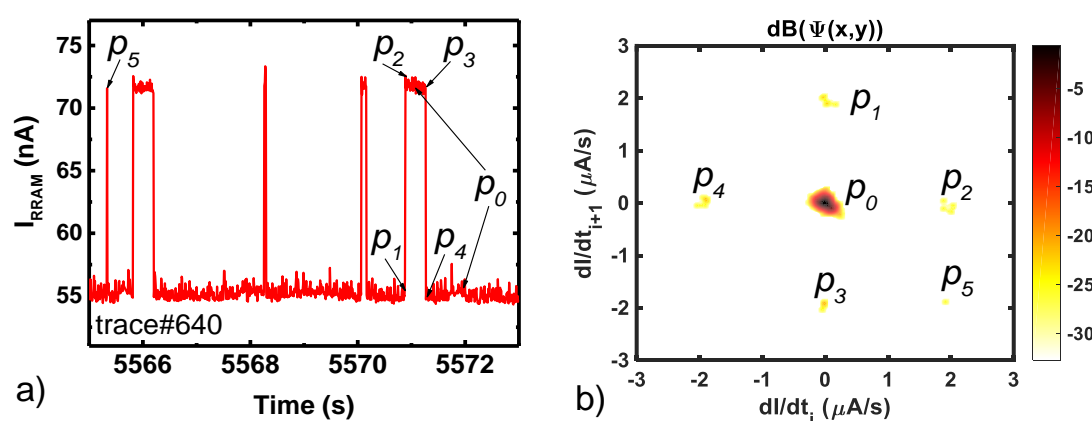
Figure 5.9 **a)** Current versus time plot of 1000 samples measured in a Ni/HfO$_2$/Si-n^{++} device (trace #640). **b)** DLWTLP (*M*=200 points M5x5, σ_f = 1.5) of the same trace [González-Cordero2019c].

Table 5.I Description of the labels employed in **Figure 5.9**

Mark	Description
p_0	Current switch between stable current levels. It is obtained for stable levels, 0 or 1
p_1	Beginning of the current transition from state 0 to state 1. The *i*-derivative is close to cero, while the following (*i+1*-derivative) is positive.
p_2	End of transition revealed by p_1 (from 0 to 1). The *i*-derivative is positive, the *i+1* one is close to cero.
p_3	Beginning of the current transition from state 1 to state 0. The *i*-derivative is close to cero, while the following (*i+1*-derivative) is negative.
p_4	End of the transition revealed by p_3 (from 1 to 0 states). The *i*-derivative is negative, the *i+1*-derivative one is close to cero.
p_5	Spike between states 0-1-0. It reveals a duration in the 1 state shorter than two sampling time steps.

This method was published in González-Cordero et al. Microelectronic Engineering (2019), the accepted preprint paper is presented below.

González-Cordero et al. Microelectronic Engineering (2019)

Quality metrics

Data base	Rating	Quartile
Web of Science	Impact factor: 2.02	Q2
Scimago	Scientific journal ranking: 0.604	Q1

Publication citations

Google Scholar	Web of Science
0	**0**

A new technique to analyze RTN signals in resistive memories

G. González-Cordero[a], M.B. González[b], F. Campabadal[b],
F. Jiménez-Molinos[a], J.B. Roldán[a,*]

[a]Departamento de Electrónica y Tecnología de Computadores, Universidad de Granada, 18071 Granada, Spain
[b]Institut de Microelectrònica de Barcelona, IMB-CNM (CSIC), Campus UAB, 08193 Bellaterra, (Spain)

ABSTRACT

A new technique to study random telegraph noise is proposed. It is based on an analysis of the variations of the sampled current instead of the current itself. These current variations are represented following a time-lag-plot scheme. The meaning of the graphical patterns obtained is discussed. Specifically, this new method is very effective for detecting current spikes due to the presence of fast traps. In addition, it can be used to easily detect an unsuitable sampling rate and achieve optimum RTN measurement conditions. This technique has been used for analyzing several current versus time traces for the state-of-the-art Resistive Random Access Memories (RRAMs). The results are analyzed and the patterns obtained with the proposed method are linked to the characteristic features of the corresponding random telegraph noise signals, showing the validity and effectiveness of the proposed method.

Keywords: Resistive RAM; random telegraph noise; RTN; time-lag-plot

*Corresponding author. Tel.:+ *34 958244071;*   *E-mail address:*jroldan@ugr.es (J.B. Roldán)

1. INTRODUCTION

RRAMs are currently one of the most outstanding technologies for non-volatile memories (NVMs). Among them, those based on volume conduction or based on filamentary conduction can be distinguished. For the latter case, the presence or destruction of one or several conductive filaments (CFs) inside an insulator allows the differentiation of two resistive states: low resistance state (LRS) and high resistance state (HRS) [1]. The formation and disruption of CFs both in metal-insulator-metal (MIM) or metal-insulator-semiconductor (MIS) structures is assumed to be the mechanism behind resistive switching (RS) in these devices.

Random telegraph noise (RTN) in filamentary RRAMs is usually related to the presence of charged traps in the oxide inside or near the CF [2-5]. Activation and deactivation of traps may produce fluctuations between different current levels [2,4,5]. RTN should be correctly modeled and taken into account because it could cause read errors in digital applications. Analog operation may be influenced by RTN as well. For instance, in analog neuromorphic applications (where RRAMs can be used as synapsis emulators), RTN would lead to random fluctuations of the synaptic weights. On the other hand, RTN can be exploited for applications such as Physically Unclonable Functions (PUF) [6] or Random Number Generation (RNG) [5].

RTN is usually characterized by means of different techniques based on Time-Lag-Plots [7], which are representations of the temporal *i+1* sampled current value versus the *i* value. In this paper, we briefly review TLP methods and present our new technique (section 2) in this context. In section 3, we describe the device fabrication and measurement processes. The results and discussion are given in section 4. Finally, the main conclusions are drawn.

2. TIME LAG PLOTS AND THE NEW CURRENT DERIVATIVE TECHNIQUE

The Time Lag Plot (TLP) is a graphic tool used to easily visualize RTN data [7]. Given a sampled current versus time trace (I_i, t_i), where $i \in [1, n]$ and n is the number of sampled data points, the current value at a certain time, I_{i+1}, is plotted versus the previous value, I_i. Therefore, stable current levels appear as clusters of points along the diagonal of the graph ($I_{i+1} = I_i$) while transitions between current levels show up outside this diagonal. However, TLP does not provide quantitative information about the number of points concentrated or even overlapped around a given region (this information would be related to the occurrence probability of current levels). Furthermore, the proximity of two stable levels and/or the background noise can produce the overlapping of points within the clusters, being the interpretation of the plot difficult in these cases [4,8,9].

In order to overcome these drawbacks, alternative methods based on TLP have been proposed. These techniques add information linked to the occurrence probability in a third axis. Among them, the Radius Time Lag Plot (RTLP) [9] considers that the value associated to a given position (I_i, I_{i+1}) in the TLP depends on the number of counts in a circular neighbourhood (defined by a certain radius). On the other hand, the Weighted Time Lag Plot (WTLP) [8] method calculates the occurrence probability in a given position of the TLP space as a weighted sum of all the sampled data. The weights are given by the distance between each position and the corresponding sampled data following a bidimensional Gaussian distribution (BGD). In this way, zones with a higher point concentration in the TLP space are highlighted by both methodologies (RTLP and WTLP).

However, both techniques are computationally expensive. In order to reduce computation time for extremely long traces, the authors of this work recently proposed the Locally Weighted Time Lag Plot (LWTLP) [10] that holds the best features of both methods, RTLP and WTLP. In the LWTLP method, a surrounding square will be defined for each position (I_i, I_{i+1}) of the TLP space. After that, the probability at a given position (I_i, I_{i+1}) is calculated taking into account the distance to points in the surrounding positions (by means of a BGD) [10]. In the present work, we propose a new technique based on a representation of the temporal numerical derivative of the current, instead of the current itself; i.e.:

$$\frac{dI_i}{dt} \approx \frac{I_{i+1}-I_i}{t_{i+1}-t_i} \ , i = 1..n-1. \tag{1}$$

Once the derivatives have been calculated, the data are represented by means of a time-lag-plot scheme. That is, the derivative corresponding to sample *i+1* is plotted versus the current derivative of sample *i*. In this work, LWTLPs [10] of the current derivative have been used to analyze the results, see Fig. 1.

LWTLP 5x5 Matrix

$\hat{y}+2$	0.16	0.33	0.41	0.33	0.16
$\hat{y}+1$	0.33	0.64	0.80	0.64	0.33
$\hat{y}$	0.41	0.80	1	0.80	0.41
$\hat{y}-1$	0.33	0.64	0.80	0.64	0.33
$\hat{y}-2$	0.16	0.33	0.41	0.33	0.16
	$\hat{x}-2$	$\hat{x}-1$	$\hat{x}$	$\hat{x}+1$	$\hat{x}+2$

Normalized coordinates   Weights used in the matrix

$$\hat{x} = int\left(\frac{I_i - I_{min}}{\Delta x}\right) \qquad w(\hat{x},\hat{y}) = e^{-\frac{\hat{x}^2+\hat{y}^2}{2\sigma_f}}$$

$$\hat{y} = int\left(\frac{I_{i+1} - I_{min}}{\Delta y}\right)$$
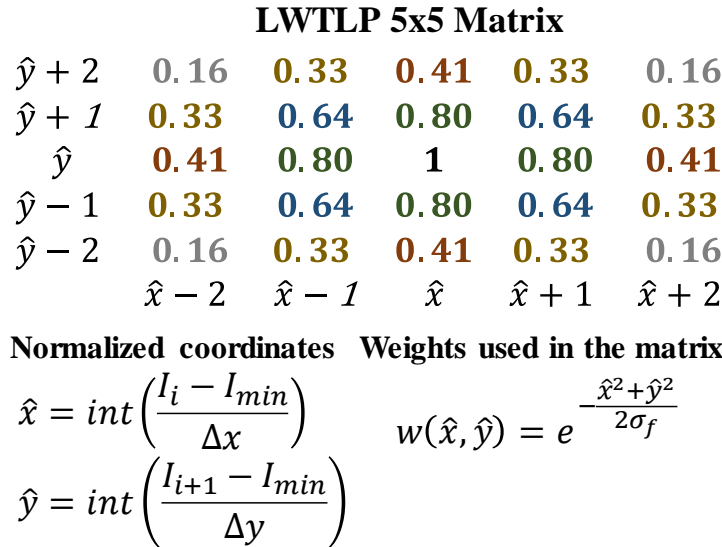
Fig.1. Summary of the LWTLP method: the time current levels were transformed in a normalized coordinate system $(\hat{x},\hat{y})$. Each point in the neighborhood was weighted by a bidimensional Gauss distribution function $w(\hat{x},\hat{y})$. An example of LWTLP 5x5 matrix is shown, similar weights are written with the same color [10].

As we will describe in section 4, this new representation allows obtaining additional information hidden in a TLP of the current, such as the presence of spikes (defined here as current level changes whose time length equals a sampling time). Basically, the new method is a representation of the current transitions between states and in this respect it would be a complementary technique to the methods described above. Note that if the sampling rate is constant, the TLP of the current derivative (Equation 1) is equal to the TLP of the current variations ($\Delta I_i = I_{i+1} - I_i$), except for a scale factor (the sampling time).

3. DEVICE FABRICATION

Devices based on a Ni/HfO$_2$/Si-n$^+$ stack were fabricated on silicon wafers with resistivity 7-13mΩ·cm. The fabricated structures are square cells of 5x5µm^2 with a 20nm-thick HfO$_2$. More detailed information about the process flow can be found in Ref [3]. These devices show unipolar resistive switching features. The RTN data were recorded using a HP-4155B semiconductor parameter analyzer controlled by an automatic software tool based in a smart procedure implemented in Matlab®. The RTN traces were measured at different biases in the HRS. Different time intervals were considered with the following features: (2000 samples, ~20s).
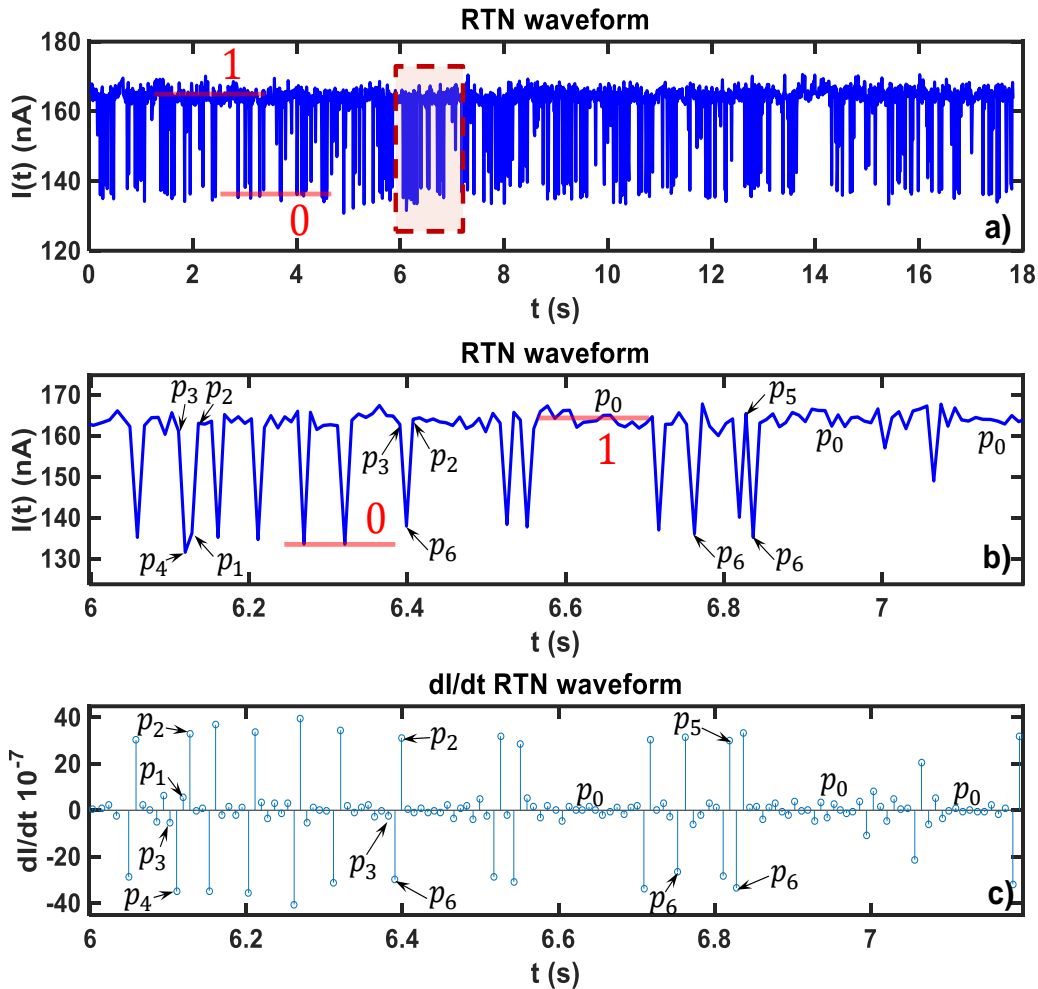
Fig.2. Typical RTN signals measured in the HRS of Ni/HfO$_2$/Si-n$^+$ devices for an applied bias V$_{RRAM}$=-0.6V. a) Current versus time plot. Two current levels can be clearly identified. b) Plot corresponding to the 100 current data points of the RTN signal highlighted in the red box in a). c) dI/dt of the signal in b), where different events are labeled according to Table I.

4. RESULTS AND DISCUSSION

Fig. 2a shows a measured RTN signal with 2000 data points at a bias of V_{RRAM}= -0.6V. Two current levels are clearly identified, around 137nA and 164nA, as indicated in the zoom-in plot of 100 current points shown in Fig. 2b. The two states are labelled '0' and '1', respectively. Fig. 1c shows the corresponding current derivative (*dI/dt*) versus time of the RTN trace.

The LWTLP of the *I-t* data is represented in Fig. 3a using a dB scale (10log$_{10}$(X/X$_{max}$), taking as a reference level the point of greatest probability [10]. The two RTN levels are revealed in the main diagonal. Fig. 3b shows the corresponding LWTLP of the *dI/dt* in dB scale, where the events indicated in Fig. 2b and 2c have been highlighted. Table I shows a description definition of the types of events found in the experimental RTN signal of Fig. 2. The events that have been detected with this new technique include information about the beginnings and ends of the current transitions and the possible spikes between states, with their relative probabilities. The presence of spikes with a large relative probability could be an indication of a too low sampling frequency. Therefore, this new technique can provide a method to determine if the sampling time is low or high in comparison with trap emission and capture times. If the sampling time is low more events associated with spikes would appear (0-1-0 or 1-0-1). On the contrary, if the sampling rate is high enough and the sampling time much shorter than the capture and emission times, the number of spike events should be reduced and events p_0 to p_4 would be more frequent.

Event	Description		Pr(dB)
p_0	No current switch between stable levels are revealed. It is obtained for both levels, 0 or 1 (Fig. 1a)		0 (ref.)
p_1	Beginning of the current transition from state 0 to state 1. The *i*-derivative is close to cero, while the following is positive.		-17.6
p_2	End of transition revealed by p_1 (from 0 to 1). The *i*-derivative is positive, the *i+1* one is close to cero.		-9.3
p_3	Beginning of the current transition from state 1 to state 0. The *i*-derivative is close to cero, while the following is negative.		-10.4
p_4	End of transition revealed by p_3 (from 1 to 0). The *i*-derivative is negative, the *i+1* one is close to cero.		-16.8
p_5	Spike between states 0-1-0. It reveals a duration in the 1 state shorter than two sample periods.		-16.7
p_6	Spike between states 1-0-1. It reveals a duration in the 0 state shorter than two sample periods.		-10.4

Table I. Description of the events detected in the RTN signal of Fig. 2 with the proposed analysis technique based on the current derivative (they correspond to the labels employed in Figs. 2 and 3). The last column shows the probability values in dB that are obtained by the following expression $10\log_{10}(X/X_{max})$ assuming the most probable event to be the reference (X_{max}), see LWTLP in Fig. 3b.
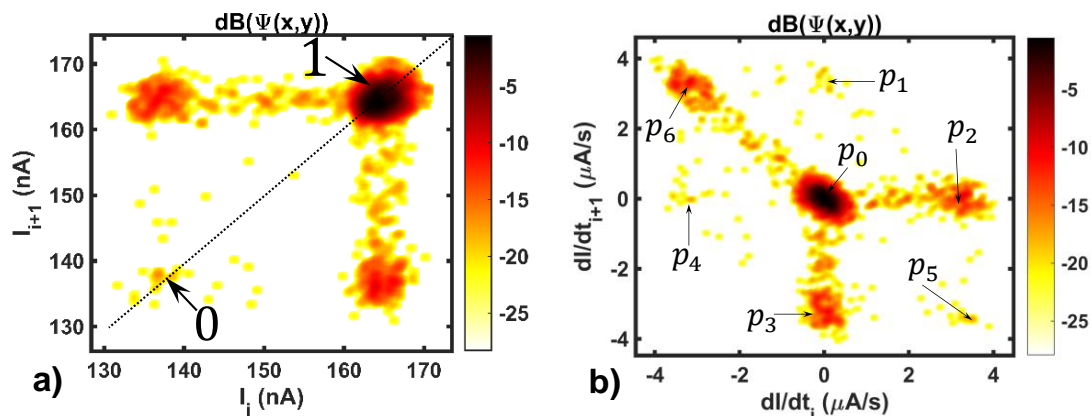
Fig.3. a) LWTLP in dB scale calculated for the data in Fig. 2. In the main diagonal the two most frequent RTN current levels are located (137nA @ -19dB and 164nA @ 0dB). b) LWTLP for the current derivative dI/dt in dB scale. The different events shown in Fig. 2b and 2c are indicated.

Note that in the LWTLP of the *I-t* trace (Fig. 3a) the two current levels result in the two clusters in the main diagonal. The lowest current level (labeled with 0) is much less probable than the other one (labeled with 1), although many transitions occur between both states, as can be seen in the clusters outside the main diagonal of Fig. 3a and in the current fluctuations of the *I-t* trace (Fig. 2a).

The current level transitions can be better described in a LWTLP of the current derivative, as shown in Fig. 3b. The different transition events and its relative frequency are indicated in Fig. 3b. For example, transitions from the high state to the low state are highlighted in the cluster labelled as p_3. It should be noticed that transitions between two states can result in two different events: p_1 or p_3 events (the current remains at least two sampled data points at the low level previous to the transition) or p_5 or p_6 events (which correspond to spikes, the current rapidly returns to the initial level). These two different cases are indistinguishable in a conventional current TLP, but they appear clearly differentiated in the TLP of the current derivative. This is due to the fact that the last one includes information about three data points of the *I-t* trace in each point of the TLP (as illustrated in the schematic figures of Table I).

Fig. 4a shows another example of RTN data (current versus time, V_{RRAM}=-0.31V). Again, two current levels are clearly seen. The corresponding current derivative time-lag-plot is shown in Fig. 4b. In the secondary diagonal, a coloured cluster (p_5) reveals the presence of spikes 0-1-0, but with much lower probability than the other highlighted events. This indicates that the RTN trace has been sampled with a suitable frequency to properly detect the RTN levels. This proposed RTN analysis can be useful to complement previously published analysis and methods [4, 8, 10, 11] and can help in the implementation of compact modeling [5, 12-14].

In order to validate the proposed technique for long traces. We employed RTN data measured at V_{RRAM}=-0.5V in the HRS of the devices during 6800s, where 1.2×10^6 samples were recorded. The obtained current-time trace is represented in Fig 5a, in the inset a more detailed plot for 100s period is shown, RTN signals are clearly observed. For these data the Time Lag Plot obtained by means of the LWTLP method with M = 400 and 5×5 neighbor matrices has been employed [10] and represented in Fig 5b. In this representation no clear conclusions can be extracted due to the high number of data and the long measurement time. This long assessment time increases the probabilities that the current levels can be slightly shifted during the RTN measurements. This current shift may increase the difficulties to detect clustered levels in the TLP of the full trace.
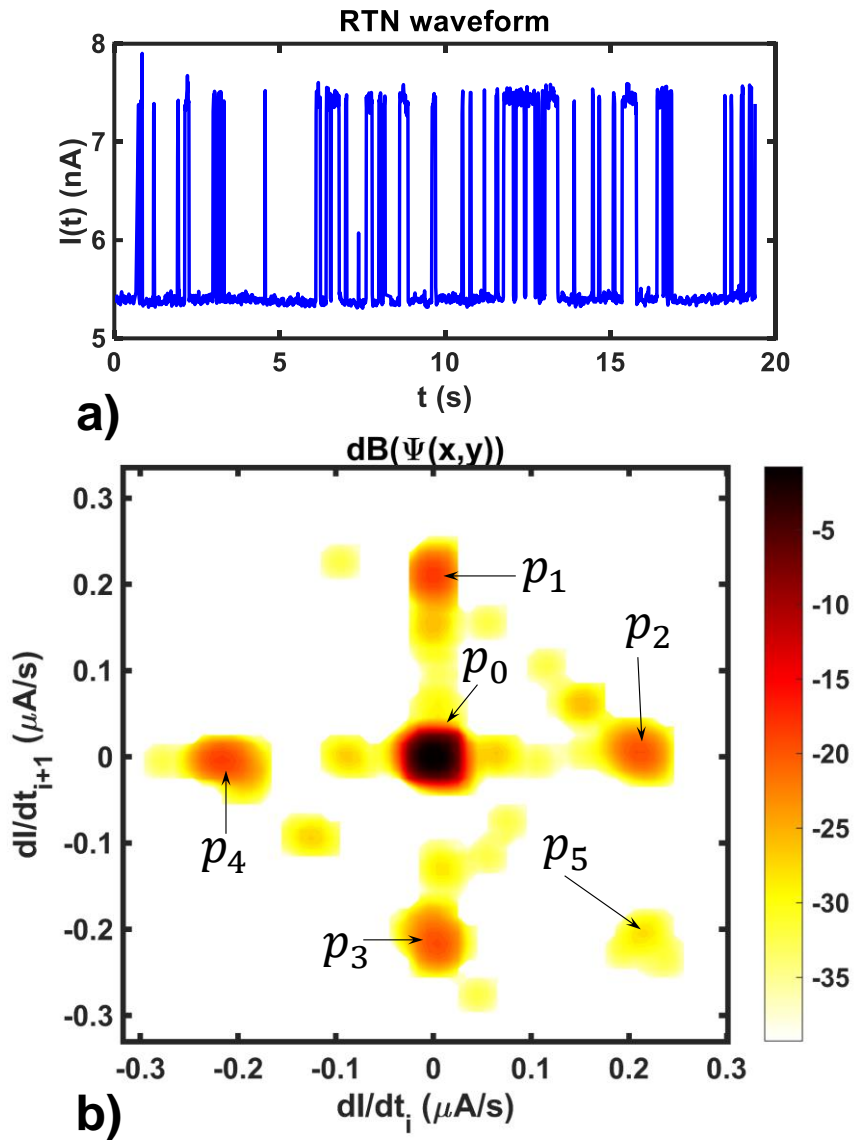
Fig. 4. RTN data measured for the studied Ni/HfO$_2$/Si-n$^+$ at V_{RRAM}=-0.31V in the HRS. a) current versus time plot, b) LWTLP for the current derivative. In the secondary diagonal appears a highlighted region (p$_5$) that indicates the presence of spikes 0-1-0 with a very low probability in relation to the other events.

In order to extract more useful information from long signals, we used the LWTLP method for the current derivative for the whole current trace under consideration, see Fig. 5. The corresponding plot suggests that there are four current levels (Fig. 6a). The first two levels 0-1 (more likely) have the associated events p_1 to p_6, these states present capture and emission times of the same order (the description of these events is shown in Table I). It is worth highlighting that there is a large probability of spikes of the type 0-1-0 (event p_6). In addition, there are two other levels (labeled 2 and 3 in Fig. 6a). For these levels, the capture and emission times are also approximately similar. These news levels have associated events q_1 to q_6 with the same interpretation as p_1 to p_6 previously described in Table I, except that instead of the 0 initial state, in the case of q events their "ground" state corresponds to current level 2 and the high current level shifts to level 3. In these states there is a greater probability of spikes of type 2-3-2 (event q_5). As can be seen, this new representation based on the LWTLP of the current derivative allows a clearer representation of some of the RTN features than with previously proposed methodologies [7-9].
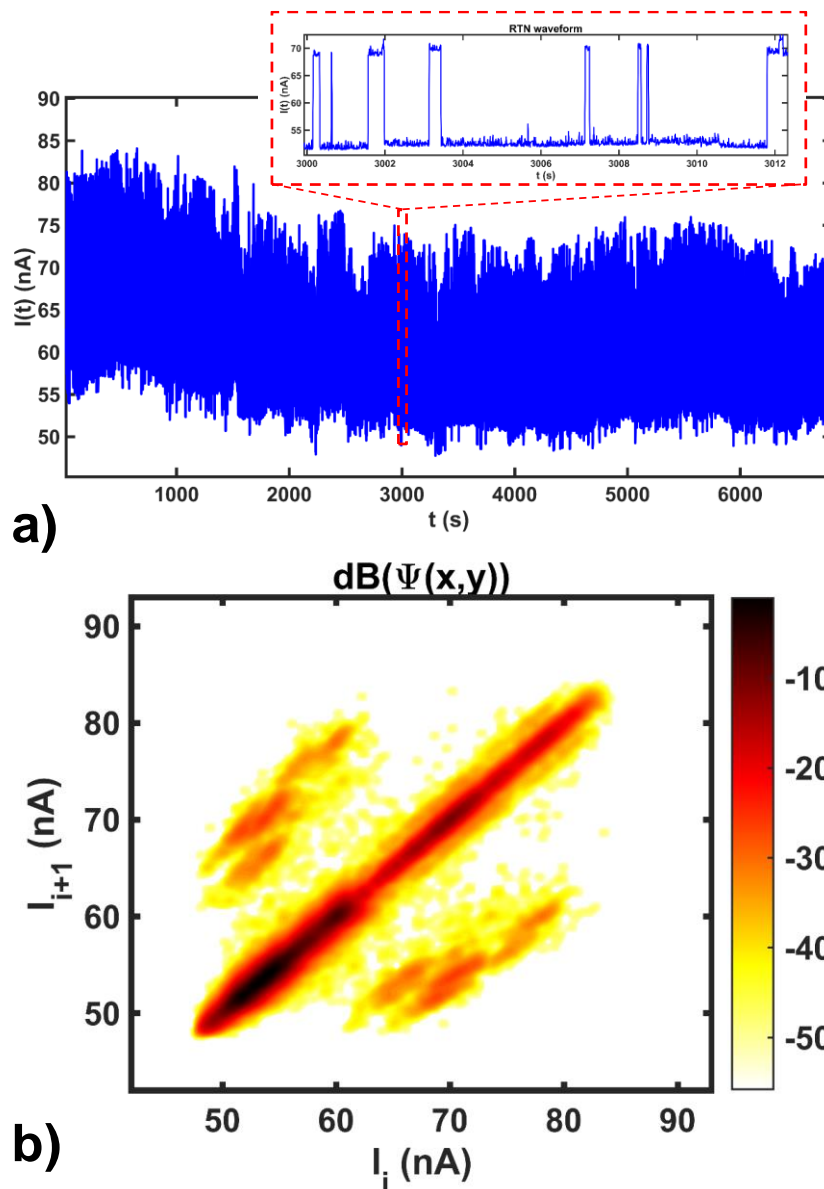
Fig. 5. a) RTN data obtained during a long measurement time. The devices were biased at V_{RRAM}=-0.5V in the HRS for a measurement time of 6800s (1.2×10^6 samples were recorded). See in the inset a detailed plot of the recorded data for a time period of 100s, RTN signals are clearly shown. b) Time Lag Plot obtained by means of the LWTLP method with M = 400 and 5×5 neighbor matrices.
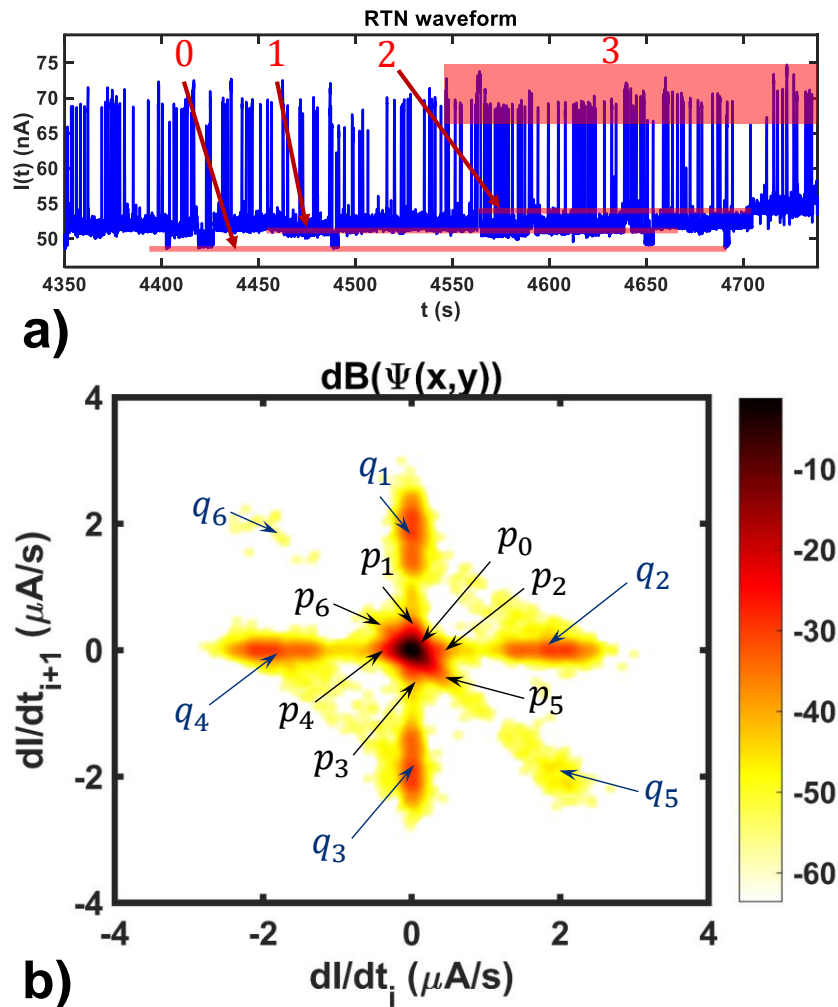
Fig. 6. a) Plot of an RTN signal for a time interval of 350s. The current levels referred to the text are shown. b) LWTLP for the current derivative obtained from the long set of RTN data measured and shown in the Fig. 5.

5. CONCLUSIONS

A new method to analyze RTN signals has been proposed. This method has been employed to study RTN traces in the HRS of Ni/HfO$_2$/Si-n$^+$ resistive switching devices. The technique is based on a time-lag-plot representation of the current derivative instead of the current itself, allowing a better understanding of the characteristic RTN signal features and better visualization of the complete range of current transitions than when a representation based on the current is considered. In addition, this new technique provides information to assess if the sampling rate is adequate to determine the presence of the electrically active defects in relation to their capture and emission times. So, it could be a complementary tool to the conventional representations employed for RTN analysis.

ACKNOWLEDGEMENTS

References

[1] M.A. Villena, J.B. Roldán, F. Jiménez-Molinos, E. Miranda, J. Suñé, M. Lanza. J. Comput. Elec. 16 (2017) 1095-1120.

[2] S. Ambrogio, S. Balatti, A. Cubeta, A. Calderoni, N. Ramaswamy and D. Ielmini, IEEE Trans. Electr. Dev. 61 (2014) 2920-2927.

[3] M.B. Gonzalez, J. Martin-Martinez, R. Rodriguez, M.C. Acero, M. Nafria, F. Campabadal, X. Aymerich. Microelec. Eng.147 (2015) 59-62.

[4] M.B. Gonzalez, J. Martin-Martinez, M. Maestro, M.C. Acero, M. Nafría, F. Campabadal. IEEE Trans. Electr. Dev. 63 (2016) 3116-3122.

[5] F.M. Puglisi, N. Zagni, L. Larcher, P. Pavan. IEEE Trans. Electr. Dev. 65 (2018) 2964-2972.

[6] D. Arumí, Á. Gómez-Pau, S. Manich, R. Rodríguez-Montañés, M.B. González, F. Campabadal. IEEE Electron Dev. Lett. 40 (2019) 341-344.

[7] T. Nagumo, K. Takeuchi, S. Yokogawa, K. Imai, Y. Hayashi, IEEE International Electron Devices Meeting (2009) 1-4.

[8] J. Martin-Martinez, J. Diaz, R. Rodriguez, M. Nafria, X. Aymerich, IEEE Electron Device Lett. 35 (2014) 479-481.

[9] C. Márquez, N. Rodríguez, F. Gámiz, R. Ruiz, A. Ohata. Solid-State Electron. 117 (2016) 60-65.

[10] G. González-Cordero, M.B. González, F. Jiménez-Molinos, F. Campabadal, J.B. Roldán. J. Vac. Sci. Technol. B. 37 (2019) 012203.

[11] F.M. Puglisi, L. Larcher, A. Padovani and P. Pavan, IEEE Trans. Electr. Dev. 62 (2015) 2606-2613.

[12] M. Lanza et al., Adv. Electron. Mater. 5 (2019) 1800143.

[13] G. González-Cordero, J.B. Roldán, F. Jiménez-Molinos, J. Suñé, S. Long, M. Liu, Semicond. Sci. Technol. 31 (2016) 115013.

[14] G. González-Cordero, F. Jiménez-Molinos, J.B. Roldán, M.B. González, F. Campabadal, J. Vac. Sci. Technol. B. 35 (2017) 01A110.

5.3. Neural Network Based Analysis of RTN with LWTLP

As explained above, the LWTLP method allows us to characterize long RTN traces with short computation efforts. However, if the recording time is very long, the RTN patterns could evolve because the number and location of active traps could change while the measurement is carried out. As a consequence, if the complete trace is divided in regular time intervals, different TLPs could be obtained. Therefore, the question that arises naturally is related to the repetition of certain patterns or if the complete trace could be characterized by a reduced set of patterns. Regarding this issue, an automatized classification of the pattern would be very valuable. In this context, an automatic classification tool based on Artificial Neural Network using Self-Organizing Maps has been developed and used in order to analyse a long $I - t$ trace with 1.2 million of samples.

This method was published in González-Cordero et al. Semiconductor Science and Technology (2019), the accepted preprint paper is presented below.

González-Cordero et al. Semiconductor Science and Technology (2019)

Quality metrics

Data base	Rating	Quartile
Web of Science	Impact factor: 2.654	Q2
Scimago	Scientific journal ranking: 0.793	Q1

Publication citations

Google Scholar	Web of Science
0	**0**

Neural network based analysis of Random Telegraph Noise in Resistive Random Access Memories

Authors: G. González-Cordero[1], M.B. González[2], A. Morell[3], F. Jiménez-Molinos[1], F. Campabadal[2], J.B. Roldán[1]

[1]Departamento de Electrónica y Tecnología de Computadores. Universidad de Granada. Facultad de Ciencias. Avd. Fuentenueva s/n, 18071 Granada, Spain.
[2]Institut de Microelectrònica de Barcelona, IMB-CNM (CSIC), Campus UAB, 08193 Bellaterra, Spain
[3]Departament de Telecomunicació i Enginyeria de Sistemes. Universitat Autònoma de Barcelona. Escola d'Enginyeira, carrer de les Sitges, S/N, 08193 Bellaterra, Spain
Electronic mail: *jroldan@ugr.es*

Abstract

The characterization of Random Telegraph Noise (RTN) signals in Resistive Random Access Memories (RRAM) is a challenge. The inherent stochastic operation of these devices, much different to what is seen in other electron devices such as MOSFETs, diodes, etc., makes this issue more complicated from the mathematical viewpoint. Nevertheless, the accurate modeling of these type of signals is essential for their use in digital and analog applications. RTN signals are revealed to be linked to the emission and capture of electrons by traps close to the conductive filament (CF) that can influence resistive switching (RS) operation in RRAMs. RTN features depend on the number of active traps, on the interaction between these traps at different times, on the occurrence of anomalous effects, etc. Using a new representation technique, the Locally Weighted Time Lag Plot (LWTLP), a highly efficient method in terms of computation, data from current-time (I-t) traces can be represented with a pattern that allows the analysis of important RTN signal features. In addition, Self-organizing maps (SOM), a neural network devoted to clustering, can be employed to perform an automatic classification of the RTN traces that have similar LWTLP patterns. This pattern analysis allows a better understanding of RTN signals and the physics underlying them. The new technique presented can be performed in a reasonable computing time and it is particularly adequate for long (I-t) traces. We introduce here this technique and the most important results that can be drawn when applied to long RTN traces experimentally obtained in RRAMs.

Keywords: Resistive memories, RRAMs, RTN signals, Time Lag Plot, LWTLP, Self organizing maps, Unsupervised learning, Clustering, Neural networks

1.- INTRODUCTION

New emerging non-volatile memory technologies are getting wide attention among electronics manufacturers and the academic community. These new devices show a set of advantages that makes the viability of high-performance and cost-effective applications a reasonable possibility [1-4]. The applications are not only linked to non-volatile storage-class memory modules but also to neuromorphic circuits and hardware security implementations [2, 5-7]. The growing prominence of mobile devices and the popularity of Internet-of-things (IoT) is pushing the technology towards the use of devices such as RRAMs that can be easily scaled and show fast read and writing times, low power operation, non-volatility and CMOS compatibility. A resistive memory is made of metal or highly doped semiconductor electrodes and a dielectric in between the electrodes that can be fabricated by different types of oxides and even 2D materials. A wide variety of materials has been employed for dielectric and electrodes [1, 2]. These devices have been successfully used at the integrated circuit level with a promising degree of scalability [8-10]. However, prior to massive industrial use, key issues such as variability and reliability have to be improved. In addition, characterization and modeling have to be pushed forward. Although great efforts from the physical simulation [3, 11-17] and compact modeling [18-22] have been made, new studies in terms of characterization and modeling are needed. With respect to modeling, noise is a significant issue to deal with, in particular RTN, a noise source that is important in RRAMs [5, 23-27].

The CF creation and rupture gives rise to resistive switching (RS) operation. The presence of single or multiple traps inside or close to the CFs influences charge conduction and produces current fluctuations that can lead to RTN [23-25]. These fluctuations can reduce noise margin in memory cell arrays [24, 25] or affect the analog behavior of the devices necessary to mimic electronic synapses in neuromorphic circuits [28], posing important hurdles to the use of these devices in highly-scaled integrated circuits. RTN fluctuations can also be beneficial, for instance, when used as entropy sources in random number generators [23, 29, 30].

Several methods to characterize RTN can be found in the literature [24, 25, 27, 31- 35]. Different facets of RTN signals can be studied making use of them; however, if long (I-t) traces are considered some of these procedures are not appropriate due to their heavy burden from the computational viewpoint. We have recently presented a methodology based on the Locally Weighted Time Lag Plot (LWTLP) [25]. This new method allows a quick analysis of (I-t) RTN signals.

Making use of an experimental (I-t) trace as a starting point, a pattern based on the LWTLP is obtained that produces information about the current levels, their frequency, the transitions between different current levels, etc [25, 32, 36]. In a long trace, different characteristic patterns can be obtained if the trace is divided in regular time intervals, since the traps that influence current fluctuations get activated or deactivated as the measurement goes on. In this respect, the number of active traps, i.e., the different RTN current levels, evolve with time. If a long (I-t) trace with millions of measurements is divided in time windows, we would obtain a characteristic pattern for each of these windows. The question that reasonably comes up is connected with the possibility of repetition of certain patterns, or if any pattern could be characterized by a finite set of patterns. In implementing this analysis, we enter in the data mining/machine learning realm and in particular we deal with a (unsupervised) clustering problem. We have adopted in this work an Artificial Neural Network (ANN) approach using Self-Organizing Maps (SOM), also known as Kohonen networks [37, 38]. SOM has been employed instead of k-Means approach [39] due to the topology preservation and 2-D visualization (as a map) properties.

The paper scheme is the following, section II describes the device fabrication and measurement procedures and section III is devoted to a summary of some of the techniques to

analyze RTN signals. In section IV, the new technique is explained and in section V the main results are discussed. Finally, the conclusions are drawn in Sec. VI.

2.- DEVICE FABRICATION AND MEASUREMENT

The fabricated devices were based on the Ni/HfO$_2$/Si stack, with n-type silicon with a resistivity of (7-13) mΩ·cm. A 20nm-thick HfO$_2$ layer was deposited by ALD at 498K using TDMAH and H$_2$O as precursors. The structures are 5x5μm^2 square cells. The cross-sectional view of the device is shown in the inset of Figure 1. More detailed information about the fabrication process flow is given in Refs. [40, 41].

The current was recorded in the time domain by means of a HP-4155B semiconductor parameter analyzer. The voltage was applied to the top Ni electrode, while the Si substrate was grounded. Both, the I-V curves for the forming process and RS cycles were measured making use of ramped voltage signals (some set/reset curves are shown in Figure 1). Two clearly differentiated resistive states were detected (see Figure 1). The low resistance state (LRS) shows up when the CF is fully formed and the two electrodes are shorted; if the CF is ruptured in a reset process, the device conductance drops off resulting in the high resistance state (HRS).
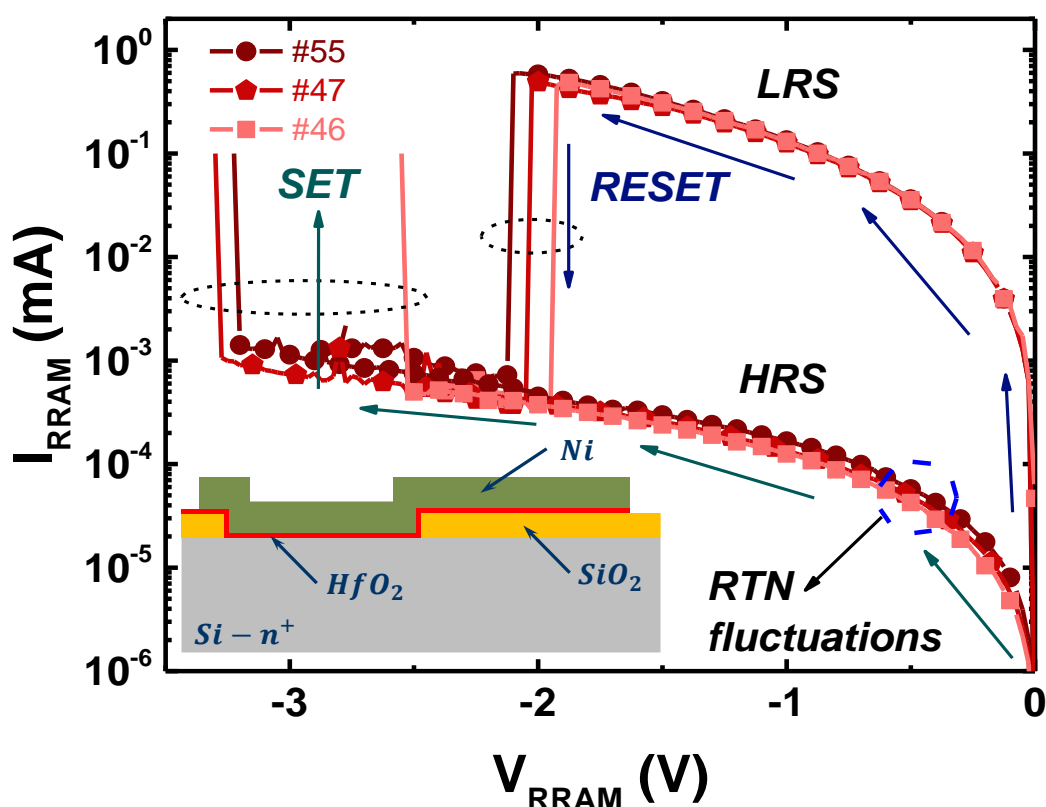
Figure 1. Current versus applied voltage for different set and reset cycles (#55, #46 and #47) within a long RS series of more than a thousand curves, I$_{CC}$=100μA. Inset: device schematic cross section. The device operation region where RTN signals are measured is highlighted.

RTN data were measured in the HRS at constant bias af V$_{RRAM}$=-0.5V for time intervals of several seconds (thousands of data were measured). The RTN signals were recorded by an automatic algorithm that considers the previous measured data making use of a smart procedure (a Matlab® software tool was employed to control the instrumentation) [41, 36]. Figure 2 shows a long register of approximately 1.2 million samples obtained for 10500 seconds and the details of two time intervals of 10 seconds (where typical RTN signals can be recognized).
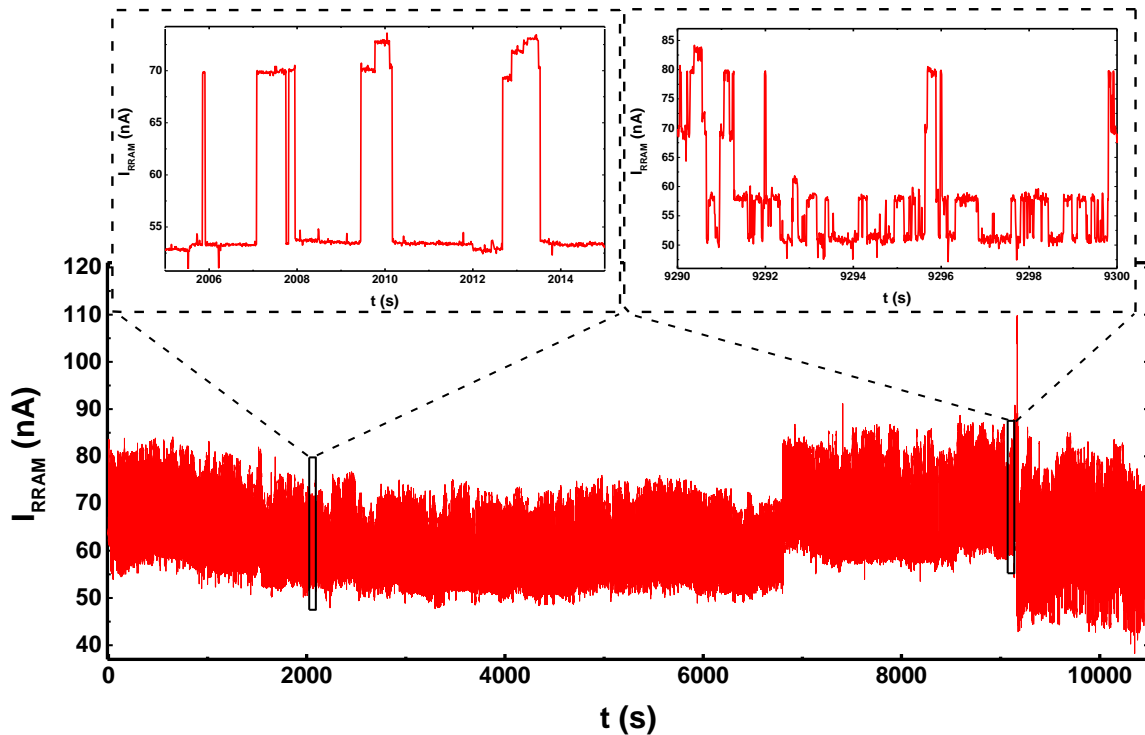
Figure 2: Current versus time for the HRS of Ni/HfO₂/Si devices at V_{RRAM}=-0.5V (more than 1.2 million data were measured in 10500 seconds). Zoomed in plots of RTN in two time windows are also shown.

3.- REVISION OF RTN ANALYSIS TECHNIQUES

The basic RTN signal representation consist of a current versus time plot. The trace consist of a series of points (I_i, t_i), where $i \in [1, N]$, being N the number of sampled data. In a basic plot it is easy to identify the number of current levels involved; in addition, a rough estimation of the more likely current states in a certain time window can be performed visually, see for instance Figure 3a (the description of the symbols employed in the Figure is presented in Table I) where a two-level RTN signal is shown in trace#640 (the original (I-t) trace was divided in 1203 intervals, from trace#1 to trace#1203). The current levels were labeled as states 0 and 1 (55nA and 72nA respectively), the 0 state being more stable than the 1 state. If the number of sampled data is high or the signal is very complex, including many current levels, irreversible states, background noise, etc., this type of plots is not adequate since much of the statistical information is not described.
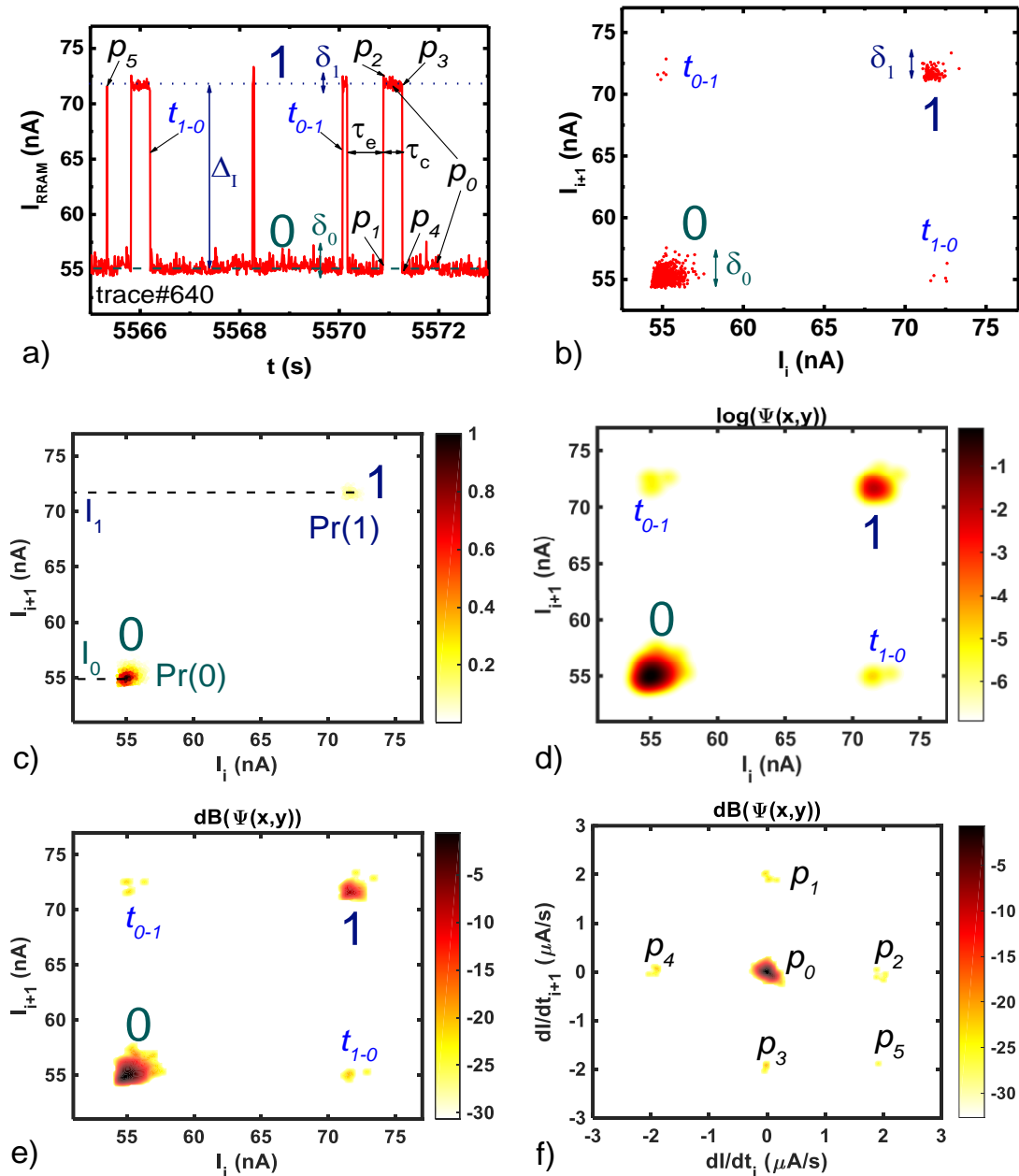
Figure 3. Different analysis methods for RTN signals. a) Current at V_{RRAM}=-0.5V versus time, trace #640 (1000 samples), b) Time lag plot (TLP) [31], c) Radius time lag plot (RTLP) [34], the most likely state is $Pr(0)$ presented by points in black, state 1 with a relative probability $Pr(1)$ close to 0.2 is shown in yellow, d) WTLP (M=200 points, α=0.1) [32,33], e) LWTLP (M=200 points, M5x5, $\sigma_f = 1.5$) [25], f) DLWTLP (M=200 points, M5x5, $\sigma_f = 1.5$) [35].

A step ahead from the direct current trace plot is the Time Lag Plot (TLP), a representation method to easily visualize some RTN features. In this type of plot, the I_{i+1} current level versus the previous value, I_i, is plotted [31], see Figure 3b. The stable current levels appear as points clusters along the diagonal of the TPL graph ($I_{i+1} = I_i$), while transitions between the current levels show up outside this diagonal. Figure 3b shows the TLP of trace#640, where two clusters represent states 0 and 1 shown in Figure 3a. Few points outside the diagonal correspond to the transitions from state 0 to state 1, t_{0-1}, and the transitions from state 1 to 0, t_{1-0}. State 0 is described by a cluster with a greater number of points and also with greater dispersion than the cluster that describes state 1 ($\delta_0 > \delta_1$).

a.- An alternative to the TLP to improve its features, known as the **Radio Time Lag Plot (RTLP)** incorporates a method to visualize the likelihood of occurrence of a point in the TLP (Figure 3c). The value associated to a given position (I_i, I_{i+1}) depends on the number of counts in the neighborhood $\xi(i,j)$, within a region described by a given radius, r, [34]. In that manner, the areas with a higher point concentration are highlighted. The method can be described by Equations 1 and 2,

$$A\big(I(i), I(i+1)\big) = \sum_{j=1}^{N-1} \xi(i,j) \tag{1}$$

$$\xi(i,j) = \begin{cases} 1 & if \quad d\{(I(j), I(j+1)), (I(i), I(i+1))\} \leq r \\ 0 & if \quad d\{(I(j), I(j+1)), (I(i), I(i+1))\} > r \end{cases} \tag{2}$$

where N is the number of samples (measured points in a (I-t) trace), d is the Euclidean distance function. The plot shows the same points as in the TLP (Figure 3b) but a colour map is employed to represent the number of points in the determined neighborhood (Pr, the relative probability normalized to unity is used).

Table I. Description of the symbols employed in Figure 3.

Mark	Description
1/0	stable states corresponding to the high/low current levels
$I_1 (I_0)$	Mean current values corresponding to the high/low current levels
Δ_I	Difference between the high and low current levels
$t_{0-1} (t_{1-0})$	Transition of low-high (high-low) current states
$\delta_1 (\delta_0)$	Variability of the high (low) current states
$\tau_e (\tau_c)$	Emission (capture) times
p_0	Current switch between stable current levels. It is obtained for stable levels, 0 or 1
p_1	Beginning of the current transition from state 0 to state 1. The *i*-derivative is close to cero, while the following (*i+1*-derivative) is positive.
p_2	End of transition revealed by p_1 (from 0 to 1). The *i*-derivative is positive, the *i+1* one is close to cero.
p_3	Beginning of the current transition from state 1 to state 0. The *i*-derivative is close to cero, while the following (*i+1*-derivative) is negative.
p_4	End of the transition revealed by p_3 (from 1 to 0 states). The *i*-derivative is negative, the *i+1*-derivative one is close to cero.
p_5	Spike between states 0-1-0. It reveals a duration in the 1 state shorter than two sampling time steps.

b.- The **Weighted Time Lag Plot (WTLP)** calculates the occurrence probability in a given position of the TLP space considering the occurrences in the rest of positions in the graph by means of the bidimensional Gaussian distribution (BGD) [32, 33, 42]. It reduces the data space (I_i, I_{i+1}) of a trace to a $M \times M$ matrix ($M < N$); that is, for each position (x, y), the probability is calculated as a weighted sum of all the sampled data (I_i, I_{i+1}). The weights are given by the distance to each occurrence and the corresponding value of the BGD. The mathematical methodology can be described by Equation 3 [32],

$$\psi(x,y) = \frac{k}{2\pi\alpha^2} \sum_{i=1}^{N-1} \exp\left(\frac{-[(I_i - x) + (I_{i+1} - y)^2]}{2\alpha^2}\right) \tag{3}$$

The values of x and y depend on the range of values to represent and the numbers of points in the matrix accordingly to Equation 4.

$$(x, y) = \left(\frac{\hat{x}}{M - 1} (I_{max} - I_{min}) + I_{min}, \frac{\hat{y}}{M - 1} (I_{max} - I_{min}) + I_{min} \right) \tag{4}$$

where $\hat{x}$ e $\hat{y}$ are the indices of the matrix of values to be displayed ($\hat{x} = 0,1, \dots M - 1$ $\hat{y} = 0,1, \dots M - 1$), and I_{max} e I_{min} are the maximum and minimum current values used in the plot. Figure 3d shows the WTLP of the trace #640 in logarithmic scale with a value of M=200. The state with the higher probability of occurrence can be easily visualized in the main diagonal making use of a color map. Both methods (RTLP and WTLP) are computationally expensive.

c.- The ***Locally Weighted Time Lag Plot*** reduces the space (I_i, I_{i+1}) to $M \times M$ points (x, y) [25], like the method WTLP (Equation 4 to discretize the space (I_i, I_{i+1}) can be also used here). For the WTLP case, instead of calculating for each point (x, y) the contribution of all the points (I_i, I_{i+1}) weighted by BGD, the coordinates $(\hat{x}, \hat{y})$ are determined for each of the $N - 1$ pairs of points (I_i, I_{i+1}) by the following equation:

$$(\hat{x}, \hat{y}) = \left(int \left(M \frac{I_i - I_{min}}{I_{max} - I_{min}} \right), int \left(M \frac{I_{i+1} - I_{min}}{I_{max} - I_{min}} \right) \right) \tag{5}$$

where $int(x)$ is the function that returns the integer closest to x. For the occurrence probability calculation, different submatrices were used (for example 3×3 or 5×5) [25]; a 5x5 matrix example is shown in Figure 4 with the corresponding weights.
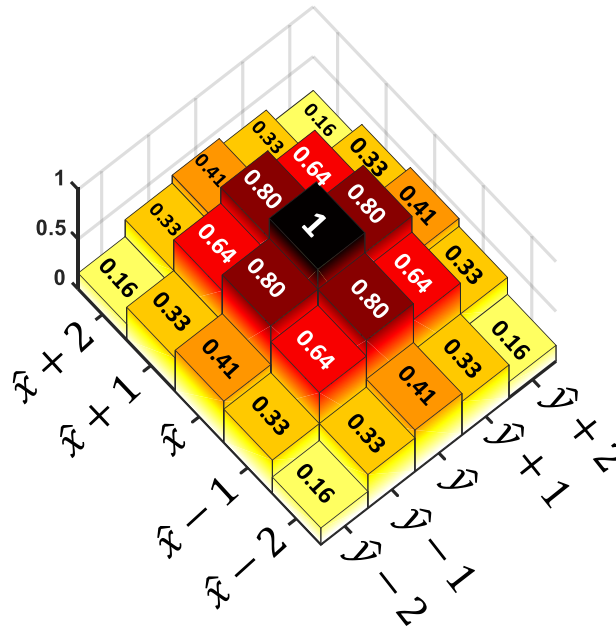
Figure 4: An example of LWTLP 5x5 matrix is shown, equal weights are plotted with the same color [25].

Figure 3e shows the LWTLP of trace #640 calculated for M=200 points and a 5x5 sub-matrix. The main virtue of this method is its computational efficiency, approximately 750 times faster than WTLP or RTLP [25].

d.- The ***Differential Locally Weighted Time Lag Plot*** (DLWTLP) is a new method of RTN representation [35] based on the numerical derivative (Equation 8) of the current with respect to time, instead of the current itself. This plot does not represent directly the RTN signal stable levels but offers information about the temporal variation sequence of current values, such as the probability of occurrence of changes between current states (p_1, p_2, p_3 and p_4) and the presence of spikes (p_5), as described in the Table I [35].

$$\frac{dI_i}{dt} \approx \frac{I_{i+1} - I_i}{t_{i+1} - t_i} \ , i = 1..N - 1. \tag{8}$$

Figure 3f shows the DLWTLP of trace #640, the occurrence of p_5 indicates the presence of spikes in the RTN signal. The marks p_1 and p_2 indicate the transition from state 0 to state 1, and the presence of marks p_3 and p_4 indicates the transition from state 1 to state 0.

4.- NEW TECHNIQUE BASED ON NEURAL NETWORK ANALYSIS

4.1.-Study of characteristic patterns in the LWTLP domain for different RTN signals

Among the methods described in the previous section, the LWTLP allows to characterize the RTN signal in a determined (I-t) trace with a low computational cost. This computation efficiency becomes evident when we need to analyze long RTN traces in comparison with other methodologies. Figure 5 shows the LWTLP (M5x5 and M=50 points) for different types of RTN signals found in the long trace in Figure 2. Figure 5a shows trace #21 (multilevel fluctuation with three current levels) and Figure 5b the corresponding LWLTP; Figure 5c shows trace #148 (representing background noise), Figure 5d shows the related LWTLP. Figure 5e represents trace #268 (a stable two current level fluctuation), Figure 5f plots the LWTLP for trace #268. Figure 5g shows trace #1074 (a multilevel (6 levels) non correlated transition fluctuation) and Figure 5h the corresponding LWTLP. It is revealed that different types of RTN signals show characteristic representations in terms of LWTLP patterns. The LWTLP patterns can be seen as a representation of RTN in a different domain that highlights important signal features with respect to the temporal domain, just as Fourier domain allows for the frequency analysis of a certain temporal signal.

The long-duration signal in Figure 2 (around 1.2 million sampled data) is divided into 1203 pieces (m=1203), for each of these pieces the LWTLP (M5x5 M= 50 points) is obtained. These LWTLP plots are the input set to train an artificial self-associative neural network. In SOM, each neuron plays the role of a cluster head and is connected to all the input variables. During training, neurons adapt the weights that connect them to inputs. Specifically, a similarity measure-based algorithm is used to determine the most similar neuron or cluster head. This neuron and their neighboring nodes slightly modify their own weights in order to increase the similarity with that particular input in the training process. The strength of the adaptation process decreases both with distance (the effect is higher on closer neurons) and time (the last training examples have less influence on the map than the first examples). After training, the patterns are clustered by mapping them to the most similar neuron. One advantage of using SOM with respect to well-known methods, such as k-means [39], and which motivated our choice, is the preservation of the topology. In our application, it is interesting to know that patterns corresponding to a certain neuron will be similar to patterns corresponding to the neighboring nodes and visualize this information in the 2D map. See the Appendix for further details.

Several network sizes have been tested for this purpose and we found that a 5x4 neurons network is an acceptable compromise between the number of clusters or classes obtained and the elements classified in each of the classes. In the training process 1203 input vectors (2500 dimension) were used for their training employing 4000 epochs (iterations for learning performed by the network, updating the weight W_i), using 31 minutes in this process (for an Intel ® Core™ i7-7700HQ CPU @2.8GHz and 24GB RAM). The graphic representation of the neural network is presented in Figure 6. The degree of connection of each neuron with its neighbors is represented by a color scale (dark black furthest, clear-yellow closer).
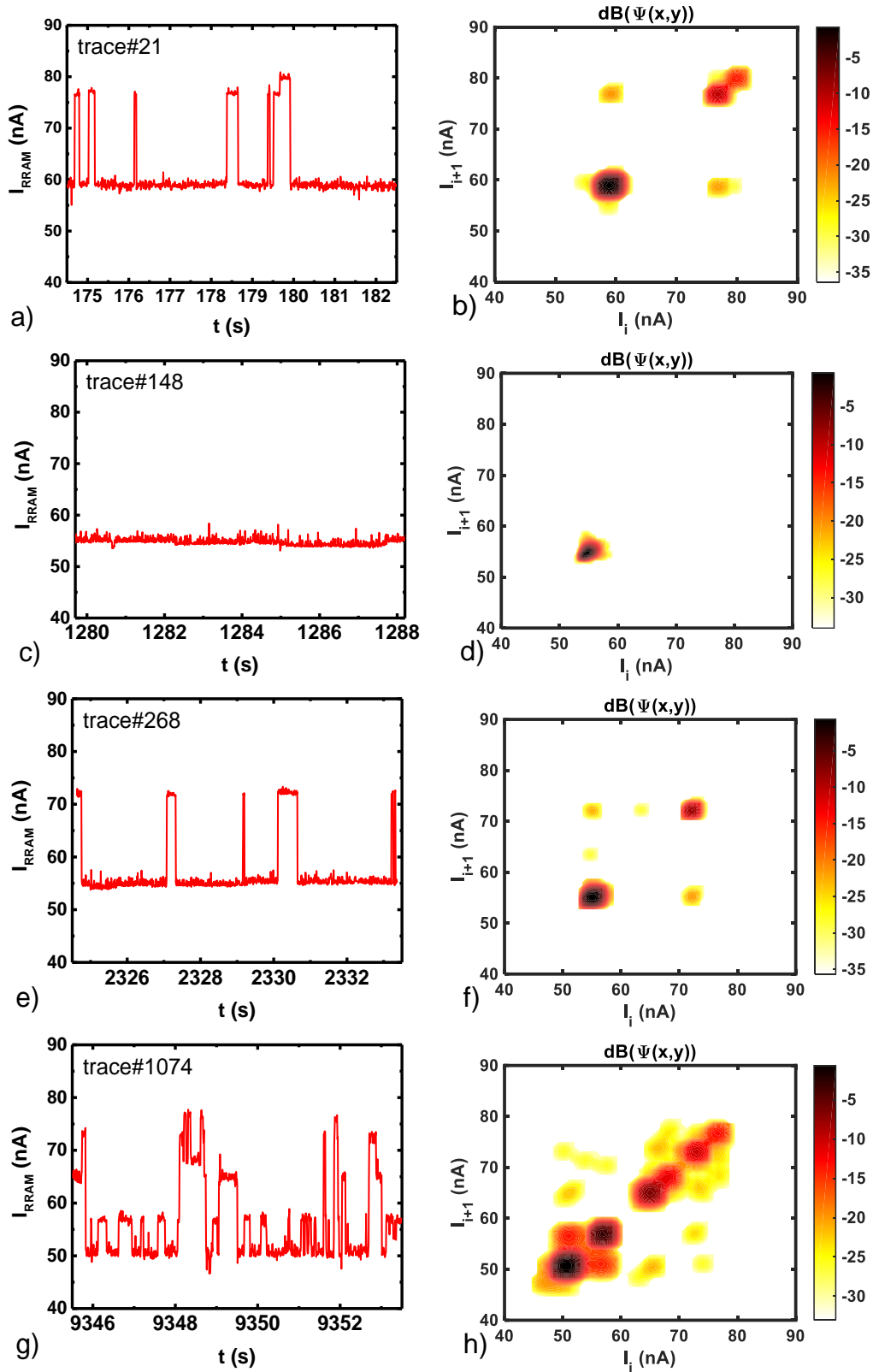
Figure 5: Examples of different types of RTN signals found in the long trace represented in Figure 2. Comparison of (I-t) trace time intervals and the corresponding LWTLPs (with M5x5 and M=50 points [25]). a) Trace #21 (multilevel fluctuation with 3 current levels), b) LWTLP of trace #21; c) Trace #148, (background noise), d) LWTLP of trace #148; e) Trace #268 (stable two current level fluctuation), f) LWTLP of trace #268; g) Trace #1074 (multilevel (6 levels) non correlated transitions fluctuation), h) LWTLP of trace #1074.
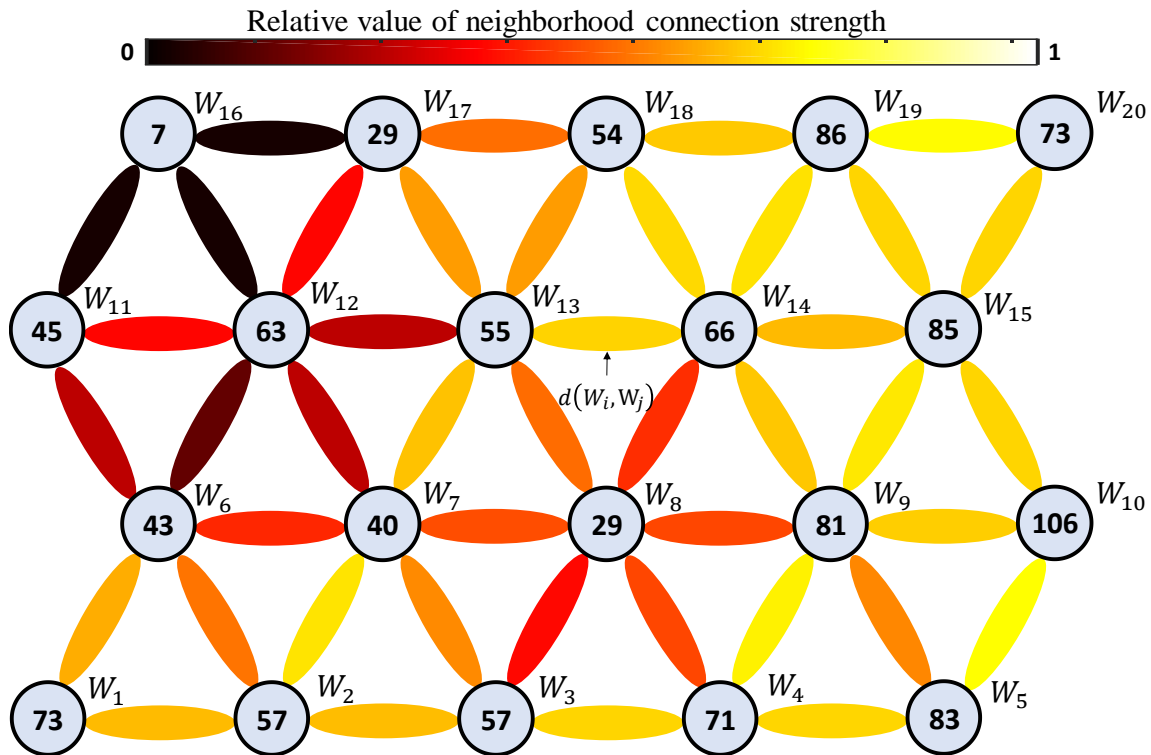
Figure 6. Representation of the SOM 5x4 neural network employed for our analysis. The circles represent the neurons, the number within the circles stand for the number of LWTLP patterns associated to each clusterhead (neurons). The neighborhood connection strength of the neurons in the self-associative network is represented in colour (a dark colour connection between the neurons corresponds to a large Euclidean distance between them, i.e., Euclidean distance of the corresponding neurons weights $d(W_i, W_j)$. On the other hand, a light colour between the neurons connection means that neurons are close to each other in terms of Euclidean distance). A two-dimensional mapping is employed for the implemented ANN, we have chosen this particular topology although others can be employed.

The neural network provides a total of 20 clusters (C#1 to C#20) to classify each of the 1203 input vectors (RTN traces), notice that the sum of the number of patterns associated to the 20 different clusters represents the 1203 traces. Figure 6 represents the number of input vectors that have been classified in each cluster, we have clusters with many associated vectors (C#10 =106) and others sparsely populated (C#16 =7).

5.- RESULTS AND DISCUSSION

The main result of the new procedure introduced here can be found at the output of the ANN training process. A set of clusters that allow the classification of the RTN signals experimentally measured is obtained. The pattern characteristics associated to each cluster represent a particular configuration of the RTN signal in terms of number of current levels, their corresponding likelihood of occurrence, current levels transitions, background noise, etc. In order to shed light on this issue, we present three examples of the patterns associated to the cluster C#1, C#11 and C#16, obtained after the ANN training process. They are shown in Figure 7, C#1: a) trace #188, b) trace #101, c) trace #868; Figure 8, C#11: a) trace #1061, b) trace #1069, c) trace #1086; and Figure 9 C#16: a) trace # 148, b) trace # 427, c) trace # 553). In these figures we can observed the (I-t) traces and the corresponding LWTLPs (calculated with M5x5 and M=50 points).
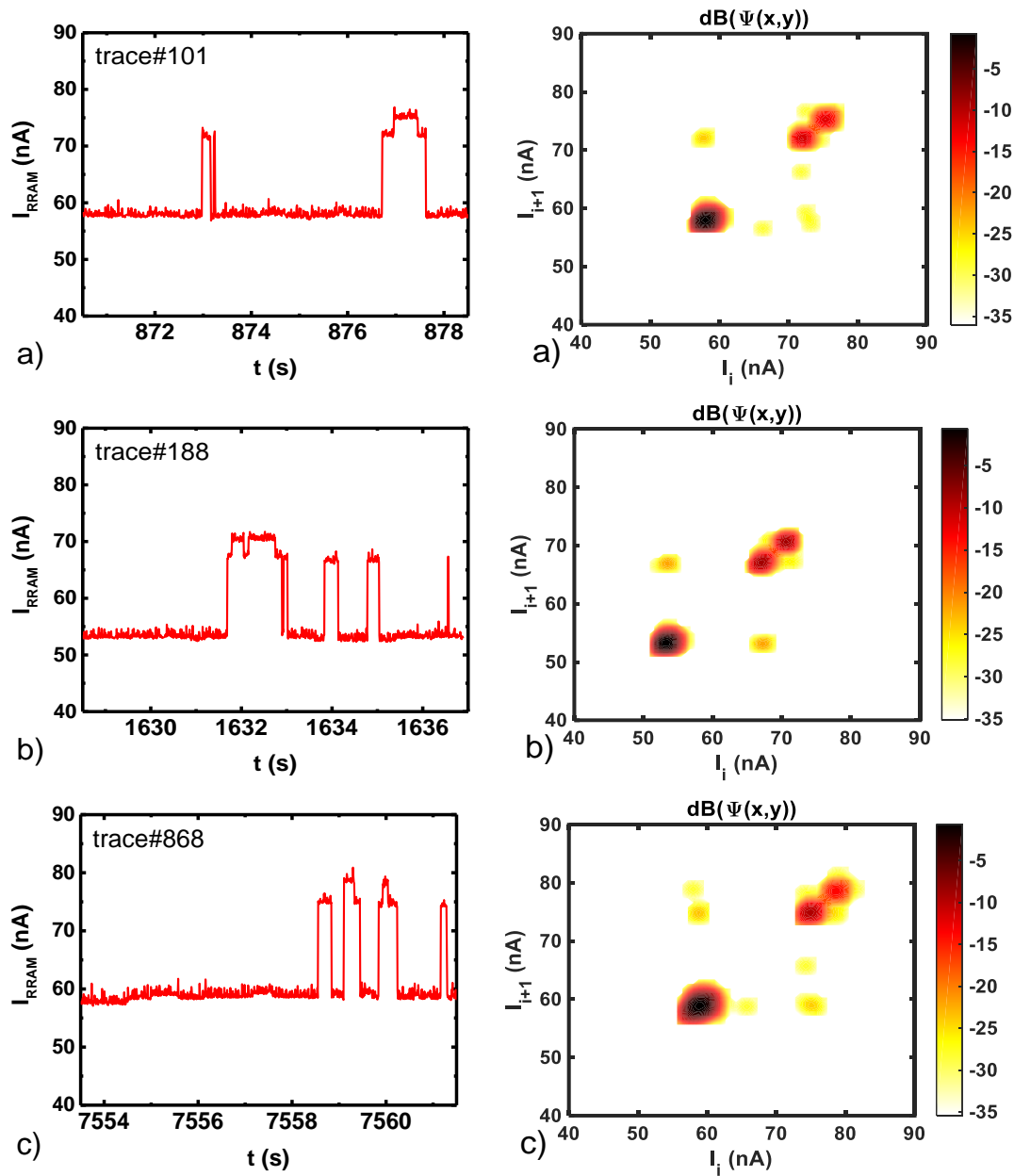
Figure 7. I-t trace plots and corresponding LWTLPs (calculated with M5x5 and M=50 points) classified in the same cluster C#1: a) trace #188, b) trace # 101, c) trace # 868.

In Figure 7 we deal with signals that show three current levels. Notice that the traces considered are just different parts of a long RTN trace (Figure 2), these traces corresponding to different time windows. The three corresponding dark clusters of points in the LWTLPs plots are clearly detected. In all cases we see this behavior, although we can distinguish certain differences in the probability of occurrence of each of these current levels.
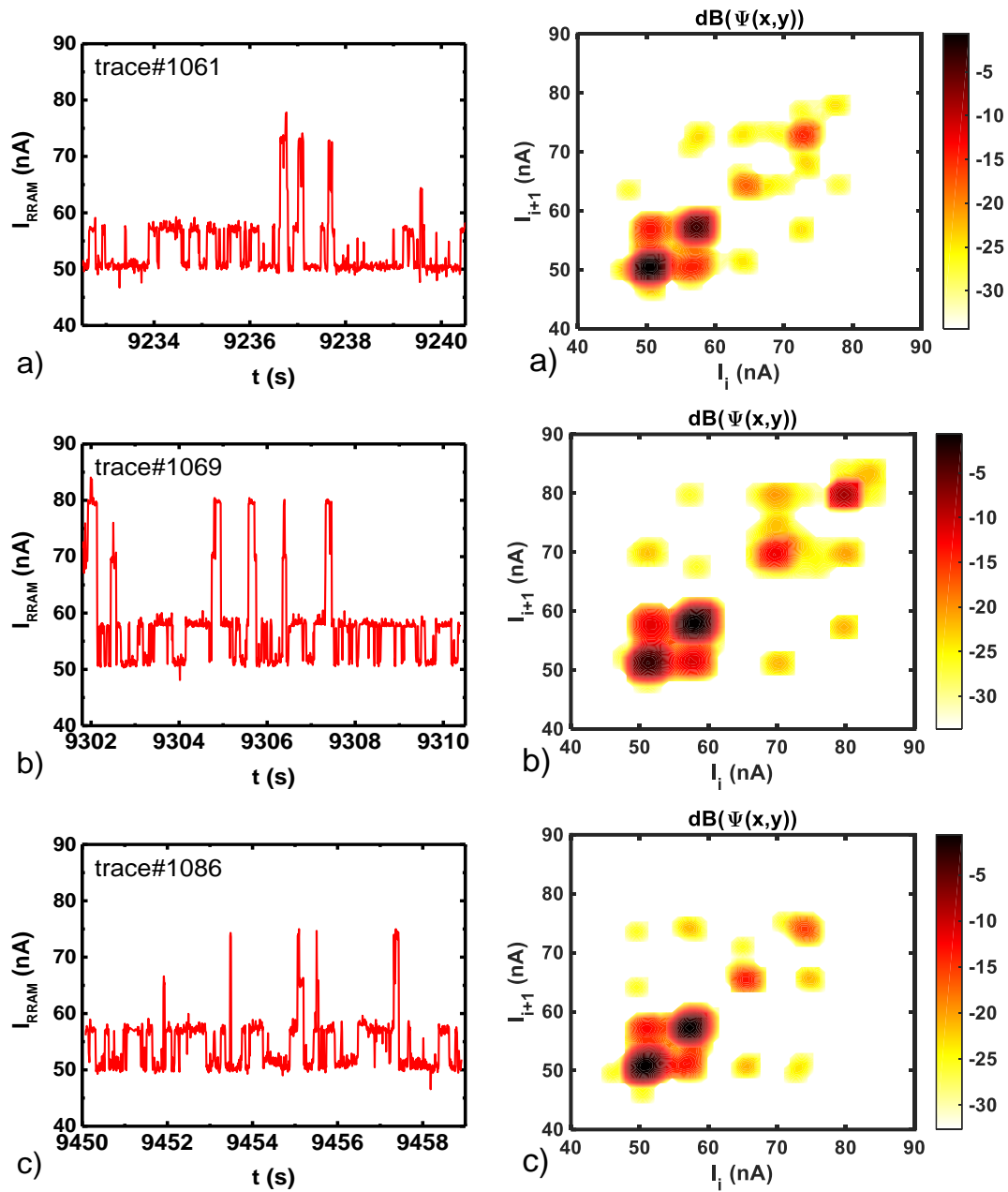
Figure 8. I-t trace plots and corresponding LWTLPs (calculated with M5x5 and M=50 points) classified in the same cluster C#11: a) trace #1061, b) trace # 1069, c) trace # 1086.

In Figure 8 the signals associated to cluster C#11 show four current levels, the LWTLP patterns clearly indicate this fact, although variance in the probability of occurrence is observed. The traps linked to the current levels seem to be independent and additive since the patterns in the LWTLP domain are stable and independent.
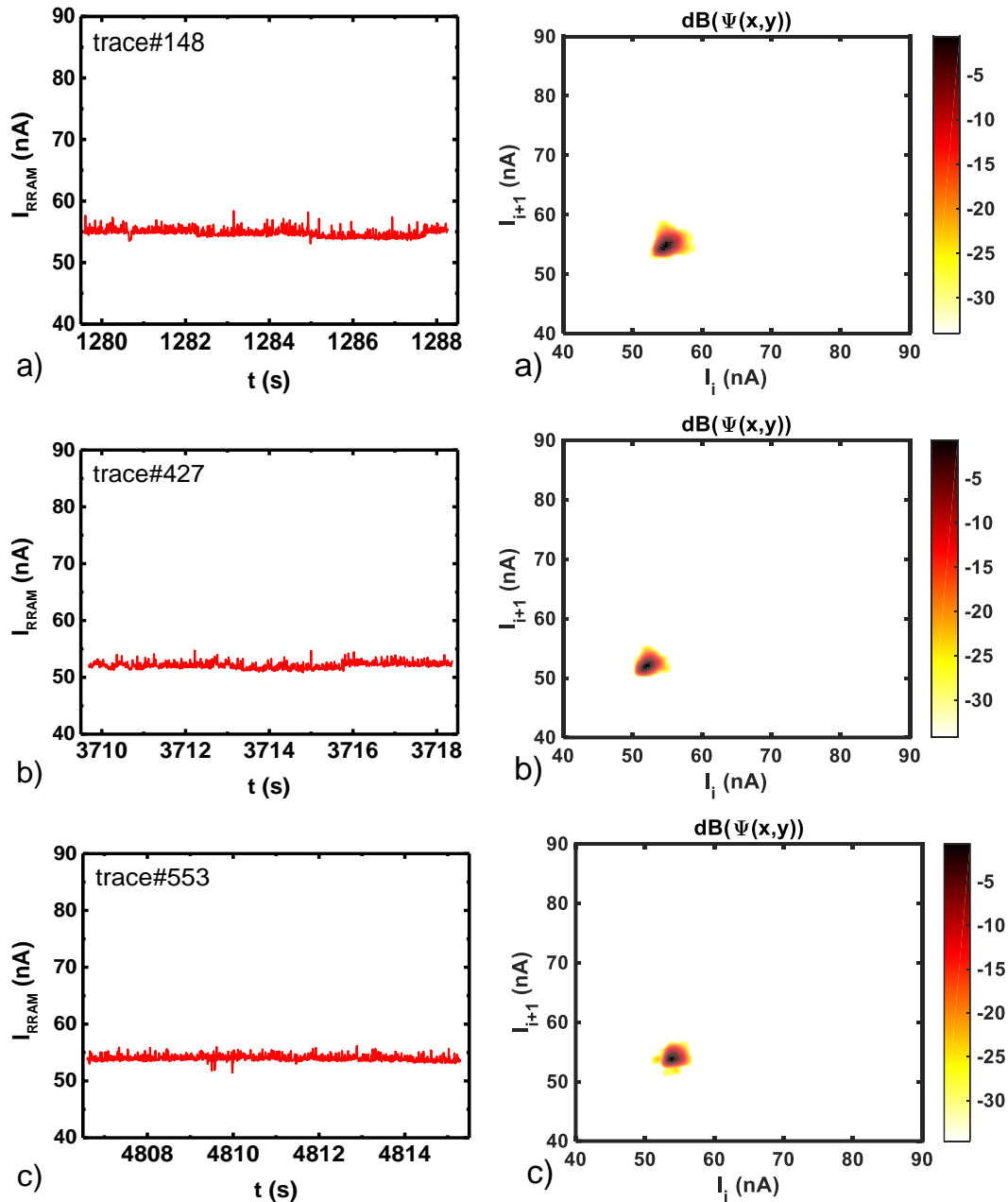
Figure 9. I-t trace plots and corresponding LWTLPs (calculated with M5x5 and M=50 points) classified in the same cluster C#16: a) trace #148, b) trace #427, c) trace # 553.

In Figure 9 the representations indicate that we are facing background noise. No clear current levels can be appreciated. As expected, a single cluster of points at the LWTLP domain center is obtained in all cases.

According to the obtained results, for the neuron set selected, the most representative LWTLP patterns (and consequently the RTN signals) are classified after the training process. In order to highlight this point, one LWTLP pattern (footprint) for each of the 20 clusters produced (C#1 to C#20) is shown in Figure 10. A general view of this figure allows to summarize the main features of the RTN signal plotted in Figure 2.

187
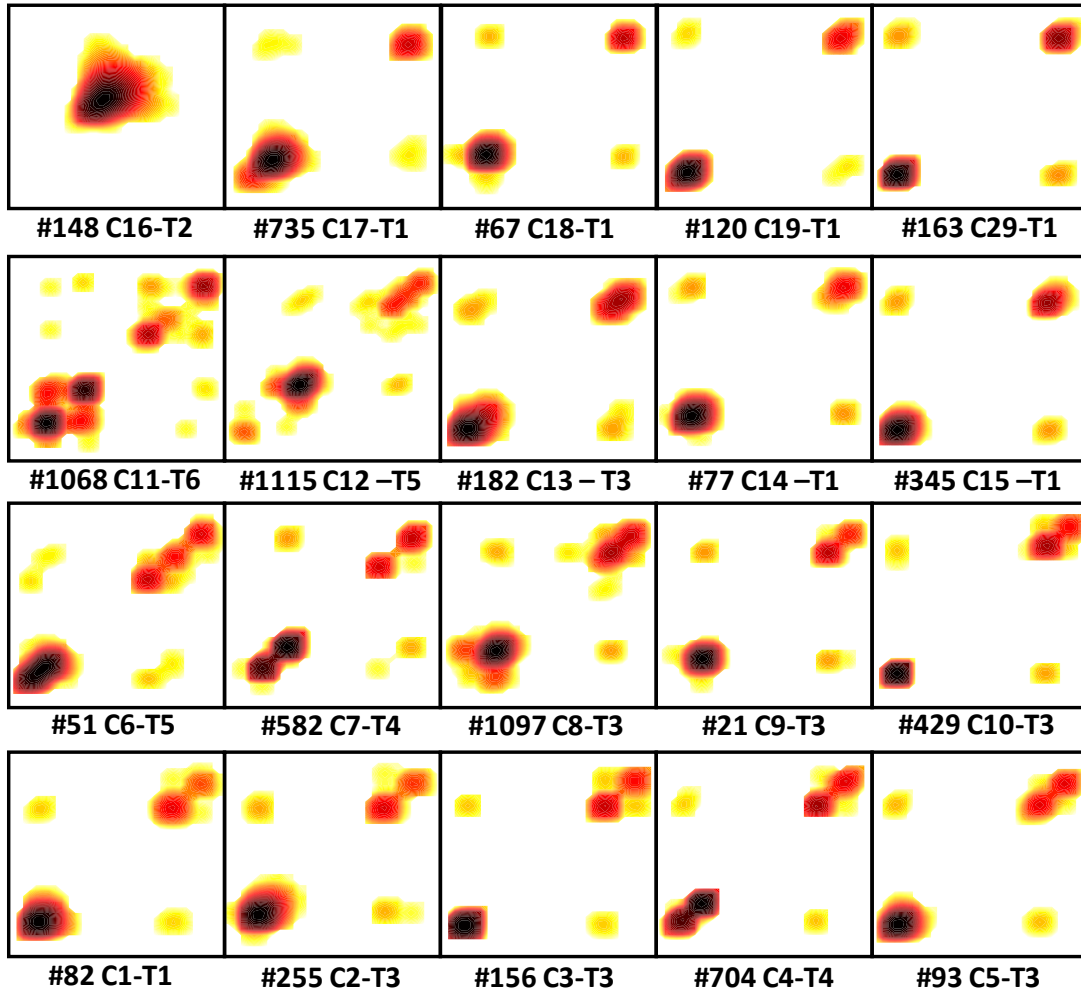
Figure 10: LWTLP pattern types for each of the 20 clusters obtained (C1 to C20) after SOM training process. The classification of the obtained RTN signal reference patterns is described in Table II.

These results are comprehensively classified in Table II, the classification of the LWTLP patterns is done by considering six different RTN signal reference types (T1 to T6). The corresponding probability for these reference types is also given for comparison purposes.

Table II. LWTLP pattern classification based on RTN fluctuation types.

Type of RTN fluctuation			Clusters #	RTN Type	%
Two-Levels	Stable-Current		14,15,17,18,19,20	T1	32,67
	Background noise		16	T2	0,58
Multilevel	Non correlated transitions	3-levels	1,2,3,5,8,9,10,13	T3	44,97
		4-levels	4,7	T4	9,23
		5-levels	6,12	T5	8,81
	Interactive defects		11	T6	3,74

Finally, the evolution of the reference fluctuation types (shown in Table II) along the RTN trace under consideration is represented in Figure 11. It can be observed that the most probable LWTLP pattern corresponds to the reference type T3 (44.97%) followed by reference type T1 (32.67%). Reference type T3 corresponds to a RTN signal with three current levels. This pattern may be explained by the activation of two defects, one generates two different current levels and

the other produces other two levels, one of them merges with one of the levels of the companion defect. Reference type T1 corresponds to a two level stable current fluctuation produced by a single active defect. These are the two most probable situations. In relation to reference type T6, it is important to highlight that interactive defects refer to defects whose fluctuation may involve changes in the occupation probability of other traps, resulting in a large distribution of switching times and RTN amplitudes [36]. In our calculations, T6 is unlikely although it can occur. T4 and T5 can be attributed to two or three active defects.
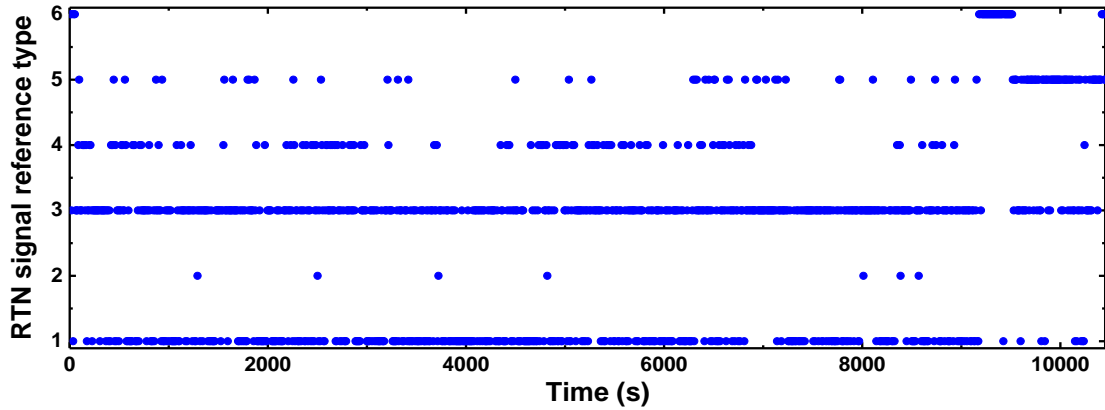
Figure 11. Evolution of the reference fluctuations types (T1-T6) employed to classify the RTN signals corresponding to the LWTLP patterns shown in Figure 10.

An interesting issue is related to the ability of the method to track the probability that a transition type is reached from another type. The evolution of the RTN signal reference types (T1-T6) shown in Figure 11 allows the determination of the state transition matrix that represents the count of observed transitions from state i to state j (i and j ∈ [T1, T6]) and can be represented graphically as a Discrete-Time Markov Chain, see Figure 12. This latter mathematical tools has been previously employed in the analysis of RTN signals [49].
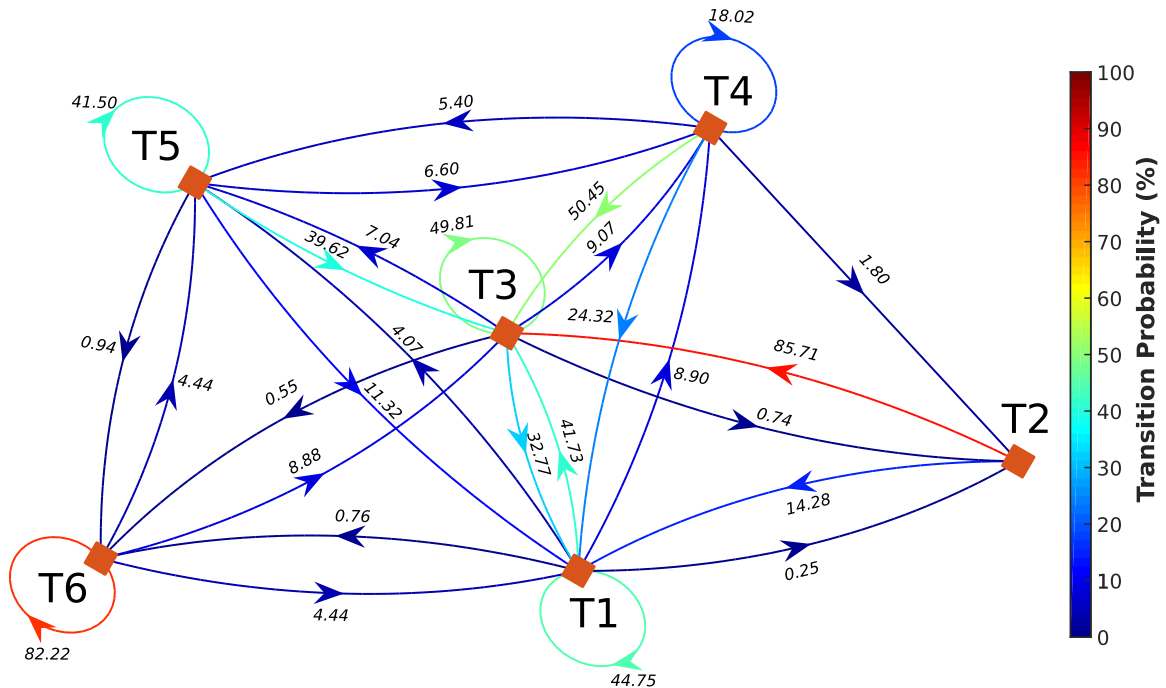
Figure 12: Discrete-Time Markov Chains extracted from evolution of the fluctuations reference types of figure 11. Notice that we have used a non-normalized transition matrix, the transition probabilities are multiplied by 100 to ease the interpretation with percentages.

Several conclusions can be drawn from the interpretation of Discrete-Time Markov Chains. Being in state T1, it is most likely to remain in T1 (44.75%) and the most probable transition from T1 is to T3 with a probability of 41.73% (this would correspond to the activation of an additional defect in addition to one currently active). Most likely, T1 will be preceded by T3 (32.77%) or T4 (24.32%) and these two latter transitions could correspond to the deactivation of a defect. The transition from T2 (14.28%) may be due to the activation of a defect in the case none were active and the transition from T5 (11.32%), corresponds to the deactivation of two defects, which has less likelihood as expected. The probability of reaching T2 is low and the most probable case would be preceded by T4 (1.8%). From T2 we will most likely end up in T3 (85.71%) as well as it is not likely to remain in T2. Other transitions can be easily described by using Figure 12. The knowledge of the state transitions and the occupancy probability of RTN reference types can be employed to deepen physically speaking on the nature of RTN signals. This is linked to the number and type of active defects in each time window. In addition, this method correlates the nature of electrically active defects with the trap response at the device level. This correlation allows to define optimal design rules to keep a defect control and optimize the device performance. The Markov chain transition matrix can also help on facets such as the use of RRAMs as entropy sources for random number generators and physical unclonable functions, used in applications such as stochastic computing or hardware security [50].

It is also interesting to comment on the issue linked to the time intervals employed to perform this study since these time intervals can be chosen at will for a determined long experimental (I-t) set of data. The length of the time intervals could affect the results obtained by the methodology presented here that is why we analyze it. The number of traces (denoted by N in previous sections) would change depending on the number of sampling points (NSP) for the time windows selected (N, as we denoted it Section 2). This choice would influence the LWTLPs obtained; therefore, there could be changes in the types of clusters obtained (Figure 10) and in the time linked to the RTN signal reference types (last column of Table II). We have tried to perform a study to clarify the impact of the NSP on the obtained results. In Fig. 13, experimental current values for a determined time interval corresponding to N=1500 (Figure 13a) are shown. It can be observed that depending on N in this particular case (i.e., the length of the time window), the associated LWTLPs are different since certain current levels can be included (or not) and this is reflected upon the LWTLP.

The whole study for intervals with different N has been performed, where no significant differences were observed regarding the clusters shown in Figure 10. With respect to the time associated to the different RTN fluctuation types, the results have been presented in Table III.

Table III. Time expressed in percentage associated to the RTN fluctuation types obtained in the SOM training process for intervals with different number of sampling points.

	NSP = 500	NSP = 750	NSP = 1000	NSP = 1250
T1 (%)	44.20	39.72	32.67	30.61
T2 (%)	6.48	1.01	0.58	-
T3 (%)	41.71	43.82	44.97	47.67
T4 (%)	4.53	7.82	9.23	8.69
T5 (%)	1.45	4.29	8.81	9.31
T6 (%)	1.62	3.34	3.74	3.72

Although some differences can be appreciated for the shorter time intervals, there is a saturation effect for $N > 750$. In this case no significant changes are obtained in the results, as can be seen in Table III. We selected N=1000 both to have a higher number of traces (m) than for N>1000, and consequently increase the number of input vectors for the ANN training process, and because of the results obtained in Table III show no significant differences to the case N=1250. In these considerations it is the optimum N value.
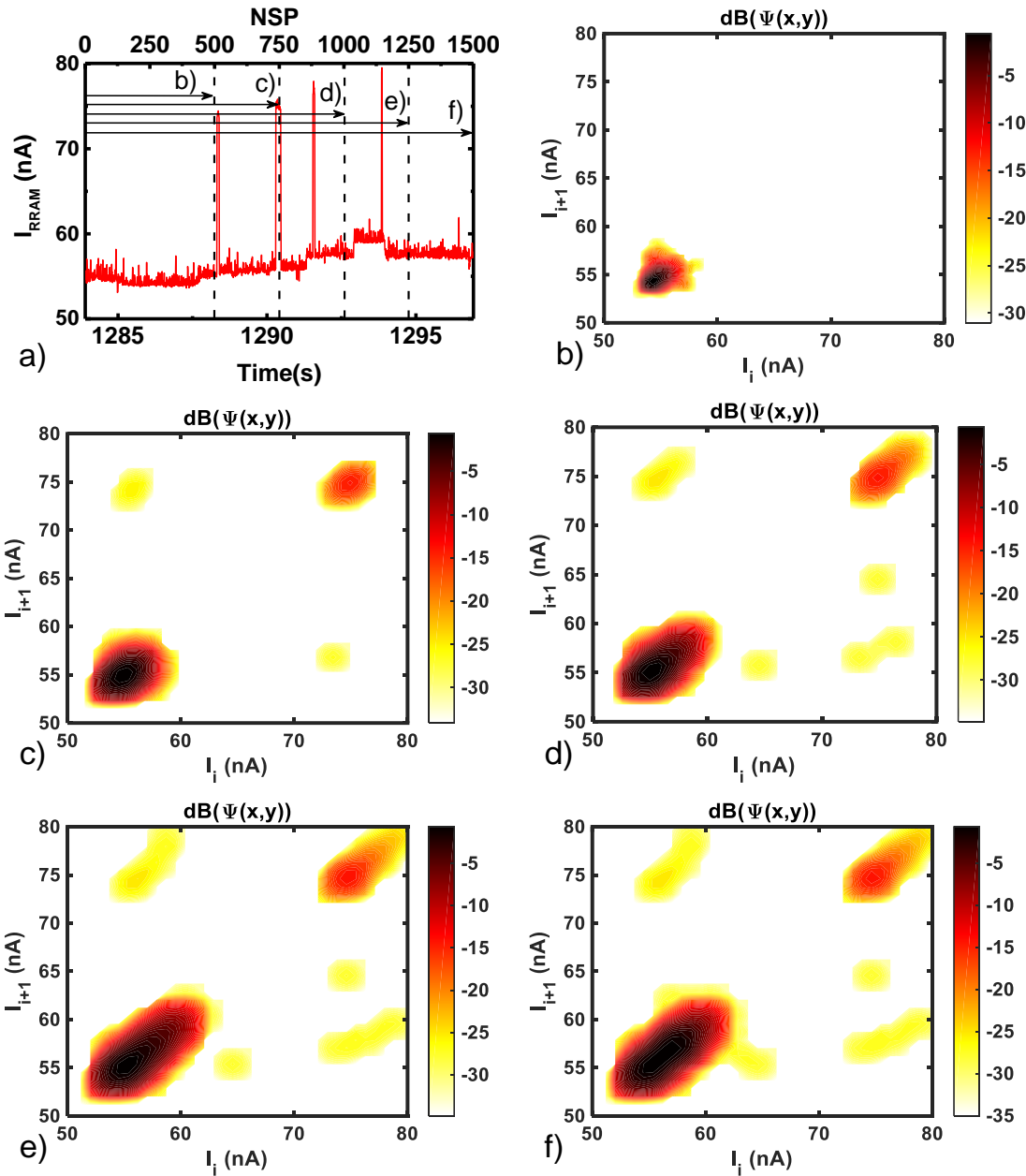
Figure 13. (a) Current versus time for the studied time intervals of measured data indicated by (b), (c), (d), (e) and (f). LWTLPs for time intervals with different N, b) 500 sampling points, c) 750 sampling points, d) 1000 sampling points, e) 1250 sampling points and f) 1500 sampling points.

5.- CONCLUSIONS

A new technique based on ANN has been implemented to analyze RTN signals. The procedure takes advantage of the analysis of SOMs based on the data obtained by means of the LWTLP technique for sets of experimental RTN data taken from a long (I-t) trace. In particular, we can graphically characterize by the LWTLP sequence of RTN data (for instance, 1000 sampled current versus time data) with a high processing speed by means of a pattern (50x50 points) set. With these pattern set, making use of its vector form, we train a SOM neural network (in our case a network made of 5x4 neurons) that allows us to classify each of the 1203 input sequences (RTN signals for a determined time window) in each of the 20 patterns that have been generated by the neural network training process. An individualized analysis of each of the 20 patterns allows the classification of the different types of current fluctuations present in a long sequence of RTN data, more than 1.2 million sampled data for our particular measurement. Once these results have been achieved, the graphical representation of the type of fluctuations that can be found at each time window in the complete long RTN signal can be determined. Finally, we concluded that six types of patterns were present in the RTN signal trace we analyzed, including stable 2-level current fluctuations, multilevel transitions and the presence of background noise.

6.- ACKNOWLEDGMENTS

7.- APPENDIX

Self-organizing maps (SOM), also namely as Kohonen networks [37, 38], are accounted among the artificial neural networks (ANN). They are bio-inspired software models based on neuron organization into the human brain [Ch. 4, 43]. In this work, SOMs are used for the task of clustering patterns as a visual alternative to other well-known approaches such as k-means [39]. Note that in the context of deep learning [44], other unsupervised approaches such as the Restricted Boltzmann Machine (RBM) [45], Variational Autoencoders (VAEs) [46] or Generative Adversarial Networks (GANs) [47] among others go beyond the clustering task and try to learn a probabilistic model of the dataset.

The training process linked to SOMs makes use of an unsupervised learning algorithm, it allows to analyze and visualize high-dimensional data into a low-dimensional discretized space (they are mostly employed in a two-dimensional domain, the designated map) that represents the input space of the training samples. Two main SOM features make them different from other widely used ANNs in supervised or semi-supervised tasks, such as the Multi-Layer Perceptron (MLP), Convolutional Neural Networks (CNNs) or Recurrent Neural Networks (RNNs) [44]. On the one hand, they are competitive neural networks that implement the winner-take-all function; on the other hand, they have a neural network plasticity that modifies the local synaptic weight as a function of the neighborhood related data.

The training expression for a neuron i with weight vector $W_i(e)$ that we have employed here is the following:

$$W_i(e+1) = W_i(e) + \Omega(i,j,e) \cdot \alpha(e) \cdot [LWTLP(t) - W_i(e)] \quad \begin{cases} \forall i = 1 \dots n \\ j \in \{1..n\} \\ \forall t = 1 \dots m \end{cases} \quad \text{(A.1)}$$

$$\Omega(i,j,e) = \begin{cases} 0 & if & d_{i,j} > d \\ 1 & if & d_{i,j} \le d \end{cases} \quad \text{(A.2)}$$

Where e is the step training index, i is the index of the actual neuron weight vector to update $W_i(e+1)$, $LWTLP(t)$ is the vector input characteristic of each RTN signal trace, j is index of

the best matching unit (BMU) that represents the neuron whose weight vector $W_j(e)$ is most similar to the input vector $LWTLP(t)$, t is the index of the input vector $LWTLP(t)$, m is the number of input vectors $LWTLP(t)$. $\alpha(e)$ is a monotonically decreasing learning coefficient (for example, we could use this analytical description $\alpha(e) = \alpha_0/(1 + k \cdot e)$, where, α_0 is the initial learning coefficient and k is a parameter, $k > 0$), $\Omega(i,j,e)$, as a function of variable e, represents the neighborhood function which gives the distance $(d_{i,j})$ between the neuron i (actually updated neuron $W_i(e+1)$) and the best matching unit j. If the neuron i is near neuron j $(d_{i,j} \leq d)$ then the neuron i is updated (Equation A.2). Variable n is the number of neurons in the network (usually $n = x \cdot y$, where x and y are integers; in this respect, although we have employed 10·10, 6·6, 5·5 topologies, we found that an optimum choice was 5·4).

The training utilizes a competitive learning method to update the weight of the network $W_i(e+1)$. When an input training vector $LWTLP(t)$ is fed to the neurons network, W_i ($\forall i = 1...n$), its Euclidean distance to all weight vectors is computed. Neuron j, whose weight vector, $W_j(e)$, is the most similar to the input vector $LWTLP(t)$ (BMU), is determined. The BMU weights and neurons close to it in the SOM grid are recalculated taking into consideration the input vector (in our particular case, as explained in section 4, we have m=1203 input vectors and 4000 epochs). The magnitude of the changes in $W_i(e+1)$ decreases with each training step (depending on function $\alpha(e)$) and with the grid-distance too (function of $\Omega(i,j,e)$) [48].
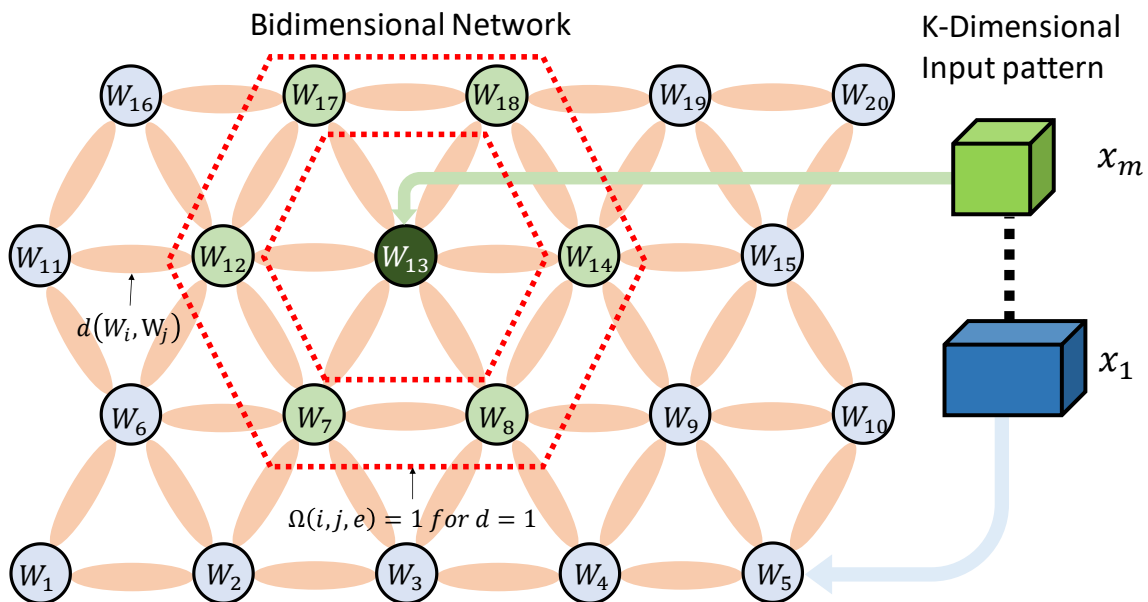
Figure A1: Example of SOM neighbors connections on a 5x4 neurons network. The connection of the neurons is done in the form of a bee panel (hexagonal arrangement), the number of inputs is an array of m values of K dimension (in our application m=1203 and K=2500). Each input pattern is assigned to the most similar neuron W_i. In training time the weight of each neuron is updated by equation A.1 (taking into account the neighborhood function described in Equation A.2). When the training process is finished, each new input pattern produces the activation of only one neuron of the network (for example, input pattern x_m produced the excitation of neuron W_{13}, the output signal of this is 1) while the rest of the neurons in the network are deactivated (producing a null output signal), the index of the active neuron determines the cluster or class assigned to the input.

The input $x(t)$ of the SOM is one K dimensional vector, the matrix LWTLP $(M \times M)$ is transformed in a K dimensional vector ($K = M \times M$), concatenating each row LWTLP matrix to the following one.

These are the ANN we have employed here to perform the analysis presented in this work. The results consisted of a set of clusters (where each neuron is a cluster head) obtained by using SOM with the goal to classify LWTLP patterns and characterize RTN signals.

References

[1] F. Pan, S. Gao, C. Chen, C. Song, F. Zeng, "Recent progress in resistive random access memories: materials, switching mechanisms and performance", Materials Science and Engineering, 83, pp. 1-59, 2014.

[2] M. Lanza, H.-S. P. Wong, E. Pop, D. Ielmini, D. Strukov, B.C. Regan, L. Larcher, M.A. Villena, J.J. Yang, L. Goux, A. Belmonte, Y. Yang, F. M. Puglisi, J. Kang, B. Magyari-Köpe, E. Yalon, A. Kenyon, M. Buckwell, A. Mehonic, A. Shluger, H. Li, T.-H. Hou, B. Hudec, D. Akinwande, R. Ge, S. Ambrogio, J.B. Roldan, E. Miranda, J. Suñe, K.L. Pey, X. Wu, N. Raghavan, E. Wu, W.D. Lu, G. Navarro, W. Zhang, H. Wu, R. Li, A. Holleitner, U. Wurstbauer, M. Lemme, M. Liu, S. Long, Q. Liu, H. Lv, A. Padovani, P. Pavan, I. Valov, X. Jing, T. Han, K. Zhu, S. Chen, F. Hui, Y. Shi, "Recommended methods to study resistive switching devices", Advanced Electronics Materials, 5, 1800143, 2019.

[3] S. Menzel, P. Kaupmann, R. Waser, "Understanding filamentary growth in electrochemical metallization memory cells using kinetic Monte Carlo simulations", Nanoscale, 7, 12673, 2015.

[4] M.A. Villena, J.B. Roldán, F. Jiménez-Molinos, E. Miranda, J. Suñé, M. Lanza," SIM2RRAM: a physical model for RRAM devices simulation", Journal of Computational Electronics, 16, p. 1095, 2017. https://doi.org/10.1007/s10825-017-1074-8

[5] D. Ielmini, R. Waser. "Resistive Switching: From Fundamentals of Nanoionic Redox Processes to Memristive Device Applications", Wiley-VCH, 2015.

[6] S. Yu, Y. Wu, R. Jeyasingh, D. Kuzum, H.-S. Wong, "An electronic synapse device based on metal oxide resistive switching memory for neuromorphic computation", IEEE Trans. Electron Devices, 58 (8), pp. 2729–2737, 2011. doi: 10.1109/TED.2011.2147791.

[7] S. Yu, "Neuro-inspired computing using resistive synaptic devices", Springer, 2017. ISBN: 978-3-319-54312-3

[8] J. Zahurak, K. Miyata, M. Fischer, M. Balakrishnan, S. Chhajed,D. Wells, Li Hong, A. Torsi, J. Lim, M. Korber, K. Nakazawa, S. Mayuzumi, M. Honda, S. Sills,S. Yasuda, A. Calderoni, B. Cook, G. Damarla, H. Tran, Bei Wang, C. Cardon, K. Karda, J. Okuno, A. Johnson, T. Kunihiro, J. Sumino, M. Tsukamoto, K. Aratani, N. Ramaswamy, W. Otsuka,K. Prall. "Process integration of a 27nm, 16Gb Cu ReRAM", Electron Devices Meeting (IEDM), pp.6.2.1-6.2.4, 2014.

[9] T.Y. Liu, T. H. Yan, R. Scheuerlein, Y. Chen, J. K. Lee, G. Balakrishnan, G. Yee, H. Zhang, A. Yap et al., "A 130.7-mm2 2-Layer 32-Gb ReRAM Memory Device in 24-nm Technology", IEEE J. Solid-State Circuits 49, pp. 140-153, 2014.

[10] A. Kawahara, R. Azuma, Y. Ikeda, K. Kawai, Y. Katoh, Y. Hayakawa, K. Tsuji, S. Yoneda, A. Himeno, et al., "An 8 Mb Multi-Layered Cross-Point ReRAM Macro With 443 MB/s Write Throughput", IEEE J. Solid-State Circuits 48, pp. 178-185, 2013.

[11] H.-S P. Wong, H.-Y. Lee, S. Yu, Y.-S. Chen, Y. Wu, P.-S. Chen, B. Lee, F. Chen, and M.-J. Tsai, "Metal–Oxide RRAM", Proceedings of IEEE, vol. 100, pp. 1951-1970, 2012, doi: 10.1109/JPROC.2012.2190369

[12] S. Aldana, P. García-Fernández, A. Rodríguez-Fernández, R. Romero-Zaliz, M.B. González, F. Jiménez-Molinos, F. Campabadal, F. Gómez-Campos, J.B. Roldán, "A 3D Kinetic Monte Carlo simulation study of Resistive Switching processes in Ni/HfO2/Si-n+-based RRAMs", Journal of Physics D: Applied Physics, 50, 335103, 2017.

[13] J. Guy, G. Molas, P. Blaise, M. Bernard, A. Roule, G. Le Carval, V. Delaye, A. Toffoli, G. Ghibaudo, Fellow, IEEE, F. Clermidy, B. De Salvo, L. Perniola , "Investigation of Forming, SET, and Data Retention of Conductive-Bridge Random-Access Memory for Stack Optimization", IEEE Transactions on Electron Devices, 62, pp. 3482-3489, 2015

[14] A. Padovani, Member, IEEE, L. Larcher, Member, IEEE, O. Pirrotta, L. Vandelli, G. Bersuker, Member, IEEE, "Microscopic Modeling of HfO x RRAM Operations: From Forming to Switching", IEEE Transactions on Electron Devices, 62(6), pp. 1998-2006, 2015.

[15] M. Bocquet, D. Deleruyelle, C. Muller, J.M. Portal, "Self-consistent physical modeling of set/reset operations in unipolar resistive-switching memories". Applied Physics Letters, 98, p. 263507, 2011.

[16] M.A. Villena, J.B. Roldán, M.B. González, P. González-Rodelas, F. Jiménez-Molinos, F. Campabadal, D. Barrera, "A new parameter to characterize the charge transport regime in Ni/HfO2/Si-n+-based RRAMs", Solid State Electronics, vol. 118, pp. 56-60, 2016.

[17] M.A. Villena, M.B. González, J.B. Roldán, F. Campabadal, F. Jiménez-Molinos, F.M. Gómez-Campos y J. Suñé, "An in-depth study of thermal effects in reset transitions in HfO2 based RRAMs", Solid State Electronics, 111, pp. 47-51, 2015.

[18] J.B. Roldán, E. Miranda, G. González-Cordero, P. García-Fernández, R. Romero-Zaliz, P. González-Rodelas, A. M. Aguilera, M.B. González, F. Jiménez-Molinos, "Multivariate analysis and extraction of parameters in resistive RAMs using the Quantum Point Contact model", Journal of Applied Physics, 123, 014501, 2018.

[19] Z. Jiang, S. Yu, Y. Wu, J. H. Engel, X. Guan, and H.-S. P. Wong, "Verilog-A Compact Model for Oxide-based Resistive Random Access Memory (RRAM)," International Conference on Simulation of Semiconductor Processes and Devices (SISPAD), pp. 41 – 44, 2014. DOI: 10.1109/SISPAD.2014.6931558

[20] Huang, X. Y. Liu, B. Chen, H. T. Li, Y. J. Wang, Y. X. Deng, K. L. Wei, L. Zeng, B. Gao, G. Du, X. Zhang, and J. F. Kang, "A Physics-Based Compact Model of Metal-Oxide-Based RRAM DC and AC Operations," IEEE Trans. Electron Devices, vol. 60, no. 12, pp. 4090–4097, Dec. 2013.

[21] G. González-Cordero, F. Jiménez-Molinos, J.B. Roldán, M.B. González and F. Campabadal, "In-depth study of the physics behind resistive switching in TiN/Ti/HfO2/W structures", Journal of Vacuum Science & Technology B 35, 01A110, 2017.

[22] G. Gonzalez-Cordero, J. B. Roldan, and F. Jimenez-Molinos, "Simulation of RRAM memory circuits, a Verilog-A compact modeling approach," in 2016 Conference on Design of Circuits and Integrated Systems (DCIS), pp. 1–6, 2016.

[23] F.M. Puglisi, N. Zagni, L. Larcher, P. Pavan, "Random Telegraph Noise in Resistive Random Access Memories: Compact Modeling and Advanced Circuit Design", IEEE Transactions on Electron Devices, 65, pp. 2964 – 2972, 2018.

[24] F.M. Puglisi, L. Larcher, A. Padovani and P. Pavan, "A Complete Statistical Investigation of RTN in HfO2-Based RRAM in High Resistive State", IEEE Transactions on Electron Devices, 62, pp. 2606-2613, 2015.

[25] G. González-Cordero, M. B. González, F. Jiménez-Molinos, F. Campabadal, and J. B. Roldán, "New method to analyze random telegraph signals in resistive random access memories", Journal of Vacuum Science & Technology B, vol. 37, no. 1, p. 012203, 2019.

[26] D. Ielmini, F. Nardi, and C. Cagli, "Resistance-dependent amplitude of random telegraph-signal noise in resistive switching memories," Appl. Phys. Lett., vol. 96, pp. 053503-1–053503-3, 2010.

[27] S. Ambrogio, S. Balatti, A. Cubeta, A. Calderoni, N. Ramaswamy, and D. Ielmini, "Statistical fluctuations in HfOx resistive-switching memory: Part II—Random telegraph noise," IEEE Trans. Electron Devices, vol. 61, no. 8, pp. 2920–2927, Aug. 2014.

[28] G. González-Cordero et al., "Analysis of resistive switching processes in TiN/Ti/HfO2/W devices to mimic electronic synapses in neuromorphic circuits", Solid-State Electronics, vol. 157, pp. 25–33, 2019.

[29] D. Arumí, S. Manich, R. Rodríguez-Montañés and M. Pehl, "RRAM based random bit generation for hardware security applications," 2016 Conference on Design of Circuits and Integrated Systems (DCIS), Granada, 2016, pp. 1-6. doi: 10.1109/DCIS.2016.7845382

[30] Z. Wei et al., "True random number generator using current difference based on a fractional stochastic model in 40-nm embedded ReRAM," 2016 IEEE International Electron Devices Meeting (IEDM), San Francisco, CA, pp. 4.8.1-4.8.4, 2016. doi: 10.1109/IEDM.2016.7838349

[31] T. Nagumo, K. Takeuchi, S. Yokogawa, K. Imai and Y. Hayashi, "New analysis

methods for comprehensive understanding of Random Telegraph Noise", IEEE International Electron Devices Meeting (IEDM), Baltimore, MD, pp. 1-4, 2009. doi: 10.1109/IEDM.2009.5424230

[32] J. Martin-Martinez, J. Diaz, R. Rodriguez, M. Nafria and X. Aymerich, "New Weighted Time Lag Method for the Analysis of Random Telegraph Signals", IEEE Electron Device Letters, vol. 35, pp. 479-481, 2014. doi: 10.1109/LED.2014.2304673

[33] J. Martin-Martinez et al., "Characterization of random telegraph noise and its impact on reliability of SRAM sense amplifiers," in Proc. 5th Eur. Workshop CMOS Variability (VARI), pp. 1–6, 2014.

[34] C. Márquez, N. Rodríguez, F. Gámiz, R. Ruiz, and A. Ohata, "Electrical characterization of Random Telegraph Noise in Fully-Depleted Silicon-On-Insulator MOSFETs under extended temperature range and back-bias operation," Solid State Electron., vol. 117, pp. 60–65, 2016.

[35] G. González-Cordero, M. B. González, F. Campabadal, F. Jiménez-Molinos, and J. B. Roldán, "A new technique to analyze RTN signals in resistive memories," Microelectronic Engineering, vol. 215, p. 110994, 2019.

[36] M. B. Gonzalez, J. Martin-Martinez, M. Maestro, M. C. Acero, M. Nafría and F. Campabadal, "Investigation of Filamentary Current Fluctuations Features in the High-Resistance State of Ni/HfO2-Based RRAM," in IEEE Transactions on Electron Devices, vol. 63, no. 8, pp. 3116-3122, Aug. 2016.

[37] T. Kohonen, "Self-organized formation of topologically correct feature maps," Biological Cybernetics, vol. 43, no. 1, pp. 59–69, 1982.

[38] T. Kohonen, Self-Organizing Maps, vol. 30. Berlin, Heidelberg: Springer Berlin Heidelberg, 2001.

[39] S. Lloyd, "Least squares quantization in PCM," IEEE Transactions on Information Theory, 28, pp. 129-137, 1982.

[40] M. B. Gonzalez, J. M. Rafí, O. Beldarrain, M. Zabala and F. Campabadal, "Analysis of the Switching Variability in Ni/HfO2 -Based RRAM Devices," in IEEE Transactions on Device and Materials Reliability, vol. 14, no. 2, pp. 769-771, June 2014. doi: 10.1109/TDMR.2014.2311231

[41] M.B. Gonzalez, J. Martin-Martinez, R. Rodriguez, M.C. Acero, M. Nafria, F. Campabadal, X. Aymerich, Dedicated random telegraph noise characterization of Ni/HfO2-based RRAM devices, Microelectronic Engineering, Volume 147, pp. 59-62, 2015, http://dx.doi.org/10.1016/j.mee.2015.04.046.

[42] M. Maestro, J. Martin-Martinez, J. Diaz, A. Crespo-Yepes, M.B. Gonzalez, R. Rodriguez, F. Campabadal, M. Nafria, X. Aymerich, Analysis of Set and Reset mechanisms in Ni/HfO2-based RRAM with fast ramped voltages, Microelectronic Engineering, volume 147, pp. 176-179, 2015. http://dx.doi.org/10.1016/j.mee.2015.04.057.

[43] T. J. Sejnowski, "The Deep Learning Revolution", MIT Press, 2018.

[44] LeCun Y, Bengio Y, Hinton G. Deep learning. Nature. 2015 May 28;521(7553):436-44. doi: 10.1038/nature14539.

[45] G. E. Hinton, R. R. Salakhutdinov, "Reducing the Dimensionality of Data with Neural Networks", Science, vol. 313, pp. 504–507, 2006.

[46] D. P. Kingma, M. Welling, "Auto-Encoding Variational Bayes". Proceedings of the 2nd International Conference on Learning Representations (ICLR), 2014.

[47] I. Goodfellow, J. Pouget-Abadie, M. Mirza, B. Xu, D. Warde-Farley, S. Ozair, A. Courville, Y. Bengio "Generative Adversarial Networks", Proceedings of Advances in neural information processing systems, 2014.

[48] C. S. Wicramasinghe, K. Amarasinghe and M. Manic, "Deep Self-Organizing Maps for Unsupervised Image Classification", IEEE Transactions on Industrial Informatics, p. 1, 2019. doi: 10.1109/TII.2019.2906083

[49] F. Puglisi, P. Pavan, "Factorial hidden Markov model analysis of Random Telegraph Noise in Resistive Random Access Memories", in IEEE Transactions on Electrical Eng., Electronicas and Communications, vol. 12, no. 1, pp. 2429, June 2014.

[50] R. Carboni, D. Ielmini, "Stochastic Memory Devices for Security and Computing", Advanced Electronics Materials, 2019. https://doi.org/10.1002/aelm.201900198

Simulation Study of Circuits Based on Resistive Switching Memristors

6.1. Introduction

This chapter describes several circuit simulations and applications of some memristor models devoted both to analog and digital approaches.

For the digital application we analyze the appropriateness of three different RRAM compact models based on the SU-VCM (described in section 3.2.), for different non-volatile circuit configurations (1T1R and 3x3 matrix). Several features are taken into account in the models: the ohmic resistance linked to the conductive filaments and a detailed thermal description assuming cylindrical and truncated cone-shaped CFs. These models have been implemented in Verilog-A and compiled in the ADS circuit simulator.

For the analog application a physically based compact model UGR-VCM (described in section 3.4. New Compact Model for Bipolar VCM (UGR-VCM)) is used to assess the device behavior as an electronic synapsis. The simulation study has been employed to describe the influence of the compliance current on the resistive switching processes. This compact modeling approach can be used to aid neuromorphic circuit designers by allowing simulations at a circuit level and a design procedure for conductance modulation for these kind of applications.

Analog and digital circuit studies were also presented by means of two compact models (IM2NP-CBM and SU-VCM, described previously in chapter 2 section 2.2. and chapter 3 section 3.2. respectively). The models are compared in depth and a description of their sub-circuit implementation in SPICE is given.

6.2. Simulation on RRAM Memory Circuits

In this section we show results of two types of circuits:

1.- A single memory cell, making use of a NMOS transistor [Chen2015] and comparing different design parameters like set, reset and read times (t_{set}, t_{reset}, t_{read}), noise margin and threshold.

2.- A memory matrix built in a 3x3 crossbar configuration [Ariza2015].

Three different RRAM compact models implemented in Verilog-A and compiled in the ADS circuit simulator (Keysight Technologies) are taken into consideration:

1.- Stanford Model (SM-VCM) [Guan2012, Guan2012b, Yu2012, Jiang2014 , Chen2015, Jiang2016], where the evolution of the gap between the bottom electrode an the metallic-like filament tip determines the average tunneling current in the device (described in the paper [González-Cordero2016f]). The model is described in section II.A and a more extensive explanation is given in section 3.2. Unidimensional Compact Model for VCM Bipolar RRAMs (SU-VCM)). A single temperature is employed for the device obtained with a simple approach based on a thermal resistance (see section D.1.).

2.- Valence Change Memory model with Cylindrical Cone (UGR-VCMCF). This model introduces a cylindrical CF [Li2014, Li2015, Huang2013] with variable length and accounts for the surrounding oxide resistance. The CF temperature is calculated solving the heat equation with this geometric CF. The thermal conductivity, a heat transfer coefficient, the average electric field, the electrical conductivity and the CF radius are considered (as described in appendix D.4. Temperature for a memristor with a Cylindrical conductive filament with Thermal Conductivity k_{th} and Heat Transfer Coefficient h).

3.- Valence Change Memory model with Truncated Cone (UGR-VCMTCF). It introduces a truncated-cone shaped conductive filament with the other features similar to the previous model.

Table 6.I shows a summary of second order effects included in each model.

Table 6.I Summary of main features of the models used for the memory circuit simulations.

Model features	SM-VCM	UGR-VCMCF	UGR-VCMTCF
CF Geometry	without shape for the filament	Cylinder	Truncated Cone
Effect of CF Resistance (R_{CF})	no	yes	yes (C.4.3.)
Effect of the resistance of the oxide surrounding the CF (R_{Ox})	no	yes	yes (C.4.4.)
Effect of the resistance of the oxide between the CF tip and the electrode (R_g)	no	yes	yes
Thermal description	R_{th} (0)	K_{th}, h (D.4.)	K_{th}, h (D.6.)
Model description	3.2. and II.A	II.B	II.C

This section was published in González-Cordero et al. Proceedings of IEEE. XXXI edition of the Design of Circuits and Integrated Systems Conference (DCIS 2016). IEEE Xplore digital library, the accepted preprint paper is presented below.

González-Cordero et al. Proceedings of IEEE. XXXI edition of the Design of Circuits and Integrated Systems Conference (DCIS 2016). IEEE Xplore digital library

Quality metrics

Data base	Rating
Scimago Journal & Country Rank	h-index:2

Publication citations

Google Scholar	Web of Science
6	**0**

Simulation of RRAM memory circuits, a Verilog-A compact modeling approach

G. González-Cordero, J.B. Roldán, F. Jiménez-Molinos

Departamento de Electrónica y Tecnología de Computadores, Universidad de Granada (Spain), *Email: jroldan@ugr.es*

Abstract— Three different compact models for resistive RAM are introduced in this work. The role of the conductive filaments ohmic resistance is introduced for different filament shapes, affecting the voltage at the gap between the filament tip and the electrode, and therefore the device hopping current. The temperature behavior of the devices under study is also described with a different degree of accuracy. These models have been implemented in Verilog-A in the ADS circuit simulator (Keysight Technologies) to analyze several non-volatile memory circuits. First, a single memory cell, making use of a NMOS transistor is studied accounting for the differences of the three RRAM models, and later on a 3x3 memory matrix is analyzed.

Keywords—Resistive RAM, crossbar array, memory cell, non-volatile memory

I. INTRODUCTION

One of the greatest research efforts currently going on in the microelectronics industry is connected to the different ways to offer competitive alternatives for fast-write and low-voltage non-volatile conventional Flash memories [1, 2]. These alternatives are needed because Flash cells face great hurdles in their roadmap due to scaling and manufacture difficulties. Phase change memories, Spin-transfer torque magnetic RAMs and Resistive RAMS (RRAMs) are some of technologies under consideration; in particular, the latter is one of the most promising.

RRAMs are considered a serious future contender in the non-volatile memory realm because of their low program/erase currents, fast speed, remarkably good endurance and their viability for 3D memory stacks [3-5]. In addition, RRAMs can be easily integrated in the BEOL of CMOS processes [1, 3, 5]. The viability of RRAM technology has been proved for single devices as well as in complete integrated circuits (ICs); e. g., a 16Gb memory circuit has been reported recently [6]. There exist many flavors of RRAMs, combining different dielectrics and electrodes; nevertheless, for most of them the electrical operation is based on the creation and disruption of conductive filaments (CFs) that can change the device resistance in several orders of magnitude [1-5]. These different resistance states can be easily distinguished in the device operation and allow the use of RRAMs as non-volatile memories [1-5].

To advance in RRAM IC development, good compact models are needed to include in circuit design simulation EDA tools. For these compact models the physics behind resistive switching (RS) mechanisms has to be taken into account. Among the important physical effects we could count thermal effects, quantum mechanical effects such as tunneling currents, series resistances, redox reactions or other processes under control of the dynamical evolution of the conductive filaments, etc. [2-5, 7]. The stochastic nature of some of the latter physical processes leads to the occurrence of current fluctuations that explain the device-to-device and cycle-to-cycle variability, one of the main issues to be addressed before this technology is introduced for massive industrial production.

Several SPICE models for RRAM simulation have been reported so far, among them the following can be a representative set [8-14]. As can be seen in the previous references, different features can be included in the model description such as: device temperature calculation at simulation time, consideration of the real shape and the number of CFs, tunneling currents, etc. Parameter extraction issues are also an important consideration with respect to compact modeling, in particular to RRAMs [15-17].

In this work we deal with different types of compact models for RRAM devices, a previous Stanford model (SM) and two other with improvements that we propose: Valence Change Memory model with Cylindrical-Cone shaped (UGR-VCMCF) and Valence Change Memory model with Truncated-Cone shaped (UGR-VCMTCF). These two new models incorporate effects not reported in the previous literature: a specific CF geometry, parasitic ohmic resistances linked to the device conductive filament (CF), surrounding oxide and gap oxide, and a more detailed description of the thermal behavior by solving the heat equation including the CF thermal conductivity as well as the lateral heat dissipation from the CF to the dielectric). A comparison of simulation results for different memory circuits is performed by employing the compact models under study here. In this respect, the simplicity-accuracy trade-off that is faced when compact models are selected to be included in a simulation tool for circuit design purposes is discussed in depth.

II. COMPACT MODELS DESCRIPTION

A. Basic modeling scheme

We have selected a model closed to the one described in [9] (Stanford Model (SM)) as the basic and first level simulation scheme employed here. A CF formed by a metallic-like cluster of oxygen vacancies is assumed in the operation of the devices modeled. The CF length is diminished in *reset* processes, increasing the distance, represented by g, between the CF tip and the electrode; in a *set* process g is reduced till the CF and the electrode get in touch, consequently reducing greatly the

device resistance (Fig. 1a, 1b and 1c). The RRAM operation is described by the equations given below.

$$\frac{dg}{dt} = -v_0 e^{-\frac{E_a}{k_b T}} sinh\left(\frac{\gamma(g)a_0 q V_g}{t_{ox} k_b T}\right) \qquad (1)$$

where g, referred above, stands for the average tunneling gap distance (see Fig. 1d, 1e, 1f), t_{ox} for the dielectric thickness, E_a for the activation energy, v_o is a fitting parameter [19], a_0 the atom spacing and V_g voltage drop at the gap g. In this model version $V_g = V_{RRAM}$, where V_{RRAM} stands for total device applied voltage; this means that no series resistance and ohmic component due to CF are considered. To account for the strong polarizability of the high-k dielectric usually employed in RRAM [3, 5] $\gamma(g)$ is introduced, where F_{min} stands for the minimum field requirement to enhance gap formation.

$$\gamma(g) = \begin{cases} \gamma_0 - \beta \cdot \left(\frac{g}{g_{ini}}\right)^3 & ,\frac{\gamma \cdot V_{RRAM}}{t_{ox}} \geq F_{min} \\ 0 & ,\frac{\gamma \cdot V_{RRAM}}{t_{ox}} < F_{min} \end{cases} \qquad (2)$$

The gap evolution (Eq. 1) depends on the device temperature. In this model it is calculated as follows [9]:

$$T = T_0 + V_{RRAM} I_{RRAM} R_{th} \qquad (3)$$

where T_0 is the room temperature and R_{th} the device thermal resistance, that accounts for the thermal effects linked to all the device region. No dependencies on the CF geometry are included here.

The device current (assumed to be a hopping current [20]) can be calculated as follows, assuming I_0, g_0 and V_0 as fitting constants.

$$I_{RRAM} = I_{hopping} = I_0 e^{-g/g_0} \sinh\left(\frac{V_g}{V_0}\right) \qquad (4)$$

where I_{RRAM} represents the DC device current. Finally, the dielectric capacitance is calculated by considering a homogeneous layer of oxide. Hence, the total current accounting also for time dependent components can be obtained as follows:

$$I_{Total} = I_{RRAM} + C_p \frac{dV}{dt} \qquad (5)$$

B. Inclusion of a cylindrical CF, new ohmic features and temperature distribution, UGR-VCMCF model.

The second compact model used here is based on the previous one; however, the ohmic features of a cylindrical CF (this shape has been used previously [14]) of variable length are included (see Fig. 1b, 1e, 1h). The equivalent ohmic resistance including the CF (R_{CF}) and surrounding oxide (R_{Ox}) roles can be calculated as follows: $R_{eq} = R_{CF}||R_{Ox}$. Therefore, the device current can be obtained from:

$$V_g = V_{RRAM} - I_{RRAM}(V_g) \cdot R_{eq} \qquad (6)$$

The temperature response is calculated in a more accurate manner than in the previous version, by solving the heat equation within the CF [18],

$$\sigma_{eq} \cdot \xi^2 = -k_{th} \frac{\partial^2 T(x)}{\partial x^2} + 2 \cdot h \frac{T(x) - T_{ox}}{r_{CF}} \qquad (7)$$

where $\boldsymbol{\sigma_{eq}}$ represents the CF electric conductivity (a usual metallic-like temperature dependence is assumed [4]), $\boldsymbol{r_{CF}}$ the CF radius (constant in this case because of the cylindrical CF shape), $\boldsymbol{\xi}$ the average electric field in the CF, $\boldsymbol{k_{th}}$ the CF thermal conductivity, and $\boldsymbol{h}$ stands for heat transfer coefficient that accounts for the lateral heat dissipation from the CF to the dielectric. The maximum temperature found solving Eq. 7 along the $\boldsymbol{x}$ CF axis (see the Fig. 1e) is given in Eq. 8 and it is assumed as the CF temperature,

$$T = T_0 + \frac{\sigma_{eq} \cdot \xi^2 \cdot r_{CF} \cdot (e^\alpha - 1)^2}{2 \cdot h \cdot (e^{2 \cdot \alpha} + 1)} \qquad (8)$$

where the α parameter is given below:

$$\alpha = \frac{t_{ox}}{2} \sqrt{\frac{2 \cdot h}{k_{th} \cdot r_{CF}}} \qquad (9)$$

The model equivalent circuit is given in Fig. 1h. $\boldsymbol{R_g}$ represents the oxide resistance in the gap region. This complemented version of the SM is called, UGR Valence Change memory Model with Cylindrical Filaments (UGR-VCMCF).
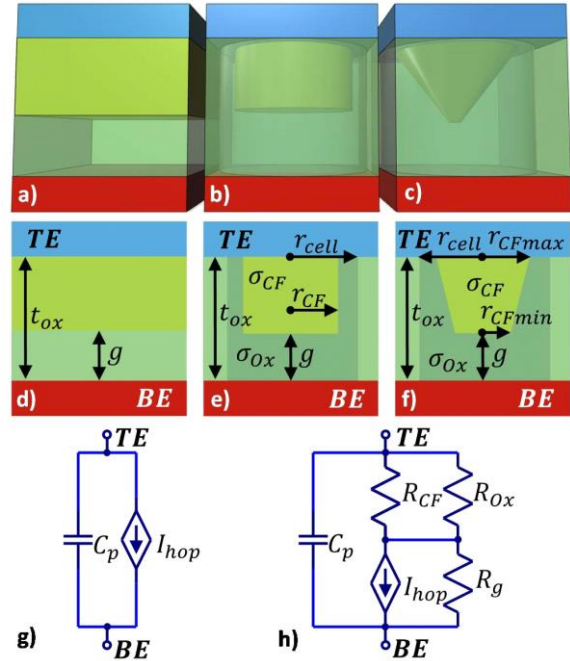
Figure 1: Three-dimensional geometrical representation of the RRAMs modeled: **a)** SM, **b)** UGR-VCMCF, **c)** UGR-VCMTCF. Geometrical parameters for the description of the models employed: **d)** SM, **e)** UGR-VCMCF, **f)** UGR-VCMTCF. Electrical equivalent circuits: **g)** SM, **h)** UGR-VCMCF, UGR-VCMTCF.

C. Inclusion of a truncated-cone shaped CF, new ohmic features and temperature distribution, UGR-VCMTCF model.

The last version of the models considered here; i. e., the UGR Valence Change Memory model with Truncated-Cone shaped Filaments (UGR-VCMTCF) is described below. In this case, the ohmic component of the CF and the solution of the heat equation are obtained assuming a truncated-cone shaped CF (see Fig. 1c and 1f).

Eq.7 cannot be solved analytically assuming a CF with this geometry. In order to obtain a compact solution we consider the following issues in the context of Eq. 7 solution:
1.-It can be shown analytically that a truncated-cone shaped CF with constant conductivity is equivalent to a cylindrical CF with a conductivity dependent on the variable along the CF main axis. With this transformation we can solve the heat equation for a truncated cone shape in an analytical manner. The radius of this equivalent cylinder can be obtained as shown in Eq. 11.
2.-The use of the previous assumption leads to an electric field dependent on the variable along the CF axis, for a fixed voltage drop in the CF. We include the electric field maximum value in Eq. 7.

Making use of these considerations the heat equation can now be solved and the maximum temperature obtained is given in Eq. 10.

$$T = T_0 + \frac{\sigma_{eq} \cdot \xi^2 \cdot r_{CFg} \cdot (e^\alpha - 1)^2}{2 \cdot h \cdot (e^{2 \cdot \alpha} + 1)} \qquad (10)$$

where α y r_{CFg} are calculated as follows:

$$\alpha = \frac{t_{ox}}{2} \sqrt{\frac{2 \cdot h}{k_{th} \cdot r_{CFg}}} \quad , r_{CFg} = \sqrt{r_{CFmax} \cdot r_{CFmin}} \qquad (11)$$

The resistances shown in Fig. 1.h (R_{CF} y R_{Ox}) are calculated making use of the real geometry of the CF; therefore, their values are different for cylindrical or truncated-cone shaped CFs. I_{RRAM} is obtained self-consistently solving Equations 1, 4, 5 and 6 by means of Newton-Raphson numerical procedure both for UGR-VCMCF and UGR-VCMTCF models.

D. Modeling results.

We have assumed bipolar RRAM devices such as the ones described in [21] although no particular curve fitting has been performed. The curves shown (Fig. 2) present current values usually found in the literature, a reasonable approach for the theoretical study presented here. We show different curves changing several parameters for the three models employed here. The input signal had the following features:$\pm 3V_{pp}$, and a $1V/s$ ramp. Figures 2.a, 2.c, and 2.e show the influence of the oxide thickness, t_{ox}, on the device current curves, see the variation of the set and reset voltages V_{set} y V_{reset} (as expected, the higher t_{ox}, the higher V_{set} and V_{reset}). The influence of thermal effects has been highlighted in Fig 2.b, 2.c and 2.d where variations of the thermal resistance and the thermal

conductivity have been introduced for the three models under study. More abrupt transitions at the reset and set processes are observed for the UGR-VCMCF y UGR-VCMTCF models due to the higher influence of changes in the thermal conductivity in the final device response.
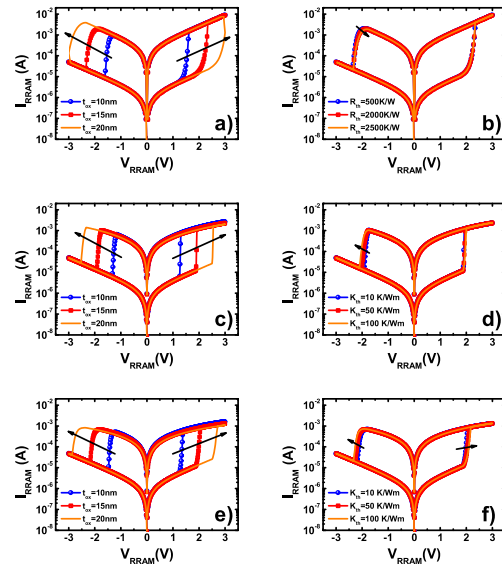
Figure 2: Current versus voltage **a)** SM for different oxide thicknesses, **b)** SM for different thermal resistances; **c)** UGR-VCMCF model for different oxide thicknesses, **d)** UGR-VCMCF model for different thermal conductivities of the CF; **e)** UGR-VCMTCF model for different oxide thicknesses, **f)** UGR-VCMTCF model for different thermal conductivities.

III. CIRCUIT SIMULATION

A. Single memory cell

The models described in the previous section have been implemented in Verilog-A and compiled for the circuit simulator memory ADS (Keysight technologies). They can be also used in other simulators (e.g.: HSPICE or SPECTRE) compiling the Verilog-A model in the compiler associated with each simulator. Making use of this simulation infrastructure, the circuit sketched in Fig. 3 has been analyzed.
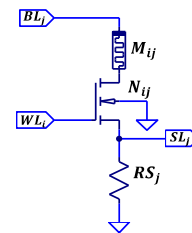
Figure 3: Basic memory cell including a RRAM based on the scheme proposed in Ref. [22]. This cell (row i and column j) could be part of a greater array where M_{ij} stands for the RRAM, N_{ij} for the nMOS transistor. WL_i is the word line signal selector of row i, BL_j is the bit line signal selector of column j, and SL_j is the sensing line of column j that connect to the sense amplifier.

We have plotted in Fig. 4 the input voltage signals and different RRAM model variables versus time. The 3V signal for the Word Line (WL) is used with the following rise and fall times: $t_r = t_f = 0.1ns$. The operation voltage in the memory cell RRAM is introduced through the Bit Line (BL) (set or reset processes and resistance state reading operations are performed). These control signals have been chosen to clearly show the operation of the circuits under study, in this respect this facet could be further optimize in future improvements.

The signals WL and BL are plotted in Fig. 4a. First, a voltage pulse to trigger a set process (a logic 1) is introduced; $V_{set} = 6V$ in BL, 40ns long with $t_r = t_f = 0.1ns$. After that, g reaches its minimum value (the CF is fully formed) and the RRAM Low Resistance State (LRS) is achieved. In case a logic 0 could be needed, then a $V_{Reset} = -6V$, 40ns long with $t_r = t_f = 0.1ns$ is introduced through BL. After this pulse, g reaches its maximum value and the RRAM High Resistance State (HRS) is achieved. The maximum and minimum g values can be fitted to reproduce experimental results for a particular RRAM device.

The cell can be read with a pulse $V_{Read} = 3V$ in the BL with the same time features described above for Set/Reset voltages. Lower voltages could be used although we have not dealt with this issue here since we have concentrated on the compact modeling facet. After the transient, t_{re} (reading time when the RRAM is in the HRS) or t_{read} (reading time when the RRAM is in the LRS) in the SL port (Fig. 4f, 4g and 4h), the voltage can be measured; since the MOS transistor operates in the saturation region, a voltage divider is formed by the RRAM resistance and the sensing resistance. If the RRAM is in LRS, this voltage will achieve a high level and the opposite would occur if the HRS is found in the RRAM. The noise margins can therefore be obtained. The median value has to be programmed in the sense amplifier to distinguish the logic levels in the memory cell.

The RRAM temperatures for the three models under study for the signals shown in Fig 4.a are shown in Figures 4.c, 4.d, 4.e. The parameter g is plotted in Fig. 4.b. It can be seen the temperature peaks in the writing processes linked to the RRAM reset transitions.

The BL signal of the memory cell is shown in red in Fig. 5, as a series of operations are performed, set-read-read-reset-read-read; the corresponding signal at the sense line is shown in blue in the same figure. The resistance chosen for the memory cell was $RS = 4500 \ \Omega$. The different time delays due to the RRAM response can be clearly observed in Figure 5. Negative voltages in the SL are due to the role played by the internal RRAM and transistor capacitances.
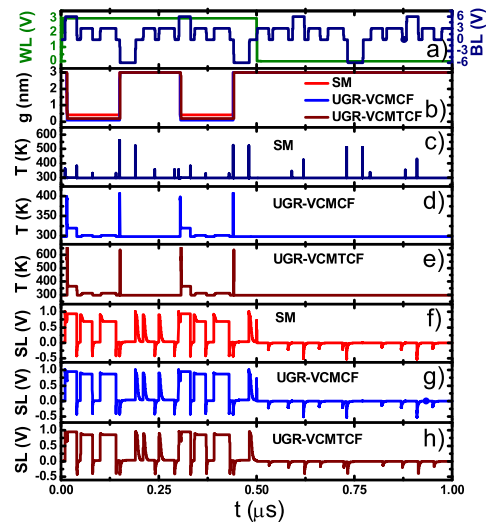
Figure 4: Voltage signals and RRAM parameters versus time. a) Word line voltage at the gate of nMOS 130nm (PTM model used for the MOS transistor [23]) and Bit line voltage at the RRAM top electrode. (Two sequences are considered: Set-read-read-Reset-read-read) b) RRAM CF gap, g, c) d) e) RRAM temperature for SM, UGR-VCMTCF and UGR-VCMCF models, f) g) h) Sense line voltage signals for SM, UGR-VCMTCF and UGR-VCMCF models.
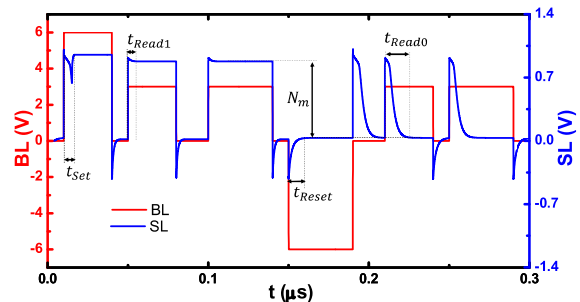
Figure 5: Graphical representation of delay time parameters in a set-read-read-reset-read-read series in the BL. The SL output is also shown for the UGR-VCMCF model. t_{set}: time to write a logic 1 in the cell (LRS in the RRAM). t_{reset}: time to write a logic 0 in the cell (HRS in the RRAM). t_{read0} time to read when the RRAM is in the HRS. t_{read1} time to read when the RRAM is in the LRS. N_m: Noise margin, difference between the high and low reading levels.

Apart from the compact model comparison in the context of Fig. 4, other studies could be performed; in particular, an interesting set of simulations could be designed. Different technological nodes for the NMOS transistors (channel length sweeping from $L = 130nm$ to $L = 16nm$) can be used employing The Predictive Technology Model (PTM) model. Files for the different nodes and interconnect technologies were used in these simulations [23]. In particular, we have chosen a fixed MOS transistor node ($65nm$) and analyzed the memory cell of Fig. 3 for different RRAM sizes (assuming square devices with side lengths sweeping from $L_{cell} = 400nm$ to $L_{cell} = 50nm$), see Fig. 6.
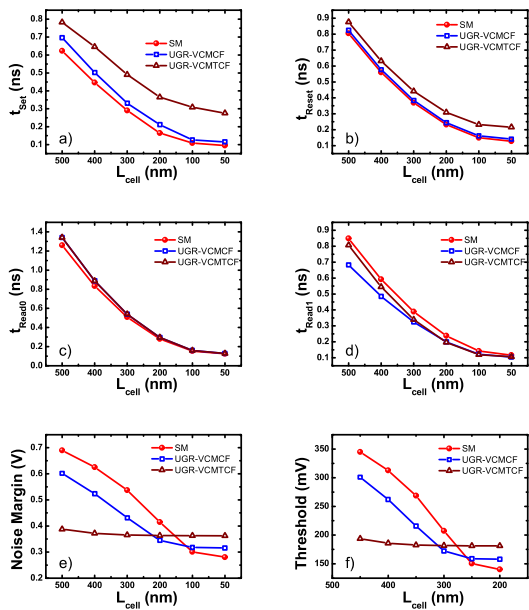
Figure 6: Memory cell characteristic parameters versus RRAM size featured by L_{cell} with nMOS 65nm. a) t_{set} b) t_{reset} c) t_{read0} d) t_{read} e) Noise margin. **f)** Threshold

It can be observed that as the RRAM size shrinks the characteristic times of the memory cell decrease; this reduction is closely related to the role of the RRAM internal capacitance.

B. Memory Array

A 3x3 memory array is shown in Fig. 7. The operation is conventional for this type of circuits. The access to a determined cell (M_{22}) requires a high voltage at WL_2 and a low voltage at WL_1 and WL_3. A control signal at BL_2 affects column 2 components (see the red part of the circuit shown in Fig. 7). The resistance variation at M_{22} makes the voltage level change in RS_2.

The decoders to randomly access the array cells have been implemented in Verilog-A. Fig. 8.a shows the control signals at WL_1, WL_2 and WL_3; the signals at BL_1, BL_2 and BL_3 are plotted in Fig. 8.b; the established sequence to write-read the memory cells is correspondingly given. In Fig. 8.c the CF gap time evolution is shown for the memory cells under consideration. The simultaneous writing or reading operations for the components in a row could increase the band width of data transfer in a memory circuit such as this one.
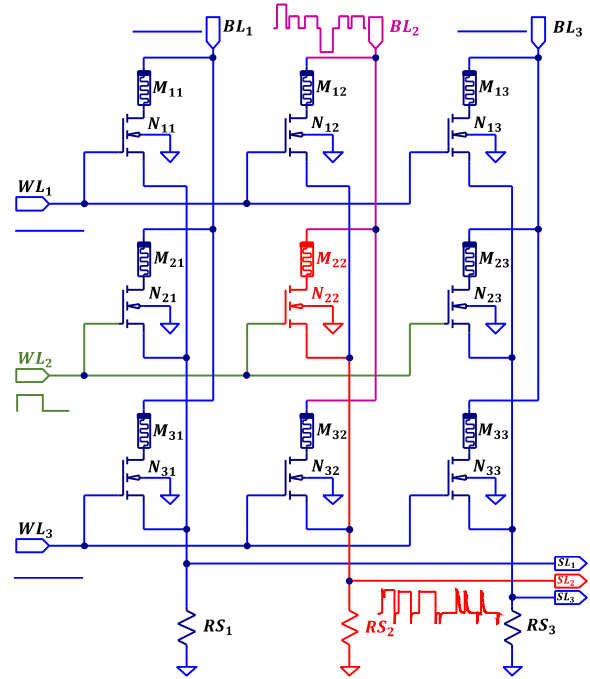
Figure 7: Memory circuit consisting of a cell matrix based on 1T1R structures with RRAMs and nMOS transistors [24]. M_{ij} stands for the RRAM, N_{ij} for the selector device, a nMOS transistor. WL_i is the word line signal of row i, BL_j the bit line signal of column j, SL_j is the sensing line of column j, RS_j stands for the sense resistor of the column j.
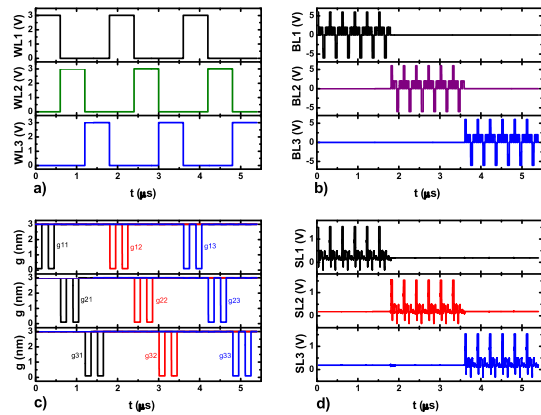
Figure 8: Sequential set-read-read-reset-read-read operation for cells $M_{11}, M_{21}, M_{31} .. M_{31}, M_{32}, M_{33}$. a) Word line temporal signal evolution (WL_1, WL_2, WL_3). b) Bit line temporal signal evolution (BL_1, BL_2, BL_3). **c)** CF gap, g, temporal evolution $g_{11}, g_{12}.. g_{32}, g_{33}$. d) Sense line signal temporal evolution (SL_1, SL_2, SL_3).

TABLE I.   PARAMETERS USED IN THE MODELS

SM	UGR-CMTCF	UGR-CMTCF
$t_{ox} = 15\,nm, T_0 = 298\,K, E_a = 0.86\,eV, V_0 = 0.8\,V, I_0 = 0.5\,mA,$ $g_0 = 0.15\,nm, v_0 = 0.5\,m/s, \gamma_0 = 12, \beta = 0.85, F_{min} = 1.4\,V/nm$		
-	$r_{cell} = 20\,nm, E_m = 0.90\,eV$ $\sigma_{CF0} = 5 \cdot 10^5\,S/m, \sigma_{Ox} = 1.65\,S/m$	
	$r_{CF} = 2.5\,nm$	-
	-	$r_{CFmax} = 10\,nm, r_{CFmin} = 3\,nm$
$R_{th} = 2100\,K/W$	$k_{th} = 10\,K/Wm, h = 10^{10}\,K/Wm^2, \alpha_T = 10^{-3}\,K^{-1}$	

IV. CONCLUSIONS

Three different compact models for resistive RAMs have been introduced in this work. Different features are taken into account in the models; in particular, the ohmic resistance linked to the conductive filaments and a detailed thermal description of the filament are included assuming cylindrical and truncated-cone shaped filaments. The inclusion of these model characteristics allowed us to analyze the voltage at the gap between the filament tip and the electrode, and therefore the device hopping current, considering valence change resistive switching mechanisms. These models have been implemented in Verilog-A in the ADS circuit simulator (Keysight Technologies) to analyze several non-volatile memory circuits. First, a single memory cell, making use of a NMOS transistor is studied accounting for the differences of the three RRAM models, comparing different design parameters (t_{set}, t_{reset}, t_{read0}, t_{read1}, noise margin and threshold). Finally, a 3x3 memory matrix is analyzed. It has been highlighted in a real circuital design context the need of accurate compact models to correctly describe RRAM based memory circuits.

ACKNOWLEDGMENTS

REFERENCES

[1] R. Waser, R. Dittmann, G. Staikov, and K. Szot, "Redox-based resistive switching memories—Nanoionic mechanisms, prospects, and challenges" Adv. Mater., vol. 21, nos. 25–26, pp. 2632–2663, 2009.

[2] H. S. P. Wong, H. Y. Lee, S. Yu. Y.-S. Chen, Y. Wu, P.-S. Chen, B. Lee, F. T. Chen and M.-J. Tsai. "Metal-Oxide RRAM" Proceedings of the IEEE, Vol. 100, Nº. 6, June 2012.

[3] J.S. Lee, S. Lee., T.W. Noh, "Resistive switching phenomena: A review of statistical physics approaches", Applied Physics Reviews, 2, 031303, 2015.

[4] Villena, M.A., Jiménez-Molinos, F., Roldán, J.B., Suñé, J., Long, S. Lian, X., Gámiz, F., And Liu,M., "An In-Depth Simulation Study Of Thermal Reset Transitions In Resistive Switching Memories", J. Appl. Phys., Vol. 114, pp. 144505-144505-8, 2013.

[5] F. Pan, S. Gao, C. Chen, C. Song, F. Zeng, "Recent progress in resistive random access memories: materials, switching mechanisms and performance", Materials Science and Engineering, 83, pp. 1-59, 2014.

[6] J. Zahurak, et al., "Process integration of a 27nm, 16Gb Cu ReRAM," Electron Devices Meeting (IEDM), 2014 IEEE International, vol., no., pp.6.2.1,6.2.4, 15-17 Dec. 2014.

[7] M.A. Villena, M.B. González, F. Jiménez-Molinos, F. Campabadal, J.B. Roldán, J. Suñé, E. Romera, E. Miranda, "Simulation of thermal reset transitions in RRAMs including quantum effects", J. Appl. Phys., vol. 115, p. 214504, 2014.

[8] Jiménez-Molinos, F., Villena, M.A., Roldán, J.B., Roldán, A.M., "A spice compact model for unipolar rram reset process analysis", IEEE Trans. Elec. Dev., vol 62, n.3, pp. 955-962, 2015.

[9] X. Guan, S. Yu, and H.S.P. Wong, "A SPICE Compact Model of Metal Oxide Resistive Switching Memory with Variations", IEEE Elec. Dev. Lett., vol. 33, pp. 1405-1407, 2012.

[10] P. Y. Chen and S. Yu, "Compact Modeling of RRAM Devices and Its Applications in 1T1R and 1S1R Array Design," in IEEE Transactions on Electron Devices, vol. 62, no. 12, pp. 4022-4028, Dec. 2015.

[11] X. Fang; X. Yang; J. Wu; X. Yi, "A Compact SPICE Model of Unipolar Memristive Devices," Nanotechnology, IEEE Transactions on, vol.12, no.5, pp.843-850, 2013.

[12] R. Picos, J.B. Roldán, M.M. Al Chawa, P. García-Fernández, F. Jiménez-Molinos, E. García-Moreno, "Semiempirical Modeling of Reset Transitions in Unipolar Resistive-Switching based Memristors", Radioengineering Journal, vol 24, nº 2, pp. 420-424, 2015.

[13] S. Menzel, U. Böttger, and R. Waser, "Simulation of multilevel switching in electrochemical metallization memory cells", J. Appl. Phys. 111, 014501/1-5, 2012.

[14] M. Bocquet, D. Deleruyelle, C. Muller and J.-M. Portal, "Self-consistent physical modeling of set/reset operations in unipolar resistive-switching memories". Appl. Phys. Letters, 98, 263507, 2011.

[15] S. Long, L. Perniola, C. Cagli, J. Buckley, X. Lian, E. Miranda, F. Pan, M. Liu and J. Suñé. "Voltage and power-controlled regimes in the progressive unipolar RESET transition of HfO2-based RRAM". Scientific reports, 3, 2013.

[16] S. Long, C. Cagli, D. Ielmini, M. Liu and J. Suñé. "Analysis and modeling of resistive switching statistics". Journal of Applied Physics, 111(7), 074508, 2012.

[17] M.A. Villena, J.B. Roldán, M.B. González, P. González-Rodelas, F. Jiménez-Molinos, F. Campabadal, D. Barrera, "A new parameter to characterize the charge transport regime in Ni/HfO2/Si-n+-based RRAMs", Solid State Electronics, pp. 56-60, 2016.

[18] M.A. Villena, M.B. González, J.B. Roldán, F. Campabadal, F. Jiménez-Molinos, F.M. Gómez-Campos, J. Suñé, "An in-depth study of thermal effects in reset transitions in HfO2 based RRAMs", Solid State Electronics, 111, pp. 47-51, 2015.

[19] S. Yu, B. Gao, Z. Fang, H. Yu, J. Kang, H.S.P. Wong, "A neuromorphic visual system using RRAM synaptic devices with sub-pj energy and tolerance to variability: experimental characterization and large-scale modeling", IEDM, pp. 239-242, 2012.

[20] P. Huang. et al., "A physics-based compat model of metal-oxide-based RRAM DC and AC operations", IEEE Trans. Elec. Dev., vol. 60, 4090, 2013.

[21] Z. Jiang; S. Yu; Y. Wu; J.H. Engel; X. Guan; H.S. P. Wong, "Verilog-A Compact Model for Oxide-based Resistive Random Access Memory," Simulation of Semiconductor Processes and Devices (SISPAD), 2014 International Conference on, vol., no., pp.41,44, 9-11 Sept. 2014

[22] H. Ariza, M. Bocquet, M. Moreau, J.M. Portal, "A built-in-self test structure (BIST) for resistive RRAMs characterization: application to bipolar OxRRAM", Solid State Electronics, 103, pp. 73-78, 2015

[23] Predictive Technology Model (PTM). Nanoscale Integration and Modeling (NIMO) Group at Arizona State University. Available: http://ptm.asu.edu/

[24] P. Y. Chen and S. Yu, "Compact Modeling of RRAM Devices and Its Applications in 1T1R and 1S1R Array Design," in IEEE Transactions on Electron Devices, vol. 62, no. 12, pp. 4022-4028, Dec. 2015.

6.3. Simulation of Circuits Including RRAMs

In this section, two different RRAM models assuming filamentary conduction are compared in depth and their implementation in a SPICE-based simulator is described. One model accounts for RRAMs where conductive filaments (CFs) change their geometry laterally, changing the radius, these models have been usually linked to Conductive Bridge Memories (CBM) [Bocquet2014, Bocquet2013] (described in section 2.2. Compact Model of Bipolar CB-RRAM (IM2NP)), although this approach could be employed for other type of devices. The other model takes into consideration vertical variations of the CF (calculating the gap between the filament tip and the electrode). This approach has been usually employed in Valence Change Memories (VCMs) where the CFs are formed by oxygen vacancies [Guan2012, Guan2012b, Yu2012, Jiang2014 , Chen2015, Jiang2016] (described in section 3.2. Unidimensional Compact Model for VCM Bipolar RRAMs (SU-VCM)).

The SPICE model for the Compact Model of Bipolar CB-RRAM (IM2NP) was made with four blocks:

1. ***Thermal Block***: this block computes the temperature of the cylinder CF by solving the heat equation takes into account the electrical conductivity, the average electric field applied to the CF, the thermal conductivity and the heat transfer coefficient that account for the lateral heat dissipation. [Villena2013, González Cordero2016a]. (See appendix 7D.4. for details).

2. ***Kinetic Block***: this block computes the CF radius variation by solving the Butler-Volmer equation for the redox processes that produce the SET and RESET events[Bocquet2014] (See appendix B.3. for more details).

3. ***Conductive Filament Resistance***: this block represents the characteristic ohmic resistance dominant in the LRS. The resistance is computed taking into account the CF geometrical features and its temperature dependence.

4. ***Other elements***: the resistance (R_c) at the top and bottom contacts, the capacitor (C_p) between the top and bottom electrodes and the current (I_{ox}) through the oxide layer surrounding the CF [González Cordero2016a] were also considered.

The SPICE model for the Compact Model of Bipolar CB-RRAM (IM2NP) was implemented employing four blocks too:

1. ***Thermal block***: this block is calculated with the same premises than the previous model. The main difference is linked to the CF length that depends on the gap (g). (See appendix D.4. for more details).

2. ***Kinetic block***: this block computes the variation of the gap (g) between the CF tip and the bottom electrode as a consequence of the migration of oxygen vacancies [Guan2012, Guan2012b, Yu2012, Jiang2014 , Chen2015, Jiang2016]. (See section 3.2. for more details).

3. ***Conductive filament resistance***: in this block we use the same features of the previous models, save the difference linked to CF length dependence on the gap (g).

4. ***Other Elements***: the resistance (R_c) at the top and bottom contacts, the capacitor (C_p) between the top and bottom electrodes, and the tunneling current (I_g) were considered in the model.

With these models different types of circuit simulations were made:

a) Extraction of I-V curves to extract the influence of physical constant such as: oxide thickness, thermal conductivity and heat transfer coefficient.

b) Response to a step voltage input to assess the device resistance response starting from an initial HRS.

c) Ramped input voltage analysis to obtain the typical DC curves and extract characteristics such as $V_{set}, V_{reset}, I_{set}, I_{reset}, R_{on}, R_{off}$.

d) Simulations in single memory cells with a NMOS transistor [Hosoi2006] selector operated by pulses with the same sequence of operations (set-read-read-reset-read-read). The noise margin was obtained as well as the temporal evolution of internal variables (for example: CF radius or gap evolution).

This section was published in González-Cordero et al. Proceedings of IEEE. 11th Spanish Conference on Electron Devices (CDE 2017). IEEE Xplore digital library, the accepted preprint paper is presented below.

González-Cordero et al. Proceedings of IEEE. 11ᵗʰ Spanish Conference on Electron Devices (CDE 2017). IEEE Xplore digital library

Quality metrics

Data base	Rating	
Google Scholar Metrics	h5-index:6	h5-median:8

Publication citations

Google Scholar	Web of Science
0	**0**

2017 Spanish Conference on Electron Devices (CDE)

SPICE simulation of RRAM circuits. A compact modeling perspective

G. González-Cordero, J.B. Roldán, F. Jiménez-Molinos

Departamento de Electrónica y Tecnología de Computadores, Universidad de Granada (Spain), *Email: jroldan@ugr.es*

Abstract— Two different compact models for resistive RAM (RRAMs) with filamentary conduction are compared in depth. One model describes RRAMs where conductive filaments (CFs) change their geometry laterally while the other model takes into consideration vertical variations of the CF. The role of the conductive filament (CF) ohmic resistance and the temperature evolution is carefully studied. The models have been implemented in SPICE to analyze circuits under step pulsed signals and voltage ramps. A single non-volatile memory cell using a NMOS transistor as selector device is studied in depth.

Keywords—Resistive RAM, crossbar array, memory cell, non-volatile memory, SPICE model, compact model.

I. INTRODUCTION

The roadmap of flash cells has reached important limits due to scaling and manufacture difficulties. Therefore, the microelectronics industry is looking for alternatives for high capacity storage systems and mobile applications where fast-write and low-voltage non-volatile memories (NVM) are key players [1, 2]. The main technologies alternatives under consideration in the International Roadmap for Semiconductor (ITRS) are Phase change memories, Spin-transfer torque magnetic RAMs and RRAMs. The latter devices are considered the contenders with more possibilities in the non-volatile memory realm because of their simple structure, their scaling potential (<10nm), their low program/erase currents, low switching voltages (<3V), fast switching speeds (<10ns), excellent retention (>10 year) and good endurance (10^{12}). In addition, RRAMs allow multi-bit storage, viability for 3D memory stacks and integration in the back-end-of-line (BEOL) of CMOS processes [1-5]. The viability of RRAM technology has been proved for single devices as well as for complete integrated circuits (ICs); e. g., a 32Gb memory circuit has been reported recently [6].

RRAMs have a top electrode-dielectric-bottom electrode device structure that can be built by means of MIM or MIS stacks. Several oxides have been reported such as: NiO, TiO_2, HfO_2, ZnO, Al_2O_3, SnO_2, ZrO_2, among others [5, 7]; in all the cases a reasonable resistive switching (RS) behavior has been reported. RS consists of a change between a high resistive state (HRS) to a low resistive state (LRS) in the SET process and the inverse in the RESET process. RRAMs can be classified in two groups: unipolar and bipolar. Unipolar RRAMs switch with the same voltage polarity (both, SET and RESET). On the contrary, for bipolar RRAMs SET and RESET show up under different voltage polarities.

To advance in RRAM IC development, good compact models are needed to include in circuit simulation tools (EDA tools). For these compact models to operate appropriately the physics behind resistive switching (RS) mechanisms has to be taken into account. Among the important physical effects we could count on thermal effects, quantum mechanical effects such as tunneling currents, series resistances, redox reactions

or other processes under control of the dynamical evolution of the conductive filaments, etc. [2-5, 8, 9]

Several SPICE models for RRAM simulation have been reported, the following can be listed [9-15]. As shown in the previous references, different features can be included in the model description such as: device temperature calculation at simulation time, real shape and number of CFs, tunneling currents, etc. Parameter extraction methods are also a key issue [16-18].

In this work we deal with different types of compact models for RRAM devices implemented in SPICE (in particular in LTspice of Linear Technology). The two models chosen here deal with the creation and disruption of the CFs that control de SET and RESET processes in a different manner. In one case a lateral variation of a cylindrical CF is considered, this kind of models has been usually linked to Electrochemical Metallization Cells (EMCs) or Conductive Bridge Memories (CBM) [4, 15]; the other model is based upon the vertical variation of the CF, this approach has been employed in Valence Change Memories (VCMs) where the CFs are formed by oxygen vacancies (Vo) [10, 19, 27]. Obviously, other modeling strategies could be employed to deal with EMCs and VCMs since there are many material combinations that lead to RRAMs that could be included in these groups and show specific characteristics that suggest differences in the physics behind their operation.

A comparison of simulation results for I-V characteristics and step signals is performed. In addition a memory cell is analyzed. The simplicity-accuracy trade-off linked to compact modeling is dealt with for both models.
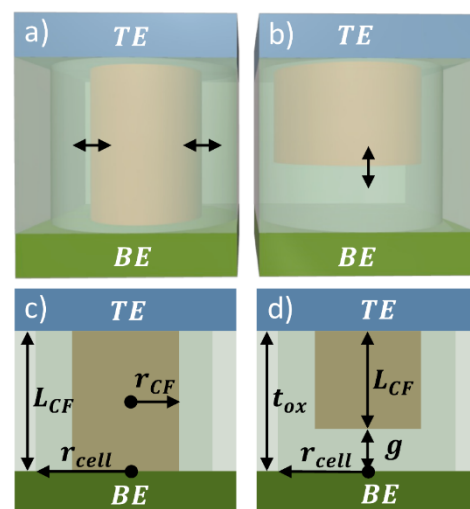
Figure 1: Three-dimensional geometrical representation of the RRAMs modeled: cylindrical CF with **(a)** lateral variation, **(b)** vertical variation, **(c)** and **(d)** geometrical parameters for the description of the models employed.

II. COMPACT MODELS DESCRIPTION

A. Basic modeling scheme

The basic device and CF geometry is represented in Fig. 1, where TE and BE stands for the Top and Bottom Electrodes. In both models the CF shape is a cylinder whose radius is r_{CF}. In the model for ECM devices (model A) the CF radius is modified while in the model for VCMs (model B), CF geometric variation is linked to the CF length.

B. Model with lateral variation of the CF.

This model is based on that presented in Ref. [20], improved with a detailed thermal description (thermal block) and a conductive filament whose electric conductivity is temperature dependent. The block diagram for SPICE simulation is shown in Fig. 2.
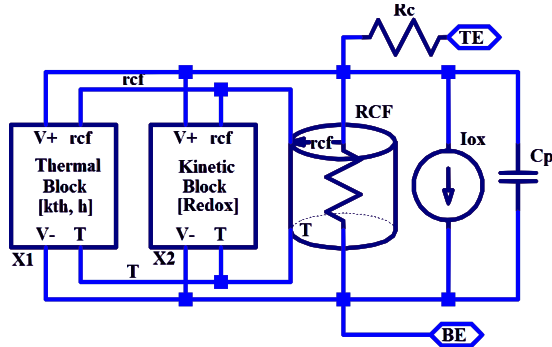
Figure 2: LTspice subcircuit block diagram of the model that considers lateral variation of the CF. Source code available in Ref. [26].

B.1. Thermal Block [kth,h] Subcircuit (X1)

The temperature response is calculated by solving the heat equation within the CF [4, 21-22],

$$\sigma_{CF} \cdot \xi^2 = -k_{th} \frac{\partial^2 T(x)}{\partial x^2} + 2 \cdot h \frac{T(x) - T_{ox}}{r_{CF}}, \quad (1)$$

where σ_{CF} represents the CF electric conductivity (a usual metallic-like temperature dependence is assumed [4, 22]), r_{CF} the CF radius (constant in this case along the CF length because of the cylindrical CF shape), ξ the average electric field in the CF, k_{th} the CF thermal conductivity and h stands for heat transfer coefficient that accounts for the lateral heat dissipation from the CF to the dielectric. The maximum temperature found solving Eq. 1 is given in Eq. 2 and it is assumed as the CF temperature,

$$T = T_0 + \frac{\sigma_{CF} \cdot \xi^2 \cdot r_{CF} \cdot (e^\beta - 1)^2}{2 \cdot h \cdot (e^{2 \cdot \beta} + 1)}, \quad (2)$$

where the β parameter is given below:

$$\beta = L_{CF} \sqrt{\frac{h}{2 \cdot k_{th} \cdot r_{CF}}}, \quad (3)$$

where L_{CF} is the length of the CF (in this case is equal to the thickness of the oxide layer t_{ox}).

B.2. Kinetic Block [Redox] subcircuit (X2)

The kinetic representation of the SET (RESET) processes can be formulated by considering the variations of the CF radius obtained by solving the adapted Butler-Volmer equation of the corresponding redox process [20].

B.3. Conductive Filament Resistance (R_{CF})

The CF resistance takes into account the temperature dependence,

$$R_{CF} = \frac{L_{CF} \cdot (1 + \alpha_T \cdot (T - T_0))}{\sigma_{CF} \cdot \pi \cdot r_{CF}^2}, \quad (4)$$

where α_T is the thermal coefficient of temperature, T_0 is the room temperature and T is the current simulation temperature.

C. Model with longitudinal variation of the CF.

This model is described in detail in Ref. [23]. We introduce here a more detailed thermal block (X1) and we considered as well the role of the ohmic component of the conductive filament where temperature dependence (X3 module) is employed. The device block diagram is shown in Fig. 3.
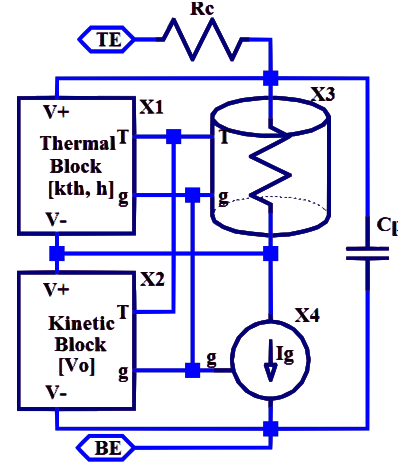
Figure 3: LTspice subcircuit block diagram of the model that considers longitudinal variation of the CF. Source code available in Ref. [26].

C.1. Thermal Block [kth,h] Subcircuit (X1)

The CF gap evolution and the resistance depend on the device temperature. It is calculated with the same premises that in the previous model. The only difference is that the effective CF length changes as follows ($L_{CF} = t_{ox} - g$), where g stands for the length of the gap between the CF tip and the electrode.

C.2. Kinetic Block Subcircuit (X2)

A CF formed by oxygen vacancies is assumed in the operation of the devices modeled. The CF length is diminished in *reset* processes, increasing the distance, represented by g, between the CF tip and the electrode; in a *set* process g is reduced till the CF and the electrode get in touch, consequently reducing greatly the device resistance. The RRAM operation is described by the equations given in Ref. [19].

C.3. Conductive Filament Resistance (X3)

The CF resistance is temperature dependent.

$$R_{CF} = \frac{(t_{ox} - g) \cdot \left(1 + \alpha_T \cdot (T - T_0)\right)}{\sigma_{CF} \cdot \pi r_{CF}^2} \quad (5)$$

C.4. Tunnel current. Subcircuit (X4)

The device current (assumed to be a hopping current [19]) can be calculated as follows, assuming I_0, g_0 and V_0 as fitting constants.

$$I_g = \pi r_{CF}^2 I_0 e^{-g/g_0} \sinh\left(\frac{V_g}{V_0}\right) \quad (6)$$

In this model the ohmic features of a cylindrical CF of variable length are included.

C.5. Parasite elements: Iox, Rc and Cp

I_{ox} represents the current through the oxide layer surrounding de CF [22], R_c is the series resistance and C_p the capacitor between the top and bottom electrodes. These considerations are valid for both models.

III. CIRCUIT SIMULATION

A. Influence of the model parameters

For each parameter or physical constant in the model we have obtained the influence on the I-V characteristic. Fig. 4 shows the I-V curves variability for three key parameters: oxide thickness (t_{ox}), thermal conductivity (k_{th}) and heat transfer coefficient (h).
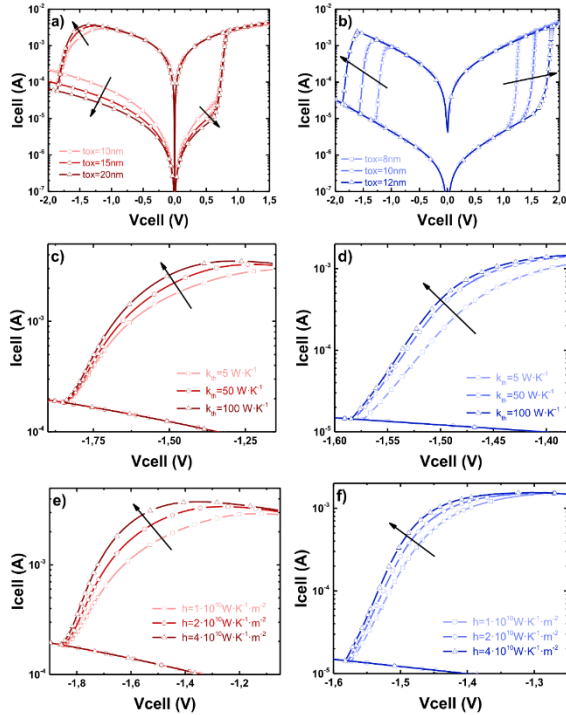
Figure 4: Current versus voltage. RRAM model A **(a)** and B **(b)** for different oxide thicknesses (t_{ox}), RRAM model A **(c)** and B **(d)** for different thermal conductivity coefficients (k_{th}), RRAM model A **(e)** and B **(f)** for different heat transfer coefficients (h).

B. Step input response

The two models are used for simulation with a simple voltage step as input to obtain the device resistance response, starting from an initial HRS. The results are shown in Fig. 5. Model A response is less abrupt than that of model B, where an exponential relationship is considered to model the tunneling current. The maximum resistance device of model B ($\sim250K\Omega$) is higher than model A ($\sim60K\Omega$), see the Table I for the parameters employed.
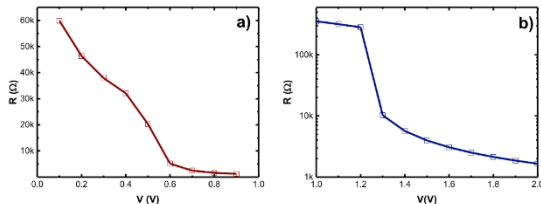
Figure 5: Device resistance for different step voltages applied for the RRAM model A **(a)** and B **(b)**.

C. Ramped input voltage response

The model parameters have been chosen to obtain the same current level in DC operation for both models. For an input signal of $\pm 2V_{pp}$, with a $1V/s$ ramp, Fig. 6 shows the time evolution of the current, the internal state variable (r_{CF} for model A and g for model B) and the temperature evolution. The set voltage is lower in model A (0.75V); in

model B set takes place at 1.5V. The reset process starts first with model B (-1.25V); for model A at -1.5V. The temperatures reached in model A are ~200K higher than in model B for the device parameters used in Table I.
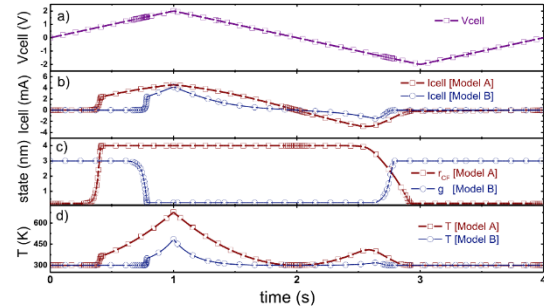
Figure 6: Temporal evolution of different model variables. **(a)** Applied voltage 1V/s ramp, **(b)** currents for RRAMs obtained with model A and B. **(c)** evolution of state variables r_{CF} for model A and g for model B. **(d)** Temperature evolution for both models.

B. Single memory cell

The circuit sketched in Fig. 7 has been analyzed. It consists of one RRAM device (X1), a cell selector NMOS transistor (M1), a sense resistor (Rsense=200Ω) was used to ease the discrimination of two digital logic states stored in the cell, "0" and "1", in the read cycles. A NMOS transistor was used to allow a low resistance path (M2) in addition to a low resistance (RRW=10Ω).
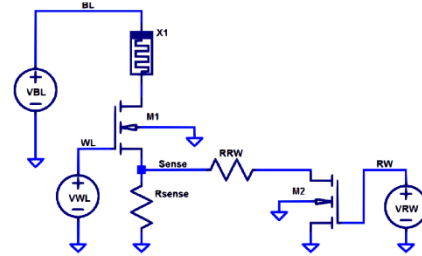
Figure 7: Basic memory cell including a RRAM, based on the scheme proposed in Ref. [25]. X1 stands for the RRAM, M1 for the nMOS transistor. *WL* is the word line signal selector (row *i* in a memory array), *BL* is the bit line signal selector (column *j* in a memory array), and *Sense* is the sensing line of column *j* that connects to the sense amplifier.

The same sequence of three cycles operation is applied in the control BL: set-read-read-reset-read-read, (see Fig. 8.a and 8.b); the line linked to the WL is activated with a single step (see Fig. 8.c and 8.d). The amplitudes needed to let the memory cell work taking into consideration the two different models employed here are: $3.5V$ for V_{set} (model A) and $4.2V$ for model B, $-3.5V$ (model A) for V_{reset} ($-3V$ for model B); an applied pulse amplitude of $0.5V$ for reading (model A) ($1.5V$ for model B) with the following temporal characteristics $t_{set} = 10ns$, and $t_{reset} = 20ns$ with rise and fall times $t_f = t_r = 1ns$ for both models, see Fig. 8.a and 8.b.

The evolution of internal variables, r_{CF} in case of model A and g for model B, is shown in Fig. 8.g and 8.h. The CF radius changes between $0.25nm$ and $1.5nm$ (HRS, LRS), while the gap, g (model B) has the following limits: $3nm$ and $0.25nm$ for HRS and LRS, respectively.

The memory cell operation is shown in terms of the response of the sensing line. This signal show different voltage levels corresponding to the HRS or LRS of the RRAM. In the case of model A (Fig. 8.i) a voltage level of $\sim400mV$ is shown corresponding to a memory state 1, while a voltage level of $\sim150mV$ is obtained for the memory state 0. For model B the voltage level of $\sim1.2V$ corresponds to a memory state 1, and a voltage level of $\sim50mV$ for a 0 value (see Fig 8.j).
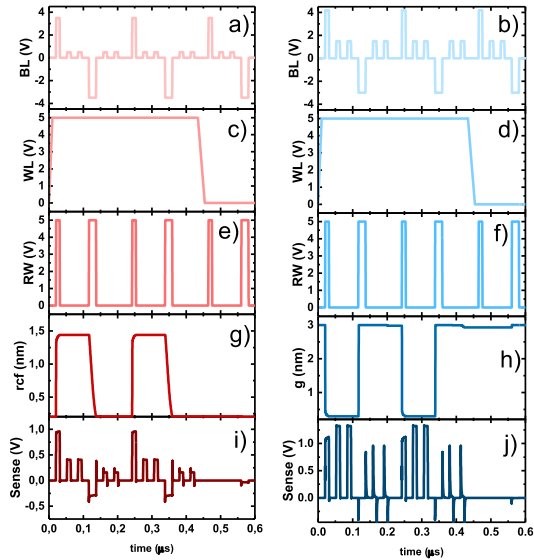
Figure 8: Time evolution of signals for the circuit shown in Fig. 7. (a) BL voltage, model A, (b) BL voltage, model B, (c) WL voltage, model A, (d) WL voltage model B, (e) RW voltage, model A, (f) RW voltage, model B, (g) internal CF radius r_{CF}, model A, (h) internal gap between the CF and the electrode, g, model B, (i) sense line voltage evolution, model A (j) sense line voltage evolution, model B.

TABLE I. PARAMETERS USED IN THE MODELS

Model A	Model B
$0.25nm \le r_{CF} \le 4nm$, $\sigma_{CF} = 3 \cdot 10^5 \, \Omega^{-1}m^{-1}$, $\sigma_{Ox} = 1.6 \, \Omega^{-1}m^{-1}, \alpha = 0.7$ $E_a = 0.75 \, eV, A_{RedOx} = 10^5 s^{-1}$, $A_{HRS} = 5 \cdot 10^{-9} \, A \cdot V^{-2}, \alpha_{HRS} = 2$	$0.25nm \le g \le 3nm$, $E_a = 0.5 \, eV, V_0 = 0.8 \, V$, $I_0 = 1 \, \mu A/nm^2, g_0 = 0.15 \, nm$, $v_0 = 0.5 \, m/s, \gamma_0 = 12, \beta = 0.85$, $F_{min} = 1.4 \, V/nm, a_0 = 0.25nm$
$t_{ox} = 10 \, nm, T_0 = 298 \, K, k_{th} = 5 \, WK^{-1}m^{-1}, h = 10^{10}WK^{-1}m^{-2}$, $\alpha_T = 10^{-3}K^{-1}, S_{cell} = 10^{-12}m^2, R_c = 1\Omega, E_r = 25$	

IV. CONCLUSIONS

Two different compact models for resistive RAMs have been analyzed in a circuit simulation context. Different device features are taken into account in the models. In particular, the ohmic resistance linked to the CFs and a detailed thermal description of the CF is included assuming cylindrical shaped filaments. The models have been implemented in SPICE using the LTspice circuit simulator to analyze a non-volatile memory circuit.

ACKNOWLEDGMENTS

REFERENCES

[1] R. Waser, R. Dittmann, G. Staikov, and K. Szot, "Redox-based resistive switching memories—Nanoionic mechanisms, prospects, and challenges", Adv. Mater., vol. 21, nos. 25–26, pp. 2632–2663, 2009.

[2] H. S. P. Wong, H. Y. Lee, S. Yu. Y.-S. Chen, Y. Wu, P.-S. Chen, B. Lee, F. T. Chen and M.-J. Tsai. "Metal-Oxide RRAM", Proceedings of the IEEE, Vol. 100, Nº. 6, June 2012.

[3] J.S. Lee, S. Lee., T.W. Noh, "Resistive switching phenomena: A review of statistical physics approaches", Applied Physics Reviews, 2, 031303, 2015.

[4] M.A. Villena, F. Jiménez-Molinos, J.B. Roldán, J. Suñé, S. Long, X. Lian, F. Gámiz, M. Liu,"An In-Depth Simulation Study Of Thermal Reset Transitions In Resistive Switching Memories", J. Appl. Phys., Vol. 114, pp. 144505-144505-8, 2013.

[5] F. Pan, S. Gao, C. Chen, C. Song, F. Zeng, "Recent progress in resistive random access memories: materials, switching mechanisms and performance", Materials Science and Engineering, 83, pp. 1-59, 2014.

[6] T.Y. Liu, T. H. Yan, R. Scheuerlein, Y. Chen, J. K. Lee, et al., "A 130.7mm² 2-layer 32 Gb ReRAM memory device in 24 nm technology", in 2013 IEEE International Solid-State Circuits Conference Digest of Technical Papers, 2013.

[7] J. Blasco, N. Ghenzi, J. Suñé, P. Levy, and E. Miranda, "Equivalent circuit modeling of the bistable conduction characteristics in electroformed thin dielectric films", Microelectron. Reliab., vol. 55, no. 1, pp. 1–14, 2015.

[8] M.A. Villena, M.B. González, F. Jiménez-Molinos, F. Campabadal, J.B. Roldán, J. Suñé, E. Romera, E. Miranda, "Simulation of thermal reset transitions in RRAMs including quantum effects", J. Appl. Phys., vol. 115, p. 214504, 2014.

[9] Jiménez-Molinos, F., Villena, M.A., Roldán, J.B., Roldán, A.M., "A spice compact model for unipolar rram reset process analysis", IEEE Trans. Elec. Dev., vol 62, n.3, pp. 955-962, 2015.

[10] X. Guan, S. Yu, and H.S.P. Wong, "A SPICE Compact Model of Metal Oxide Resistive Switching Memory with Variations", IEEE Elec. Dev. Lett., vol. 33, pp. 1405-1407, 2012.

[11] P. Y. Chen and S. Yu, "Compact Modeling of RRAM Devices and Its Applications in 1T1R and 1S1R Array Design", in IEEE Transactions on Electron Devices, vol. 62, no. 12, pp. 4022-4028, Dec. 2015.

[12] X. Fang; X. Yang; J. Wu; X. Yi, "A Compact SPICE Model of Unipolar Memristive Devices", IEEE Transactions on Nanotechnology, vol.12, no.5, pp.843-850, 2013.

[13] R. Picos, J.B. Roldán, M.M. et al, "Semiempirical Modeling of Reset Transitions in Unipolar Resistive-Switching based Memristors", Radioengineering Journal, vol 24, nº 2, pp. 420-424, 2015.

[14] S. Menzel, U. Böttger, and R. Waser, "Simulation of multilevel switching in electrochemical metallization memory cells", J. Appl. Phys. 111, 014501/1-5, 2012.

[15] M. Bocquet, D. Deleruyelle, C. Muller and J.M. Portal, "Self-consistent physical modeling of set/reset operations in unipolar resistive-switching memories", Appl. Phys. Letters, 98, 263507, 2011.

[16] S. Long, L. Perniola, C. Cagli, J. Buckley, X. Lian, E. Miranda, F. Pan, M. Liu and J. Suñé. "Voltage and power-controlled regimes in the progressive unipolar RESET transition of HfO2-based RRAM", Scientific reports, 3, 2013.

[17] S. Long, C. Cagli, D. Ielmini, M. Liu and J. Suñé. "Analysis and modeling of resistive switching statistics", Journal of Applied Physics, 111(7), 074508, 2012.

[18] M.A. Villena, J.B. Roldán, M.B. González, P. González-Rodelas, F. Jiménez-Molinos, F. Campabadal, D. Barrera, "A new parameter to characterize the charge transport regime in Ni/HfO₂/Si-n⁺-based RRAMs", Solid State Electronics, pp. 56-60, 2016.

[19] P. Huang. et al., "A physics-based compat model of metal-oxide-based RRAM DC and AC operations", IEEE Trans. Elec. Dev., vol. 60, 4090, 2013.

[20] M. Bocquet, H. Aziza, W. Zhao, Y. Zhang, S. Onkaraiah, C. Muller, M. Reyboz, D. Deleruyelle, F. Clermidy, and J.-M. Portal, "Compact Modeling Solutions for Oxide-Based Resistive Switching Memories (OxRAM)," J. Low Power Electron. Appl., vol. 4, no. 1, pp. 1–14, 2014.

[21] G. González-Cordero, J. B. Roldan, and F. Jiménez-Molinos, "Simulation of RRAM memory circuits, a Verilog-A compact modeling approach", in XXXI Edition of the Design of Circuits and Integrated Systems Conference, 2016.

[22] G. Gonzalez-Cordero, J. B. Roldan, F. Jimenez-Molinos, J. Suñé, S. Long, and M. Liu, "A new compact model for bipolar RRAMs based on truncated cone conductive filaments, a Verilog-A approach", Semicond. Sci. Technol., vol. 31, no. 11, pp. 1–13, 2016.

[23] Z. Jiang; S. Yu, Y. Wu, J.H. Engel, X. Guan, H.S. P. Wong, "Verilog-A Compact Model for Oxide-based Resistive Random Access Memory", Simulation of Semiconductor Processes and Devices (SISPAD), 2014 International Conference on, vol., no., pp.41,44, 9-11 Sept. 2014

[24] M.A. Villena, M.B. González, J.B. Roldán, F. Campabadal, F. Jiménez-Molinos, F.M. Gómez-Campos, J. Suñé, "An in-depth study of thermal effects in reset transitions in HfO₂ based RRAMs", Solid State Electronics, 111, pp. 47-51, 2015.

[25] Y. Hosoi, Y. Tamai, T. Ohnishi, et al. "High speed unipolar switching resistance RAM (RRAM) technology," Tech. Dig. Int. Electron Devices Meet. IEDM, no. 1, pp. 6–9, 2006.

[26] "RRAM Modeling", available: http://wpd.ugr.es/~rram_modeling/.

[27] G. González-Cordero, F. Jiménez-Molinos, J. B. Roldan, M. B. González and F. Campabadal "In-depth study of the physics behind resistive switching in TiN/Ti/HfO2/W structures", J. Vac. Sci. Technol. B 35, 01A110, 2017.

[28] G. González-Cordero, F. Jiménez-Molinos, J. B. Roldan, M. B. González and F. Campabadal, "Transient SPICE simulation of Ni/HfO2/Si-n+ resistive memories", in XXXI edition of the Design of Circuits and Integrated Systems Conference, 2017.

6.4. Electronic Synapses Based on Resistive Switching Devices.

As discussed above, resistive switching devices have similarities in their functional behavior to biological synapses, therefore, these synapses can be easily mimicked [Huang2017]. **Figure 6.1** show a sketch of a biological synapse and the implementation in a cross-bar architecture of electronic synapses based on RRAMs for the construction of an Artificial Neural Network (ANN) [Huang2017].
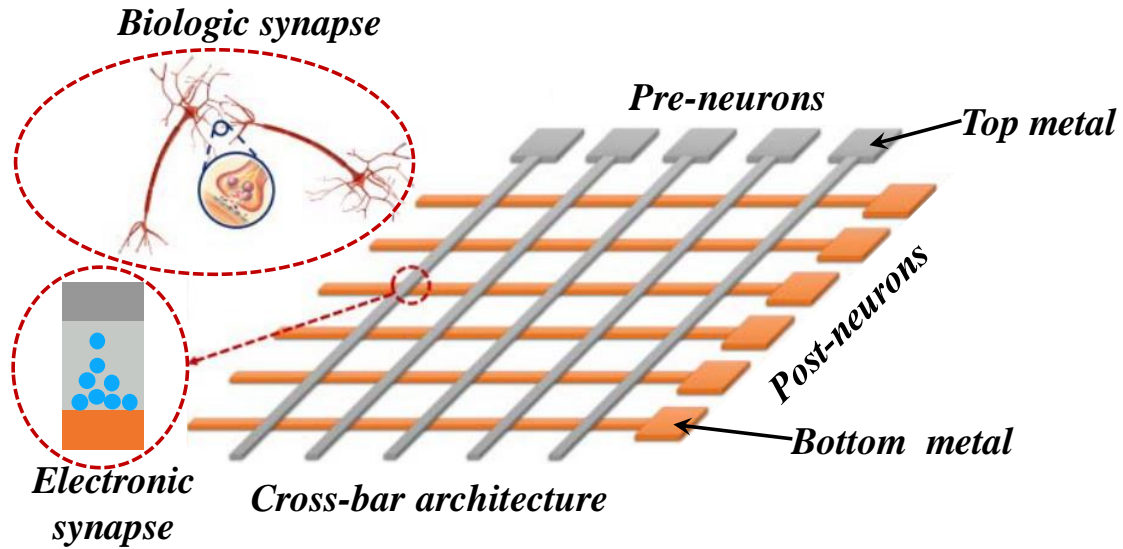
Figure 6.1 Artificial Neural Network based in a cross-bar architecture with electronic synapses implemented with memristor located in the intersection of horizontal bottom metal and vertical top metal. [Huang2017].

A more detail representation of an artificial neural network is shown in **Figure 6.2**, the weights w_{ij} are implemented in a hardware approach by means of memristors controlling their conductivity [Park2016].
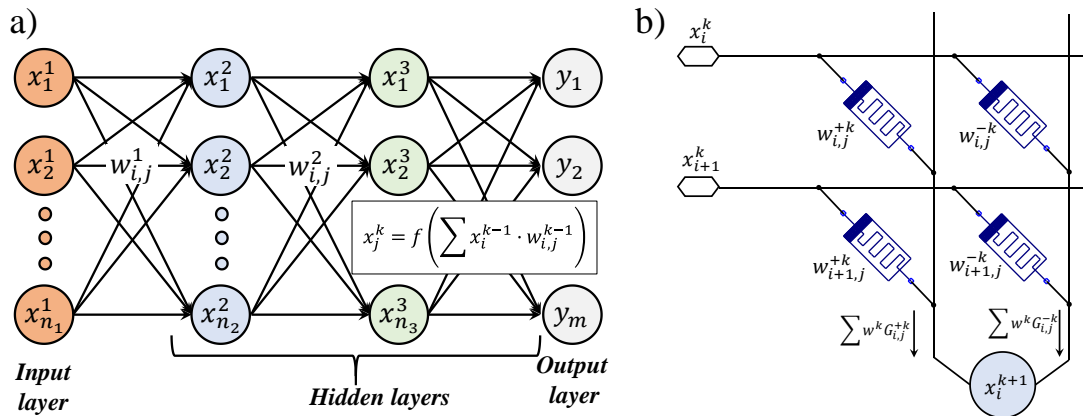
Figure 6.2 a) Schematic diagram of an artificial neural network with three layer (denoted by the super indices 1 to 3 in the weight w_{ij}) with an input signal x^l_i and an output signals y_i. **b)** Schematic diagram of an electronic synaptic devices implemented with memristor [Park2016].

Different methods to modulate the memristor conductivity have been reported in the literature:

   1.- Conductance modulation by means of V_{stop} [Yu2012]: the device is assumed to be in LRS (previously, a set process is undertaken). After that, an applied ramped voltage with a limited voltage V_{stop} provokes the reset process; however, not all the V_{stop} values lead the device to a full HRS. In this respect, different conductance values can be achieved. An example of four current levels is shown in **Figure 6.3**.
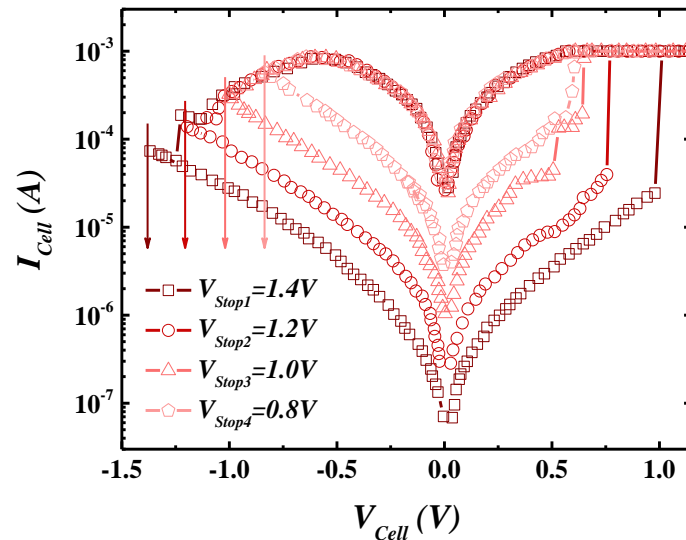
Figure 6.3 Example of a multilevel approach (four levels) represented in the I-V curves with different V_{stop} voltages (obtained from Yu et al. [Yu2012]).

   2.- Conductance control by means of I_{CC} [Pedro2017, González-Cordero2019b] : the device is assumed to be in the HRS (after a previous reset process). Later on an applied ramped voltage with a compliance current I_{CC} provokes the set process. Nevertheless, not all I_{CC} values produce a full LRS. Different device conductance values can be achieved. An example of eight current levels obtained with this procedure are shown in **Figure 6.4**.
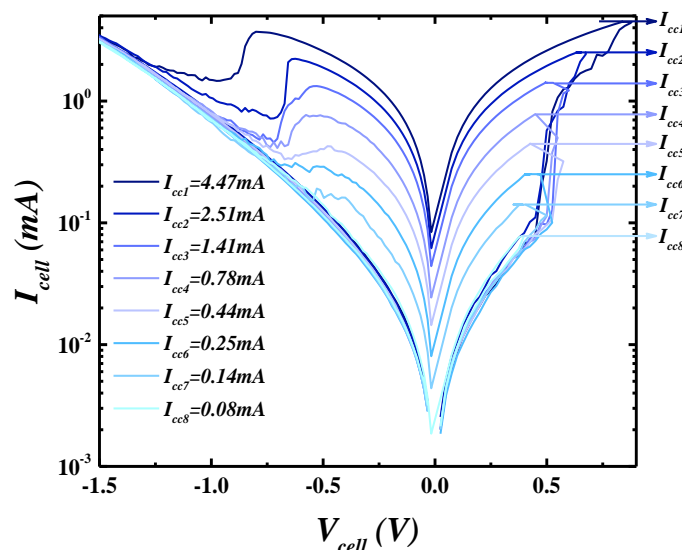
Figure 6.4 Eight current levels by controlling the conductivity are plotted versus voltage (different I_{cc} currents were used) [Pedro2017, González-Cordero2019b].

   These methods can be implemented in and 1T1R cell architecture [Chiang2015]. In this case I_{CC} depends on the voltage applied to the NMOS transistor gate (see **Figure 6.5 b**).
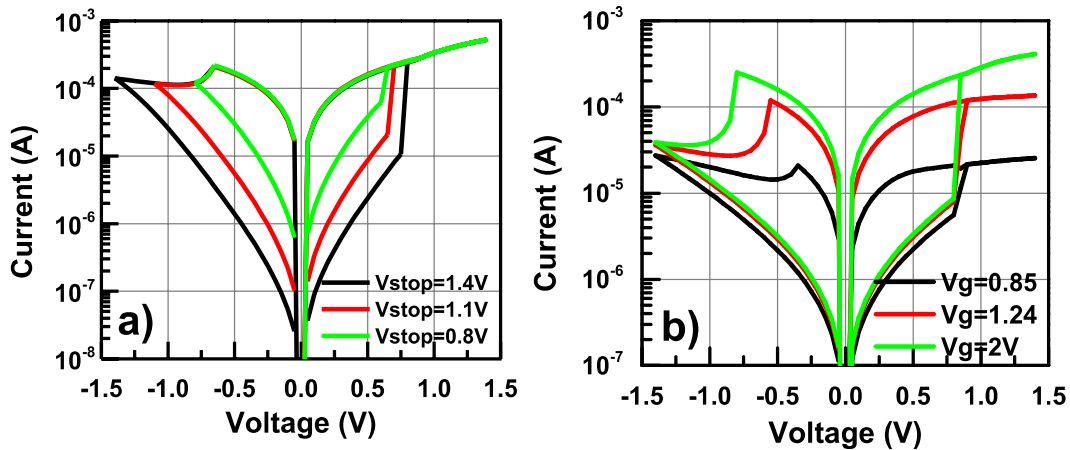
Figure 6.5 Conductance control in memristors within 1T1R circuits, **a)** three levels obtained by three different V_{stop} , **b)** three levels obtained by three different biases on the transistor gate [Chiang2015].

3.- Conductance control by means of voltage pulse modulation [Park2016]: with voltage pulses of different amplitudes (assuming a constant time scheme for the pulses) is possible to control dynamically RRAM conductance. On bipolar resistive switching devices, if the pulse is positive, a rising conductance is obtained (potentiation), in the case of negative pulses a decreasing conductance is achieved (depression). **Figure 6.6** shows an example of 64 level conductivity control with this technique [Park2016].
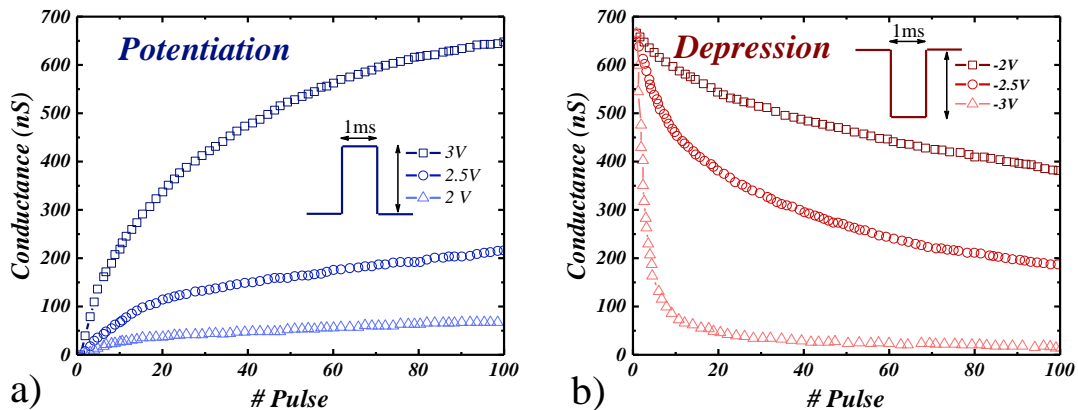
Figure 6.6 Example of 64 levels control by using sequences of different voltage pulse amplitudes. **a)** Potentiation increases the conductivity through positives pulses. **b)** Depression decreases the conductivity through negative pulses [Park2016].

4.- Other method of conductance control: Stathopoulos et al. reported a 92 levels of conductance control (6.5 bits memory per unitary cell) in a Al_xO_y/TiO_2 RRAM by an incremental step pulse with verify algorithm (ISPVA) [Stathopoulos2017]. Perez et al. reported in the table 1 at [Perez2019] different methods to control the conductance of a memristor and proposed a new method named multi incremental step pulse with verify algorithm (M-ISPVA).

An implementation based on TiN/Ti/HfO$_2$/W stacks using the control of I_{CC} is employed to mimic synapses operation. The fabrication and measurement set-up for these devices is described in the section A.2. TiN/Ti/HfO$_2$/W Devices. We used the UGR-VCM model (described in section 3.4. New Compact Model for Bipolar VCM (UGR-VCM)) to fit a complete series of 890 RS cycles with different compliance currents values (I_{CC}) with the help of parameter fitting using a gradient descent algorithm. A good fit between experimental and modeled I-V curves for each I_{CC} under study was obtained.

The results of this section were published in González-Cordero et al. Solid State Electronics (2019), the accepted preprint paper is presented below.

González-Cordero et al. Solid State Electronics (2019)

Quality metrics

Data base	Rating	Quartile
Web of Science	Impact factor: 1.666	Q3
Scimago	Scientific journal ranking: 0.492	Q2

Publication citations

Google Scholar	Web of Science
1	**0**

Analysis of resistive switching processes in TiN/Ti/HfO₂/W devices to mimic electronic synapses in neuromorphic circuits

Authors: G. González-Cordero[1], M. Pedro[2], J. Martin-Martinez[2], M.B. González[3], F. Jiménez-Molinos[1], F. Campabadal[3], N. Nafría[2], J.B. Roldán[1]

Address:
[1]Departamento de Electrónica y Tecnología de Computadores. Universidad de Granada. Facultad de Ciencias. Avd. Fuentenueva s/n, 18071 GRANADA, Spain. Email: jroldan@ugr.es
[2]Dept. Enginyeria Electrònica. Universitat Autònoma de Barcelona, Edifici Q. 08193 Bellaterra, Spain
[3]Institut de Microelectrònica de Barcelona, IMB-CNM (CSIC), Campus UAB, 08193 Bellaterra, Spain

Abstract:

The potential of resistive switching (RS) devices based on TiN/Ti/HfO₂/W stacks to mimic synapses within a neuromorphic applications context is analyzed in depth. The fabrication and characterization process are explained and a physically-based modeling description is performed to understand the devices resistive switching operation and conductance modulation. The model employed considers truncated-cone shaped conductive filament (CF) geometries and parasitic ohmic resistances linked to the device conductive filaments in addition to device capacitances. The temporal evolution is analysed assuming a valence change memory operation, where the oxide surrounding the CF is considered as well as the CF thermal description. A complete series of RS cycles has been fitted with the model by means of the gradient descent algorithm to study the compliance current effects on the conductance modulation. To do so, experimental and modeled results are extensively compared.

Index Terms — Conductive filaments, Neuromorphic applications, Parameter extraction, Physical model, Resistive switching memory, RRAM.

I. INTRODUCTION

RRAM technology has been proved to be suitable for the implementation of electronic synapses in a neuromorphic architecture, because of its non-volatile memory properties, the analog control of its conductivity state, scalability and compatibility with CMOS technology [1-3]. Moreover, its device-level variability, which is a well-known issue in these devices [4, 5], could be mitigated by the learning algorithms employed in artificial neural networks, leading to a system with high resilience to device variability. In order to optimize the device operating point, electrical characterization and further modeling is needed to understand the underlying mechanisms of resistive switching (RS) phenomena. RS mastering is one of the keys for the implementation of an electronic synapse, where, analog control of the conductance is required to imitate the potentiation and depression processes that take place in the connections between neurons [3, 6]. This analog control allows to build a stronger or weaker link between neuronal circuits, mimicking the variation of the synaptic weight, i.e., the connection strength between neurons.

In this context, the use of simulations at both device and system-level can be essential to deepen on the physics behind RS and the operation of circuits based on RS devices. The information obtained by means of simulators can be used to explore the capabilities of RRAM technology for neuromorphic applications [3]. In this respect, we make use in this work of a previously developed RRAM physically-based model [7, 8] to characterize the device operation as synapses within a neuromorphic hardware landscape where electronic circuits are thought to be employed in neuro-inspired computing. This compact model, once its capacity to work correctly by reproducing the behavior and main characteristics of the studied devices as electronic synapsis is proved, could be used in the future to aid the design of new neuromorphic circuits based on the technology presented here.

The model employed here has been previously described and validated [7-9] and includes important physical effects involved in the RS operation of the devices under consideration [7, 8]. Thermal effects and quantum mechanical effects, such as tunneling currents, are included along with redox reactions to control the dynamics of CF rupture and rejuvenation [5, 7, 9, 10-13]. Parasitic effects such as series resistances and capacitances are also incorporated in the physical description. In addition, the model, in a compact form, has been implemented in circuit simulators [7, 9] with the purpose of analyzing RS cycles with a fixed compliance current. In this work, RS cycles under variable compliance currents are experimentally obtained and analyzed with our model in order to characterize TiN/Ti/HfO$_2$/W devices. We have studied the possibilities to modulate the device conductance state by means of the compliance current and assess the devices potential to be employed as electronic synapses.

The fabrication technology and measurement details are explained in section II, the model main features are described in section III and results and discussion are given in section IV. Finally, we extract the main conclusions in section V.

II. DEVICE DESCRIPTION AND MEASUREMENT SET-UP

The devices employed in this study are TiN/Ti/HfO$_2$/W Metal-Insulator-Metal (MIM) structures in a single device cross-bar configuration and an area of 5×5 μm^2 (see Figure 1) [7, 8]. They were fabricated on 100 mm-diameter Si wafers. The fabrication process started with a thermal oxidation, leading to a 200 nm SiO$_2$ layer to isolate the MIM devices from the Si substrate. Next, the bottom electrode, consisting of a 200 nm-thick W layer was deposited by magnetron sputtering and patterned by photolithography and dry etching. Then, a 10 nm HfO$_2$ insulator layer was deposited by atomic layer deposition (ALD) at 225 °C using TDMAH and H$_2$O as precursors and N$_2$ as carrier and purge gas. After the ALD process, the top electrode, consisting of 200nm TiN and 10nm Ti, was deposited by magnetron sputtering and patterned by photolithography and

dry etching. Finally, the contact area to the bottom electrode was defined by photolithography and dry etching of the HfO₂ film on top of the W layer.
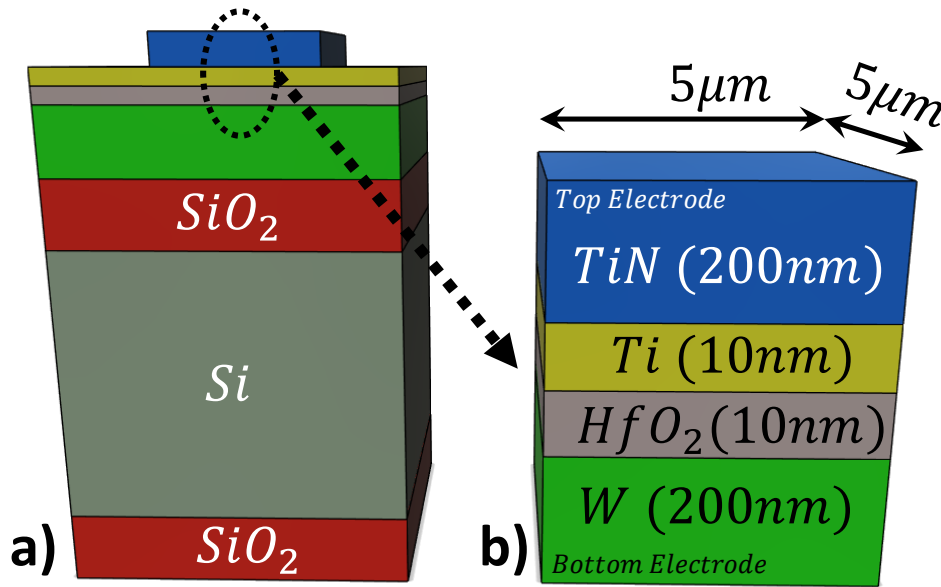
Figure 1. a) Stack structure built on the silicon wafer, b) schematic of the TiN/Ti/HfO₂/W Metal-Insulator-Metal (MIM) RRAM devices.

A particular measurement scheme was used here involving smart control of the compliance current (I_{CC}) of each RS cycle. Ad hoc software was developed for this purpose making use of a Semiconductor Parameter Analyzer (Ag4156C) [1]. The voltage was applied to the top electrode, while the bottom electrode was grounded. After a forming process of $I_{cc} = 100\mu A$, a ramped voltage was employed and the negative stop voltage was fixed to -1.6V, to make sure the devices reach the high resistance state (HRS) within the reset process. The smart control of the measurement allows taking decisions during the set process depending on the current, i.e., the voltage will increase until the measured current reaches I_{CC}. At this point the ramped voltage is reversed. In Figure 2a the I-V curves of complete RS cycles are shown for different current compliances. A gradual modification of the compliance current was considered by means of the ramped signal shown in Figure 2b.
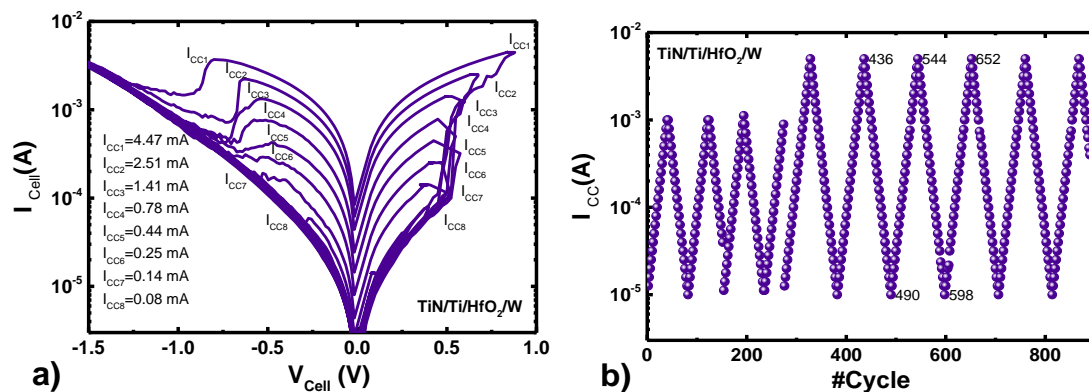
Figure 2. a) I-V curves from RS cycles 545 to 595. The curves were selected in steps of 5 cycles, and they correspond to measurements for different compliance currents. b) I_{CC} variation for the series of 890 RS cycles employed in this manuscript.

As expected, the higher I_{cc} the higher I_{Set} (and I_{Reset}) due to the formation of thicker conductive filaments and correspondingly lower device resistances in the low resistance state (LRS) [4, 5, 14, 15]. A universal trend behind this behavior has been reported previously [16, 17].

III. PHYSICAL MODEL

The model employed here has been described previously [8, 9] and the devices used in the fitting process reported in [7, 8] are similar. Therefore, the fitting constants reported in the latter references are also used here. The devices are modeled making use of a truncated-cone filament whose shape changes through the RS cycle (reset and set processes) as depicted in Figure 3 [8]. The approach based on the variation of the CF size is in line with previous models found in the literature [5, 12, 13, 17-20]. In this respect, single cylinders [5, 12], truncated-cone-shaped filaments [5, 18] and two cylinder structures in which the smaller cylinder modifies its length and radius [13, 20] and the bigger one is fixed are employed as conductive filaments.
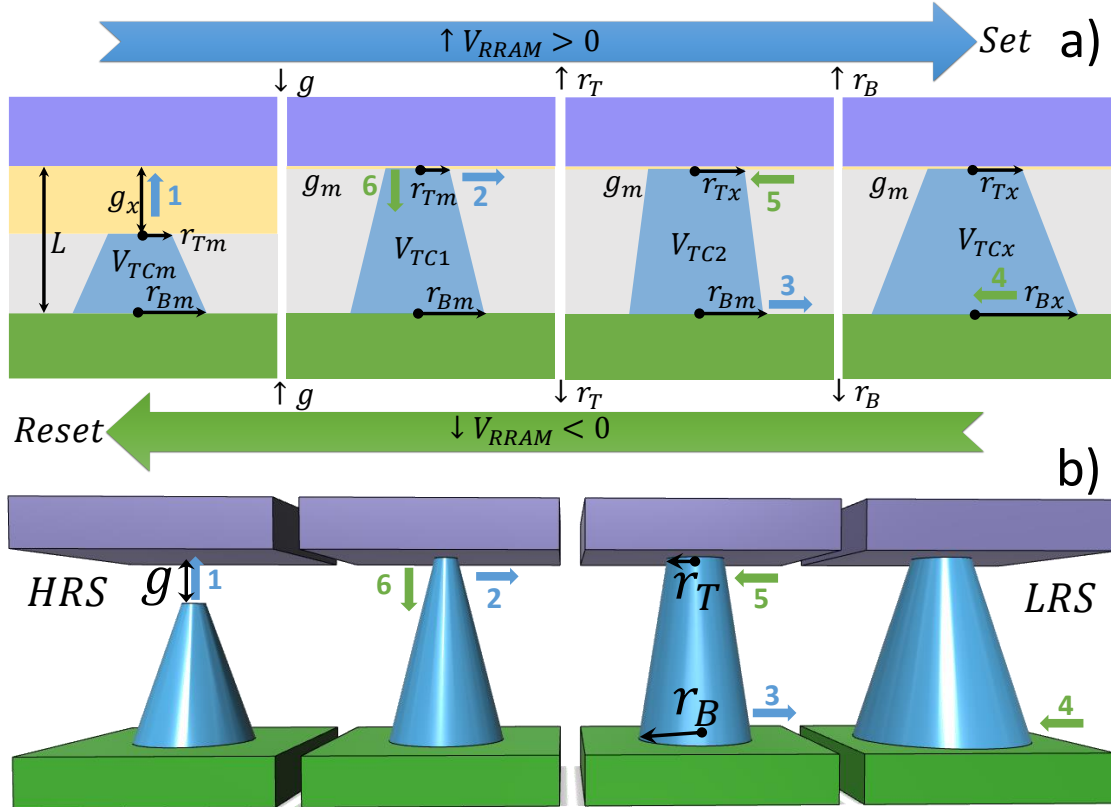
Figure 3. Conductive filament geometry evolution in the model employed to describe RS cycling. The filament volume of the truncated-cone depends on gap (g), the top radius (r_T) and the bottom radius (r_B) that evolve according to equations (1) and (2) following the fixed schema shown in the figure. a) (HRS) Initial CF geometry at its minimum value during the cycle, characterized by a gap length higher than the minimum value (g_m) and close to the maximum (g_x), the minimum top radius (r_{Tm}) and the minimum bottom radius (r_{Bm}). A positive voltage increase leads to a reduction of the gap between the filament tip and the electrode (process 1), until its minimum value, g_m, is reached; if the applied voltage keeps on rising, the CF volume continues its growth by increasing its top radius, r_T (process 2). This parameter is limited by two determined values, $r_{Tm} < r_T < r_{Tx}$. Finally, once r_T reaches its maximum value, it is the bottom radius, r_B, the one that rises till the CF is fully formed (process 3) (the volume reaches its maximum value) and the set process is over. The limits for this radius are the following: $r_{Bm} < r_B < r_{Bx}$. In this case, the LRS is achieved. If the device voltage changes its polarity, the process would lead to a CF volume reduction (a reset process initiates) that would be translated first to a change in r_B, a (process 4) reduction till $r_B=r_{Bm}$. Later on, a reduction of r_T takes place (process 5) and, finally, a g increase (process 6). At this point, the CF volume reduction is over (the reset process is finished). b) 3D scheme of the CF volume growth (set process, represented by blue arrows, corresponding to positive voltages in Figure 2a) and volume decrease (reset process, represented by green arrows, corresponding to negative voltages in Figure 2a).

The CF geometrical features are shown in Fig 3. We have assumed a truncated-cone shaped CF in line with previous studies involving devices based on Ag/ZrO$_2$/Pt [21] and Pt/TiO$_2$/Pt [22] stacks. The CF, with a metallic-like conductivity, is assumed to be made of oxygen vacancies. The migration of oxygen ions, the generation of oxygen vacancies and the recombination of both species are assumed in simplified the formulation of the Equations 1 and

2, as reported previously [7, 8]. In this work, the evolution of the CF is described by means of Equations 1 and 2 and it is formulated in terms of the CF volume. Taking into consideration the geometrical particularities of our model (Figure 3), we use a three dimensional approximation that allows the description of the truncated-cone shaped CF geometric parameters [23, 24] instead of the variation of the CF radius as was employed in Refs. [5, 12, 25, 26] or the gap between the CF tip and the electrode, as described in Ref. [27].

For the set process, the main physical mechanism that controls the filament evolution is the generation of oxygen vacancies [13, 27]. However, the reset is determined by three processes [13]: electrode release of oxygen ions, movement of the oxygen ions in the oxide layer (via hopping) and recombination between oxygen ions and vacancies. The three processes are also thermally activated. For the sake of simplicity and compactness in the mathematical formulation, we merged in a single equation the previous components [7]. In this respect, we call the reader's attention to the fact that our development falls in the compact modeling approach; an accuracy-simplicity trade-off has been considered since the model is thought to be implemented in simulators to analyze circuits with a very high number of devices.

Therefore, the CF volume temporal evolution is obtained by means of the following equations,

$$\frac{dV_{TC}}{dt} = v_0 \exp\left(-\frac{E_a - \alpha_a Z q \xi}{k_b T}\right) \quad (set) \tag{1}$$

$$\frac{dV_{TC}}{dt} = -v_0 \exp\left(-\frac{E_r - \alpha_r(g) Z q \xi}{k_b T}\right) \quad (reset) \tag{2}$$

where V_{TC} stands for the CF volume, v_0 for the product of the oxygen ion vibration frequency and the approximated separation between oxygen vacancies, E_a is the average activation energy for oxygen vacancies generation, α_a is the enhancement factor of the electric field, Z is the charge number of oxygen ions, q is the unit charge, ξ is the electric field and k_b is the Boltzmann's constant. The local field strength can be bigger than the average electric field. For this reason, it is usual to employ α_a as a fitting parameter [13], [7]; in addition, it accounts for the polarizability of the dielectric. T is the local temperature obtained by means of the approach detailed in references [7, 8]. In this case the heat equation is solved, and for this purpose a simplifying procedure that considers an equivalent cylinder instead of a truncated-cone shape is employed in order to obtain an analytical expression for the temperature. E_r stands for the average energy that accounts for the aforementioned processes involved in the RESET event. Note that the factor $\alpha_r(g)$, which takes into account the local electric field enhancement depends on the gap because it is expected that the local electric field enhancement in the gap region was bigger than the average electric field as the gap is narrower [27]. For each I-V curve and voltage point, once the CF state has been determined, the current is calculated [7]-[8]. The RRAM equivalent circuit for the current calculation is sketched in Figure 4a. The current sources I_{g1} and I_{g2} correspond to hopping currents through the gap between the filament and the top electrode and from the sides from the filament to the top electrode, respectively. They are calculated according with expression (19) in [13]. In addition, the top and bottom electrode resistances are represented by R_{CT}, R_{CB}, while R_{CF} is the ohmic resistance due to the formed filament. Finally, R_{ox} and R_g are the resistances linked to the dielectric surrounding the CF and to the dielectric region filling the gap, respectively [7]-[8].
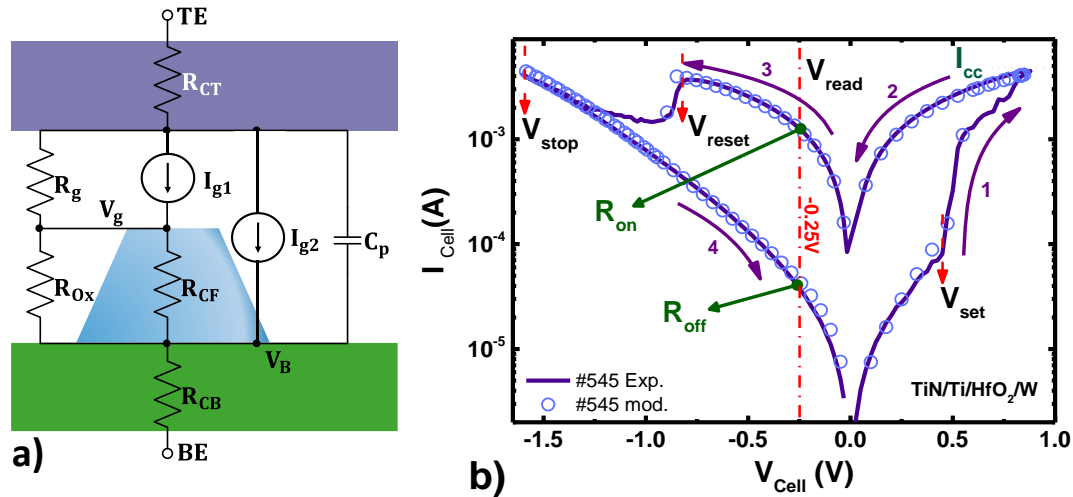
Figure 4. a) Circuit representation of the different electrical components included in the model [7, 8]. b) Description of the I-V curve of a modeled cycle (experimental data are shown in solid lines and modeled data in symbols). Initially, the RRAM is in the HRS. Section 1 of the I-V characteristic and the previous curve region represent a current rise due to a positive ramped voltage applied to the device, a set process takes place when the applied voltage equals V_{Set} (the device enters the LRS). The maximum current is limited by I_{cc}. In section 2, a negative ramped voltage is applied to the RRAM, still with positive voltage values. In section 3, a negative voltage ramp is employed with negative voltages; a final voltage value, V_{Stop}=-1.6V is used. For V_{Cell}=-0.25V (section 3) the R_{on} resistance is measured, and when the voltage reaches V_{Reset} the RRAM changes to the HRS. In section 4, a positive voltage ramp is used increasing voltage values. For V_{Cell}=-0.25V, R_{off} resistance is determined.

IV. RESULTS AND DISCUSSION

The modeling results for a selected set of experimental I-V curves are shown in Figure 4b and Figure 5 for different I_{CC} values. A good fit is obtained.
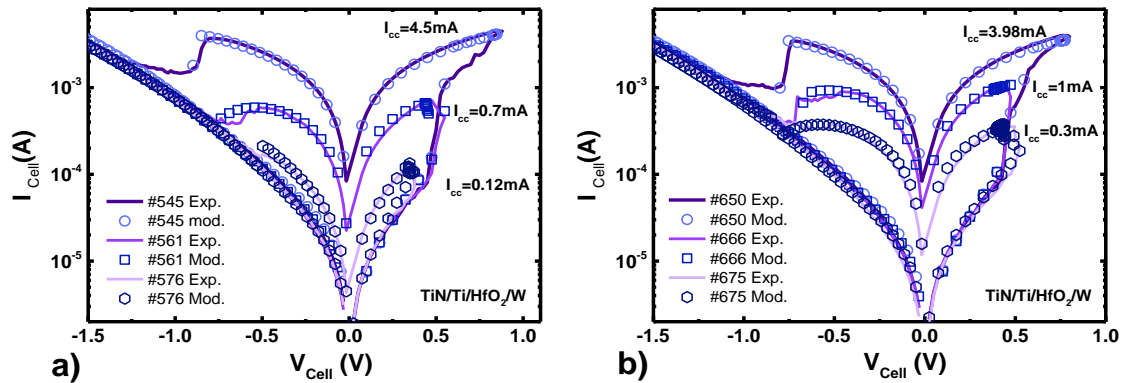
Figure 5. RRAM current versus applied voltage. Experimental data (lines) and modeled data (symbols) are shown for different compliance currents: a) cycle #545 - I_{cc}=4.5mA, cycle #561 - I_{cc}= 0.7mA and cycle #576 - I_{cc}=0.12mA, b) cycle #650 - I_{cc}=3.98mA, cycle #666 - I_{cc}= 1mA and cycle #675 - I_{cc}=0.3mA.

A massive fitting of the 890 RS cycles obtained for the I_{cc} depicted in Figure 2b has been performed. A general framework for the modeling procedure was established by selecting the following geometrical parameters for the truncated-cone shaped CFs: The minimum filament volume is determined by the maximum gap length (g_x=5.4nm) and the minimum top and bottom radii (r_{Tm} =1nm and r_{Bm}=12nm, respectively). The device is in the HRS and during the set process a single oxygen vacancy could close a percolation path, therefore these geometrical values are reasonable. The cycle-to-cycle variability and the different compliance currents used for each cycle lead to different initial and final filament sizes. A different fit was performed for each experimental I-V curve as follows: given an I-V curve, we assume a set of parameters for the model. With these parameters, we obtain (for the same experimental voltages) an array (I_{mod}) of current values provided by the model for each voltage. Taking into account the Euclidean distance

between this array and the array given by the corresponding experimental curves (I_{exp}), the relative error m_I (Equation 3) is determined [28].

$$m_I = \frac{||I_{exp} - I_{mod}||}{||I_{exp}||} \qquad (3)$$

where $||...||$ represents the norm of the corresponding vector. This value gives us a measure of the error between the experimental and modeled data. A method based on gradient descent algorithm [29] is employed to change the model parameters until a local minimum for m_I is obtained. Figure 6 shows the geometrical parameters corresponding to the state of the filament once the compliance current and maximum positive voltage have been reached. As can be seen, at low compliance currents, the filament barely changes ($g \sim g_x$, $r_T = r_{Tm}$, $r_B = r_{Bm}$).

If the compliance current is higher than 0.055 mA, the filament is allowed to evolve, entering in the tunable region (Figure 6). The higher the compliance current, the lower the final gap length. Once the gap reaches its minimum value, the top radius is allowed to grow to its maximum value and, after that, the bottom radius grows. Therefore, for the cycles where the set process is well completed and the LRS reached, the gap is minimum, the top radii maximum and the bottom radius takes a value between its minimum and maximum values that determines the current in the LRS for each cycle. Note that the CF volume obtained for each I-V curve is different, as expected, and that, because of the scheme we have followed in order to reproduce the CF evolution, the dispersion in the values of the current for completely formed CFs is reflected as a dispersion in the values of the radii, while a variation in the values of the gap (g) reproduces the dispersion in the values corresponding to the HRS. This result is coherent with the role that I_{cc} plays in limiting the current in each RS cycle and therefore fixing R_{on} value (I_{Reset} is linked to I_{CC} because of this [16]). The region where the gap starts to be reduced is signaled by a vertical dashed line. In these cases an operation region with tunable conductivity is entered and RS effects can be employed to mimic synaptic potential in the devices [1, 3] within a neuromorphic circuit context.
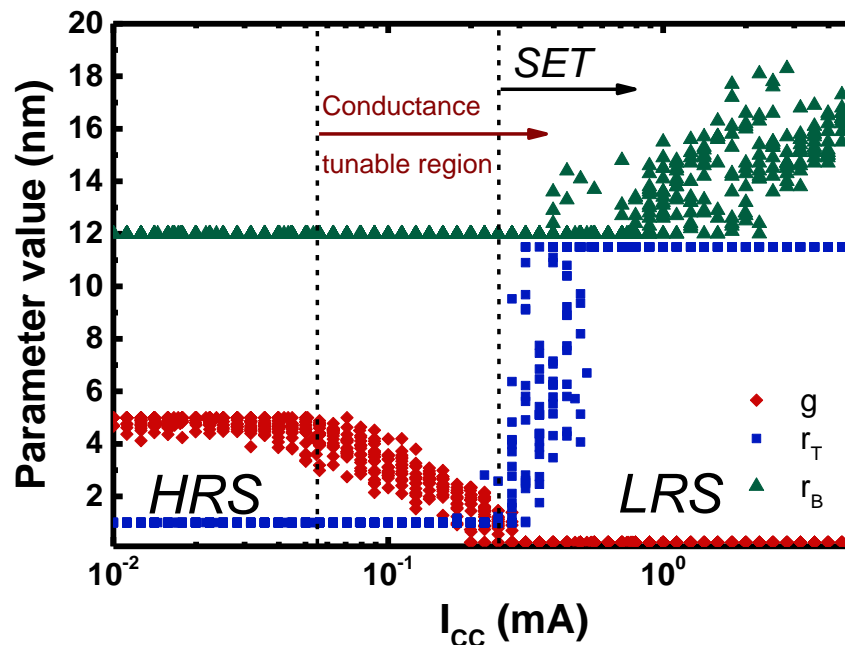
Figure 6: Filament size after the compliance current and the maximum positive voltages are reached (set process), as a function of the compliance current for some of the fitted cycles. The filament final size is given by the gap length (g) and the top and bottom CF radii (r_T and r_B, respectively). In the low I_{CC} region a complete set process is not performed since there is a gap between the CF and the electrode. The tunable region starts when the CF geometry changes (indicated by a dashed line).

A comparison between measured and modeled (after the fitting process) resistances, both in the LRS and HRS, is plotted in Figure 7 to show the goodness of the modeling technique presented for the RS series under study.
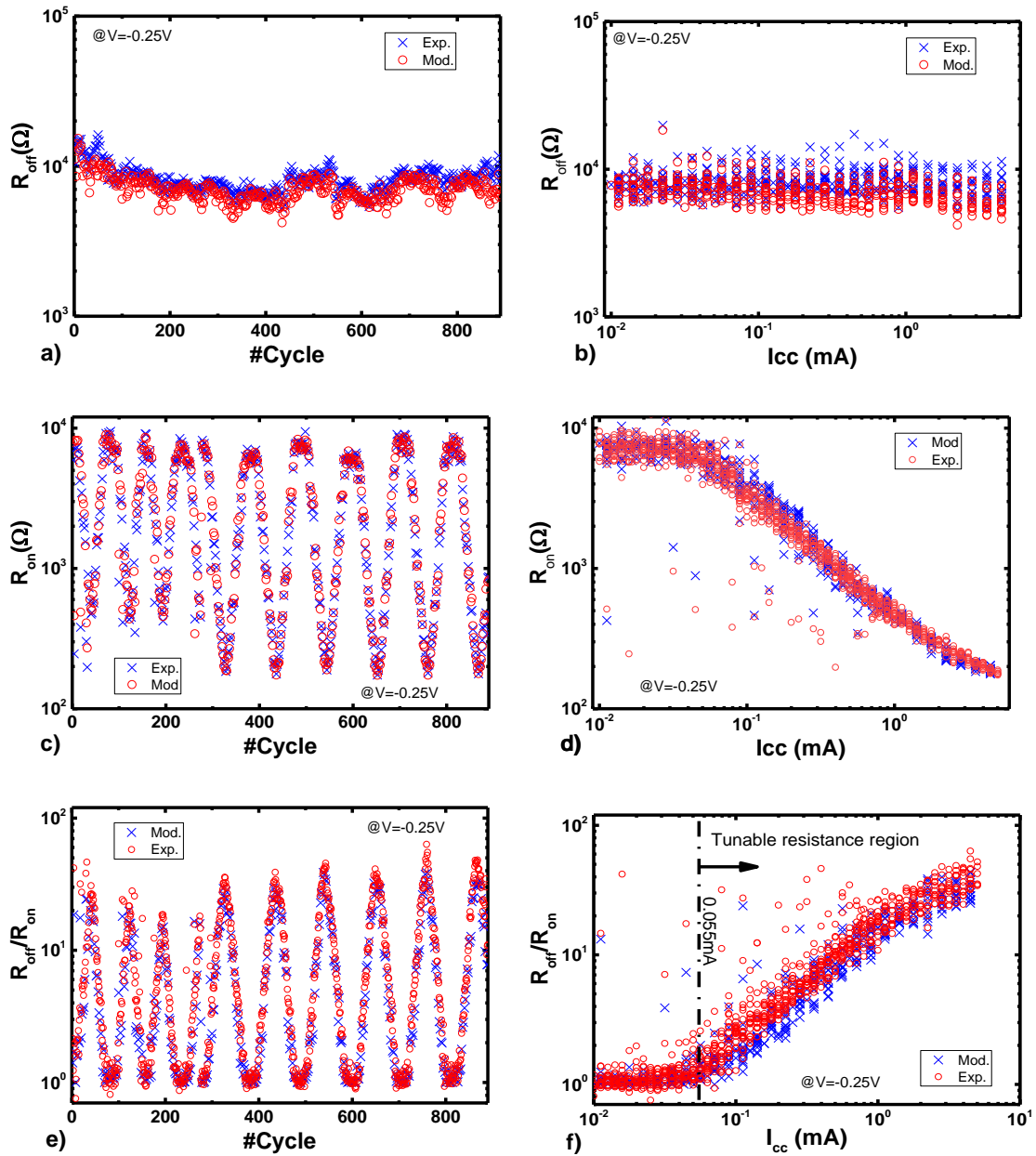
Figure 7. a) R_{off} evolution for the 890 cycles under consideration (measured at V_{Cell}=-0.25V), experimental (modeled) data are shown in blue crosses (red circles), b) R_{off} versus I_{cc} for the cycles considered, c) R_{on} evolution for the 890 cycles under consideration (measured at V_{Cell}=-0.25V), d) R_{on} versus I_{cc}, e) R_{off}/R_{on} ratio versus cycle number, f) R_{off}/R_{on} versus I_{cc}.

A narrow set of R_{off} values is obtained, centered around 10kΩ. The R_{on} value is similar to R_{off} for I_{cc} values below 0.055mA. As highlighted above, it is clear that for these low compliance currents the set process is not performed, therefore $R_{on} \approx R_{off}$ (see Figure 7f). The values for parameter *g* shown in Figure 6 show clearly the non-zero distance from the filament tip to the electrode; in fact, the gap is not modified in these cases. On the contrary, for I_{cc} values higher than 0.055mA, a difference between R_{on} and R_{off} can be seen.

The R_{off}/R_{on} ratio is a measure used by analog circuit designers to determine the level of tuning that the device supports. In our case, this measure shows a two orders of magnitude maximum. Depending on the application, there may be sufficient margin (e.g. to fix weights in neural network implementations). Another issue to highlight here is linked to the possibilities in the realm of multilevel memory circuits.

The histogram and cumulative probability for R_{off} have been shown in Figure 8. It can be seen that the fitting obtained allowed us to reproduce the values accurately.
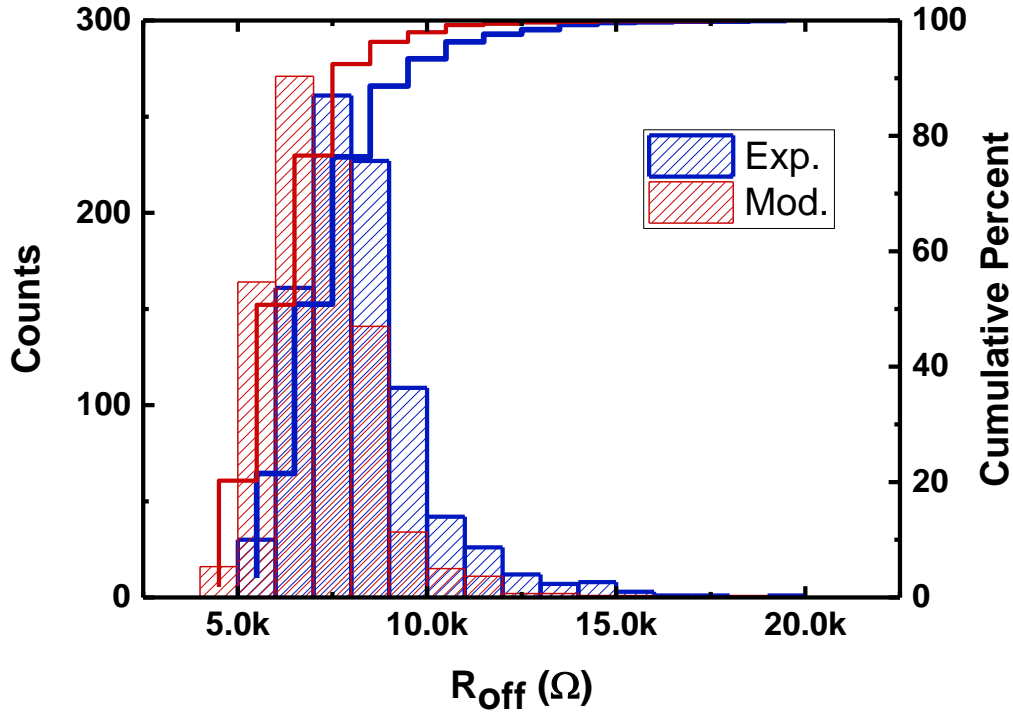
Figure 8. Histogram and cumulative probability for the R_{off} obtained in a set of 890 RS cycles for different I_{cc} values, experimental data (blue) and modeled data (red).

R_{on} versus I_{cc} has been plotted in Figure 9 for modeled and experimental data. The expected values and dependencies are obtained. The plateau observed at low I_{cc} values corresponds to the region where the set process is far from being reached (g remains at its higher value g_x in Figure 6). The on resistance behavior versus the compliance current, $R_{on}(I_{cc})$, can be semiempirically modeled making use of the following analytical expression, with I_{cc} as independent variable,

$$R_{on}(I_{cc}) = \frac{R_o}{1 + \frac{I_{cc}}{I_o}} \tag{4}$$

The paremeter R_o is linked to the HRS resistance (this expression gives a resistance of R_o at low compliance currents). Equation (4) points out how the ratio R_{off}/R_{on} can be modulated by means of the compliance current, I_{CC}. This fact suggests a promising potential for neuromorphic circuit applications taking into consideration the capacity to tune the device conductance (as illustrated by the fitting shown in Figure 9). Comparison of Figures 9a and 9b highlights again the accuracy of the modeling procedure.

Note that Expression (4) reduces to the well known relationship $R_{on} = R_o \cdot I_0/I_{CC}$ [30], for $I_{CC} \gg I_0$. Furthermore, with the values used in this work, the product $R_o \cdot I_0$ is 0.6-0.7V, in the order of $V_C = 0.4$V in the expression $R_{on} = V_C/I_{CC}$ [20]. In the relation we propose in this work (Expression 4), the parameter I_0 represents a compliance current limit. For compliance currents much lower than this limit, the CF would remain basically unchanged.
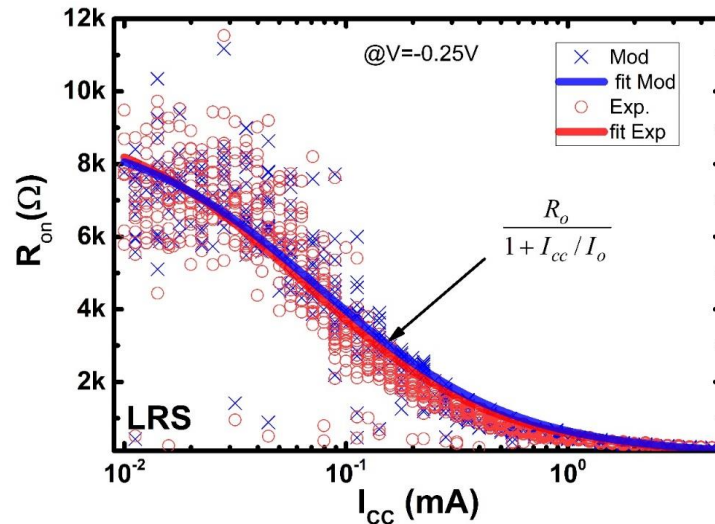
Figure 9. R_{on} versus I_{cc} for the RS series under consideration. Blue crosses and line are used for modeled data, the fitting curve shown (Equation 4) is obtained by means of the following parameters ($R_o = 9461\Omega$, $I_o = 64.41\mu A$); red circles and line are used for experimental data, the fitting curve shown (Equation 4) is obtained making use of the following parameters ($R_o = 9105\Omega$, $I_o = 77.05\mu A$). In both cases the fit reflects 95% confidence bounds.

As explained above, the CF volume was assumed in Equations 1 and 2 as the variable to be calculated in order to describe RS in the devices under study. The volume reached by the filament after a SET process has been plotted in Figure 10.
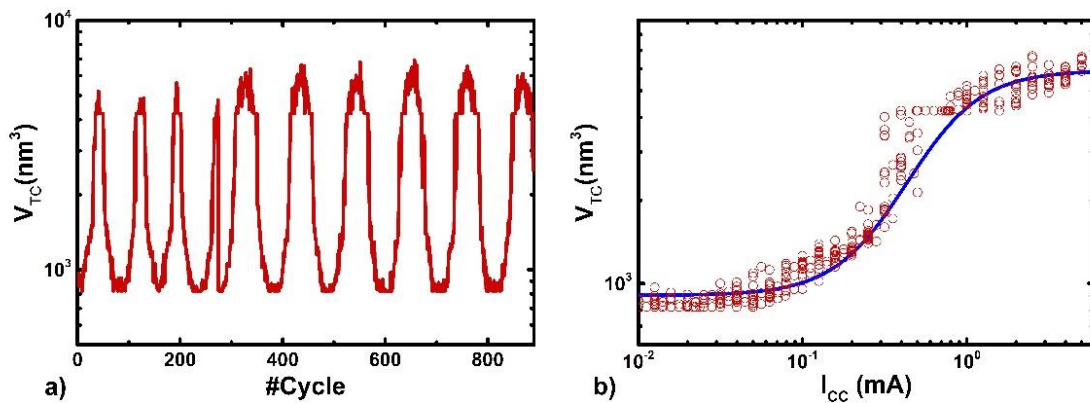
Figure 10: CF volume when the compliance current and the maximum voltage have been reached versus cycle number (a) and versus I_{CC} (b). The shape of the modeled data can be reproduced by a sigmoid function (Equation 5) in a log-log scale. We have performed the fitting with the following parameters (a=8.69, b=6.81, c=14.87 and d=0.52).

See that the CF volume follows the I_{CC} signal employed in the measurement technique, as expected (Figure 10a). The CF volume increases as I_{CC} rises, once a threshold value is reached (the tunable region starts around 0.055 mA, as it can be also seen in Figure 6). This higher volume is reflected in the R_{on} reduction as shown in Figure 9. However, for the highest compliance currents, a certain degree of saturation of the final volume (or resistance) versus compliance current plots appears. That fact is linked to the enhancement of the side components of the current at the highest voltages (modeled by means of I_{g2}, see Figure 4) at the expense of the main current component I_{g1} (which is, therefore, limited by the growing of that side component and that mainly determines the evolution of the filament). This behavior make the shape of the V_{TC}-I_{CC} plot resemble an "S" and, therefore, the distribution of CF volume data shown in Figure 10b can be well fitted with a sigmoid function within a semiempirical approach. In this respect, we have proposed the function given in Equation 5. The fitting is reasonably good, as can be seen in Figure 10b.

$$V_{TC}(I_{CC}) = exp\left(\frac{a-b}{1 + exp\left(-\left(\frac{ln(I_{cc})}{d} + c\right)\right)} + b\right) \qquad (5)$$

The previous explanation concerning the two hopping currents (I_{g1}, I_{g2}) is coherent with the CF truncated-cone shapes reported in the literature and also with the consideration of other CF shapes, such as tree-branch shapes, where tunneling current components can be found in parallel with ohmic ones due to role played by intermediate oxygen vacant clusters close to the percolation paths.

It has been highlighted that when small variation of the compliance current is employed, a better control of the device resistance is achieved in comparison with random variations of the compliance current [1]. A coherent explanation of this effect can be given in the context of RS Kinetic Monte Carlo simulation [4, 11, 31-34]. It is seen that reduction (oxidation) activation energies of ion (atoms) within the dielectric that contribute to the percolation paths and configure the CFs depend on the number of atoms surrounding them [4, 31]. Therefore, the cluster formation, that constitutes the first stage in percolation path evolution, can be favored if small variations of I_{CC} are employed in a cycle-to-cycle basis. In this manner, better control of the density of defects in the CF is achieved and consequently the device conductivity can be modulated more easily. It was also addressed the issue connected to the different manners of defining the end of reset processes [1]. One of them fixing a stop voltage allows better control of R_{off}; while other processes, which are stopped when a current drop is detected, does not allow control of R_{off}. This effect can be explained if we concentrate our reasoning on the parameter g in our model (the gap distance, see Figure 3). In this respect, the current drop is produced by the sudden increase of the gap between the filament tip and the electrode. Since the device current depends exponentially on g [8], we would find out different gaps if the reset process is stopped when the device current drops off. Consequently, different gaps could be formed and very different currents (since the current depends exponentially on the gap distance) would be obtained, this could lead to a great R_{off} variability.

Finally, we can assess the maximum temperature obtained in the set process for each of the I_{CC} modeled. It has been plotted in Figure 11. The temperature was obtained by solving the 1D heat equation considering a cylindrical shaped CF. We include a term weighted by a heat transfer coefficient to account for the lateral heat dissipation from the CF to the dielectric. The Joule heating was calculated by means of the electrical conductivity and the electric field in the CF. More details are given in Ref. 8.
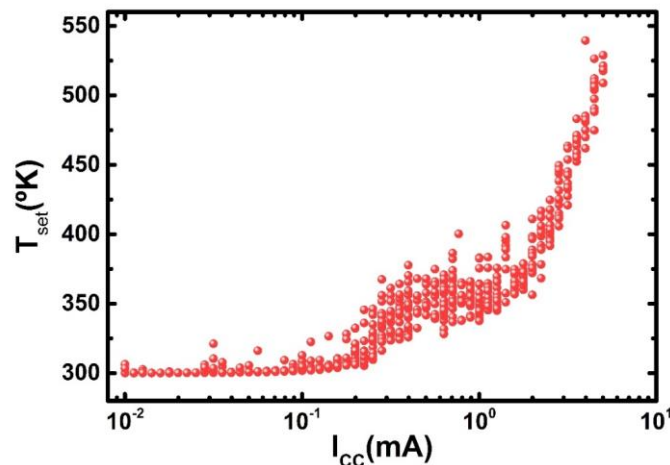
Figure 11. Maximum temperature in the set process versus compliance current.

As expected, at low compliance currents the temperature does not increase due to the lower currents achieved and the low Joule heating effects. However, once the gap parameter achieves its minimum value, the current, heating effects and CF temperature go up.

V. CONCLUSIONS

A physical compact model to analyze electronic synapses based on resistive switching devices has been employed to describe the influence of the compliance current on the resistive switching processes. The modelling approach makes use of truncated-cone shaped CF geometries and parasitic ohmic resistances. A new measurement procedure was employed to gradually change the compliance current. The analysis consisted of a massive fitting of 890 RS cycles to understand the effects of compliance current variation. An in-depth comparison between measured and modeled data was performed to show the accuracy of the modeling technique in reproducing a modulation ratio of the resistance and the compliance current in two decades. Therefore, the results helped to clarify the devices potential to work as synaptic elements in neuromorphic circuits taking into consideration the conductivity gradual control capacity observed. As shown, this compact modeling approach could be used to aid neuromorphic circuit designers by allowing simulations at a circuit level.

VI. ACKNOWLEDGMENTS

REFERENCES

[1] M. Pedro, J. Martin-Martinez, M.B. Gonzalez, R. Rodriguez, F. Campabadal, M. Nafria, Xavier Aymerich, "Tuning the conductivity of resistive switching devices for electronic synapses", Microelectronic Engineering, Vol. 178, pp. 89-92, 2017.

[2] S. Yu, Y. Wu, R. Jeyasingh, D. Kuzum, H.-S. Wong, "An electronic synapse device based on metal oxide resistive switching memory for neuromorphic computation", IEEE Trans. Electron Devices, 58 (8), pp. 2729–2737, 2011. DOI: 10.1109/TED.2011.2147791.

[3] S. Yu, "Neuro-inspired computing using resistive synaptic devices", Springer, 2017. ISBN: 978-3-319-54312-3

[4] F. Pan, S. Gao, C. Chen, C. Song, F. Zeng, "Recent progress in resistive random access memories: materials, switching mechanisms and performance", Materials Science and Engineering, 83, pp. 1-59, 2014. DOI: 10.1016/j.mser.2014.06.002

[5] M.A. Villena, J.B. Roldán, F. Jiménez-Molinos, E. Miranda, J. Suñé, M. Lanza, "SIM^{2}RRAM: a physical model for RRAM devices simulation", Journal of Computational Electronics, 2017. DOI: 10.1007/s10825-017-1074-8

[6] N. Suri, "Advances in neuromorphic hardware exploiting emergin nanoscale devices", Springer, 2017. DOI:10.1007/978-81-322-3703-7

[7] G. González-Cordero, F. Jiménez-Molinos, J.B. Roldan, M.B. González and F. Campabadal, "In-depth study of the physics behind resistive switching in TiN/Ti/HfO2/W structures". J. Vac. Sci. Technol. B 35, 01A110, 2017 DOI: 10.1116/1.4973372.

[8] G. González-Cordero, M.B. González, H. García, F. Campabadal, S. Dueñas, H. Castán, F. Jiménez-Molinos, J.B. Roldán, "A physically based model for resistive memories including a detailed temperature and variability description", Microelectronic Engineering, Vol. 178, pp. 26-29, 2017. DOI: 10.1016/j.mee.2017.04.019

[9] G. González-Cordero, M. B. González, H. García, F. Jiménez-Molinos, F. Campabadal, S. Dueñas, H. Castán and J. B. Roldán, "A Physically Based Model to describe Resistive Switching in different RRAM technologies", in 11th edition of the Spanish Conference on Electron Devices (CDE), in Barcelona, Spain, 2017. DOI: 10.1109/CDE.2017.7905223

[10] M.A. Villena, J.B. Roldán, M.B. González, P. González-Rodelas, F. Jiménez-Molinos, F. Campabadal, D. Barrera, "A new parameter to characterize the charge transport regime in Ni/HfO_2/Si-n$^+$-based RRAMs", Solid State Electronics, vol. 118, pp. 56-60, 2016. DOI: 10.1007/s10825-017-1074-8

[11] A. Padovani, L. Larcher, O. Pirrotta, L. Vandelli and G. Bersuker, "Microscopic Modeling of HfOx RRAM Operations: From Forming to Switching", IEEE Transactions on Electron Devices, 62(6), pp. 1998-2006, 2015. DOI: 10.1109/TED.2015.2418114

[12] M. Bocquet, D. Deleruyelle, H. Aziza, C. Muller, J. Portal, T. Cabout, E. Jalaguier, "Robust compact model for bipolar oxide-based resistive switching memories", IEEE Transactions on Electron Devices, 61, pp. 674-681, 2014. DOI: 10.1109/FTFC.2013.6577779

[13] P. Huang, X. Y. Liu, B. Chen, H.T. Li, Y. J. Wang, Y.X. Deng, K.L. Wei, L. Zeng, B. Gao, G. Du, X. Zhang, J.F. Kang, "A Physics-Based Compact Model of Metal-Oxide-Based RRAM DC and AC Operations," Electron Devices, IEEE Transactions on, vol.60, no.12, pp. 4090-4097, 2013. DOI: 10.1109/TED.2013.2287755

[14] M. Lanza, "A Review on Resistive Switching in High-k Dielectrics: A Nanoscale point of View Using Conductive Atomic Force Microscope", Materials 7, pp. 2155-2182, 2014. DOI: 10.3390/ma7032155.

[15] M.A. Villena, M.B. González, F. Jiménez-Molinos, F. Campabadal, J.B. Roldán, J. Suñé, E. Romera, E. Miranda, "Simulation of thermal reset transitions in RRAMs including quantum effects", Journal of Applied Physics, vol. 115, pp. 214504, 2014. DOI: 10.1063/1.4881500

[16] D. Ielmini, R. Waser. "Resistive Switching: From Fundamentals of Nanoionic Redox Processes to Memristive Device Applications", Wiley-VCH, 2015. DOI: 10.1002/9783527680870

[17] F. Nardi, S. Larentis, S. Balatti, D. C. Gilmer, and D. Ielmini, "Resistive Switching by Voltage-Driven Ion Migration in Bipolar RRAM—Part I: Experimental Study", IEEE Trans. Elec. Dev., vol 59, p. 2461, 2012. DOI: 10.1109/TED.2012.2202319

[18] G. Gonzalez-Cordero, J. B. Roldan, F. Jimenez-Molinos, J. Suñé, S. Long and M. Liu, "A new compact model for bipolar RRAMs based on truncated cone conductive filaments, a Verilog-A approach," Semicond. Sci. Technol., vol. 31, no. 11, pp. 1–13, 2016. DOI: 10.1088/0268-1242/31/11/115013

[19] F. Jiménez-Molinos, M.A. Villena, J.B. Roldán, A.M. Roldán, "A Spice Compact Model For Unipolar RRAM Reset Process Analysis", IEEE Trans. Elec. Dev., vol 62, pp. 955-962, 2015. DOI: 10.1109/TED.2014.2387429

[20] D. Ielmini, "Modeling the Universal Set/Reset Characteristics of Bipolar RRAM by Field- and Temperature-Driven Filament Growth", IEEE Transactions on Electron Devices, vol 58, no. 12, pp. 4309-4317, 2011.

[21] J. Sun, X. Wu, Q. Liu, M. Liu, L.T. Sun, "Real time observation of nanoscale multiple conductive filaments in RRAM by using advanced in-situ TEM", 2013 20th IEEE International Symposium on the Physical and Failure Analysis of Integrated Circuits (IPFA), pp. 560–562, 2013. DOI: 10.1109/IPFA.2013.6599223

[22] D.-H. Kwon, K. M. Kim, J. H. Jang, J. M. Jeon, M. H. Lee, G. H. Kim, X.-S. Li, G.-S. Park, B. Lee, S. Han, M. Kim, and C. S. Hwang, "Atomic structure of conducting nanofilaments in TiO2 resistive switching memory," Nat. Nanotechnol., vol. 5, no. 2, pp. 148–153, Feb. 2010. DOI: 10.1038/nnano.2009.456

[23] K.M. Kim, C.S. Hwang, "The conical shape filament growth model in unipolar resistance switching of TiO2 thin film", Applied Physics Letters, 94(12), PP. 10–13, 2009. DOI: 10.1063/1.3108088.

[24] K.M. Kim, M.H. Lee, G.H. Kim, S.J. Song, J.Y. Seok, J.H. Yoon, C.S. Hwang, "Understanding structure-property relationship of resistive switching oxide thin films using a conical filament model", Applied Physics Letters, 97(16), 2010. DOI: 10.1063/1.3505354

[25] M.A. Villena, M.B. González, J.B. Roldán, F. Campabadal, F. Jiménez-Molinos, F.M. Gómez-Campos y J. Suñé, "An in-depth study of thermal effects in reset transitions in HfO2 based RRAMs", Solid State Electronics, 111, pp. 47-51, 2015. DOI: 10.1016/j.sse.2015.04.008.

[26] M. Bocquet, D. Deleruyelle, C. Muller, J.M. Portal, "Self-consistent physical modeling of set/reset operations in unipolar resistive-switching memories". *Applied Physics Letters*, *98*, p. 263507, 2011. DOI: 10.1063/1.3605591

[27] Guan, Ximeng, Shimeng Yu, and H-S. Philip Wong. "A SPICE compact model of metal oxide resistive switching memory with variations." IEEE electron device letters 33.10, pp. 1405-1407, 2012. DOI: 10.1109/LED.2012.2210856

[28] S. Kvatinsky, M. Ramadan, E. G. Friedman and A. Kolodny, "VTEAM: A General Model for Voltage-Controlled Memristors," in IEEE Transactions on Circuits and Systems II: Express Briefs, vol. 62, no. 8, pp. 786-790, Aug. 2015. DOI: 10.1109/TCSII.2015.2433536

[29] R.W. Cottle, M.N. Thapa, "Descent methods. In Linear and Nonlinear Optimization", (1st ed., pp. 317–368). New York: Springer-Verlag, 2017. DOI: 10.1007/978-1-4939-7055-1_10

[30] S. Kim, C. Du, P. Sheridan, W. Ma, S. Choi, W. D. Lu, "Experimental Demonstration of a Second-Order Memristor and Its Ability to Biorealistically Implement Synaptic Plasticity" *Nano Lett. 15*, 2203, 2015.

[31] S. Aldana, P. García-Fernández, A. Rodríguez-Fernández, R. Romero-Zaliz, M.B. González, F. Jiménez-Molinos, F. Campabadal, F. Gómez-Campos, J.B. Roldán, "A 3D Kinetic Monte Carlo simulation study of Resistive Switching processes in Ni/HfO2/Si-n+-based RRAMs", Journal of Physics D: Applied Physics, 50, 335103, 2017. DOI: 10.1088/1361-6463/aa7939

[32] X. Guan, S. Yu and H.-P. Wong, "On the switching parameter variation of metal-oxide RRAM—Part I: Physical modeling and simulation methodology", IEEE Transactions on Electron Devices, 59, pp. 1172-1182, 2012. DOI: 0.1109/TED.2012.2184545

[33] S. Yu, X. Guan, H.S. Philip Wong, "On the switching parameter variation of metal oxide RRAM—Part II: Model corroboration and device design strategy", IEEE Transactions on Electron Devices, 59, pp. 1183-1188, 2012. DOI: 10.1109/TED.2012.2184544

[34] J. Guy, G. Molas, P. Blaise, M. Bernard, A. Roule, G. Le Carval, V. Delaye, A. Toffoli, G. Ghibaudo, *Fellow, IEEE*, F. Clermidy, B. De Salvo, L. Perniola , "Investigation of Forming, SET, and Data Retention of Conductive-Bridge Random-Access Memory for Stack Optimization", IEEE Transactions on Electron Devices, *62*(11), pp. 3482-3489, 2015. DOI: 10.1109/TED.2015.2476825

Conclusions

In the current electronic industry there is a growing demand for temporary (volatile) and permanent (non-volatile) data storage, in portable devices this demand is even higher and also requires low power consumption. This memory demand becomes evident in smartphones, laptops, internet of things (IoT) devices, solid-state drives (SSD), cloud storage, data mining, artificial intelligence, among others applications [Gupta2019]. RRAMs are the main memory emerging technology since it is the more viable alternative due to its ease of integration into the current CMOS technology in the Back-End-Of-Line (BEOL), good scalability, data retention, endurance, speed and latency, low energy consumption and the possibility of 3D integration and multibit programming.

In this doctoral thesis we have focused on the modeling of memristors based on resistive switching devices implemented with different technologies. The models are used both for analog and digital applications. This doctoral thesis includes *eight publications* in scientific journals indexed in the *Journal Citation Report of Science Citation Index*, *five Proceedings* published in *IEEE Xplore digital library* and *twelve contributions* to *International Conferences*.

More precisely, the summary of the main results obtained here are the following:

Three new RRAM compact models have been implemented: *UGR-CBM*, *UGR-VCM* and *UGR-QPC*. The models take into consideration different facets regarding the device operation bias (bipolar and unipolar) and account for different conduction mechanisms in the dielectric layer (ohmic, tunneling and QPC conduction components).

1.- The *UGR-CBM* model was implemented in Verilog A and includes second order effects. Among its main features, the following can be counted:

▪ Truncated cone-shaped CFs with a non-linear resistor that includes thermal dependence.
▪ Inclusion of the oxide resistance surrounding the CF, series resistance and the capacitance formed between the electrodes. General dielectric conduction mechanisms are used.
▪ Development of a new thermal model that accounts for the CF temperature evolution at the two regions close to the electrodes. This allows the description of the rupture process at the

conductive filament narrowest part and also the correct calculation of the main CF body electrical conductivity.

The ***UGR-CBM*** model allows multiple conductive filaments to be incorporated. The results have been compared to a long RS series of 128 I-V measured curves obtained from $Ti/ZrO_2/Pt$ RRAM devices. A good fit was achieved in all cases. It has been proven that the ***UGR-CBM*** model is efficient in a real circuit simulation environment and can be used to implement a memory cell with a 1T1R architecture.

2.- The ***UGR-VCM*** model implemented in Verilog-A and Matlab©. It includes second order effects and has the following characteristics:

▪ It is based on the creation and destruction of conductive filaments formed by oxygen vacancies in the context of Valence Change Memories. The main equation employed to articulate the model describes the CF volume evolution by controlling the dynamics of resistive switching in these devices. The truncated-cone shaped filaments can be changed in terms of radii and the gap between the filament tip and the electrodes. The CFs are metallic-like and the transport mechanisms combine ohmic conduction and hoping currents. Series resistances are also included.

▪ The model was tested for several RRAM technologies based on HfO_2 dielectrics or multilayer stacks such as $TiO_2/Al_2O_3/TiO_2$, with different combinations of layer thicknesses. A good agreement was obtained in the comparison with hundreds of experimental curves for the technologies analyzed.

▪ A random component was employed to variate the CF, it was described by a thermally activate mechanism to account for the device cycle to cycle variability. A good fit of experimental data was obtained.

▪ The ***UGR-VCM*** model was easily adapted to account for $Au/Ti/TiO_2/SiO_x/Si-n^{++}$. In this devices both filamentary and bulk distributed conduction takes place. A semiempirical current source was employed for the latter conduction mechanism. A good fit between experimental and modeled results was achieved in terms of I-V curves as well as in reset and set voltages and R_{on} and R_{off} distributions.

▪ The ***UGR-VCM*** model could be used to aid neuromorphic circuit designers by allowing simulations at a circuit level. The electronic synapses based on resistive switching $TiN/Ti/HfO_2/W$ devices have been employed to describe the compliance current influence on the resistive switching processes with a massive fitting of 890 RS cycles. The conductivity gradual control capacity observed helped to clarify that the devices have potential to work as synaptic elements.

3.- The ***UGR-QPC*** model was implemented in a SPICE-based simulator. It includes the QPC conduction mechanism and two different thermal models were considered. The main features are given below:

3.1. The first model describes the conductive filament formed by two cylindrical sections of variable geometry (radius) under the premise of a thermal approach that makes use of variable equivalent thermal resistances that depend on the two cylindrical sections radii. This modeling scheme allows to fit the static I-V characteristics of $Ni/HfO_2/Si-n+$ devices.

3.2. The second model, implemented also in a SPICE-based simulator uses the same basis of the previous one, but includes a variable thermal capacity that allows a more precise characterization of the thermal response working in a pulsed voltage operation regime. The model worked well when compared with $Ni/HfO_2/Si-n+$ device measurements.

Wrapping up the results linked to the models developed. The following facts can be highlighted:

Five RRAM technologies have been modeled. The devices are based on the following stacks: Ti/ZrO$_2$/Pt, TiN/Ti/HfO$_2$/W, Ni/HfO$_2$/Si-n+, Au/Ti/TiO$_2$/SiO$_X$/n^{++}Si and Pt/TiO$_2$/Al$_2$O$_3$/TiO$_2$/RuO$_X$/TiN. A compact model capable of describing the main operation features has been provided and the fitting of experimental data measured in DC and AC conditions was good along RS series.

Two SPICE-like models (**UGR-BTS** and **UGR-SMS**) reported in the literature have been implemented and the variability in the transfer function I-V was studied. A comparison of the models against different inputs of pulsed and ramped voltages was performed. The model performance in a 1T1R memory simulation was analyzed.

Three models were implemented in Verilog-A (**UGR-VCMCF**, **UGR-VCMTCF** and **UGR-SMVA**). Different CF shape configurations (cylinder, truncated-cone and the one proposed in the Stanford model) were employed with the purpose of comparing the characteristics at the behavioral level. 1T1R memory cells and 3x3 memory arrays for different RRAM technological nodes were considered. A 65nm NMOS transistor was included as a selector device. Read and write times, noise margin and thresholds for the different models were implemented.

Table 7.I shows the summary of models implemented in this doctoral thesis and theirs associated publications.

Table 7.I Summary of models implemented.

Model Name	Devices used to test	Implementation	Polarity type	References
UGR-CBM	Ti/ZrO$_2$/Pt	Verilog-A/Matlab	Bipolar	[González-Cordero2016a]
UGR-VCM	TiN/Ti/HfO$_2$/W Pt/TiO$_2$/Al$_2$O$_3$/TiO$_2$/RuO$_X$/TiN Au/Ti/TiO$_2$/SiO$_X$/n^{++}Si	Verilog-A/Matlab	Bipolar	[González-Cordero2017a, González-Cordero2017b, González-Cordero2017d, González-Cordero2019b]
UGR-QPC	Ni/HfO$_2$/Si-n+	Spice	Unipolar	[González-Cordero2016e, Jiménez-Molinos2017]
UGR-VCMCF	-	Verilog-A	Bipolar	[González-Cordero2016f]
UGR-VCMTCF	-	Verilog-A	Bipolar	
UGR-SMVA	-	Verilog-A	Bipolar	
UGR-BTS	-	Spice	Bipolar	[González-Cordero2017c]
UGR-SMS	-	Spice	Bipolar	

We have also developed activity in the context of parameter extraction and measurement characterization. The more important results are given below:

Three methodologies have been implemented for the analysis of RTN signals. The **LWTLP**, **DLWTLP** and a procedure based on the use of neural networks for the classification of RTN traces in a long-term sequence. **Table 7.II** shows the summary of methods implemented with theirs associated publications.

The first technique reported above is named **Locally Weighted Time Lag Plot** (LWTLP). It allows the calculation of the probability associated to each position in the (I_i, I_{i+1}) TLP plot taking into consideration the occurrences in the neighborhood of the current points with a computation time much lower than previous methods reported in the literature. The procedure is used to study I-t traces measured in Ni/HfO$_2$/Si-n+-based RRAMs with a massive number of data.

The second method is named **differential Locally Weighted Time Lag Plot** (DLWTLP). It is based on a TLP representation of the current derivative, allowing the visualization of the complete range of current transitions. This new method provides information to assess if the sampling rate is adequate to determine the presence of the electrically active defects in relation to their capture and emission times. It has been employed to study RTN traces in Ni/HfO$_2$/Si-n+ devices operating in the HRS with a massive number of data.

The third method is devoted to the classification of traces of RTN based on Artificial Neural Network, using SOM networks. Employing 1203 input experimental traces in a long trace measured in a Ni/HfO$_2$/Si-n+ device in the HRS and characterizing by the LWTLP patterns, 20 clusters were obtained that allow the classification of entire input RTN patterns into six types of RTN signals: stable 2-level current fluctuations, multilevel transitions with 3, 4 and 5 levels, background noise and interactive defects.

A new method based on the use of the QPC model to detect the presence of tunnelling effects in RRAM conduction has been presented. The presence of conduction able to be modeled by the QPC current model is built upon the calculation of the current second derivative of experimental data. The model parameter extraction is performed with a genetic algorithm using the Euclidean distance between the current modeled and experimental current, and the modeled and experimental second derivative of the current. The procedure was tested with a series of more than 2800 measurements RS cycles in a Ni/HfO$_2$/Si-n+ device.

Table 7.II Summary of parameter extraction methods development in this doctoral thesis tested with Ni/HfO$_2$/Si-n$^+$ devices.

Method	References
QPC parameters extraction	[Roldán2018]
Locally Weighted Time Lag Plot (LWTLP)	[González-Cordero2019a]
Differential Locally Weighted Time Lag Plot (DLWTLP)	[González-Cordero2019c]
Neural Network Based Analysis of RTN	[González-Cordero2019d]

Device Fabrication and Measurement Description

This appendix describes the fabrication processes and measurement set-ups for the different experimental devices used in this thesis and summarized in **Table A.1**. The publications derived from the modeling of this devices are shown in **Table A.2**.

Table A.1 Summary of main characteristics of fabricated devices used in this work.

Device	#1	#2	#3		#4	#5
Top electrode	Ti	Ti/TiN	Pt		Au/Ti	Ni
Dielectric TMO	ZrO_2	HfO_2	$TiO_2/Al_2O_3/TiO_2$		TiO_2/SiO_X	HfO_2
Dielectric Thickness (*nm*)	15	10	28.2-TiO_2 0.2-Al_2O_3	19.2-TiO_2 0.4-Al_2O_3	2-TiO_2 1.5-SiO_X	20
Bottom electrode	Pt	W	Ru/Si		$n^{++}Si$	Si-n+
Switching polarity	Bipolar	Bipolar	Bipolar		Bipolar	Unipolar
Cycles set/reset[*]	128	728	9	15	100	2800
Pulses[**]	yes	no	no		no	no
RTN[**]	no	no	no		no	yes
Fabricated by	F1	F2	F3		F4	F2
Measured by			F5			
Used in sections	2.4.	3.4.	3.4.2.		3.4.4.	4.4. , 4.5. 5.2.7. 5.2.8. and 5.3.

Notes:

[*] Number of cycles of the resistive switching series employed in this thesis.

[**] These rows indicate if these features (pulsed operation/RTN) have been modeled in this thesis.

F1: Lab of Nanofabrication and Novel Device Integration, Institute of Microelectronics, Chinese Academy of Sciences, Beijing.

F2: Institut de Microelectrònica de Barcelona IMB-CNM (CSIC) Bellaterra, Spain.

F3: Institute of Physics, University of Tartu, Ravila, Estonia.

F4: Institute of Functional Nano & Soft Materials (FUNSOM), Collaborative Innovation Center of Suzhou Nano Science & Technology, Soochow University, China.

F5: Departamento de Electrónica, Universidad de Valladolid, Spain.

Table A.2 Summary publications associated with the devices used in this work.

#	TMO	Publications (references)
1	ZrO$_2$	[González-Cordero2016a]
2	HfO$_2$	[González-Cordero2017a, González-Cordero2017b, González-Cordero2017d, González-Cordero2019b]
4	TiO$_2$/Al$_2$O$_3$/TiO$_2$	[González-Cordero2017b, González-Cordero2017d]
5	Ni/HfO$_2$/Si-n+	[González-Cordero2016e, Jiménez-Molinos2017, Roldán2018, González-Cordero2019a, González-Cordero2019c, González-Cordero2019d]

A.1. Ti/ZrO$_2$/Pt Devices

A.1.1. Fabrication Process

These devices were made in the Laboratory of Nanofabrication and Novel Device Integration, Institute of Microelectronics, Chinese Academy of Sciences, Beijing. The steps of the fabrication process of the Ti/ZrO$_2$/Pt stack are described in **Table A.3**. (more details are given in reference [Wang2015])

Table A.3 Main fabrication processes for Ti/ZrO$_2$/Pt RRAM. The devices have an area of 100x100 μm^2

RRAM	Step	Layer (*nm*)	Description
	Cleaning wafer		Chemical cleaning
	Deposited SiO$_2$	100	Thermally grown by dry oxidation
BE	Deposited Ti	30	E-beam evaporation
	Deposited Pt	70	
TMO	Grown ZrO$_2$	15	Ion-beam sputtering
TE	Deposited Ti	10	E-beam evaporation and patterned by lift-off
	Deposited Pt	70	process

A.1.2. Mesurement Set-up

The electrical characteristics of the Ti/ZrO$_2$/Pt devices were obtained by the measuring equipment and the connection scheme shown in **Figure A.1**. The voltage was applied to the TE while the BE is grounded through a load resistance, R_{load}.
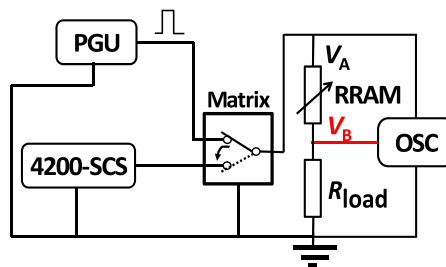
Figure A.1 Connection scheme of the measuring equipment of Ti/ZrO$_2$/Pt RRAMs [Wang2015].

The measuring equipment consisted of:
- PGU: it is an Agilent B1525A HV-SPGU used in order to study pulsed operation: set/reset transitions are caused by means of AC signals in the form of square pulses (with programmable rise/fall times, pulse duration and amplitude).
- 4200-SCS: it is a Keithley 4200-SCS semiconductor characterization system. It generates DC voltage sweeps in order to obtain the characteristic I-V curves of the devices.
- Matrix: it is a matrix Keithley 707A that allows to select the signal source applied to the device.

- OSC: is a Tektronix DPO7104 digital oscilloscope used to capture the switching transient signals produced during the set/reset processes in the device.

The DC measurements obtained with the 4200-SCS are shown in **Figure A.2**. A symmetrical voltage ramp of $\pm 1V$ was used, limiting the set current to $I_{CC} = 5mA$ and carrying out a total of 128 set/reset cycles.
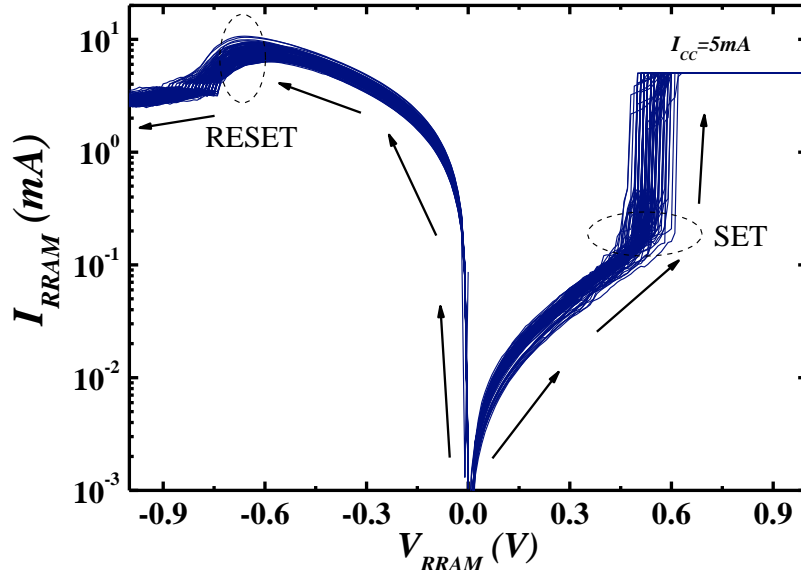
Figure A.2 Experimental *I–V* curves of 128 consecutive resistive switching set/reset processes in a Ti/ZrO$_2$/Pt RRAM device.

The AC measurements obtained with the two oscilloscope channels (V_A corresponds to the top electrode voltage and V_B to the bottom electrode voltage) when the matrix selects the PGU instrument, see **Figure A.3**.
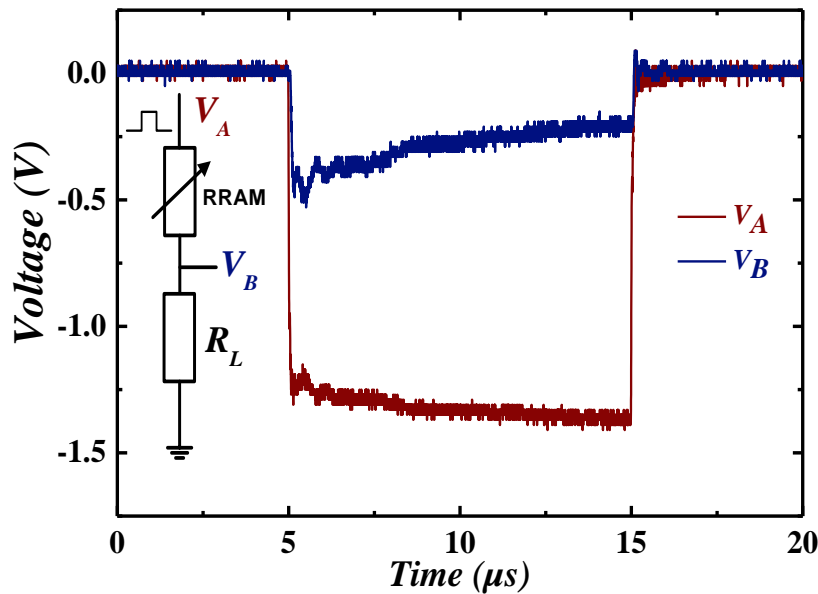
Figure A.3 Experimental measurement of pulsed operation in a Ti/ZrO$_2$/Pt RRAM device.

These experimental measurements are used to calibrate de model described in section 2.4. New Bipolar CB-RRAM Compact Model (UGR-CB).

A.2. TiN/Ti/HfO₂/W Devices

A.2.1. Fabrication Process

These devices were fabricated at the Institut de Microelectrònica de Barcelona IMB-CNM (CSIC) Bellaterra, Spain. The main fabrication process of the TiN/Ti/HfO₂/W stack are described in **Table A.4**. (more details are given in reference [Poblador2017]).

Table A.4 Main fabrication steps for the TiN/Ti/HfO₂/W RRAMs.

RRAM	Step	Layer (nm)	Description
	Initial Wafer		(100) p-type CZ silicon wafers
	Cleaning wafer		With a standard wafer cleaning
	Deposited SiO₂	200	Wet thermal oxidation process at 1100 °C
BE	Deposited W	200	Magnetron sputtering and patterned by photolithography and lift-off process for deposit W
TMO	Deposited HfO₂	10	Atomic layer deposition (ALD) at 225 °C with precursors TDMAH and H₂O, and a carrier and purge gas N₂
TE	Deposited Ti	10	Magnetron sputtering and patterned by photolithography and lift-off
	Deposited TiN	200	TE: deposited by magnetron sputtering and patterned by photolithography and lift-off
	Open Contact		Dry etching of the HfO₂ layer

A representation of the device cross-section is shown in **Figure A.4**. The device structures are square cells of $15\times15\mu m^2$, $5\times5\mu m^2$ and $2\times2\mu m^2$.
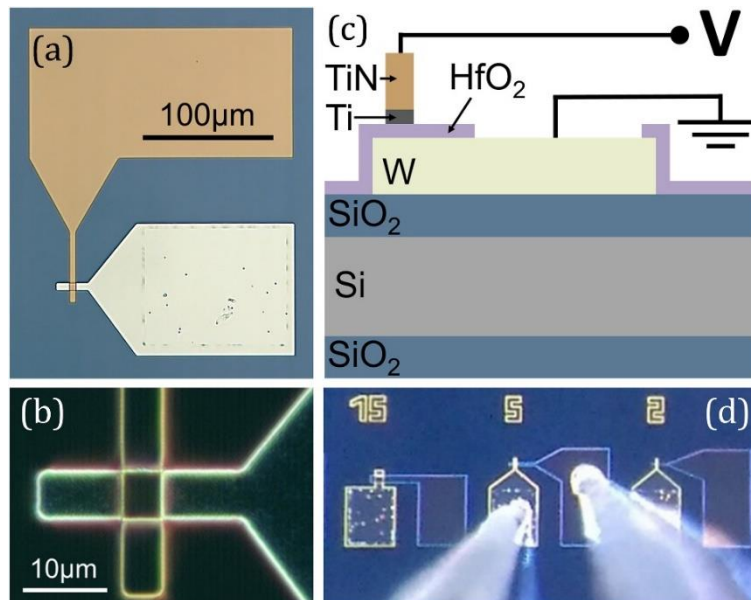
Figure A.4 **(a)** Optical image of the TiN/Ti/HfO₂/W devices with a 100µm reference line. **(b)** Detailed dark field image of the crossbar architecture. **(c)** Cross-section diagram of the device structure. **(d)** Optical image during the measurement process and marked dimensions of square cells of $15\times15\mu m^2$, $5\times5\mu m^2$ and $2\times2\mu m^2$ [Poblador2017].

A.2.2. Measurement Set-up

The electrical characteristics of the TiN/Ti/HfO$_2$/W devices were obtained by means of a HP-4155B semiconductor parameter analyzer controlled via a General Purpose Instrumentation Bus (GPIB) by a software tool developed and implemented in a Matlab script.

The measure procedure was performed as follows:

1. The HP-4155B is connected to the TiN/Ti top electrode while the W bottom electrode was grounded.
2. A voltage weep is applied to the fresh devices to guarantee the formation process with a compliance current $I_{CC} = 100\mu A$.
3. A positive ramped voltage with an amplitude of 1 V is applied to force the set process.
4. A negative ramped voltage with an amplitude of -1.8 V is applied to force the reset process.
5. Steps 3 and 4 are repeated to obtain hundreds of RS cycles in the same RS series.

The 728 measurements cycles obtained with this procedure are shown in **Figure A.5**.
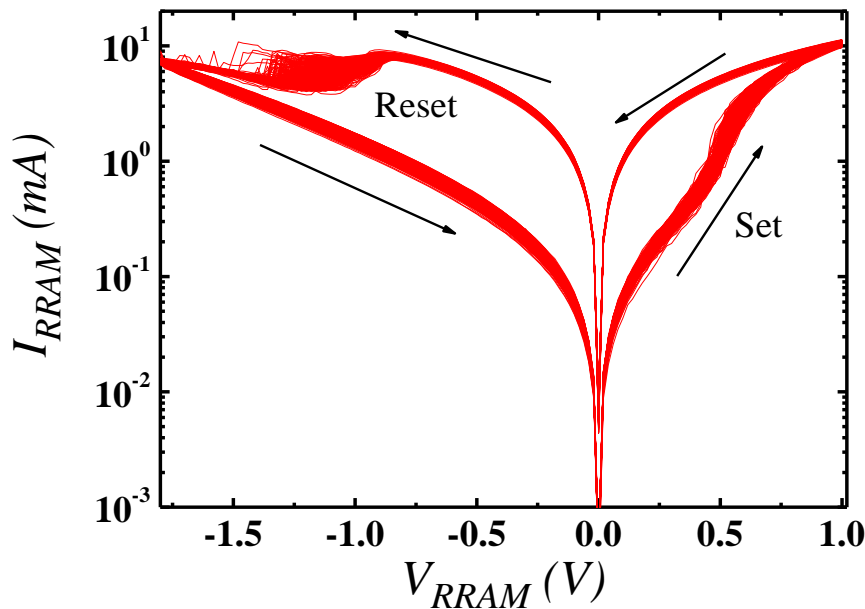
Figure A.5 Current versus applied voltage for a set of 728 experimental measured cycles of a TiN/Ti/HfO$_2$/W device.

This experimental measured are used to calibrate de model described in section 3.4. New Compact Model for Bipolar VCM (UGR-VCM).

A.3. Pt/TiO₂/Al₂O₃/TiO₂/RuOₓ/TiN Devices

A.3.1. Fabrication Process

These devices were fabricated at the Institute of Physics, University of Tartu, Ravila, Estonia. The steps of the fabrication process of the Pt/TiO$_2$/Al$_2$O$_3$/TiO$_2$/RuO$_x$/TiN stack are described in **Table A.5**.A.3. The dielectric layer thicknesses depend on the number of cycles uses in the ALD process (see **Table A.6**).

Table A.5 Main fabrication processes of the following stack TiO$_2$/Al$_2$O$_3$/TiO$_2$.

Step	Layer (*nm*)	Description
Initial substrate		
TiN	10	Assumed previous deposited layer of TiN and RuO$_2$
RuO$_2$	15	
Deposited TiO$_2$	See **Table A.6**	Atomic Layer deposition (ALD) performed in a flow-type reactor (with substrate at 350 °C). Ti precursor was TiCl$_4$ and H$_2$O was used as oxygen source
Deposited Al$_2$O$_3$	See **Table A.6**	Atomic Layer deposition (ALD) performed in a flow-type reactor (with substrate at 350 °C). Al precursor was TMA and H$_2$O was used as oxygen source
Deposited TiO$_2$	See **Table A.6**	Atomic Layer deposition (ALD) performed in a flow-type reactor (with substrate at 350 °C). Ti precursor was TiCl$_4$ and H$_2$O was used as oxygen source

Table A.6 Deposited layer thicknesses of the thin films of TiO$_2$ and Al$_2$O$_3$ as a function of the number of cycles of TiCl$_4$+H$_2$O and TMA+H$_2$O respectively [González-Cordero2017b, González-Cordero2017d].

TiCl$_4$+H$_2$O cycles	Deposited TiO$_2$ (*nm*)	TMA+H$_2$O cycles	Deposited Al$_2$O$_3$ (*nm*)
300	28.2	1	0.2
300	19.2	2	0.4

A.3.2. Measurement Set-up

These devices were measured at Departamento de Electrónica at the Universidad de Valladolid, Spain. The electrical characteristics of Pt/TiO$_2$/Al$_2$O$_3$/TiO$_2$/RuO$_x$/TiN devices were obtained by using a HP-4155B semiconductor parameter analyzer. The measurement process was as follows:

1.- The HP-4155B is connected to the Pt top electrode while the TiN bottom electrode was grounded, with a compliance current of 0.1 A for both HRS and LRS states.

2.- A positive ramped voltage with an amplitude of 3 V is applied to force the set process with a compliance current of 0.1 A.

4.- A negative ramped voltage with and amplitude of -4 V is applied to force the set process with a compliance current of 0.1 A.

5.- Steps 3 and 4 are repeated to obtain different RS cycles.

The results with different oxide thicknesses are shown in **Figure A.6** and **Figure A.7**.
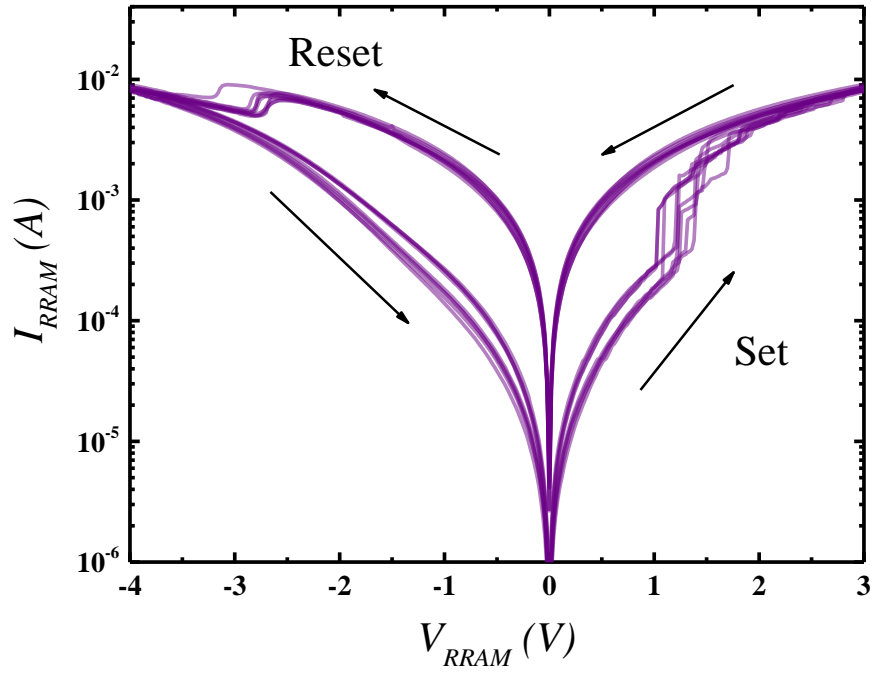
Figure A.6 Current versus applied voltage for a set of 9 cycles of Pt/TiO$_2$ (28.2nm)/Al$_2$O$_3$(0.2nm)/TiO$_2$(28.2nm)/RuO$_x$/TiN devices.
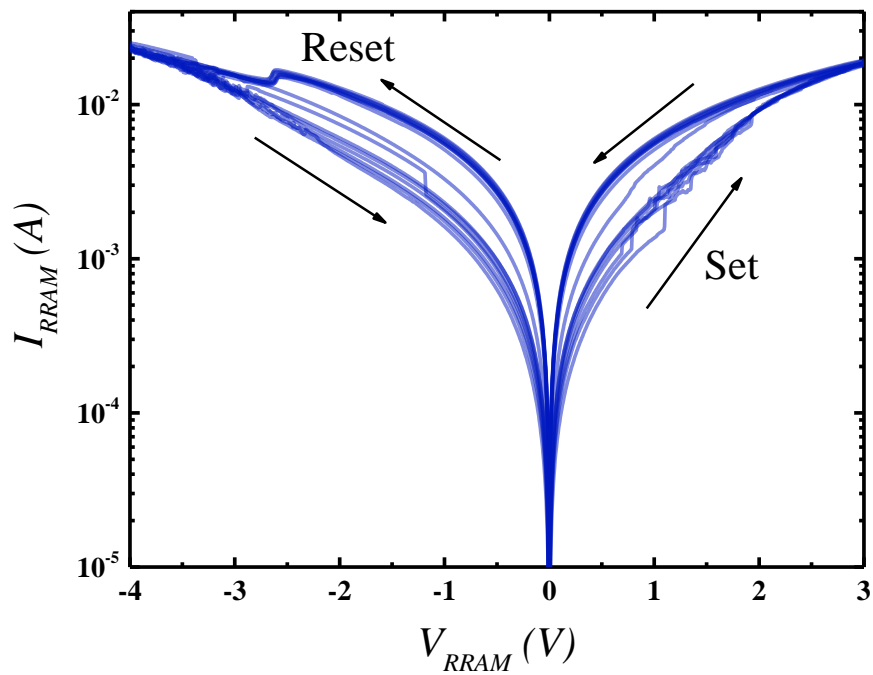
Figure A.7 Current versus applied voltage for a set of 15 cycles of a Pt/TiO$_2$(19.2nm)/Al$_2$O$_3$(0.4nm)/TiO$_2$(19.2nm)/RuO$_x$/TiN stack device.

These experimental measurements were used in section 3.4.2. UGR-VCM Model Validation with other Technologies.

A.4. Au/Ti/TiO₂/SiOₓ/n⁺⁺Si Devices

A.4.1. Fabrication Process

These devices were made at Institute of Functional Nano & Soft Materials (FUNSOM), Collaborative Innovation Center of Suzhou Nano Science & Technology, Soochow University, China. The steps of the fabrication process of the Au/Ti/TiO₂/SiOₓ/n⁺⁺Si RRAMs are described in **Table A.7** (more details are given in reference [Xiao2017]). The cross section TEM view and the SEM image of the squared devices are shown in **Figure A.8**.

Table A.7 Main fabrication processes of Au/Ti/TiO₂/SiOₓ/n⁺⁺Si RRAMs with areas of 100 μm×100 μm, 50 μm ×50μm and 25μm×25μm.

RRAM	Step	Layer (*nm*)	Description
	Initial wafer		Highly doped (n⁺⁺) n-type Si (N100)
BE	n++ Si		resistivity between 0.008 and 0.02 Ω·cm⁻¹
TMO	SiOₓ	1.5	with native SiOₓ oxide
	Cleaning wafer		HF solution for 2 min
	Deposited TiO₂	2	Plasma-enhanced atomic layer deposition (PEALD) at 200ºC 40 cycles using Tetrakis(Dimethylamido) Titanium (Ti(NMe₂)₄) and oxygen inductively coupled discharge as Ti and O sources
TE	Ti	20	Deposited by electron beam evaporator and a
	Au	40	laser-patterned shadow mask was used
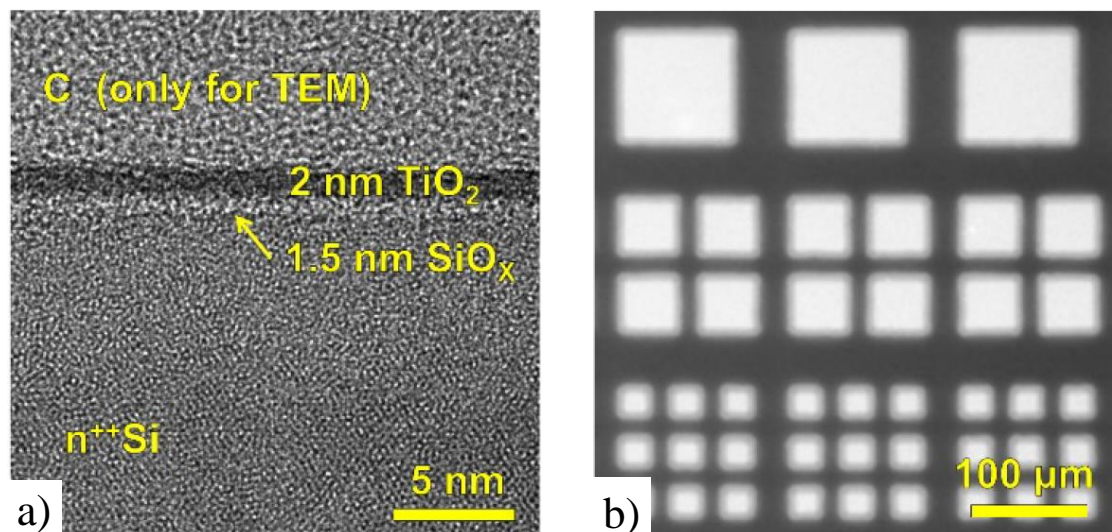
Figure A.8 a) Cross sectional TEM images of TiO₂/SiOₓ/n⁺⁺Si stacks. **b)** SEM image of the squared Au/Ti/TiO₂/SiOₓ/n⁺⁺Si resistive switching cells [Xiao2017].

A.4.2. Measurement set-up

The electrical measurement of Au/Ti/TiO$_2$/SiO$_X$/n^{++}Si RRAM devices were made by means of a probe station M150 from Cascade and a Keithley 4200 Semiconductor Parameter Analyzer. The n^{++}Si substrate was grounded, and the voltage was applied to the Au/Ti electrode. **Figure A.9** shows the semilogarithmic representation of the current of the Au/Ti/TiO$_2$/SiO$_X$/n^{++}Si RRAMs. A set of 100 cycles were obtained with a voltage sweep range from −4 to 2.4 V. Note that these devices perform the set process under a negative voltage, while the reset requires a positive voltage.
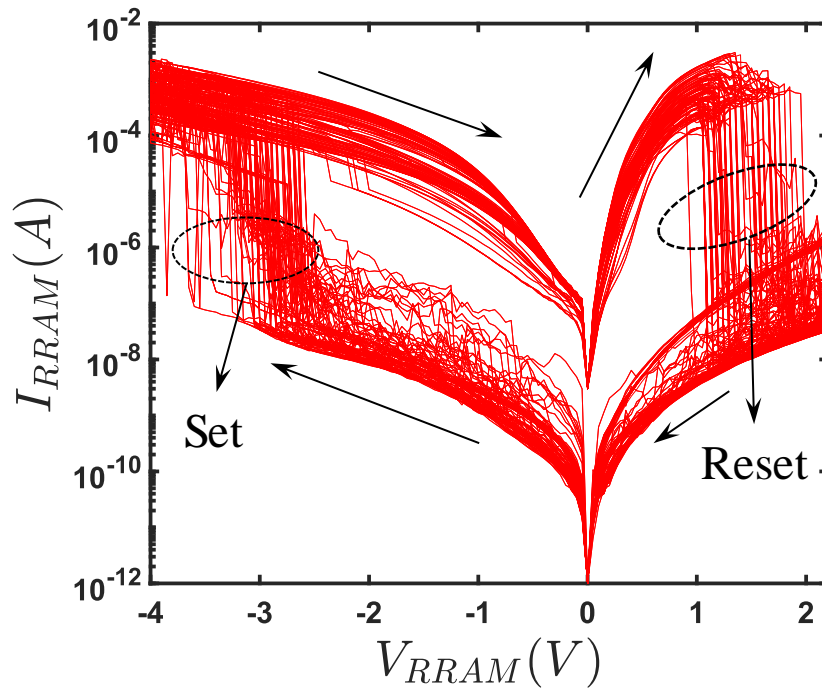
Figure A.9 Current versus applied voltage for a set of 100 experimental measured cycles of a TiO$_2$/SiO$_X$/n^{++}Si device.

These measurements are used to calibrate de model described in section 3.4. New Compact Model for Bipolar VCM (UGR-VCM). The results are used in section 3.4.4. UGR-VCM Model Improvement to Include Distributed Currents

A.5. Ni/HfO₂/Si-n⁺⁺ Devices

A.5.1. Fabrication Process

These devices were fabricated at the Institut de Microelectrònica de Barcelona IMB-CNM (CSIC) Bellaterra, Spain. The main fabrication steps of Ni/HfO₂/Si-n⁺⁺ devices are described in **Table A.8**. (more details are given in references [Gonzalez2014, Gonzalez2015]).

Table A.8 Main fabrication processes of Ni/HfO₂/Si-n⁺⁺ devices, different areas were employed.

RRAM	Step	Layer (*nm*)	Description
BE	Initial wafer		Highly doped (n⁺⁺) n-type Czochralski Si (N100) resistivity between 0.007 and 0.013 $\Omega \cdot cm^{-1}$
	Wafer cleaning		
	Deposited SiO₂	200	Wet thermal oxidation at 1100°C and patterned by photolithography and wet etching
	Cleaning		With H_2O_2/H_2SO_4 and a dip in HF(5%)
TMO	HfO₂ deposition	20	Atomic layer deposition at 225°C using tetrakis (Dimethylamido)-hafnium (TDMAH) and H₂O as precursors and N₂ as carrier and purge gas
TE	Deposited Ni	200	Magnetron sputtering

A.5.2. Measurement Set-up

The electrical measurements of Ni/HfO₂/Si-n++ RRAMs were made by means of a HP-4155B semiconductor parameter analyzer, controlled by a computer using a Matlab script and connected to the instruments by a GPIB bus. The n⁺⁺Si substrate was grounded, and the voltage was applied to the Ni electrode. **Figure A.10** shows three representative current versus voltage curves, (thousands of consecutives curves were measured) with a voltage sweep range from 0V to -4V and a compliance current of 100µA.
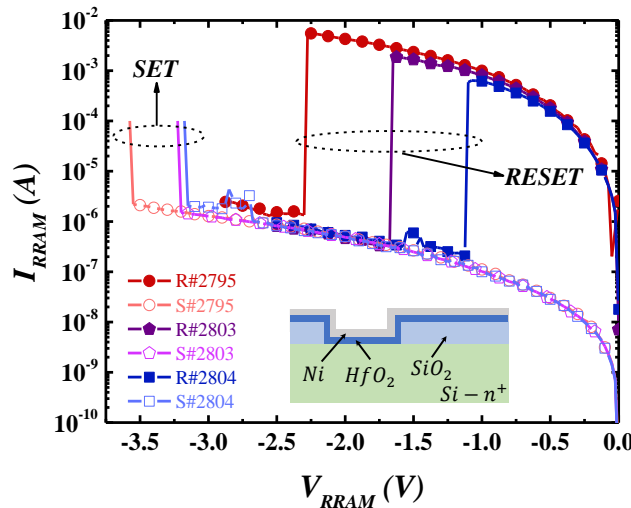
Figure A.10 Current versus applied voltage for different set and reset cycles (#2795, #2803 and #2804) within a long RS series of more than a thousand curves, I_{CC}=100µA. Inset: schematic cross section of Ni/HfO₂/Si-n⁺⁺ stack structure device.

These experimental measurements are used in sections: 4.4. Parameter Extraction, 4.5. UGR-QPC1 model and 4.6. UGR-QPC2 models.

Additional measurements of RTN signals were performed. Different time intervals were considered (details in Table A.9): traces with 20 seconds (2000 samples) and long traces with 11660 seconds (1.3 million of samples) were recorded. An example piece of long time trace of 6800 seconds with a RRAM bias of -0.5 V is presented in **Figure A.11**.
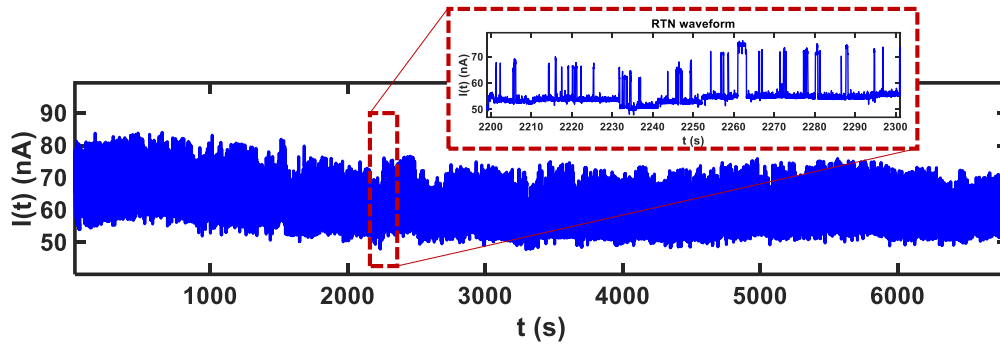
Figure A.11 Current versus time plot measured at an applied voltage of - 0.5V for 6800 seconds. A detail of a time period of 100 seconds is shown, where RTN signals are apparent.
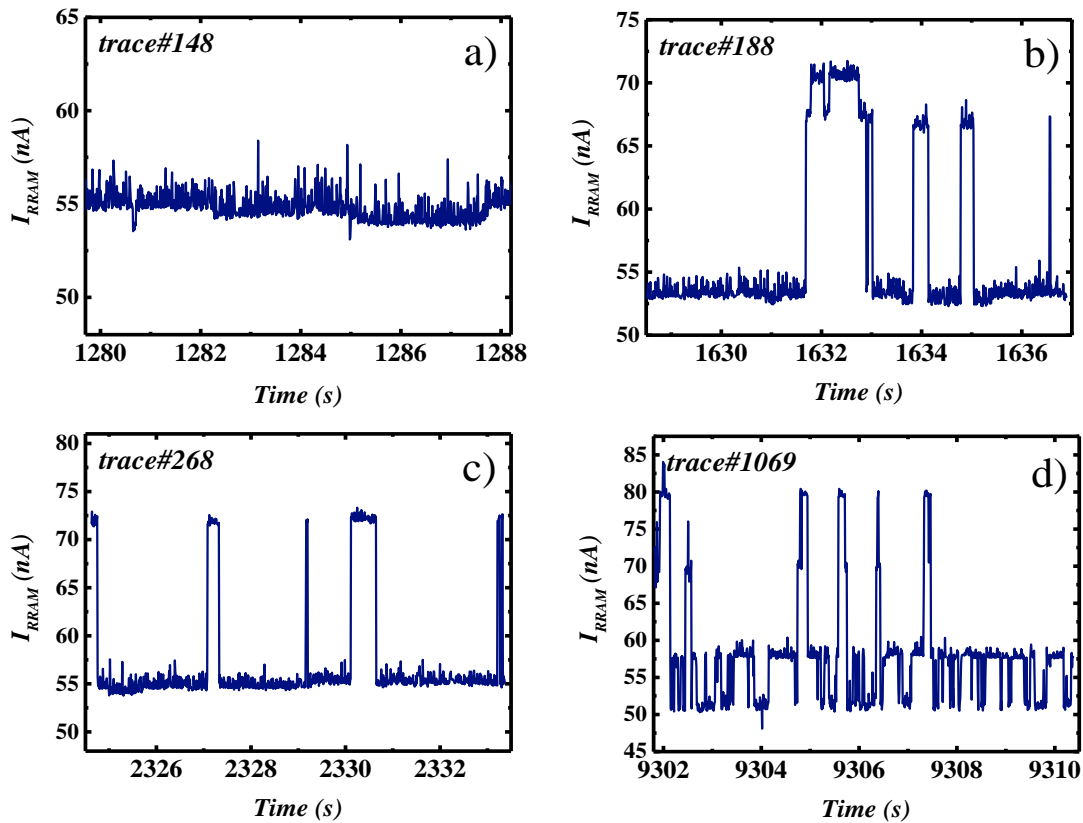
Figure A.12 Detail of 1000 sample of RTN of a long time trace measured on Ni/HfO$_2$/Si-n^{++} stack structure device: **a)** anomalous RTN **b)** Three levels stable RTN **c)** Two levels stable RTN **d)** four levels RTN (based on RTN classification proposed in [González2016]).

These measurements are used in sections:

5.2.7. The Locally Weighted Time Lag Plot.
5.2.8. Differential Locally Weighted Time Lag Plot.
5.3. Neural Network Based Analysis of RTN with LWTLP.

Table A.9 Catalogue of RTN measurements performed on the Ni/HfO$_2$/Si-n^{++} device.

Measure Ref.	V_{RRAM} (V)	Samples #	Observation Time (s)	RTN type*
1	-0.50	2000	17.3738	Noncorrelated transtion
2	-0.28	2000	18.9488	Irreversible digital-like current changes
3	-0.46	2000	18.2301	Interacting defects
4	-0.47	2000	18.3743	Interacting defects
5	-0.48	2000	18.4323	Interacting defects
6	-0.59	2000	17.9474	Activation and deactivation
7	-0.60	2000	17.7738	Stable current fluctuation
8	-0.61	2000	17.518	Activation and deactivation
9	-0.62	2000	17.4576	Activation and deactivation
10	-0.29	2000	19.2055	Noncorrelated transtion
11	-0.30	2000	19.1426	Noncorrelated transtion
12	-0.31	2000	19.3012	Stable current fluctuation
13	-0.32	2000	19.1083	Stable current fluctuation
14	-0.33	2000	19.1337	Stable current fluctuation
15	-0.34	2000	19.0137	Stable current fluctuation
16	-0.35	2000	19.3301	Stable current fluctuation
17	-0.36	2000	19.0829	Stable current fluctuation
18	-0.37	2000	19.2792	Stable current fluctuation
19	-0.38	2000	19.2803	Noncorrelated transtion
20	-0.50	1334237	11660.4	Long time serie

*RTN types is described in reference [Gonzalez2016].

The samples were recorded in plain text files, using scientific notation separated by space with fixed precision of six decimal digits for the argument and three digits for the exponent. The first column represents the voltage applied to the RRAM in volts, the second column the current flowing in amps and the third column the elapsed time in seconds. The detail of the first four lines of a measure register file is shown as follow:

```
-5.000000e-001 6.420370e-008 6.712802e-002
-5.000000e-001 6.716610e-008 7.580191e-002
-5.000000e-001 6.549200e-008 8.452412e-002
-5.000000e-001 6.334480e-008 9.313828e-002
```


a) b)
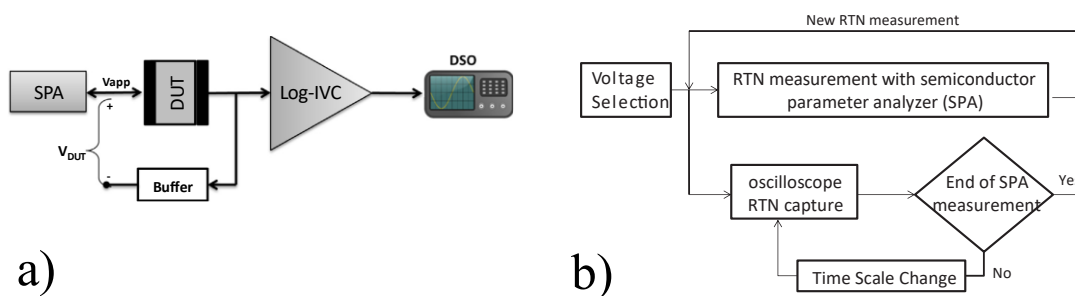
Figure A.13 a) Schematics of the connection of the measuring instruments. SPA is a semiconductor parameter analyzers (Agilent 4156C), DSO is a digital storage oscilloscope (Tektronix TDS220), DUT is device under test (Ni/HfO$_2$/Si-n^{++} stack) and Log-IVC is logarithmic current-to-voltage converter. **b)** Flow chart of the RTN measurement process [Maestro2016].

Additional Developments to the CB-RRAM Model

In this appendix we introduce some additional developments assumed in the literature which are fundamental to fully understand the modeling process of the CB-RRAM device described in Modeling of Conductive Bridge RRAMs.

B.1. Equivalent Electrical Conductivity of CF

Figure B.1 shows the sketch of the geometrical representation of the device to calculate the equivalent electrical conductivity assuming a cylindrical CF proposed in reference [Bocquet2013].
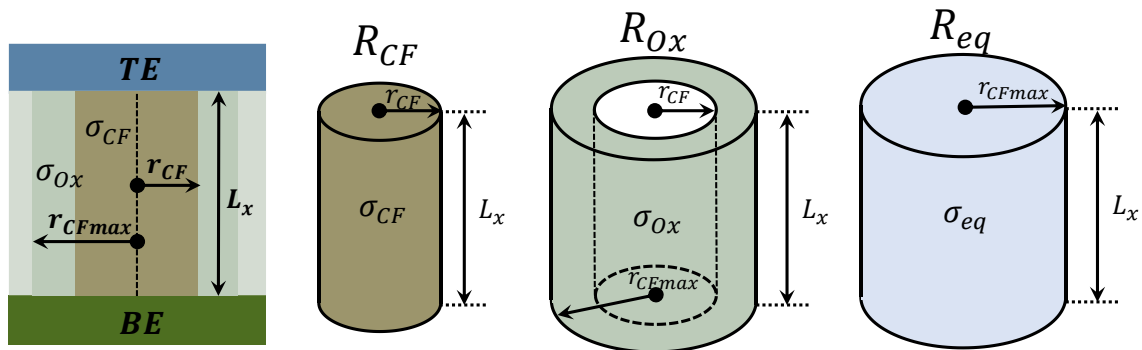
Figure B.1 Geometrical representation of the RRAM for the device resistance calculation [Bocquet2013].

The electrical resistance of a cylinder with radius r_{CF} and height L_x, with electrical conductivity σ_{CF} can be calculated as follows:

$$R_{CF} = \frac{L_x}{\sigma_{CF} \cdot \pi \cdot r_{CF}^2}$$

(B.1)

The oxide surrounding layer is a hollow cylinder of radius r_{CFmax} and height L_x, and the electrical conductivity is assumed to be σ_{Ox}. The conductive filament is assumed to be within the oxide, i.e., a cylinder with radius r_{CF} and height L_x. Therefore, the oxide resistance can be obtained as:

$$R_{Ox} = \frac{L_x}{\sigma_{Ox} \cdot \pi \cdot (r_{CFmax}^2 - r_{CF}^2)} \tag{B.2}$$

As the two resistances are connected in parallel, the equivalent resistance for the devices can be obtained as

$$R_{eq} = \frac{R_{CF} \cdot R_{Ox}}{R_{CF} + R_{Ox}} = \frac{L_x}{\sigma_{CF} \cdot \pi \cdot r_{CF}^2 + \sigma_{Ox} \cdot \pi \cdot (r_{CFmax}^2 - r_{CF}^2)} \tag{B.3}$$

Now, we assume that there is a cylinder with radius r_{CFmax} and height L_x with a uniform equivalent electrical conductivity σ_{eq} (see **Figure B.1**). The value of this electrical resistance can be expressed as follows,

$$R_{eq} = \frac{L_x}{\sigma_{eq} \cdot \pi \cdot r_{CFmax}^2} \tag{B.4}$$

Matching both expressions

$$\frac{L_x}{\sigma_{eq} \cdot \pi \cdot r_{CFmax}^2} = \frac{L_x}{\sigma_{CF} \cdot \pi \cdot r_{CF}^2 + \sigma_{Ox} \cdot \pi \cdot (r_{CFmax}^2 - r_{CF}^2)} \tag{B.5}$$

The equivalent electrical conductivity σ_{eq} is calculated as follows,

$$\sigma_{eq} = \frac{\sigma_{CF} \cdot r_{CF}^2 + \sigma_{Ox}(r_{CFmax}^2 - r_{CF}^2)}{r_{CFmax}^2} \tag{B.6}$$

The source current I_{CF} can be calculated starting from the equations (B.4) and (B.6)

$$I_{CF} = \frac{V_{cell}}{R_{eq}} = \frac{V_{cell}}{L_x} [r_{CF}^2 \cdot \pi \cdot (\sigma_{CF} - \sigma_{Ox}) + r_{CFmax}^2 \cdot \pi \cdot \sigma_{Ox}] \tag{B.7}$$

B.2. Equivalent Electrical Conductivity of CF Including the Work Area

Figure B.2 shows the sketch diagram to calculate the equivalent electrical conductivity of a cylindrical CF, proposed in reference [Bocquet2014]. In this case the equivalent cylinder has a radio r_{work}. This case is very similar to the previous one, although it is included here for the sake of completeness.
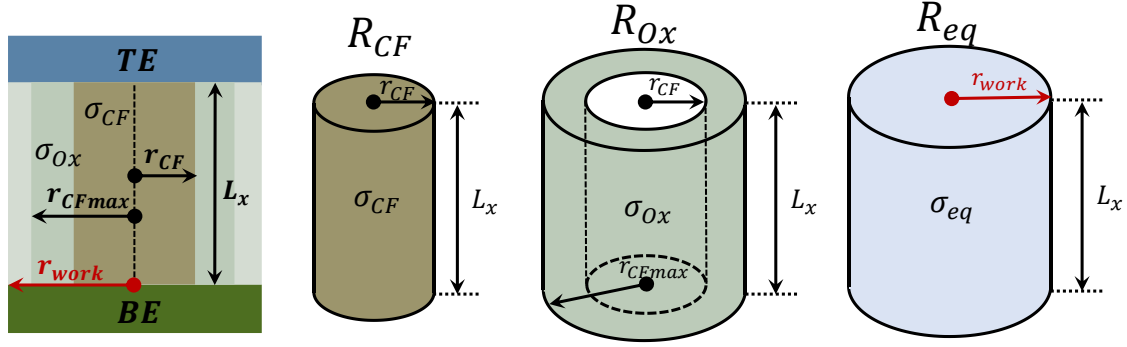
Figure B.2 Geometrical representation of the RRAM for the device resistance calculation [Bocquet2014].

With this new description of the device, equations (B.1), (B.2) and (B.3) are the same, and (B.4) now is replaced by

$$R_{eq} = \frac{L_x}{\sigma_{eq} \cdot \pi \cdot r_{work}^2} \tag{B.8}$$

Matching both expressions (B.8) and (B.3)

$$R_{eq} = \frac{L_x}{\sigma_{CF} \cdot \pi \cdot r_{CF}^2 + \sigma_{Ox} \cdot \pi \cdot (r_{CFmax}^2 - r_{CF}^2)} = \frac{L_x}{\sigma_{eq} \cdot \pi \cdot r_{work}^2} \tag{B.9}$$

The equivalent electrical conductivity σ_{eq} is calculated

$$\sigma_{eq} = \sigma_{CF} \frac{r_{CF}^2}{r_{work}^2} + \sigma_{Ox} \frac{r_{CFmax}^2 - r_{CF}^2}{r_{work}^2} \tag{B.10}$$

The r_{work} is fixed in the forming process described in [Bocquet2014]. It can be seen that the case described in appendix B.1. is a particular case to the one highlighted here if $r_{work} = r_{CFmax}$.

B.3. Dynamics of Oxidation-Reduction Reactions

The reduction-oxidation (redox) process is a reversible electrochemical reaction described by equation (B.11). This reaction is the basis of the formation and rupture of conductive filaments in many different resistive memories.

$$R \underset{Red}{\overset{Ox}{\rightleftarrows}} O^{z+} + ze^-$$ (B.11)

R are reductant species, O^{z+} are the oxidized ionic species and ze^- are the number of charges delivered/trapped in the corresponding reaction. During the oxidation reaction, the reductant specie R are transformed into and ionic oxidized species O^{z+} with delivery of z electrons ($R \to O^{z+} + ze^-$). When the reduction reaction takes place, the electrochemical reaction is driven in the reverse direction ($O^{z+} + ze^- \to R$), the oxidant species O^{z+} with z trapped electrons ze^- produces the reductant species R. Denoted $C_R(C_O)$ the dimensionless concentration of ionic(reduced) species, the oxidation/reduction reaction rates v_{Ox} (v_{Red}) can be calculated as [Bocquet2014],

$$v_{Ox} = k_0 e^{-\frac{\Delta rG_0 - (1-\alpha)\cdot z \cdot F \cdot (E-E_{eq})}{R \cdot T}} \cdot C_R$$ (B.12)

$$v_{Red} = k_0 e^{-\frac{\Delta rG_0 + \alpha \cdot z \cdot F \cdot (E-E_{eq})}{R \cdot T}} \cdot C_O$$ (B.13)

Where standard G_0 is the Gibbs energy, α is the charge transfer coefficient, z is the number of electrons involved in the reaction, F is the Faraday constant, R is the universal gas constant, E is the energy and T is the temperature.

At each time in the chemical reaction the following relations is fulfilled,

$$C_O = 1 - C_R$$ (B.14)

The rate of change of species C_A is expressed as:

$$\frac{dC_A}{dt} = v_{Red} - v_{Ox}$$ (B.15)

The current density J in the redox reaction is described by the Butler-Volmer formulation [Bocquet2014]:

$$J = J_0 \cdot \left[e^{\frac{\alpha \cdot z \cdot F \cdot}{R \cdot T}(E-E_{eq})} - e^{\frac{(1-\alpha)\cdot z \cdot F \cdot}{R \cdot T}(E-E_{eq})} \right]$$ (B.16)

Where J_0 is the exchange current density, α is a dimensionless charge transfer coefficient, z is the numbers of electrons delivered/trapped in the reaction, F is the constant of Faraday, E is the electrode potential, E_{eq} is the potential at equilibrium, R is the universal gas constant and T is the absolute temperature.

Bocquet et al. [Bocquet2013, Bocquet2014] assume, that the of oxidation (reduction) constant times τ_{Ox} (τ_{Red}) can be expressed as

$$\tau_{Ox} = \tau_{RedOx}e^{\frac{E_a + q\cdot(1-\alpha)\cdot V_{cell}}{k_b\cdot T}} \tag{B.17}$$

$$\tau_{Red} = \tau_{RedOx}e^{\frac{E_a - q\cdot\alpha\cdot V_{cell}}{k_b\cdot T}} \tag{B.18}$$

Where τ_{Red} (τ_{Ox}) is the time constant for electrochemical reduction (oxidation) rate, τ_{RedOx} is the nominal redox rate, E_a is the activation energy, q is the unitary charge of the electron, α is the transfer coefficient (with values between 0 to 1), k_b is the Boltzmann constant, T is the absolute temperature and V_{cell} is the applied voltage.

At this point it is important to note that equations (B.17) and (B.18) are equivalent to the classic equations (B.12) and (B.13) that govern chemical oxidation/reduction reactions, under the following considerations:

1.- The oxidation (reduction) mechanism is isotropic and therefore the redox potential is assumed to be equal to the applied voltage

$$E - E_{eq} = -|V_{Cell}| \tag{B.19}$$

2.- The following constant values can be matched,

$$\frac{1}{\tau_{RedOx}} = k_0 \, , \, E_a = \frac{\Delta rG_0}{R}k_b \tag{B.20}$$

matching the equations (B.18) and (B.13)

$$k_0e^{-\frac{\Delta rG_0 + \alpha\cdot z\cdot F\cdot(E-E_{eq})}{R\cdot T}} = \frac{1}{\tau_{RedOx}}e^{-\frac{E_a - q\cdot\alpha\cdot V_{cell}}{k_b\cdot T}} \tag{B.21}$$

matching the equations (B.17) and (B.12)

$$k_0e^{-\frac{\Delta rG_0 - (1-\alpha)\cdot z\cdot F\cdot(E-E_{eq})}{R\cdot T}} = \frac{1}{\tau_{RedOx}}e^{-\frac{E_a + q\cdot(1-\alpha)\cdot V_{cell}}{k_b\cdot T}} \tag{B.22}$$

Then, the oxidation/reduction reaction rates v_{Ox} (v_{Red}) of equation (B.12), (B.13) as a function of the oxidation and reduction times (equation (B.17) and (B.18)) can be simplified as equations (B.23) and (B.24)

$$v_{Red} = \frac{C_o}{\tau_{Red}} = \frac{1 - C_R}{\tau_{Red}} \tag{B.23}$$

$$v_{Ox} = \frac{C_R}{\tau_{Ox}} \tag{B.24}$$

And equation (B.15) can be written as

$$\frac{dC_A}{dt} = \frac{1 - C_R}{\tau_{Red}} - \frac{C_R}{\tau_{Ox}} \tag{B.25}$$

If we consider that the dimensionless concentration of reduced species (C_R) is proportional (r_{CFmax}) to the conductive filament radius (r_{CF}):

$$r_{CF} = r_{CFmax} \cdot C_R \tag{B.26}$$

Then, the dimensionless concentration of reduced species is a function of two radii (r_{CF}, r_{CFmax}),

$$C_R = \frac{r_{CF}}{r_{CFmax}} \tag{B.27}$$

Expressing equation (B.25) in terms of equation (B.27), we obtain,

$$\frac{dC_A}{dt} = \frac{1 - \dfrac{r_{CF}}{r_{CFmax}}}{\tau_{Red}} - \frac{\dfrac{r_{CF}}{r_{CFmax}}}{\tau_{Ox}} \tag{B.28}$$

In an infinitesimal time interval, from the equation (B.26), the rate of change of the filament radius is obtained,

$$\frac{dr_{CF}}{dt} = r_{CFmax} \cdot \frac{dC_R}{dt} \tag{B.29}$$

And finally, replacing the equation (B.28) into the equation (B.29), we get the master equation of the rate of change of r_{CF}

$$\frac{dr_{CF}}{dt} = \frac{r_{CFmax} - r_{CF}}{\tau_{Red}} - \frac{r_{CF}}{\tau_{Ox}} \tag{B.30}$$

B.4. Dynamics of Oxidation Reduction Reactions with Local Diffusion of Metallic Species (k_{dif})

In this section the diffusion of the metallic species is taken into account, then the rate of reduction of species C_R in equation (B.15) needs a new term v_{dif}

$$\frac{dC_A}{dt} = v_{Red} - v_{Ox} - v_{dif} \tag{B.31}$$

Where v_{dif} is the ratio of local diffusion of the metallic species, that can be expressed as follows,

$$v_{dif} = k_{dif} \cdot e^{-\frac{E_{ad}}{k_b \cdot T}} \cdot C_R \tag{B.32}$$

Where E_{ad} is the diffusion activation energy and k_{dif} is the diffusion coefficient rate. The constant time of diffusion is consequently expressed as,

$$\tau_{dif} = \frac{1}{k_{dif}} \cdot e^{\frac{E_{ad}}{k_b \cdot T}} \tag{B.33}$$

Then the ratio of local diffusion of the metallic species is rewritten as,

$$v_{dif} = \frac{C_R}{\tau_{dif}} \tag{B.34}$$

And including equations (B.23), (B.24) and (B.34) into equation (B.31), we obtain,

$$\frac{dC_A}{dt} = \frac{1 - C_R}{\tau_{Red}} - \frac{C_R}{\tau_{Ox}} - \frac{C_R}{\tau_{dif}} \tag{B.35}$$

naming the equivalent time constant oxide as τ_{Oxeq}

$$\frac{1}{\tau_{Oxeq}} = \frac{1}{\tau_{Ox}} + \frac{1}{\tau_{dif}} \tag{B.36}$$

And regrouping terms,

$$\frac{dC_A}{dt} = \frac{1 - C_R}{\tau_{Red}} - \frac{C_R}{\tau_{Oxeq}} \tag{B.37}$$

Finally, replacing equations (B.37) and (B.28) into (B.29), we get the master equation of the rate of change of r_{CF} including metallic species local diffusion:

$$\frac{dr_{CF}}{dt} = \frac{r_{CFmax} - r_{CF}}{\tau_{Red}} - \frac{r_{CF}}{\tau_{Oxeq}} \tag{B.38}$$

B.5. Analytical Solution of the Conductive Filament Radius Time Evolution

The master equation obtained in the sections B.3. and B.4. show the following formulation,

$$\frac{dr_{CF}(t)}{dt} = \frac{r_{CFmax} - r_{CF}(t)}{\tau_{Red}} - \frac{r_{CF}(t)}{\tau_{Ox}} \tag{B.39}$$

To improve the efficiency of the simulator, equation (B.39) could be solved analytically with help of the following symbolic Matlab live script, although other programming languages, such as C, R or python could be used. In these appendices we show Matlab code as an example.

```
clc, clear
% Declaration of symbolic variables
syms r_CF(t) r_CFmax tau_red tau_Ox r_i
% Solve the diffetential equation
r_i1=dsolve(diff(r_CF,1)==((r_CFmax-r_CF)/tau_red-
r_CF/tau_Ox),r_CF(0)==r_i)
```

r_i1 =

$$\frac{r_{CFmax}\,\tau_{Ox} + e^{-\frac{t\,(\tau_{Ox}+\tau_{red})}{\tau_{Ox}\,\tau_{red}}}(r_i\,\tau_{Ox} - r_{CFmax}\,\tau_{Ox} + r_i\,\tau_{red})}{\tau_{Ox} + \tau_{red}}$$

If we rename the variables as follows,

$$\tau_{eq} = \frac{\tau_{Red} \cdot \tau_{Ox}}{\tau_{Red} + \tau_{Ox}} \tag{B.40}$$

Then

$$\frac{\tau_{Ox}}{\tau_{Red} + \tau_{Ox}} = \tau_{eq}/\tau_{Red} \tag{B.41}$$

The following equation is obtained,

$$r_{CF(t)} = \left(r_i - r_{CFmax} \cdot \frac{\tau_{eq}}{\tau_{Red}}\right)e^{-t/\tau_{eq}} + r_{CFmax} \cdot \frac{\tau_{eq}}{\tau_{Red}} \tag{B.42}$$

It can be described iteratively,

$$r_{CF_{i+1}} = \left(r_{CF_i} - r_{CFmax} \cdot \frac{\tau_{eq}}{\tau_{Red}}\right)e^{-\Delta t/\tau_{eq}} + r_{CFmax} \cdot \frac{\tau_{eq}}{\tau_{Red}} \tag{B.43}$$

Note that τ_{eq}, τ_{Red} and τ_{Ox} change in each iteration, because they depends on applied voltage, and temperature (see equations (B.17) and (B.18)).

Additional Developments to the UGR-VCM Model

In this appendix we introduced some additional calculations we used in order to develop the UGR-VCM model. (Presented in Chapter 3. Modeling of Valence Change Memories. Electrochemical Memories).

C.1. Volume of Truncated-Cone CF (V_{TC})

A truncated cone is the object obtained when a cone is cut by a plane parallel to its base, after removing the new resulting cone (see **Figure C.1**). The volume V_{TC} of a truncated cone can be expressed as

$$V_{TC} = \frac{\pi}{3} \cdot L_{CF} \cdot r_x \tag{C.1}$$

where r_x is given by

$$r_x = r_T^2 + r_B^2 + r_T r_B \tag{C.2}$$

where L_{CF} is the length of a line segment that connects the two bases perpendicularly, r_T is the radius of the top basis and r_B , the bottom basis radius. Note that r_x has unit of area.
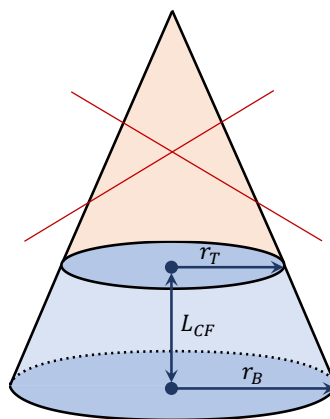
Figure C.1 Truncated cone drawing with the definition of the three geometric dimensions.

C.2. Modeling the Physical Processes of Resistive Switching in VCM

The resistive switching is described by the creation and disruption of a conductive filament in the most frequent case of filamentary conduction. Its geometry is intimately related to the oxygen vacancies (V_o) located in the oxide layer. Therefore the processes of generation, recombination and migration of oxygen vacancies determine the shape of the conductive paths and, consequently, the charge transport mechanisms [Yu2012c, Vandelli2011, Huang2012e]. **Figure C.2** shows a sketch of the processes of RS in the oxide layer, taking into account the generation of oxygen vacancies, movement of oxygen ions, absorption and generation of ions in the electrodes and recombination between oxygen vacancies and oxygen ions (adapted from [Chen2015, Huang2012e, Huang2013]). When the conductive filament is partially formed, there is a gap between the filament tip and the electrode, a dielectric region without oxygen vacancies is shown as the gap (g) in the Figure below.
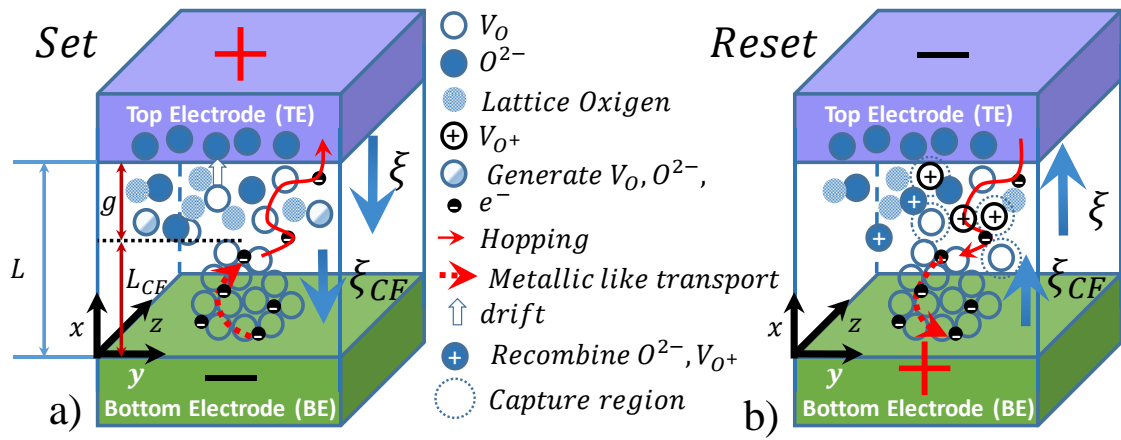
Figure C.2 Sketch model the process of RS in the oxide layer, taking into account the generation of oxygen vacancies, movement of oxygen ions, absorption and generation of ions in the electrodes and recombination between oxygen vacancies and oxygen ions (adapted from [Chen2015, Huang2012e, Huang2013]). **a)** Set process, the gap (*g*) is reduced and the length of CF (*L_CF*) increased to maximum value of oxide thickness (*L*) **b)** reset process.

C.2.1. Physical Description and Modeling of the Set Process

During the Set process, oxygen vacancies (V_0) are generated and dissociated oxygen ions (O^{2-}) drift toward the TE electrode. As a consequence, a CF of oxygen vacancies is formed between the top and bottom electrodes (TE and BE). Thus, the device state switches from HRS to LRS (see **Figure C.2 a**). The probability of generation of V_O oxygen vacancies (P_g), subjected to an electric field ξ, during an infinitesimal interval of time dt, can be determined by the following equation [Huang2013]

$$dP_g = f \cdot e^{-\frac{E_a - \alpha_a \cdot Z \cdot e \cdot \xi}{k_b \cdot T}} \cdot dt \qquad \text{(C.3)}$$

where f is the vibration frequency of the oxygen atom, T is the temperature, E_a is the activation energy, α_a is an enhacement factor of the electric field, Z is the charge number of the oxygen ion (2), e is the electron charge, k_b is the Boltzmann constant and ξ is the electric field in the gap between the filament tip and the electrode ($\xi = V_g/g$) [Huang2013].

C.2.2. Physical Description and Modeling of the Reset Process

The reset switching requires three processes:

1.- Ion release (O^{2-}) from the upper electrode TE (see **Figure C.2 b**). Its probability P_m during an infinitesimal time interval, dt, is determined by the expression [Huang2013]

$$dP_m = f \cdot e^{-\frac{E_i - \gamma \cdot Z \cdot e \cdot V_g}{k_b \cdot T}} \cdot dt \tag{C.4}$$

where E_i is the activation energy of O^{2-} ions release from the TE, and γ is a multiplier coefficient of the voltage V_g.

2.- Hopping of dissociated negative ions, O^{2-} (see **Figure C.2 b**). Its probability P_h in the oxide layer when an electric field ξ is applied during an infinitesimal time interval dt is determined by the expression [Huang2013],

$$dP_h = f \cdot e^{-\frac{E_h - \alpha_h \cdot Z \cdot e \cdot \xi}{k_b \cdot T}} \cdot dt \tag{C.5}$$

where E_h is the hopping activation energy of the negative ions O^{2-} and α_h is a multiplier coefficient of the applied field ξ.

3.- Recombination between oxygen vacancies V_O and ions O^{2-} (see **Figure C.2 b**). Its probability P_r in the oxide layer during an infinitesimal time interval dt is determined by the expression [Huang2013],

$$dP_r = f \cdot e^{-\frac{\Delta E_r}{k_b \cdot T}} \cdot dt \tag{C.6}$$

where ΔE_r is the relaxation energy of the recombination process of oxygen vacancies, V_O, and oxygen ions, O^{2-}.

C.3. Evolution of Truncated Cone CF

C.3.1. Description of SET Process Evolution

Given the probability of generation, P_g, of oxygen vacancies V_O in a region under the influence of an electric field ξ, the increase of volume of the filament can be calculated by means of equation (C.7)

$$\frac{dV_{TC}}{dt} = a_0^3 \cdot \frac{dP_g}{dt} \tag{C.7}$$

where a_0 is the average distance between two oxygen vacancies that are close together, it could be also considered as the average oxygen vacancy size. We have assumed that a cluster of vacancies has been formed and that its concentration is saturated in a region of the oxide, where the conductive filament is formed. Using equation (C.3), the following expression is obtained:

$$\frac{dV_{TC}}{dt} = v_0 \cdot e^{-\frac{E_a - \alpha_a \cdot Z \cdot e \cdot \xi}{k_b \cdot T}} \tag{C.8}$$

where v_0 is a constant equal to $a_0^3 \cdot f$. By numerical integration of equation (C.8), volume V_{TC} is calculated. Assuming a truncated-cone shaped CF, its state is determined by three variables (g, r_T and r_B, see **Figure C.1**). In order to get an accurate compact model, we assumed that the set process follows these consecutive steps: firstly the increase in volume is located in the area of the gap (g), which is narrowed down until its minimum value is reached (set step 1); then, the minor radius, r_T, is increased from its minimum value until its maximum allowed value (set step 2); and finally, the bottom radius r_B is increased (set step 3).

Set step 1

If the gap length, g, is higher than a given minimum value, g_m, the change of the filament volume is applied on the gap distance. Considering that $L_{CF} = L - g$, g is calculated from equation (C.1):

$$g = \begin{cases} L - \dfrac{3 \cdot V_{TC}}{\pi \cdot r_x} & , g \geq g_m \\ \\ g_m & , g < g_m \end{cases} \tag{C.9}$$

Note that r_x has unit of area and that r_T and r_B are constant during set step 1.

Set step 2

If the gap reaches its minimum value, g_m, the increase of the filament volume is translated into a growth of the smaller radius r_T until it reaches its maximum value, r_{Tx}. From equation (C.1), the following expression for r_T is obtained (taking the positive solution from the two possible results):

$$r_T = \begin{cases} \sqrt{\dfrac{3 \cdot V_{TC}}{\pi \cdot (L - g_m)} - \dfrac{3 \cdot r_B^2}{4}} - \dfrac{r_B}{2} & , r_T \leq r_{Tx} \\ \\ r_{Tx} & , r_T \geq r_{Tx} \end{cases} \tag{C.10}$$

Set step 3

If $r_T = r_{Tx}$, the smaller radius of the truncated cone will stop growing and any increase in the volume will be translated to an increase in the greater radius, r_B (until it reaches the maximum value, r_{Bx}). From equation (C.1), r_B is calculated (taking the positive solution from the two possible results):

$$r_B = \begin{cases} \sqrt{\dfrac{3 \cdot V_{TC}}{\pi \cdot (L - g_m)} - \dfrac{3 \cdot r_T^2}{4}} - \dfrac{r_T}{2} & , r_B \leq r_{Bx} \\ \\ r_{Bx} & , r_B \geq r_{Bx} \end{cases} \tag{C.11}$$

After this final step (if the maximum value of r_B, r_{Bx} is reached), the filament will remain fixed until the voltage is reversed and the volume is reduced again.

C.3.2. Description of Reset Process Evolution

The filament volume decrease can be determined with the conditional probability of the three processes: probability P_m of release of O^{2-} ions in the upper electrode TE, probability of hopping P_h in the oxide layer subjected to an electric field ξ and probability of recombination P_r of oxygen vacancies V_O and O^{2-} ions.

$$\frac{dV_{TC}}{dt} = -a^3 \cdot \frac{d}{dt}(P_m \cdot P_h \cdot P_r) \tag{C.12}$$

Developing and regrouping terms we get (using equations (C.4), (C.5) and (C.6)):

$$\frac{dV_{TC}}{dt} = -v_0 \cdot e^{-\frac{E_r - \alpha_r(g) \cdot Z \cdot e \cdot \xi}{k_b \cdot T}} \tag{C.13}$$

Where:

$$E_r = E_i + E_h + \Delta E_r \tag{C.14}$$

and

$$\alpha_r(g) = \gamma \cdot g + \alpha_h \tag{C.15}$$

The electric field applied in the gap is calculated by means of the next equation:

$$\xi = \frac{V_g}{g} \tag{C.16}$$

The change of the volume of the truncated cone in the reset process is translated to its geometry parameters following a reverse order to that described in the set process.

Reset step 1

Reduction of r_B until it reaches its minimum value, r_{Bm}

$$r_B = \begin{cases} \sqrt{\frac{3 \cdot V_{TC}}{\pi \cdot (L - g_m)} - \frac{3 \cdot r_T^2}{4}} - \frac{r_T}{2} & , r_B \geq r_{Bm} \\ \\ r_{Bm} & , r_B \leq r_{Bm} \end{cases} \tag{C.17}$$

Reset step 2

Reduction of r_T until it reaches its minimum value, r_{Tm}

$$r_T = \begin{cases} \sqrt{\frac{3 \cdot V_{TC}}{\pi \cdot (L - g_m)} - \frac{3 \cdot r_B^2}{4}} - \frac{r_B}{2} & , r_T \geq r_{Tm} \\ \\ r_{Tm} & , r_T \leq r_{Tm} \end{cases} \tag{C.18}$$

Reset step 3

Increase of g until it reaches the maximum value g_x

$$g = \begin{cases} L - \dfrac{3 \cdot V_{TC}}{\pi \cdot r_x} & , g \leq g_x \\[2em] g_x & , g > g_x \end{cases} \tag{C.19}$$

C.4. Electrical Sub-Circuit of UGR-VCM Model

This section described the different element that are included in the UGR-VCM sub-circuit model and determine their mathematical expression. **Figure C.3 a)** shows the scheme of the geometry assumed in a RRAM cell, and in **Figure C.3 b)** the equivalent circuit proposed.
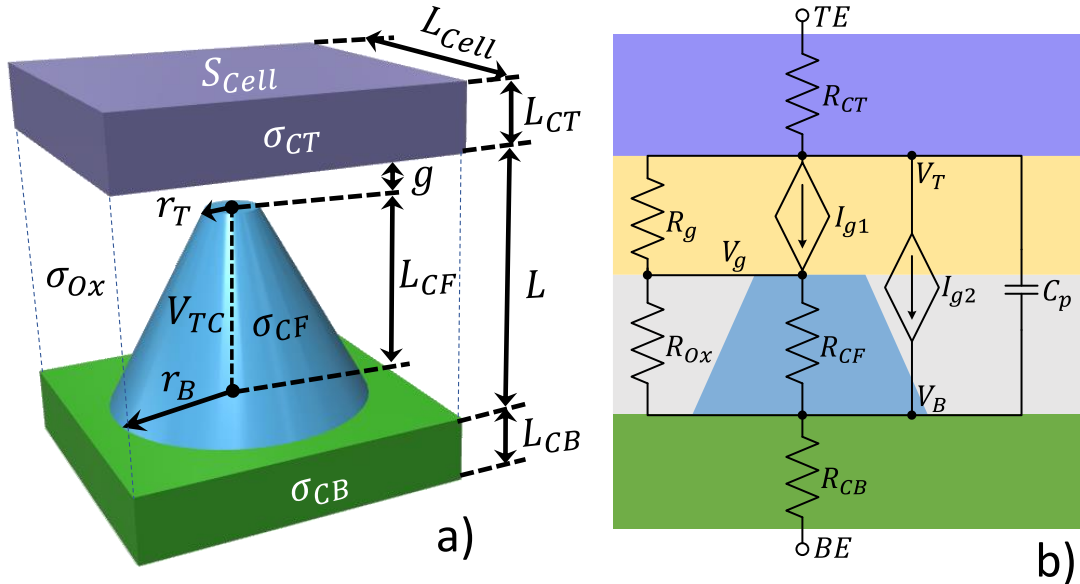
Figure C.3 a) RRAM scheme, CF geometry and main model variables. **b)** Circuit representation of the different electrical components included in the model.

C.4.1. Electrode Resistors R_{CT} and R_{CB}

The resistance of the top and bottom electrodes, R_{CT} and R_{CB}, are constants and are determined by the technological processes of the RRAM fabrication, under the corresponding approximations to considered that their geometries are rectangular parallelepipeds. Taking into account the dimensions and electrical characteristics described in **Figure C.3 a)**, the following equations are obtained,

$$R_{CT} = \frac{L_{CT}}{\sigma_{CT} \cdot S_{cell}} \tag{C.20}$$

$$R_{CB} = \frac{L_{CB}}{\sigma_{CB} \cdot S_{cell}} \tag{C.21}$$

Where σ_{CT} (σ_{CB}) is the electrical conductivity of the top (bottom) electrode, L_{CT} (L_{CB}) is the thickness of the top (bottom) contact and S_{cell} the device area.

C.4.2. Gap Resistor R_g

R_g takes into account the resistance linked to the conductive path between the top electrode and the top of the conductive filament through the oxide layer. For the sake of simplicity, an ohmic behavior has been assumed. The value of the resistance is variable and depends on g:

$$R_g = \frac{g}{\sigma_{Ox} \cdot S_{Cell}} \tag{C.22}$$

where σ_{Ox} is the electrical conductivity of the oxide layer.

C.4.3. Resistance of a Truncated-Cone Conductive Filament

The main geometrical features of a truncated-cone shaped CF, taken into account to calculate its ohmic resistance, are sketched in **Figure C.4.a)**
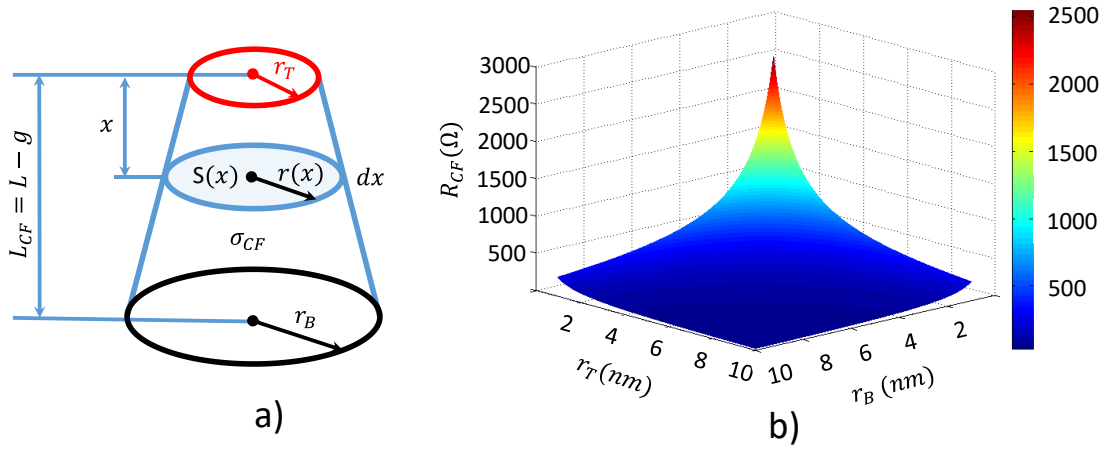
Figure C.4. a) Schematic diagram to compute the equivalent resistance of the truncated-cone shaped CF (R_{CF}) as a function of the top and bottom radii (r_T, r_B), the CF length (L_{CF}) and the electrical conductivity (σ_{CF}). **b)** 3D plot of the R_{CF} calculated for $\sigma_{CF} = 12.5 \ 10^5 m^{-1}\Omega^{-1}$ and $L_{CF} = 10nm$.

The resistance of each infinitesimal section dx can be expressed as follows, assuming a homogeneous electrical conductivity, σ_{CF}:

$$dR_{CF} = \frac{dx}{\sigma_{CF} \cdot S(x)} \tag{C.23}$$

Where $S(x)$ is the area at x and $r(x)$ is the corresponding radius.

$$S(x) = \pi \cdot r(x)^2 \tag{C.24}$$

The radius $r(x)$ is given by:

$$r(x) = \frac{r_B - r_T}{L_{CF}} \cdot x + r_T \tag{C.25}$$

Then, the overall resistance R_{CF} is determined by integration of expression (C.23) between $x = 0$ and $x = L_{CF}$

$$R_{CF} = \frac{1}{\pi \cdot \sigma_{CF}} \int_0^{L_{CF}} \frac{dx}{\left[\frac{r_B - r_T}{L_{CF}} \cdot x + r_T\right]^2} \tag{C.26}$$

Solving the integral with a change of variable $u = \frac{r_B - r_T}{L_{CF}} \cdot x + r_T$ we obtain:

$$R_{CF} = \frac{L_{CF}}{\pi \cdot \sigma_{CF} \cdot r_T \cdot r_B} \tag{C.27}$$

Figure C.4.b) shows the values calculated by means of (C.27) with $\sigma_{CF} = 12.5 \ 10^5 m^{-1}\Omega^{-1}$ and $L_{CF} = 10nm$, as a function of r_T and r_B.

C.4.4. Resistance of Oxide Surrounding the Truncated-Cone CF

In this section we perform the calculation of the resistance (R_{ox}) corresponding to the oxide surrounding the CF, as sketched in light blue in **Figure C.5.a).**

a)   b)
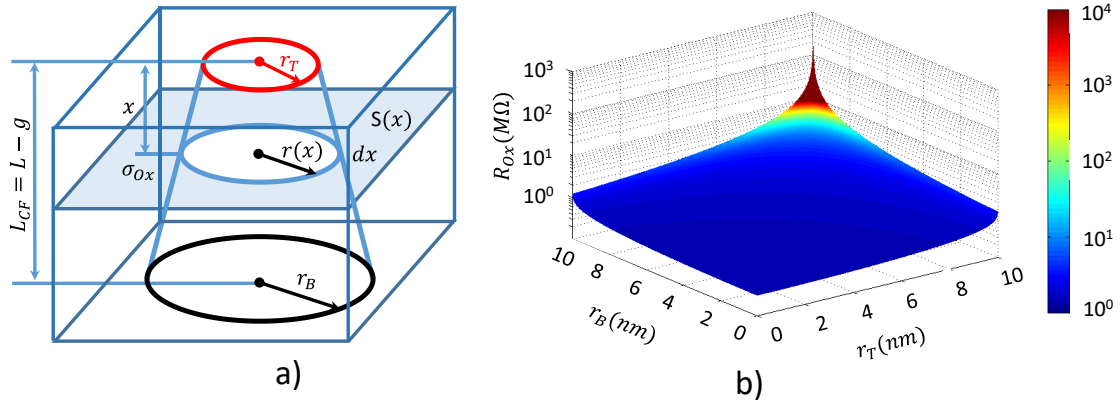
Figure C.5. **a)** Schematic diagram to compute the equivalent resistance of the oxide surrounding the truncated cone shaped CF (R_{ox}) as a function of the top and bottom CF (r_T, r_B), the CF length (L_{CF}) and oxide electric conductivity(σ_{ox}). **b)** 3D plot of the R_{ox} calculated for an example value of the oxide conductivity $\sigma_{ox} = 0.1 \ m^{-1}\Omega^{-1}$ and $L_{CF}=10nm$.

As in the previous appendix section, the resistance of a slice of oxide of infinitesimal height can be calculated as follows:

$$dR_{ox} = \frac{dx}{\sigma_{CF} \cdot S(x)} \tag{C.28}$$

Where $S(x)$ can be obtained from the following expression:

$$S(x) = S_{Cell} - \pi \cdot \left[\frac{r_B - r_T}{L_{CF}} \cdot x + r_T\right]^2 \tag{C.29}$$

Then overall resistance R_{Ox} is determined by integrating between the values $x = 0$ and $x = L_{CF}$

$$R_{CF} = \frac{1}{\sigma_{CF}} \int_0^{L_{CF}} \frac{dx}{S_{Cell} - \pi \cdot \left[\frac{r_B - r_T}{L_{CF}} \cdot x + r_T\right]^2} \tag{C.30}$$

Solving the integral with a change of variable $u = \frac{r_B - r_T}{L_{CF}} \cdot x + r_T$ we obtain:

$$R_{Ox} = \begin{cases} \dfrac{L_{CF} \cdot \delta \cdot [tanh^{-1}(r_T \cdot \delta) - tanh^{-1}(r_B \cdot \delta)]}{\sigma_{ox} \cdot \pi \cdot (r_T - r_B)} & ,r_T \neq r_B \\[4mm] \dfrac{L_{CF}}{\sigma_{ox} \cdot (S_{cell} - \pi \cdot r_T^2)} & ,r_T = r_B \end{cases}$$ (C.31)

Where

$$\delta = \sqrt{\dfrac{\pi}{S_{cell}}}$$ (C.32)

Figure C.5. b) shows the resistance of the oxide surrounding the truncated-cone CF values obtained with and electrical oxide conductivity $\sigma_{Ox} = 0.1\ m^{-1}\Omega^{-1}$ and $L_{CF} = 10nm$, as a function of r_T and r_B.

C.4.5. Tunnel Current Along the Truncated Cone-Shaped Conductive Filament

In this section we analyze the possible paths of the tunnel currents that can be generated through the cone-shaped filament structure represented in **Figure C.6 a).**
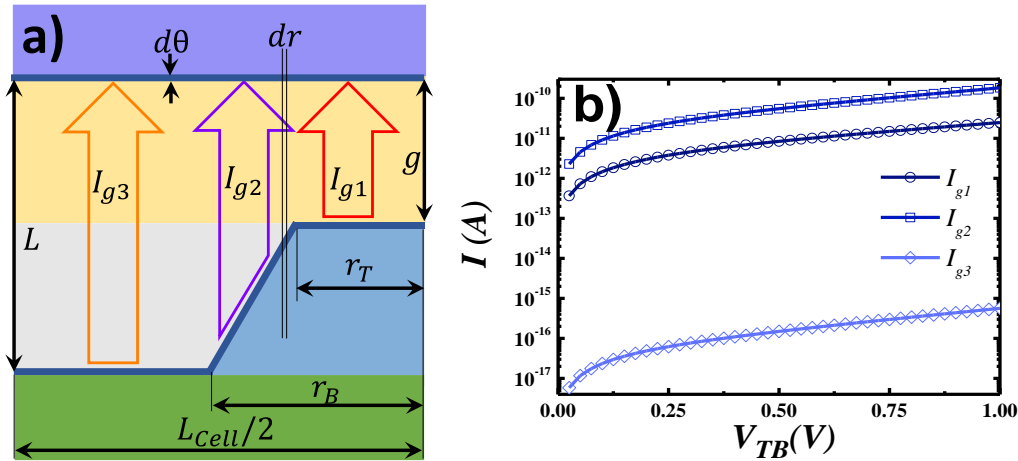
Figure C.6 a) Scheme of the possible paths of tunnel currents in the half part of a truncated cone conductive filament **b)** graphical representation of the three components of the tunnel current with $I_0 = 1\text{mA}/\mu\text{m}^2$, $g_0 = 0.5\text{nm}$, $V_0 = 0.4\text{V}$, $r_T = 1\text{nm}$, $r_B = 30\text{nm}$, $g = 3\text{nm}$, $L = 15$ nm, $V_{TB} = 0$ to 1 V; $V_g = V_{TB} \cdot 0.75$ V. (Computed by equations(C.37), (C.42) and (C.45)). The relation between the current components depends on the CF shape in each particular case.

Taking cylindrical coordinates from the center axis of the truncated cone in an infinitesimal section of radius dr and angle $d\theta$, we assume that there may be differential current dI_g due to a Generalized Tunneling effect (described by equation (1.29)), which can be expressed as,

$$dI_g = I_0 \cdot e^{-\frac{g(r)}{g_0}} \cdot \sinh\left(\frac{V_g}{V_0}\right) \cdot r \cdot dr \cdot d$$ (C.33)

where I_0 is a current density.

The total current can be divided in three components

$$I_g = I_{g1} + I_{g2} + I_{g3}$$ (C.34)

267

First component, I_{g1}.

In this case, the area is delimited by the smaller radius r_T for all angle θ. In this region the gap is constant $g(r) = g$. Let's integrate equation (C.33) with these boundary conditions,

$$I_{g1} = \int_{r=0}^{r=r_T} \int_{\theta=0}^{\theta=2\cdot\pi} I_0 \cdot e^{-\frac{g(r)}{g_0}} \cdot \sinh\left(\frac{V_g}{V_0}\right) \cdot r \cdot dr \cdot d\theta \tag{C.35}$$

Taking from the integrals the constant terms:

$$I_{g1} = I_0 \cdot e^{-\frac{g}{g_0}} \cdot \sinh\left(\frac{V_g}{V_0}\right) \int_{r=0}^{r=r_T} r \cdot dr \int_{\theta=0}^{\theta=2\cdot\pi} d\theta \tag{C.36}$$

Integrating we get the value of I_{g1}:

$$I_{g1} = \pi \cdot r_T^2 \cdot I_0 \cdot e^{-\frac{g}{g_0}} \cdot \sinh\left(\frac{V_g}{V_0}\right) \tag{C.37}$$

Second component, I_{g2}

In this area the region is delimited between the radii r_T and r_B for any angle, θ. In this region the gap depends linearly on r

$$g(r) = m \cdot r + n \tag{C.38}$$

Were m and n are determined by solving the linear equation (C.38) with the conditions $g(r_T) = g$ and $g(r_B) = L$

$$m = \frac{L - g}{r_B - r_T} \quad , \quad n = \frac{g \cdot r_B - L \cdot r_T}{r_B - r_T} \tag{C.39}$$

For obtaining an analytical solution of the integral, we assumed that the voltage applied in this stretch is constant V_g^* and equal to the median of voltages in the extremes V_{TB} and V_g

$$V_g^* = \frac{V_{TB} + V_g}{2} \tag{C.40}$$

Let's solve the integral in equation (C.33) with the following boundary conditions:

$$I_{g2} = I_0 \sinh\left(\frac{V_g^*}{V_0}\right) e^{-\frac{n}{g_0}} \int_{r=r_T}^{r=r_B} e^{-\frac{m\cdot r}{g_0}} \cdot r \cdot dr \int_{\theta=0}^{\theta=2\cdot\pi} \cdot d\theta \tag{C.41}$$

Integrating by parts, the following expression is obtained as a result:

$$I_{g2} = 2 \cdot \pi \cdot I_0 \sinh\left(\frac{V_g^*}{V_0}\right) \cdot F \tag{C.42}$$

where

$$F = \frac{e^{-\psi\cdot r_T - \chi} \cdot (r_T \cdot \psi + 1) - e^{-\psi\cdot r_B - \chi} \cdot (r_B \cdot \psi + 1)}{\psi^2} \tag{C.43}$$

and

$$\psi = \frac{m}{g_0} \quad , \chi = \frac{n}{g_0} \tag{C.44}$$

Third component, I_{g3}.

The third component is determined by the cell area (once the bottom basis area has been subtracted) and the distance between the two electrodes, L.

$$I_{g3} = (S_{cell} - \pi \cdot r_B^2) \cdot I_0 \cdot e^{-\frac{L}{g_0}} \cdot \sinh\left(\frac{V_{TB}}{V_0}\right) \tag{C.45}$$

Figure C.6 b) shows the three current components calculated according to (C.37), (C.42) and (C.45). Note that I_{g3} is negligible in relation to I_{g1} and I_{g2}

C.4.6. Capacitor C_p

The capacitor C_p in **Figure C.3 b)** takes into account the capacity of the parallel flat plate capacitor formed by the upper and lower electrodes, with the oxide layer as insulator. Its value is determined by the expression

$$C_p = \epsilon_0 \cdot \epsilon_{ox} \frac{S_{cell}}{L} \tag{C.46}$$

where ϵ_0 is the vacuum permittivity and ϵ_{ox} is the relative permittivity of the dielectric oxide layer.

C.5. Numerical Procedure to Computed the Device Current (I_{RRAM})

In this section, we will show a multidimensional Newton-Raphson based procedure for the numerical resolution of the device current, I_{RRAM}. This procedure is suitable for implementing the model into non electrical simulators, Mathematica, R, phyton and Matlab can be employed.

For the sake of clarity we do not use I_{g3} here, just I_{g1} and I_{g2}.
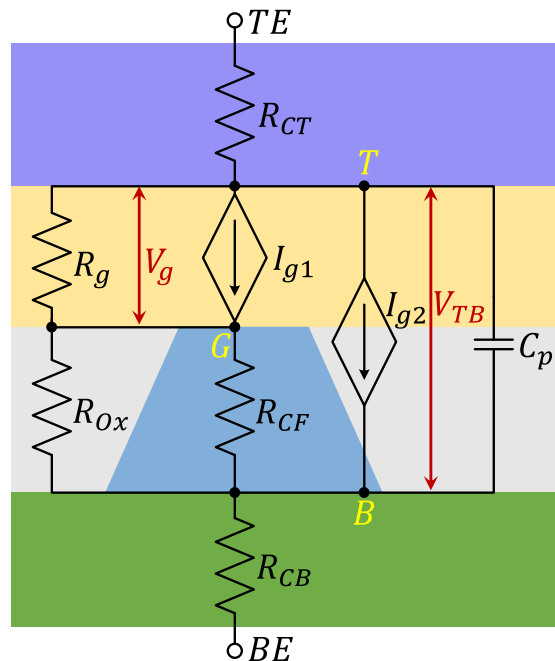
Figure C.7 Representation of nodes, voltages and currents of the electrical circuit to be solved.

The current flowing through the RRAM can be determined (observing node T in **Figure C.7**)

$$I_{RRAM} = \frac{V_g}{R_g} + I_{g1}(V_g) + I_{g2}(V_g, V_{TB})$$

(C.47)

I_{RRAM} depends on voltages V_g and V_{TB}. Looking at node G, the voltage V_g has dependencies on I_{g1} and on the voltage between the top and bottom electrode V_{TB}. From this node we can build a function of the type $f_1(V_g, V_{TB}) = 0$

$$f_1(V_g, V_{TB}) = V_{TB} - \left(I_{g1}(V_g) + \frac{V_g}{R_g} \right) \cdot R_{FO} - V_g$$

(C.48)

Where R_{FO} is the equivalent resistor of the parallel connection of R_{CF} and R_{Ox}

$$R_{FO} = \frac{R_{CF} \cdot R_{Ox}}{R_{CF} + R_{Ox}}$$

(C.49)

To determine the voltage V_{TB}, we analyze the voltage drop in the resistors of the electrodes (R_{CB}, R_{CT}) when applying a voltage to the device V_{RRAM} between the top and bottom contacts (see **Figure C.7**). With this relationship, we can build a second function $f_2(V_g, V_{TB}) = 0$

$$f_2(V_g, V_{TB}) = V_{RRAM} - \left(I_{g1}(V_g) + I_{g2}(V_g, V_{TB}) + \frac{V_g}{R_g} \right) \cdot R_C - V_{TB}$$

(C.50)

Where R_C is the equivalent resistor of the serial connection of R_{CT} and R_{CB}.

$$R_C = R_{CT} + R_{CB}$$

(C.51)

Equations (C.48) and (C.50) form a system of coupled nonlinear equations. For its solution, the multidimensional Newton-Raphson method is used:

$$\begin{bmatrix} V_g^{i+1} \\ V_{TB}^{i+1} \end{bmatrix} = \begin{bmatrix} V_g^i \\ V_{TB}^i \end{bmatrix} - \begin{bmatrix} \dfrac{\partial f_1(V_g^i, V_{TB}^i)}{\partial V_g} & \dfrac{\partial f_1(V_g^i, V_{TB}^i)}{\partial V_{TB}} \\ \dfrac{\partial f_2(V_g^i, V_{TB}^i)}{\partial V_g} & \dfrac{\partial f_2(V_g^i, V_{TB}^i)}{\partial V_{TB}} \end{bmatrix}^{-1} \begin{bmatrix} f_1(V_g^i, V_{TB}^i) \\ f_2(V_g^i, V_{TB}^i) \end{bmatrix}$$

(C.52)

Particularizing the method for our problem, we follow an iterative scheme. In each iteration we get a better approximation of V_g^{i+1} and V_{TB}^{i+1} based on initial values $V_g^i = V_{RRAM}/2$ and $V_{TB}^i = V_{RRAM}$

The Jacobian J matrix is obtained after performing the partial derivatives of the functions $f_1(V_g, V_{TB}), f_2(V_g, V_{TB}),$

$$J = \begin{bmatrix} -R_{FO}\left(\dfrac{k_1}{V_0}\cosh\left(\dfrac{V_g}{V_0}\right) + \dfrac{1}{R_g}\right) - 1 & 1 \\ -R_C\left(\dfrac{k_2}{2V_0}\cosh\left(\dfrac{V_{TB}+V_g}{2V_0}\right) + \dfrac{k_1}{V_0}\cosh\left(\dfrac{V_g}{V_0}\right) + \dfrac{1}{R_g}\right) & -\dfrac{k_2 R_C}{2V_0}\cosh\left(\dfrac{V_{TB}+V_g}{2V_0}\right) - 1 \end{bmatrix} \quad \text{(C.53)}$$

Where the values of k_1 and k_2 are

$$k_1 = \pi r_T^2 I_0 e^{-g/g_0} \quad , \quad k_2 = 2\pi I_0 F \qquad \text{(C.54)}$$

The next step is to calculate the inverse matrix J^{-1} numerically to obtain the solution of the proposed system of equations (C.53) , as follow

$$J^{-1} = \begin{bmatrix} \dfrac{J_{22}}{J_{11}\cdot J_{22} - J_{21}} & \dfrac{-1}{J_{11}\cdot J_{22} - J_{21}} \\ \dfrac{-J_{21}}{J_{11}\cdot J_{22} - J_{21}} & \dfrac{J_{11}}{J_{11}\cdot J_{22} - J_{21}} \end{bmatrix} \qquad \text{(C.55)}$$

The absolute error of each iteration can be calculated by means of this equation:

$$\left\| e^i \right\| = \left\| V^i - V^{i-1} \right\| \qquad \text{(C.56)}$$

And the relative error is determinate by

$$\left\| e_r^i \right\| = \frac{\left\| V^i - V^{i-1} \right\|}{\left\| V^{i-1} \right\|} < \varepsilon \qquad \text{(C.57)}$$

The iterative process finishes when a solution is achieved with a relative error below a predefined value ε.

C.6. Description of UGR-VCM Model Parameters

The following table summarizes the model parameters and their default values

Table C.1 Technological parameters and fitting constants used in the model.

Parameter	Description	Value	Unit
L	Oxide thickness	10	nm
$[L_{CT}, L_{CB}]$	[Top, Bottom] electrode thickness	$[210, 200]$	nm
$[g_m, r_{Tm}, r_{Bm}]$	Minimum [gap, Top, Bottom] radii	$[0.25, 0.25, 25]$	nm
L_{cell}	Side of the RRAM cell	15	μm
$[E_a, E_r]$	Average active energy of generation oxygen vacancies, Equivalent reset energy	$[1.12, 1.35]$	eV
v_0	Volume velocity ($a_0^3 \cdot f$)	156.25	$\mu m^3/s$
$[\alpha_a, \alpha_h]$	Enhancement factor of electric field for lowering of $[E_a, E_h]$	$[0.005, 0.054]$	nm
γ	Enhancement factor of voltage during the O^{2-} release process	0.25	
$[T_0, T_C]$	[Initial room, Critical] temperature	$[300, 780]$	K
k_{th}	Thermal conductivity	5	$\dfrac{W}{K \cdot m}$
h	Heat transfer coefficient	10^9	$\dfrac{W}{K \cdot m^2}$
α_T	Thermal conductivity coefficient	1.10^{-3}	K^{-1}
$[\sigma_{Ox}, \sigma_{CF0}]$	[Oxide, C.F.] electrical conductivity	$[0.013, 5 \cdot 10^5]$	S/m
$[\sigma_{CB}, \sigma_{CT}]$	[Bottom,Top] electrode electrical conductivity	$[18 \cdot 10^6, 10^6]$	S/m
I_0	Current coefficient	10	$A/\mu m^2$
g_0	Gap coefficient	1	nm
V_0	Voltage coefficient	0.30	V

Thermal Description Used in the Devices Under Study

This appendix describes the different approaches reported in the literature to describe the temperature evolution of the studied devices (memristors based on resistive switching devices) and presents some new approaches followed in this doctoral thesis. (D.4. Temperature for a memristor with a Cylindrical conductive filament with Thermal Conductivity k_{th} and Heat Transfer Coefficient h, D.5. Thermal model of a memristor with a Cylindrical Conductive Filament with Thermal Conductivity k_{th} and Heat Transfer Coefficient h by using Laplace Transform, and D.6. Thermal Description of a memristor with a Truncated-Cone Shaped Conductive Filament).

Some memristor models do not take into account thermal effects, but a behavioural description of the electrical characteristic of the devices is carried out [Chua1971, Chua1976, Benderli2009, Biolek2009, Joglekar2009, Pickett2009, Miller2010, Oblea2010, Pino2010, Radwan2010 Lehtonen2010c, Rák2010, Jo2010, Sharifi2010, Laiho2010, Mahvash2010, Yakopcic2011, Abdalla2011, Chang2011, Kavehei2011, Kvatinsky2012, Kvatinsky2013, Fang2013, Kvatinsky2015, Garcia-Moreno2015].

However, since most of the physical mechanisms which control resistive switching are thermally activated, an accurate device modeling requires a good thermal model. The calculation of the memristor temperature in the context of compact modeling is based on one-dimensional simplifications of the thermal flux caused by dissipated energy in the device, this latter effect is assumed to be the only heat source avaliable [Ielmini2016].

If more precise results were required, the conductive filament shape and a three-dimensional approach should be considered by means of the Fourier equation [Ielmini2016]

$$-\nabla k_{Th} \nabla T = |\sigma \nabla \Psi|^2 \qquad (D.1)$$

Where k_{Th} is the thermal conductivity, the term $|\sigma \nabla \Psi|^2$ represents the local dissipated power density given by the product of the electric field $\nabla \Psi$ and the electrical conductivity σ, while the term $\nabla k_{Th} \nabla T$ corresponds to the space variation of the heat flow (∇T) due to thermal conduction (∇k_{Th}). This equation can be solved following a finite element method, as it is the case of some macroscopic simulators [Panda2018, Russo2009, Aldana2017, Aldana2018, Cazorla2019].

Also, in the case of circuits with several devices that are dissipating heat simultaneously, the coupled influence of all heat sources that exist in the vicinity of each device must be taken into account. One example of the temperature distribution in a crossbar configuration is presented in [Deshmukh2015], where the thermal influence across two nearby RRAM cells is shown.

D.1. Models with a Lumped Thermal Resistance

This is the simplest concentrated parameters model to calculate the temperature in one device. It is characterized by a single thermal resistance, R_{th}. It is used in different RRAM compact models [Sheridan2011, Huang2013, Li2014, Jiang2014, Jiang2015, Jiang2016, Chen2016]. Its main advantage is due to be a very simple thermal description and differential equations have not to be solved. Therefore, it is a model computationally very efficient. The device is thermally characterized with a unique temperature.

The thermal resistance is defined as the temperature difference $(T - T_0)$ across a structure when a unit of heat energy (1 Watt) flows through it during a unit of time [Moran2011, Walker2007]. It is measured in the International System of Units in W/K. It is assumed that heat energy is due to the power dissipation by the Joule effect. Therefore, the relationship between temperature increase and heat flux can be calculated as [Moran2011, Walker2007]

$$R_{Th} = \frac{T - T_0}{V \cdot I} \tag{D.2}$$

where V is the applied voltage and I is the flowing current through the device.

With this simple model, the device temperature can be calculated from (D.2) as [Sheridan2011, Huang2013, Li2014, Jiang2014, Jiang2015, Jiang2016, Chen2016]

$$T = T_0 + R_{Th} \cdot V \cdot I \tag{D.3}$$

From a simulation point of view, equation (D.3) can be implemented with the equivalent electrical sub-circuit show in **Figure D.1**: the heat power is represented by a dependent current source of value $G_{pw} = V \cdot I$, where the voltage is sensed by the two input sub-circuit terminals V^+ and V^-, and the current is sensed by a cero voltage source V_{sense} between the input terminals I^+ and I^-. The thermal resistance is represented by and electrical resistance R_{th}, and the room temperature by a constant voltage source $T0$ with an assigned value equal to the value of the absolute room temperature (T_0), in K. The output sub-circuit terminal (T) provides a voltage that represents the temperature T (in K).
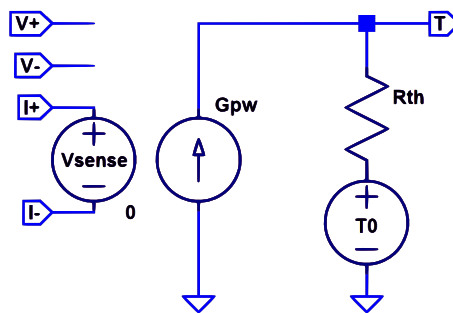
Figure D.1 Equivalent electric circuit for the temperature model based on a thermal resistance R_{th}

This approach does not take into account the conductive filament geometry. Furthermore, it does not include thermal inertia, which it could be relevant in pulsed operation.

D.2. Models with a Lumped Thermal Inertia

Thermal models based only on a thermal resistance do not provide memory effects, the temperature depends only on the instantaneous dissipated heat. In order to include thermal inertia in the model a capacitor is added. Its capacitance, C_{th}, represents the thermal capacitance of the device. This approach is used in different RRAMs compact models [Guan2012, Chen2015, Chiang2015]. As in the models described in the previous section, the device is thermally characterized by a sole homogeneous temperature.

The ability of a material to store thermal energy is linked to the thermal capacitance or heat capacity (C_{th}). It is defined as the amount of heat needed for a mass to produce a unitary temperature change. It is measured in the International System of Units in J/K or J/K (or also in $J/°C$) [Moran2011, Walker2007]. It is assumed that heat energy in one device is due to the power dissipated by the Joule effect ($V \cdot I$), and taking into account the thermal capacitance (C_{th}) and thermal resistance (R_{th}), the thermal balance can be expressed as [Moran2011, Walker2007],

$$V \cdot I = \frac{T - T_0}{R_{th}} + C_{th}\frac{dT}{dt} \qquad (D.4)$$

From this equation we obtain the equivalent electrical circuit shown in the **Figure D.2**. [Guan2012, Chen2015, Chiang2015]. Solving the temperature we obtain the expression given in equation (D.5)

$$T = T_0 + V \cdot I \cdot R_{th} - \tau_{th}\frac{dT}{dt} \qquad (D.5)$$

Where τ_{th} is the time constant of thermal inertia defined as follow,

$$\tau_{th} = C_{th}R_{th} \qquad (D.6)$$

From a simulation point of view, equation (D.5) can be implemented with the equivalent electrical sub-circuit showed in **Figure D.2**. The values of the different electric elements and the role of the pins is the same as in **Figure D.1**. However, a capacitor has been added in order to reproduce the behavior of the thermal capacitance..
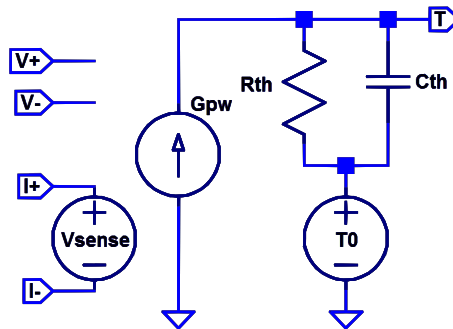
Figure D.2 Equivalent electric circuit of temperature model based on a lumped inertial thermal for a SPICE-like circuit simulator.

Again, this approach does not take into account the conductive filament geometry. However, it is provide a simple description of thermal effects, including thermal inertia.

D.3. Temperature of a memristor Cylindrical Filament with Thermal Conductivity k_{th}

The thermal conductivity (K_{th}) is a material property that describes the efficiency of heat transport through a conductive material as the result of a temperature difference, as follows [Moran2011]:

$$q = -K_{th}\nabla T \tag{D.7}$$

where q is the heat flux and ∇T is the temperature gradient. It is measured in the International System of Units in $W/m \cdot K$.

In this thermal model, the filament temperature is calculated along the filament assuming that it has a cylindrical geometry with constant electrical and thermal conductivities. Boundary conditions T_{in} and T_{out} are imposed at the extremes of the filament ($z = 0$ and z=L_{CF}, respectively), see **Figure D.3**. The following Fourier equation (D.8) is obtained with these assumptions [Bocquet2014, Bocquet2013]:

$$\sigma_{CF}\xi^2 = -K_{th}\frac{\partial^2 T_{CF}(z)}{\partial z^2} \tag{D.8}$$

where ξ is the electric field.
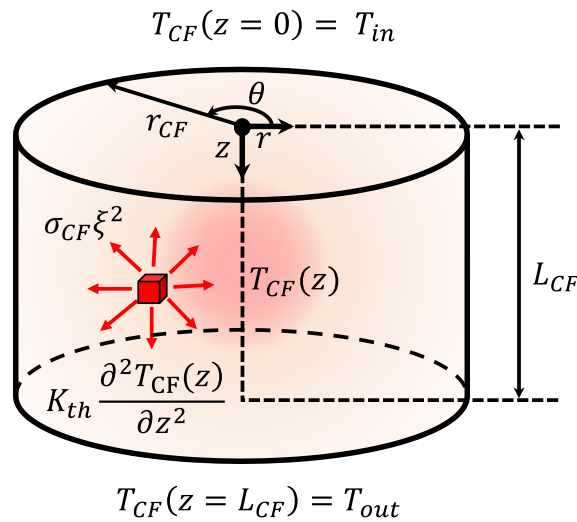
Figure D.3 Schema showing the different elements taken into account in order to solve Fourier equation in a cylindrical and homogenous conductive filament.

Table D.1 Procedure for obtain the temperature solving the heat equation.

Step	Description
1	Select the effect that include in the thermal study (K_{th},h) generally 1D simplification in compact modelling approach.
2	Select the geometry and boundary conditions eg. $T(z = 0) = T_0$, $T(Z = L_{CF}) = T_0$. Its good idea to represent graphically. (see **Figure D.3**).
3	Solve the ordinary differential equation (with Laplace Transform or standard differential equation methods). Obtain a general expression of the temperature as a function of the spatial coordinate. For example: $T(z) = f(z)$
4	Verify that the expression obtained $T(z) = f(z)$ satisfies the boundary conditions imposed on the step 2.
5	Derive $T(z)$ respect to z and find the value of z_{max} that $dT(z_{max})/dz = 0$.
6	Obtain the maximum value of $T(z_{max})$. It will be considered in simulation time as the device temperature.

Equation (D.8) was solved with with a Matlab live script, following the steps described in **Table D.1**. Other programming tools such a R or python could have been used.

```
clc, clear
% Declaration of symbolic variables
syms TCF(x) sigma K_th T_0 xi L_CF T_in T_out T_0;
% Solve the diffetential equation of calor
Tx=dsolve(diff(TCF,2) ==-sigma*xi^2/K_th ,TCF(0)==T_in, TCF(L_CF)==T_out)
Tx =
```

$$T_{\text{in}} - \frac{\sigma\, x^2\, \xi^2}{2\, K_{\text{th}}} + \frac{x\,\left(\sigma\, L_{\text{CF}}{}^2\, \xi^2 - 2\, K_{\text{th}}\, T_{\text{in}} + 2\, K_{\text{th}}\, T_{\text{out}}\right)}{2\, K_{\text{th}}\, L_{\text{CF}}}$$

```
% Simplity and represent T(x)
Txs=simplify(Tx,'steps',1000)
Txs =
```

$$T_{\text{in}} - \frac{x\,\left(T_{\text{in}} - T_{\text{out}}\right)}{L_{\text{CF}}} + \frac{\sigma\, x\, \xi^2\,\left(L_{\text{CF}} - x\right)}{2\, K_{\text{th}}}$$

```
% Calculate the derivative dT(x)/dx to obtain the value of the maximum
value of T(x)
simplify(diff(Txs,1),'steps',1000)
ans =
```

$$\frac{\sigma\, \xi^2\,\left(L_{\text{CF}} - 2\, x\right)}{2\, K_{\text{th}}} - \frac{T_{\text{in}} - T_{\text{out}}}{L_{\text{CF}}}$$

```
% Find the value of xmax
xmax=solve(diff(Txs,1))
xmax =
```

$$-\frac{K_{\text{th}}\,\left(\dfrac{T_{\text{in}} - T_{\text{out}}}{L_{\text{CF}}} - \dfrac{L_{\text{CF}}\, \sigma\, \xi^2}{2\, K_{\text{th}}}\right)}{\sigma\, \xi^2}$$

```
% Value of Temperature for x=xmax T(xmax)
T_max=simplify(subs(Txs,{x},xmax),'steps',1000)
T_max =
```

$$\frac{\sigma\, L_{\text{CF}}{}^2\, \xi^2 + 4\, K_{\text{th}}\, T_{\text{in}} + 4\, K_{\text{th}}\, T_{\text{out}}}{8\, K_{\text{th}}} + \frac{K_{\text{th}}\,\left(T_{\text{in}} - T_{\text{out}}\right)^2}{2\, L_{\text{CF}}{}^2\, \sigma\, \xi^2}$$

```
% Verify the contour value T(x=0)
simplify(subs(Txs,{x},{0}))
ans = 
```
T_{in}

```
% Verify the contour value T(x=L_CF)
simplify(subs(Txs,{x},{L_CF}))
ans = 
```
T_{out}

```
% Value of Temperature for x=xmax T(xmax) if T_in=T_out=T_0
Tm0=simplify(subs(Txs,{T_out,T_in},{T_0,T_0}),'steps',1000)
Tm0 =
```

$$T_0 + \frac{\sigma\, x\, \xi^2\,\left(L_{\text{CF}} - x\right)}{2\, K_{\text{th}}}$$

```
% Verify the contour value T(x=0)
simplify(subs(Tm0,{x},{0}))
ans = 
```
T_0

```
% Verify the contour value T(x=L_CF)
simplify(subs(Tm0,{x},{L_CF}))
ans = 
```
T_0

The general solution for the maximum temperature in the CF, with different boundary temperatures, is:

$$T_{max} = \frac{T_{in} + T_{out}}{2} + \frac{\sigma_{CF} L_{CF}^2 \xi^2}{8k_{th}} + \frac{K_{th}(T_{in} - T_{out})^2}{2L_{CF}^2 \sigma_{CF} \xi^2} \tag{D.9}$$

For the particular case in which $T_{in} = T_{out} = T_0$, the following expression is obtained:

$$T_{max} = T_0 + \frac{\sigma_{CF} \cdot L_{CF}^2 \cdot \xi^2}{8K_{th}} \tag{D.10}$$

and calculating the electric field as a function of the applied voltage ($\xi = V_{cell}/L_{CF}$), equation (D.11) is obtained:

$$T_{max} = T_0 + \frac{\sigma_{CF} V_{cell}^2}{8K_{th}} \tag{D.11}$$

This temperature description for the CF is used in section 2.2. Compact Model of Bipolar CB-RRAM (IM2NP) equation (2.9).

D.4. Temperature for a memristor with a Cylindrical conductive filament with Thermal Conductivity k_{th} and Heat Transfer Coefficient h

In the previous model, heat transfer to the surrounding insulator is not taken into account. In this section, this heat losses are included by means of the heat transfer coefficient (h), given by the ratio between the heat lateral flux and the temperature difference between the filament and the surrounding dielectric [Moran2011],

$$h = \frac{q}{\Delta T} \tag{D.12}$$

where q is the lateral heat flux and ΔT is the difference of temperature between the considered filament and the surrounding oxide. It is measured in the International System of Units in $W/m^2 \cdot K$.

In this thermal model, the filament temperature is calculated along its length assuming that it has a cylindrical geometry with constant electrical and thermal conductivities. As said before, the heat transfer towards the surrounding oxide is included by means of the coefficient h. Boundary conditions T_{in} and T_{out} are imposed at the extremes of the filament ($z=0$ and $z=L_{CF}$, respectively), see **Figure D.3**. The following Fourier equation (D.8) is obtained with these assumptions [Bocquet2011, Villena2013, Jiménez-Molinos2015, González-Cordero2016f, González-Cordero2017c]:

$$\sigma \cdot \xi^2 = -K_{th}\frac{\partial^2 T(x)}{\partial x^2} + 2h\frac{T - T_{ox}}{r_{CF}} \tag{D.13}$$
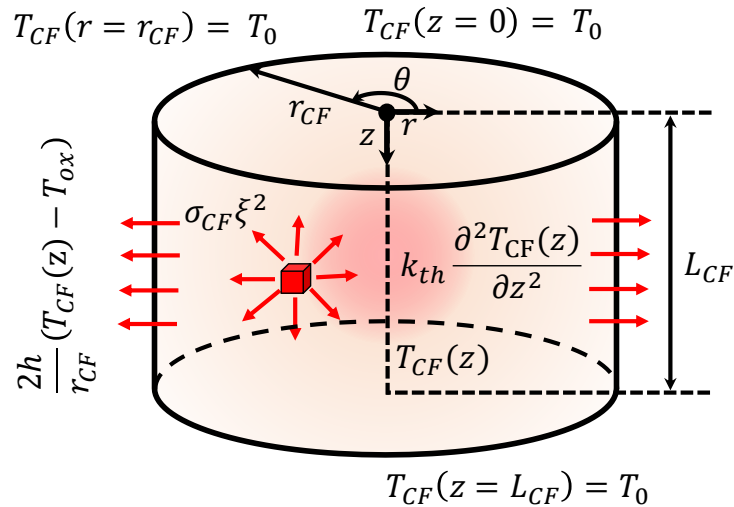
Figure D.4 Sketch of a cylindrical filament with thermal conductivity k_{th} and heat transfer coefficient h to solve the 1D heat equation.

Equation (D.13) is solved with help of symbolic Matlab live script, following the steps described in the procedure described in the **Table D.1**.

```
clc, clear
% Declaration of symbolic variables
syms T_CF(x) sigma K_th T_0 xi L_CF h r_CF
% Solve the diffetential equation of calor
Tx=dsolve(diff(T_CF,2) ==-sigma*xi^2/K_th +2*h/(r_CF*K_th)*(T_CF-T_0),
T_CF(0)==T_0, T_CF(L_CF)==T_0)
```
Tx =

$$
\frac{K_{th}\, r_{CF}\left(\frac{\sigma\,\xi^2}{K_{th}}+\frac{2\,T_0\,h}{K_{th}\,r_{CF}}\right)}{2\,h} - \frac{\mathrm{e}^{\sigma_1}\left(r_{CF}\,\sigma\,\xi^2 - r_{CF}\,\sigma\,\xi^2\,\mathrm{e}^{-\sigma_3}\right)}{\sigma_2} + \frac{\mathrm{e}^{-\sigma_1}\left(r_{CF}\,\sigma\,\xi^2 - r_{CF}\,\sigma\,\xi^2\,\mathrm{e}^{\sigma_3}\right)}{\sigma_2}
$$

where

$$
\sigma_2 = 2\,h\left(\mathrm{e}^{\sigma_3}-\mathrm{e}^{-\sigma_3}\right)
$$

$$
\sigma_1 = \frac{\sqrt{2}\,x\,\sqrt{K_{th}\,h\,r_{CF}}}{K_{th}\,r_{CF}}
$$

$$
\sigma_3 = \frac{\sqrt{2}\,L_{CF}\,\sqrt{K_{th}\,h\,r_{CF}}}{K_{th}\,r_{CF}}
$$

```
% Simplity and represent T(x)
Txs=simplify(Tx,'steps',4000)
```
Txs =

$$
T_0 + \frac{r_{CF}\,\sigma\,\xi^2\,\mathrm{e}^{-\sigma_2}\left(\sigma_1-\mathrm{e}^{\sigma_2}\right)\left(\mathrm{e}^{\sigma_2}-1\right)}{2\,h\left(\sigma_1+1\right)}
$$

where

$$
\sigma_1 = \mathrm{e}^{\frac{L_{CF}\,\sqrt{2\,K_{th}\,h\,r_{CF}}}{K_{th}\,r_{CF}}}
$$

$$
\sigma_2 = \frac{x\,\sqrt{2\,K_{th}\,h\,r_{CF}}}{K_{th}\,r_{CF}}
$$

```
% Calculate the derivative dT(x)/dx to obtain the value of the maximum
value of T(x)
simplify(diff(Txs,1),'steps',4000)
```
ans =

$$
\frac{\sigma\,\xi^2\,\mathrm{e}^{-\frac{x\,\sqrt{2\,K_{th}\,h\,r_{CF}}}{K_{th}\,r_{CF}}}\left(\mathrm{e}^{\frac{L_{CF}\,\sqrt{2\,K_{th}\,h\,r_{CF}}}{K_{th}\,r_{CF}}} - \mathrm{e}^{\frac{2\,x\,\sqrt{2\,K_{th}\,h\,r_{CF}}}{K_{th}\,r_{CF}}}\right)\sqrt{2\,K_{th}\,h\,r_{CF}}}{2\,K_{th}\,h\left(\mathrm{e}^{\frac{L_{CF}\,\sqrt{2\,K_{th}\,h\,r_{CF}}}{K_{th}\,r_{CF}}}+1\right)}
$$

```
% Find the value of dT(x)/dx=0 (xmax)
xmax=solve(diff(Txs,1))
```
xmax =

$$\left(\frac{K_{\text{th}}\, r_{\text{CF}} \log\left(-e^{\frac{\sqrt{2}\, L_{\text{CF}}\, \sqrt{K_{\text{th}}\, h\, r_{\text{CF}}}}{2\, K_{\text{th}}\, r_{\text{CF}}}}\right)}{\dfrac{\sqrt{2\, K_{\text{th}}\, h\, r_{\text{CF}}}}{\sqrt{2}\, L_{\text{CF}}\, \sqrt{K_{\text{th}}\, h\, r_{\text{CF}}}}} \right)$$

```
% Value of Temperature for x=xmax T(xmax)
Tmax=simplify(subs(Txs,{x},xmax),'steps',1000)
```

Tmax =

$$\left(\begin{array}{c} T_0 + \dfrac{r_{\text{CF}}\, \sigma\, \xi^2 \left(e^{\frac{L_{\text{CF}}\sqrt{2\,K_{\text{th}}\,h\,r_{\text{CF}}}}{2\,K_{\text{th}}\,r_{\text{CF}}}} + 1\right)^2}{\sigma_1} \\[4ex] T_0 + \dfrac{r_{\text{CF}}\, \sigma\, \xi^2 \left(e^{\frac{L_{\text{CF}}\sqrt{2\,K_{\text{th}}\,h\,r_{\text{CF}}}}{2\,K_{\text{th}}\,r_{\text{CF}}}} - 1\right)^2}{\sigma_1} \end{array} \right)$$

where

$$\sigma_1 = 2\, h \left(e^{\frac{L_{\text{CF}}\sqrt{2\,K_{\text{th}}\,h\,r_{\text{CF}}}}{K_{\text{th}}\,r_{\text{CF}}}} + 1\right)$$

```
% Verify the contour value T(x=0)
simplify(subs(Txs,{x},{0}))
```
ans = T_0
```
% Verify the contour value T(x=L_CF)
simplify(subs(Txs,{x},{L_CF}))
```
ans = T_0

$$T_{max} = T_0 + \frac{\sigma_{CF} \cdot \xi^2 \cdot r_{CF} \cdot (e^\alpha - 1)^2}{2 \cdot h(e^{2\alpha} + 1)} \tag{D.14}$$

Where

$$\alpha = \frac{L_{CF}}{2}\sqrt{\frac{2 \cdot h}{k_{th} \cdot r_{CF}}} \tag{D.15}$$

This thermal model is used in sections:

6.2. Simulation on RRAM Memory Circuits and in the reference 6.2. [González-Cordero2016f].
6.3. Simulation of Circuits Including RRAMs and in the reference[González-Cordero2017c].

D.5. Thermal model of a memristor with a Cylindrical Conductive Filament with Thermal Conductivity k_{th} and Heat Transfer Coefficient h by using Laplace Transform

In this section we work on equations ([11](#)), ([12](#)) and ([13](#)) of paper included in the section 2.4. New Bipolar CB-RRAM Compact Model (UGR-CB) and in the reference 2.4. [González-Cordero2016a].

Using the symbolic Matlab© live script the heat equation (D.13) is solved used Laplace Transform, The analytical expression obtained is equivalent to the one extracted in the previous section.

```
%% Analytical Resolution of the Heat Equation with Laplace Transform
clear, clc
% Symbolic variables
syms s sigma_CF xi_z h r_CF T T_ox K_th z L_CF LT T_0 d_T0;
% definition of Ordinary Diferenctial Ecuation (ODE)
eq ='sigmaCF*xi_z^2-2*h/r_CF*(T(z)-T_ox)=-K_th*D(D(T))(z)'
```

```
eq = 'sigmaCF*xi_z^2-2*h/r_CF*(T(z)-T_ox)=-K_th*D(D(T))(z)'
```

```
% Laplace Transform of ODE
ltode=laplace(eq,z,s)
```

ltode =

$$\frac{2\,h\left(\dfrac{T_{\text{ox}}}{s}-\text{laplace}(T(z),z,s)\right)}{r_{\text{CF}}}+\frac{\text{sigmaCF}\,\xi_z{}^2}{s}=K_{\text{th}}\left(s\,T(0)+\left(\left(\frac{\partial}{\partial z}\,T(z)\right)\Big|_{z=0}\right)-s^2\,\text{laplace}(T(z),z,s)\right)$$

```
%% Change some Symbolic expresion
% LT <- laplace(T(z), z, s)
% d_T0 <- subs(diff(T(z), z), z, 0)
% T_0 <- T(0)
eqn=(sigma_CF*xi_z^2)/s + (2*h*(T_0/s - LT))/r_CF == K_th*(s*T_0 + d_T0 -
s^2*LT)
```

eqn =

$$\frac{\sigma_{\text{CF}}\,\xi_z{}^2}{s}-\frac{2\,h\left(\text{LT}-\dfrac{T_0}{s}\right)}{r_{\text{CF}}}=K_{\text{th}}\left(-\text{LT}\,s^2+T_0\,s+d_{\text{T0}}\right)$$

```
%% solve LT
T2=solve(eqn,LT)
```

T2 =

$$-\frac{\dfrac{\sigma_{\text{CF}}\,\xi_z{}^2}{s}-K_{\text{th}}\left(d_{\text{T0}}+T_0\,s\right)+\dfrac{2\,T_0\,h}{r_{\text{CF}}\,s}}{K_{\text{th}}\,s^2-\dfrac{2\,h}{r_{\text{CF}}}}$$

```
%% inverse Laplace Transform -> T(z)
TZ=ilaplace(T2,s,z)
```

TZ =

$$\frac{r_{\text{CF}}\,\sigma_{\text{CF}}\,\xi_z{}^2+2\,T_0\,h}{2\,h}-\frac{r_{\text{CF}}\,\sigma_{\text{CF}}\,\xi_z{}^2\cosh\left(\dfrac{\sqrt{2}\ \sqrt{h}\ z}{\sqrt{K_{\text{th}}}\ \sqrt{r_{\text{CF}}}}\right)-\sqrt{2}\ \sqrt{K_{\text{th}}}\,d_{\text{T0}}\,\sqrt{h}\ \sqrt{r_{\text{CF}}}\,\sinh\left(\dfrac{\sqrt{2}\ \sqrt{h}\ z}{\sqrt{K_{\text{th}}}\ \sqrt{r_{\text{CF}}}}\right)}{2\,h}$$

```
% Verification z=0 -> T(z)=T0
TZ0=simplify(eval(subs(TZ,{'z'},0)))
```

TZ0 = T_0

```
%% with T(z=L_CF)=T0 -> solve dT0
TzL=subs(TZ,{'z'},{'L_CF'});
```

```
Tzls=simplify(eval(TzL-T_0),2000)
Tzls =
```

$$\frac{\sqrt{2}\ \sqrt{K_{th}}\ d_{T0}\ \sqrt{r_{CF}}\ \sinh\left(\frac{\sqrt{2}\ L_{CF}\ \sqrt{h}}{\sqrt{K_{th}}\ \sqrt{r_{CF}}}\right)}{2\ \sqrt{h}} - \frac{r_{CF}\ \sigma_{CF}\ \xi_z^{\,2}\ \sinh\left(\frac{\sqrt{2}\ L_{CF}\ \sqrt{h}}{2\ \sqrt{K_{th}}\ \sqrt{r_{CF}}}\right)^2}{h}$$

```
%% solve dT0
dt0=simplify(solve(Tzls,d_T0),2000)
dt0 =
```

$$\frac{\sqrt{2}\ \sqrt{r_{CF}}\ \sigma_{CF}\ \xi_z^{\,2}\ \tanh\left(\frac{\sqrt{2}\ L_{CF}\ \sqrt{h}}{2\ \sqrt{K_{th}}\ \sqrt{r_{CF}}}\right)}{2\ \sqrt{K_{th}}\ \sqrt{h}}$$

```
%% Find the maximum value of T(z)
Tzdto=subs(TZ,{d_T0},dt0);
% determine dT(z)/dz
DTzdx=simplify(eval(diff(Tzdto,z)))
DTzdx =
```

$$-\frac{\sqrt{2}\ \sqrt{r_{CF}}\ \sigma_{CF}\ \xi_z^{\,2}\ \left(\sinh\left(\frac{\sqrt{2}\ \sqrt{h}\ z}{\sqrt{K_{th}}\ \sqrt{r_{CF}}}\right) - \tanh\left(\frac{\sqrt{2}\ L_{CF}\ \sqrt{h}}{2\ \sqrt{K_{th}}\ \sqrt{r_{CF}}}\right)\cosh\left(\frac{\sqrt{2}\ \sqrt{h}\ z}{\sqrt{K_{th}}\ \sqrt{r_{CF}}}\right)\right)}{2\ \sqrt{K_{th}}\ \sqrt{h}}$$

```
%% solve dT(z)/dz=0
zmax=simplify(solve(DTzdx,z),2000)
zmax =
```

$$\left(\begin{array}{c} \dfrac{L_{CF}}{2} \\[4ex] \dfrac{\sqrt{2}\ \sqrt{K_{th}}\ \sqrt{r_{CF}}\ \log\left(-e^{\frac{\sqrt{2}\,L_{CF}\,\sqrt{h}}{2\,\sqrt{K_{th}}\,\sqrt{r_{CF}}}}\right)}{2\ \sqrt{h}} \end{array}\right)$$

```
%% Tmax=T(zmax)
Tmax=subs(TZ,{z},{L_CF/2})
Tmax =
```

$$\frac{r_{CF}\ \sigma_{CF}\ \xi_z^{\,2} + 2\ T_0\ h}{2\ h} - \frac{r_{CF}\ \sigma_{CF}\ \xi_z^{\,2}\ \cosh\left(\frac{\sqrt{2}\ L_{CF}\ \sqrt{h}}{2\ \sqrt{K_{th}}\ \sqrt{r_{CF}}}\right) - \sqrt{2}\ \sqrt{K_{th}}\ d_{T0}\ \sqrt{h}\ \sqrt{r_{CF}}\ \sinh\left(\frac{\sqrt{2}\ L_{CF}\ \sqrt{h}}{2\ \sqrt{K_{th}}\ \sqrt{r_{CF}}}\right)}{2\ h}$$

Namely (equation (12))

$$\alpha = \sqrt{\frac{2h}{k_{th}\cdot r_{CF}}} \tag{D.16}$$

The value of `dt0` obtained can be rewiten as (same as the equation (13)),

$$dT_0 = \frac{\sigma_{CF}\cdot r_{CF}\cdot \xi^2 tanh\left(\frac{\alpha L}{2}\right)}{\sqrt{2\cdot K_{th}\cdot h\cdot r_{CF}}} \tag{D.17}$$

The maximum temperature (`Tmax`) taking out the term $\sigma_{CF} r_{CF} \xi^2$ as a common factor and replacing α parameter, can be rewritten as (same as the equation (11)),

$$T_{CF} = T_0 + \frac{\sigma_{CF} r_{CF}\xi^2}{2h}\left(1 - cosh\left(\frac{\alpha L_{CF}}{2}\right)\right) + \frac{dT_0}{\alpha}sinh\left(\frac{\alpha L_{CF}}{2}\right) \tag{D.18}$$

D.6. Thermal Description of a memristor with a Truncated-Cone Shaped Conductive Filament

In this section we describe the thermal model assumed for a memristor with a CF with truncated-cone shape. The boundary condition are shown in **Figure D.5 a)**. Notice that the radius $r_{CF}(x)$ of the truncated cone depends on the x position. The heat equation taken into account thermal conductivity K_{th} and a heat transfer coefficient h is expressed as follows,

$$\sigma_{CF}(x) \cdot \xi_{CF}(x)^2 - \frac{2h}{r_{CF}(x)}(T_{CF}(x) - T_0) = -K_{th}\frac{\partial^2 T_{CF}(x)}{\partial x^2} \tag{D.19}$$

This equation cannot be solved analytically with a variable $r_{CF}(x)$. In order to obtain an approximated analytical solution, we consider that a truncated-cone shaped CF with constant conductivity is equivalent to a cylinder with radio $(r_g = \sqrt{r_T \cdot r_B})$ with variable conductivity $\sigma_{CF}(x)$, see **Figure D.5 b)**. For a fixed applied voltage, we include the electric field maximum, that is a value affected by the ratio between the two truncated cone radii ($\eta = r_T/r_B$). The following simplified heat equation

$$\frac{\sigma_{CF} \cdot V_{CF}^2}{L_{CF}^2 \cdot \eta} - \frac{2h}{r_g}(T_{CF}(x) - T_0) = -K_{th}\frac{\partial^2 T_{CF}(x)}{\partial x^2} \tag{D.20}$$
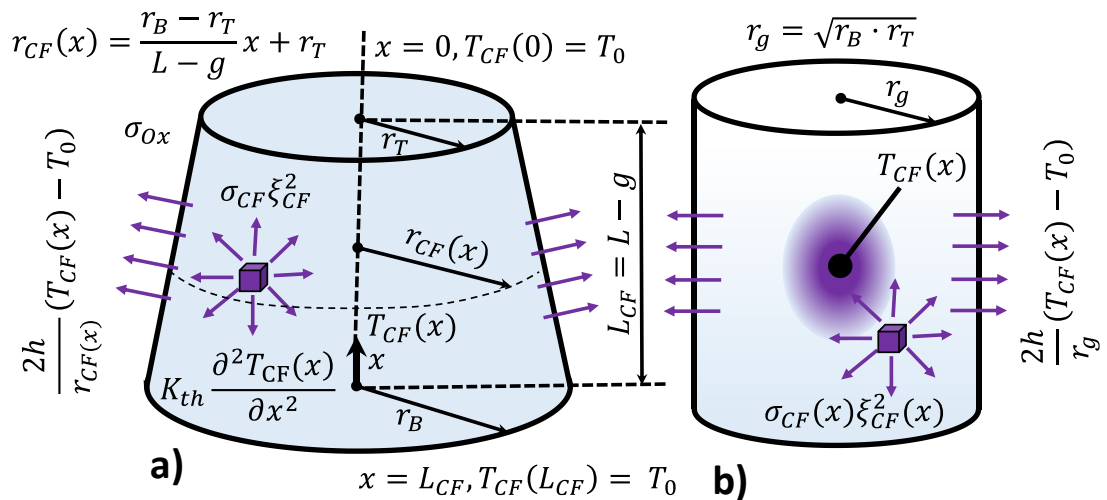
Figure D.5 a) Energy dissipation terms included in the heat equation and geometrical domain for the CF thermal description, **b)** Cylindrical CF equivalent employed to simplify the heat equation solution and obtain a compact analytical expression for the CF temperature.

Equation (D.20) is solved with help of a symbolic Matlab live script, following the steps described in **Table D.1**.

```
% Declaration of symbolic variables
syms T_CF(x) sigma_CF K_th T_0 xi L_CF h r_g eta
% Solve the diffetential equation of calor
Tx=dsolve(diff(T_CF,2) ==-sigma_CF*xi^2/(K_th *eta)
+2*h/(r_g*K_th)*(T_CF-T_0), T_CF(0)==T_0, T_CF(L_CF)==T_0)
```

Tx =

$$\frac{K_{th}\, r_g \left(\dfrac{\sigma_{CF}\, \xi^2}{K_{th}\, \eta} + \dfrac{2\, T_0\, h}{K_{th}\, r_g} \right)}{2\, h} - \frac{e^{\sigma_1} \left(r_g\, \sigma_{CF}\, \xi^2 - r_g\, \sigma_{CF}\, \xi^2\, e^{-\sigma_3} \right)}{\sigma_2} + \frac{e^{-\sigma_1} \left(r_g\, \sigma_{CF}\, \xi^2 - r_g\, \sigma_{CF}\, \xi^2\, e^{\sigma_3} \right)}{\sigma_2}$$

where
$$\sigma_2 = 2\,\eta\,h\,\left(e^{\sigma_3} - e^{-\sigma_3}\right)$$

$$\sigma_1 = \frac{\sqrt{2}\,x\,\sqrt{K_{th}\,h\,r_g}}{K_{th}\,r_g} \qquad \sigma_3 = \frac{\sqrt{2}\,L_{CF}\,\sqrt{K_{th}\,h\,r_g}}{K_{th}\,r_g}$$

```
% Simplity and represent T(x)
Txs=simplify(Tx,'steps',1000)
Txs =
```

$$\frac{\dfrac{r_g\,\sigma_{CF}\,\xi^2}{2} + T_0\,\eta\,h - \sigma_1}{\eta\,h} - \frac{\dfrac{r_g\,\sigma_{CF}\,\xi^2\,e^{\frac{x\,\sqrt{2\,K_{th}\,h\,r_g}}{K_{th}\,r_g}}}{2} - \sigma_1}{\eta\,h\,\left(e^{\frac{L_{CF}\,\sqrt{2\,K_{th}\,h\,r_g}}{K_{th}\,r_g}} + 1\right)}$$

where

$$\sigma_1 = \frac{r_g\,\sigma_{CF}\,\xi^2\,e^{-\frac{x\,\sqrt{2\,K_{th}\,h\,r_g}}{K_{th}\,r_g}}}{2}$$

```
% Calculate the derivative dT(x)/dx to obtain the value of the maximum
value of T(x)
simplify(diff(Txs,1),'steps',4000)
ans =
```

$$\frac{\sigma_{CF}\,\xi^2\,e^{-\frac{x\,\sqrt{2\,K_{th}\,h\,r_g}}{K_{th}\,r_g}}\left(e^{\frac{L_{CF}\,\sqrt{2\,K_{th}\,h\,r_g}}{K_{th}\,r_g}} - e^{\frac{2\,x\,\sqrt{2\,K_{th}\,h\,r_g}}{K_{th}\,r_g}}\right)\sqrt{2\,K_{th}\,h\,r_g}}{2\,K_{th}\,\eta\,h\,\left(e^{\frac{L_{CF}\,\sqrt{2\,K_{th}\,h\,r_g}}{K_{th}\,r_g}} + 1\right)}$$

```
% Find the value of dT(x)/dx=0 (xmax)
xmax=simplify(solve(diff(Txs,1)),1000)
xmax =
```

$$\left(\frac{\dfrac{K_{th}\,r_g\,\log\left(-e^{\frac{L_{CF}\,\sqrt{2\,K_{th}\,h\,r_g}}{2\,K_{th}\,r_g}}\right)}{\sqrt{2\,K_{th}\,h\,r_g}}}{\dfrac{L_{CF}}{2}}\right)$$

```
% Value of Temperature for x=xmax T(xmax)
Tmax=simplify(subs(Txs,{x},{L_CF/2}),'steps',1000)
Tmax =
```

$$\frac{r_g\,\sigma_{CF}\,\xi^2 + 2\,T_0\,\eta\,h}{2\,\eta\,h} - \frac{r_g\,\sigma_{CF}\,\xi^2\,e^{\frac{L_{CF}\,\sqrt{2\,K_{th}\,h\,r_g}}{2\,K_{th}\,r_g}}}{\eta\,h\,\left(e^{\frac{L_{CF}\,\sqrt{2\,K_{th}\,h\,r_g}}{K_{th}\,r_g}} + 1\right)}$$

```
% Verify the contour value T(x=0)
simplify(subs(Txs,{x},{0}))
ans = 
```
T_0
```
% Verify the contour value T(x=L_CF)
simplify(subs(Txs,{x},{L_CF}))
ans = 
```
T_0

Namely: (Equation ([5]) of section 3.4.3. UGR-VCM Model with Variability)

$$\alpha = L_{CF}\sqrt{\frac{2h}{k_{th}r_g}} \tag{D.21}$$

The value of Tmax obtained can be rewritten as (same as the equation ([4])).

$$T = T_0 + \frac{r_g \sigma_{CF} \xi^2}{\eta h}\left[\frac{1}{2} - \frac{e^{\frac{\alpha}{2}}}{e^{\alpha} + 1}\right] \tag{D.22}$$

This thermal model is used in sections:

3.4.1. Model Development and in the reference [González-Cordero2017a]
3.4.2. UGR-VCM Model Validation with other Technologies and in the reference [González-Cordero2017d]
3.4.3. UGR-VCM Model with Variability and in the reference [González-Cordero2017b,]
3.4.4. UGR-VCM Model Improvement to Include Distributed Currents
6.4. Electronic Synapses Based on Resistive Switching Devices. and in the reference [González-Cordero2019b]

References

[Abdalla2011] Abdalla, H., & Pickett, M. D. (2011). SPICE modeling of memristors. In *2011 IEEE International Symposium of Circuits and Systems (*ISCAS*)* (pp. 1832–1835). IEEE. DOI: 10.1109/ISCAS.2011.5937942

[Acal2019] Acal, C., Ruiz-Castro, J. E., Aguilera, A. M., Jiménez-Molinos, F., & Roldán, J. B. (2019). Phase-type distributions for studying variability in resistive memories. *Journal of Computational and Applied Mathematics*, *345*, 23–32. DOI: 10.1016/j.cam.2018.06.010

[Aguilera-Morillo2019] Aguilera-Morillo, M. C., Aguilera, A. M., Jiménez-Molinos, F., & Roldán, J. B. (2019). Stochastic modeling of Random Access Memories reset transitions. *Mathematics and Computers in Simulation*, *159*, 197–209. DOI: 10.1016/j.matcom.2018.11.016

[Aldana2017] Aldana, S., García-Fernández, P., Rodríguez-Fernández, A., Romero-Zaliz, R., González, M. B., Jiménez-Molinos, F., … Roldán, J. B. (2017). A 3D kinetic Monte Carlo simulation study of resistive switching processes in Ni/HfO$_2$ /Si-n$^+$ -based RRAMs. *Journal of Physics D: Applied Physics*, *50*(33), 335103. DOI: 10.1088/1361-6463/aa7939

[Aldana2018] Aldana, S., Roldán, J. B., García-Fernández, P., Suñe, J., Romero-Zaliz, R., Jiménez-Molinos, F., … Liu, M. (2018). An in-depth description of bipolar resistive switching in Cu/HfO$_x$/Pt devices, a 3D kinetic Monte Carlo simulation approach. *Journal of Applied Physics*, *123*(15). DOI: 10.1063/1.5020148

[Aldana2018b] Aldana, S., García-Fernández, P., Romero-Zaliz, R., Jiménez-Molinos, F., Gómez-Campos, F., & Roldán, J. B. (2018). Analysis of conductive filament density in resistive random access memories: a 3D kinetic Monte Carlo approach. *Journal of Vacuum Science & Technology B*, *36*(6), 062201. DOI: 10.1116/1.5049213

[Al-Chawa2017] Al chawa, M. M., Picos, R., Roldan, J. B., Jimenez-Molinos, F., Villena, M. A., & de Benito, C. (2017). Exploring resistive switching-based memristors in the charge-flux domain: A modeling approach. *International Journal of Circuit Theory and Applications*. DOI:10.1002/cta.2397

[Allen2002] Allen J. Bard and Larry R. Faulkner. (2002). A Electrochemical Methods: Fundamentals and Applications, New York: Wiley, 2001, 2nd ed. *Russian Journal of Electrochemistry*, *38*(12), 809. DOI: 10.1023/A:1021637209564

[Arita2012] Arita, M., Kaji, H., Fujii, T., & Takahashi, Y. (2012). Resistance switching properties of molybdenum oxide films. *Thin Solid Films*, *520*(14), 4762–4767. DOI: 10.1016/j.tsf.2011.10.174

[Aratani2007] Aratani, K., Ohba, K., Mizuguchi, T., Yasuda, S., Shiimoto, T., Tsushima, T., … Narisawa, H. (2007). A novel resistance memory with high scalability and nanosecond switching. In *Technical Digest - International Electron Devices Meeting, IEDM* (pp. 783–786). IEEE. DOI: 10.1109/IEDM.2007.4419064

[Arumi2016] Arumi, D., Manich, S., Rodriguez-Montanes, R., & Pehl, M. (2016). RRAM based random bit generation for hardware security applications. In *2016 Conference on Design of Circuits and Integrated Systems, DCIS 2016 - Proceedings* (pp. 219–224). DOI: 10.1109/DCIS.2016.7845382

[Arumi2019]Arumi, D., Gomez-Pau, A., Manich, S., Rodriguez-Montanes, R., Gonzalez, M. B., & Campabadal, F. (2019). Unpredictable Bits Generation Based on RRAM Parallel Configuration. *IEEE Electron Device Letters*, *40*(2), 341–344. DOI: 10.1109/LED.2018.2886396

[Ambrogio2014] Ambrogio, S., Balatti, S., Gilmer, D. C., & Ielmini, D. (2014). Analytical modeling of oxide-based bipolar resistive memories and complementary resistive switches. *IEEE Transactions on Electron Devices*, 61(7), 2378–2386. DOI: 10.1109/TED.2014.2325531

[Ambrogio2016] Ambrogio, S., Balatti, S., Milo, V., Carboni, R., Wang, Z.-Q., Calderoni, A., … Ielmini, D. (2016). Neuromorphic Learning and Recognition With One-Transistor-One-Resistor Synapses and Bistable Metal Oxide RRAM. IEEE Transactions on Electron Devices, 63(4), 1508–1515. DOI: 10.1109/TED.2016.2526647

References

[Ariza2015] Aziza, H., Bocquet, M., Moreau, M., & Portal, J.-M. (2015). A Built-In Self-Test Structure (BIST) for Resistive RAMs characterization: Application to bipolar OxRRAM. Solid-State Electronics, 103, 73–78. DOI: 10.1016/j.sse.2014.09.005

[Ascoli2013] Ascoli, A., Tetzlaff, R., Corinto, F., Mirchev, M., & Gilli, M. (2013). Memristor-based filtering applications. LATW 2013 - 14th IEEE Latin-American Test Workshop, 20(1), 1–6. DOI: 10.1109/LATW.2013.6562672

[Aziza2014] Aziza, H., Ayari, H., Onkaraiah, S., Portal, J. M., Moreau, M., & Bocquet, M. (2014). Oxide based resistive RAM: ON/OFF resistance analysis versus circuit variability. Proceedings - IEEE International Symposium on Defect and Fault Tolerance in VLSI Systems, 81–85. DOI: 10.1109/DFT.2014.6962107

[Awais2013] Awais, M. N., & Choi, K. H. (2013). Memristive Behavior in Electrohydrodynamic Atomized Layers of Poly[2-methoxy-5-(2'-ethylhexyloxy)–(*p* -phenylenevinylene)] for Next Generation Printed Electronics. *Japanese Journal of Applied Physics*, *52*(5S1), 05DA05. DOI: 10.7567/JJAP.52.05DA05

[Baek2004] Baek, I. G., Lee, M. S., Sco, S., Lee, M. J., Seo, D. H., Suh, D.-S., … Moon, J. T. (2004). Highly scalable non-volatile resistive memory using simple binary oxide driven by asymmetric unipolar voltage pulses. In IEDM Technical Digest. IEEE *International Electron Devices Meeting*, 2004. (pp. 587–590). IEEE. DOI: 10.1109/IEDM.2004.1419228

[Baek2007] Baek, S., Lee, D., Kim, J., Hong, S. H., Kim, O., & Ree, M. (2007). Novel digital nonvolatile memory devices based on semiconducting polymer thin films. *Advanced Functional Materials*, *17*(15), 2637–2644. DOI: 10.1002/adfm.200600892

[Baek2013] Baek, H., Lee, C., Choi, J., & Cho, J. (2013). Nonvolatile memory devices prepared from sol-gel derived niobium pentoxide films. *Langmuir*, *29*(1), 380–386. DOI: 10.1021/la303857b

[Baikalov2003] Baikalov, A., Wang, Y. Q., Shen, B., Lorenz, B., Tsui, S., Sun, Y. Y., … Chu, C. W. (2003). Field-driven hysteretic and reversible resistive switch at the Ag–Pr0.7Ca0.3MnO3 interface. Applied Physics Letters, 83(5), 957–959. DOI: 10.1063/1.1590741

[Balachandran2008] Balachandran, G. K., & Barnett, R. E. (2008). A 440-nA true random number generator for passive RFID tags. IEEE *Transactions on Circuits and Systems I*: Regular Papers, 55(11), 3723–3732. DOI: 10.1109/TCSI.2008.927220

[Balatti2015] Balatti, S., Ambrogio, S., & Ielmini, D. (2015). Normally-off Logic Based on Resistive Switches—Part I: Logic Gates. IEEE *Transactions on Electron Devices*, 62(6), 1831–1838. DOI: 10.1109/TED.2015.2422999

[Bandyopadhyay2003] Bandyopadhyay, A., & Pal, A. J. (2003). Large conductance switching and memory effects in organic molecules for data-storage applications. *Applied Physics Letters*, *82*(8), 1215–1217. DOI: 10.1063/1.1555263

[Bandhopadhyay2003b] Bandhopadhyay, A., & Pal, A. J. (2003). Large conductance switching and binary operation in organic devices: Role of functional groups. *Journal of Physical Chemistry B*, *107*(11), 2531–2536. DOI: 10.1021/jp027369q

[Bao2011] Bao, B., Ma, Z., Xu, J., Liu, Z., & Xu, Q. (2011). A simple memristor chaotic circuit with complex dynamics. *International Journal of Bifurcation and Chaos*, *21*(9), 2629–2645. DOI: 10.1142/S0218127411029999

[Baral2008] Baral, J. K., Majumdar, H. S., Laiho, A., Jiang, H., Kauppinen, E. I., Ras, R. H. A., … Österbacka, R. (2008). Organic memory using [6,6]-phenyl-C61 butyric acid methyl ester: Morphology, thickness and concentration dependence studies. *Nanotechnology*, *19*(3). DOI: 10.1088/0957-4484/19/03/035203

[Bard2001] A. J. Bard and L. R. Faulkner (2001), Electrochemical Methods: Fundamentals and Applications. New York, NY, USA: Wiley. ISBN: 978-0-471-04372-0

[Barrera2017] Barrera, D., Ibáñez, M. J., Roldán, A. M., Roldán, J. B., & Yáñez, R. (2017). Polynomial pattern finding in scattered data. *Journal of Computational and Applied Mathematics*, *318*, 107–116. DOI: 10.1016/j.cam.2016.11.021

288

[Barrera2019] Barrera, D., Ibáñez, M. J., Jiménez-Molinos, F., Roldán, A. M., & Roldán, J. B. (2019). A spline quasi-interpolation based method to obtain the reset voltage in Resistive RAMs in the charge-flux domain. *Journal of Computational and Applied Mathematics*, *354*, 326–333. DOI: 10.1016/j.cam.2017.12.020

[Benderli2009] Benderli, S., & Wey, T. a. (2009). On SPICE macromodelling of TiO_2 memristors. *Electronics Letters*, *45*(7), 377. DOI: 10.1049/el.2009.3511

[Bersuker2011] Bersuker, G., Yum, J., Vandelli, L., Padovani, A., Larcher, L., Iglesias, V., … Jammy, R. (2011). Grain boundary-driven leakage path formation in HfO_2 dielectrics. *Solid-State Electronics*, 65–66(1), 146–150. DOI: 10.1016/j.sse.2011.06.031

[Bersuker2011b] Bersuker, G., Gilmer, D. C., Veksler, D., Kirsch, P., Vandelli, L., Padovani, A., … Nafría, M. (2011). Metal oxide resistive memory switching mechanism based on conductive filament properties. *Journal of Applied Physics*, *110*(12), 124518. DOI: 10.1063/1.3671565

[Bertaud2012] Bertaud, T., Walczyk, D., Walczyk, C., Kubotsch, S., Sowinska, M., Schroeder, T., … Grampeix, H. (2012). Resistive switching of HfO_2-based Metal–Insulator–Metal diodes: Impact of the top electrode material. *Thin Solid Films*, 520(14), 4551–4555. DOI: 10.1016/j.tsf.2011.10.183

[Blasco2015] Blasco, J., Ghenzi, N., Suñé, J., Levy, P., & Miranda, E. (2015). Equivalent circuit modeling of the bistable conduction characteristics in electroformed thin dielectric films. *Microelectronics Reliability*, 55(1), 1–14. DOI: 10.1016/j.microrel.2014.10.017

[Bickerstaff2010] Bickerstaff, K., & Swartzlander, E. E. (2010). Memristor-based arithmetic. Conference Record - *Asilomar Conference on Signals, Systems and Computers*, 1173–1177. DOI: 10.1109/ACSSC.2010.5757715

[Biju2011] Biju, K. P., Liu, X., Kim, S., Jung, S., Park, J., & Hwang, H. (2011). Coexistence of filamentary and homogeneous resistive switching in graded WOx thin films. *Physical Status Solidi - Rapid Research Letters*, 5(3), 89–91. DOI:10.1002/pssr.201004455

[Biolek2009] Biolek, Z., Biolek, D., & Biolková, V. (2009). SPICE model of memristor with nonlinear dopant drift. *Radioengineering*, *18*(2), 210–214.

[Bishop2012] Bishop, S. M., Bakhru, H., Capulong, J. O., & Cady, N. C. (2012). Influence of the SET current on the resistive switching properties of tantalum oxide created by oxygen implantation. *Applied Physics Letters*, *100*(14). DOI: 10.1063/1.3701154

[Bocquet2011] Bocquet, M., Deleruyelle, D., Muller, C., & Portal, J.-M. (2011). Self-consistent physical modeling of set/reset operations in unipolar resistive-switching memories. *Applied Physics Letters*, *98*(26), 263507. DOI: 10.1063/1.3605591

[Bocquet2013] Bocquet, M., Deleruyelle, D., Aziza, H., Muller, C., & Portal, J.-M. (2013). Compact modeling solutions for OxRAM memories. In *2013 IEEE Faible Tension Faible Consommation* (pp. 1–4). IEEE. DOI: 10.1109/FTFC.2013.6577779

[Bocquet2014] Bocquet, M., Deleruyelle, D., Aziza, H., Muller, C., Portal, J. M., Cabout, T., & Jalaguier, E. (2014). Robust compact model for bipolar oxide-based resistive switching memories. IEEE *Transactions on Electron Devices*, 61(3), 674–681. DOI: 10.1109/TED.2013.2296793

[Bocquet2014b] Bocquet, M., Aziza, H., Zhao, W., Zhang, Y., Onkaraiah, S., Muller, C., … Portal, J.-M. (2014). Compact Modeling Solutions for Oxide-Based Resistive Switching Memories (OxRAM). *Journal of Low Power Electronics and Applications*, *4*(1), 1–14. DOI: 10.3390/jlpea4010001

[Bojnordi2017] Bojnordi, M. N., & Ipek, E. (2017). Memristive Boltzmann machine: A hardware accelerator for combinatorial optimization and deep learning. In *2017 Fifth Berkeley Symposium on Energy Efficient Electronic Systems & Steep Transistors Workshop (E3S)* (Vol. 2018-Janua, pp. 1–3). IEEE. DOI: 10.1109/E3S.2017.8246178

[Brederlow2006] Brederlow, R., Prakash, R., Paulus, C., & Thewes, R. (2006). A low-power true random number generator using random telegraph noise of single oxide-traps. In *2006 IEEE International Solid State Circuits Conference* - Digest of Technical Papers (pp. 1666–1675). IEEE. DOI: 10.1109/ISSCC.2006.1696222

References

[Buscarino2012] Buscarino, A., Fortuna, L., Frasca, M., & Valentina Gambuzza, L. (2012). A chaotic circuit based on Hewlett-Packard memristor. *Chaos: An Interdisciplinary Journal of Nonlinear Science*, 22(2), 023136. DOI: 10.1063/1.4729135

[Cao2009] X. Cao, X. M. Li, X. D. Gao, Y. W. Zhang, X. J. Liu, Q. Wang y L. D. Chen, "Effects of the compliance current on the resistive switching behavior of TiO_2 thin films", *Appl. Phys. A,* vol. 97, nº 4, pp. 883-887, jul 2009. DOI: 10.1007/s00339-009-5351-7

[Carboni2019] Carboni, R., & Ielmini, D. (2019). Stochastic Memory Devices for Security and Computing. *Advanced Electronic Materials*, 5(9), 1900198. DOI: 10.1002/aelm.201900198

[Carrara2012] S. Carrara, D. Sacchetto, M.A. Doucey, C. Baj-Rossi, G. De Micheli and Y. Leblebici, "Applications of Multi-Terminal Memristive Devices: A Review", Sensor Actuat. B-Chem. 171-172: 449-457, 2012 DOI: 10.1109/MCAS.2013.2256258

[Castán2018] Castán, H., Dueñas, S., García, H., Ossorio, O. G., Domínguez, L. A., Sahelices, B., … Campabadal, F. (2018). Analysis and control of the intermediate memory states of RRAM devices by means of admittance parameters. *Journal of Applied Physics*, 124(15), 152101. DOI: 10.1063/1.5024836

[Cazorla2019] Cazorla, M., Aldana, S., Maestro, M., González, M. B., Campabadal, F., Moreno, E., … Roldán, J. B. (2019). Thermal study of multilayer resistive random access memories based on HfO_2 and Al_2O_3 oxides . *Journal of Vacuum Science & Technology B*, 37(1), 012204. DOI: 10.1116/1.5058294

[Celano2014] U. Celano, L. Goux, A. Belmonte, K. Opsomer, A. Franquet, A. Shulze, C Detavernier, O. Richard, H. Bender, M. Jurczak, W. Vandervorst, "Three-Dimensional Observation of the Conductive Filament in Nanoscaled Resistive Memory Devices", Nanoletters, 14, pp. 2401-2406, 2014. DOI: 10.1021/nl500049g

[Chao2010] Y. Chao Yang, F. Pan y F. Zeng, "Bipolar resistance switching in high-performance Cu/ZnO:Mn/Pt nonvolatile memories: active region and influence of Joule heating", *New Journal of Physics,* vol. 12, nº 2, p. 023008, 2010. DOI: 10.1088/1367-2630/12/2/023008

[Chan2008] M. Y. Chan, T. Zhang, V. Ho y P. S. Lee, "Resistive switching effects of HfO_2 high-k dielectric", *Microelectronic Engineering ,* vol. 85, nº 12, pp. 2420-2424, 2008. DOI: 10.1016/j.mee.2008.09.021

[Chandrakishore2014] Chandrakishore, S., & Pandurangan, A. (2014). Facile synthesis of carbon nanotubes and their use in the fabrication of resistive switching memory devices. *RSC Advances*, 4(20), 9905–9911. DOI: 10.1039/c3ra45359f

[Chang2008] W.-Y. Chang, Y.-C. Lai, T.-B. Wu, S.-F. Wang, F. Chen y M.-J. Tsai, "Unipolar resistive switching characteristics of ZnO thin films for nonvolatile memory applications", *Appl. Phys. Lett.,* vol. 92, nº 2, p. 022110, 2008. DOI: 10.1063/1.2834852

[Chang2009] W.-Y. Chang, J.-H. Liao, Y.-S. Lo y T.-B. Wu, "Resistive switching characteristics in $Pr_{0.7}Ca_{0.3}MnO_3$ thin films on $LaNiO_3$-electrodized Si substrate", *Applied Physics Letters,* vol. 94, nº 17, p. 172107, 2009. DOI: 10.1063/1.3126057

[Chang2010] Chang, T. Y., Cheng, Y. W., & Lee, P. T. (2010). Electrical characteristics of an organic bistable device using an Al/Alq3/nanostructured MoO3/Alq3/p +-Si structure. *Applied Physics Letters*, 96(4), 043309. DOI: 10.1063/1.3299265

[Chang2011] Chang, T., Jo, S.-H., Kim, K.-H., Sheridan, P., Gaba, S., & Lu, W. (2011). Synaptic behaviors and modeling of a metal oxide memristive device. *Applied Physics A*, 102(4), 857–863. DOI: 10.1007/s00339-011-6296-1

[Chang2012] Chang, M.-F., Wu, C.-W., Kuo, C.-C., Shen, S.-J., Lin, K.-F., Yang, S.-M., … Chih, Y.-D. (2012). A 0.5V 4Mb logic-process compatible embedded resistive RAM (ReRAM) in 65nm CMOS using low-voltage current-mode sensing scheme with 45ns random read time. In *2012 IEEE International Solid-State Circuits Conference* (Vol. 55, pp. 434–436). IEEE. DOI: 10.1109/ISSCC.2012.6177079

[Chang2012b] Chang, Y.-F., Chen, P.-Y., Chen, Y.-T., Xue, F., Wang, Y., Zhou, F., … Lee, J. C. (2012). Study of polarity effect in SiOx -based resistive switching memory. *Applied Physics Letters*, 101(5), 052111. DOI: 10.1063/1.4742894

[Chang2013] Chang, T., Yang, Y., & Lu, W. (2013). Building Neuromorphic Circuits with Memristive Devices. IEEE *Circuits and Systems Magazine*, 13(2), 56–73. DOI: 10.1109/MCAS.2013.2256260

[Chang2013b] Chang, Y. F., Ji, L., Wu, Z. J., Zhou, F., Wang, Y., Xue, F., … Lee, J. C. (2013). Oxygen-induced bi-modal failure phenomenon in SiOx-based resistive switching memory. *Applied Physics Letters*, 103(3). DOI: 10.1063/1.4816162

[Chang2015] Chang, M.-F., Lin, C.-C., Lee, A., Kuo, C.-C., Yang, G.-H., Tsai, H.-J., … Ku, T.-K. (2015). 17.5 A 3T1R nonvolatile TCAM using MLC ReRAM with Sub-1ns search time. In *2015 IEEE International Solid-State Circuits Conference - (ISSCC) Digest of Technical Papers* (Vol. 58, pp. 1–3). IEEE. DOI: 10.1109/ISSCC.2015.7063054

[Chang2016] Chang, M. F., Huang, L. Y., Lin, W. Z., Chiang, Y. N., Kuo, C. C., Chuang, C. H., … Sheu, S. S. (2016). A ReRAM-Based 4T2R Nonvolatile TCAM Using RC-Filtered Stress-Decoupled Scheme for Frequent-OFF Instant-ON Search Engines Used in IoT and Big-Data Processing. *IEEE Journal of Solid-State Circuits*, *51*(11), 2786–2789. DOI: 10.1109/JSSC.2016.2602218

[Chang2016b] Chang, Y.-F., Fowler, B., Chen, Y.-C., Zhou, F., Pan, C.-H., Chang, K.-C., … Lee, J. C. (2016). A synaptic device built in one diode–one resistor (1D–1R) architecture with intrinsic SiOx-based resistive switching memory. *Physical Sciences Reviews*, *1*(4), 1–11. DOI: https://doi.org/10.1515/psr-2016-0012

[Chang2017] Chang, M.-F., Lin, C.-C., Lee, A., Chiang, Y.-N., Kuo, C.-C., Yang, G.-H., … Sheu, S.-S. (2017). A 3T1R Nonvolatile TCAM Using MLC ReRAM for Frequent-Off Instant-On Filters in IoT and Big-Data Processing. *IEEE Journal of Solid-State Circuits*, 52(6), 1664–1679. DOI: 10.1109/JSSC.2017.2681458

[Chawa2016] Chawa, M. M. A., Picos, R., Garcia-Moreno, E., Stavrinides, S. G., Roldan, J. B., & Jimenez-Molinos, F. (2016). An analytical energy model for the reset transition in unipolar resistive-switching RAMs. *Proceedings of the 18th Mediterranean Electrotechnical Conference: Intelligent and Efficient Technologies and Services for the Citizen, MELECON 2016*, (April), 1–4. DOI: 10.1109/MELCON.2016.7495318

[Chawa2018] Al Chawa, M. M., Picos, R., Roldan, J. B., Jimenez-Molinos, F., Villena, M. A., & de Benito, C. (2018). Exploring resistive switching-based memristors in the charge–flux domain: A modeling approach. *International Journal of Circuit Theory and Applications*, *46*(1), 29–38. DOI: https://doi.org/10.1002/cta.2397

[Chen2005] Chen, A., Haddad, S., Wu, Y. C., Fang, T. N., Lan, Z., Avanzino, S., … Taguchi, M. (2005). Non-volatile resistive switching for advanced memory applications. *Technical Digest - International Electron Devices Meeting, IEDM*, *2005*(c), 746–749. DOI: 10.1109/IEDM.2005.1609461

[Chen2006] Chen, J., & Ma, D. (2006). Performance improvement by charge trapping of doping fluorescent dyes in organic memory devices. *Journal of Applied Physics*, *100*(3), 034512.DOI: 10.1063/1.2234541

[Chen2008] Chen, A., Haddad, S., Wu, Y. C., Fang, T. N., Kaza, S., & Lan, Z. (2008). Erasing characteristics of Cu2 O metal-insulator-metal resistive switching memory. *Applied Physics Letters*, *92*(1). DOI: 10.1063/1.2828864

[Chen2009] Chen, Y. S., Wu, T. Y., Tzeng, P. J., Chen, P. S., Lee, H. Y., Lin, C. H., … Tsai, M. J. (2009). Forming-free HfO2 bipolar RRAM device with improved endurance and high speed operation. International *Symposium on VLSI Technology, Systems, and Applications, Proceedings*, *29*, 37–38. DOI: 10.1109/VTSA.2009.5159281

[Chen2010] Chen, P. S., Lee, H. Y., Chen, Y. S., Chen, F., & Tsai, M. J. (2010). Improved bipolar resistive switching of HfOx/TiN stack with a reactive metal layer and post metal annealing. *Japanese Journal of Applied Physics*, 49(4 PART 2). DOI: 10.1143/JJAP.49.04DD18

[Chen2010b] Chen, C., Yang, Y. C., Zeng, F., & Pan, F. (2010). Bipolar resistive switching in Cu/AlN/Pt nonvolatile memory device. *Applied Physics Letters*, *97*(8), 2008–2011. DOI: 10.1063/1.3483158

References

[Chen2010c] Chen, Y. S., Chen, B., Gao, B., Zhang, F. F., Qiu, Y. J., Lian, G. J., … Kang, J. F. (2010). Anticrosstalk characteristics correlated with the set process for α -Fe$_2$O$_3$ /Nb-SrTiO$_3$ stack-based resistive switching device. *Applied Physics Letters*, *97*(26), 2008–2011. DOI: 10.1063/1.3532970

[Chen2011] Chen, Y. Y., Pourtois, G., Wang, X. P., Adelmann, C., Goux, L., Govoreanu, B., … Wouters, D. J. (2011). Switching by Ni filaments in a HfO$_2$ matrix: A new pathway to improved unipolar switching RRAM. *2011 3rd IEEE International Memory Workshop, IMW 2011*, 1–4. DOI: 10.1109/IMW.2011.5873223

[Chen2011b] Chen, S. C., Chang, T. C., Chen, S. Y., Chen, C. W., Chen, S. C., Sze, S. M., … Yeh, F. S. (2011). Bipolar resistive switching of chromium oxide for resistive random access memory. *Solid-State Electronics*, *62*(1), 40–43. DOI: 10.1016/j.sse.2010.12.014

[Chen2012] Chen, Y. Y., Pourtois, G., Wang, X. P., Adelmann, C., Goux, L., Govoreanu, B., … Wouters, D. J. (2011). Switching by Ni filaments in a HfO2 matrix: A new pathway to improved unipolar switching RRAM. *2011 3rd IEEE International Memory Workshop*, IMW 2011, 1–4. DOI: https://doi.org/10.1109/IMW.2011.5873223

[Chen2012b] Chen, H.-Y., Yu, S., Gao, B., Huang, P., Kang, J., & Wong, H.-S. P. (2012). HfOx based vertical resistive random access memory for cost-effective 3D cross-point architecture without cell selector. In *2012 International Electron Devices Meeting* (Vol. 2, pp. 20.7.1-20.7.4). IEEE. DOI: 10.1109/IEDM.2012.6479083

[Chen2012c] Chen, C., Gao, S., Tang, G., Song, C., Zeng, F., & Pan, F. (2012). Cu-embedded AlN-based nonpolar nonvolatile resistive switching memory. *IEEE Electron Device Letters*, *33*(12), 1711–1713. DOI: 10.1109/LED.2012.2220953

[Chen2013] Chen, C., Gao, S., Zeng, F., Wang, G. Y., Li, S. Z., Song, C., & Pan, F. (2013). Conductance quantization in oxygen-anion-migration-based resistive switching memory devices. *Applied Physics Letters*, *103*(4). DOI: 10.1063/1.4816747

[Chen2013b] Chen, Y. Y., Goux, L., Clima, S., Govoreanu, B., Degraeve, R., Kar, G. S., … Jurczak, M. (2013). Endurance/retention trade-off on HfO$_2$\metal cap 1T1R bipolar RRAM. *IEEE Transactions on Electron Devices*, *60*(3), 1114–1121. DOI: 10.1109/TED.2013.2241064

[Chen2015] Chen, P.-Y., & Yu, S. (2015). Compact Modeling of RRAM Devices and Its Applications in 1T1R and 1S1R Array Design. IEEE Transactions on Electron Devices, 62(12), 4022–4028. DOI: 10.1109/TED.2015.2492421

[Chen2015b] Chen, Z., Yin, W., & Boyle, K. (2015). True Random Number Generator in 0.35 μm for RFID applications. In *2015 IEEE International Conference on Electron Devices and Solid-State Circuits (EDSSC)* (Vol. 5, pp. 625–628). IEEE. DOI: 10.1109/EDSSC.2015.7285193

[Chen2016] Chen, A. (2016). A review of emerging non-volatile memory (NVM) technologies and applications. *Solid-State Electronics*, *125*, 25–38. DOI: 10.1016/j.sse.2016.07.006

[Cheng2011] Cheng, C. H., Chin, A., & Yeh, F. S. (2011). Ultralow switching energy Ni/GeO$_x$/HfON/TaN RRAM. *IEEE Electron Device Letters*, *32*(3), 366–368. DOI: 10.1109/LED.2010.2095820

[Chevallier2010] Chevallier, C. J., Siau, C. H., Lim, S. F., Namala, S. R., Matsuoka, M., Bateman, B. L., & Rinerson, D. (2010). A 0.13μm 64Mb multi-layered conductive metal-oxide memory. In *2010 IEEE International Solid-State Circuits Conference - (ISSCC)* (Vol. 53, pp. 260–261). IEEE. DOI: 10.1109/ISSCC.2010.5433945

[Chiang2015] Chiang, M.-H., Hsu, K.-H., Ding, W.-W., & Yang, B.-R. (2015). A Predictive Compact Model of Bipolar RRAM Cells for Circuit Simulations. *IEEE Transactions on Electron Devices*, *62*(7), 2176–2183. DOI: 10.1109/TED.2015.2428293

[Chien2010] Chien, W. C., Chen, Y. C., Lai, E. K., Yao, Y. D., Lin, P., Horng, S. F., … Chih-Yuan Lu. (2010). Unipolar Switching Behaviors of RTO WOX RRAM. *IEEE Electron Device Letters*, 31(2), 126–128. DOI: 10.1109/LED.2009.2037593

[Chiu2012] Chiu, F. C., Li, P. W., & Chang, W. Y. (2012). Reliability characteristics and conduction mechanisms in resistive switching memory devices using ZnO thin films. *Nanoscale Research Letters*, *7*(1), 1–9. DOI: 10.1186/1556-276X-7-178

292

[Chiu2012b] Chiu, F.-C., Shih, W.-C., & Feng, J.-J. (2012). Conduction mechanism of resistive switching films in MgO memory devices. *Journal of Applied Physics*, 111(9), 094104. DOI: 10.1063/1.471228

[Chiu2014] Chiu, F.-C. (2014). A Review on Conduction Mechanisms in Dielectric Films. *Advances in Materials Science and Engineering*, *2014*, 1–18. DOI: 10.1155/2014/578168

[Choi2005] Choi, B. J., Jeong, D. S., Kim, S. K., Rohde, C., Choi, S., Oh, J. H., … Tiedke, S. (2005). Resistive switching mechanism of TiO_2 thin films grown by atomic-layer deposition. *Journal of Applied Physics*, *98*(3), 033715. DOI: 10.1063/1.2001146

[Choi2006] Choi, D., Lee, D., Sim, H., Chang, M., & Hwang, H. (2006). Reversible resistive switching of $SrTiO_x$ thin films for nonvolatile memory applications. *Applied Physics Letters*, *88*(8), 082904. DOI: 10.1063/1.2178405

[Choi2009] Choi, J.-H., Das, S. N., & Myoung, J.-M. (2009). Controllable resistance switching behavior of NiO/SiO_2 double layers for nonvolatile memory applications. *Applied Physics Letters*, *95*(6), 062105. DOI: 10.1063/1.3204450

[Choi2009b] Choi, J. S., Kim, J. S., Hwang, I. R., Hong, S. H., Jeon, S. H., Kang, S. O., … Seo, S. (2009). Different resistance switching behaviors of NiO thin films deposited on Pt and $SrRuO_3$ electrodes. *Applied Physics Letters*, *95*(2). DOI: 10.1063/1.3173813

[Choi2013] Choi, B. J., Torrezan, A. C., Norris, K. J., Miao, F., Strachan, J. P., Zhang, M. X., … Williams, R. S. (2013). Electrical performance and scalability of Pt dispersed SiO_2 nanometallic resistance switch. *Nano Letters*, *13*(7), 3213–3217. DOI: 10.1021/nl401283q

[Chu2005] Chu, C. W., Ouyang, J., Tseng, J. H., & Yang, Y. (2005). Organic donor-acceptor system exhibiting electrical bistability for use in memory devices. *Advanced Materials*, *17*(11), 1440–1443. DOI: 10.1002/adma.200500225

[Chua1971] Chua, L. (1971). Memristor-The missing circuit element. *IEEE Transactions on Circuit Theory*, *18*(5), 507–519. DOI: 10.1109/TCT.1971.1083337

[Chua1976] Chua, L. O., & Sung Mo Kang. (1976). Memristive devices and systems. *Proceedings of the IEEE*, *64*(2), 209–223. DOI: 10.1109/PROC.1976.10092

[Chua2011] Chua, L. (2011). Resistance switching memories are memristors. *Applied Physics A: Materials* Science *and Processing*, *102*(4), 765–783. DOI: 10.1007/s00339-011-6264-9

[Chua2012] Chua, L. O. (2012). The fourth element. Proceedings of the IEEE, 100(6), 1920–1927. DOI: 10.1109/JPROC.2012.2190814

[Chua2013] Chua, L. (2013). Memristor, hodgkin-huxley, and edge of chaos. *Nanotechnology*, *24*(38). DOI: 10.1088/0957-4484/24/38/383001

[Chung2011] Chung, Y. L., Lai, P. Y., Chen, Y. C., & Chen, J. S. (2011). Schottky barrier mediated single-polarity resistive switching in Pt layer-included TiO_x memory device. *ACS Applied Materials and Interfaces*, *3*(6), 1918–1924. DOI: 10.1021/am200106z

[Chung2011b] Chung, H., Jeong, B. H., Min, B. J., Choi, Y., Cho, B. H., Shin, J., … Jun, Y. H. (2011). A 58nm 1.8V 1Gb PRAM with 6.4MB/s program BW. *Digest of Technical Papers - IEEE International Solid-State Circuits Conference*, 500–501. DOI: 10.1109/ISSCC.2011.5746415

[Corinto2012] Corinto, F., & Ascoli, A. (2012). Memristive diode bridge with LCR filter. *Electronics Letters*, *48*(14), 824. DOI: 10.1049/el.2012.1480

[Cottle2017] Cottle, R. W., & Thapa, M. N. (2017). DESCENT METHODS (1st ed., pp. 317–368). New York: Springer-Verlag, DOI: 10.1007/978-1-4939-7055-1_10

[Datta1997] Datta, S. (1997). *Electronic* transport *in mesoscopic systems*. Cambridge University Press.

[Deshmukh2015] Deshmukh, S., Islam, R., Chen, C., Yalon, E., Saraswat, K. C., & Pop, E. (2015). Thermal modeling of metal oxides for highly scaled nanoscale RRAM. In *2015 International Conference on Simulation of Semiconductor Processes and Devices (SISPAD)* (Vol. 2015-Octob, pp. 281–284). IEEE. DOI: 10.1109/SISPAD.2015.7292314

References

[Dittmann2012] Dittmann, R., Muenstermann, R., Krug, I., Park, D., Menke, T., Mayer, J., … Waser, R. (2012). Scaling potential of local redox processes in memristive $SrTiO_3$ thin-film devices. *Proceedings of the IEEE*, *100*(6), 1979–1990. DOI: 10.1109/JPROC.2012.2188771

[Dittmann2019] Dittmann, R., & Strachan, J. P. (2019). Redox-based memristive devices for new computing paradigm. *APL Materials*, *7*(11), 110903. DOI: 10.1063/1.5129101

[Driscoll2010] Driscoll, T., Quinn, J., Klein, S., Kim, H. T., Kim, B. J., Pershin, Y. V., … Basov, D. N. (2010). Memristive adaptive filters. *Applied Physics Letters*, *97*(9), 093502. DOI: 10.1063/1.3485060

[Driscoll2011] Driscoll, T., Pershin, Y. V., Basov, D. N., & Di Ventra, M. (2011). Chaotic memristor. *Applied Physics A*, *102*(4), 885–889. DOI: 10.1007/s00339-011-6318-z

[Dong2007] Dong, R., Lee, D. S., Xiang, W. F., Oh, S. J., Seong, D. J., Heo, S. H., … Hwang, H. (2007). Reproducible hysteresis and resistive switching in metal- Cu_xO -metal heterostructures. *Applied Physics Letters*, *90*(4). DOI: 10.1063/1.2436720

[Dou2012] Dou, C., Kakushima, K., Ahmet, P., Tsutsui, K., Nishiyama, A., Sugii, N., … Iwai, H. (2012). Resistive switching behavior of a CeO_2 based ReRAM cell incorporated with Si buffer layer. Microelectronics *Reliability*, *52*(4), 688–691. DOI: 10.1016/j.microrel.2011.10.019

[Duan2013] Duan, S., Hu, X., Wang, L., Gao, S., & Li, C. (2014). Hybrid memristor/RTD structure-based cellular neural networks with applications in image processing. *Neural Computing and Applications*, *25*(2), 291–296. DOI: 10.1007/s00521-013-1484-x

[Emara2014] Emara, A., Ghoneima, M., & El-Dessouky, M. (2014). Differential 1T2M memristor memory cell for single/multi-bit RRAM modules. In *2014 6th Computer Science and Electronic Engineering Conference (CEEC)* (pp. 69–72). IEEE. DOI: 10.1109/CEEC.2014.6958557

[Emara2015] Emara, A., & Ghoneima, M. (2015). A reference-less multilevel memristor based RRAM module. In *2015 IEEE 58th International Midwest Symposium on Circuits and Systems (MWSCAS)* (Vol. 2015-Septe, pp. 1–4). IEEE. DOI: 10.1109/MWSCAS.2015.7282147

[Eshraghian2011] Eshraghian, K., Cho, K.-R., Kavehei, O., Kang, S.-K., Abbott, D., & Kang, S.-M. S. (2011). Memristor MOS Content Addressable Memory (MCAM): Hybrid Architecture for Future High Performance Search Engines. *IEEE Transactions on Very Large Scale Integration (VLSI) Systems*, *19*(8), 1407–1417. DOI: 10.1109/TVLSI.2010.2049867

[Fackenthal2014] Fackenthal, R., Kitagawa, M., Otsuka, W., Prall, K., Mills, D., Tsutsui, K., … Hush, G. (2014). 19.7 A 16Gb ReRAM with 200MB/s write and 1GB/s read in 27nm technology. In *2014 IEEE International Solid-State Circuits Conference Digest of Technical Papers (ISSCC)* (Vol. 57, pp. 338–339). IEEE. DOI: 10.1109/ISSCC.2014.6757460

[Fang2010] Fang, Z., Yu, H. Y., Liu, W. J., Pey, K. L., Li, X., Wu, L., … Kang, J. F. (2010). Bias temperature instability of binary oxide based ReRAM. In *2010 IEEE International Reliability Physics Symposium* (Vol. 453, pp. 964–965). IEEE. DOI: 10.1109/IRPS.2010.5488697

[Fang2011] Fang, Z., Yu, H. Y., Li, X., Singh, N., Lo, G. Q., & Kwong, D. L. (2011). $HfO_x/TiO_x/HfO_x/TiO_x$ multilayer-based forming-free RRAM devices with excellent uniformity. *IEEE Electron Device Letters*, *32*(4), 566–568. DOI: 10.1109/LED.2011.2109033

[Fang2013] Fang, X., Yang, X., Wu, J., & Yi, X. (2013). A compact SPICE model of unipolar memristive devices. *IEEE Transactions on Nanotechnology*, *12*(5), 843–850. DOI: 10.1109/TNANO.2013.2275178

[Fang2015] Fang, R., Chen, W., Gao, L., Yu, W., & Yu, S. (2015). Low-Temperature Characteristics of HfO_x -Based Resistive Random Access Memory. *IEEE Electron Device Letters*, *36*(6), 567–569. DOI: 10.1109/LED.2015.2420665

[Fujita2004] Fujita, S., Uchida, K., Yasuda, S., Ohba, R., Nozaki, H., & Tanamoto, T. (2004). Si nanodevices for random number generating circuits for cryptographic security. In *2004 IEEE International Solid-State Circuits Conference (IEEE Cat. No.04CH37519)* (pp. 294–295). DOI: 10.1109/ISSCC.2004.1332710

[Fu2011] Fu, D., Xie, D., Feng, T., Zhang, C., Niu, J., Qian, H., & Liu, L. (2011). Unipolar resistive switching properties of diamondlike carbon-based RRAM devices. *IEEE Electron Device Letters*, *32*(6), 803–805. DOI: 10.1109/LED.2011.2132750

[Fu2014]. Fu, Y. J., Xia, F. J., Jia, Y. L., Jia, C. J., Li, J. Y., Dai, X. H., … Liu, B. T. (2014). Bipolar resistive switching behavior of $La_{0.5}Sr_{0.5}CoO_{3-\sigma}$ films for nonvolatile memory applications. *Applied Physics Letters*, *104*(22), 223505. DOI: 10.1063/1.4881720

[Fusi2000] Fusi, S., Annunziato, M., Badoni, D., Salamon, A., & Amit, D. J. (2000). Spike-Driven Synaptic Plasticity: Theory, Simulation, VLSI Implementation. *Neural Computation*, *12*(10), 2227–2258. DOI: 10.1162/089976600300014917

[Gaillardon2012] Gaillardon, P.-E., Sacchetto, D., Bobba, S., Leblebici, Y., & De Micheli, G. (2012). GMS: Generic memristive structure for non-volatile FPGAs. In *2012 IEEE/IFIP 20th International Conference on VLSI and System-on-Chip (VLSI-SoC)* (Vol. 07-10-Octo, pp. 94–98). IEEE. DOI: 10.1109/VLSI-SoC.2012.7332083

[Gao2010] Gao, X., Guo, H., Xia, Y., Yin, J., & Liu, Z. (2010). Unipolar resistive switching characteristics in Co_3O_4 films. *Thin Solid Films*, *519*(1), 450–452. DOI: 10.1016/j.tsf.2010.07.075

[Gao2010b] Gao, X., Xia, Y., Xu, B., Kong, J., Guo, H., Li, K., … Liu, Z. (2010). Unipolar resistive switching behaviors in amorphous lutetium oxide films. *Journal of Applied Physics*, *108*(7). DOI: 10.1063/1.3490758

[Gao2012] Gao, S., Song, C., Chen, C., Zeng, F., & Pan, F. (2012). Dynamic processes of resistive switching in metallic filament-based organic memory devices. *Journal of Physical Chemistry C*, *116*(33), 17955–17959. DOI: 10.1021/jp305482c

[Gao2013] Gao, S., Zeng, F., Chen, C., Tang, G., Lin, Y., Zheng, Z., … Pan, F. (2013). Conductance quantization in a Ag filament-based polymer resistive memory. *Nanotechnology*, *24*(33). DOI: 10.1088/0957-4484/24/33/335201

[Gao2018] Gao, S., Liu, G., Chen, Q., Xue, W., Yang, H., Shang, J., … Li, R.-W. (2018). Improving Unipolar Resistive Switching Uniformity with Cone-Shaped Conducting Filaments and Its Logic-In-Memory Application. *ACS Applied Materials & Interfaces*, *10*(7), 6453–6462. DOI: 10.1021/acsami.7b19586

[Garcia-Moreno2015] Garcia-Moreno, E., Picos, R., & Al-Chawa, M. M. (2015). SPICE model for unipolar RRAM based on a flux-controlled memristor. In *2015 IEEE International Autumn Meeting on Power, Electronics and Computing (ROPEC)* (pp. 1–4). IEEE. DOI: 10.1109/ROPEC.2015.7395128

[Garcia-Redondo2016] Garcia-Redondo, F., Gowers, R. P., Crespo-Yepes, A., Lopez-Vallejo, M., & Jiang, L. (2016). SPICE Compact Modeling of Bipolar/Unipolar Memristor Switching Governed by Electrical Thresholds. *IEEE Transactions on Circuits and Systems I: Regular Papers*, *63*(8), 1255–1264. DOI: 10.1109/TCSI.2016.2564703

[Geresdi2011] Geresdi, A., Halbritter, A., Gyenis, A., Makk, P., & Mihály, G. (2011). From stochastic single atomic switch to nanoscale resistive memory device. *Nanoscale*, *3*(4), 1504–1507. DOI: 10.1039/c0nr00951b

[Ghenzi2014] Ghenzi, N., Sánchez, M. J., Rubi, D., Rozenberg, M. J., Urdaniz, C., Weissman, M., & Levy, P. (2014). Tailoring conductive filaments by electroforming polarity in memristive based TiO_2 junctions. *Applied Physics Letters*, *104*(18), 183505. DOI: 10.1063/1.4875559

[Gismatulin2019] Gismatulin, A. A., Kruchinin, V. N., Gritsenko, V. A., Prosvirin, I. P., Yen, T.-J., & Chin, A. (2019). Charge transport mechanism of high-resistive state in RRAM based on SiO_x. *Applied Physics Letters*, *114*(3), 033503. DOI: 10.1063/1.5074116

[Gonon2010] Gonon, P., Mougenot, M., Vallée, C., Jorel, C., Jousseaume, V., Grampeix, H., & El Kamel, F. (2010). Resistance switching in HfO_2 metal-insulator-metal devices. *Journal of Applied Physics*, *107*(7), 074507. DOI: 10.1063/1.3357283

[Gonzalez2014] González, M.B., Rafí, J.M. , Beldarrain, O., Zabala, M., and Campabadal, F. (2014) Analysis of the Switching Variability in Ni/HfO_2-based RRAM Devices. *IEEE Transactions on devices and material reliability*. DOI: 10.1109/TDMR.2014.2311231

[Gonzalez2015] Gonzalez, M. B., Martin-Martinez, J., Rodriguez, R., Acero, M. C., Nafria, M., Campabadal, F., & Aymerich, X. (2015). Dedicated random telegraph noise characterization of Ni/HfO2-based RRAM devices. *Microelectronic Engineering*, *147*, 59–62. DOI: 10.1016/j.mee.2015.04.046

References

[Gonzalez2016] Gonzalez, M. B., Martin-Martinez, J., Maestro, M., Acero, M. C., Nafría, M., & Campabadal, F. (2016). Investigation of Filamentary Current Fluctuations Features in the High-Resistance State of Ni/HfO$_2$-Based RRAM. *IEEE Transactions on Electron Devices*, *63*(8), 3116–3122. DOI: 10.1109/TED.2016.2583924

[**González-Cordero2016a**] **G. González-Cordero**, J. B. Roldan, F. Jimenez-Molinos, J. Suñé, S. Long and M. Liu. (2016). A new compact model for bipolar RRAMs based on truncated cone conductive filaments, a Verilog-A approach, *Semiconductor Science and Technology*, vol. 31, no. 11, pp. 1–13, DOI: 10.1088/0268-1242/31/11/115013

[**González-Cordero2016b**] **G. González-Cordero**, J. B. Roldan and F. Jiménez-Molinos (2016). A model for circuit simulation of bipolar RRAMs based on conductive filaments with truncated cone shapes. In *Jornadas de Investigadores en Formación Fomentando la interdisciplinariedad (JIFFI)*. Granada, Spain.

[**González-Cordero2016c**] **G. González-Cordero**, M. B. González, F. Jiménez-Molinos, F. Campabadal, and J. B. Roldan. (2016) An in-depth study of the physics behind resistive switching in TiN/Ti/HfO$_2$/W structures. In *19th Workshop on Dielectrics in Microelectronics (Wodim)*. Catania, Italy.

[**González-Cordero2016d**] **G. González-Cordero**, F. Jiménez-Molinos, M. A. Villena and J. B. Roldan. (2016) SPICE simulation of thermal reset transitions in Ni/HfO$_2$/Si-n+ RRAMs including quantum effects. In *19th Workshop on Dielectrics in Microelectronics (Wodim)*. Catania, Italy.

[**González-Cordero2016e**] **G. González-Cordero**, F. Jiménez-Molinos, J. B. Roldan, M. B. González and F. Campabadal (2016) Transient SPICE simulation of Ni/HfO$_2$/Si-n+ resistive memories. In *XXXI edition of the Design of Circuits and Integrated Systems Conference (DCIS)*, Granada, Spain. DOI: 10.1109/DCIS.2016.7845384

[**González-Cordero2016f**] **G. González-Cordero**, J. B. Roldan, and F. Jiménez-Molinos. (2016). Simulation of RRAM memory circuits, a Verilog-A compact modeling approach. in *XXXI edition of the Design of Circuits and Integrated Systems Conference (DCIS)*, Granada, Spain. DOI: 10.1109/DCIS.2016.7845386

[**González-Cordero2017a**] **G. González-Cordero**, F. Jiménez-Molinos, J. B. Roldan, M. B. González and F. Campabadal. (2017). In-depth study of the physics behind resistive switching in TiN/Ti/HfO$_2$/W structures. *Journal of Vacuum Science and Technology B.* 35, 01A110. DOI: 10.1116/1.4973372

[**González-Cordero2017b**] **G. González-Cordero**, M. B. González, H. García, F. Campabadal, S. Dueñas, H. Castán, F. Jiménez-Molinos and J. B. Roldán. (2017). A physically based model for resistive memories including a detailed temperature and variability description, *Microelectronic Engineering*, Volume 178, 25 June 2017, Pages 26-29, ISSN 0167-9317, DOI: 10.1016/j.mee.2017.04.019

[**González-Cordero2017c**] **G. González-Cordero**, J. B. Roldán, F. Jiménez-Molinos. (2017). SPICE simulation of RRAM circuits. A compact modeling perspective. In *11th edition of the Spanish Conference on Electron Devices (CDE)*, Barcelona, Spain. DOI: 10.1109/CDE.2017.7905250

[**González-Cordero2017d**] **G. González-Cordero**, M. B. González, H. García, F. Jiménez-Molinos, F. Campabadal, S. Dueñas, H. Castán and J. B. Roldán. (2017). A Physically Based Model to describe Resistive Switching in different RRAM technologies", in *11th edition of the Spanish Conference on Electron Devices (CDE)*, Barcelona, Spain. DOI: 10.1109/CDE.2017.7905223

[**González-Cordero2017e**] **G. González-Cordero**, M. B. González, H. García, F. Campabadal, S. Dueñas, H. Castán, F. Jiménez-Molinos and J. B. Roldán. (2017). A physically based model for resistive memories including a detailed temperature and variability description. In *20th Conference on "Insulating Films on Semiconductors" (INFOS)*, Potsdam, Germany

[**González-Cordero2017f**] **G. González-Cordero**, J. B. Roldán, F. Jiménez-Molinos. (2017). A time dependent thermal model for RRAM circuit simulation. In *20th Conference on "Insulating Films on Semiconductors (INFOS)*, Potsdam, Germany

[**González-Cordero2019a**]**G. González-Cordero,** Mireia B. González, Francisco Jiménez-Molinos, Francesca Campabadal, and Juan Bautista Roldán. (2019). New method to analyze random telegraph signals in resistive random access memories. *Journal of Vacuum Science and Technology B*. 37, 012203. DOI: 10.1116/1.50593840

[González-Cordero2019b] **G. González-Cordero**, M. Pedro, J. Martin-Martinez, M.B. González, F. Jiménez-Molinos, F. Campabadal, N. Nafría, J.B. Roldán. (2019). Analysis of resistive switching processes in TiN/Ti/HfO$_2$/W devices to mimic electronic synapses in neuromorphic circuits. *Solid State Electronics*, Volume 157, July 2019, Pages 25-33. DOI: 10.1016/j.sse.2019.04.001

[González-Cordero2019c] **G. González-Cordero**, M.B. González, F. Campabadal, F. Jiménez-Molinos, J.B. Roldán. (2019). A new technique to analyze RTN signals in resistive memories. *Microelectronic Engineering*. Volume 215, 15 July 2019, 110994 DOI: 10.1016/j.mee.2019.110994

[González-Cordero2019d] **G. Gonzalez-Cordero**, M.B. González, A. Morell, F. Jiménez-Molinos, F. Campabadal, J.B. Roldán. (2019). Neural network based analysis of Random Telegraph Noise in Resistive Random Access Memories. *Semiconductor Science and Technology*. (Accepted for publication on December 4, 2019).

[Govoreanu2013] Govoreanu, B., Clima, S., Radu, I. P., Chen, Y. Y., Wouters, D. J., & Jurczak, M. (2013). Complementary role of field and temperature in triggering ON/OFF switching mechanisms in Hf/HfO$_2$ Resistive RAM cells. *IEEE Transactions on Electron Devices*, *60*(8), 2471–2478. DOI: 10.1109/TED.2013.2266357

[Grossi2016] Grossi, A., Zambelli, C., Olivo, P., Miranda, E., Stikanov, V., Walczyk, C., & Wenger, C. (2016). Electrical characterization and modeling of pulse-based forming techniques in RRAM arrays. *Solid-State Electronics*, *115*, 17–25. DOI: 10.1016/j.sse.2015.10.003

[Gregory2015] Gregory, M. D., & Werner, D. H. (2015). Application of the Memristor in Reconfigurable Electromagnetic Devices. *IEEE Antennas and Propagation Magazine*, *57*(1), 239–248. DOI: 10.1109/MAP.2015.2397153

[Guan2008] Guan, W., Long, S., Liu, Q., Liu, M., & Wang, W. (2008). Nonpolar nonvolatile resistive switching in Cu doped ZrO$_2$. *IEEE Electron Device Letters*, *29*(5), 434–437. DOI: 10.1109/LED.2008.919602

[Guan2012] Guan, X., Yu, S., & Wong, H.-S. P. (2012). A SPICE Compact Model of Metal Oxide Resistive Switching Memory With Variations. IEEE Electron Device Letters, 33(10), 1405–1407. DOI: 10.1109/LED.2012.2210856

[Guan2012b] Guan, X., Yu, S., & Wong, H. S. P. (2012). On the variability of HfO$_x$ RRAM: From numerical simulation to compact modeling. Technical Proceedings of the 2012 NSTI Nanotechnology Conference and Expo, NSTI-Nanotech 2012, 2, 815–820.

[Guo2007] Guo, H. X., Yang, B., Chen, L., Xia, Y. D., Yin, K. B., Liu, Z. G., & Yin, J. (2007). Resistive switching devices based on nanocrystalline solid electrolyte (AgI)$_{0.5}$ (AgPO$_3$) $_{0.5}$. *Applied Physics Letters*, *91*(24), 2–5. DOI: 10.1063/1.2825273

[Guo2012] Guo, X. (2012). Roles of Schottky barrier and oxygen vacancies in the electroforming of SrTiO$_3$. *Applied Physics Letters*, *101*(15), 152903. DOI: 10.1063/1.4759030

[Guo2015] Guo, T., Tan, T., & Liu, Z. (2015). The improved resistive switching of HfO$_2$:Cu film with multilevel storage. *Journal of Materials Science*, *50*(21), 7043–7047. DOI: 10.1007/s10853-015-9257-9

[Guo2015b] Guo, D. Y., Wu, Z. P., An, Y. H., Li, P. G., Wang, P. C., Chu, X. L., … Tang, W. H. (2015). Unipolar resistive switching behavior of amorphous gallium oxide thin films for nonvolatile memory applications. *Applied Physics Letters*, *106*(4), 042105. DOI: 10.1063/1.4907174

[Gupta2019] Gupta, V., Kapur, S., Saurabh, S., & Grover, A. (2019). Resistive Random Access Memory: A Review of Device Challenges. *IETE Technical Review (Institution of Electronics and Telecommunication Engineers, India)*, *0*(0), 1–14. DOI: 10.1080/02564602.2019.1629341

[Goux2010] Goux, L., Chen, Y.-Y., Pantisano, L., Wang, X.-P., Groeseneken, G., Jurczak, M., & Wouters, D. J. (2010). On the Gradual Unipolar and Bipolar Resistive Switching of TiN\HfO$_2$\Pt Memory Systems. *Electrochemical and Solid-State Letters*, *13*(6), G54. DOI: 10.1149/1.3373529

[Guy2015] Guy, J., Molas, G., Blaise, P., Bernard, M., Roule, A., Le Carval, G., … Perniola, L. (2015). Investigation of Forming, SET, and Data Retention of Conductive-Bridge Random-Access Memory for Stack Optimization. *IEEE Transactions on Electron Devices*, *62*(11), 3482–3489. DOI: 10.1109/TED.2015.2476825

References

[Ha2008] Ha, H., & Kim, O. (2008). Bipolar switching characteristics of nonvolatile memory devices based on poly(3,4-ethylenedioxythiophene):poly(styrenesulfonate) thin film. *Applied Physics Letters*, *93*(3), 033309. DOI: 10.1063/1.2960998

[Haemori2009] Haemori, M., Nagata, T., Chikyow, T., T. Sakamoto, H. S. H. K. T. H. T. N. and M. A., N. Banno, T. S. T. H. K. T. and M. A., K. Terabe, T. H. T. N. and M. A., … K. Tsunoda, Y. F. J. R. J. Z. W. P. B. G. and Y. N. (2009). Impact of Cu Electrode on Switching Behavior in a Cu/HfO$_2$/Pt Structure and Resultant Cu Ion Diffusion. *Applied Physics Express*, *2*(6), 061401. DOI: 10.1143/APEX.2.061401

[Hajto1991] Hajto, J., Rose, M. J., Snell, A. J., Osborne, I. S., Owen, A. E., & Lecomber, P. G. (1991). Quantised electron effects in metal/a-Si:H/metal thin film structures. *Journal of Non-Crystalline Solids*, *137–138*(PART 1), 499–502. DOI: 10.1016/S0022-3093(05)80164-4

[Hajto1996] Hajto, J., McAuley, B., Snell, A. J., & Owen, A. E. (1996). Theory of room temperature quantized resistance effects in metal-a-Si:H-metal thin film structures. *Journal of Non-Crystalline Solids*, *198–200*, 825–828. DOI: 10.1016/0022-3093(96)00048-8

[Hasan2008] Hasan, M., Dong, R., Choi, H. J., Lee, D. S., Seong, D. J., Pyun, M. B., & Hwang, H. (2008). Uniform resistive switching with a thin reactive metal interface layer in metal-La$_{0.7}$Ca$_{0.3}$MnO$_3$-metal heterostructures. *Applied Physics Letters*, *92*(20). DOI: 10.1063/1.2932148

[Hatem2015] Hatem, F. O., Ho, P. W. C., Kumar, T. N., & Almurib, H. A. F. (2015). Modeling of bipolar resistive switching of a nonlinear MISM memristor. *Semiconductor Science and Technology*, *30*(11), 115009. DOI: 10.1088/0268-1242/30/11/115009

[He2013] He, X., & Li, X. (2013). Field-induced resistive switching of (Ba$_{0.6}$Sr $_{0.4}$)TiO$_3$ thin films based on switching of conducting domains model. *Applied Physics Letters*, *102*(22), 0–3. DOI: 10.1063/1.4809532

[Hsieh2015] Hsieh, W.-K., Lam, K.-T., & Chang, S.-J. (2015). Bipolar Ni/ZnO/HfO$_2$/Ni RRAM with multilevel characteristic by different reset bias. *Materials Science in Semiconductor Processing*, *35*, 30–33. DOI: 10.1016/j.mssp.2015.02.073

[Ho2007] Ho, C., Lai, E. K., Lee, M. D., Pan, C. L., Yao, Y. D., Hsieh, K. Y., … Lu, C. Y. (2007). A Highly Reliable Self-Aligned Graded Oxide WO$_x$ Resistance Memory: Conduction Mechanisms and Reliability. In *2007 IEEE Symposium on VLSI Technology* (pp. 228–229). IEEE. DOI: 10.1109/VLSIT.2007.4339703

[Ho2010] Ho, C. H., Hsu, C. L., Chen, C. C., Liu, J. T., Wu, C. S., Huang, C. C., … Yang, F. L. (2010). 9nm half-pitch functional resistive memory cell with <1μA programming current using thermally oxidized sub-stoichiometric WO$_x$ film. *Technical Digest - International Electron Devices Meeting, IEDM*, 19.1.1-19.1.4. DOI: 10.1109/IEDM.2010.5703389

[Hong2015] Hong, S. M., Kim, H.-D., Yun, M. J., Park, J. H., Jeon, D. S., & Kim, T. G. (2015). Improved resistive switching properties by nitrogen doping in tungsten oxide thin films. *Thin Solid Films*, *583*(1), 81–85. DOI: 10.1016/j.tsf.2015.03.049

[Hosoi2006] Hosoi, Y., Tamai, Y., Ohnishi, T., Ishihara, K., Shibuya, T., Inoue, Y., … Tokura, Y. (2006). High Speed Unipolar Switching Resistance RAM (RRAM) Technology. In *2006 International Electron Devices Meeting* (pp. 1–4). IEEE. DOI: 10.1109/IEDM.2006.346732

[Hu2011] Hu, P., Li, X. Y., Lu, J. Q., Yang, M., Lv, Q. B., & Li, S. W. (2011). Oxygen deficiency effect on resistive switching characteristics of copper oxide thin films. *Physics Letters, Section A: General, Atomic and Solid State Physics*, *375*(18), 1898–1902. DOI: 10.1016/j.physleta.2011.03.033

[Hu2012] Hu, B., Quhe, R., Chen, C., Zhuge, F., Zhu, X., Peng, S., … Li, R. W. (2012). Electrically controlled electron transfer and resistance switching in reduced graphene oxide noncovalently functionalized with thionine. *Journal of Materials Chemistry*, *22*(32), 16422–16430. DOI: 10.1039/c2jm32121a

[Hu2013] Hu, C., McDaniel, M. D., Ekerdt, J. G., & Yu, E. T. (2013). High ON/OFF ratio and quantized conductance in resistive switching of TiO$_2$ on silicon. *IEEE Electron Device Letters*, *34*(11), 1385–1387. DOI: 10.1109/LED.2013.2282154

[Huang2008] Huang, L., Qu, B., & Liu, L. (2008). Bistable resistive switching of pulsed laser deposited polycrystalline la$_{0.67}$Sr$_{0.33}$MnO$_3$ films. *International Conference on Solid-State and Integrated Circuits Technology Proceedings, ICSICT*, 936–939. DOI: 10.1109/ICSICT.2008.4734688

[Huang2010] Huang, J.-J., Kuo, C.-W., Chang, W.-C., & Hou, T.-H. (2010). Transition of stable rectification to resistive-switching in Ti/TiO$_2$/Pt oxide diode. *Applied Physics Letters*, *96*(26), 262901. DOI: 10.1063/1.3457866

[Huang2010b] Huang, H. H., Shih, W. C., & Lai, C. H. (2010). Nonpolar resistive switching in the Pt/MgO/Pt nonvolatile memory device. *Applied Physics Letters*, *96*(19). DOI: 10.1063/1.3429024

[Huang2012] Huang, C., Shen, W. C., Tseng, Y., King, Y., & Lin, C. (2012). A Contact-Resistive Random-Access-Memory-Based True Random Number Generator. *IEEE Electron Device Letters*, *33*(8), 1108–1110. DOI: 10.1109/LED.2012.2199734

[Huang2012b] Huang, Y., Huang, R., Pan, Y., Zhang, L., Cai, Y., Yang, G., & Wang, Y. (2012). A New Dynamic Selector Based on the Bipolar RRAM for the Crossbar Array Application. *IEEE Transactions on Electron Devices*, *59*(8), 2277–2280. DOI: 10.1109/TED.2012.2201158

[Huang2012c] Huang, R., Tang, Y., Kuang, Y., Ding, W., Zhang, L., & Wang, Y. (2012). Resistive switching in organic memory device based on parylene-c with highly compatible process for high-density and low-cost memory applications. *IEEE Transactions on Electron Devices*, *59*(12), 3578–3582. DOI: 10.1109/TED.2012.2220142

[Huang2012d] Huang, Y. C., Chen, P. Y., Chin, T. S., Liu, R. S., Huang, C. Y., & Lai, C. H. (2012). Improvement of resistive switching in NiO-based nanowires by inserting Pt layers. *Applied Physics Letters*, *101*(15). DOI: 10.1063/1.4758482

[Huang2012e] Huang, P., Gao, B., Chen, B., Zhang, F., Liu, L., & Du, G. (2012). Stochastic simulation of forming, SET and RESET process for transition metal oxide-based resistive switching memory. *Sispad 2012*, (2011), 312–315. Retrieved from http://in4.iue.tuwien.ac.at/pdfs/sispad2012/16-4.pdf

[Huang2013] Huang, P., Liu, X. Y., Chen, B., Li, H. T., Wang, Y. J., Deng, Y. X., … Kang, J. F. (2013). A Physics-Based Compact Model of Metal-Oxide-Based RRAM DC and AC Operations. *IEEE Transactions on Electron Devices*, *60*(12), 4090–4097. DOI: 10.1109/TED.2013.2287755

[Huang2014] Li-Yue Huang, Meng-Fan Chang, Ching-Hao Chuang, Chia-Chen Kuo, Chien-Fu Chen, Geng-Hau Yang, … Ming-Jer Kao. (2014). ReRAM-based 4T2R nonvolatile TCAM with 7x NVM-stress reduction, and 4x improvement in speed-wordlength-capacity for normally-off instant-on filter-based search engines used in big-data processing. In *2014 Symposium on VLSI Circuits Digest of Technical Papers* (pp. 1–2). IEEE. DOI: 10.1109/VLSIC.2014.6858404

[Huang2017] Huang, P., Zhu, D., Chen, S., Zhou, Z., Chen, Z., Gao, B., … Kang, J. (2017). Compact Model of HfO$_X$-Based Electronic Synaptic Devices for Neuromorphic Computing. *IEEE Transactions on Electron Devices*, *64*(2), 614–621. DOI: 10.1109/TED.2016.2643162

[Hudec2014] Hudec, B., Paskaleva, A., Jančovič, P., Dérer, J., Fedor, J., Rosová, A., … Fröhlich, K. (2014). Resistive switching in TiO$_2$-based metal–insulator–metal structures with Al$_2$O$_3$ barrier layer at the metal/dielectric interface. *Thin Solid Films*, *563*, 10–14. DOI: 10.1016/j.tsf.2014.02.030

[Hwang2012] Hwang, I., Lee, M.-J., Bae, J., Hong, S., Kim, J.-S., Choi, J., … Park, B. H. (2012). Effects of a Load Resistor on Conducting Filament Characteristics and Unipolar Resistive Switching Behaviors in a Pt/NiO/Pt Structure. *IEEE Electron Device Letters*, *33*(6), 881–883. DOI: 10.1109/LED.2012.2190259

[Hwang2012b] Hwang, S. K., Lee, J. M., Kim, S., Park, J. S., Park, H. Il, Ahn, C. W., … Kim, S. O. (2012). Flexible multilevel resistive memory with controlled charge trap B- and N-doped carbon nanotubes. *Nano Letters*, *12*(5), 2217–2221. DOI: 10.1021/nl204039q

[Ibáñez2019] Ibáñez, M. J., Jiménez-Molinos, F., Roldán, J. B., & Yáñez, R. (2019). Estimation of the reset voltage in resistive RAMs using the charge–flux domain and a numerical method based on quasi-interpolation and discrete orthogonal polynomials. *Mathematics and Computers in Simulation*, *164*, 120–130. DOI: 10.1016/j.matcom.2018.09.028

References

[Ielmini2015] Ielmini, D., & Waser, R. (2016). *Resistive Switching*. (D. Ielmini & R. Waser, Eds.). Weinheim, Germany: Wiley-VCH Verlag GmbH & Co. KGaA. ISBN: 978-3-527-33417-9. DOI: 10.1002/9783527680870

[Ielmini2016] Ielmini, D. (2016). Resistive switching memories based on metal oxides: mechanisms, reliability and scaling. *Semiconductor Science and Technology*, *31*(6), 063002. DOI: 10.1088/0268-1242/31/6/063002

[Ielmini2017] Ielmini, D., & Milo, V. (2017). Physics-based modeling approaches of resistive switching devices for memory and in-memory computing applications. *Journal of Computational Electronics*, *16*(4), 1121–1143. DOI: 10.1007/s10825-017-1101-9

[Indiveri2013] Indiveri, G., Linares-Barranco, B., Legenstein, R., Deligeorgis, G., & Prodromakis, T. (2013). Integration of nanoscale memristor synapses in neuromorphic computing architectures. *Nanotechnology*, *24*(38), 384010. DOI: 10.1088/0957-4484/24/38/384010

[Ismail2014] Ismail, M., Huang, C.-Y., Panda, D., Hung, C.-J., Tsai, T.-L., Jieng, J.-H., … Tseng, T.-Y. (2014). Forming-free bipolar resistive switching in nonstoichiometric ceria films. *Nanoscale Research Letters*, *9*(1), 45 DOI: 10.1186/1556-276X-9-45

[Ismail2015] Ismail, M., Ahmed, E., Rana, A. M., Talib, I., Khan, T., Iqbal, K., & Nadeem, M. Y. (2015). Role of tantalum nitride as active top electrode in electroforming-free bipolar resistive switching behavior of cerium oxide-based memory cells. *Thin Solid Films*, *583*(1), 95–101. DOI: 10.1016/j.tsf.2015.03.059

[Itoh2008] Itoh, M., & Chua, L. O. (2008). Memristor oscillators. *International Journal of Bifurcation and Chaos*, 18(11), 3183–3206. DOI: 10.1142/S0218127408022354

[Iu2011a] Iu, H. H. C., Yu, D. S., Fitch, A. L., & Sreeram, V. (2011). Chaos control in a memristor based circuit. *Proceedings - IEEE International Symposium on Circuits and Systems*, 2946–2949. DOI: 10.1109/ISCAS.2011.5938209

[Iu2011b] Iu, H. H. C., Yu, D. S., Fitch, A. L., Sreeram, V., & Chen, H. (2011). Controlling Chaos in a Memristor Based Circuit Using a Twin-T Notch Filter. *IEEE Transactions on Circuits and Systems I: Regular Papers*, *58*(6), 1337–1344. DOI: 10.1109/TCSI.2010.2097771

[Jacobs2013] Jacobs, T. D. B., & Carpick, R. W. (2013). Nanoscale wear as a stress-assisted chemical reaction. *Nature Nanotechnology*, *8*(2), 108–112. DOI: 10.1038/nnano.2012.255

[Jagath2018] Jagath, A. L., Nandha Kumar, T., & Almurib, H. A. F. (2018). Modeling of Current Conduction during RESET Phase of $Pt/Ta_2O_5/TaO_x/Pt$ Bipolar Resistive RAM Devices. In *2018 IEEE 7th Non-Volatile Memory Systems and Applications Symposium (NVMSA)* (pp. 55–60). IEEE. DOI: 10.1109/NVMSA.2018.00014

[Jakobsson2007] Jakobsson, F. L. E., Crispin, X., Cölle, M., Büchel, M., de Leeuw, D. M., & Berggren, M. (2007). On the switching mechanism in Rose Bengal-based memory devices. *Organic Electronics*, *8*(5), 559–565. DOI: 10.1016/J.ORGEL.2007.04.002

[Jameson2012] Jameson, J. R., Gilbert, N., Koushan, F., Saenz, J., Wang, J., Hollmer, S., … Derhacobian, N. (2012). Quantized conductance in $Ag/GeS_2/W$ conductive-bridge memory cells. *IEEE Electron Device Letters*, *33*(2), 257–259. DOI: 10.1109/LED.2011.2177803

[Jeon2014]. Jeon, H., Park, J., Jang, W., Kim, H., Kang, C., Song, H., … Jeon, H. (2014). Resistive switching of a $TaO_x/TaON$ double layer via ionic control of carrier tunneling. *Applied Physics Letters*, *104*(15), 151603. DOI: 10.1063/1.4871692

[Jeong2006] Jeong, K. W., Do, Y. H., Yoon, K. S., & Hong, C. O. K. and J. P. (2006). Resistive Switching Characteristics of Unique Binary-Oxide MgO_x Films. *Journal of the Korean Physical Society*, *48*(6), 1501.

[Jeong2007] Jeong, D. S., Schroeder, H., & Waser, R. (2007). Coexistence of Bipolar and Unipolar Resistive Switching Behaviors in a $Pt/TiO_2/Pt$ Stack. *Electrochemical and Solid-State Letters*, *10*(8), G51. DOI: 10.1149/1.2742989

[Jeong2008] Jeong, D. S., Schroeder, H., Breuer, U., & Waser, R. (2008). Characteristic electroforming behavior in $Pt/TiO_2/Pt$ resistive switching cells depending on atmosphere. *Journal of Applied Physics*, *104*(12), 123716. DOI: 10.1063/1.3043879

[Jeong2009] Jeong, D. S., Schroeder, H., & Waser, R. (2009). Mechanism for bipolar switching in a Pt/TiO$_2$/Pt resistive switching cell. *Physical Review B*, *79*(19), 195317. DOI: 10.1103/PhysRevB.79.195317

[Jiang2014] Jiang, Z., Yu, S., Wu, Y., Engel, J. H., Guan, X., & Wong, H.-S. P. (2014). Verilog-A compact model for oxide-based resistive random access memory (RRAM). In *2014 International Conference on Simulation of Semiconductor Processes and Devices (SISPAD)* (pp. 41–44). IEEE. DOI: 10.1109/SISPAD.2014.6931558

[Jiang2015] Li, H., Jiang, Z., Huang, P., Wu, Y., Chen, H.-Y., Gao, B., … Wong, H.-S. P. (2015). Variation-Aware, Reliability-Emphasized Design and Optimization of RRAM using SPICE Model. In *Design, Automation & Test in Europe Conference & Exhibition (DATE), 2015* (pp. 1425–1430). New Jersey: IEEE Conference Publications. DOI: 10.7873/DATE.2015.0362

[Jiang2016] Jiang, Z., Wu, Y., Yu, S., Yang, L., Song, K., Karim, Z., & Wong, H.-S. P. (2016). A Compact Model for Metal–Oxide Resistive Random Access Memory With Experiment Verification. IEEE Transactions on Electron Devices, 63(5), 1884–1892. DOI: 10.1109/TED.2016.2545412

[Jiménez-Molinos2015] Jiménez-Molinos, F., Villena, M. A., Roldan, J. B., & Roldan, A. M. (2015). A SPICE Compact Model for Unipolar RRAM Reset Process Analysis. *IEEE Transactions on Electron Devices*, *62*(3), 955–962. DOI: 10.1109/TED.2014.2387429

[Jiménez-Molinos2017] Jiménez-Molinos, F., **G. Gonzalez-Cordero**, G., Cartujo-Cassinello, P., & Roldan, J. B. (2017). SPICE modeling of RRAM thermal reset transitions for circuit simulation purposes. In *2017 Spanish Conference on Electron Devices (CDE)* (pp. 1–4). DOI: 10.1109/CDE.2017.7905227

[Jin2012] Jin, C., Lee, J., Lee, E., Hwang, E., & Lee, H. (2012). Nonvolatile resistive memory of ferrocene covalently bonded to reduced graphene oxide. *Chemical Communications*, *48*(35), 4235–4237. DOI: 10.1039/c2cc30973d

[Jin2013] Jin, Z., Liu, G., & Wang, J. (2013). Organic nonvolatile resistive memory devices based on thermally deposited Au nanoparticle. *AIP Advances*, *3*(5), 052113. DOI: 10.1063/1.4804948

[Jo2008] Jo, S. H., & Lu, W. (2008). CMOS compatible nanoscale nonvolatile resistance switching memory. *Nano Letters*, *8*(2), 392–397. DOI: 10.1021/nl073225h

[Jo2010] Jo, S. H., Chang, T., Ebong, I., Bhadviya, B. B., Mazumder, P., & Lu, W. (2010). Nanoscale Memristor Device as Synapse in Neuromorphic Systems. *Nano Letters*, *10*(4), 1297–1301. DOI: 10.1021/nl904092h

[Joo2006] Joo, W. J., Choi, T. L., Lee, J., Lee, S. K., Jung, M. S., Kim, N., & Kim, J. M. (2006). Metal filament growth in electrically conductive polymers for nonvolatile memory application. *Journal of Physical Chemistry B*, *110*(47), 23812–23816. DOI: 10.1021/jp0649899

[Joo2007] Joo, W. J., Choi, T. L., Lee, K. H., & Chung, Y. (2007). Study on threshold behavior of operation voltage in metal filament-based polymer memory. *Journal of Physical Chemistry B*, *111*(27), 7756–7760. DOI: 10.1021/jp0684933

[Joshua2009] Joshua Yang, J., Miao, F., Pickett, M. D., Ohlberg, D. A. A., Stewart, D. R., Lau, C. N., & Williams, R. S. (2009). The mechanism of electroforming of metal oxide memristive switches. *Nanotechnology*, *20*(21), 215201. DOI: 10.1088/0957-4484/20/21/215201

[Joglekar2009] Joglekar, Y. N., & Wolf, S. J. (2009). The elusive memristor: properties of basic electrical circuits. European Journal of Physics, 30(4), 661–675. DOI 10.1088/0143-0807/30/4/001

[Kang2015] Kang, J. F., Li, H. T., Huang, P., Chen, Z., Gao, B., Liu, X. Y., … Wong, H.-S. P. (2015). Modeling and design optimization of ReRAM. In *The 20th Asia and South Pacific Design Automation Conference* (Vol. 1, pp. 576–581). IEEE. DOI: 10.1109/ASPDAC.2015.7059070

[Kano2005] Kano, M., Orito, S., Tsuruoka, Y., & Ueno, N. (2005). Nonvolatile memory effect of an Al/2-Amino-4,5-dicyanoimidazole/Al structure. *Synthetic Metals*, *153*(1–3), 265–268. DOI: 10.1016/J.SYNTHMET.2005.07.090

[Kaushik2017] Kaushik, B. K., Verma, S., Kulkarni, A. A., & Prajapati, S. (2017). Emerging Memory Technologies. In Y. Xie (Ed.), *Springer Briefs in Applied Sciences and Technology* (pp. 1–12). DOI: 10.1007/978-981-10-2720-8_1

References

[Kvatinsky2014] Kvatinsky, S., Satat, G., Wald, N., Friedman, E. G., Kolodny, A., & Weiser, U. C. (2014). Memristor-based material implication (IMPLY) logic: Design principles and methodologies. *IEEE Transactions on Very Large Scale Integration (VLSI) Systems*, *22*(10), 2054–2066. DOI: 10.1109/TVLSI.2013.2282132

[Kavehei2011] Kavehei, O., Cho, K., Lee, S., Kim, S.-J., Al-Sarawi, S., Abbott, D., & Eshraghian, K. (2011). Fabrication and modeling of Ag/TiO$_2$/ITO memristor. In *2011 IEEE 54th International Midwest Symposium on Circuits and Systems (MWSCAS)* (pp. 1–4). IEEE. DOI: 10.1109/MWSCAS.2011.6026575

[Kawabata2010] Kawabata, S., Nakura, M., Yamazaki, S., Shibuya, T., Inoue, Y., Onishi, J., … Awaya, N. (2010). CoO$_x$-RRAM memory cell technology using recess structure for 128Kbits memory array. In *2010 IEEE International Memory Workshop* (pp. 1–2). IEEE. DOI: 10.1109/IMW.2010.5488319

[Kawahara2012] Kawahara, A., Azuma, R., Ikeda, Y., Kawai, K., Katoh, Y., Tanabe, K., … Aono, K. (2012). An 8Mb multi-layered cross-point ReRAM macro with 443MB/s write throughput. In *2012 IEEE International Solid-State Circuits Conference* (Vol. 55, pp. 432–434). DOI: 10.1109/ISSCC.2012.6177078

[Kever2006] Kever, T., Nauenheim, C., Böttger, U., & Waser, R. (2006). Preparation and characterisation of amorphous Cu:7,7,8,8-Tetracyanoquinodimethane thin films with low surface roughness via thermal co-deposition. *Thin Solid Films*, *515*(4), 1893–1896. DOI:10.1016/J.TSF.2006.07.028

[Kim2005] Kim, Y.-T., Hwang, Y.-N., Lee, K.-H., Lee, S.-H., Jeong, C.-W., Ahn, S.-J., … Kong, J.-T. (2005). Programming Characteristics of Phase Change Random Access Memory Using Phase Change Simulations. *Japanese Journal of Applied Physics*, *44*(4B), 2701–2705. DOI: 10.1143/JJAP.44.2701

[Kim2006] Kim, K. R., Park, I. S., Hong, J. P., Lee, S. S., Choi, B. L., & Ahn, J. (2006). Resistive switching characteristics of HfO$_2$ grown by atomic layer deposition. *Journal of the Korean Physical Society*, *49* (SUPPL. 2).

[Kim2006b] Kim, K. M., Choi, B. J., Jeong, D. S., Hwang, C. S., & Han, S. (2006). Influence of carrier injection on resistive switching of TiO$_2$ thin films with Pt electrodes. Applied Physics Letters, 89(16). DOI: 10.1063/1.2361268

[Kim2006c] Kim, K. M., Choi, B. J., Koo, B. W., Choi, S., Jeong, D. S., & Hwang, C. S. (2006). Resistive Switching in Pt∕Al$_2$O$_3$∕TiO$_2$∕Ru Stacked Structures. *Electrochemical and Solid-State Letters*, *9*(12), G343. DOI: 10.1149/1.2353899

[Kim2007] Kim, K. M., Choi, B. J., & Hwang, C. S. (2007). Localized switching mechanism in resistive switching of atomic-layer-deposited TiO$_2$ thin films. *Applied Physics Letters*, *90*(24), 242906. DOI: 10.1063/1.2748312

[Kim2008] Kim, Y.-M., & Lee, J.-S. (2008). Reproducible resistance switching characteristics of hafnium oxide-based nonvolatile memory devices. *Journal of Applied Physics*, *104*(11), 114115. DOI: 10.1063/1.3041475

[Kim2009] Kim, K. M., & Hwang, C. S. (2009). The conical shape filament growth model in unipolar resistance switching of TiO$_2$ thin film. *Applied Physics Letters*, *94*(12), 122109. DOI: 10.1063/1.3108088

[Kim2009b] Kim, S., & Choi, Y.-K. (2009). A Comprehensive Study of the Resistive Switching Mechanism in Al/TiO$_x$/TiO$_2$/Al Structured RRAM. *IEEE Transactions on Electron Devices*, *56*(12), 3049–3054. DOI: 10.1109/TED.2009.2032597

[Kim2009c] Kim, M., & Kim, O. (2009). Unipolar resistance switching in polymeric resistance random access memories. *Japanese Journal of Applied Physics*, *48*(6 PART 2), 8–11. DOI: 10.1143/JJAP.48.06FD02

[Kim2010] Kim, K. M., Lee, M. H., Kim, G. H., Song, S. J., Seok, J. Y., Yoon, J. H., & Hwang, C. S. (2010). Understanding structure-property relationship of resistive switching oxide thin films using a conical filament model. *Applied Physics Letters*, *97*(16), 162912. DOI: 10.1063/1.3505354

302

[Kim2010b] Kim, S., Jeong, H. Y., Choi, S.-Y., & Choi, Y.-K. (2010). Comprehensive modeling of resistive switching in the Al/TiO$_x$/TiO$_2$/Al heterostructure based on space-charge-limited conduction. *Applied Physics Letters*, *97*(3), 033508. DOI: 10.1063/1.3467461

[Kim2010c] Kim, K. M., Kim, G. H., Song, S. J., Seok, J. Y., Lee, M. H., Yoon, J. H., & Hwang, C. S. (2010). Electrically configurable electroforming and bipolar resistive switching in Pt/TiO$_2$/Pt structures. *Nanotechnology*, *21*(30), 305203. DOI: 10.1088/0957-4484/21/30/305203

[Kim2010d] Kim, T. W., Oh, S. H., Choi, H., Wang, G., Kim, D. Y., Hwang, H., & Lee, T. (2010). Effect of Ag Nanoparticles on resistive switching of polyfluorene-based organic non-volatile memory devices. *Journal of the Korean Physical Society*, *56*(1), 128–132. DOI: 10.3938/jkps.56.128

[Kim2010e] Kim, T. W., Oh, S. H., Lee, J., Choi, H., Wang, G., Park, J., … Lee, T. (2010). Effect of metal ions on the switching performance of polyfluorene-based organic non-volatile memory devices. *Organic Electronics: Physics, Materials, Applications*, *11*(1), 109–114. DOI: 10.1016/j.orgel.2009.10.006

[Kim2010f] Kim, H. D., An, H. M., Kim, K. C., Seo, Y., Nam, K. H., Chung, H. B., … Kim, T. G. (2010). Large resistive-switching phenomena observed in Ag/Si$_3$N$_4$/Al memory cells. *Semiconductor Science and Technology*, *25*(6). DOI: 10.1088/0268-1242/25/6/065002

[Kim2010g] Kim, K. H., Hyun Jo, S., Gaba, S., & Lu, W. (2010). Nanoscale resistive memory with intrinsic diode characteristics and long endurance. *Applied Physics Letters*, *96*(5). DOI: /10.1063/1.3294625

[Kim2011] Kim, K., Shin, S., & Kang, S.-M. (2011). Field Programmable Stateful Logic Array. *IEEE Transactions on Computer-Aided Design of Integrated Circuits and Systems*, *30*(12), 1800–1813. DOI: 10.1109/TCAD.2011.2165067

[Kim2011b] Kim, Y. S., Kim, J.-S., Choi, J. S., Hwang, I. R., Hong, S. H., Kang, S.-O., & Park, B. H. (2011). Resistive switching behaviors of NiO films with controlled number of conducting filaments. *Applied Physics Letters*, *98*(19), 192104. DOI: 10.1063/1.3589825

[Kim2011c] Kim, H. D., An, H. M., Seo, Y., & Kim, T. G. (2011). Transparent resistive switching memory using ITO/AlN/ITO capacitors. *IEEE Electron Device Letters*, *32*(8), 1125–1127. DOI: 10.1109/LED.2011.2158056

[Kim2012] Kim, T. W., Zeigler, D. F., Acton, O., Yip, H. L., Ma, H., & Jen, A. K. Y. (2012). All-organic photopatterned one diode-one resistor cell array for advanced organic nonvolatile memory applications. *Advanced Materials*, *24*(6), 828–833. DOI: 10.1002/adma.201104266

[Kim2012b] Kim, H. D., An, H. M., Hong, S. M., & Kim, T. G. (2012). Unipolar resistive switching phenomena in fully transparent SiN-based memory cells. *Semiconductor Science and Technology*, *27*(12). DOI: 10.1088/0268-1242/27/12/125020

[Kim2013] Kim, S., Kim, S.-J., Kim, K. M., Lee, S. R., Chang, M., Cho, E., … Yoo, I.-K. (2013). Physical electro-thermal model of resistive switching in bi-layered resistance-change memory. *Scientific Reports*, *3*(1), 1680. DOI: 10.1038/srep01680

[Kim2013b] Kim, H. D., An, H. M., Seo, Y., & Kim, T. G. (2011). Transparent resistive switching memory using ITO/AlN/ITO capacitors. *IEEE Electron Device Letters*, *32*(8), 1125–1127. DOI: 10.1109/LED.2011.2158056

[Kim2013c] Kim, H. D., An, H. M., Hong, S. M., & Kim, T. G. (2013). Forming-free SiN-based resistive switching memory prepared by RF sputtering. *Physica Status Solidi (A) Applications and Materials Science*, *210*(9), 1822–1827. DOI: 10.1002/pssa.20132902

[Kim2014] Kim, W., Park, S. Il, Zhang, Z., & Wong, S. (2014). Current Conduction Mechanism of Nitrogen-Doped AlO$_x$ RRAM. *IEEE Transactions on Electron Devices*, *61*(6), 2158–2163. DOI: 10.1109/TED.2014.2319074

[Kim2014b] Kim, S., Choi, S., & Lu, W. (2014). Comprehensive Physical Model of Dynamic Resistive Switching in an Oxide Memristor. *ACS Nano*, *8*(3), 2369–2376. DOI: 10.1021/nn405827t

[Kinoshita2006] Kinoshita, K., Tamura, T., Aoki, M., Sugiyama, Y., & Tanaka, H. (2006). Bias polarity dependent data retention of resistive random access memory consisting of binary transition metal oxide. *Applied Physics Letters*, *89*(10), 103509. DOI: 10.1063/1.2339032

References

[Kondo2008] Kondo, T., Lee, S. M., Malicki, M., Domercq, B., Marder, S. R., & Kippelen, B. (2008). A nonvolatile organic memory device using ITO surfaces modified by Ag-nanodots. *Advanced Functional Materials*, *18*(7), 1112–1118. DOI: 10.1002/adfm.200700567

[Kosta2011] Kosta, S. P., Kosta, Y. P., Bhatele, M., Dubey, Y. M., Gaur, A., Kosta, S., … Patel, B. (2011). Human blood liquid memristor. International Journal of Medical Engineering and Informatics, 3(1), 16. DOI: 10.1504/IJMEI.2011.039073

[Kozicki2005] Kozicki, M. N., Park, M., & Mitkova, M. (2005). Nanoscale memory elements based on solid-state electrolytes. *IEEE Transactions on Nanotechnology*, *4*(3), 331–338. DOI: 10.1109/TNANO.2005.846936

[Kozma2012] Kozma, R., Pino, R. E., & Pazienza, G. E. (2012). *Advances in Neuromorphic Memristor Science and Applications*. (R. Kozma, R. E. Pino, & G. E. Pazienza, Eds.). Dordrecht: Springer Netherlands. DOI: 10.1007/978-94-007-4491-2

[Kuang2010] Kuang, Y., Huang, R., Tang, Y., Ding, W., Zhang, L., & Wang, Y. (2010). Flexible single-component-polymer resistive memory for ultrafast and highly compatible nonvolatile memory applications. *IEEE Electron Device Letters*, *31*(7), 758–760. DOI: 10.1109/LED.2010.2048297

[Kugeler2008] Kugeler, C., Nauenheim, C., Meier, M., Rudiger, A., & Waser, R. (2008). Fast resistance switching of TiO_2 and MSQ thin films for non-volatile memory applications (RRAM). In *2008 9th Annual Non-Volatile Memory Technology Symposium (NVMTS)* (Vol. 00, pp. 1–6). IEEE. DOI: 10.1109/NVMT.2008.4731195

[Kund2005] Kund, M., Beitel, G., Pinnow, C. U., Röhr, T., Schumann, J., Symanczyk, R., … Müller, G. (2005). Conductive bridging RAM (CBRAM): An emerging non-volatile memory technology scalable to sub 20nm. *Technical Digest - International Electron Devices Meeting, IEDM*, *2005*(1), 754–757. DOI: 10.1109/IEDM.2005.1609463

[Kurnia2011] Kurnia, F., Hadiyawarman, Jung, C. U., Jung, R., & Liu, C. (2011). Composition dependence of unipolar resistance switching in TaOx thin films. *Physica Status Solidi - Rapid Research Letters*, *5*(7), 253–255. DOI: 10.1002/pssr.201105253

[Kurnia2013] Kurnia, F., Liu, C., Jung, C. U., & Lee, B. W. (2013). The evolution of conducting filaments in forming-free resistive switching $Pt/TaO_x/Pt$ structures. *Applied Physics Letters*, *102*(15). DOI: 10.1063/1.4802263

[Kurnia2015] Kurnia, F., Jung, C. U., Lee, B. W., & Liu, C. (2015). Compliance current induced non-reversible transition from unipolar to bipolar resistive switching in a $Cu/TaO_x/Pt$ structure. *Applied Physics Letters*, *107*(7), 073501. DOI: 10.1063/1.4928913

[Kvatinsky2010] Kvatinsky, S., Ramadan, M., Friedman, E. G., & Kolodny, A. (2015). VTEAM: A General Model for Voltage-Controlled Memristors. *IEEE Transactions on Circuits and Systems II: Express Briefs*, *62*(8), 786–790. DOI: 10.1109/TCSII.2015.2433536

[Kvatinsky2011] Kvatinsky S, Talisveyberg K, Fliter D, Friedman EG, Kolodny A, Weiser UC. Verilog-A for memristor models. CCIT Tech Rep. 2011;8. Available from: http://webee.technion.ac.il/people/skva/Memristor Models/VerilogA models technical report.pdf

[Kvatinsky2012] Kvatinsky, S., Talisveyberg, K., Fliter, D., Kolodny, A., Weiser, U. C., & Friedman, E. G. (2012). Models of memristors for SPICE simulations. In *2012 IEEE 27th Convention of Electrical and Electronics Engineers in Israel* (pp. 1–5). IEEE. DOI: 10.1109/EEEI.2012.6377081

[Kvatinsky2013] Kvatinsky, S., Friedman, E. G., Kolodny, A., & Weiser, U. C. (2013). TEAM: ThrEshold Adaptive Memristor Model. *IEEE Transactions on Circuits and Systems I: Regular Papers*, *60*(1), 211–221. DOI: 10.1109/TCSI.2012.2215714

[Kvatinsky2015] Kvatinsky, S., Ramadan, M., Friedman, E. G., & Kolodny, A. (2015). VTEAM: A General Model for Voltage-Controlled Memristors. *IEEE Transactions on Circuits and Systems II: Express Briefs*, *62*(8), 786–790. DOI: 10.1109/TCSII.2015.2433536

[Kwak2010] Kwak, J. S., Do, Y. H., Bae, Y. C., Im, H., & Hong, J. P. (2010). Reproducible unipolar resistive switching behaviors in the metal-deficient CoO_x thin film. *Thin Solid Films*, *518*(22), 6437–6440. DOI: 10.1016/j.tsf.2010.03.050

[Kwon2010] Kwon, D., Kim, K. M., Jang, J. H., Jeon, J. M., Lee, M. H., Kim, G. H., … Hwang, C. S. (2010). Atomic structure of conducting nanofilaments in TiO_2 resistive switching memory. *Nature Nanotechnology*, *5*(2), 148–153. DOI: 10.1038/nnano.2009.456

[Laiho2010] Laiho, M., Lehtonen, E., Russell, A., & Dudek, P. (2010). Memristive synapses are becoming reality. *The Neuromorphic Engineer*, 10–12. https://doi.org/10.2417/1201011.003396

[Laiho2010b] Laiho, M., & Lehtonen, E. (2010). Arithmetic operations within memristor-based analog memory. In *2010 12th International Workshop on Cellular Nanoscale Networks and their Applications (CNNA 2010)* (pp. 1–4). IEEE. DOI: 10.1109/CNNA.2010.5430319

[Lai2006] Lai, Q., Zhu, Z., Chen, Y., Patil, S., & Wudl, F. (2006). Organic nonvolatile memory by dopant-configurable polymer. *Applied Physics Letters*, *88*(13), 133515. DOI: 10.1063/1.2191874

[Lai2011] Lai, P. Y., & Chen, J. S. (2011). Ultrahigh on/off -current ratio for resistive memory devices with poly(N-Vinylcarbazole)/poly(3, 4-ethylenedioxythiophene)poly(styrenesulfonate) stacking bilayer. *IEEE Electron Device Letters*, *32*(3), 387–389. DOI: 10.1109/LED.2010.2099102

[Lai2013] Lai, Y. C., Wang, D. Y., Huang, I. S., Chen, Y. T., Hsu, Y. H., Lin, T. Y., … Chen, Y. F. (2013). Low operation voltage macromolecular composite memory assisted by graphene nanoflakes. *Journal of Materials Chemistry C*, *1*(3), 552–559. DOI: 10.1039/c2tc00010e

[Lanza2014] Lanza, M. (2014). A Review on Resistive Switching in High-k Dielectrics: A Nanoscale Point of View Using Conductive Atomic Force Microscope. *Materials*, *7*(3), 2155–2182. DOI: 10.3390/ma7032155

[Lanza2019] Lanza, M., Wong, H.-S. P., Pop, E., Ielmini, D., Strukov, D., Regan, B. C., … Shi, Y. (2019). Recommended Methods to Study Resistive Switching Devices. *Advanced Electronic Materials*, *5*(1), 1800143. DOI: 10.1002/aelm.201800143

[Larentis2012] Larentis, S., Nardi, F., Balatti, S., Gilmer, D. C., & Ielmini, D. (2012). Resistive Switching by Voltage-Driven Ion Migration in Bipolar RRAM—Part II: Modeling. *IEEE Transactions on Electron Devices*, *59*(9), 2468–2475. DOI: 10.1109/TED.2012.2202320

[Lauters2005] Lauters, M., McCarthy, B., Sarid, D., & Jabbour, G. E. (2005). Nonvolatile multilevel conductance and memory effects in organic thin films. *Applied Physics Letters*, *87*(23), 231105. DOI: 10.1063/1.2138809

[Lauters2006] Lauters, M., McCarthy, B., Sarid, D., & Jabbour, G. E. (2006). Multilevel conductance switching in polymer films. *Applied Physics Letters*, *89*(1), 013507. DOI: 10.1063/1.2219338

[Lee2005] Dongsoo Lee, Hyejung Choi, Hyunjun Sim, Dooho Choi, Hyunsang Hwang, Myoung-Jae Lee, … Yoo, I. K. (2005). Resistance switching of the nonstoichiometric zirconium oxide for nonvolatile memory applications. *IEEE Electron Device Letters*, *26*(10), 719–721. DOI: 10.1109/LED.2005.854397

[Lee2007] Lee, H.-Y., Chen, P.-S., Wang, C.-C., Maikap, S., Tzeng, P.-J., Lin, C.-H., … Tsai, M.-J. (2007). Low-Power Switching of Nonvolatile Resistive Memory Using Hafnium Oxide. *Japanese Journal of Applied Physics*, *46*(4B), 2175–2179. DOI: 10.1143/JJAP.46.2175

[Lee2007b], M. J., Park, Y., Suh, D. S., Lee, E. H., Seo, S., Kim, D. C., … Park, B. H. (2007). Two series oxide resistors applicable to high speed and high density nonvolatile memory. *Advanced Materials*, *19*(22), 3919–3923. DOI: 10.1002/adma.200700251

[Lee2007c] Lee, D., Seong, D. J., Jo, I., Xiang, F., Dong, R., Oh, S., & Hwang, H. (2007). Resistance switching of copper doped MoO_x films for nonvolatile memory applications. *Applied Physics Letters*, *90*(12), 1–4. DOI: 10.1063/1.2715002

[Lee2008] Lee, S., Kim, W.-G., Rhee, S.-W., & Yong, K. (2008). Resistance Switching Behaviors of Hafnium Oxide Films Grown by MOCVD for Nonvolatile Memory Applications. *Journal of The Electrochemical Society*, *155*(2), H92. DOI: 10.1149/1.2814153

[Lee2008b] Lee, H. Y., Chen, P. S., Wu, T. Y., Chen, Y. S., Wang, C. C., Tzeng, P. J., … Tsai, M.-J. (2008). Low power and high speed bipolar switching with a thin reactive Ti buffer layer in robust HfO_2 based RRAM. In *2008 IEEE International Electron Devices Meeting* (pp. 1–4). IEEE. DOI: 10.1109/IEDM.2008.4796677

References

[Lee2008c] Lee, P. T., Chang, T. Y., & Chen, S. Y. (2008). Tuning of the electrical characteristics of organic bistable devices by varying the deposition rate of Alq_3 thin film. *Organic Electronics: Physics, Materials, Applications*, *9*(5), 916–920. DOI: 10.1016/j.orgel.2008.06.003

[Lee2008d] Lee, D., Baek, S., Ree, M., & Kim, O. (2008). Effect of the electrode material on the electrical-switching characteristics of nonvolatile memory devices based on poly(o-anthranilic acid) thin films. *IEEE Electron Device Letters*, *29*(7), 694–697. DOI: 10.1109/LED.2008.2000667

[Lee2009] Lee, B., & Wong, H. S. P. (2009). NiO resistance change memory with a novel structure for 3D integration and improved confinement of conduction path. *Digest of Technical Papers - Symposium on VLSI Technology*, 28–29.

[Lee2009b] Lee, S., Kim, H., Yun, D.-J., Rhee, S.-W., & Yong, K. (2009). Resistive switching characteristics of ZnO thin film grown on stainless steel for flexible nonvolatile memory devices. *Applied Physics Letters*, *95*(26), 262113. DOI: 10.1063/1.3280864

[Lee2010] Lee, H. Y., Chen, Y. S., Chen, P. S., Gu, P. Y., Hsu, Y. Y., Wang, S. M., … Tsai, M. J. (2010). Evidence and solution of over-RESET problem for HfO_x based resistive memory with sub-ns switching speed and high endurance. In Technical Digest - International Electron Devices Meeting, IEDM (pp. 19.7.1-19.7.4). IEEE. DOI: 10.1109/IEDM.2010.5703395

[Lee2011] Lee, W., Jo, G., Lee, S., Park, J., Jo, M., Lee, J., … Hwang, H. (2011). Nonvolatile resistive switching in $Pr_{0.7}Ca_{0.3}MnO_3$ devices using multilayer graphene electrodes. *Applied Physics Letters*, *98*(3), 032105. DOI: 10.1063/1.3544051

[Lee2011b] Lee, M. J., Lee, C. B., Lee, D., Lee, S. R., Chang, M., Hur, J. H., … Kim, K. (2011). A fast, high-endurance and scalable non-volatile memory device made from asymmetric Ta_2O_{5-x}/TaO_{2-x} bilayer structures. *Nature Materials*, *10*(8), 625–630. DOI: 10.1038/nmat3070

[Lee2012] Lee, H. D., Kim, S. G., Cho, K., Hwang, H., Choi, H., Lee, J., … Hong, S.-J. (2012). Integration of 4F2 selector-less crossbar array 2Mb ReRAM based on transition metal oxides for high density memory applications. In *2012 Symposium on VLSI Technology (VLSIT)* (pp. 151–152). IEEE. DOI: 10.1109/VLSIT.2012.6242506

[Lee2012b] Lee, J.-K., Jung, S., Park, J., Chung, S.-W., Sung Roh, J., Hong, S.-J., … Lee, J.-H. (2012). Accurate analysis of conduction and resistive-switching mechanisms in double-layered resistive-switching memory devices. *Applied Physics Letters*, *101*(10), DOI: 10.1063/1.4751248

[Lee2014] Lee, S., Woo, J., Lee, D., Cha, E., & Hwang, H. (2014). Internal resistor of multi-functional tunnel barrier for selectivity and switching uniformity in resistive random access memory. *Nanoscale Research Letters*, *9*(1), 364. DOI: 10.1186/1556-276X-9-364

[Lee2015] Lee, J. S., Lee, S., & Noh, T. W. (2015). Resistive switching phenomena: A review of statistical physics approaches. *Applied Physics Reviews*, *2*(3), 031303. DOI: 10.1063/1.4929512

[Lee2015b] Lee, A., Chang, M.-F., Lin, C.-C., Chen, C.-F., Ho, M.-S., Kuo, C.-C., … Ku, T.-K. (2015). RRAM-based 7T1R nonvolatile SRAM with 2x reduction in store energy and 94x reduction in restore energy for frequent-off instant-on applications. In *2015 Symposium on VLSI Circuits (VLSI Circuits)* (Vol. 2015-Augus, pp. C76–C77). IEEE. DOI: 10.1109/VLSIC.2015.7231368

[Lehtonen2009] Lehtonen, E., & Laiho, M. (2009). Stateful implication logic with memristors. In *2009 IEEE/ACM International Symposium on Nanoscale Architectures* (pp. 33–36). IEEE. DOI: 10.1109/NANOARCH.2009.5226356

[Lehtonen2010a] Lehtonen, E., Laiho, M., & Poikonen, J. (2010). A chaotic memristor circuit. In *2010 12th International Workshop on Cellular Nanoscale Networks and their Applications (CNNA 2010)* (pp. 1–3). IEEE. DOI: 10.1109/CNNA.2010.5430322

[Lehtonen2010c] Lehtonen, E., & Laiho, M. (2010). CNN using memristors for neighborhood connections. In 2010 12th International Workshop on Cellular Nanoscale Networks and their Applications (CNNA 2010) (pp. 1–4). IEEE. DOI: 10.1109/CNNA.2010.5430304

[Lekshmi2019] Lekshmi Jagath, A., Hock Leong, C., Kumar, T. N., & Almurib, H. F. (2019). Insight into physics-based RRAM models – review. The Journal of Engineering, 2019(7), 4644–4652. DOI: 10.1049/joe.2018.5234

[Lei2009] Lei, B., Kwan, W. L., Shao, Y., & Yang, Y. (2009). Statistical characterization of the memory effect in polyfluorene based non-volatile resistive memory devices. *Organic Electronics: Physics, Materials, Applications*, *10*(6), 1048–1053.DOI: 10.1016/j.orgel.2009.05.015

[Li2008] Li, Y., Sinitskii, A., & Tour, J. M. (2008). Electronic two-terminal bistable graphitic memories. *Nature Materials*, *7*(12), 966–971. DOI: 10.1038/nmat2331

[Li2010] Li, Y., Long, S., Zhang, M., Liu, Q., Shao, L., Zhang, S., … Liu, M. (2010). Resistive switching properties of Au/ZrO2/Ag structure for low-voltage nonvolatile memory applications. *IEEE Electron Device Letters*, *31*(2), 117–119. DOI: 10.1109/LED.2009.2036276

[Li2013] Li, Y., Lv, H., Liu, Q., Long, S., Wang, M., Xie, H., … Liu, M. (2013). Bipolar one diode–one resistor integration for high-density resistive memory applications. *Nanoscale*, *5*(11), 4785. DOI: 10.1039/c3nr33370a

[Li2013b] Li, Z.-J., & Zeng, Y.-C. (2013). A memristor oscillator based on a twin-T network. *Chinese Physics B*, *22*(4), 040502. DOI: 10.1088/1674-1056/22/4/040502

[Li2014] Li, H., Huang, P., Gao, B., Chen, B., Liu, X., & Kang, J. (2014). A SPICE Model of Resistive Random Access Memory for Large-Scale Memory Array Simulation. IEEE Electron Device Letters, 35(2), 211–213. DOI: 10.1109/LED.2013.2293354

[Li2014b] Kai-Shin Li, Ho, C., Ming-Taou Lee, Min-Cheng Chen, Cho-Lun Hsu, Lu, J. M., … Fu-Liang Yang. (2014). Utilizing Sub-5 nm sidewall electrode technology for atomic-scale resistive memory fabrication. In *2014 Symposium on VLSI Technology (VLSI-Technology): Digest of Technical Papers* (pp. 1–2). IEEE. DOI: 10.1109/VLSIT.2014.6894402

[Li2015] Li, H., Jiang, Z., Huang, P., Wu, Y., Chen, H.-Y., Gao, B., … Wong, H.-S. P. (2015). Variation-Aware, Reliability-Emphasized Design and Optimization of RRAM using SPICE Model. In Design, Automation & Test in Europe Conference & Exhibition (DATE), 2015 (Vol. 2015-April, pp. 1425–1430). New Jersey: IEEE Conference Publications. DOI: 10.7873/DATE.2015.0362

[Li2015b] Li, Y., Long, S., Liu, Y., Hu, C., Teng, J., Liu, Q., … Liu, M. (2015). Conductance Quantization in Resistive Random Access Memory. *Nanoscale Research Letters*, *10*(1). DOI: 10.1186/s11671-015-1118-6

[Li2019] Li, B., Yan, B., & Li, H. (2019). An Overview of In-memory Processing with Emerging Non-volatile Memory for Data-intensive Applications. In *Proceedings of the 2019 on Great Lakes Symposium on VLSI - GLSVLSI '19* (pp. 381–386). New York, New York, USA: ACM Press. DOI: 10.1145/3299874.3319452

[Liao2011] Liao, Z., Gao, P., Meng, Y., Zhao, H., Bai, X., Zhang, J., & Chen, D. (2011). Electroforming and endurance behavior of Al/Pr$_{0.7}$Ca$_{0.3}$MnO /Pt devices. *Applied Physics Letters*, *99*(11), 1–4. DOI:10.1063/1.3638059

[Lian2012] Lian, X., Long, S., Cagli, C., Buckley, J., Miranda, E., Liu, M., & Suñe, J. (2012). Quantum point contact model of filamentary conduction in resistive switching memories. *2012 13th International Conference on Ultimate Integration on Silicon, ULIS 2012*, *1*(1), 101–104. DOI: 10.1109/ULIS.2012.6193367

[Lian2014] Lian, X., Cartoixà, X., Miranda, E., Perniola, L., Rurali, R., Long, S., … Suñé, J. (2014). Multi-scale quantum point contact model for filamentary conduction in resistive random access memories devices. *Journal of Applied Physics*, *115*(24), 244507. DOI: 10.1063/1.4885419

[Lim2015] Lim, E., & Ismail, R. (2015). Conduction Mechanism of Valence Change Resistive Switching Memory: A Survey. *Electronics*, *4*(3), 586–613. DOI: 10.3390/electronics4030586

[Lim2015b] Lim, W. F., Quah, H. J., Sreenivasan, S., & Cheong, K. Y. (2015). Investigation of Aloe Vera as active layer for development of organic based memory devices. *Materials Technology*, *30*(A1), A29–A35. https://doi.org/10.1179/1753555714Y.0000000259

[Lim2017] Lim, Z. X., Sreenivasan, S., Wong, Y. H., Zhao, F., & Cheong, K. Y. (2017). Filamentary Conduction in Aloe Vera Film for Memory Application. *Procedia Engineering*, *184*, 655–662. DOI: 10.1016/J.PROENG.2017.04.133

References

[Lin2007] Lin, C.-Y., Wu, C.-Y., Wu, C.-Y., Hu, C., & Tseng, T.-Y. (2007). Bistable Resistive Switching in Al_2O_3 Memory Thin Films. *Journal of The Electrochemical Society*, *154*(9), G189. DOI: 10.1149/1.2750450

[Lin2007b] Lin, C.-C., Lin, C.-Y., Lin, M.-H., Lin, C., & Tseng, T.-Y. (2007). Voltage-Polarity-Independent and High-Speed Resistive Switching Properties of V-Doped $SrZrO_3$ Thin Films. *IEEE Transactions on Electron Devices*, *54*(12), 3146–3151. DOI: 10.1109/TED.2007.908867

[Lin2007c] Lin, C. Y., Wu, C. Y., Wu, C. Y. C. Y., Lee, T. C., Yang, F. L., Hu, C., & Tseng, T. Y. (2007). Effect of top electrode material on resistive switching properties of ZrO_2 film memory devices. *IEEE Electron Device Letters*, *28*(5), 366–368. DOI: 10.1109/LED.2007.894652

[Lin2008] Lin, C. Y., Lee, D. Y., Wang, S. Y., Lin, C. C., & Tseng, T. Y. (2008). Reproducible resistive switching behavior in sputtered CeO_2 polycrystalline films. *Surface and Coatings Technology*, *203*(5–7), 480–483. DOI: 10.1016/j.surfcoat.2008.07.004

[Lin2009] Lin, Z.-H., Wang, H.-X. (2009). Image encryption based on chaos with PWL memristor in Chua's circuit. In *2009 International Conference on Communications, Circuits and Systems* (Vol. 0, pp. 964–968). DOI: 10.1109/ICCCAS.2009.5250354

[Lin2010] Lin, Zhaohui & Wang, Hongxia. (2010). Efficient Image Encryption Using a Chaos-based PWL Memristor. *IETE Technical Review*. 27. 10.4103/0256-4602.64605.

[Lin2011] Lin, C. W., Pan, T. S., Chen, M. C., Yang, Y. J., Tai, Y., & Chen, Y. F. (2011). Organic bistable memory based on Au nanoparticle/ZnO nanorods composite embedded in poly (vinylpyrrolidone) layer. *Applied Physics Letters*, *99*(2), 1–4. DOI: 10.1063/1.3605596

[Lin2011b] Lin, K.-L., Hou, T.-H., Shieh, J., Lin, J.-H., Chou, C.-T., & Lee, Y.-J. (2011). Electrode dependence of filament formation in HfO_2 resistive-switching memory. *Journal of Applied Physics*, *109*(8), 084104. DOI: 10.1063/1.3567915

[Liu2009] Liu, M., Abid, Z., Wang, W., He, X., Liu, Q., & Guan, W. (2009). Multilevel resistive switching with ionic and metallic filaments. *Applied Physics Letters*, *94*(23), 1–4. DOI: 10.1063/1.3151822

[Liu2009b] Liu, Q., Long, S., Wang, W., Zuo, Q., Zhang, S., Chen, J., & Liu, M. (2009). Improvement of Resistive Switching Properties in ZrO_2-Based ReRAM With Implanted Ti Ions. *IEEE Electron Device Letters*, *30*(12), 1335–1337. DOI: 10.1109/led.2009.2032566

[Liu2010] Liu, X., Biju, K. P., Bourim, E. M., Park, S., Lee, W., Shin, J., & Hwang, H. (2010). Low programming voltage resistive switching in reactive metal/polycrystalline $Pr_{0.7}Ca_{0.3}MnO_3$ devices. *Solid State Communications*, *150*(45–46), 2231–2235. DOI: 10.1016/j.ssc.2010.09.036

[Liu2011] Liu, K. C., Tzeng, W. H., Chang, K. M., Huang, J. J., Lee, Y. J., Yeh, P. H., … Tsai, M. J. (2011). Investigation of the effect of different oxygen partial pressure to $LaAlO_3$ thin film properties and resistive switching characteristics. *Thin Solid Films*, *520*(4), 1246–1250. DOI: 10.1016/j.tsf.2011.04.205

[Liu2012] Liu, L., Zhang, S., Luo, Y., Yuan, G., Liu, J., Yin, J., & Liu, Z. (2012). Coexistence of unipolar and bipolar resistive switching in $BiFeO_3$ and $Bi_{0.8}Ca_{0.2}FeO_3$ films. *Journal of Applied Physics*, *111*(10), 104103. DOI: 10.1063/1.4716867

[Liu2013] Tz-Yi Liu, Tian Hong Yan, Scheuerlein, R., Yingchang Chen, Lee, J. K., Balakrishnan, G., … Quader, K. (2013). A 130.7mm^2 2-layer 32Gb ReRAM memory device in 24nm technology. In *2013 IEEE International Solid-State Circuits Conference Digest of Technical Papers* (pp. 210–211). IEEE. DOI: 10.1109/ISSCC.2013.6487703

[Liu2013b] Liu, S. H., Yang, W. L., Wu, C. C., Chao, T. S., Ye, M. R., Su, Y. Y., … Tsai, M. J. (2013). High-performance polyimide-based ReRAM for nonvolatile memory application. *IEEE Electron Device Letters*, *34*(1), 123–125. DOI: 10.1109/LED.2012.2224633

[Liu2013c] Liu, D., Cheng, H., Zhu, X., Wang, G., & Wang, N. (2013). Analog memristors based on thickening/thinning of Ag nanofilaments in amorphous manganite thin films. *ACS Applied Materials and Interfaces*, *5*(21), 11258–11264. DOI: 10.1021/am403497y

[Liu2014] Liu, T., Yan, T. H., Scheuerlein, R., Chen, Y., Lee, J. K., Balakrishnan, G., … Fasoli, L. (2014). A 130.7-mm^2 2-layer 32-gb ReRAM memory device in 24-nm technology. *IEEE Journal of Solid-State Circuits*, *49*(1), 140–153. DOI: 10.1109/JSSC.2013.2280296

[Liu2016] Liu, D., Liu, Z., Li, L., & Zou, X. (2016). A Low-Cost Low-Power Ring Oscillator-Based Truly Random Number Generator for Encryption on Smart Cards. *IEEE Transactions on Circuits and Systems II: Express Briefs*, *63*(6), 608–612. DOI: 10.1109/TCSII.2016.2530800

[Long2012] Long, S., Cagli, C., Ielmini, D., Liu, M., & Suñé, J. (2012). Analysis and modeling of resistive switching statistics. *Journal of Applied Physics*, *111*(7). DOI: 10.1063/1.3699369

[Long2012b] Long, B., Li, Y., Mandal, S., Jha, R., & Leedy, K. (2012). Switching dynamics and charge transport studies of resistive random access memory devices. *Applied Physics Letters*, *101*(11). DOI: 10.1063/1.4749809

[Long2013] Long, S., Perniola, L., Cagli, C., Buckley, J., Lian, X., Miranda, E., … Suñé, J. (2013). Voltage and power-controlled regimes in the progressive unipolar RESET transition of HfO$_2$-based RRAM. *Scientific Reports*, *3*, 1–8. DOI: 10.1038/srep02929

[Long2013b] Long, S., Lian, X., Cagli, C., Cartoixà, X., Rurali, R., Miranda, E., … Suñé, J. (2013). Quantum-size effects in hafnium-oxide resistive switching. *Applied Physics Letters*, *102*(18). DOI: 10.1063/1.4802265

[Lu2014] Lu, Y., & Chen, M. (2014). Synchronizing Chaos in Memristor Based van der Pol Oscillation Circuits, 0–4. DOI: 10.1109/PEAC.2014.7038023

[Lv2015] Lv, H., Xu, X., Sun, P., Liu, H., Luo, Q., Liu, Q., … Liu, M. (2015). Atomic View of Filament Growth in Electrochemical Memristive Elements. *Scientific Reports*, *5*(1), 13311. DOI: 10.1038/srep13311

[Ma2002] Ma, L. P., Liu, J., & Yang, Y. (2002). Organic electrical bistable devices and rewritable memory cells. *Applied Physics Letters*, *80*(16), 2997–2999. DOI: 10.1063/1.1473234

[Ma2014] G. Ma, X. Tang, H. Su, Y. Li, H. Zhang and Z. Zhong. (2014). Effects of Standard Free Energy on NiO Bipolar Resistive Switching Devices. *IEEE Transactions on Electron Devices*, *61*(5), 1237–1240. DOI: 10.1109/TED.2014.2309975

[Ma2015] Ma, X., Wu, H., Wu, D., & Qian, H. (2015). A 16 Mb RRAM test chip based on analog power system with tunable write pulses. In *2015 15th Non-Volatile Memory Technology Symposium (NVMTS)* (pp. 1–3). DOI: 10.1109/NVMTS.2015.7457478

[Ma2016] Ma, W., Zhou, Z., Zhu, D., & Liu, L. (2016). Quaternary non-volatile adder implemented with HfO$_x$/TiO$_x$/HfO$_x$/TiO$_x$ multilayer-based resistive RAM. *Electronics Letters*, *52*(12), 1073–1074. DOI: 10.1049/el.2015.4198

[Mahapatra2015] Mahapatra, R., Maji, S., Horsfall, A. B., & Wright, N. G. (2015). Temperature impact on switching characteristics of resistive memory devices with HfO$_x$/TiO$_x$/HfO$_x$ stack dielectric. *Microelectronic Engineering*, *138*, 118–121. DOI: 10.1016/j.mee.2015.03.008

[Mähne2012] Mähne, H., Berger, L., Martin, D., Klemm, V., Slesazeck, S., Jakschik, S., … Mikolajick, T. (2012). Filamentary resistive switching in amorphous and polycrystalline Nb$_2$O$_5$thin films. *Solid-State Electronics*, *72*, 73–77. DOI: 10.1016/j.sse.2012.01.005

[Mahvash2010] Mahvash, M., & Parker, A. C. (2010). A memristor SPICE model for designing memristor circuits. In *2010 53rd IEEE International Midwest Symposium on Circuits and Systems* (pp. 989–992). IEEE. DOI: 10.1109/MWSCAS.2010.5548803

[Maestro2015] Maestro, M., Martin-Martinez, J., Diaz, J., Crespo-Yepes, A., Gonzalez, M. B., Rodriguez, R., … Aymerich, X. (2015). Analysis of set and reset mechanisms in Ni/HfO$_2$-based RRAM with fast ramped voltages. *Microelectronic Engineering*, *147*, 176–179. DOI: 10.1016/j.mee.2015.04.057

[Maestro2016] Maestro, M., Diaz, J., Crespo-Yepes, A., Gonzalez, M. B., Martin-Martinez, J., Rodriguez, R., … Aymerich, X. (2016). New high resolution Random Telegraph Noise (RTN) characterization method for resistive RAM. *Solid-State Electronics*, *115*, 140–145. 10.1016/j.sse.2015.08.010

[Maestro-Izquierdo2019] Maestro-Izquierdo, M., Gonzalez, M. B., & Campabadal, F. (2019). Mimicking the spike-timing dependent plasticity in HfO$_2$-based memristors at multiple time scales. *Microelectronic Engineering*, *215*(April), 111014. DOI: 10.1016/j.mee.2019.111014

References

[Makarov2011] Makarov, A., Sverdlov, V., & Selberherr, S. (2011). Stochastic model of the resistive switching mechanism in bipolar resistive random access memory: Monte Carlo simulations. *Journal of Vacuum Science & Technology B, Nanotechnology and Microelectronics: Materials, Processing, Measurement, and Phenomena*, *29*(1), 01AD03. DOI: 10.1116/1.3521503

[Maldonado2019] Maldonado, D., Roldán, A. M., González, M. B., Jiménez-Molinos, F., Campabadal, F., & Roldán, J. B. (2019). Influence of magnetic field on the operation of TiN/Ti/HfO$_2$/W resistive memories. *Microelectronic Engineering*, *215*(April). DOI: 10.1016/j.mee.2019.110983

[Marotta2010] Marotta, G. G., Macerola, A., D'Alessandro, A., Torsi, A., Cerafogli, C., Lattaro, C., … Roohparvar, F. (2010). A 3bit/Cell 32Gb NAND flash memory at 34nm with 6mb/s program throughput and with dynamic 2b/cell blocks configuration mode for a program throughput increase up to 13MB/s. *Digest of Technical Papers - IEEE International Solid-State Circuits Conference*, *53*, 444–445. DOI: 10.1109/ISSCC.2010.5433949

[Márquez2016] Márquez, C., Rodriguez, N., Gamiz, F., Ruiz, R., & Ohata, A. (2016). Electrical characterization of Random Telegraph Noise in Fully-Depleted Silicon-On-Insulator MOSFETs under extended temperature range and back-bias operation. *Solid-State Electronics*, *117*, 60–65. DOI: 10.1016/j.sse.2015.11.022

[Martín-Martínez2014] Martín-Martínez, J., Diaz, J., Rodriguez, R., Nafria, M., & Aymerich, X. (2014). New Weighted Time Lag Method for the Analysis of Random Telegraph Signals. *IEEE Electron Device Letters*, *35*(4), 479–481. DOI: 10.1109/LED.2014.2304673

[Martín-Martínez2014b] Martín-Martínez, J., Diaz, J., Rodriguez, R., Nafria, M., Aymerich, X., Roca, E., … Rubio, A. (2014). Characterization of random telegraph noise and its impact on reliability of SRAM sense amplifiers. In *2014 5th European Workshop on CMOS Variability (VARI)* (pp. 1–6). IEEE. DOI: 10.1109/VARI.2014.6957088

[Matveyev2016] Matveyev, Y., Kirtaev, R., Fetisova, A., Zakharchenko, S., Negrov, D., & Zenkevich, A. (2016). Crossbar Nanoscale HfO$_2$-Based Electronic Synapses. *Nanoscale Research Letters*, 11(1), 147. DOI: 10.1186/s11671-016-1360-6

[Mazumder2012] Mazumder, P., Kang, S. M., & Waser, R. (2012). Memristors: Devices, models, and applications. *Proceedings of the IEEE*, *100*(6), 1911–1919. 10.1109/JPROC.2012.2190812

[Mehonic2012] Mehonic, A., Cueff, S., Wojdak, M., Hudziak, S., Labbé, C., Rizk, R., & Kenyon, A. J. (2012). Electrically tailored resistance switching in silicon oxide. *Nanotechnology*, *23*(45), 455201. DOI: 10.1088/0957-4484/23/45/455201

[Mehonic2013] Mehonic, A., Vrajitoarea, A., Cueff, S., Hudziak, S., Howe, H., Labbé, C., … Kenyon, A. J. (2013). Quantum conductance in silicon oxide resistive memory devices. *Scientific Reports*, *3*, 1–8. DOI: 10.1038/srep02708

[Menzel2012] Menzel, S., Böttger, U., & Waser, R. (2012). Simulation of multilevel switching in electrochemical metallization memory cells. *Journal of Applied Physics*, *111*(1), 014501. DOI: 10.1063/1.3673239

[Menzel2015] Menzel, S., Kaupmann, P., & Waser, R. (2015). Understanding filamentary growth in electrochemical metallization memory cells using kinetic Monte Carlo simulations. *Nanoscale*, *7*(29), 12673–12681. DOI: 10.1039/C5NR02258D

[Miller2010] Miller, K. J. (2010). Fabrication and modeling of thin-film anodic titania memristors. Iowa State University. Iowa State University, Digital Repository, Ames. DOI: 10.31274/etd-180810-2909

[Milo2019] Milo, V., Zambelli, C., Olivo, P., Perez, E., Ossorio, O. G., Wenger, C., & Ielmini, D. (2019). Low-energy inference machine with multilevel HfO 2 RRAM arrays. In *ESSDERC 2019 - 49th European Solid-State Device Research Conference (ESSDERC)* (pp. 174–177). IEEE. DOI: 10.1109/ESSDERC.2019.8901818

[Miranda2001] Miranda, E., & Suñé, J. (2001). Analytic modeling of leakage current through multiple breakdown paths in SiO$_2$ films. *IEEE International Reliability Physics Symposium Proceedings*, *2001-January*, 367–379. DOI: 10.1109/RELPHY.2001.922929

[Miranda2010] Miranda, E. A., Walczyk, C., Wenger, C., & Schroeder, T. (2010). Model for the resistive switching effect in HfO$_2$ MIM structures based on the transmission properties of narrow constrictions. *IEEE Electron Device Letters*, *31*(6), 609–611. DOI: 10.1109/LED.2010.2046310

[Miranda2012] Miranda, E., Kano, S., Dou, C., Kakushima, K., Suñé, J., & Iwai, H. (2012). Nonlinear conductance quantization effects in CeO_x/SiO_2 -based resistive switching devices. *Applied Physics Letters*, *101*(1), 012910. DOI: 10.1063/1.4733356

[Mondal2012], S., Chen, H. Y., Her, J. L., Ko, F. H., & Pan, T. M. (2012). Effect of Ti doping concentration on resistive switching behaviors of Yb_2O_3 memory cell. *Applied Physics Letters*, *101*(8), 1–5. DOI: 10.1063/1.4747695

[Mondal2012b] Mondal, S., Her, J. L., Ko, F. H., & Pan, T. M. (2012). The effect of Al and Ni top electrodes in resistive switching behaviors of Yb_2O_3-based memory cells. *ECS Solid State Letters*, *1*(2), P22–P25. DOI: 10.1149/2.005202ssl

[Mondal2014] Mondal, S., Chueh, C.-H., & Pan, T.-M. (2014). Current conduction and resistive switching characteristics of Sm_2O_3 and Lu_2O_3 thin films for low-power flexible memory applications. *Journal of Applied Physics*, *115*(1), 014501. DOI: 10.1063/1.4858417

[Montesi2016] Montesi, L., Buckwell, M., Zarudnyi, K., Garnett, L., Hudziak, S., Mehonic, A., & Kenyon, A. J. (2016). Nanosecond analog programming of substoichiometric silicon oxide resistive RAM. *IEEE Transactions on Nanotechnology*, *15*(3), 428–434. DOI: 10.1109/TNANO.2016.2539925

[Morales-Masis2009] Morales-Masis, M., van der Molen, S. J., Fu, W. T., Hesselberth, M. B., & van Ruitenbeek, J. M. (2009). Conductance switching in Ag_2S devices fabricated by in situ sulfurization . *Nanotechnology*, *20*(9), 095710. DOI: 10.1088/0957-4484/20/9/095710

[Moran2011] Moran, M. J., Shapiro, H. N., Munson, B. R., Dewitt, D. P., Wiley, J., Hepburn, K., … Fleming, L. (2011). *Introduction to Thermal Systems Engineering : and Heat Transfer*. *John Wiley & Sons, Inc.* (Vol. 169). New York: John Wiley & Sons, Inc. ISBN: 0471204900

[Mott1950] Mott, N.F. and Gurney, R.W. (1950), Electronic Processes in Ionic Crystal, 2nd ed. Oxford University Press, Oxford, 1950.

[Muenstermann2010] Muenstermann, R., Menke, T., Dittmann, R., & Waser, R. (2010). Coexistence of Filamentary and Homogeneous Resistive Switching in Fe-Doped $SrTiO_3$ Thin-Film Memristive Devices. *Advanced Materials*, *22*(43), 4819– DOI: 10.1002/adma.201001872

[Munjal2019] Munjal, S., & Khare, N. (2019). Advances in resistive switching based memory devices. *Journal of Physics D: Applied Physics*, *52*(43), 433002. DOI: 10.1088/1361-6463/ab2e9e

[Muraoka2007] Muraoka, S., Osano, K., Kanzawa, Y., Mitani, S., Fujii, S., Katayama, K., … Takagi, T. (2007). Fast switching and long retention Fe-O ReRAM and its switching mechanism. *Technical Digest - International Electron Devices Meeting, IEDM*, (1), 779–782. DOI: 10.1109/IEDM.2007.4419063

[Muthuswamy2009] Muthuswamy, B., & Kokate, P. (2009). Memristor-Based Chaotic Circuits. *IETE Technical Review*, *26*(6), 417. DOI: 10.4103/0256-4602.57827

[Muthuswamy2010] B. Muthuswamy. (2010). Implementing Memristor Based Chaotic Circuits. *International Journal of Bifurcation and Chaos*, vol. 20, no. 5, pp. 1335–1350, 2010. DOI: 10.1142/S0218127410026514

[Muthuswamy2010b] B. Muthuswamy and L. O. Chua (2010). Simplest chaotic circuit. *International Journal of Bifurcation and Chaos*, vol. 20, no. 5, pp. 1567–1580, 2010. DOI: 10.1142/S0218127410027076

[Nagashima2009] Nagashima, K., Yanagida, T., Oka, K., & Kawai, T. (2009). Unipolar resistive switching characteristics of room temperature grown SnO_2 thin films. *Applied Physics Letters*, *94*(24), 242902. DOI: 10.1063/1.3156863

[Nagumo2009] Nagumo, T., Takeuchi, K., Yokogawa, S., Imai, K., & Hayashi, Y. (2009). New analysis methods for comprehensive understanding of random telegraph noise. *Technical Digest - International Electron Devices Meeting, IEDM*, 1–4. DOI: 10.1109/IEDM.2009.5424230

[Nandakumar2016] Nandakumar, S. R., & Rajendran, B. (2016). Verilog-A compact model for a novel Cu/SiO_2W quantum memristor. In 2016 International Conference on Simulation of Semiconductor Processes and Devices (SISPAD) (pp. 169–172). IEEE. DOI: 10.1109/SISPAD.2016.7605174

References

[Nardi2012] Nardi, F., Larentis, S., Balatti, S., Gilmer, D. C., & Ielmini, D. (2012). Resistive switching by voltage-driven ion migration in bipolar RRAMPart I: Experimental study. *IEEE Transactions on Electron Devices*, *59*(9), 2461–2467. DOI: 10.1109/TED.2012.2202319

[Nebashi2009] Nebashi, R., Sakimura, N., Honjo, H., Saito, S., Ito, Y., Miura, S., … Kasai, N. (2009). A 90nm 12ns 32Mb 2T1MTJ MRAM. *Digest of Technical Papers - IEEE International Solid-State Circuits Conference*, 462–464. DOI: 10.1109/ISSCC.2009.4977508

[Niu2016] Niu, G., Calka, P., Auf Der Maur, M., Santoni, F., Guha, S., Fraschke, M., … Schroeder, T. (2016). Geometric conductive filament confinement by nanotips for resistive switching of HfO_2-RRAM devices with high performance. *Scientific Reports*, *6*(April), 1–9. DOI: 10.1038/srep25757

[Oblea2010] Oblea, A. S., Timilsina, A., Moore, D., & Campbell, K. A. (2010). Silver chalcogenide based memristor devices. In The 2010 International Joint Conference on Neural Networks (IJCNN) (Vol. 3, pp. 1–3). IEEE. DOI: 10.1109/IJCNN.2010.5596775

[Oldham2011] Oldham, K. B., Myland, J. C., & Bond, A. M. (2011). *Electrochemical Science and Technology: Fundamentals and Applications*. Chichester, UK: John Wiley & Sons, Ltd. DOI: 10.1002/9781119965992

[Onofrio2015] Onofrio, N., Guzman, D., & Strachan, A. (2015). Atomic origin of ultrafast resistance switching in nanoscale electrometallization cells. *Nature Materials*, *14*(4), 440–446. DOI: 10.1038/nmat4221

[Otsuka2011] Otsuka, W., Miyata, K., Kitagawa, M., Tsutsui, K., Tsushima, T., Yoshihara, H., … Ogata, K. (2011). A 4Mb conductive-bridge resistive memory with 2.3GB/s read-throughput and 216MB/s program-throughput. In *2011 IEEE International Solid-State Circuits Conference* (pp. 210–211). IEEE. DOI: 10.1109/ISSCC.2011.5746286

[Ouyang2004] Ouyang, J., Chu, C. W., Szmanda, C. R., Ma, L., & Yang, Y. (2004). Programmable polymer thin film and non-volatile memory device. *Nature Materials*, *3*(12), 918–922. DOI: 10.1038/nmat1269

[Oyamada2003]Oyamada, T., Tanaka, H., Matsushige, K., Sasabe, H., & Adachi, C. (2003). Switching effect in Cu:TCNQ charge transfer-complex thin films by vacuum codeposition. *Applied Physics Letters*, *83*(6), 1252–1254. DOI: 10.1063/1.1600848

[Padovani2015] Padovani, A., Larcher, L., Pirrotta, O., Vandelli, L., & Bersuker, G. (2015). Microscopic Modeling of HfO_x RRAM Operations: From Forming to Switching. *IEEE Transactions on Electron Devices*, *62*(6), 1998–2006. DOI: 10.1109/TED.2015.2418114

[Pan2011] Pan, F., Yin, S., & Subramanian, V. (2011). A Detailed Study of the Forming Stage of an Electrochemical Resistive Switching Memory by KMC Simulation. *IEEE Electron Device Letters*, *32*(7), 949–951. DOI: 10.1109/LED.2011.2143691

[Pan2012] Pan, T. M., Lu, C. H., Mondal, S., & Ko, F. H. (2012). Resistive switching characteristics of Tm_2O_3, Yb_2O_3, and Lu_2O_3-based metal-insulator-metal memory devices. *IEEE Transactions on Nanotechnology*, *11*(5), 1040–1046. https://doi.org/10.1109/TNANO.2012.2211893

[Pan2014] Pan, F., Gao, S., Chen, C., Song, C., & Zeng, F. (2014). Recent progress in resistive random access memories: Materials, switching mechanisms, and performance. *Materials Science and Engineering: R: Reports*, *83*(1), 1–59. DOI: 10.1016/j.mser.2014.06.002

[Pan2015] Pan, H. W., Huang, K. P., Chen, S. Y., Peng, P. C., Yang, Z. S., Kuo, C., … Lin, C. J. (2015). 1Kbit FinFET Dielectric (FIND) RRAM in pure 16nm FinFET CMOS logic process. In *2015 IEEE International Electron Devices Meeting (IEDM)* (pp. 10.5.1-10.5.4). IEEE. DOI: 10.1109/IEDM.2015.7409670

[Panda2018] Panda, D., Sahu, P. P., & Tseng, T. Y. (2018). A Collective Study on Modeling and Simulation of Resistive Random Access Memory. *Nanoscale Research Letters*, *13*(1), 8. DOI: 10.1186/s11671-017-2419-8

[Park2007] Park, G.-S., Li, X.-S., Kim, D.-C., Jung, R.-J., Lee, M.-J., & Seo, S. (2007). Observation of electric-field induced Ni filament channels in polycrystalline NiO_x film. *Applied Physics Letters*, *91*(22), 222103. DOI: 10.1063/1.2813617

[Park2012] Park, J., Jung, S., Lee, W., Kim, S., Shin, J., Lee, D., … Hwang, H. (2012). Improved Switching Variability and Stability by Activating a Single Conductive Filament. *IEEE Electron Device Letters*, *33*(5), 646–648. DOI: 10.1109/LED.2012.2188373

[Park2012b] Park, S.-G., Yang, M. K., Ju, H., Seong, D.-J., Lee, J. M., Kim, E., … Chung, C. (2012). A non-linear ReRAM cell with sub-1µA ultralow operating current for high density vertical resistive memory (VRRAM). In *2012 International Electron Devices Meeting* (pp. 20.8.1-20.8.4). IEEE. DOI: 10.1109/IEDM.2012.6479084

[Park2016], J., Kwak, M., Moon, K., Woo, J., Lee, D., & Hwang, H. (2016). TiO_x-Based RRAM Synapse With 64-Levels of Conductance and Symmetric Conductance Change by Adopting a Hybrid Pulse Scheme for Neuromorphic Computing. *IEEE Electron Device Letters*, *37*(12), 1559–1562. DOI: 10.1109/LED.2016.2622716

[Paul2006] Paul, S., Kanwal, A., & Chhowalla, M. (2006). Memory effect in thin films of insulating polymer and C60 nanocomposites. *Nanotechnology*, *17*(1), 145–151. DOI: https://doi.org/10.1088/0957-4484/17/1/023

[Pedro2017] Pedro, M., Martin-Martinez, J., Gonzalez, M. B., Rodriguez, R., Campabadal, F., Nafria, M., & Aymerich, X. (2017). Tuning the conductivity of resistive switching devices for electronic synapses. *Microelectronic Engineering*, *178*, 89–92. DOI: 10.1016/j.mee.2017.04.040

[Pedro2018] Pedro, M., Martin-Martinez, J., Miranda, E., Rodriguez, R., Nafria, M., Gonzalez, M. B., & Campabadal, F. (2018). Device variability tolerance of a RRAM-based self-organizing neuromorphic system. In *2018 IEEE International Reliability Physics Symposium (IRPS)* (Vol. 2018-March, p. P-CR.4-1-P-CR.4-5). IEEE. DOI: 10.1109/IRPS.2018.8353657

[Pedro2019] Pedró, M., Martín-Martínez, J., Maestro-Izquierdo, M., Rodríguez, R., & Nafría, M. (2019). Self-Organizing Neural Networks Based on OxRAM Devices under a Fully Unsupervised Training Scheme. *Materials*, *12*(21), 3482. DOI: 10.3390/ma12213482

[Pedro2019b] Pedro, M., Martin-Martinez, J., Rodriguez, R., Gonzalez, M. B., Campabadal, F., & Nafria, M. (2019). A flexible characterization methodology of RRAM: Application to the modeling of the conductivity changes as synaptic weight updates. *Solid-State Electronics*, *159*(March), 57–62. DOI: 10.1016/j.sse.2019.03.035

[Pedro2019c] Pedro, M., Martin-Martinez, J., Rodriguez, R., Gonzalez, M. B., Campabadal, F., & Nafria, M. (2019). An unsupervised and probabilistic approach to Pavlov's dog experiment with OxRAM devices. *Microelectronic Engineering*, *215*(April), 111024. DOI: 10.1016/j.mee.2019.111024

[Peng2009] Peng, H., & Wu, T. (2009). Nonvolatile resistive switching in spinel $ZnMn_2O_4$ and ilmenite $ZnMnO_3$. *Applied Physics Letters*, *95*(15), 152106. DOI: 10.1063/1.3249630

[Peng2013] Peng, H. Y., Pu, L., Wu, J. C., Cha, D., Hong, J. H., Lin, W. N., … Wu, T. (2013). Effects of electrode material and configuration on the characteristics of planar resistive switching devices. *APL Materials*, *1*(5), 052106. DOI: 10.1063/1.4827597

[Perez2019] Perez, E., Zambelli, C., Mahadevaiah, M. K., Olivo, P., & Wenger, C. (2019). Toward Reliable Multi-Level Operation in RRAM Arrays: Improving Post-Algorithm Stability and Assessing Endurance/Data Retention. *IEEE Journal of the Electron Devices Society*, *7* (July), 740–747. DOI: 10.1109/JEDS.2019.2931769

[Perez2019b] Pérez, E., Maldonado, D., Acal, C., Ruiz-Castro, J. E., Alonso, F. J., Aguilera, A. M., … Roldán, J. B. (2019). Analysis of the statistics of device-to-device and cycle-to-cycle variability in TiN/Ti/Al:HfO_2/TiN RRAMs. *Microelectronic Engineering*, *214*(April), 104–109. DOI: 10.1016/j.mee.2019.05.004

[Pershin2009] Pershin, Y. V., La Fontaine, S., & Di Ventra, M. (2009). Memristive model of amoeba learning. *Physical Review E*, *80*(2), 021926. DOI: 10.1103/PhysRevE.80.021926

[Pershin2010] Pershin, Y. V., & Di Ventra, M. (2010). Experimental demonstration of associative memory with memristive neural networks. *Neural Networks*, *23*(7), 881–886. DOI: 10.1016/j.neunet.2010.05.001

[Pershin2010b] Pershin, Y. V., & Di Ventra, M. (2010). Practical Approach to Programmable Analog Circuits With Memristors. *IEEE Transactions on Circuits and Systems I: Regular Papers*, *57*(8), 1857–1864. DOI: 10.1109/TCSI.2009.2038539

References

[Pham2015] Pham, V.-T., Volos, C. K., Vaidyanathan, S., Le, T. P., & Vu, V. Y. (2015). A Memristor - Based Hyperchaotic System with Hidden Attractors : Dynamics , Synchronization and Circuital Emulating. *Journal of Engineering Science and Technology Review*, 8(2), 205–214. DOI: 10.25103/jestr.082.26

[Pickett2009] Pickett, M. D., Strukov, D. B., Borghetti, J. L., Yang, J. J., Snider, G. S., Stewart, D. R., & Williams, R. S. (2009). Switching dynamics in titanium dioxide memristive devices. Journal of Applied Physics, 106(7), 074508. DOI: 10.1063/1.3236506

[Picos2015] Picos, R., Roldan, J. B., Al Chawa, M. M., Garcia-Fernandez, P., Jimenez-Molinos, F., & Garcia-Moreno, E. (2015). Semiempirical Modeling of Reset Transitions in Unipolar Resistive-Switching based Memristors. *Radioengineering*, 24(2), 420–424. DOI: 10.13164/re.2015.0420

[Picos2016] Picos, R., Roldan, J. B., Chawa, M. M. Al, Jimenez-Molinos, F., & Garcia-Moreno, E. (2016). A physically based circuit model to account for variability in memristors with resistive switching operation. In *2016 Conference on Design of Circuits and Integrated Systems (DCIS)* (pp. 1–6). IEEE. DOI: 10.1109/DCIS.2016.7845383

[Pino2010] Pino, R. E., Bohl, J. W., McDonald, N., Wysocki, B., Rozwood, P., Campbell, K. A., … Timilsina, A. (2010). Compact method for modeling and simulation of memristor devices: Ion conductor chalcogenide-based memristor devices. In 2010 IEEE/ACM International Symposium on Nanoscale Architectures (pp. 1–4). IEEE. DOI: 10.1109/NANOARCH.2010.5510936

[Poblador2017] Poblador, S., Gonzalez, M. B., & Campabadal, F. (2018). Investigation of the multilevel capability of TiN/Ti/HfO$_2$/W resistive switching devices by sweep and pulse programming. *Microelectronic Engineering*, 187–188, 148–153. DOI: 10.1016/j.mee.2017.11.007

[Potember1979] Potember, R. S., Poehler, T. O., & Cowan, D. O. (1979). Electrical switching and memory phenomena in Cu-TCNQ thin films. *Applied Physics Letters*, 34(6), 405–407. DOI: 10.1063/1.90814

[Prócel2013] Prócel, L. M., Trojman, L., Moreno, J., Crupi, F., Maccaronio, V., Degraeve, R., … Simoen, E. (2013). Experimental evidence of the quantum point contact theory in the conduction mechanism of bipolar HfO$_2$-based resistive random access memories. *Journal of Applied Physics*, 114(7). DOI: 10.1063/1.4818499

[PTM2016] Predictive Technology Model (PTM). Nanoscale Integration and Modeling (NIMO) Group at Arizona State University. Available: http://ptm.asu.edu Accessed:2016-08-25

[Puglisi2013] Puglisi, F. M., Pavan, P., Padovani, A., Larcher, L., & Bersuker, G. (2013). RTS noise characterization of HfO$_x$ RRAM in high resistive state. *Solid-State Electronics*, 84, 160–166. DOI: 10.1016/j.sse.2013.02.023

[Puglisi2015] Puglisi, F. M., Pavan, P., Vandelli, L., Padovani, A., Bertocchi, M., & Larcher, L. (2015). A microscopic physical description of RTN current fluctuations in HfO$_x$ RRAM. *IEEE International Reliability Physics Symposium Proceedings*, 2015-May, 5B51-5B56. DOI: 10.1109/IRPS.2015.7112746

[Puglisi2018] Puglisi, F. M., Zagni, N., Larcher, L., & Pavan, P. (2018). Random Telegraph Noise in Resistive Random Access Memories: Compact Modeling and Advanced Circuit Design. *IEEE Transactions on Electron Devices*, 65(7), 2964–2972. DOI: 10.1109/TED.2018.2833208

[Qazi2011] Qazi, M., Clinton, M., Bartling, S., & Chandrakasan, A. P. (2011). A low-voltage 1Mb FeRAM in 0.13µm CMOS featuring time-to-digital sensing for expanded operating margin in scaled CMOS. *Digest of Technical Papers - IEEE International Solid-State Circuits Conference*, 208–209. DOI: 10.1109/ISSCC.2011.5746285

[Qiao2018] Qiao, X., Cao, X., Yang, H., Song, L., & Li, H. (2018). Atomlayer: A Universal ReRAM-Based CNN Accelerator with Atomic Layer Computation. In *Proceedings of the 55th Annual Design Automation Conference on - DAC '18* (Vol. Part F1377, pp. 1–6). New York, New York, USA: ACM Press. DOI: 10.1145/3195970.3195998

[Quintero2007] Quintero, M., Levy, P., Leyva, A. G., & Rozenberg, M. J. (2007). Mechanism of Electric-Pulse-Induced Resistance Switching in Manganites. *Physical Review Letters*, 98(11), 116601. DOI: 10.1103/PhysRevLett.98.116601

[Quinteros2014] Quinteros, C., Zazpe, R., Marlasca, F. G., Golmar, F., Casanova, F., Stoliar, P., … Levy, P. (2014). HfO$_2$ based memory devices with rectifying capabilities. *Journal of Applied Physics*, *115*(2), 024501. DOI: 10.1063/1.4861167

[Radwan2010] Radwan, A. G., Zidan, M. A., & Salama, K. N. (2010). On the mathematical modeling of memristors. In *2010 International Conference on Microelectronics* (Vol. 8, pp. 284–287). IEEE. DOI: 10.1109/ICM.2010.5696139

[Rahaman2012] Rahaman, S. Z., Maikap, S., Chen, W. S., Lee, H. Y., Chen, F. T., Kao, M. J., & Tsai, M. J. (2012). Repeatable unipolar/bipolar resistive memory characteristics and switching mechanism using a Cu nanofilament in a GeO$_x$ film. *Applied Physics Letters*, *101*(7), 1–6. DOI: 10.1063/1.4745783

[Rajendran2010] Rajendran, J., Manem, H., Karri, R., & Rose, G. S. (2010). Memristor based programmable threshold logic array. In *2010 IEEE/ACM International Symposium on Nanoscale Architectures* (pp. 5–10). IEEE. DOI: 10.1109/NANOARCH.2010.5510933

[Rák2010] Rak, Á., & Cserey, G. (2010). Macromodeling of the Memristor in SPICE. *IEEE Transactions on Computer-Aided Design of Integrated Circuits and Systems*, *29*(4), 632–636. DOI: 10.1109/TCAD.2010.2042900

[Realov2013] Realov, S., & Shepard, K. L. (2013). Analysis of random telegraph noise in 45-nm CMOS using on-chip characterization system. *IEEE Transactions on Electron Devices*, *60*(5), 1716–1722. DOI: 10.1109/TED.2013.2254118

[Reuben2019] Reuben, J., Fey, D., & Wenger, C. (2019). A Modeling Methodology for Resistive RAM Based on Stanford-PKU Model With Extended Multilevel Capability. IEEE Transactions on Nanotechnology, 18, 647–656. DOI: 10.1109/TNANO.2019.2922838

[Rizk2019] Rizk, R., Rizk, D., Kumar, A., & Bayoumi, M. (2019). Demystifying emerging nonvolatile memory technologies: Understanding advantages, challenges, trends, and novel applications. *Proceedings - IEEE International Symposium on Circuits and Systems*, *2019-May*. DOI: 10.1109/ISCAS.2019.8702390

[Rodriguez-Fernandez2017] Rodriguez-Fernandez, A., Aldana, S., Campabadal, F., Sune, J., Miranda, E., Jimenez-Molinos, F., … Gonzalez, M. B. (2017). Resistive Switching with Self-Rectifying Tunability and Influence of the Oxide Layer Thickness in Ni/HfO$_2$/n$^+$-Si RRAM Devices. *IEEE Transactions on Electron Devices*, *64*(8), 3159–3166. DOI: 10.1109/TED.2017.2717497

[Rodriguez-Fernandez2018] Rodriguez-Fernandez, A., Suñé, J., Miranda, E., Gonzalez, M. B., Campabadal, F., Chawa, M. M. Al, & Picos, R. (2018). SPICE model for the ramp rate effect in the reset characteristic of memristive devices. *2017 32nd Conference on Design of Circuits and Integrated Systems, DCIS 2017 - Proceedings*, *2017-November*, 1–4. DOI: 10.1109/DCIS.2017.8311635

[Rohde2005] Rohde, C., Choi, B. J., Jeong, D. S., Choi, S., Zhao, J.-S., & Hwang, C. S. (2005). Identification of a determining parameter for resistive switching of TiO$_2$ thin films. *Applied Physics Letters*, *86*(26), 262907. DOI: 10.1063/1.1968416

[Rose2012] Rose, G. S., Rajendran, J., Manem, H., Karri, R., & Pino, R. E. (2012). Leveraging Memristive Systems in the Construction of Digital Logic Circuits. *Proceedings of the IEEE*, *100*(6), 2033–2049. DOI:10.1109/JPROC.2011.2167489

[Roldán2018] Roldán, J. B., Miranda, E., **González-Cordero, G**., García-Fernández, P., Romero-Zaliz, R., González-Rodelas, P., … Jiménez-Molinos, F. (2018). Multivariate analysis and extraction of parameters in resistive RAMs using the Quantum Point Contact model. *Journal of Applied Physics*, *123*(1), 014501. DOI: 10.1063/1.5006995

[Roldán2019] Roldán, J. B., Alonso, F. J., Aguilera, A. M., Maldonado, D., & Lanza, M. (2019). Time series statistical analysis: A powerful tool to evaluate the variability of resistive switching memories. *Journal of Applied Physics*, *125*(17), 174504. DOI: 10.1063/1.5079409

[Russo2007] Russo, U., Ielmini, D., Cagli, C., Lacaita, A. L., Spiga, S., Wiemer, C., … Fanciulli, M. (2007). Conductive-filament switching analysis and self-accelerated thermal dissolution model for reset in NiO-based RRAM. In *2007 IEEE International Electron Devices Meeting* (pp. 775–778). IEEE. DOI: 10.1109/IEDM.2007.4419062

References

[Russo2009] Russo, U., Ielmini, D., Cagli, C., & Lacaita, A. L. (2009). Self-accelerated thermal dissolution model for reset programming in unipolar resistive-switching memory (RRAM) devices. *IEEE Transactions on Electron Devices*, *56*(2), 193–200. DOI: 10.1109/TED.2008.2010584

[Russo2009b] Russo, U., Ielmini, D., Cagli, C., & Lacaita, A. L. (2009). Filament Conduction and Reset Mechanism in NiO-Based Resistive-Switching Memory (RRAM) Devices. *IEEE Transactions on Electron Devices*, *56*(2), 186–192. DOI: 10.1109/TED.2008.2010583

[Sacchetto2010] Sacchetto, D., Ben-Jamaa, M. H., Carrara, S., De Micheli, G., & Leblebici, Y. (2010). Memristive devices fabricated with silicon nanowire schottky barrier transistors. In *Proceedings of 2010 IEEE International Symposium on Circuits and Systems* (pp. 9–12). IEEE. DOI: 10.1109/ISCAS.2010.5537146

[Sacchetto2011] Sacchetto, D., Doucey, M.-A., De Micheli, G., Leblebici, Y., & Carrara, S. (2011). New Insight on Bio-sensing by Nano-fabricated Memristors. *BioNanoScience*, *1*(1–2), 1–3. DOI: 10.1007/s12668-011-0002-9

[Sacchetto2013] Sacchetto, D., Gaillardon, P., Zervas, M., Carrara, S., De Micheli, G., & Leblebici, Y. (2013). Applications of Multi-Terminal Memristive Devices: A Review. *IEEE Circuits and Systems Magazine*, *13*(2), 23–41. DOI: 10.1109/MCAS.2013.2256258

[Sadaf2012] Sadaf, S. M., Liu, X., Son, M., Park, S., Choudhury, S. H., Cha, E., … Hwang, H. (2012). Highly uniform and reliable resistance switching properties in bilayer WO_x/NbO_x RRAM devices. *Physica Status Solidi (A) Applications and Materials Science*, *209*(6), 1179–1183. DOI: 10.1002/pssa.201127659

[Sakamoto2003] Sakamoto, T., Sunamura, H., Kawaura, H., Hasegawa, T., Nakayama, T., & Aonob, M. (2003). Nanometer-scale switches using copper sulfide. *Applied Physics Letters*, *82*(18), 3032–3034. DOI: 10.1063/1.1572964

[Sakamoto2007] Sakamoto, T., Lister, K., Banno, N., Hasegawa, T., Terabe, K., & Aono, M. (2007). Electronic transport in Ta_2O_5 resistive switch. *Applied Physics Letters*, *91*(9). DOI: 10.1063/1.2777170

[Sangho2011] Sangho S., Kyungmin K., Sung-Mo Kang S. (2011). Memristor Applications for Programmable Analog ICs. *IEEE Transactions on Nanotechnology*, *10*(2), 266–274. DOI: 10.1109/TNANO.2009.2038610

[Saremi2016] Saremi, M. (2016). A physical-based simulation for the dynamic behavior of photodoping mechanism in chalcogenide materials used in the lateral programmable metallization cells. *Solid State Ionics*, *290*, 1–5. DOI: 10.1016/j.ssi.2016.04.002

[Sawa2004] Sawa, A., Fujii, T., Kawasaki, M., & Tokura, Y. (2004). Hysteretic current–voltage characteristics and resistance switching at a rectifying $Ti/Pr_{0.7}Ca_{0.3}MnO_3$ interface. *Applied Physics Letters*, *85*(18), 4073–4075. DOI: 10.1063/1.1812580

[Schindler2007] Schindler, C., Thermadam, S. C. P., Waser, R., & Kozicki, M. N. (2007). Bipolar and Unipolar Resistive Switching in Cu-Doped SIO_2. *IEEE Transactions on Electron Devices*, *54*(10), 2762–2768. DOI: 10.1109/TED.2007.904402

[Schönhals2017] Schönhals, A., Rosário, C. M. M., Hoffmann-Eifert, S., Waser, R., Menzel, S., & Wouters, D. J. (2018). Role of the Electrode Material on the RESET Limitation in Oxide ReRAM Devices. *Advanced Electronic Materials*, *4*(2), 1–11. DOI: 10.1002/aelm.201700243

[Secco2016] Secco, J., Farina, M., Demarchi, D., Corinto, F., & Gilli, M. (2016). Memristor cellular automata for image pattern recognition and clinical applications. In *2016 IEEE International Symposium on Circuits and Systems (ISCAS)* (pp. 1378–1381). IEEE. DOI: 10.1109/ISCAS.2016.7527506

[Sekar2014] Sekar, D. C., Bateman, B., Raghuram, U., Bowyer, S., Bai, Y., Calarrudo, M., … Bronner, G. (2014). Technology and circuit optimization of resistive RAM for low-power, reproducible operation. In *2014 IEEE International Electron Devices Meeting* (Vol. 2015-Febru, pp. 28.3.1-28.3.4). IEEE. DOI: 10.1109/IEDM.2014.7047125

[Seo2004] Seo, S., Lee, M. J., Seo, D. H., Jeoung, E. J., Suh, D.-S., Joung, Y. S., … Park, B. H. (2004). Reproducible resistance switching in polycrystalline NiO films. *Applied Physics Letters*, *85*(23), 5655–5657. DOI: 10.1063/1.1831560

316

[Seo2005] Seo, S., Lee, M. J., Seo, D. H., Choi, S. K., Suh, D.-S., Joung, Y. S., … Park, B. H. (2005). Conductivity switching characteristics and reset currents in NiO films. *Applied Physics Letters*, *86*(9), 093509. DOI: 10.1063/1.1872217

[Seo2005b] Seo, S., Lee, M. J., Kim, D. C., Ahn, S. E., Park, B.-H., Kim, Y. S., … Park, B. H. (2005). Electrode dependence of resistance switching in polycrystalline NiO films. *Applied Physics Letters*, *87*(26), 263507. DOI: 10.1063/1.2150580

[Seong2007] Seong, D., Jo, M., Lee, D., & Hwang, H. (2007). HPHA Effect on Reversible Resistive Switching of Pt∕Nb-Doped $SrTiO_3$ Schottky Junction for Nonvolatile Memory Application. *Electrochemical and Solid-State Letters*, *10*(6), H168. DOI: 10.1149/1.2718396

[Shafiee2016] Shafiee, A., Nag, A., Muralimanohar, N., Balasubramonian, R., Strachan, J. P., Hu, M., … Srikumar, V. (2016). ISAAC: A Convolutional Neural Network Accelerator with In-Situ Analog Arithmetic in Crossbars. In *2016 ACM/IEEE 43rd Annual International Symposium on Computer Architecture (ISCA)* (pp. 14–26). IEEE. DOI: 10.1109/ISCA.2016.12

[Sharifi2010] Sharifi, m. J., & Banadaki, y. M. (2010). General spice models for memristor and application to circuit simulation of memristor-based synapses and memory cells. *Journal of Circuits, Systems and Computers*, *19*(02), 407–424. DOI: 10.1142/S0218126610006141

[Sharma2014] Sharma, Y., Misra, P., Pavunny, S. P., & Katiyar, R. S. (2015). Unipolar resistive switching behavior of high-k ternary rare-earth oxide $LaHoO_3$ thin films for non-volatile memory applications. *MRS Proceedings*, *1729*(1972), 23–28. DOI: 10.1557/opl.2015.92

[Sheridan2011] Sheridan, P., Kim, K.-H., Gaba, S., Chang, T., Chen, L., & Lu, W. (2011). Device and SPICE modeling of RRAM devices. *Nanoscale*, *3*(9), 3833. DOI: 10.1039/c1nr10557d

[Sheu2009] Sheu, S.-S., Chiang, P.-C., Lin, W.-P., Lee, H.-Y., Chen, P.-S., Chen, Y.-S., … Tsai, M.-J. (2009). A 5ns fast write multi-level non-volatile 1 K bits RRAM memory with advance write scheme. *2009 Symposium on VLSI Circuits*, 2008–2009.

[Sheu2011] Sheu, S.-S., Chang, M.-F., Lin, K.-F., Wu, C.-W., Chen, Y.-S., Chiu, P.-F., … Tsai, M.-J. (2011). A 4Mb embedded SLC resistive-RAM macro with 7.2ns read-write random-access time and 160ns MLC-access capability. In *2011 IEEE International Solid-State Circuits Conference* (Vol. 2010, pp. 200–202). IEEE. DOI: 10.1109/ISSCC.2011.5746281

[Shi2011] Shi, L. P., Yi, K. J., Ramanathan, K., Zhao, R., Ning, N., Ding, D., & Chong, T. C. (2011). Artificial cognitive memory—changing from density driven to functionality driven. *Applied Physics A*, *102*(4), 865–875. DOI: 10.1007/s00339-011-6297-0

[Shim2016] Shim, Y., Sengupta, A., & Roy, K. (2016). Low-power approximate convolution computing unit with domain-wall motion based "spin-memristor" for image processing applications. In *Proceedings of the 53rd Annual Design Automation Conference on - DAC '16* (pp. 1–6). New York, New York, USA: ACM Press. DOI: 10.1145/2897937.2898042

[Shima2007] Shima, H., Takano, F., Akinaga, H., Tamai, Y., Inoue, I. H., & Takagi, H. (2007). Resistance switching in the metal deficient-type oxides: NiO and CoO. *Applied Physics Letters*, *91*(1), 012901. DOI: 10.1063/1.2753101

[Shima2008] Shima, H., Takano, F., Muramatsu, H., Akinaga, H., Tamai, Y., Inque, I. H., & Takagi, H. (2008). Voltage polarity dependent low-power and high-speed resistance switching in CoO resistance random access memory with Ta electrode. *Applied Physics Letters*, *93*(11), 91–94. DOI: 10.1063/1.2982426

[Shima2009] Shima, H., Zhong, N., & Akinaga, H. (2009). Switchable rectifier built with Pt/TiO_x/Pt trilayer. *Applied Physics Letters*, *94*(8), 082905. DOI: 10.1063/1.3068754

[Shin2009] Shin, S., Kim, K., & Kang, S.-M. (2009). Memristor-based fine resolution programmable resistance and its applications. In *2009 International Conference on Communications, Circuits and Systems* (pp. 948–951). IEEE. DOI: 10.1109/ICCCAS.2009.5250376

[Shin2011] Shin, S., Kim, K., & Kang, S.-M. (2009). Memristor-based fine resolution programmable resistance and its applications. In *2009 International Conference on Communications, Circuits and Systems* (pp. 948–951). IEEE. DOI: 10.1109/TNANO.2009.2038610

References

[Shkabko2009] Shkabko, A., Aguirre, M. H., Marozau, I., Lippert, T., & Weidenkaff, A. (2009). Measurements of current-voltage-induced heating in the Al/SrTiO$_{3-x}$N$_y$/Al memristor during electroformation and resistance switching. *Applied Physics Letters*, *95*(15), 152109. DOI: 10.1063/1.3238563

[Shirolkar2014] Shirolkar, M. M., Hao, C., Dong, X., Guo, T., Zhang, L., Li, M., & Wang, H. (2014). Tunable multiferroic and bistable/complementary resistive switching properties of dilutely Li-doped BiFeO$_3$ nanoparticles: An effect of aliovalent substitution. *Nanoscale*, *6*(9), 4735–4744. DOI: 10.1039/c3nr05973a

[Siemon2014] Siemon, A., Menzel, S., Marchewka, A., Nishi, Y., Waser, R., & Linn, E. (2014). Simulation of TaO$_x$-based complementary resistive switches by a physics-based memristive model. In *2014 IEEE International Symposium on Circuits and Systems (ISCAS)* (pp. 1420–1423). IEEE. DOI: 10.1109/ISCAS.2014.6865411

[Silva2009] Silva, H., Gomes, H. L., Pogorelov, Y. G., Stallinga, P., de Leeuw, D. M., Araujo, J. P., … Freitas, P. P. (2009). Resistive switching in nanostructured thin films. *Applied Physics Letters*, *94*(20), 202107. DOI: 10.1063/1.3134484

[Sim2005a] Sim, H., Choi, D., Lee, D., Hasan, M., Samantaray, C. B., & Hwang, H. (2005). Reproducible resistance switching characteristics of pulsed laserdeposited polycrystalline Nb$_2$O$_5$. *Microelectronic Engineering*, *80*(SUPPL.), 260–263. DOI:10.1016/j.mee.2005.04.012

[Sim2005b] Sim, H., Choi, D., Lee, D., Seo, S., Lee, M. J., Yoo, I. K., & Hwang, H. (2005). Resistance-switching characteristics of polycrystalline Nb$_2$O$_5$ for nonvolatile memory application. *IEEE Electron Device Letters*, *26*(5), 292–294. DOI: 10.1109/LED.2005.846592

[Sim2005c] Hyunjun Sim, Hyejung Choi, Dongsoo Lee, Man Chang, Dooho Choi, Yunik Son, … Hyunsang Hwang. (2005). Excellent resistance switching characteristics of Pt/SrTiO$_3$ schottky junction for multi-bit nonvolatile memory application. In *IEEE InternationalElectron Devices Meeting, 2005. IEDM Technical Digest.* (Vol. 2005, pp. 758–761). IEEE. DOI: 10.1109/IEDM.2005.1609464

[Sokirko1996] Sokirko, A. V., & Bark, F. H. (1995). Diffusion-migration transport in a system with butler-volmer kinetics, an exact solution. *Electrochimica Acta*, *40*(12), 1983–1996. DOI: 10.1016/0013-4686(94)00359-9

[Son2010] Son, D. I., Kim, T. W., Shim, J. H., Jung, J. H., Lee, D. U., Lee, J. M., … Choi, W. K. (2010). Flexible organic bistable devices based on graphene embedded in an insulating poly(methyl methacrylate) polymer layer. *Nano Letters*, *10*(7), 2441–2447. DOI: 10.1021/nl1006036

[Song2012] Song, M. Y., Seo, Y., Kim, Y. S., Kim, H. D., An, H. M., Park, B. H., … Kim, T. G. (2012). Realization of one-diode-type resistive-switching memory with Cr-SrTiO$_3$ film. *Applied Physics Express*, *5*(9), 8–11. DOI: 10.1143/APEX.5.091202

[Song2013] Song, S. J., Seok, J. Y., Yoon, J. H., Kim, K. M., Kim, G. H., Lee, M. H., & Hwang, C. S. (2013). Real-time identification of the evolution of conducting nano-filaments in TiO$_2$ thin film ReRAM. *Scientific Reports*, *3*, 1–6. DOI: 10.1038/srep03443

[Song2017] Song, L., Qian, X., Li, H., & Chen, Y. (2017). PipeLayer: A Pipelined ReRAM-Based Accelerator for Deep Learning. In *2017 IEEE International Symposium on High Performance Computer Architecture (HPCA)* (pp. 541–552). IEEE. DOI: 10.1109/HPCA.2017.55

[Song2018] Song, L., Zhuo, Y., Qian, X., Li, H., & Chen, Y. (2018). GraphR: Accelerating Graph Processing Using ReRAM. In *2018 IEEE International Symposium on High Performance Computer Architecture (HPCA)* (Vol. 2018-Febru, pp. 531–543). IEEE. DOI: 10.1109/HPCA.2018.00052

[Sony2019] Sony to aims to commercialize 128GB and 256GB ReRAM drives in 2020 | RRAM-Info. (n.d.). Retrieved December 3, 2019, from https://www.rram-info.com/sony-aims-commercialize-128gb-and-256gb-reram-drives-2020

[Stathopoulos2017] Stathopoulos, S., Khiat, A., Trapatseli, M., Cortese, S., Serb, A., Valov, I., & Prodromakis, T. (2017). Multibit memory operation of metal-oxide bi-layer memristors. *Scientific Reports*, *7*(1), 17532. DOI: 10.1038/s41598-017-17785-1

[Stille2012] Stille, S., Lenser, C., Dittmann, R., Koehl, A., Krug, I., Muenstermann, R., … Waser, R. (2012). Detection of filament formation in forming-free resistive switching SrTiO$_3$devices with Ti top electrodes. *Applied Physics Letters*, *100*(22), 223503. DOI: 10.1063/1.4724108

[Strukov2008] Strukov, D. B., Snider, G. S., Stewart, D. R., & Williams, R. S. (2008). The missing memristor found. *Nature*, 453(7191), 80–83. DOI: 10.1038/nature06932

[Strukov2009] Strukov, D. B., & Williams, R. S. (2009). Exponential ionic drift: Fast switching and low volatility of thin-film memristors. *Applied Physics A: Materials Science and Processing*, *94*(3), 515–519. DOI: 10.1007/s00339-008-4975-3

[Sun2009] Sun, X., Sun, B., Liu, L., Xu, N., Liu, X., Han, R., … Ma, T. P. (2009). Resistive switching in CeO$_x$ films for nonvolatile memory application. *IEEE Electron Device Letters*, *30*(4), 334–336. DOI: 10.1109/LED.2009.2014256

[Sun2009b] Sun, B., Liu, Y. X., Liu, L. F., Xu, N., Wang, Y., Liu, X. Y., … Kang, J. F. (2009). Highly uniform resistive switching characteristics of TiN/ZrO$_2$/Pt memory devices. *Journal of Applied Physics*, *105*(6), 1–5. DOI: 10.1063/1.3055414

[Sun2011] Sun, Q.-Q., Gu, J.-J., Chen, L., Zhou, P., Wang, P.-F., Ding, S.-J., & Zhang, D. W. (2011). Controllable Filament With Electric Field Engineering for Resistive Switching Uniformity. *IEEE Electron Device Letters*, *32*(9), 1167–1169. DOI: 10.1109/LED.2011.2159770

[Sun2013] Sun, J., Wu, X., Liu, Q., Liu, M., & Sun, L. T. (2013). Real time observation of nanoscale multiple conductive filaments in RRAM by using advanced in-situ TEM. In *Proceedings of the 20th IEEE International Symposium on the Physical and Failure Analysis of Integrated Circuits (IPFA)* (Vol. 7, pp. 560–562). IEEE. DOI: 10.1109/IPFA.2013.6599223

[Sun2013b] Sun, J., Shen, Y., Yin, Q., & Xu, C. (2013). Compound synchronization of four memristor chaotic oscillator systems and secure communication. *Chaos: An Interdisciplinary Journal of Nonlinear Science*, *23*(1), 013140. DOI: 10.1063/1.4794794

[Sun2014] Sun, K., Zhang, K., Wang, F., Sun, W., Lu, T., Wang, B., & Cheng, W. (2014). An Increasing High Resistance State Phenomenon in Al/VO$_x$/Cu Resistive Switching Device. *ECS Transactions*, *60*(1), 1057–1062. DOI: 10.1149/06001.1057ecst

[Sun2014b] Sun, P., Liu, S., Li, L., & Liu, M. (2014). Simulation study of conductive filament growth dynamics in oxide-electrolyte-based ReRAM. *Journal of Semiconductors*, *35*(10), 104007. DOI: 10.1088/1674-4926/35/10/104007

[Suri2017] Suri, M. (2017). *Advances in Neuromorphic Hardware Exploiting Emerging Nanoscale Devices*. (M. Suri, Ed.) (Vol. 31). New Delhi: Springer India. DOI:10.1007/978-81-322-3703-7

[Symanczyk2007] Symanczyk, R., Dittrich, R., Keller, J., Kund, M., Muller, G., Ruf, B., … Duch, A. (2007). Conductive Bridging Memory Development from Single Cells to 2Mbit Memory Arrays. In *2007 Non-Volatile Memory Technology Symposium* (Vol. 00, pp. 71–75). IEEE. DOI: 10.1109/NVMT.2007.4389950

[Syu2013] Syu, Y. E., Chang, T. C., Lou, J. H., Tsai, T. M., Chang, K. C., Tsai, M. J., … Sze, S. M. (2013). Atomic-level quantized reaction of HfOx memristor. Applied Physics Letters, 102(17). DOI: 10.1063/1.4802821

[Syu2013b] Syu, Y. E., Zhang, R., Chang, T. C., Tsai, T. M., Chang, K. C., Lou, J. C., … Sze, S. M. (2013). Endurance improvement technology with nitrogen implanted in the interface of WSiO$_x$ resistance switching device. *IEEE Electron Device Letters*, *34*(7), 864–866. DOI: 10.1109/LED.2013.2260125

[Szot2006] Szot, K., Speier, W., Bihlmayer, G., & Waser, R. (2006). Switching the electrical resistance of individual dislocations in single-crystalline SrTiO3. *Nature Materials*, *5*(4), 312–320. DOI: 10.1038/nmat1614

[Tamura2006] Tamura, T., Hasegawa, T., Terabe, K., Nakayama, T., Sakamoto, T., Sunamura, H., … Aono, M. (2006). Switching property of atomic switch controlled by solid electrochemical reaction. *Japanese Journal of Applied Physics, Part 2: Letters*, *45*(12–16). DOI: 10.1143/JJAP.45.L364

References

[Tappertzhofen2012] Tappertzhofen, S., Valov, I., & Waser, R. (2012). Quantum conductance and switching kinetics of AgI-based microcrossbar cells. *Nanotechnology*, *23*(14). DOI: 10.1088/0957-4484/23/14/145703

[Tappertzhofen2015] Tappertzhofen, S., Linn, E., Menzel, S., Kenyon, A. J., Waser, R., & Valov, I. (2015). Modeling of Quantized Conductance Effects in Electrochemical Metallization Cells. *IEEE Transactions on Nanotechnology*, *14*(3), 505–512. DOI: 10.1109/TNANO.2015.2411774

[Terai2010] Terai, M., Sakotsubo, Y., Kotsuji, S., & Hada, H. (2010). Resistance Controllability of Ta_2O_5/TiO_2 Stack ReRAM for Low-Voltage and Multilevel Operation. *IEEE Electron Device Letters*, *31*(3), 204–206. DOI: 10.1109/LED.2009.2039021

[Terabe2005] Terabe, K., Hasegawa, T., Nakayama, T., & Aono, M. (2005). Quantized conductance atomic switch. *Nature*, *433*(7021), 47–50. DOI: 10.1038/nature03190

[Tetzlaff2013] Tetzlaff, R. (2013). *Memristors and memristive systems*. (R. Tetzlaff, Ed.), *Memristors and Memristive Systems* (Vol. 9781461490). New York, NY: Springer New York. DOI: 10.1007/978-1-4614-9068-5

[Tian2011] Tian, H. F., Zhao, Y. G., Jiang, X. L., Shi, J. P., Zhang, H. J., & Sun, J. R. (2011). Resistance switching effect in $LaAlO_3$/Nb-doped $SrTiO_3$ heterostructure. *Applied Physics A: Materials Science and Processing*, *102*(4), 939–942. DOI: 10.1007/s00339-011-6276-5

[Torrezan2011] Torrezan, A. C., Strachan, J. P., Medeiros-Ribeiro, G., & Williams, R. S. (2011). Sub-nanosecond switching of a tantalum oxide memristor. *Nanotechnology*, *22*(48). DOI: 10.1088/0957-4484/22/48/485203

[Tseng2009] Yuan Heng Tseng, Chia-En Huang, Kuo, C.-H., Chih, Y.-D., & Chrong Jung Lin. (2009). High density and ultra small cell size of Contact ReRAM (CR-RAM) in 90nm CMOS logic technology and circuits. In *2009 IEEE International Electron Devices Meeting (IEDM)* (Vol. 2, pp. 1–4). IEEE. DOI: 10.1109/IEDM.2009.5424408

[Tseng2011] Tseng, H.-C., Chang, T.-C., Huang, J.-J., Yang, P.-C., Chen, Y.-T., Jian, F.-Y., … Tsai, M.-J. (2011). Investigating the improvement of resistive switching trends after post-forming negative bias stress treatment. *Applied Physics Letters*, *99*(13), 132104. DOI: 10.1063/1.3645004

[Tsuruoka2012] Tsuruoka, T., Hasegawa, T., Terabe, K., & Aono, M. (2012). Conductance quantization and synaptic behavior in a Ta_2O_5-based atomic switch. *Nanotechnology*, 23(43). DOI: 10.1088/0957-4484/23/43/435705

[Valle2018] Del Valle, J., Ramírez, J. G., Rozenberg, M. J., & Schuller, I. K. (2018). Challenges in materials and devices for resistive-switching-based neuromorphic computing. *Journal of Applied Physics*, *124*(21). DOI: 10.1063/1.5047800

[Valov2013] Valov, I., Linn, E., Tappertzhofen, S., Schmelzer, S., Van Den Hurk, J., Lentz, F., & Waser, R. (2013). Nanobatteries in redox-based resistive switches require extension of memristor theory. Nature Communications, 4, 1771–1779. DOI: 10.1038/ncomms2784

[Vandelli2011] Vandelli, L., Padovani, A., Larcher, L., Broglia, G., Ori, G., Montorsi, M., … Pavan, P. (2011). Comprehensive physical modeling of forming and switching operations in HfO_2 RRAM devices. In *2011 International Electron Devices Meeting* (pp. 17.5.1-17.5.4). IEEE. DOI: 10.1109/IEDM.2011.6131574

[Verwey1935] Verwey, E. J. W. (1935). Electrolytic conduction of a solid insulator at high fields The formation of the anodic oxide film on aluminium. *Physica*, *2*(1–12), 1059–1063. DOI: 10.1016/S0031-8914(35)90193-8

[Villena2013] Villena, M. A., Jiménez-Molinos, F., Roldán, J. B., Suñé, J., Long, S., Lian, X., … Liu, M. (2013). An in-depth simulation study of thermal reset transitions in resistive switching memories. Journal of Applied Physics, 114(14), 144505. DOI: 10.1063/1.4824292

[Villena2014] Villena, M. A., González, M. B., Jiménez-Molinos, F., Campabadal, F., Roldán, J. B., Suñé, J., … Miranda, E. (2014). Simulation of thermal reset transitions in resistive switching memories including quantum effects. *Journal of Applied Physics*, *115*(21). DOI: 10.1063/1.4881500

[Villena2014b] Villena, M. A., Roldán, J. B., Jimenez-Molinos, F., Suñé, J., Long, S., Miranda, E., & Liu, M. (2014). A comprehensive analysis on progressive reset transitions in RRAMs. *Journal of Physics D: Applied Physics*, *47*(20). DOI: 10.1088/0022-3727/47/20/205102

[Villena2015] Villena, M. A., González, M. B., Roldán, J. B., Campabadal, F., Jiménez-Molinos, F., Gómez-Campos, F. M., & Suñé, J. (2015). An in-depth study of thermal effects in reset transitions in HfO$_2$ based RRAMs. *Solid-State Electronics*, *111*, 47–51. DOI: 10.1016/j.sse.2015.04.008

[Villena2016] Villena, M. A., Roldán, J. B., González, M. B., González-Rodelas, P., Jiménez-Molinos, F., Campabadal, F., & Barrera, D. (2016). A new parameter to characterize the charge transport regime in Ni/HfO$_2$/Si-n$^+$ -based RRAMs. *Solid-State Electronics*, *118*, 56–60. DOI: 10.1016/j.sse.2016.01.007

[Villena2017] Villena, M. A., Roldán, J. B., Jiménez-Molinos, F., Miranda, E., Suñé, J., & Lanza, M. (2017). SIM2RRAM : a physical model for RRAM devices simulation. Journal of Computational Electronics, 16(4), 1095–1120. DOI: 10.1007/s10825-017-1074-8

[Villena2017b] Villena, M. A., Roldán, J. B., García-Fernández, P., & Jiménez-Molinos, F. (2017). Effects of the extension of conductive filaments, a simulation approach. *Journal of Vacuum Science & Technology B, Nanotechnology and Microelectronics: Materials, Processing, Measurement, and Phenomena*, *35*(1), 01A105. DOI: 10.1116/1.4971384

[Wagenaar2012] Wagenaar, J. J. T., Morales-Masis, M., & Van Ruitenbeek, J. M. (2012). Observing quantized conductance steps in silver sulfide: Two parallel resistive switching mechanisms. *Journal of Applied Physics*, *111*(1). DOI: 10.1063/1.3672824

[Walczyk2009] Walczyk, C., Wenger, C., Sohal, R., Lukosius, M., Fox, A., Dąbrowski, J., … Schroeder, T. (2009). Pulse-induced low-power resistive switching in HfO$_2$ metal-insulator-metal diodes for nonvolatile memory applications. *Journal of Applied Physics*, *105*(11), 114103. DOI: 10.1063/1.3139282

[Walker2007] Walker, J., (2007). *Fundamentals of Physics Halliday & resnick 10ed*. Wiley. ISBN: 9781118230725

[Wang2009] Weidong Wang, Qin Yu, Chunxiang Xu, & Yuhong Cui. (2009). Study of filter characteristics based on PWL memristor. In *2009 International Conference on Communications, Circuits and Systems* (pp. 969–973). IEEE. DOI: 10.1109/ICCCAS.2009.5250355

[Wang2010] Wang, Y., Liu, Q., Long, S., Wang, W., Wang, Q., Zhang, M., … Liu, M. (2010). Investigation of resistive switching in Cu-doped HfO$_2$ thin film for multilevel non-volatile memory applications. *Nanotechnology*, *21*(4), 045202. DOI: 10.1088/0957-4484/21/4/045202

[Wang2010b] Wang, S.-Y., Huang, C.-W., Lee, D.-Y., Tseng, T.-Y., & Chang, T.-C. (2010). Multilevel resistive switching in Ti/Cu$_x$O/Pt memory devices. *Journal of Applied Physics*, *108*(11), 114110. DOI: 10.1063/1.3518514

[Wang2010c] Wang, S. Y., Lee, D. Y., Huang, T. Y., Wu, J. W., & Tseng, T. Y. (2010). Controllable oxygen vacancies to enhance resistive switching performance in a ZrO$_2$-based RRAM with embedded Mo layer. *Nanotechnology*, *21*(49). DOI: 10.1088/0957-4484/21/49/495201

[Wang2011] Wang, Z. Q., Xu, H. Y., Li, X. H., Zhang, X. T., Liu, Y. X., & Liu, Y. C. (2011). Flexible resistive switching memory device based on amorphous InGaZnO film with excellent mechanical endurance. *IEEE Electron Device Letters*, *32*(10), 1442–1444. DOI: 10.1109/LED.2011.2162311

[Wang2015] Wang, G., Long, S., Yu, Z., Zhang, M., Ye, T., Li, Y., … Liu, M. (2015). Improving resistance uniformity and endurance of resistive switching memory by accurately controlling the stress time of pulse program operation. *Applied Physics Letters*, *106*(9), 092103. DOI: 10.1063/1.4907604

[Waser2007] Waser, R., & Aono, M. (2007). Nanoionics-based resistive switching memories. *Nature Materials*, *6*(11), 833–840. DOI: 10.1038/nmat2023

[Waser2009] Waser, R., Dittmann, R., Staikov, G., & Szot, K. (2009). Redox-Based Resistive Switching Memories - Nanoionic Mechanisms, Prospects, and Challenges. *Advanced Materials*, *21*(25–26), 2632–2663. DOI: 10.1166/jnn.2012.6652

References

[Waser2012] Waser, R. (2012). *Nanoelectronics and information technology : advanced electronic materials and novel devices*. Wiley-VCH, Berlin, 2012. ISBN: 978-3-527-40927-3

[Wei2007] Wei, L. K., Tseng, R. J., Wu, W., Pei, Q., & Yang, Y. (2007). Stackable resistive memory device using photo cross-linkable copolymer. *Technical Digest - International Electron Devices Meeting, IEDM*, 237–240. DOI: 10.1109/IEDM.2007.4418911

[Wei2011] Wei, Z., Takagi, T., Kanzawa, Y., Katoh, Y., Ninomiya, T., Kawai, K., … Aono, K. (2011). Demonstration of high-density ReRAM ensuring 10-year retention at 85°C based on a newly developed reliability model. In *2011 International Electron Devices Meeting* (pp. 31.4.1-31.4.4). IEEE. DOI: 10.1109/IEDM.2011.6131650

[Wei2016] Wei, Z., Katoh, Y., Ogasahara, S., Yoshimoto, Y., Kawai, K., Ikeda, Y., … Yoneda, S. (2016). True random number generator using current difference based on a fractional stochastic model in 40-nm embedded ReRAM. In *2016 IEEE International Electron Devices Meeting (IEDM)* (pp. 4.8.1-4.8.4). IEEE. DOI: 10.1109/IEDM.2016.7838349

[Wen2011] Shiping Wen, Yi Shen, Zhigang Zeng, & Yanxia Cai. (2011). Chaos analysis and control in a chaotic circuit with a PWL memristor. In *International Conference on Information Science and Technology* (Vol. 5, pp. 1030–1033). IEEE. DOI: 10.1109/ICIST.2011.5765147

[Wen2013] Wen, S., Zeng, Z., Huang, T., & Chen, Y. (2013). Fuzzy modeling and synchronization of different memristor-based chaotic circuits. *Physics Letters A*, *377*(34–36), 2016–2021. DOI: 10.1016/j.physleta.2013.05.046

[Williams2013] Williams, R. S., Pickett, M. D., & Strachan, J. P. (2013). Physics-based memristor models. In *2013 IEEE International Symposium on Circuits and Systems (ISCAS2013)* (pp. 217–220). IEEE. DOI: 10.1109/ISCAS.2013.6571821

[Witrisal2009a] Witrisal, K. (2009). A memristor-based multicarrier UWB receiver. In *2009 IEEE International Conference on Ultra-Wideband* (Vol. 2009, pp. 679–683). IEEE. DOI: 10.1109/ICUWB.2009.5288703

[Witrisal2009b] Witrisal, K. (2009). Memristor-based stored-reference receiver–the UWB solution? *Electronics Letters*, *45*(14), 713. DOI: 10.1049/el.2009.0123

[Wong2010] Wong, H.-S. P., Raoux, S., Kim, S., Liang, J., Reifenberg, J. P., Rajendran, B., … Goodson, K. E. (2010). Phase Change Memory. *Proceedings of the IEEE*, *98*(12), 2201–2227. DOI: 10.1109/JPROC.2010.2070050

[Wong2012] Wong, H. S. P., Lee, H. Y., Yu, S., Chen, Y. S., Wu, Y., Chen, P. S., … Tsai, M. J. (2012). Metal-oxide RRAM. In *Proceedings of the IEEE* (Vol. 100, pp. 1951–1970). DOI: 10.1109/JPROC.2012.2190369

[Wong2015] Wong, H. S. P., & Salahuddin, S. (2015). Memory leads the way to better computing. *Nature Nanotechnology*, *10*(3), 191–194. DOI: 10.1038/nnano.2015.29

[Wu2011] Wu, C., Li, F., Guo, T., Qu, B., Chen, Z., & Gong, Q. (2011). Efficient nonvolatile rewritable memories based on three-dimensionally confined Au quantum dots embedded in ultrathin polyimide layers. *Japanese Journal of Applied Physics*, *50*(3), 8–11. DOI: 10.1143/JJAP.50.030204

[Wu2011b] Wu, W. T., Wu, J. J., & Chen, J. S. (2011). Resistive switching behavior and multiple transmittance states in solution-processed tungsten oxide. *ACS Applied Materials and Interfaces*, *3*(7), 2616–2621. DOI: 10.1021/am200430y

[Wu2012] Wu, J., Cao, J., Han, W. Q., Janotti, A., & Kim, H. C. (2012). *Functional Metal Oxide Nanostructures*. *Springer Series in Materials Science* (Vol. 149). DOI: 10.1007/978-1-4419-9931-3

[Wu2013] Wu, X., Cha, D., Bosman, M., Raghavan, N., Migas, D. B., Borisenko, V. E., … Pey, K. L. (2013). Intrinsic nanofilamentation in resistive switching. *Journal of Applied Physics*, *113*(11). DOI:10.1063/1.4794519

[Wu2019] Wu, T. F., Le, B. Q., Radway, R., Bartolo, A., Hwang, W., Jeong, S., … Mitra, S. (2019). 14.3 A 43pJ/Cycle Non-Volatile Microcontroller with 4.7µs Shutdown/Wake-up Integrating 2.3-bit/Cell Resistive RAM and Resilience Techniques. In *2019 IEEE International Solid- State Circuits Conference - (ISSCC)* (Vol. 2019-Febru, pp. 226–228). IEEE. DOI: 10.1109/ISSCC.2019.8662402

[Xiao2017] Xiao, N., Villena, M. A., Yuan, B., Chen, S., Wang, B., Eliáš, M., … Lanza, M. (2017). Resistive Random Access Memory Cells with a Bilayer TiO_2 /SiO_x Insulating Stack for Simultaneous Filamentary and Distributed Resistive Switching. *Advanced Functional Materials*, *27*(33), 1700384. DOI: 10.1002/adfm.201700384

[Xie2013] Xie, C., Nie, B., Zhu, L., Zeng, L. H., Yu, Y. Q., Wang, X. H., … Wu, Y. C. (2013). High-performance nonvolatile Al/AlO_x/CdTe:Sb nanowire memory device. *Nanotechnology*, *24*(35). DOI: 10.1088/0957-4484/24/35/355203

[Xiong2016] Xiong, W., & Huang, J. (2016). Finite-time control and synchronization for memristor-based chaotic system via impulsive adaptive strategy. *Advances in Difference Equations*, *2016*(1), 101. DOI: 10.1186/s13662-016-0789-3

[Xu2008] Xu, N., Liu, L. F., Sun, X., Chen, C., Wang, Y., Han, D. D., … Yu, B. (2008). Bipolar switching behavior in TiN/ZnO/Pt resistive nonvolatile memory with fast switching and long retention. *Semiconductor Science and Technology*, *23*(7), 075019. DOI: 10.1088/0268-1242/23/7/075019

[Xie2014] Xie, Y. (2014). Introduction. In Emerging Memory Technologies (pp. 1–14). New York, NY: Springer New York. DOI: 10.1007/978-1-4419-9551-3_1

[Yakopcic2011] Yakopcic, C., Taha, T. M., Subramanyam, G., Pino, R. E., & Rogers, S. (2011). A Memristor Device Model. *IEEE Electron Device Letters*, *32*(10), 1436–1438. DOI: 10.1109/LED.2011.2163292

[Yakopcic2013] Yakopcic, C., Taha, T. M., Subramanyam, G., & Pino, R. E. (2013). Generalized Memristive Device SPICE Model and its Application in Circuit Design. *IEEE Transactions on Computer-Aided Design of Integrated Circuits and Systems*, *32*(8), 1201–1214. DOI: 10.1109/TCAD.2013.2252057

[Yan2011] Yan, Z., Guo, Y., Zhang, G., & Liu, J. M. (2011). High-performance programmable memory devices based on Co-doped $BaTiO_3$. *Advanced Materials*, *23*(11), 1351–1355. DOI: 10.1002/adma.201004306

[Yan2015] Yan, P., Li, Y., Hui, Y. J., Zhong, S. J., Zhou, Y. X., Xu, L., … Miao, X. S. (2015). Conducting mechanisms of forming-free TiW/Cu_2O/Cu memristive devices. *Applied Physics Letters*, *107*(8), 083501. DOI: 10.1063/1.4928979

[Yang2008] Yang, J. J., Pickett, M. D., Li, X., Ohlberg, D. A. A., Stewart, D. R., & Williams, R. S. (2008). Memristive switching mechanism for metal/oxide/metal nanodevices. *Nature Nanotechnology*, *3*(7), 429–433. DOI: 10.1038/nnano.2008.160

[Yang2009] Yang, J. J., Borghetti, J., Murphy, D., Stewart, D. R., & Williams, R. S. (2009). A Family of Electronically Reconfigurable Nanodevices. *Advanced Materials*, *21*(37), 3754–3758. DOI: 10.1002/adma.200900822

[Yang2009b] Yang, R., Li, X. M., Yu, W. D., Gao, X. D., Liu, X. J., Cao, X., … Chen, L. D. (2009). Stable bipolar resistance switching behaviour induced by a soft breakdown process at the Al/$La_{0.7}Ca_{0.3}MnO_3$ interface. *Journal of Physics D: Applied Physics*, *42*(17), 175408. DOI: 10.1088/0022-3727/42/17/175408

[Yang2009c], M. K., Park, J. W., Ko, T. K., & Lee, J. K. (2009). Bipolar resistive switching behavior in Ti/ MnO2 /Pt structure for nonvolatile memory devices. *Applied Physics Letters*, *95*(4), 1–4. DOI: 10.1063/1.3191674

[Yang2009d] Yang, Y. C., Pan, F., Liu, Q., Liu, M., & Zeng, F. (2009). Fully room-temperature-fabricated nonvolatile resistive memory for ultrafast and high-density memory application. *Nano Letters*, *9*(4), 1636–1643. DOI: 10.1021/nl900006g

[Yang2010] Yang, J. J., Zhang, M.-X., Strachan, J. P., Miao, F., Pickett, M. D., Kelley, R. D., … Williams, R. S. (2010). High switching endurance in TaO_x memristive devices. *Applied Physics Letters*, *97*(23), 232102. DOI: 10.1063/1.3524521

References

[Yang2012] Yang, Y., Sheridan, P., & Lu, W. (2012). Complementary resistive switching in tantalum oxide-based resistive memory devices. *Applied Physics Letters*, *100*(20). DOI: 10.1063/1.4719198

[Yang2013] Yang, Y., & Lu, W. (2013). Nanoscale resistive switching devices: mechanisms and modeling. *Nanoscale*, *5*(21), 10076. DOI: 10.1039/c3nr03472k

[Yang2013b] Yang, J. B., Chang, T. C., Huang, J. J., Chen, S. C., Yang, P. C., Chen, Y. T., … Tsai, M. J. (2013). Resistive switching characteristics of gallium oxide for nonvolatile memory application. *Thin Solid Films*, *529*, 200–204. DOI: 10.1016/j.tsf.2012.10.026

[Yang2015] Yang, J., Xu, J., Wang, B., Xue, X., Huang, R., Zhou, Q., … Lin, Y. (2015). A low cost and high reliability true random number generator based on resistive random access memory. In *2015 IEEE 11th International Conference on ASIC (ASICON)* (pp. 1–4). IEEE. DOI: 10.1109/ASICON.2015.7516996

[Ye2010] Ye, J. Y., Li, Y. Q., Gao, J., Peng, H. Y., Wu, S. X., & Wu, T. (2010). Nanoscale resistive switching and filamentary conduction in NiO thin films. *Applied Physics Letters*, *97*(13), 132108. DOI: 10.1063/1.3494267

[Yen2019] Yen, T. J., Gismatulin, A., Volodin, V., Gritsenko, V., & Chin, A. (2019). All Nonmetal Resistive Random Access Memory. *Scientific Reports*, *9*(1), 6144. DOI: 10.1038/s41598-019-42706-9

[Yi2011] Yi, J., Choi, H., Lee, S., Lee, J., Son, D., Lee, S., … Hong, S. J. (2011). Highly reliable and fast nonvolatile hybrid switching ReRAM memory using thin Al 2 O 3 demonstrated at 54nm memory array. Digest of Technical Papers - Symposium on VLSI Technology, 48–49.

[Yin2008] Yin, M., Zhou, P., Lv, H. B., Tang, T. A., Chen, B. A., Lin, Y. Y., … Chi, M. H. (2008). Enhancement of endurance for Cu_xO based RRAM cell. In *2008 9th International Conference on Solid-State and Integrated-Circuit Technology* (pp. 917–920). IEEE. DOI: 10.1109/ICSICT.2008.4734695

[Yin2012] Yin Chen, Y., Pourtois, G., Adelmann, C., Goux, L., Govoreanu, B., Degreave, R., … Wouters, D. J. (2012). Insights into Ni-filament formation in unipolar-switching Ni/HfO 2 /TiN resistive random access memory device. *Applied Physics Letters*, *100*(11), 113513. DOI: 10.1063/1.3695078

[Yoshida2007] Yoshida, C., Tsunoda, K., Noshiro, H., & Sugiyama, Y. (2007). High speed resistive switching in Pt/Ti/ /O₂/TiN film for nonvolatile memory application. *Applied Physics Letters*, *91*(22), 89–92. DOI: https://doi.org/10.1063/1.2818691

[Yoshida2008] Yoshida, C., Kurasawa, M., Lee, Y. M., Aoki, M., & Sugiyama, Y. (2008). Unipolar resistive switching in CoFeBMgOCoFeB magnetic tunnel junction. *Applied Physics Letters*, *92*(11), 6–9. DOI: 10.1063/1.2898514

[Yoshida2008b], C., Kinoshita, K., Yamasaki, T., & Sugiyama, Y. (2008). Direct observation of oxygen movement during resistance switching in NiO/Pt film. *Applied Physics Letters*, *93*(4). DOI: 10.1063/1.2966141

[Yu2008] Lee-Eun Yu, Sungho Kim, Min-Ki Ryu, Sung-Yool Choi, & Yang-Kyu Choi. (2008). Structure Effects on Resistive Switching of Al/TiOₓ/Al Devices for RRAM Applications. *IEEE Electron Device Letters*, *29*(4), 331–333. DOI: 10.1109/LED.2008.918253

[Yu2010] Yu, S., Gao, B., Dai, H., Sun, B., Liu, L., Liu, X., … Yu, B. (2010). Improved Uniformity of Resistive Switching Behaviors in HfO₂Thin Films with Embedded Al Layers. *Electrochemical and Solid-State Letters*, *13*(2), H36. DOI: 10.1149/1.3267050

[Yu2011] Yu, S., Wu, Y., Jeyasingh, R., Kuzum, D., & Wong, H.-S. P. (2011). An Electronic Synapse Device Based on Metal Oxide Resistive Switching Memory for Neuromorphic Computation. *IEEE Transactions on Electron Devices*, *58*(8), 2729–2737. DOI: 10.1109/TED.2011.2147791

[Yu2011b] Yu, S., Guan, X., & Wong, H. S. P. (2011). Conduction mechanism of TiNHfOₓPt resistive switching memory: A trap-assisted-tunneling model. *Applied Physics Letters*, *99*(6), 16–19. DOI: 10.1063/1.3624472

[Yu2011c] Yu, S., Wu, Y., Chai, Y., Provine, J., & Wong, H. S. P. (2011). Characterization of switching parameters and multilevel capability in HfO$_x$/AlO$_x$ bi-layer RRAM devices. *International Symposium on VLSI Technology, Systems, and Applications, Proceedings*, 106–107. DOI: 10.1109/VTSA.2011.5872251

[Yu2011d] Yu, S., Ximeng Guan, & Wong, H.-S. P. (2011). On the stochastic nature of resistive switching in metal oxide RRAM: Physical modeling, monte carlo simulation, and experimental characterization. In *2011 International Electron Devices Meeting* (pp. 17.3.1-17.3.4). IEEE. DOI: 10.1109/IEDM.2011.6131572

[Yu2012] Yu, S., Gao, B., Fang, Z., Yu, H., Kang, J., & Wong, H.-S. P. (2012). A neuromorphic visual system using RRAM synaptic devices with Sub-pJ energy and tolerance to variability: Experimental characterization and large-scale modeling. In *2012 International Electron Devices Meeting* (pp. 10.4.1-10.4.4). IEEE. DOI: 10.1109/IEDM.2012.6479018

[Yu2012b] Yu, S., Yin Chen, Y., Guan, X., Philip Wong, H.-S., & Kittl, J. A. (2012). A Monte Carlo study of the low resistance state retention of HfO$_x$ based resistive switching memory. *Applied Physics Letters*, *100*(4), 043507. DOI: 10.1063/1.3679610

[Yu2012c] Yu, S., Guan, X., & Wong, H.-S. P. (2012). On the Switching Parameter Variation of Metal Oxide RRAM—Part II: Model Corroboration and Device Design Strategy. *IEEE Transactions on Electron Devices*, *59*(4), 1183–1188. DOI: 10.1109/TED.2012.2184544

[Yu2014] Yu, H., & Wang, Y. (2014). Design exploration of emerging nano-scale non-volatile memory. Design Exploration of Emerging Nano-Scale Non-Volatile Memory (Vol. 9781493905515, pp. 1–192). Springer New York. DOI: 10.1007/978-1-4939-0551-5

[Yu2017] Yu, S. (Electrical engineer). (2017). *Neuro-inspired Computing Using Resistive Synaptic Devices*. (S. Yu, Ed.), Cham: Springer International Publishing. ISBN: 978-3-319-54312-3. DOI: 10.1007/978-3-319-54313-0

[Yun1993] Yun, E., Becker, M. F., & Walser, R. M. (1993). Room temperature conductance quantization in V‖amorphous-V$_2$O$_5$‖V thin film structures. *Applied Physics Letters*, *63*(18), 2493–2495. DOI: 10.1063/1.110459

[Zahurak2014] Zahurak, J., Miyata, K., Fischer, M., Balakrishnan, M., Chhajed, S., Wells, D., … Prall, K. (2014). Process integration of a 27nm, 16Gb Cu ReRAM. In *2014 IEEE International Electron Devices Meeting* (pp. 6.2.1-6.2.4). IEEE. DOI: 10.1109/IEDM.2014.7046994

[Zangeneh2014] Zangeneh, M., & Joshi, A. (2014). Design and optimization of nonvolatile multibit 1T1R resistive RAM. *IEEE Transactions on Very Large Scale Integration (VLSI) Systems*, *22*(8), 1815–1828. DOI: 10.1109/TVLSI.2013.2277715

[Zeng2014]. Zeng, B., Xu, D., Tang, M., Xiao, Y., Zhou, Y., Xiong, R., … Zhou, Y. (2014). Improvement of resistive switching performances via an amorphous ZrO$_2$ layer formation in TiO$_2$ -based forming-free resistive random access memory. Journal of Applied Physics, 116(12), 124514. DOI: 10.1063/1.4896402

[Zha2017] Zha, Y., Wei, Z., & Li, J. (2017). Recent progress in RRAM technology: From compact models to applications. *China Semiconductor Technology International Conference 2017, CSTIC 2017*, 1–4. DOI: 10.1109/CSTIC.2017.7919731

[Zhang2009] Lijie Zhang, Ru Huang, Dejin Gao, Dake Wu, Yongbian Kuang, Poren Tang, … Yangyuan Wang. (2009). Unipolar Resistive Switch Based on Silicon Monoxide Realized by CMOS Technology. *IEEE Electron Device Letters*, *30*(8), 870–872. DOI: 10.1109/LED.2009.2024650

[Zhang2011] Zhang, X. T., Yu, Q. X., Yao, Y. P., & Li, X. G. (2010). Ultrafast resistive switching in SrTiO3:Nb single crystal. *Applied Physics Letters*, *97*(22), 3–6. DOI: 10.1063/1.3524216

[Zhang2014] Zhang, Y., Deng, N., Wu, H., Yu, Z., Zhang, J., & Qian, H. (2014). Metallic to hopping conduction transition in Ta$_2$O$_{5-x}$/TaO$_y$ y resistive switching device. *Applied Physics Letters*, *105*(6), 063508. DOI: 10.1063/1.4893325

[Zhang2014b] Zhang, R., Young, T.-F., Chen, M.-C., Chen, H.-L., Liang, S.-P., Syu, Y.-E., … Chen, J.-H. (2014). Characterization of Oxygen Accumulation in Indium-Tin-Oxide for Resistance Random Access Memory. *IEEE Electron Device Letters*, *35*(6), 630–632. DOI: 10.1109/LED.2014.2316806

References

[Zhao2012] Zhao, W., Chaudhuri, S., Accoto, C., Klein, J.-O., Ravelosona, D., Chappert, C., & Mazoyer, P. (2012). High Density Spin-Transfer Torque (STT)-MRAM Based on Cross-Point Architecture. In *2012 4th IEEE International Memory Workshop* (pp. 1–4). IEEE. DOI: 10.1109/IMW.2012.6213618

[Zhao2014] Zhao, L., Zizhen Jiang, Chen, H.-Y., Sohn, J., Okabe, K., Magyari-Kope, B., … Nishi, Y. (2014). Ultrathin (2nm) HfO$_x$ as the fundamental resistive switching element: Thickness scaling limit, stack engineering and 3D integration. In *2014 IEEE International Electron Devices Meeting* (Vol. 2015-Febru, pp. 6.6.1-6.6.4). IEEE. DOI: 10.1109/IEDM.2014.7046998

[Zhao2016] Zhao, Y., Jiang, Y., Feng, J., & Wu, L. (2016). Modeling of memristor-based chaotic systems using nonlinear Wiener adaptive filters based on backslash operator. *Chaos, Solitons & Fractals*, *87*, 12–16. DOI: 10.1016/j.chaos.2016.03.004

[Zhao2016b] Zhao, Y. D., Huang, P., Guo, Z. H., Lun, Z. Y., Gao, B., Liu, X. Y., & Kang, J. F. (2016). Atomic Monte-Carlo simulation for CBRAM with various filament geometries. In *2016 International Conference on Simulation of Semiconductor Processes and Devices (SISPAD)* (pp. 153–156). IEEE. DOI: 10.1109/SISPAD.2016.7605170

[Zhong2014] Zhong, L., Reed, P. A., Huang, R., de Groot, C. H., & Jiang, L. (2014). Resistive switching of Cu/SiC/Au memory devices with a high ON/OFF ratio. *Solid-State Electronics*, *94*, 98–102. DOI: 10.1016/j.sse.2014.02.013

[Zhong2014b] Zhong, L., Jiang, L., Huang, R., & de Groot, C. H. (2014). Nonpolar resistive switching in Cu/SiC/Au non-volatile resistive memory devices. *Applied Physics Letters*, *104*(9), 093507. DOI: 10.1063/1.4867198

[Zhou2012] Zhou, Q., & Zhai, J. (2012). Study of the resistive switching characteristics and mechanisms of Pt/CeO$_x$/TiN structure for RRAM applications. In *Integrated Ferroelectrics* (Vol. 140, pp. 16–22). Taylor & Francis Group. DOI: 10.1080/10584587.2012.741372

[Zhou2014] Zhou, Q., & Zhai, J. (2014). Study of the bipolar resistive-switching behaviors in Pt/GdO$_x$/TaN$_x$ structure for RRAM application. *Physica Status Solidi (A) Applications and Materials Science*, *211*(1), 173–179. DOI: 10.1002/pssa.201330098

[Zhu2009] Zhu, W., Chen, T. P., Liu, Z., Yang, M., Liu, Y., & Fung, S. (2009). Resistive switching in aluminum/anodized aluminum film structure without forming process. *Journal of Applied Physics*, *106*(9). DOI: 10.1063/1.3253722

[Zhu2012] Zhu, X., Su, W., Liu, Y., Hu, B., Pan, L., Lu, W., … Li, R. W. (2012). Observation of conductance quantization in oxide-based resistive switching memory. Advanced Materials, 24(29), 3941–3946. DOI: 10.1002/adma.201201506

[Zhu2012b] W., Chen, T. P., Yang, M., Liu, Y., & Fung, S. (2012). Resistive switching behavior of partially anodized aluminum thin film at elevated temperatures. *IEEE Transactions on Electron Devices*, *59*(9), 2363–2367. DOI: 10.1109/TED.2012.2205692

[Zhuge2010] Zhuge, F., Dai, W., He, C. L., Wang, A. Y., Liu, Y. W., Li, M., … Li, R. W. (2010). Nonvolatile resistive switching memory based on amorphous carbon. *Applied Physics Letters*, *96*(16). DOI: 10.1063/1.3406121

[Zhuge2011] Zhuge, F., Peng, S., He, C., Zhu, X., Chen, X., Liu, Y., & Li, R.-W. (2011). Improvement of resistive switching in Cu/ZnO/Pt sandwiches by weakening the randomicity of the formation/rupture of Cu filaments. *Nanotechnology*, *22*(27), 275204. DOI:10.1088/0957-4484/22/27/275204